

Journal of
Geophysical
Research

VOLUME 66

MARCH 1961

NUMBER 3

THE SCIENTIFIC PUBLICATION
OF THE AMERICAN GEOPHYSICAL UNION

Journal of Geophysical Research

An International Scientific Publication

OFFICERS OF THE UNION

LLOYD V. BERKNER, *President*
THOMAS F. MALONE, *Vice President*
A. NELSON SAYRE, *General Secretary*
WALDO E. SMITH, *Executive Secretary*

OFFICERS OF THE SECTIONS

Geodesy

CHARLES PIERCE, *President*
FLOYD W. HOUGH, *Vice President*
BUFORD K. MEADE, *Secretary*

Seismology

LEONARD M. MURPHY, *President*
JAMES A. PEOPLES, JR., *Vice President*
BENJAMIN F. HOWELL, JR., *Secretary*

Meteorology

THOMAS F. MALONE, *President*
GORDON E. DUNN, *Vice President*
WOODBOW C. JACOBS, *Secretary*

Geomagnetism and Aeronomy

L. R. ALLDREDGE, *President*
C. T. ELVEY, *Vice President*
J. HUGH NELSON, *Secretary*

Oceanography

WALTER H. MUNK, *President*
DONALD W. PRITCHARD, *Vice President*
EUGENE C. LAFOND, *Secretary*

Volcanology, Geochemistry, and Petrology

ALFRED O. C. NIER, *President*
FRANCIS J. TURNER, *Vice President*
IRVING FRIEDMAN, *Secretary*

Hydrology

WALTER B. LANGBEIN, *President*
WILLIAM C. ACKERMANN, *Vice President*
CHARLES C. McDONALD, *Secretary*

Technophysics

PATRICK M. HURLEY, *President*
LOUIS B. SLICHTER, *Vice President*
H. RICHARD GAULT, *Secretary*

BOARD OF EDITORS

Editors: PHILIP H. ABELSON and J. A. PEOPLES, JR.

ASSOCIATE EDITORS

1959-1961

HENRI BADER	T. NAGATA
K. E. BULLEN	FRANK PRESS
CONRAD P. MOOK	A. NELSON SAYRE
WALTER H. MUNK	MERLE A. TUVE
JAMES A. VAN ALLEN	

1960-1962

JULIUS BARTELS	L. A. MANNING
V. V. BELOUSOV	TOR J. NORDENSON
E. G. BOWEN	E. N. PARKER
JOHN E. CHAPPELEAR	GEORGE P. RIGSBY
G. D. GARLAND	WALTER O. ROBERTS
GORDON J. F. MACDONALD	C. N. TOUTART
JAMES R. WAIT	

1961-1963

FRANKLIN I. BADGLEY	ROBERT O. REID
HENRY G. BOOKER	BRUNO ROSSI
JOSEPH W. CHAMBERLAIN	GEORGE H. SUTTON
HERBERT FRIEDMAN	DAVID K. TODD
MARK F. MEIER	VICTOR VACQUIER
ARTHUR H. WAYNICK	

The Editors of the *Journal of Geophysical Research* welcome original scientific contributions on the physics of the earth and its environment.

Manuscripts should be submitted in triplicate to J. A. Peoples, Jr., Department of Geology, University of Kansas, Lawrence, Kansas. Authors' institutions, if in the United States or Canada, are requested to pay a publication charge of \$25 per page, which, if honored, entitles them to 100 free reprints.

Subscriptions to the *Journal of Geophysical Research* and *Transactions*, AGU are included in membership dues.

Non-member subscriptions, *Journal of Geophysical Research*.. \$30 for back Volume of 1959, \$42 for back Volume of 1960, \$4 for this issue; \$20 for the calendar year 1961.

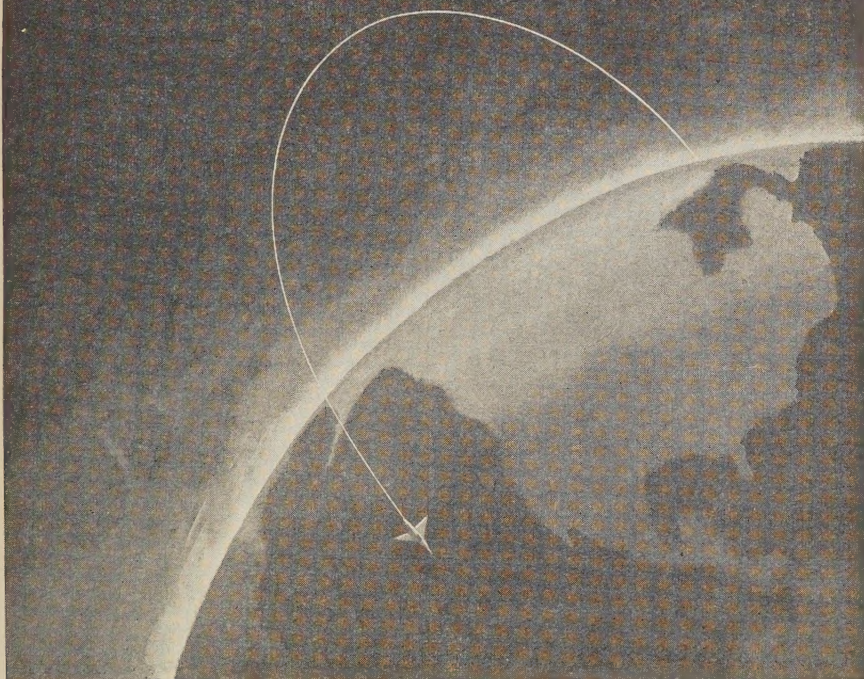
Non-member subscriptions, *Transactions*, AGU.... \$4 per calendar year, \$1.25 per copy. Subscriptions, renewals, and orders for back numbers should be addressed to American Geophysical Union, 1515 Massachusetts Ave., Northwest, Washington 5, D. C. Suggestions to authors are available on request.

Advertising Representative: Howland and Howland, Inc., 230 Park Ave., New York 17, N. Y.

Beginning with the January 1959 issue (Vol. 64, No. 1) the *Journal of Geophysical Research* is published monthly by the American Geophysical Union, the U. S. National Committee of the International Union of Geodesy and Geophysics organized under the National Academy of Sciences-National Research Council as the U. S. national adhering body. Publication of this journal is supported by the National Science Foundation and the Carnegie Institution of Washington. The new monthly combines the type of scientific material formerly published in the bi-monthly *Transactions*, *American Geophysical Union*, and the quarterly *Journal of Geophysical Research*. The *Transactions*, *American Geophysical Union* will continue as a quarterly publication for Union business and items of interest to members of the Union.

Published monthly by the American Geophysical Union from 1407 Sherwood Avenue, Richmond, Virginia. Second class postage paid at Richmond, Virginia.

We can now measure gravity from the air



Another achievement in gravity measurement from LaCoste & Romberg

Now for the first time, gravity surveys of inaccessible areas can be made from the air, using a LaCoste & Romberg airborne gravity meter. This new meter requires no gyroscopic stabilization platform. Its accuracy is better than 10 milligals.

Commercial airborne surveys are now available from Fairchild LaCoste Gravity Surveys, Inc.

LaCoste & Romberg 6606 NO. LAMAR AUSTIN, TEXAS

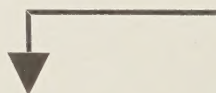
Manufacturers of airborne, submarine, shipborne and surface gravity meters for both exploration and geodetic surveys

Please mention JOURNAL OF GEOPHYSICAL RESEARCH, when writing to advertisers



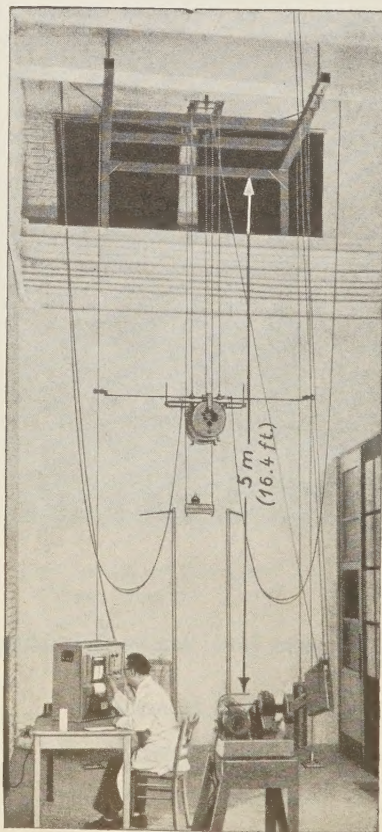
ASKANIA SEA GRAVIMETER Gss 2 AFTER GRAF

Considerably improved version

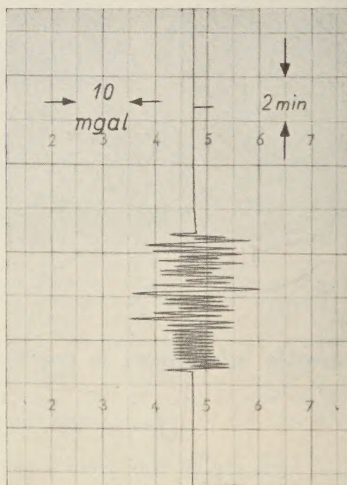


tested at accelerations up to
 $\pm 100,000$ mgals
(periods of 6 to 10 seconds)

Example of recording:
irregular accelerations with
peaks up to 200,000 mgals



The new 5-meter Sine Lift in the laboratory
of the Askania-Werke



Write for detailed information
also on our Land Gravimeters Gs
11 / Gs 12, and Earth Tide Re-
cording Gravimeters

Askania-Werke
Division of Continental Elektroindustrie A. G.
U. S. BRANCH
4913 Cordell Avenue Bethesda 14, Maryland

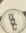


UNUSUAL AS SNOW IN HOUSTON

General Geophysical's Laboratory has the unusual facilities and know-how to custom-build equipment to meet your special requirements. Through research we continually develop, design and manufacture a complete range of unusual seismic instruments and other equipment necessary for geophysical work.

- We can quickly produce specially designed or modified instruments and equipment to fit the special needs of your job, and to fit the geographic and geological characteristics of the area to be worked.

Find out for yourself the reasons behind General's reputation for success in the unusual. Call General today . . .

General 
GEOPHYSICAL COMPANY
 Houston Club Bldg. • Houston, Texas

Paris, France
 Edmonton, Alberta
 Nassau, Bahamas
 Tripoli, Libya

When your contract is with General, the percentage for successful exploration is in your favor!

Please mention JOURNAL OF GEOPHYSICAL RESEARCH, when writing to advertisers

PORTABLE, ACCURATE, EASY TO OPERATE Sprengnether's Blast and Vibration Seismograph

Ideal for recording all types of vibrations caused by blasting, pile driving, heavy industrial machinery and other sources of strong motion vibrations.

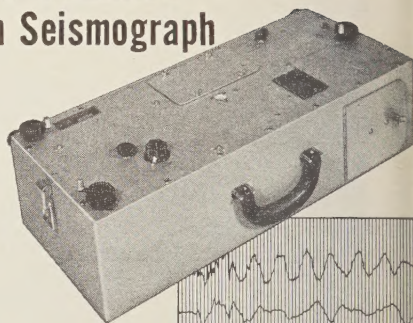
Portability (38 lbs. — 25 x 10 x 8 in.) Unit is self contained and free from external power source.

Extremely Accurate To guard against error, each instrument is tested and calibration data furnished. Frequency response, 3 to 200 cycles per second. Timing lines are across record at intervals of 0.02 seconds with accuracy of 0.1%.

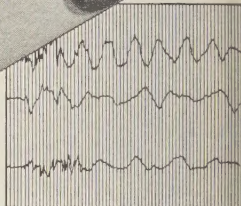
Easy to Operate: All controls are easily accessible. Instrument can be set up, leveled and made ready to operate within minutes.

Seismometer System: A mechanical, optical seismometer employing three independent pendulum systems with magnetic damping. System is contained within unit, hence, no need for external geophones.

Recording System: Photographic recording of all three components appearing on 2¾ inch wide paper. Cartridge type cameras are replaceable and can be pre-loaded to facilitate in the field camera replacement.



Write today for
complete
information.



OTHER SPECIFICATIONS

Natural Period (All Components)..... 0.75 sec

Damping (Fraction of Critical)..... .55

Static Magnification..... *

*May be specified by purchaser from 50 to 200.
Two ranges in one instrument available.

Internationally Known Mfrs. of Seismological, Geophysical Instruments.

W.F. SPRENGNETHER INSTRUMENT CO., INC.
4567 SWAN AVENUE • ST. LOUIS 10, MO.

GEODESY AND CARTOGRAPHY, 1959

(Geodezia i Kartografiya)

The leading monthly journal of Geodesy and Cartography in the USSR is being translated and published in an English edition, *for the year 1959*, by the American Geophysical Union, aided by a grant from the National Science Foundation.

Subscription price, \$20.00 for the volume of 12 numbers

Send subscription requests to

AMERICAN GEOPHYSICAL UNION

1515 Massachusetts Avenue, N.W.

Washington 5, D. C., U.S.A.

Other publications of the AGU include

- JOURNAL OF GEOPHYSICAL RESEARCH (monthly), 4800 pages anticipated for 1961, subscription \$30.00
- TRANSACTIONS (quarterly), \$4.00 per calendar year
- GEOPHYSICAL MONOGRAPH SERIES (occasional volumes), No. 5 (issued in 1960)
Physics of Precipitation (proceedings of the Cloud Physics Conference, Woods Hole, Massachusetts, June 3-5, 1959), 435 pp., \$12.50
- IZVESTIYA, Academy of Sciences, USSR, Geophysics series, English edition (monthly), \$25.00 per calendar year, available for 1957, 1958, 1959, and 1960

Please mention JOURNAL OF GEOPHYSICAL RESEARCH, when writing to advertisers

★ Space Science Resident Research Appointments ★

CALIFORNIA INSTITUTE OF TECHNOLOGY

The Jet Propulsion Laboratory of the California Institute of Technology is accepting applications for resident research appointments in the space sciences. These appointments are open to U.S. citizens and foreign nationals. Security clearance is not required. Applicants must have training equivalent to that represented by a doctorate degree and must have demonstrated superior ability for creative research.

JPL has the responsibility of executing the lunar, planetary, and interplanetary space exploration programs for the National Aeronautics and Space Administration, and is supporting research activities related to these programs.

The stipend for research appointments to highly qualified scientific personnel starts at \$10,000 per annum. For a foreign award, the basis would be equivalent to the salary of the researcher's American counterpart.

An appropriate travel grant will be provided.

Applications will be accepted for positions in the following areas of research and development:

Instrumentation...

design, development, and preparation of scientific instruments for space research; research on and development of concepts and techniques applicable to space research.

Field and Particle Measurements...

gravitational, magnetic, and electric fields; ionospheres of the earth and other planets; energetic particles; micrometeorites.

Astronomy...

development of new astronomical instruments for use on space probes; cosmology; celestial mechanics.

Exobiology...

nature of extraterrestrial life forms; techniques of sterilization and decontamination of space probes.

Solar Physics...

solar-terrestrial relationships; measurements in the ultra-violet and x-ray regions of the spectrum; magnetohydrodynamics.

Geology, Geophysics and Geochemistry...

chemical and physical nature of lunar and planetary surface and subsurface material; study of lunar and planetary interiors.

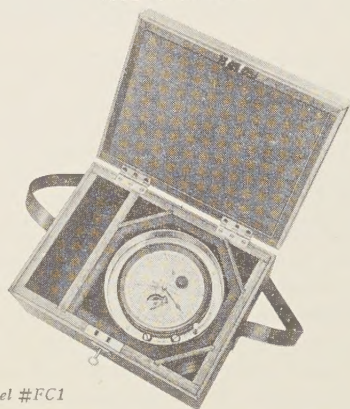
Planetary Atmospheres...

pressure, temperature, density, and composition of the atmosphere of the planets and the moon; the study of meteors and comets.

Theoretical and experimental scientists may obtain further information and application forms by addressing requests to...

Professor W. H. PICKERING, Director
JET PROPULSION LABORATORY
California Institute of Technology
4800 OAK GROVE DRIVE • PASADENA • CALIFORNIA

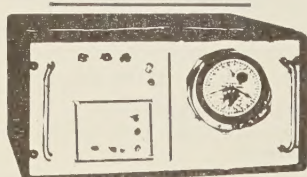
Reliable because it is
Mechanical



Model #FC1

FIELD CHRONOMETER—PROGRAMMER

- Provides Chronometer time and any desired sequence of programmed time marks in hours, minutes and seconds
- Provides stable 60 cycle for precision field recording or control when used with (optional) synchronous inverter.
- Winding, setting, stop-start and blocking for shipment is easily accessible from the top of the Field Chronometer. (Optional remote control stop-start).
- The Field Chronometer Programmer's most unique characteristic is that it is entirely mechanical which provides the most reliable operation and long life service.
- Shock-proof carry case suitable for use alone or for inclusion with associated equipment.



Model
#AVP1

AUTOMATIC VERTICAL FIELD CHRONOMETER PROGRAMMER

- Vertical Face for shelf or rack mounting
- Automatic (battery) with 6 hour mechanical reserve; and mechanical wind
- Provides any programmed time marks to the absolute accuracy of the Chronometer
- Remote controlled stop-start
- Unattended operation capability for 6 months or 1 year
- Stable sixty cycle for precision field recording or control

Dear Ad reader: You are cordially invited to the Waldorf-Astoria, at our suite to meet our people, talk shop, partake and view a display including Seismometer, Timing System, Blastorder, Helicorder, Data Transmission Equipment, Data Tape Recorder, Instantaneous Film Processor and Associated equipment.

Please fill out and mail coupon below
SUITE 1315

M. LOW, Inc.
44 Fulton St. New York 38, N. Y.
COrtlandt 7-5480

To: **M. LOW, Inc.** 44 Fulton St. New York 38, N. Y.
COrtlandt 7-5480 Cable: EMLOWINK

<input type="checkbox"/> Send me Literature	20 March	21 March	22 March	23 March
<input type="checkbox"/> I can attend	Mon	Tues	Wed	Thurs
<input type="checkbox"/> I might attend	<input type="checkbox"/>	<input type="checkbox"/>	<input type="checkbox"/>	<input type="checkbox"/>

Name _____ please print

Position _____

Company Address _____

Telephone _____

ARE YOU A MEMBER of AGU?

If you are a reader or user of either of the publications noted below, you should look into this matter.

Members regularly receive
the monthly

**Journal of
Geophysical Research**

the quarterly

**Transactions
American Geophysical Union**

Members are entitled to special discounts on other publications of AGU such as

- **Geophysical Monograph Series** (Nos. 1 to 5 available)
- **Izvestiya of the Academy of Sciences, USSR; Geophysics Series** for the years 1957, 1958, 1959, and 1960
- **Geodesy and Cartography, USSR, 1959**

- Annual meeting in Washington in late April or early May each year
- Regional meeting in the Pacific Northwest in autumn
- Regional meeting in the Pacific Southwest in winter
- National Western Meeting, December 1961

For application forms and other information regarding membership, meetings, and other matters, write to

AMERICAN GEOPHYSICAL UNION
1515 Massachusetts Ave., N.W.
Washington 5, D. C.

(An application form is also inserted in the closing pages of this issue.)

The first six years of Space Technology Leadership

Since 1954, when the Air Force ballistic missile program was accorded top national priority, Space Technology Laboratories has been engaged in virtually every major phase of research, development, testing and technical management of missile and space systems • STL's contributions have hastened the day of operational capability for Air Force ballistic missiles, and have been applied as well in satellite projects and space probes • Today, as STL's activities expand in significance and scope, STL offers exceptional opportunity to the outstanding scientist and engineer whose talents and training will add to, and benefit from, the accumulated experience that has enabled STL to conceive and accomplish major advances in the state-of-the-art • STL's creative flexibility, anticipating and responding to the demands of space progress, ranges in application from abstract analysis to complex hardware fabrication for military and civilian space projects • STL invites scientists and engineers to consider career opportunities in the atmosphere of Space Technology Leadership. Resumes and inquiries will receive meticulous attention.

SPACE TECHNOLOGY LABORATORIES, INC.

a subsidiary of Thompson Ramo Wooldridge Inc.

P. O. BOX 95005JK LOS ANGELES 45, CALIFORNIA

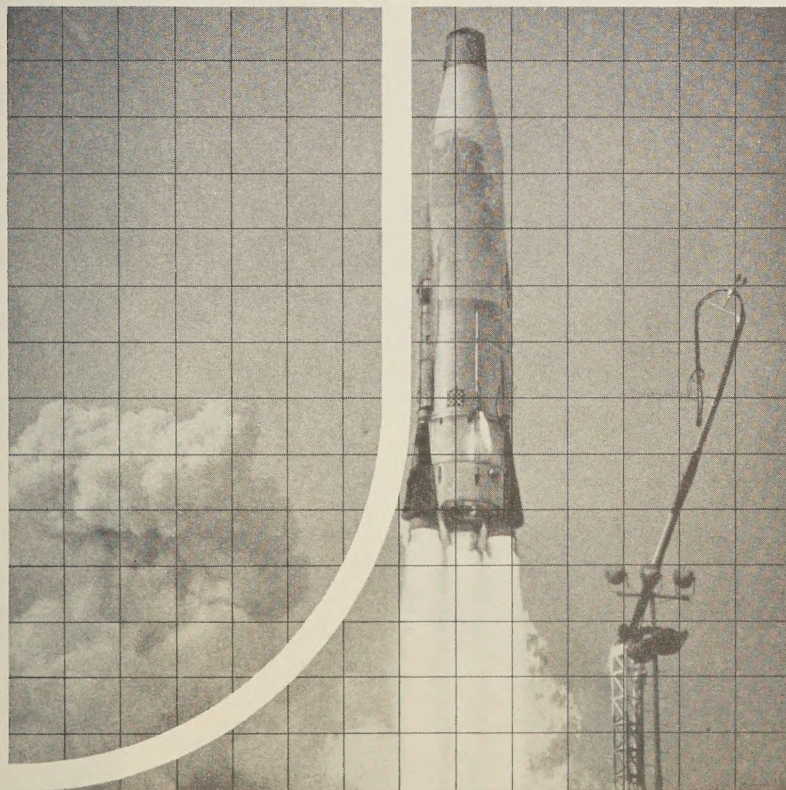
El Segundo • Santa Maria

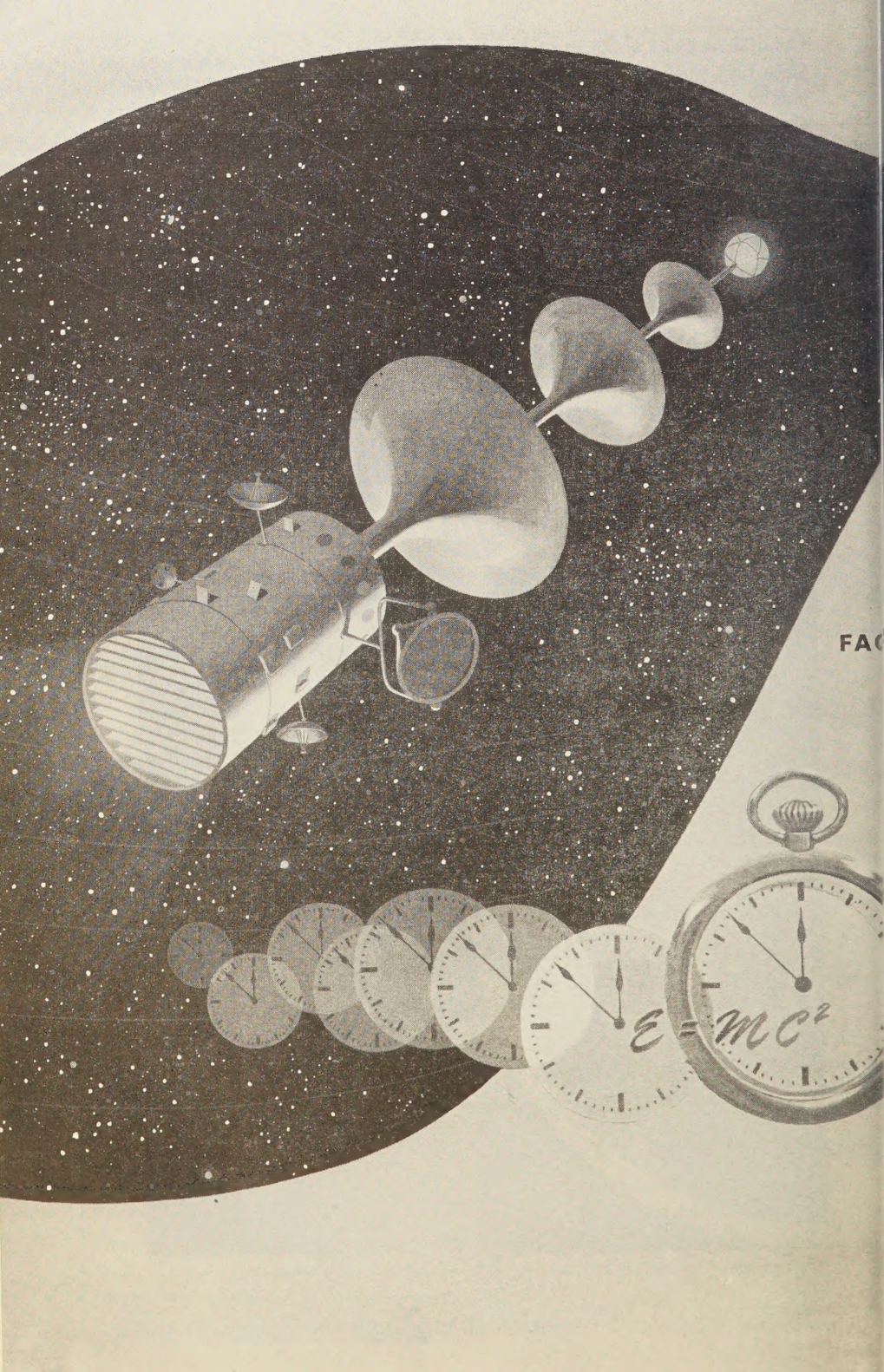
Edwards Rocket Base • Canoga Park



Cape Canaveral • Hawaii

Manchester, England • Singapore





FAC



FOURTH DIMENSION IN PROPULSION DEVELOPMENT

Whether the universe has a "saddle shape," or any shape at all, is a matter of interesting conjecture. The matter of space travel, however, is the subject of intense experimentation. A nuclear/thermionic/ionic propulsion system, currently being studied at Lockheed Missiles and Space Division, might well become the power source for space vehicles.

Its design incorporates a nuclear reactor only one foot in diameter, generating heat at a temperature of 1850°K . This is transmitted to banks of thermionic generators, converting the heat directly into electrical energy for the ion beam motor which uses cesium vapor as a fuel. The entire system is designed without any moving parts, minimizing the possibility of failure.

Lockheed's investigation of propulsion covers a number of potential systems. They include: plasma, ionic, nuclear, unique concepts in chemical systems involving high-energy solid and liquid propellents, combined solid-liquid chemical systems. The fundamentals of magnetohydrodynamics as they might eventually apply to propulsion systems, are also being examined. Just as thoroughly, Lockheed probes all missile and space disciplines in depth. The extensive facilities of the research and development laboratories—together with the opportunity of working with men who are acknowledged leaders in their fields—make association with Lockheed truly rewarding and satisfying.

Lockheed Missiles and Space Division in Sunnyvale and Palo Alto, on the beautiful San Francisco Peninsula, is an exciting and challenging place to work. For further information, write Research and Development Staff, Department M-24E, 962 West El Camino Real, Sunnyvale, California. U.S. citizenship or existing Department of Defense industrial security clearance required.

Lockheed / MISSILES AND SPACE DIVISION

Systems Manager for the Navy POLARIS FBM and the Air Force AGENA Satellite in the DISCOVERER and MIDAS Programs

Journal of Geophysical Research

BACK ISSUES AVAILABLE

Volume 64, 1959 **Total 2488 pages**

Complete Volume	\$30.00
January, 132 pp.	\$2.00
February, 138 pp.	\$2.00
March, 112 pp.	\$2.00
April, 106 pp.	\$2.00
May, 98 pp.	\$2.00
June, 110 pp.	\$2.00
July, 168 pp.	\$2.00
August, 268 pp.	\$4.00
September, 230 pp.	\$3.00
October, 284 pp.	\$4.00
November, 390 pp.	\$5.00
December, 452 pp.	\$6.00

Volume 65, 1960 **Total 4248 pages**

Complete Volume	\$42.00
January, 384 pp.	\$5.00
February, 414 pp.	\$5.00
March, 284 pp.	\$4.00
April, 248 pp.	\$4.00
May, 314 pp.	\$4.00
June, 220 pp.	\$4.00
July, 348 pp.	\$4.00
August, 350 pp.	\$4.00
September, 462 pp.	\$6.00
October, 490 pp.	\$6.00
November, 344 pp.	\$4.00
December, 390 pp.	\$5.00

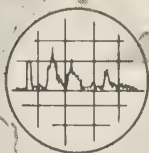
SYMPOSIA REPRINTED from JGR

International Symposium on Electronic Distance-Measuring Techniques (144-page Symposium reprinted from the February 1960 issue)	\$3.50
Symposium on Sferics and Thunderstorm Electricity (102-page Symposium reprinted from the July 1960 issue)	\$3.50
Symposium on the Exosphere and Upper <i>F</i> Region (74-page Symposium reprinted from the September 1960 issue)	\$2.50
Scientific Effects of Artificially Introduced Radiations at High Altitudes (74-page Symposium reprinted from the August 1959 issue)	\$1.50
International Symposium on Fluid Mechanics in the Ionosphere (202-page Symposium reprinted from the December 1959 issue)	\$4.50

AMERICAN GEOPHYSICAL UNION

1515 Massachusetts Avenue, N.W., Washington 5, D. C.

To obtain back issues for 1958 and earlier years, write to
Walter J. Johnson, Inc., 111 Fifth Avenue, New York 3, New York.



IONOSPHERIC PROPAGATION AND HF COMMUNICATIONS

If you have the background, the imagination and the desire to contribute to important programs in these fields, you are invited to join a carefully selected team of outstanding scientists and engineers now contributing significantly to current knowledge through advanced research.

Our present needs are for:

SENIOR IONOSPHERIC PHYSICISTS

Ph.D. preferred, with several years' experience in the study of Ionospheric phenomena. Should be familiar with present knowledge of upper atmosphere physics and possess an understanding of current programs using rockets and satellites for studies in F-region and beyond. Qualified individuals with supervisory abilities will have an exceptional opportunity to assume project leadership duties on HF projects already under way involving F-layer propagation studies backed by a substantial experimental program.

SENIOR DEVELOPMENT PHYSICISTS

Advanced degree in Physics or E.E. preferred. Must be familiar with latest techniques in the design of advanced HF receivers and transmitters and possess working knowledge of modern HF networks employing ferrites and metallic tape cores. Strong theoretical background in modern linear circuit theory desired. Will carry out laboratory development and implementation of new HF communications systems.

SENIOR ELECTRONIC ENGINEERS

Advanced degree in E.E. preferred. Must be familiar with conventional pulse circuit designs and applications. Technical background should include substantial experience in data process and data recovery systems using both analog and digital techniques. Knowledge of principles and application of modern information theory including correlation techniques helpful. Will be responsible for the design of sub-systems.

These programs are being conducted at our ELECTRO-PHYSICS LABORATORIES in the suburban Washington, D.C. area, ideally located from the viewpoint of advanced study which may be conducted at one of several nearby universities; for readily available housing in pleasant residential neighborhoods; and for the general amenities of living offered by this important Metropolitan center.

*For a prompt reply to your inquiry,
please forward resume
in confidence to:*

W. T. WHELAN
Director of Research
& Development

ACF ELECTRONICS DIVISION
ACF INDUSTRIES
RIVERDALE, MARYLAND

During the
IRE SHOW
visit the
ACF Suite
in the
convention hotel
MARCH 20-23

International Geophysics Series

Edited by J. VAN MIEGHEM, Royal Belgian Meteorological Institute

Physics of the Aurora and Airglow

By JOSEPH W. CHAMBERLAIN,

Yerkes Observatory, University of Chicago, Williams Bay, Wisconsin

Spring 1961, about 700 pp., illus., \$16.50

This monograph discusses completely the physics of the aurora and airglow, emphasizing those subjects not covered extensively elsewhere in the literature. The bibliography of more than 1500 entries is complete to January 1960, and contains selected references to the literature published later. The book requires only a background in classical and atomic physics. It will be of great interest to all scientists active in the field, and will be suitable as a textbook in graduate courses, for which both practical and theoretical problems are given at the ends of the chapters.

Radiation in Spectral Lines

Scattering of Radiation in Finite Atmospheres
Magnetic Fields, Charged Particles, and the
Upper Atmosphere

Occurrence of Aurorae in Space and Time

Auroral Spectroscopy and Photometry
The Radio-Aurora

Physical Processes in the Auroral Atmosphere

Auroral Particles in Space

The Airglow Spectrum

Analysis of Twilight Observations for
Emission Heights

Theory of the Twilight and Day Airglow

Spectral Photometry of the Nightglow

Excitation of the Nightglow

APPENDICES:

A Table of Constants

The Rayleigh:

A Photometric Unit for the Aurora and
Airglow

A Short List of Airglow-Aurora Observing
Stations

Temperature, Density, and Composition of
the Upper Atmosphere

The Ionosphere

Forbidden Atomic Oxygen and Nitrogen Lines

Glossary of Symbols

A List of Books and Review Articles on the
Aurora and Airglow

BIBLIOGRAPHY

SUBJECT INDEX

Physics of the Earth's Interior

By BENO GUTENBERG

Review:

1959, 240 pp., illus., \$8.50

"This volume, a well written, clear, concise, and authoritative summary of present knowledge and opinion on the nature of the earth's interior, is a work that every earth scientist will want to read cover to cover. It is the eloquent swan song of an eminent scientist who, over the past 50 years, contributed substantially to every phase of the 'physics of the earth's interior.'"

"We are, indeed, fortunate to have, in this book, his final summing up of a lifetime of research."

—*Science*

Forthcoming Titles in the Series:

The Upper Atmosphere, By RICHARD A. CRAIG, *The Florida State University*

Radioastronomy, By R. COUTREZ, *Observatoire Royal de Belgique*

Thermodynamics of Clouds, By L. DUFOUR, *Royal Belgian Meteorological Institute*
and R. DEFAY, *University of Bruxelles*

Detailed literature available upon request



ACADEMIC PRESS

111 Fifth Avenue, New York 3

New York and London

17 Old Queen Street, London, S.W. 1

Journal of GEOPHYSICAL RESEARCH

VOLUME 66

MARCH 1961

No. 3

Cosmic-Ray Neutron Demography

W. N. HESS, E. H. CANFIELD, AND R. E. LINGENFELTER

*Lawrence Radiation Laboratory, University of California
Livermore, California*

Abstract. The equilibrium spatial and energy distribution is calculated for neutrons made in the earth's atmosphere by cosmic rays. The neutron current leaking into space is found, and the density of neutron decays in the vicinity of the earth is computed for a future determination of importance as a source for the Van Allen belts. The spectrum and the leakage current below 10 Mev are determined from multigroup diffusion theory; the leakage above 10 Mev (<1 per cent of total) is approximated from geometrical arguments. An integrated source over each square centimeter of earth surface (at geomagnetic latitude 44°N) of 6.2 neutrons/sec (1.2 from 'knock-on' processes above 10 Mev and 5.0 from evaporation processes below 10 Mev) gives an equilibrium spectrum in agreement with the ± 25 per cent accuracy of measured values. This source corresponds to a global average of 4.6 neutrons/cm²/sec, of which 0.8 leaks into space, 2.9 form C^{14} , and 0.9 is absorbed in other processes. Gravitationally trapped neutrons (<0.66 ev) amount to less than 1 per cent of the total leakage, but they contribute substantially to the decay density near the earth (e.g., 40 per cent of total decays at $\frac{1}{2}$ earth radius).

INTRODUCTION

We wish to discuss here the birth, life history, and fate of cosmic-ray neutrons produced in the atmosphere of the earth by the interactions of primary cosmic rays with nitrogen and oxygen (few neutrons reach the earth from far away because of their 12-minute half-life). Special attention is paid to the neutrons that escape from the top of the atmosphere, because they are one of the sources of the trapped particles in the Van Allen radiation belts.

Cosmic-ray neutrons are produced by two kinds of reactions. Fast neutrons made by direct interactions of high-energy cosmic rays are called knock-on neutrons and have energies from about 1 Mev to 1 bev or more. A larger source of neutrons is the evaporation process. Neutron emission is the most probable de-excitation reaction when nitrogen and oxygen are excited to energies above about 8 Mev by cosmic rays. These evaporation neutrons have a roughly Maxwellian energy distribution peaked at about 1 Mev.

These neutron sources, together with the losses from leakage from the atmosphere and the

absorptions during thermalization, result in an equilibrium spectrum. Below 10 Mev this spectrum can be computed rather precisely by multigroup diffusion theory, but the anisotropy of the higher-energy neutrons will not permit such an analysis. However, from an analogy to high-energy proton data we can estimate the percentage of knock-on neutrons that are degraded in energy to less than 10 Mev. These are then added to the evaporation source for the diffusion analysis. The relative strength of the knock-on and evaporation sources (about 1 : 4) was determined from experimental measurements of the equilibrium spectrum.

The diffusion calculations also give the leakage current as a function of energy and angle. The trajectories of these exit neutrons in the gravitational field of the earth are found, and the density of decays is given for different altitudes and magnetic latitudes.

EQUILIBRIUM SPECTRUM IN THE ATMOSPHERE

Recent experiments by Hess, Patterson, Wallace, and Chupp [1959] have measured the absolute neutron-energy spectrum from sea level to

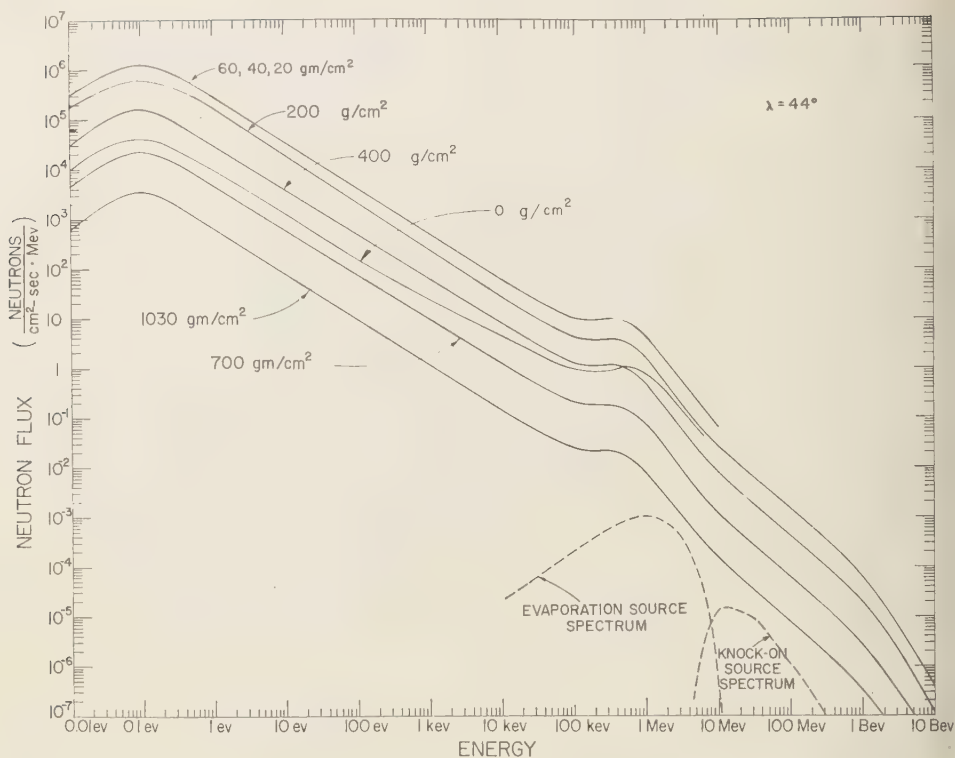


Fig. 1. The equilibrium neutron flux versus energy at different depths in the atmosphere for geomagnetic latitude 44° . The energy spectra for 200 to 1030 g/cm^2 are experimental values [Hess, Patterson, Wallace, and Chupp, 1959]. For depths less than 200 g/cm^2 the spectra are calculated. The shapes of the two neutron source spectra are also shown. Above 500 Mev the curves are based on the work of Messel [1954]. See Figure 2 for the same data plotted vs. altitude.

within 200 g/cm^2 from the top of the atmosphere for energies ranging from thermal to 500 Mev. This measured spectrum, shown for altitudes $< 200 \text{ g}/\text{cm}^2$ in Figures 1 and 2, is an equilibrium spectrum; that is, the processes of production, slowing down, and absorption are in equilibrium. The bump seen at about 1 Mev is the softened peak of the evaporation-source spectrum. The thermalized neutrons are largely captured by an $\text{N}^{14}(n, p)\text{C}^{14}$ reaction. This strong capture probability shifts the peak of the thermal spectrum from the thermal energy of about 0.02 ev to about 0.1 ev.

The spectrum has been extended from 500 Mev to higher energies by using the work of Messel [1954] that shows that above about 500 Mev the energy spectrum of secondary particles (such as

neutrons) closely resembles the energy spectrum of the primary cosmic-ray protons.

Figure 1 also shows the assumed spectra of the knock-on and evaporation neutrons as well as the results of the calculations to be described.

The neutron equilibrium spectrum can be calculated for a given time-independent source of cosmic-ray neutrons. The spatial and energy dependence of this source must be chosen so that the equilibrium spectrum agrees with measured values. The exact solution involves solving the Boltzmann transport equation—a formidable task. For energies below 10 Mev, however, the atmosphere is a moderator admirably suited to treatment by diffusion theory, an approximation to transport theory which assumes that the neutron flux is not highly anisotropic. Since mos

the neutrons in the equilibrium spectrum have energies in this range, the treatment of neutrons at higher energies will be limited to estimates of their leakage and their contribution to the source below 10 Mev. Our calculations show that below about 1 Mev only the magnitude (but not the shape) of the spectrum is affected by the details of the high-energy spectrum.

Low-energy neutrons (<10 Mev). The steady-state diffusion equation for the scalar neutron flux $\phi(E, r)$ may be written

$$-\nabla \cdot D(E, r) \nabla \phi(E, r) + \Sigma(E, r) \phi(E, r) - \int_0^\infty dE' \Sigma(E' \rightarrow E, r) \phi(E', r) = S(E, r) \quad (1)$$

where

$$\phi(E, r) = n(E, r) v.$$

$n(E, r) dE$ = number of neutrons per cubic centimeter in the energy interval $E, E + dE$.

$\Sigma(E, r)$ = total macroscopic cross section.

$\Sigma(E' \rightarrow E, r)$ = macroscopic cross section for scattering from $dE' \rightarrow dE$.

$D(E, r)$ = diffusion coefficient = $1/[3\Sigma_{TR}(E, r)]$.

$\Sigma_{TR}(E, r)$ = macroscopic transport cross section.

$S(E, r)$ = neutron source = number of neutrons per cubic centimeter per second fed into the system.

Multiply by dE , and integrate from E_{i-1} to E_i to obtain the usual multigroup equation for neutrons in the i th energy group ($E_{i-1} < E < E_i$):

$$-\nabla \cdot D^i(r) \nabla \phi^i(r) + \sum_i (r) \phi^i(r) - (\text{Sum})_i \sum_{ij} (r) \phi^j(r) = S^i(r) \quad (2)$$

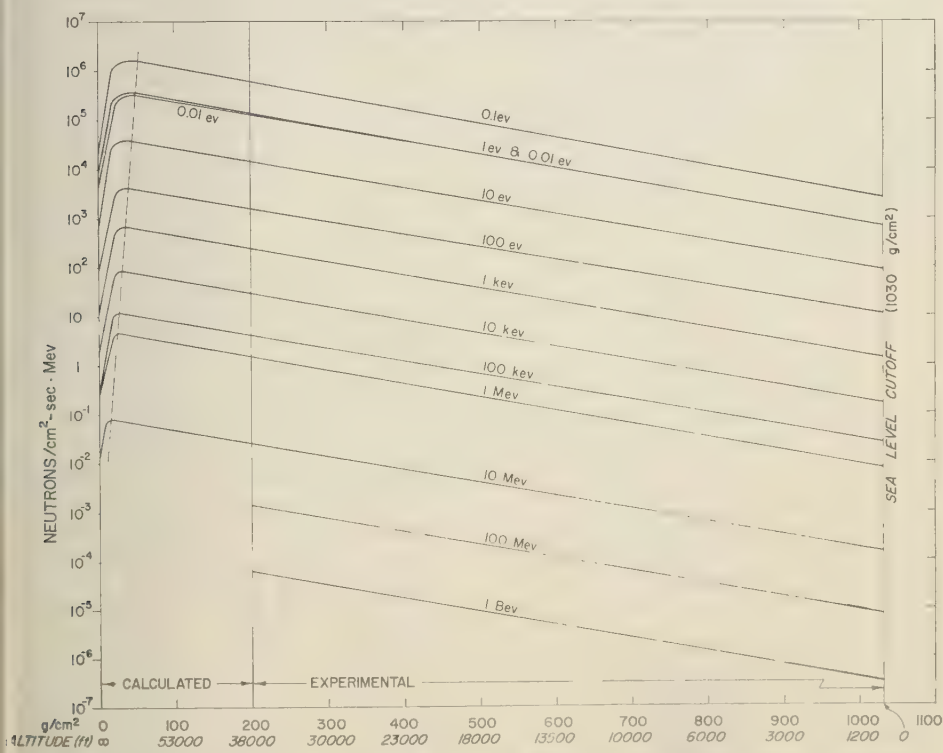


Fig. 2. The equilibrium neutron flux vs. altitude at different neutron energies for geomagnetic latitude 44° . The data for altitudes above the 200-g/cm² level are calculated; the rest are experimental (same data as Fig. 1).

where

$$\phi^i(r) = \int_{E_{i-1}}^{E_i} \phi(E, r) dE$$

= group scalar flux.

$$S^i(r) = \int_{E_{i-1}}^{E_i} S(E, r) dE$$

= group source.

$$D^i(r) = \frac{1}{\phi^i(r)} \int_{E_{i-1}}^{E_i} D(E, r) \phi(E, r) dE$$

= group diffusion coefficient.

$$\sum^i(r) = \frac{1}{\phi^i(r)} \int_{E_{i-1}}^{E_i} \sum(E, r) \phi(E, r) dE$$

= group total cross section.

$\Sigma^{ij}(r)$ = group cross section for scattering from j to i .

The atmosphere is a sufficiently thin layer on the earth's surface to be accurately represented as a slab, infinite in two directions. For calculational and interpretational convenience, it is advantageous to restate equation 2 in so-called mass units. If x is the mass of a column of air extending r cm above 1 cm^2 of earth, equation 2 can be expressed in the new variable x through $d/dr = (dx/dr)(d/dx)$:

$$-\frac{dx}{dr} \frac{d}{dx} D^i(r) \frac{dx}{dr} \frac{d}{dx} \phi^i(r) + \sum^i(r) \phi^i(r) - (\text{Sum})_i \sum^{ij}(r) \phi^j(r) = S^i(r) \quad (3)$$

Define $n(x) dx$ = number of neutrons between x and $x + dx$, and $S(x) dx$ = number of source neutrons per second introduced into dx . By definition,

$$\left. \begin{aligned} S(x) dx &= S(r) dr \\ n(x) dx &= n(r) dr \end{aligned} \right\} \quad (4)$$

Then

$$n(x) \frac{dx}{dt} = n(r) \frac{dr}{dt}$$

or

$$\phi(x) = \phi(r) \quad (5)$$

Furthermore,

$$\sum(r) \frac{dr}{dx} = \text{macroscopic cross section/gram} \quad (6)$$

Inserting (4), (5), and (6) into (3), we have

$$-\frac{d}{dx} D^i(x) \frac{d}{dx} \phi^i(x) + \sum^i(x) \phi^i(x) - (\text{Sum})_i \sum^{ij}(x) \phi^j(x) = S^i(x) \quad (7)$$

where all cross sections refer to a unit mass.

This formulation is equivalent to condensing the atmosphere to a uniform density of 1 g/cc . Then x is the unit of height in this atmosphere. In the calculations, 20 cm of water was inserted below the atmosphere to approximate the effect of the (very small) interaction between the neutrons and the earth's surface.

It should be noted that this constant-density atmosphere gives the same neutron flux (neutrons passing $1 \text{ cm}^2/\text{sec}$) as a diffuse atmosphere. However, the spatial contraction will reduce the actual number of neutrons above 1 cm^2 of earth at any one time because of the decreased slowing-down time. (Consider the opposite extreme, a highly diffuse atmosphere with the same number of neutrons per second introduced above each square centimeter. If the source is turned on, many neutrons enter the system before any collisions occur; yet eventually equilibrium is reached, and the resultant flux, which is what our counters measure, is dependent only on the source strength. The neutron is influenced only by the number of mean free paths of matter facing it.)

The atmosphere, 80 per cent nitrogen and 20 per cent oxygen, was treated as a uniform density slab. The temperature variation of the standard atmosphere with altitude [Shapiro, 1953] was approximated by dividing the atmosphere into four temperature zones:

- 280°K, 0–301 g above sea level.
- 260°K, 301–545 g above sea level.
- 234°K, 545–789 g above sea level.
- 219°K, 789–1033 g above sea level.

Zoom, a neutron-diffusion code [Stuart, Canfield, Dougherty, and Stone, 1958] developed for the IBM 704 at the University of California's Lawrence Radiation Laboratory (LRL) at Livermore, was used for solving the multigroup equations 7.

Cross sections are essentially those from BNL 325, weighted with the observed neutron spectrum. Transfer coefficients for scattering between energy groups are based on the assumption that the atmosphere is a Maxwell gas moderator that scatters isotropically in the center of mass. These coefficients were calculated with Sophist I, another IBM 704 code developed by LRL. Above 1 Mev, the effects of anisotropy in the elastic scattering were compensated for by corrections linear in the average value of the cosine of the scattering angle.

The diffusion coefficients are determined from

$$D = \sum_a / K^2$$

where K^2 is found from the one-group equation misprinted in *Glasstone and Edlund*, 1952]

$$\frac{\sum_s}{2K} \ln \left[\frac{\sum_s + K}{\sum_s - K} \right] = \frac{K^2 + 3 \sum_a \sum_s \bar{\mu}_0}{K^2 + 3 \sum_a \sum_s \bar{\mu}_0}$$

The symbols Σ , Σ_a , and Σ_s are, respectively, the total, absorption, and scattering cross section, and $\bar{\mu}_0$ is the average cosine of the scattering angle in the laboratory system. A correct multigroup treatment, including sources, might change these coefficients by several per cent.

The principal source used in the diffusion calculation was a neutron evaporation spectrum

$$N(E) dE \propto E e^{-E/\theta} dE \quad (8)$$

where $N(E)$ is the number of neutrons per second produced in the energy interval dE . The nuclear temperature $\theta = 1$ Mev was chosen to agree with the neutron spectrum arising from 190-Mev protons incident on carbon [Gross, 1956] and with the calculations of *LeCouteur* [1952]. To this was added a small contribution from the higher-energy knock-on source (to be discussed later).

Since the slowing-down length for neutrons in the atmosphere is small compared with 155 grams, the altitude dependence of the source was chosen to agree with the measured equilibrium spectrum value of $e^{-d/155}$, where d is the depth into the atmosphere in grams [Hess, Patterson, Wallace, and Chupp, 1959].

High-energy neutrons (>10 Mev). The anisotropy of the neutron flux above 10 Mev makes diffusion theory a poor approximation, so that it is difficult to determine an equilibrium flux throughout the atmosphere. But from simple

conservation calculations the percentage of these neutrons that become degraded in energy to less than 10 Mev can be estimated. These, then, may be added to the low-energy source function and included in the diffusion calculation.

Within an energy range ΔE the neutron sources (knock-on and scatter-down from higher energies) must balance the losses (leakage, absorption, and scatter-down). Neutron cross-section data for absorption and for elastic and inelastic scattering are available in the published literature for oxygen and nitrogen up to several hundred Mev. But the spectrum of the scattered neutrons must be inferred from proton data. Above 10 Mev the principal mechanism of neutron degradation is inelastic collisions. The spectra of neutrons resulting from inelastic reactions are assumed to be similar to those for protons. Figure 3 shows spectra from experiments performed on high-energy accelerators at energies of 14, 96, and 300 Mev averaged over angle of scattering [Smith, 1954; Strauch and Titus, 1956; Hess and Moyer, 1956]; they are the basis of the energy transfer probabilities used in the conservation calculation.

The characteristics of the low-energy neutron source (evaporation source) are well understood

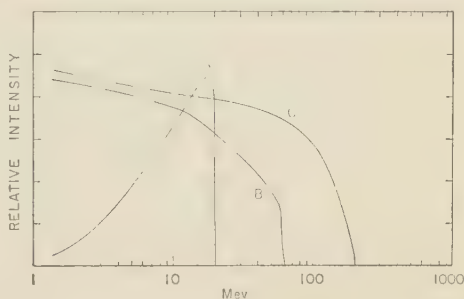


Fig. 3. Spectra of high-energy scattered neutrons used to calculate the equilibrium neutron-energy spectra. Curve A is from the work of Smith [1954] for 14-Mev neutrons on nitrogen (modified to represent 20-Mev neutrons). Curve B is from the work of Strauch and Titus [1956] for 96-Mev protons incident on carbon (modified to represent 60-Mev protons). Curve C is from the work of Hess and Moyer [1956] for 300-Mev protons on carbon (modified to represent 200-Mev protons). All spectra have been averaged over the angle of scattering. The scattering spectra shown in curves A, B, and C were assumed to be typical for neutrons in the energy ranges 10 to 31.6 Mev, 31.6 to 100 Mev, and 100 to 316 Mev, respectively.

theoretically and are experimentally verified, but there is no direct cosmic-ray information about the higher-energy neutron source spectrum. Neutron spectra have been measured by *Graves and Rosen* [1953], using 14-Mev neutrons bombarding various elements, and by *Gross* [1956], using 190-Mev protons bombarding various elements. These authors find that below 3 or 4 Mev the neutrons are clearly identified as evaporation neutrons but that above 4 Mev the yield of neutrons is higher than expected from evaporation, and that the neutrons come off preferentially forward. These higher-energy neutrons are made by direct interaction processes, and they are called knock-on neutrons. It is expected that high-energy knock-on neutrons and protons will be made with equal yields, although at low energies there are more neutrons because proton emission is suppressed by the Coulomb barrier.

Camerini, Fowler, Lock, and Muirhead [1950] measured the proton spectrum from cosmic rays bombarding emulsion nuclei. *Rossi* [1952] fitted these data above 50 Mev with

$$N_p(E) dE = k(E + 50)^{-2} dE$$

where E is in Mev. An equally good fit to the high-energy data, one that should be applicable to lower-energy neutrons as well, is

$$N(E) dE = kE^{-2} \exp(-160 E^{-2}) dE$$

where a Gamow barrier penetration factor has been added to suppress direct neutron emission at low energies. This is the knock-on neutron spectrum used in these calculations. Fortunately the information derived from this source is rather insensitive to the form of the spectrum.

The (small) probability of escape through the top of the atmosphere is approximated by an interpolation between the 3- to 10-Mev leakage (8 per cent) obtained from the diffusion calculations and an estimate (1 per cent) for the very-high-energy (bev range) exit current calculated from geometrical arguments later in this paper.

The result of the conservation calculation was that, of the knock-on neutrons, about 43 per cent are absorbed and 5 per cent leak out above 10 Mev; the other 52 per cent are degraded to less than 10 Mev (44 per cent between 10 and 3.16 Mev, 6 per cent between 3.16 and 1 Mev, 2 per cent below 1 Mev).

A ratio of evaporation to knock-on sources $E/K = 4.1$ was found necessary to give the

experimental ratio of fluxes in the knock-on region to the evaporation region. Then the source for the diffusion calculation is an evaporation spectrum (equation 8) of strength E , plus a contribution from the knock-on source of magnitude $(0.52) \times E/4.1$.

Results. Normalizing the calculated equilibrium flux to the measured equilibrium flux at $\lambda = 44^\circ$, we find that a total source strength, $S = K + E = 6.2$ neutrons/cm²/sec ($K = 1.2$, $E = 5.0$) gives an absolute equilibrium flux which agrees with the measured flux to well within the ± 25 per cent accuracy of the measurements, over eight orders of magnitude in energy range from 10 Mev to thermal. This agreement extends from sea level to within 200 g/cm² of the top of the atmosphere, the upper limit of the experimental data. The calculated spectrum from 200 g/cm², up is also shown in Figures 1 and 2. The spatial dependence to approximately 50 g/cm² is the same as the measured shape below 200 g/cm². The rapid drop-off at the top of the atmosphere is caused by the leakage.

TABLE 1

	Below 1 Mev	1 to 10 Mev	Above 10 Mev	Total
Captured to form C ¹⁴	3.86	0.11	0	3.97
Captured by other processes	0.18	0.49	0.53	1.20
Leak out of the atmosphere	0.62	0.35	0.06	1.03
Strike earth and are captured	<0.01
Total	4.66	0.95	0.59	6.20

Our calculations, which start with the neutron sources K and E , follow the neutrons as they slow down, are captured, or escape from the atmosphere. A summary of the fates of the neutrons is given in Table 1. The entries in the table are neutrons/cm²/sec for $\lambda = 44^\circ$.

These values are for $\lambda = 44^\circ$. To convert to a global average we multiply by 0.75 [*Anderson, 1953*], which gives a total global-average source $\bar{S} = 4.6$ neutrons/cm²/sec. This can be translated to the rate of capture in nitrogen to form C¹⁴ by multiplying by 3.97/6.2 (see Table 1),

which gives the global average C^{14} source, $\bar{Q} = 2.9$ neutrons/cm²/sec, with an accuracy of about ± 25 per cent. This figure of 2.9 is in reasonable agreement with the value of $\bar{Q} = 2.6$ given by Anderson [1953], which has a quoted error of about ± 15 per cent.

The total leakage, 1.03 neutrons/cm²/sec at 14° (Table 1), corresponds to a leakage of about 0.4 at the equator and about 1.8 at the pole. These are about 20 times the values obtained by Kellogg [1959]. Kellogg used the neutron spectrum of Bethe, Korff, and Placzek [1940], which is valid only below approximately 100 kev. Above 100 kev this spectrum greatly underestimates the flux, whereas our analysis indicates that about 90 per cent of the leakage neutrons have energies above this.

One result of this study is to show that the global average total-neutron-source strength $\bar{S} = 4.6$ is a fair amount larger than the C^{14} -production-source strength $\bar{Q} = 2.9$ neutron/cm²/sec. This is new information, but it in no way affects the C^{14} dating, because \bar{Q} is the source strength that should be used in calculating the production of C^{14} .

NEUTRONS IN SPACE

Angular distribution of neutron leakage (<10 Mev). Precise specification of the angular distribution of neutrons leaking out the top of the atmosphere depends on knowing the transport vector flux. Diffusion theory is an approximation to transport theory involving only the two leading terms in a spherical harmonic expansion of the vector flux. The usual diffusion boundary condition, that the boundary flux extrapolate to zero at a distance $0.71\lambda_{TR} = 2.13D$, is chosen so that the net leakage of neutrons is correct even though the angular distribution is no longer precise [Glasstone and Edlund, 1952, p. 403].

In the diffusion approximation the vector flux is given by

$$\begin{aligned} F(x, \mu) &= \sum_{l=0}^1 \frac{2l+1}{2} P_l(\mu) F_l(x) \\ &= \frac{1}{2} F_0(x) + \frac{3}{2} \mu F_1(x) \end{aligned}$$

where $F(x, \mu) d\mu$ is the number of neutrons per second leaving a unit sphere through a ring element of area $2\pi d\mu$ with direction cosines between μ and $\mu + d\mu$.

But

$$F_0(x) = \phi(x)$$

the neutron scalar flux, and

$$F_1(x) = J(x) = -D \frac{d}{dx} \phi(x)$$

the net neutron current density.

As was stated above, the diffusion boundary condition at the outside boundary (the top of the atmosphere) gives

$$\left. \frac{d\phi}{dx} \right|_{x=R} = \frac{\phi(R + 2.13D) - \phi(R)}{(R + 2.13D) - R} = -\frac{\phi(R)}{2.13D}$$

Therefore,

$$\begin{aligned} F(R, \mu) &= \frac{1}{2} \phi(R) + \frac{3}{2} \mu \frac{\phi(R)}{2.13} \\ &= \frac{1}{2} \phi(R) \left[1 + \frac{3\mu}{2.13} \right] \end{aligned}$$

The number of neutrons per cubic centimeter per second passing a unit area of boundary surface is

$$\frac{\mu}{2\pi} F(R, \mu) = \text{constant} \left(\mu + \frac{3\mu^2}{2.13} \right) = J(R, \mu)$$

where $\mu = \cos \theta$, and θ is the zenith angle. The angular distribution of leakage neutrons, $J(R, \mu)$, has been normalized to unity at $\theta = 0$ and plotted in Figure 4 along with the function μ^2 . The close agreement of these curves allows us to

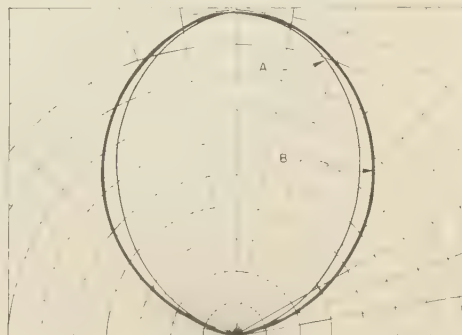


Fig. 4. Angular distribution of slow neutrons leaking out of the atmosphere of the earth is shown in curve B. A $\cos^2 \theta$ angular distribution, curve A, is shown for comparison. θ is the zenith angle.



Fig. 5. Production of very-high-energy neutrons by very-high-energy protons striking glancing blows on the atmosphere. The dotted line represents the angular distribution of the very-high-energy neutrons leaving a unit area at the top of the atmosphere.

assume for ease of calculation that the leakage is of the simpler form

$$J(R, \mu) = f(R)\mu^2$$

The normalizing constant $f(R)$ is chosen so that

$$\begin{aligned} J(R) &= -D \left. \frac{d\phi}{dx} \right|_{x=R} \\ &= \int_0^1 J(R, \mu) 2\pi d\mu = \frac{2\pi}{3} f(R) \end{aligned}$$

Hence,

$$\begin{aligned} J(R, \mu) &= \frac{3J(R)}{2\pi} \mu^2 \\ &= \text{neutrons/cm}^2/\text{sec/Mev/steradian emerging from the top of the atmosphere.} \end{aligned}$$

This formulation loses its usefulness above 10 Mev, where the anisotropy of the neutron knock-on source makes diffusion theory invalid.

Angular distribution of neutron leakage (> 10 Mev). The production angular distribution for high-energy knock-on neutrons is highly anisotropic. We can calculate the angular distribution of the very-high-energy leakage neutrons by geometric considerations. For very-high-energy neutrons the production angular distribution is very strongly peaked in the forward direction. The Brookhaven cosmotron's 2-bev protons make high-energy neutrons [Coor, Hill, Hornyak, Smith, and Snow, 1955] with a half-angle at half maximum of 6° . The half-angle of elastic scattering of neutrons on carbon (which is similar to scattering on air) for 5-bev neutrons is about 1° [Atkinson, Hess, Perez-Mendez, and Wallace, 1959]. Therefore, we can say that 10-bev neutrons will travel essentially in the direction of the incident nucleon. Because of this, only the very-high-energy neutrons produced by fast nucleons striking glancing blows on the atmosphere (Fig. 5) leak out of the atmosphere. Those with steeper angles are stopped by the denser atmosphere or the earth.

The angular distribution of high-energy neu-

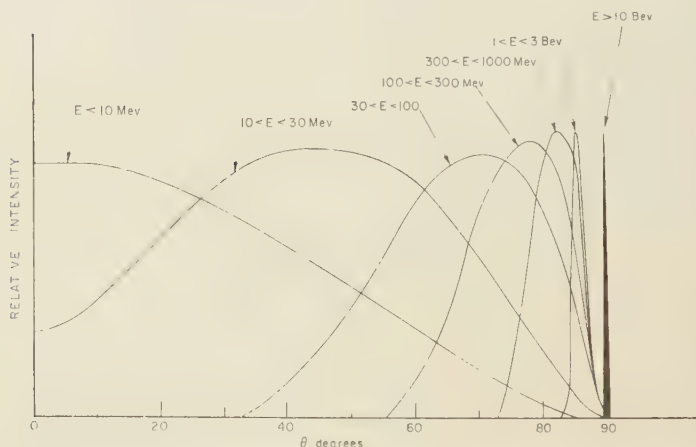


Fig. 6 Angular distributions of neutrons of different energies leaking out of the atmosphere of the earth. θ is the zenith angle.

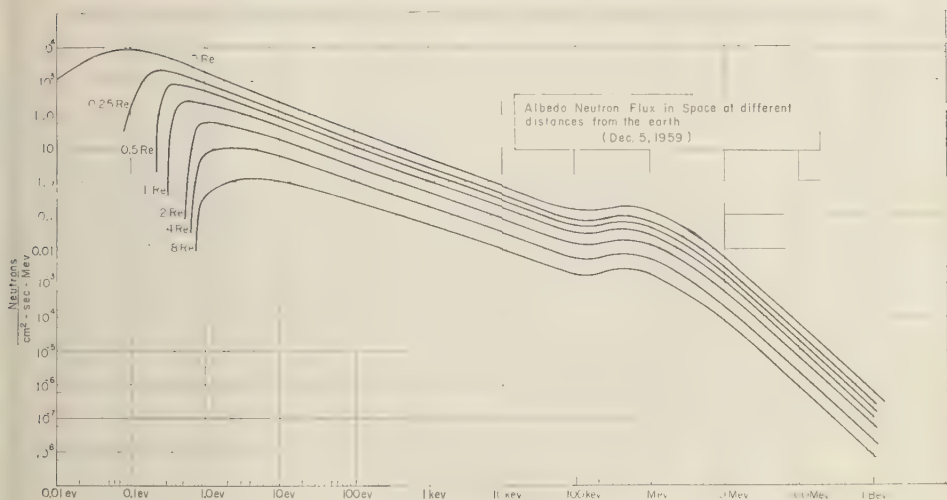


Fig. 7. Neutron energy spectra in space at different distances from the earth above the geomagnetic equator. Distance unit is radius of the earth (Re). The 0 Re curve is for the top of the atmosphere, which is roughly 100 km.

trons has been calculated in the geometrical limit of forward production and no scattering, using production and absorption mean free paths of 155 g/cm². The neutron current out of a slab of atmosphere of thickness t and uniform density, produced by a beam of protons incident upon the slab, is given by

$$J = \int_0^t [e^{-x/\lambda_p}] \frac{dx}{\lambda_p} e^{-(t-x)/\lambda_n}$$

$$= \frac{t}{\lambda} e^{-t/\lambda} \quad \text{for } \lambda_n = \lambda_p$$

In the calculation of the angular distribution the variation of density with altitude is considered, and the neutron production for different glancing paths near the edge of the atmosphere (see Fig. 5) is calculated by means of the expression above. By comparing the neutron production from different paths we can get the angular distribution of very-high-energy neutrons. The result is shown in Figure 6 by the curve for $E > 10$ bev. For neutrons with energies between 10 Mev and 10 bev, interpolated guesses at the angular distributions are shown in Figure 6. The widths of these curves are taken to be in the ratio of the production angular-distribution widths as determined by high-energy accelerators. The results that we are interested in, the neutron

flux and neutron decay density in space, are not very dependent on the angular distributions.

The absolute magnitude of $J(R, \mu)$, the leakage neutron current for the very-high-energy neutrons, has been determined by calculating the ratio of particles passing down through the 200-g/cm² level of the atmosphere to particles leaking out of the atmosphere by a geometrical calculation as sketched above. Then, using the measured value of the equilibrium neutron flux at 200 g/cm² from Figure 1, we can get $J(R, \mu)$.

The neutron current in space. Now consider the neutrons leaking out of the atmosphere of the earth. We can use the known values of the leakage current density to study the neutrons in space. The latitude dependence of the source we will take as that measured by Simpson [1951], although it may be somewhat time dependent [Haymes, 1959] or altitude dependent [Lord, 1951]. Starting with the source $J(\mu, E, \lambda)$ we calculate the neutron current J passing through a sphere of 1 cm² cross section at any position in space by integrating the source over the surface of the earth.

$$J(R, \lambda, E) = \int_{\text{earth}} J(\mu, E, \lambda) e^{-L/\lambda} \cdot \left[\frac{1}{L^2} \right] dA \text{ neutrons/cm}^2/\text{sec/Mev}$$

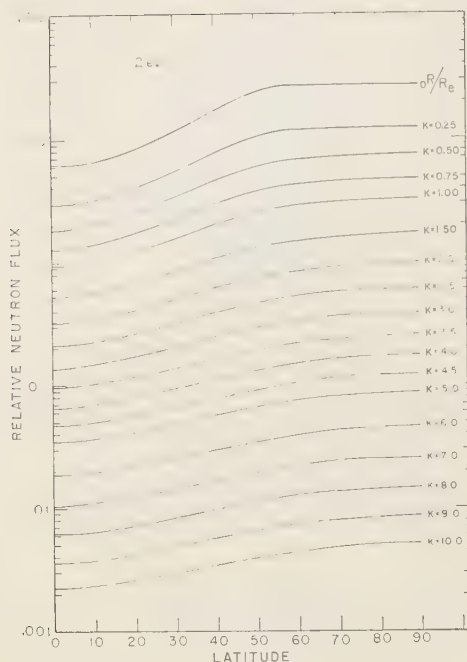


Fig. 8a. Variation of the neutron flux in space with latitude and altitude for 2-ev neutrons.

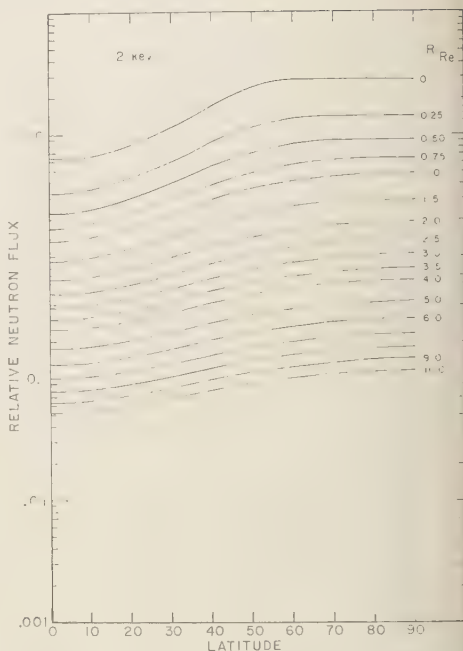


Fig. 8b. Variation of the neutron flux in space with latitude and altitude for 2-kev neutrons.

where

L = distance from source to point of observation.

R = distance from the center of the earth.

τ = mean life of neutron.

v = velocity of neutron.

The neutron source is given by

$$J(\mu, E, \lambda) = kF_1(\mu)F_2(E)F_3(\lambda)$$

neutrons/cm²/sec/Mev/ster

$F_1(\mu)$ is the angular distribution of the neutrons (see Fig. 4); $F_2(E)$ is the energy spectrum given in Figure 7 for $R_e = 0$; $F_3(\lambda)$ is the latitude variation given by Simpson [1951]; and k is a normalizing constant. The integral has been evaluated by an IBM 650. The resulting neutron energy spectra in space at different distances from the earth are shown in Figure 7. The variation in 2-ev and 2-kev neutron fluxes with latitude and altitude is shown in Figure 8. As is evident from this figure, the latitude variation of flux seen at the surface of the earth decreases with altitude.

From Figures 8a and 7 the 2-ev neutron flux is seen to decrease faster with altitude than the 2-kev flux shown in Figure 8b; this is because more of the slower-traveling neutrons decay in traveling a given distance.

Gravitationally trapped neutrons. One important feature of the neutrons leaking out of the atmosphere is that some of the low-energy neutrons are trapped by the gravitational field of the earth. A neutron having 0.66-ev kinetic energy and moving vertically has just enough energy to escape from the earth. The neutrons in space below 1 ev have been treated separately in the calculations because of this gravitational trapping. These neutrons move upward from the top of the atmosphere in elliptical orbits and stay aloft for many minutes. For example, a 0.35-ev neutron moving vertically stays up 80 minutes. This is 6.6 half-lives. Nearly all these neutrons decay before they return to earth. Typical elliptical orbits for 0.15-, 0.25-, and 0.35-ev neutrons are shown in Figure 9. In our calculations we have approximated these orbits by having the neutrons move in straight lines away

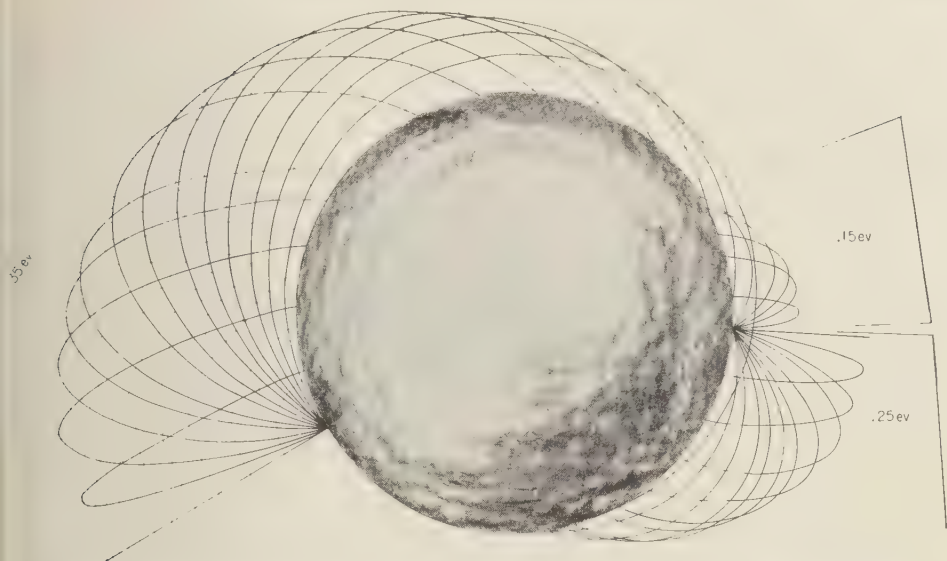


Fig. 9. Orbits of neutrons gravitationally trapped in space near the earth. Three sets of orbits are shown for neutrons of three different energies: $E_n = 0.35, 0.25$, and 0.15 ev. Marks are made along the 0.35 -ev neutron orbits for every 200 seconds of flight time.

from the source point but with a velocity that decreases with altitude in the proper way. Sample calculations show that this approximation is quite good except at very low energies, roughly below 0.15 ev, where the neutrons get to 1500 -km

altitude at most, and therefore are not important in considerations of the Van Allen radiation belt. Figure 9 shows that the orbits of most of the trapped particles are, for a few half-lives, nearly straight lines.

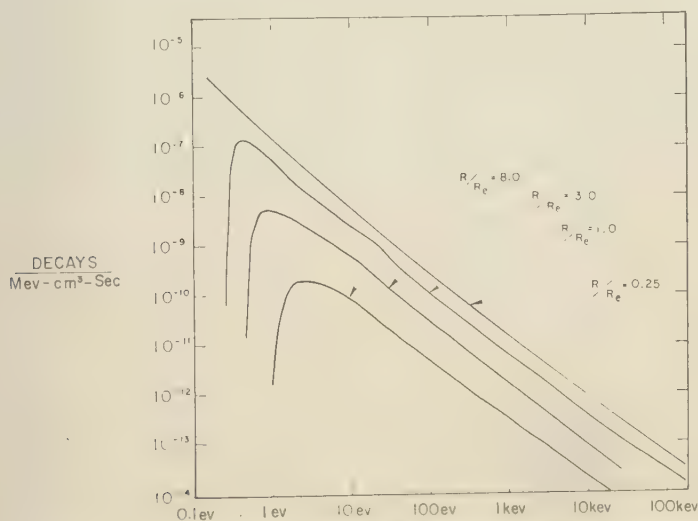


Fig. 10. Energy spectrum of neutrons that decay at different distances from the surface of the earth above the geomagnetic equator.

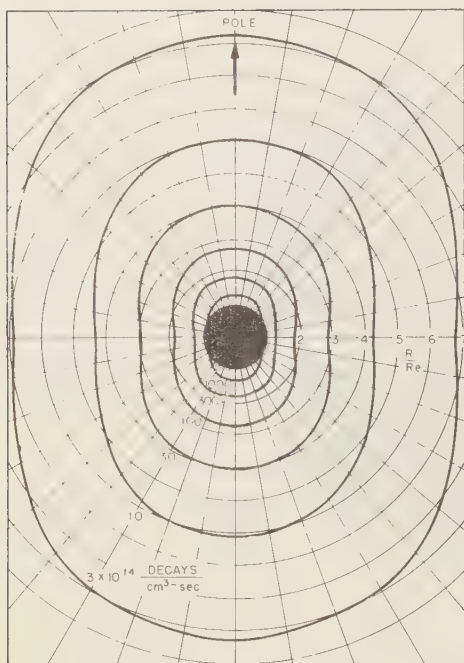


Fig. 11. Values of dn/dV , the neutron decay density summed for neutrons of all energies, at different altitudes and magnetic latitudes.

The fluxes of gravitationally trapped neutrons in space are included in the spectra shown in Figure 7. The intensity of these low-energy neutrons falls off faster with altitude than the intensity of the higher-energy neutrons, because the former travel more slowly and therefore more of them decay.

The neutron-decay density. To understand the Van Allen radiation belts, we want to know how important the injection of particles by neutron decay is. When a neutron decays, a proton and electron are made. If the neutron decays in space near the earth, the electron and proton can be trapped in the radiation zone.

We can calculate the neutron-decay density dn/dV (particles decaying per cubic centimeter per second) at all positions in space directly from the neutron current in space by

$$\frac{d}{dV} n(\lambda, E, R) = \frac{1}{v\tau} [J(\lambda, E, R)]$$

where v = neutron velocity and τ = neutron mean life. The energy spectrum of the neutrons that decay at different altitudes is shown in Figure 10. In studying the electrons injected into the radiation belt, we see that all neutron decays produce electrons of essentially the same energy, independent of the neutron energy. Because of this, the neutron-decay density summed over energy is important. It is given by

$$\frac{d}{dV} n(\lambda, R) = \int \frac{d}{dV} n(\lambda, R, E) dE$$

The variation of $(d/dV)n(\lambda, R)$ with position in space is shown in Figure 11. The gravitationally trapped neutrons contribute substantially to the decay density since they spend so much time in space near the earth. For example, at 0.5 earth radius from the earth's surface the gravitationally trapped neutrons produce 40 per cent of the decays, although they amount to less than 1 per cent of the neutron leakage (the global average total leakage is about 0.8 neutron/cm²/sec).

If the gravitational field of the earth were to be turned off, the neutron-decay rate would decrease about 40 per cent at 0.25 earth radius, increase about 70 per cent at 0.5 earth radius, and increase more farther out from the earth.

The neutron-decay density obtained is larger than that calculated by Kellogg [1959]. There are several reasons why this is so. First, he did not consider gravitational trapping of neutrons, which we find to be worth almost a factor of 2 at 0.5 earth radius. Second, all his neutrons traveled radially outward instead of with the $\cos^2 \theta$ distribution we found, so that his neutrons tended to decay farther from the earth. Finally, his fluxes in the kev and Mev ranges were about 1/20 of ours (as discussed previously).

SUMMARY

A reasonable guess about the spectrum of neutrons created by cosmic rays enabled us to calculate the equilibrium neutron spectrum in the atmosphere. Normalizing this calculated equilibrium spectrum to the experimental values, we find the necessary neutron source strength to be 6.2 ± 1.5 neutrons/cm²/sec of earth surface at $\lambda = 44^\circ$. This corresponds to a global average of 4.6 neutrons/cm²/sec, about 50 per cent higher than quoted values which ignore leakage and absorption other than $N^{14}(n, p)C^{14}$.

Of the cosmic-ray neutrons born in the atmos-

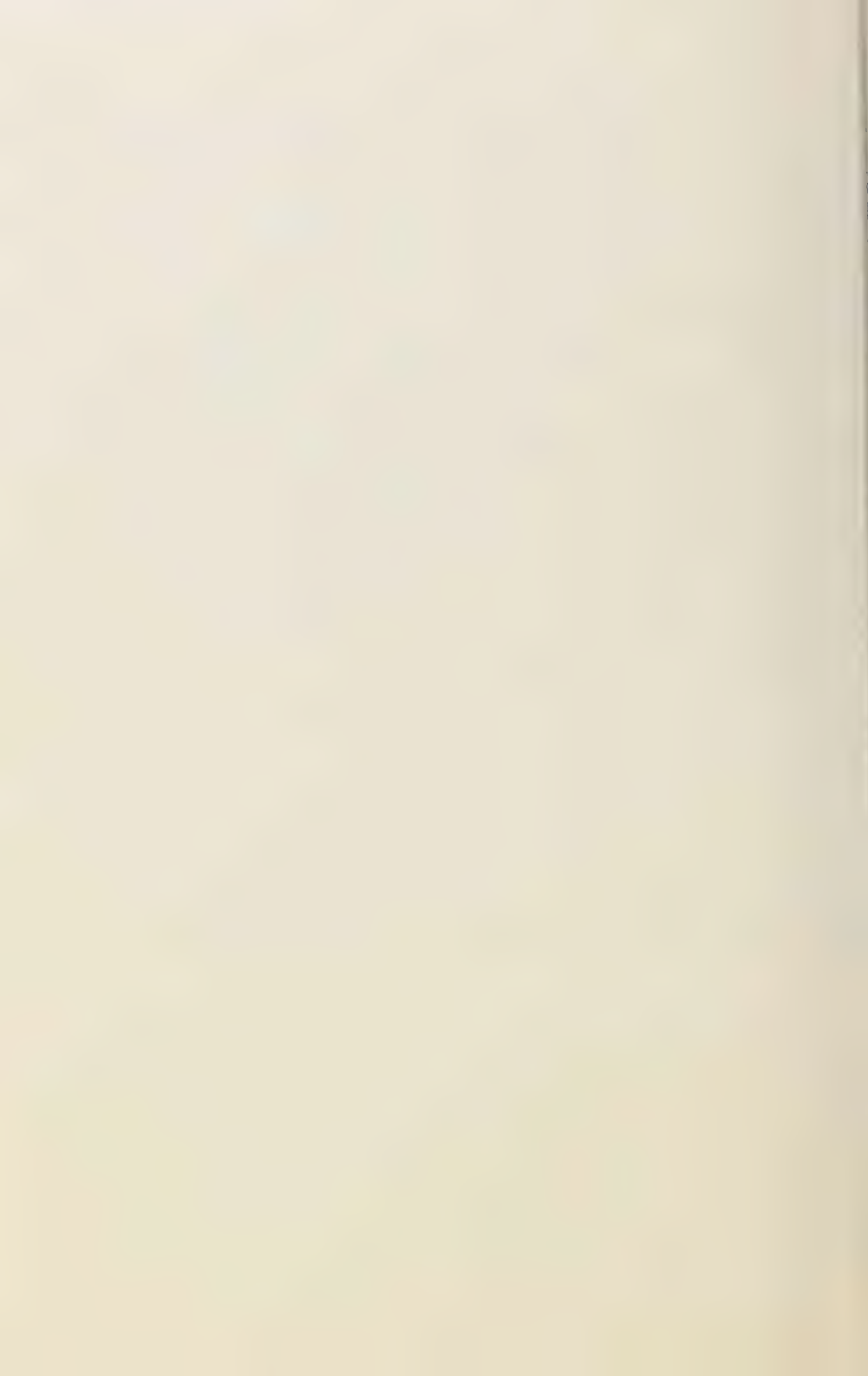
where, 64 per cent are captured by $N^{14}(n, p)C^{14}$, 19 per cent are captured by $N(n, \gamma)$, $N(n, \alpha)$, and $O(n, \alpha)$ reactions, 17 per cent leak out of the atmosphere, and less than 0.2 per cent are captured by the earth.

From the energy spectrum and angular distribution of leakage neutrons we have calculated the neutron flux and decay density of all points in space. This demography of cosmic-ray neutrons allows us to proceed with the study of the importance of cosmic-ray neutron decays as a source of the Van Allen radiation belts.

REFERENCES

- Anderson, E. C., The production and distribution of natural radiocarbon, *Ann. Rev. Nuclear Sci.*, **2**, 63, 1953.
- Atkinson, J. H., W. N. Hess, V. Perez-Mendez, and R. W. Wallace, Neutron cross-section measurements at 4.5 Bev, *Phys. Rev. Letters*, **2**, 168, 1959.
- Bethe, H. A., S. A. Korff, and G. Placzek, On the interpretation of neutron measurements in cosmic radiation, *Phys. Rev.*, **57**, 573, 1940.
- Camerini, U., P. H. Fowler, W. O. Lock, and H. Muirhead, Nuclear transmutations produced by cosmic-ray particles of great energy, IV, The distribution in energy, and the secondary interactions of the particles emitted from stars, *Phil. Mag.*, **41**, 413, 1950.
- Coor, T., D. A. Hill, W. F. Hornyak, L. W. Smith, and G. Snow, Nuclear cross sections for 1.4-Bev neutrons, *Phys. Rev.*, **98**, 1369, 1955.
- Glasstone, S., and M. C. Edlund, *The Elements of Nuclear Reactor Theory*, pp. 395-396, D. Van Nostrand, Co., Princeton, N. J., 1952.
- Graves, E. R., and L. Rosen, Distribution in energy of the neutrons from the interaction of 14-Mev neutrons with some elements, *Phys. Rev.*, **89**, 343, 1953.
- Gross, E., The absolute yield of low-energy neutrons from 190-Mev proton bombardment of gold, silver, nickel, aluminum, and carbon, *Lawrence Radiation Lab. (Berkeley, Calif.), Rept. UCRL-3330*, Feb. 29, 1956 (OTS).
- Haymes, R. C., High altitude neutron intensity diurnal variation, *Phys. Rev.*, **116**, 1231, 1959.
- Hess, W. N., and B. J. Moyer, Production of deuterons in high-energy nucleon bombardment of nuclei and its bearing on nuclear charge distribution, *Phys. Rev.*, **101**, 337, 1956.
- Hess, W. N., H. W. Patterson, R. Wallace, and E. L. Chupp, Cosmic-ray neutron energy spectrum, *Phys. Rev.*, **116**, 445, 1959.
- Kellogg, P. J., Possible explanation of the radiation observed by Van Allen at high altitudes in satellites, *Nuovo cimento*, **11**, 48, 1959.
- LeCouteur, K. J., Statistical fluctuations in nuclear evaporations, *Proc. Phys. Soc. London, A*, **65**, 718, 1952.
- Lord, J. J., The altitude and latitude variation in the rate of occurrence of nuclear disintegrations produced in the stratosphere by cosmic rays, *Phys. Rev.*, **81**, 901, 1951.
- Messel, H., *Progress in Cosmic Ray Physics*, vol. 2, p. 1761, Interscience Publishers, New York, 1954.
- Rossi, B., *High Energy Particles*, p. 488, Prentice-Hall, New York, 1952.
- Shapiro, A. H., *The Dynamics and Thermodynamics of Compressible Fluid Flow*, vol. 1, app. B, pp. 612-613, Ronald Press, New York, 1953.
- Simpson, J. A., Neutrons produced in the atmosphere by the cosmic radiations, *Phys. Rev.*, **83**, 1175, 1951.
- Smith, J. R., Scattering of 14-Mev neutrons in helium, hydrogen, and nitrogen, *Phys. Rev.*, **95**, 730, 1954.
- Strauch, K., and F. Titus, Inelastic scattering of 96-Mev protons, *Phys. Rev.*, **104**, 191, 1956.
- Stuart, R. N., E. H. Canfield, E. E. Dougherty, and S. P. Stone, Zoom: a one-dimensional, multi-group, neutron diffusion theory reactor code for the IBM-704, *Lawrence Radiation Lab. (Livermore, Calif.), Rept. UCRL-5293*, Nov. 19, 1958 (OTS).

(Manuscript received May 31, 1960;
revised November 30, 1960.)



Scintillation-Counter Observations of Auroral X Rays during the Geomagnetic Storm of May 12, 1959

P. D. BHAVSAR¹

*School of Physics, University of Minnesota
Minneapolis, Minnesota*

Abstract. Auroral X rays were observed at 10 g/cm² atmospheric depth over Minneapolis on May 12, 1959, with a balloon-borne NaI scintillation spectrometer in the energy range 22 to 263 kev. This event accompanied the low-energy solar cosmic rays that also produced some γ rays in the atmosphere. Energy spectra of the X rays were obtained after correcting for the presence of these γ rays. The peak in the auroral X-ray intensity was found to be associated with the passage of the aurora at the zenith. The electron spectrum responsible for the X rays has been determined and found to be in agreement with the observations of electron spectrum of the outer radiation belt.

Introduction. During the great magnetic storm of May 12, 1959, several balloon flights were made from Minneapolis, Minnesota, to study the incoming radiation at high altitudes. The results obtained from the ionization chamber and Geiger-counter observations made during these flights, together with a brief account of scintillation-counter observations, have already been reported by *Winckler and Bhavsar* [1960]. In this paper the scintillation-counter observations will be discussed in more detail. Because a NaI scintillation crystal detector has a very high efficiency for the detection of photons, this is the study, particularly, of the photonic component during the storm.

The observed photonic component in the atmosphere, as will be shown below, was produced during the storm by two different processes. The high-energy γ rays were produced as a result of the nuclear reactions of solar protons with the air nuclei. At certain times, accompanying a strong aurora, a low-energy component in the energy range from 22 kev to about 200 kev (the auroral X rays) was also observed. Such X rays had already been observed on several occasions by *Winckler* [1960] during the IGY period. These auroral X rays are presumed to be produced as bremsstrahlung of the electrons lumped from the Van Allen outer zone during the magnetic storm. In addition, there is always a photonic background present which is secondary to the galactic cosmic rays.

Because of the continuous arrival of the solar protons during this storm at times when the aurora was also present, the auroral X ray observations are polluted by the pulses due to high-energy γ rays not losing their total energy in the crystal, and due to multiple-scattered γ rays sufficiently degraded in energy to fall into the energy region of the auroral X rays.

The X-ray observations have been corrected for these γ -ray effects by studying the pulse-height spectra obtained during the periods when there was no visible aurora present above about 30° elevation. All excess photon pulses observed at those times were assumed to be due to the γ rays alone. From the auroral X-ray spectrum obtained in this way we have calculated the electron spectrum striking the top of the atmosphere and producing these X rays.

Apparatus. Figure 1 shows the block diagram of the scintillation detector. It was a small integral pulse-height spectrometer utilizing a cylindrical NaI(Tl) crystal of 12.70-mm thickness and 45.45-mm diameter. The crystal was coupled to an RCA-6655 photomultiplier tube. The high voltage was provided by 30V midget batteries connected in series. The output of the photomultiplier was fed to an amplifier through an emitter follower and a cycling attenuator. The amplifier output was fed to a fixed discriminator. Thus at a particular instant the discriminator passed only those pulses above a certain height determined by the calibration of the attenuator position at that time. The attenuator was a simple potentiometer coupled to a constant speed motor that took it through one complete

¹ On leave from Physical Research Laboratory, India. Supported by Fulbright travel grant.

SCHEMATIC OF SCINTILLATION COUNTER

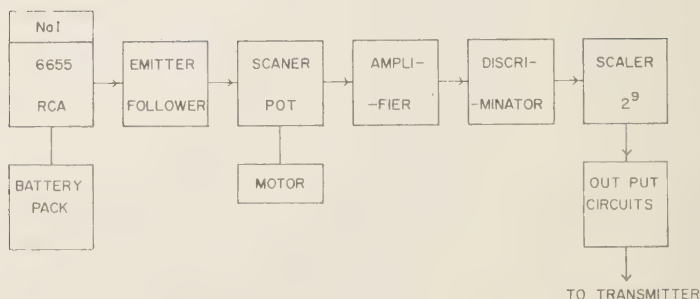


Fig. 1. Block diagram of NaI scintillation spectrometer used for auroral X-ray measurements.

cycle in about 10 minutes. The lower and the upper cutoff levels at the two ends of the potentiometer were set at pulse-heights equivalent to energy loss of 22 and 263 kev in the scintillation crystal. The pulse-height values for different energies were obtained by studying the pulses due to fluorescent X rays of 8-, 18-, and 22-kev energy from copper, molybdenum, and silver targets, respectively, and to γ rays of Co^{57} and Cs^{137} of energies 123 and 661 kev, respectively. The pulse-height was found to change linearly with energy in this range. Time-versus-energy discrimination calibration for the different positions during a cycle of the attenuator potentiometer was obtained with a calibrated pulser after setting the upper and the lower limits. Figure 2 shows the results obtained in the laboratory by the above-mentioned instrument with different X ray and γ -ray sources.

The output of the discriminator was fed to a train of binaries and the scaled-down rates were telemetered. This instrument was flown with the standard IGY cosmic-ray monitoring gear described by *Winckler, Peterson, and Howard* [1958]. The detector had a good temperature characteristic. The calibration was found to change not more than about 2 per cent for a temperature change of $+20^{\circ}\text{C}$ to -10°C . This was achieved by using selected good transistors for the amplifier and the discriminator circuits.

Experimental results. Figure 3 shows the counting rates of different instruments carried on balloon Flight IGC-8 on May 12, 1959, as a function of Universal Time. A time-altitude curve for the whole flight is plotted, showing that this was a good level flight. On the same diagram also

is plotted the H component of the earth's magnetic field as observed at the Fredericksburg Observatory, and the sea-level neutron intensity during this period as observed by the monitor at Deep River, Canada. The counting rate of the single Geiger counter is not corrected for the dead-time. The counting rate of the scintillation counter indicated on the diagram is the rate at the beginning of each scanning cycle and shows the rate of occurrence of events with energy losses > 22 kev in the scintillation crystal. The general features of this diagram were discussed in the earlier communication by *Winckler and Bhavsar* [1960].

For studying the excess photonic component it is necessary to remove the background rates from the total counting rate observed. The background rate is composed of counts due to photons secondary to the galactic cosmic rays plus counts due to direct cosmic-ray-particle radiation and solar protons. The particles give almost all large pulses. An estimation shows that their contribution to the pulses with energy loss in the crystal less than 263 kev is only about 1.3 per cent of the total counting rate due to particles. The counting rate due to the secondary photons of galactic cosmic rays can be taken as the photon rate observed on a quiet-day flight. To get the rate due to excess photons with pulse-height equivalent to energy loss E ($22 < E < 263$ kev) or more in the crystal, we have only to subtract the quiet day photonic rate at this energy plus the total particle rate from the observed counting rate at this energy. The total number of counts due to particles only was estimated by reducing the total counting rate of the single Geiger counter

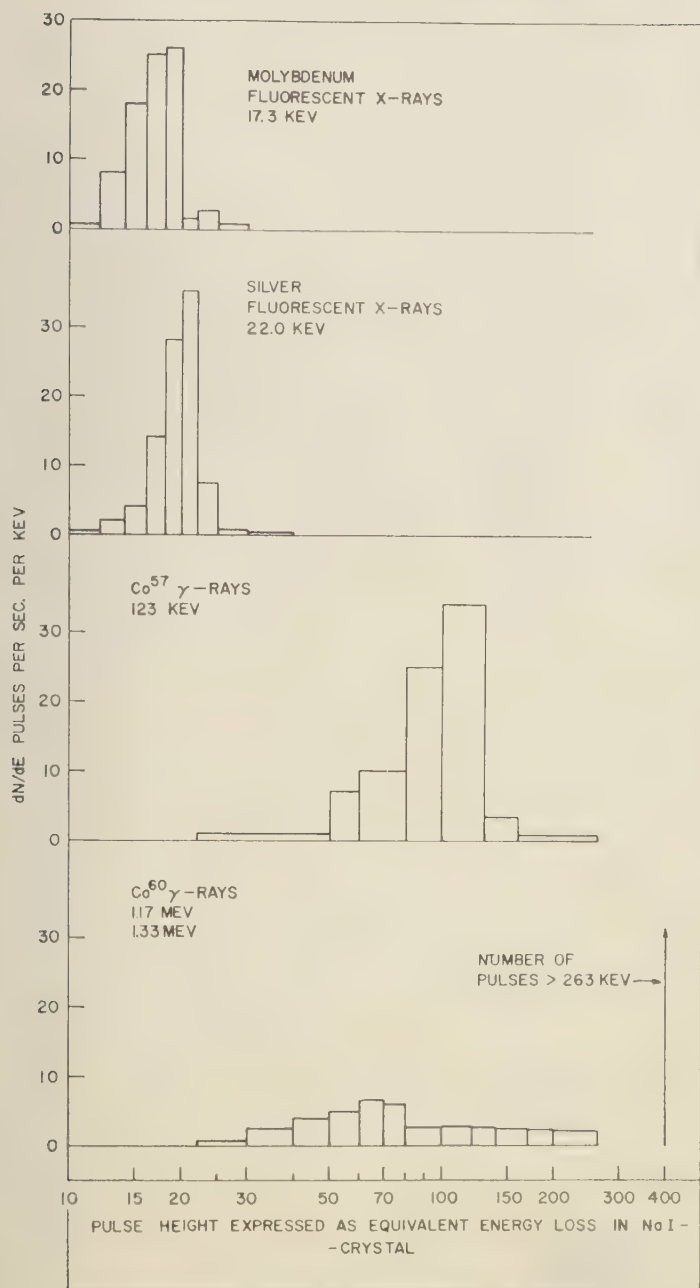


Fig. 2. Pulse-height spectra of X rays and γ rays obtained in the laboratory with the detector used for present investigation.

to the scintillator geometry. The quiet-day rates were obtained from a balloon flight made 5 days before this flight, a day which was magnetically quiet. Thus

$$N(>E)_{\text{photon excess during storm}} = N(>E)_{\text{total rate}}^{\text{scintillator}} - N(>E)_{\text{photon quiet day}} - N_{\text{particle}}$$

Excess photons observed during the balloon ascent. First let us confine our attention to the results obtained during the balloon ascent shown in Figure 4. Here are plotted the excess photon rates at the time of the storm versus atmospheric depth. The four photon rate plots, from top to bottom, are for pulses with energy loss >22 kev, >35 kev, >50 kev, and >263 kev, respectively. In the same figure is also plotted the excess counting rate of the single Geiger counter corrected for the dead-time losses, but not reduced to the scintillator geometry. Excess Geiger counter rate is almost entirely due to solar protons, since the counter has a very low efficiency for photon detection. The excess photons, as can be seen from the diagram, are first observed deep in the atmosphere around 120 g/cm^2 depth, which is much deeper than where the solar protons made their presence known by direct detection as an increase in the single counter rate. As an approximation we can say that all four photon excess plots for different energy losses have almost the same slopes, indicating most of the pulses observed in the energy range 22 to 263 kev during the ascent are due to photons of higher energy (>263 kev) which produce pulses in the low-energy range, either by losing a part of their energy in the crystal by Compton scattering, or by the process of multiple Compton scattering in it. If there are primary photons of low energy, then the slopes of the four curves in Figure 4 have to be greatly different from each other.

These photons can be of three different origins. (1) They can be primary, that is, not originating in the earth's environment. (2) They can originate in the bremsstrahlung radiation of energetic electrons striking at the top of the atmosphere. (3) They can have their origin in the nuclear reactions of the solar protons with air nuclei.

From the rate-altitude plot of the ≥ 263 -kev energy loss pulses we get an average absorption coefficient $-0.023 \text{ cm}^2/\text{gm}$ for air, which is the absorption coefficient for about 2-Mev γ rays. We cannot attach much importance to this num-

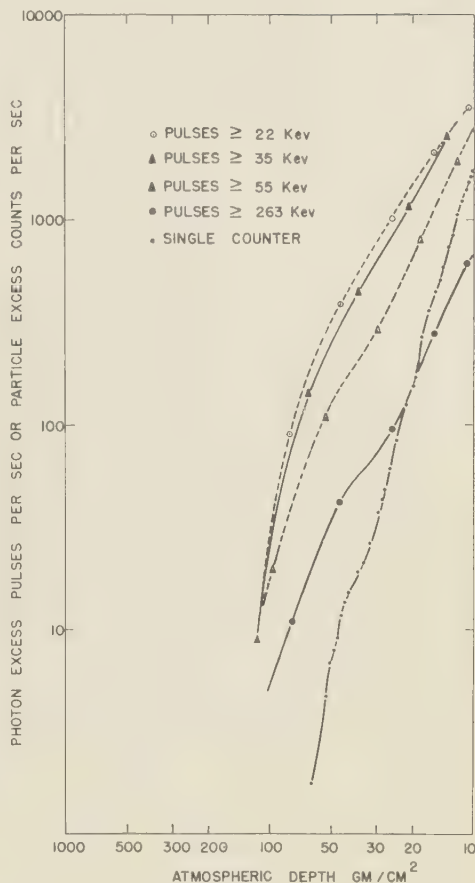


Fig. 4. Excess photon rates plotted as a function of atmospheric depth. Particle excess as recorded by the Geiger counter is also plotted for comparison. All four photon excess curves have the same approximate slope.

ber, however, for we have no means to correct the rates for any time variation that may be superimposed on it; this will not allow the true determination of absorption coefficient.

The first type of origin for these photons can be ruled out, and the decision is between the other two probable modes of production. For this it is necessary to examine more closely the rate-altitude plots. We have determined the absorption coefficients as obtained from these plots between different atmospheric depths. The values thus obtained are given in Table 1. As can be seen, the absorption coefficient values are

TABLE 1. Absorption Coefficient μ in cm^2/g between Different Atmospheric Depths

Plot	10 to 30 g/cm^2	30 to 50 g/cm^2	50 to 100 g/cm^2
>22 kev	-0.034	-0.019	-0.021
>35 kev	-0.038	-0.020	-0.020
>55 kev	-0.050	-0.018	-0.017
>263 kev	-0.049	-0.016	-0.015

about the same for all the energies at depths greater than 30 g/cm^2 , and the average value is about $-0.018 \text{ g}/\text{cm}^2$, which is the absorption coefficient for 5-Mev γ rays. As stated earlier, not much importance can be attached to these individual values of absorption coefficient; however, the unknown time-variation effect will be the same for all the plots, and therefore some definite conclusions can be drawn from the comparison of these values. If these photons are produced by the second type of production, that is, by the process of bremsstrahlung, we need electrons of at least 5-Mev energy to produce the γ rays of that energy. Electrons of this energy can penetrate in the atmosphere up to 2.8 g/cm^2 depth, so all photon production will take place high in the atmosphere beyond this depth. Also, there will be many more low-energy photons produced by bremsstrahlung, compared with the high-energy ones. At depths greater than 2.8 g/cm^2 there will be no more photon production, and because of the larger absorption of the low-energy photons higher values of absorption coefficient from the lower energy loss plot should be expected. Quite contrary to this, between the depths 10 to 30 g/cm^2 we get lower absorption coefficient values for low-energy loss plot. This rules out the second type of production and leads to the third type, where, from the nuclear reactions of solar protons with the oxygen and nitrogen nuclei, more high-energy γ rays will be produced than low-energy ones. The number of protons crossing any particular atmospheric level decreases very rapidly deep in the atmosphere, and so the production of high-energy photons also decreases with depth. As these high-energy photons penetrate deep in the atmosphere, a low-energy degraded photon flux, which is more efficiently detected than its high-energy parent, builds up. This qualitatively explains the strange behavior of the absorption coefficient for the

low-energy loss pulses. This also supports our view that the photons observed during the ascent of the balloon are initially of high energy and therefore γ rays produced in nuclear reactions. Brown and D'Arcy [1959] have observed a similar γ -ray effect accompanying a solar proton event during July 1959, and they also estimate the energy of these γ rays as 3-5 Mev.

The problem of production of γ rays in the interactions of solar protons with air has been examined in more detail, and for the constant altitude part of the flight quantitative estimates show that all the observed γ rays can be accounted for from production by the nuclear processes (Bhavsar, to be published). Neutrons also are produced in these interactions and have been observed in the emulsions (Freier, to be published).

We have not attempted any quantitative analyses for the ascent part of the flight because there are many uncertainties involved, such as unknown time variation and the complicated nature of degradation in air of γ rays of energy between about 5 Mev and 40-50 kev.

Photons during the aurora and the constant altitude part of the balloon flight. In Figure 5 the excess photon rates are shown against UT for the period when significant excess photons were observed. On the same figure, at the bottom, are also two more plots showing the ratios between photon excess >22 kev/particle excess, and photon excess >263 kev/particle excess. For the calculations of these ratios the particle excess rates were reduced to the scintillator geometry.

The balloon reached ceiling at 0535 UT. As can be seen, from this time to about 0730 UT the plots of ratios are parallel to each other. Also, the ratios are almost constant compared with the large decrease in the counting rates of the Geiger counter at this time, which can be seen in Figure 3. This points to the fact that the excess photons during this time were in balance with the coming solar proton intensity, we may conclude, therefore, that they were produced by these solar protons in the atmosphere. Also, at this time the low-energy and high-energy loss pulses had the same trend, indicating that the low-energy pulses are dependent on the high-energy ones. This supports our previous conclusion derived from the rate-altitude plot.

The situation changes around 0730 UT, when the departure between the two ratio plots is seen.

about 0800 UT this separation becomes more prominent, with a very sharp peak around 0835 U.T. The upper four curves show the increase in separation at this time, indicating an increase

in low-energy loss pulses compared with those of high energy. The time of occurrence coincides with the visual observation of the aurora at zenith. The total counting rate of the scintillation

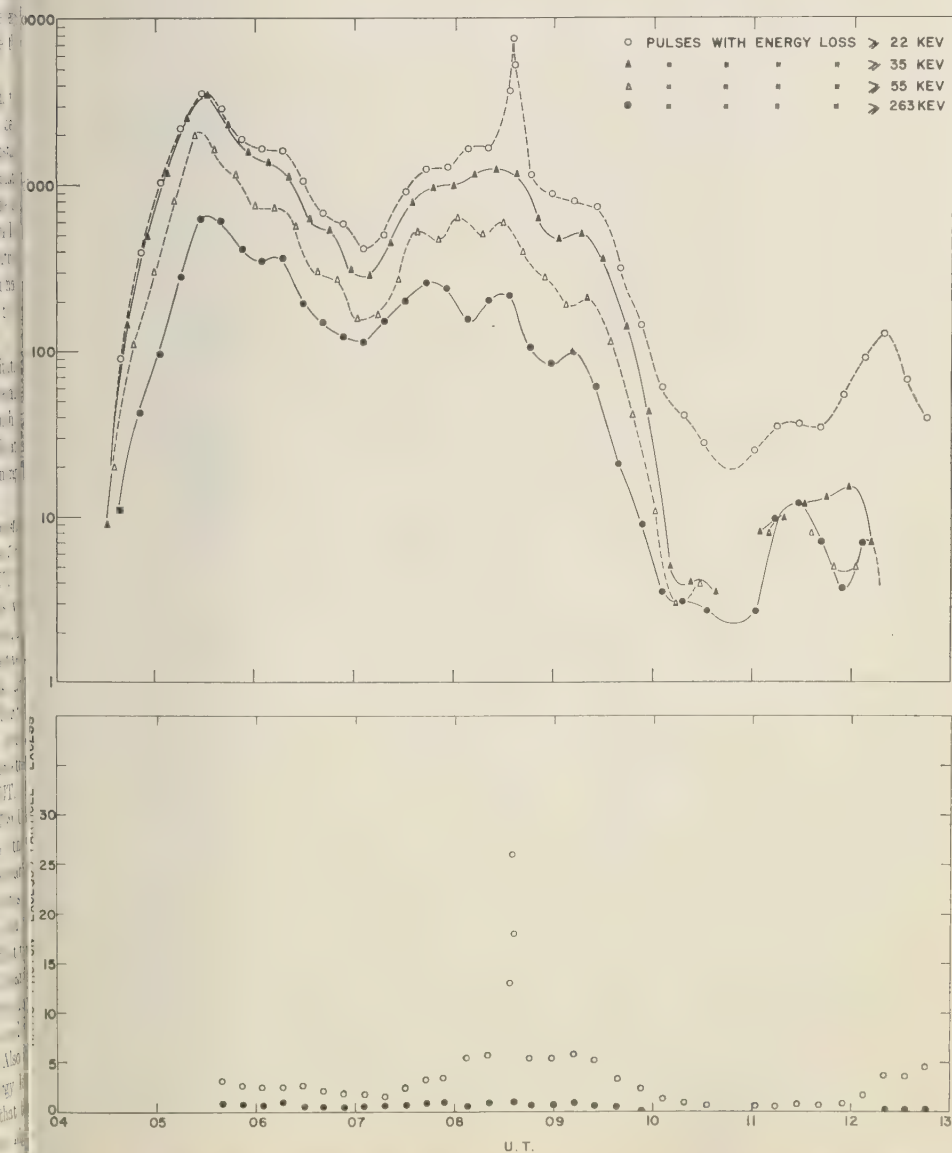


Fig. 5. Upper section: excess photon rates plotted as a function of time. Lower section: ratio of excess photon rates to particle excess for two X-ray energy levels, 22 and 263 kev. Note the change in ratio of 22 kev to particle excess at the time of the aurora. The other ratio plot is not affected.

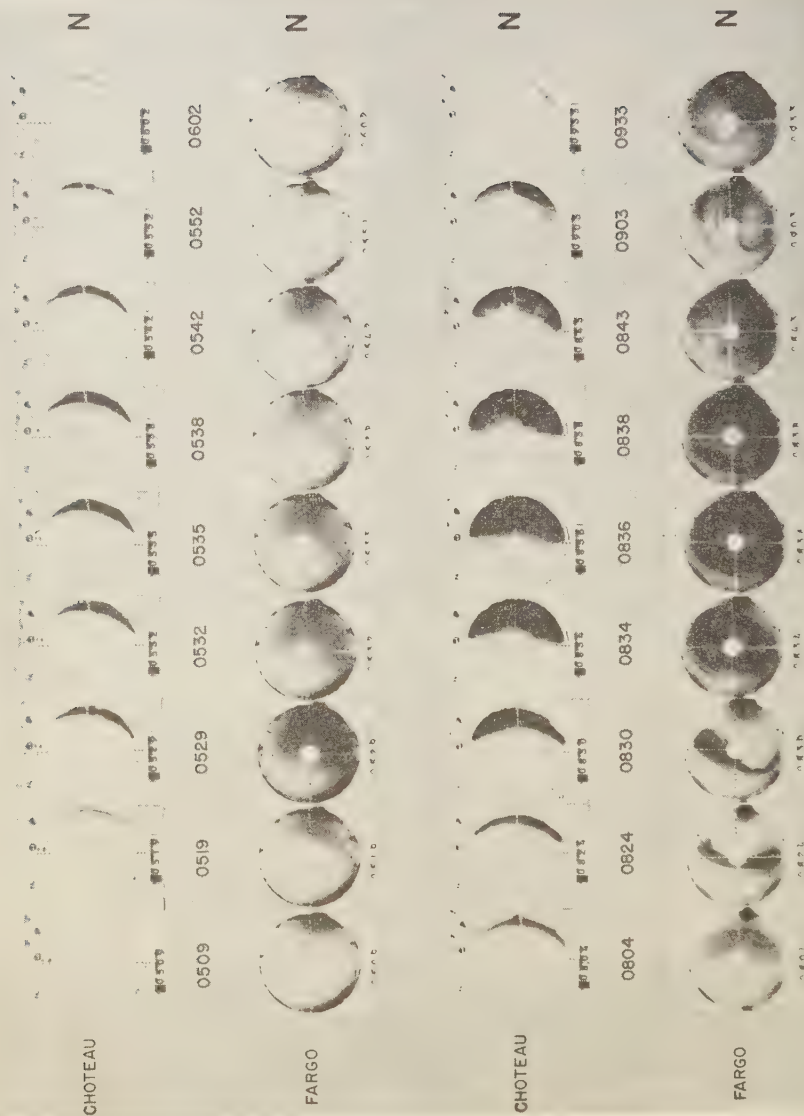


Fig. 6. Auroral all-sky camera records of the May 12 aurora from stations adjacent to Minneapolis. Upper two sections: early auroral buildup with maximum at 0534 UT. Lower two sections: great auroral buildup during balloon flight with maximum at 0836 UT. These photographs correlate well with visual observations at Minneapolis. The maxima agree within 1 minute with the time of the X-ray bursts accompanying the aurora.

counter for pulses >22 kev was 8000 counts/sec at the peak of this X-ray event. At this time the whole sky was luminous with corona and flickering bands across the zenith. Both red and green colors were present in the visible aurora. On previous occasions also, when auroral X rays

were observed, such red spectral lines were present in an aurora [Winckler, 1960]. All this leads to the confirmation that this increase in the low-energy photon intensity was due to the auroral X rays.

The all-sky camera records of the aurora (Fig.

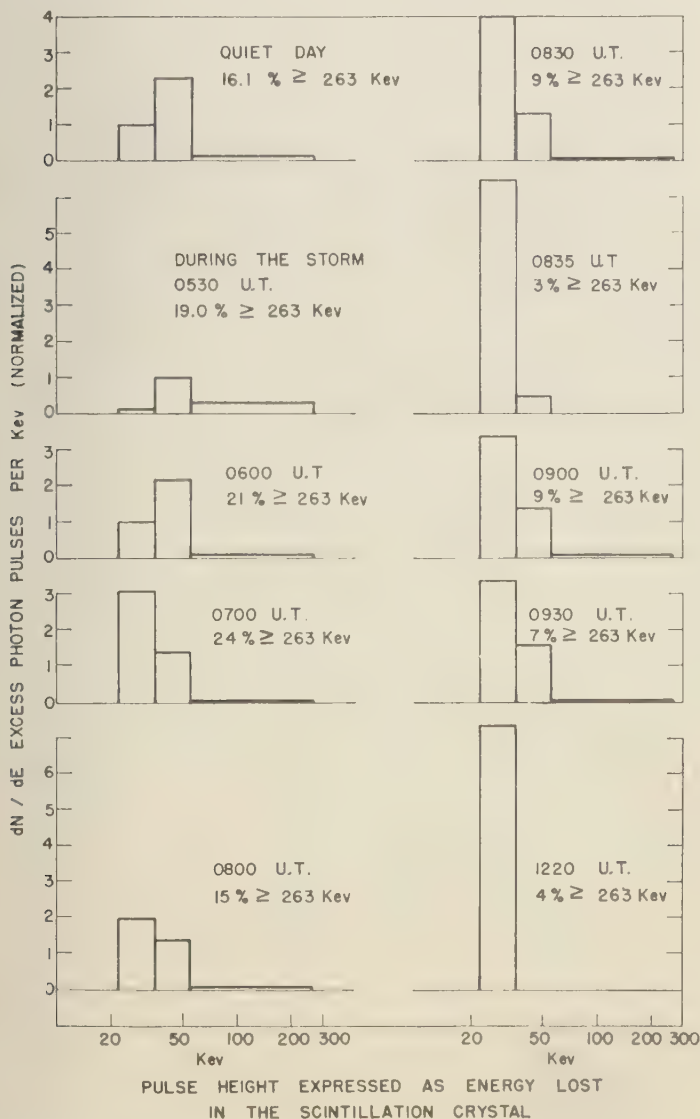


Fig. 7. Differential pulse-height spectra for excess photons as observed at different times of the flight IGC-8. A quiet-day photon spectrum is also shown (top, left) for comparison. All the spectra are normalized for better comparison.

6) taken at this time at Choteau, Montana, and at Fargo, North Dakota, have been studied. In both sets of records the auroral activity reaches the zenith within a few minutes of the observation of auroral X-ray peak at Minneapolis. When the all-sky records from the Fargo station were projected with a movie projector, the very spectacular movement of the ribbon-like form at zenith between 0830 and 0834 UT could be seen. This broke up into an intense luminosity around 0835 UT and then subsided. The aurora at Minneapolis started receding toward the north, where by 1030 UT it had formed a low arc. The early dawn at that time of the year ended visual observations of the aurora at Minneapolis. A small increase in the low-energy loss pulses was observed again around 1215 UT. No visual auroral observations are available at this time because of the daylight.

Figure 3 plots the horizontal component of the earth's magnetic field as observed at Fredericksburg Observatory. There are no other magnetogram records available from a nearby station, and no correlation between the fine structure of the magnetic intensity variations and the visible aurora and X rays has been established. This is understandable, however, as Fredericksburg is farther south than Minneapolis in latitude and the separation in longitude is about 21° .

Energy spectrum of the auroral X rays and of electrons producing these X rays. From the time-intensity plots of Figure 5, the integral pulse-height spectrum of the photon pulses observed at a certain time may be obtained by reading out the values on the different plots for that time. From this the differential pulse-height spectrum at a particular instant may be obtained. The spectra at different times of the flight have been determined and are shown in Figure 7. They have been normalized to total 100 pulses of >22 -kev energy loss for a better comparison between each spectrum.

The uppermost spectrum on the left-hand side shows the quiet-day pulse-height spectrum at 10 g/cm^2 atmospheric depth, which is due to photons secondary to the galactic cosmic rays. The other spectra are those observed during Flight IGC-8, and the times of observations are indicated on each plot.

It is easy to see that the first three differential energy spectra on the left-hand side (from top to bottom) are similar in character to each other,

but are quite different from the rest of the spectra in the diagram. The first, as observed on a quiet day, is due to high-energy photons and their degraded low-energy progeny produced in the earth's atmosphere by the galactic cosmic rays. The similarity of the next two spectra lends more confidence to our conclusion that during the earlier hours of the flight the photons observed were the high energy ones, secondary to the solar protons. That the three spectra are not exactly identical can be understood from the fact that the nuclear processes responsible for the production of the photons on a quiet day are different from the processes responsible for the γ -ray production due to solar protons, and although both types of photons are of high energy compared with auroral X rays, the quiet-day photons are much more energetic. The dissimilarity between the spectra at 0530 and 0600 UT may be due to the fact that the smooth curves in Figure 5, from which these spectra are obtained, are obtained from points about 10 minutes apart. Therefore, there is a possibility of introduction of error in the rates obtained from these plots.

The peculiarity of the first three spectra in Figure 7, which are due to high-energy photons in the atmosphere, is the peak around 50 kev resulting from the buildup in the intensity of multiple-scattered degraded photons of energy equal to the energy when the Compton cross section in the absorbing medium is equal to the photoelectric cross section. The spectra observed after 0700 UT are different from the earlier spectra with a very high relative intensity in the low-energy region between 22 and 35 kev. They do not show the peak around 50 kev, which confirms the fact that they are due to low-energy photons of the same low energy at production.

For correcting the X-ray spectra for the γ -ray effects, an average spectrum of the observed pulse-heights was determined for the period 0530 to 0600 UT, and the average excess proton rate for the same period was also determined. The at any instant the spectrum due to γ -ray effect was taken as equivalent to the average spectrum with intensity normalized to the excess proton rates at that particular instant. The spectrum obtained in this manner was subtracted from the observed spectrum at that time, and the residual spectrum thus obtained was taken as the representative spectrum of auroral X rays.

TABLE 2. Integral Energy Spectra of Photons at 10 g/cm² Atmospheric Depth

	Photon Energy, kev	Total Excess Photons, cm ⁻² ·sec ⁻¹	γ-Ray Photons, cm ⁻² ·sec ⁻¹	X-Ray Photons, cm ⁻² ·sec ⁻¹
At the peak of the aurora at 0835 UT	>22	593.0 ± 10.0	54.0	539.0
	>35	94.9 ± 1.6	46.8	48.1
	>55	42.7 ± 1.0	23.7	19.0
	>263	17.4 ± 0.6	11.3	6.1
Average for the period 0805 UT to 0925 UT	>22	114.5 ± 2.0	43.0	71.5
	>35	62.1 ± 1.0	37.3	24.8
	>55	31.6 ± 0.7	18.8	12.8
	>263	10.4 ± 0.4	9.1	1.3

Using the above-described method, we have determined the X-ray spectrum at the time of the auroral peak at 0835 UT, and an average γ-ray spectrum for the period 0805 to 0925 UT when the auroral activity was very prominent. The differential number-spectra thus obtained are tabulated in Table 2. These auroral X-ray spectra obtained are those observed at an atmospheric depth of 10 g/cm², from which we have determined the spectra at the top of the atmosphere by correcting for the loss of photons in the atmosphere. For these corrections the absorption coefficients compiled in the *Handbook of Chemistry and Physics* were used. The corrected integral energy spectra for the auroral peak and the average are shown in Figure 8. Assuming that these X rays are the bremsstrahlung radiation of the electrons striking the top of the atmosphere, and that these electrons have a kinetic energy spectrum obeying a power law of the type

$$N(>E) = CE^{-\gamma}$$

we have calculated the X-ray spectra produced by electron spectra with three different values for the exponent γ . These calculated X-ray spectra are also shown in Figure 8. For these calculations we have used computed integral number-energy spectra for the photons produced by the electrons during traversal of their entire ranges in air as calculated by J. E. Kasper (State University of Iowa, private communication).

From Figure 8 it can be seen that in the low-energy region the peak auroral X-ray spectrum agrees well with the X rays produced by electron spectrum with an exponent $\gamma \approx 7$, while the

average spectrum agrees with that due to the electron spectrum with an exponent $\gamma \approx 5$. This agreement is not very good for photon energies above about 80 kev, and it seems that the high-energy photons are due to a much less steep electron spectrum. We have also calculated the number of electrons dumped at the top of the atmosphere, and the values are as given below.

$\sim 10^9$ /cm²·sec electrons of $KE > 22$ kev at the peak of the aurora at 0835 UT

$\sim 10^{12}$ /cm² electrons of $KE > 22$ kev for the total period of 1 hr 20 min (0805 to 0925 UT)

Discussion. The auroral X rays now have been observed on many occasions at the latitude of Minneapolis when there was a visible aurora present at or near the zenith. It is believed that such subauroral-zone auroras are probably caused by the discharge of trapped electrons from the outer radiation zone. Quantitative measurements of this effect by Arnoldy, Hoffman, and Winkler [1960], based on the Explorer VI observations, show that enough electrons are dumped during a magnetic storm to cause a strong subauroral-zone X-ray storm at balloon altitudes.

In the present instance, it is possible to estimate the total energy incident on the atmosphere during the storm in the form of electrons of energy ≥ 22 kev. It is reasonable that an aurora of this intensity extended 2000 miles in longitude and 1000 miles in latitude for the 1-hr 20-min period, and both the area and the time may be lower limits. As stated before, about 10^{12} electrons/cm² of energy $E \geq 22$ kev were incident

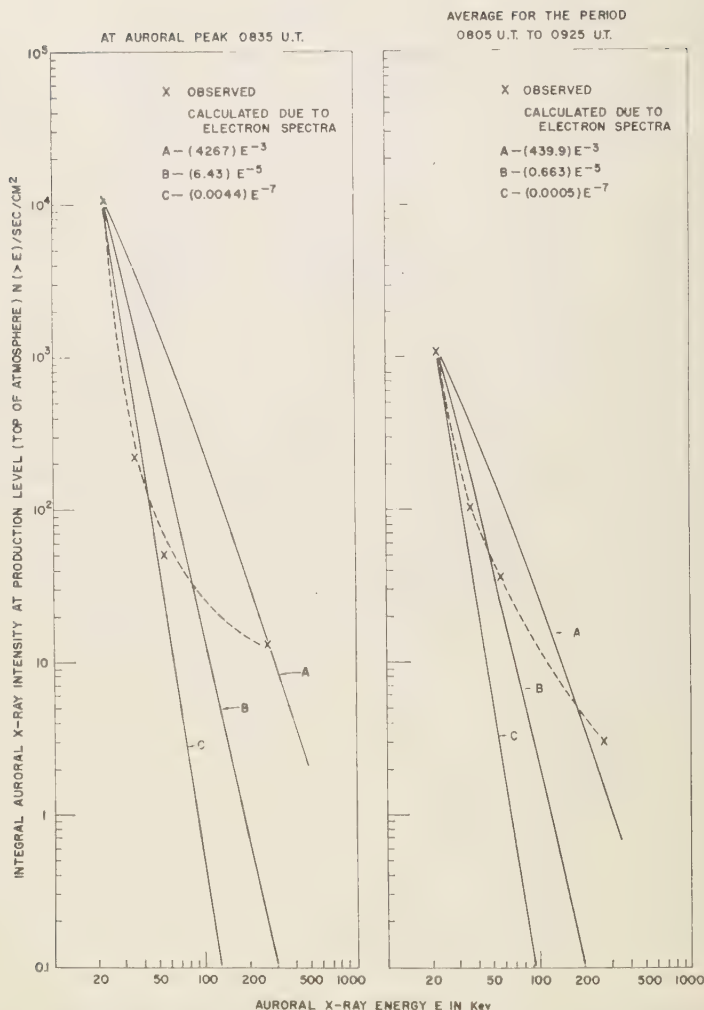


Fig. 8. Integral energy spectrum of the auroral X rays at the top of the atmosphere: at the peak of the aurora (left-hand side), and the average spectrum (right-hand side) for the period when auroral activity was predominant. Assuming that the electron spectrum responsible for the X rays obeys a power law, calculated X-ray spectra due to the electron spectrum with three different exponential values are also shown.

during the whole period at Minneapolis. This gives

E_{total}

$$= 5 \times 10^{16} \text{ cm}^2 \times 10^{12} \times 22 \times 10^3 \text{ ev} \\ \approx 10^{33} \text{ ev}$$

for the above time and area. This number appears

to be of the same order of magnitude as the energy-density value obtained for the Explorer VI observations of the outer radiation belt by *Arnoldy, Hoffman and Winckler* [1960]. Detailed comparison is postponed, however, until laboratory calibration results are available for the X-ray detection efficiency of the Explorer V payload.

We have already shown above that the electron spectrum responsible for the auroral X rays, as measured for the average X-ray spectrum, can be represented by a power law of the type

$$N(>E) = CE^{-5} \quad 22 < E < 80 \text{ kev}$$

and it seems that the spectrum becomes flatter above about 80-kev kinetic energy.

Vernov and Chudakov [1960] have measured the spectrum of the outer-radiation-zone electrons from observations made from the Soviet satellites. According to their measurements, the electron spectrum can be represented as

$$\begin{aligned} N(>E) &\sim E^{-5} & 22 < E < 100 \text{ kev} \\ N(>E) &\sim E^{-2} & \text{for electrons of higher} \\ & & \text{energy up to several Mev} \end{aligned}$$

Rocket observations of Walt, Chase, Cladis, Imhof, and Knecht [1960] also show that the energy spectrum of the outer-radiation-zone electrons becomes flat at higher energies, although, according to their results, this flattening takes place above about 500-kev electron KE energy.

Thus, our measurements of the electron spectrum responsible for the X rays observed during an auroral storm over Minneapolis are in good agreement with the electron spectrum measurements in the outer trapped-radiation zone. This strongly supports the view that the auroral X rays are caused by the dumping of the more energetic electrons from the outer radiation zone.

At the peak of the aurora, a much steeper spectrum ($\gamma \approx 7$) was observed. This may be due, however, to the way in which the observed X-ray spectrum is obtained from the telemetered data with points about 10 minutes apart. This uncertainty is reduced for the average spectrum.

Direct observations of the particles responsible for the subauroral zone auroras have not yet been attempted. Observations made in the auroral zone on two different occasions [McIlwain, 1960; Davis, Berg, and Meredith, 1960] have shown, however, that the auroras observed were produced entirely by electrons incident in the atmosphere in the energy range from about 5 to 50 kev. X-ray observations in the auroral zone made by Anderson [1960], and by Anderson and Enemark [1960], have shown that the X rays are much less intense and of lower energy compared with those observed with subauroral zone auroras. Anderson's observations, however, do not estab-

lish any connection between the X rays and the visible auroras. The less intense X rays in the auroral zone may be due to lower number density and energy of electrons trapped on the lines of force which join the auroral zone to the outer radiation zone.

Vestine and Sibley [1959] and Vestine [1960] have suggested that, during a disturbed period, trapped particles might have their lowest mirror points near magnetic midnight. Chamberlain, Kern, and Vestine [1960] suggest that because of this effect, auroral primaries may be the particles expelled from a trapped radiation zone. No detailed theory has been established on this line as yet.

Soviet satellite results [Vernov and Chudakov, 1960] have shown that at great distances the outer boundary of the outer radiation zone corresponds to the lines of force of the earth's dipole field. However, near the earth's surface the boundaries deviate from the geomagnetic parallels and coincide with the auroral isochasms.

It is premature at this point to say that all auroras are caused by the release of radiation from the outer radiation zone. There may be two types of auroras, one caused by the release from the outer radiation zone and therefore predominantly due to electrons, and a second type caused by the low-energy auroral protons and therefore predominantly due to protons. This may be also related to different forms of observed auroras at different times.

Acknowledgments. This work was supported by the joint program of the Office of Naval Research and the U. S. Atomic Energy Commission under contract Nonr-710(19). I wish to thank Professor John R. Winckler for his keen interest and helpful discussions and to acknowledge the help of Mr. R. L. Howard in designing and building the electronics for this experiment. Thanks are extended also to L. Peterson, W. Huch, and T. May; to all students of the balloon group who assisted with the preparation and launching of the balloon flight; and to all members of the Cosmic Ray Group at the University of Minnesota for their cooperation and kind help in various ways.

REFERENCES

- Anderson, K. A., Balloon observations of X rays in the auroral zone I, *J. Geophys. Research*, **65**, 551-564, 1960.
- Anderson, K. A., and D. C. Enemark, Observations of X rays at 40 km height in the auroral zone, *Space Research: Proceedings of the First International Space Science Symposium, Nice, 1960*,

- North Holland Publishing Company, Amsterdam, pp. 702-714, 1960.
- Arnoldy, R. L., R. A. Hoffman, and J. R. Winckler, Observations of the Van Allen radiation regions during August and September 1959, I, *J. Geophys. Research*, *65*, 1361-1376, 1960.
- Brown, R. R., and R. G. D'Arcy, Observations of solar flare radiation at high latitude during the period July 10-17, 1959, *Phys. Rev. Letters*, *3*, 390-392, 1959.
- Chamberlain, J. W., J. Kern, and E. M. Vestine, Some consequences of local acceleration of auroral primaries, *J. Geophys. Research*, *65*, 2535-2537, 1960.
- Davis, L. R., O. E. Berg, and L. H. Meredith, Direct measurements of particle fluxes in and near auroras, *Space Research: Proceedings of the First International Space Science Symposium, Nice, 1960*, North Holland Publishing Company, Amsterdam, pp. 721-735, 1960.
- McIlwain, Carl E., Direct measurement of protons and electrons in visible aurorae, *Space Research: Proceedings of the First International Space Science Symposium, Nice, 1960*, North Holland Publishing Company, Amsterdam, pp. 715-720, 1960.
- Vernov, S. N., and A. E. Chudakov, Terrestrial corpuscular radiation and cosmic rays, *Space Research: Proceedings of the First International Space Science Symposium, Nice, 1960*, North Holland Publishing Company, Amsterdam, pp. 751-796, 1960.
- Vestine, E. M., Polar auroral, geomagnetic, and ionospheric disturbances, *J. Geophys. Research*, *65*, 360-362, 1960.
- Vestine, E. H., and W. L. Sibley, Remarks on auroral isochoasms, *J. Geophys. Research*, *64*, 1333-1339, 1959.
- Walt, M., L. F. Chase, Jr., J. B. Cladis, W. L. Imhof, and D. J. Knecht, Energy spectra and altitude dependence of electrons trapped in the earth's magnetic field, *Space Research: Proceedings of the First International Space Science Symposium, Nice, 1960*, North Holland Publishing Company, Amsterdam, pp. 910-920, 1960.
- Winckler, J. R., Balloon study of high-altitude radiations during the International Geophysical Year, *J. Geophys. Research*, *65*, 1331-1359, 1960.
- Winckler, J. R., and P. D. Bhavsar, Low-energy solar cosmic rays and the geomagnetic storm of May 12, 1959, *J. Geophys. Research*, *65*, 2637-2655, 1960.
- Winckler, J. R., L. E. Peterson, and R. L. Howard, Balloon gear monitors cosmic radiation, *Electronics*, *31*, 76-79, 1958.

(Manuscript received January 3, 1961.)

Effect of Hydromagnetic Waves in a Dipole Field on the Longitudinal Invariant

E. N. PARKER

*Enrico Fermi Institute for Nuclear Studies and Department of Physics
University of Chicago, Chicago 37, Illinois*

Abstract. Hydromagnetic wave violation of the longitudinal invariant of a particle trapped in a mirror magnetic field is investigated quantitatively. It is shown that the passage of hydromagnetic waves across the region of mirroring leads to a diffusion of the individual-particle mirror points. If the relative wave amplitude $\Delta B/B$ is maintained throughout the mirror field, particles released in the field will soon diffuse out through the mirror and be lost. Application to thermonuclear devices is obvious. Confining our attention principally to the charged particles trapped in the geomagnetic field, it is shown that high-energy (10^6 -ev) electrons in the outer Van Allen radiation zone are caused to diffuse along the lines of force with a characteristic time of 4 months by hydromagnetic waves of 1 cps and an amplitude of 10^{-4} gauss. Hydromagnetic diffusion appears to be more important than collisions in determining the electron lifetime and distribution in the outer Van Allen radiation zone. Different wave distributions along the lines of force can give radically different particle distributions. It is shown that, if the hydromagnetic disturbances extend throughout the geomagnetic field, then, rather than yielding particle acceleration, they result in a net loss of particle energy. But if we assume a region of hydromagnetic disturbance localized inside the geomagnetic field, limited particle acceleration may result.

1. INTRODUCTION

We showed in an earlier paper [Parker, 1960] that violation of the third invariant [Northrup and Teller, 1959] of the motion of charged particles trapped in the geomagnetic field leads to significant outward diffusion of the particles. In this paper we consider violation of the second, or longitudinal, invariant, arriving at the conclusion that violations both of the second and of the third invariants by geomagnetic fluctuations play an important role in determining the equilibrium distribution of energetic particles in the outer Van Allen radiation zone, where collisional effects are negligible. We will find that the passage of hydromagnetic waves across the mirror points of trapped particles influences the distribution of Van Allen particles along the geomagnetic lines of force, just as the sudden commencement of magnetic storms, etc., was shown earlier to influence the distribution perpendicular to the lines of force.

As in our earlier paper on violation of the third invariant, we find that diffusion and particle loss proceeds much more rapidly than acceleration, so that the total energy of the particles remaining in the field decreases as a result of hydromagnetic disturbances. A general distribution of hydromagnetic waves does not constitute an accel-

erating mechanism capable of raising the total particle energy.

The concept of trapped particles scattering from hydromagnetic waves has been familiar for many years. Singer [1956] was perhaps the first to comment on the possibility of scattering and Fermi acceleration of trapped particles of solar origin. Vernov, Chudakov, Lebedinsky, and Ivanenko [1959] and Vernov and Chudakov [1960] have considered the hydromagnetic wave scattering in connection with the observed trapped electron and proton distributions in the Van Allen radiation zones. Dessler has recently been concerned with the effect of the scattering on the mirror-point distribution, which is particularly important in the theory of the gap in the outer radiation belt, discovered by Fan, Meyer, and Simpson [1960] and subsequently verified by Arnoldy, Hoffman, and Winckler [1960]. The passage of a hydromagnetic wave across the region in which a geomagnetically trapped particle is mirroring will put the mirror position in motion at the time of particle reflection. The wave will cause the mirror point to be ascending in the part of the wave in which the field is increasing, and descending where the field is decreasing. Thus the particle is reflected from a moving mirror point. The longitudinal invariant

is violated, and the result is particle acceleration by the familiar Fermi mechanism [Fermi, 1949]. The particle motion along the field gains energy from the head-on reflection, when the mirror point is ascending, and loses energy from the overtaking reflection, when the mirror is descending. There is on the average a net energy gain to the particle motion along the field. Thus Dessler concluded that the effect of hydromagnetic waves should be a systematic lowering of the mirror points.

The effect is limited to hydromagnetic waves with periods of the same order of magnitude as the particle transit time between mirror points (about 1 sec for a 100-kev electron in the outer Van Allen radiation zone). Thus the enormous magnetic excursions of 10^{-2} gauss or more, which occur with periods of half an hour during the active phase of a geomagnetic storm, are unimportant. Their only effect is on the third invariant, as discussed earlier. On the other hand, we expect [Dungey, 1955, 1958] to find hydromagnetic waves at higher frequencies, where they violate the longitudinal invariant, but unfortunately where they do not penetrate significantly through the ionosphere to be recorded directly on the ground. We have shown theoretically [Parker, 1958] that instability of the outer boundary of the geomagnetic field in the solar wind should lead to hydromagnetic waves with lengths \geq proton Larmor radius, or 100 km at about 5 earth's radii where the Alfvén velocity is roughly 500 km/sec. The wave amplitude is comparable to the field strength, $B \cong 10^{-3}$ gauss. Thus we expect theoretically to find waves with frequencies up to 5 cps, and with $\Delta B/B$ comparable to 1, at 5 earth's radii. Large-amplitude magnetic fluctuations up to about 0.5 cps have been observed beyond 5 earth's radii by the STL magnetometer studies from Pioneer I and V and Explorer VI [Coleman, Sonett, Judge, and Smith, 1960; Sonett, Smith, and Sims, 1960]. It is not clear that the observed waves are to be identified with the theoretical waves, but in any case magnetic agitation and hydromagnetic waves with $\Delta B/B \sim 1$ appear to be a normal state in the outer geomagnetic field. Propagation of such waves toward the earth involves, among other things, refraction, except at frequencies well below 1 cps, so that $\Delta B/B$ is difficult to estimate below altitudes of a few thousand kilometers.

Neglecting refraction, we estimate in section 3 that $\Delta B/B$ may be 10^{-3} near the earth.

The rate at which waves of this amplitude will redistribute the particle mirror points along the lines of force is given in correct order of magnitude by the following idealized argument: Suppose that the number of head-on reflections of a trapped particle per unit time is p_1 , and the number of overtaking reflections is p_2 . If the mirror point speed is v , the net rate of gain of energy of a particle of mass m and velocity w_{\parallel} along the field is readily shown to be

$$\frac{dE_{\parallel}}{dt} = 4E_{\parallel} \frac{v}{w_{\parallel}} \left[(p_1 - p_2) + \frac{v}{w_{\parallel}} (p_1 + p_2) \right]$$

where E_{\parallel} is the energy of motion along the field. Suppose that the hydromagnetic waves are of large scale so that along any given line of force they compress (or rarefy) the field across the entire mirror region all at the same time. Then we would expect that $p_1 = p_2$, yielding

$$dE_{\parallel}/dt = 8E_{\parallel} p_1 (v^2/w_{\parallel}^2)$$

There are much more complicated cases that could be considered, of course, involving small-scale hydromagnetic waves. But note that there is no configuration of *stable* hydromagnetic waves that will cause the energy of the random particles to *decrease* systematically, transferring energy from the individual particles to the individual massive waves. Such a circumstance would violate the second law of thermodynamics. Thus, the net effect must always be to increase the particle energy E_{\parallel} along the field, lowering the mirror point of each particle, and contributing to eventual loss of the particle by collision in the increasing density of the outer terrestrial atmosphere.

The number of reflections per unit time is of the order of w_{\parallel} divided by the distance along the lines of force from the northern to the southern mirror points, w_{\parallel}/l . A large-scale wave region yields a mirror-point motion

$$\frac{ds}{dt} = -\frac{\partial B/\partial t}{\partial B/\partial s} = 0 \left(\frac{\omega \Delta B}{\partial B/\partial s} \right)$$

To evaluate this in a dipole field we note that the field density is

$$B = B_0 \frac{(1 + 3 \cos^2 \theta)^{1/2}}{\sin^6 \theta}$$

along the line of force

$$r = a \sin^2 \theta$$

which crosses the equatorial plane at $r = a$ where $B = B_0$. Then, since arc length ds along a line of force is

$$ds = a(1 + 3 \cos^2 \theta)^{1/2} \sin \theta d\theta$$

we have

$$\partial B / \partial s = (dB/d\theta)(d\theta/ds)$$

and with $\epsilon = \Delta B/B$ we have

$$\frac{ds}{dt} \cong a\omega\epsilon \frac{\sin^2 \theta (1 + 3 \cos^2 \theta)^{3/2}}{3 \cos \theta (3 + 5 \cos^2 \theta)}$$

Taking the value at 45° as a rough estimate of the effective value of ds/dt , we have

$$\frac{ds}{dt} \cong \frac{5\sqrt{5}}{66} a\omega\epsilon \cong 0.2a\omega\epsilon$$

Thus,

$$\frac{1}{E_{\parallel}} \frac{dE_{\parallel}}{dt} = 0 \left(0.3\epsilon^2 \frac{w_{\parallel}}{l} \right) \times \frac{a^2 \omega^2}{w_{\parallel}^2}$$

If $l \cong a$ for this large-scale compression by waves with periods comparable to the transit time, l/w_{\parallel} , then we have ω/w_{\parallel} of the order of 1 and,

$$\frac{1}{E_{\parallel}} \frac{dE_{\parallel}}{dt} = 0 \left(0.3\epsilon^2 \frac{w_{\parallel}}{l} \right)$$

For electrons of 100 kev the transit time between mirror points is typically $l/w_{\parallel} \cong 1$ sec the outer Van Allen radiation zone, so that

$$(1/E_{\parallel})(dE_{\parallel}/dt) = 0(0.3\epsilon^2)$$

for the large-scale compression. If we suppose that $\Delta B/B \cong 10^{-3}$ at an altitude of 10^4 km, the characteristic diffusion time is 3×10^4 sec, or about 1 month. This is somewhat less than the estimated diffusion time [Wentworth, MacDonald, and Singer, 1959] of 3×10^5 sec resulting from collisions with the ions of the terrestrial atmosphere, or geocorona. It would appear from these crude order-of-magnitude estimates that it is principally hydromagnetic diffusion (due to violation of both the second and the third invariants) that influences the distribution and limits the life of the electrons in the outer Van Allen zone.

To put this general speculation on a firm

foundation we need, eventually, direct observation of the hydromagnetic wave spectrum throughout the geomagnetic field. With each trapped-particle energy and pitch angle there is a frequency band of hydromagnetic waves with periods comparable to the transit time between mirror points, which will be effective in scattering and accelerating the particle; waves of very long period do not violate the longitudinal invariant; waves of very short period can affect the motion only for a very brief period on each side reflection, when $w_{\parallel} \cong 0$.

As we will see from the formal calculations in the next section, it is of basic importance to know how well the hydromagnetic waves are able to penetrate into the dense atmosphere below altitudes of a few thousand kilometers, because the mirror points can diffuse downward only as far as the hydromagnetic waves extend: if at times the waves should propagate down to levels where particle collisions with the atmosphere are important, the mirror points will be lowered to where the particles are lost by collision with the atoms and ions of the atmosphere; if the waves are refracted and reflected back before such atmospheric depths are reached, there will be no lowering of mirror points into the atmosphere and no enhanced particle loss by collision. The calculations show the particle density to decrease along the lines of force toward increasing field strength in the former case, and to be increasing nearly proportional to the field in the latter case. It may prove possible to observe these effects in the laboratory mirror machine, to which the formal calculations should be roughly applicable, demonstrating the particle diffusion under various hydromagnetic wave conditions.

To formulate the basic problem at hand, consider an electron trapped in the geomagnetic field and oscillating along the lines of force between mirror points in the northern and southern hemispheres. We inquire into the conditions necessary to alter the longitudinal invariant I_L ,

$$I_L \equiv \oint ds \cdot w \quad (1)$$

where the integration is along the line of force between mirror points and w is the particle velocity. It can be shown [Northrup and Teller, 1959] that, if the magnetic field along the line of

force on which the particle is moving should change in a time which is not long compared with the transit time,

$$T \equiv \frac{1}{2} \oint \frac{ds}{w_{\parallel}}$$

between mirror points, then I_L may vary with time. There results a systematic change in the component w_{\parallel} of the particle velocity along the line of force, with a corresponding change in location of the mirror points. The velocity of a 10^2 -kev electron is of the order of 10^{10} cm/sec. The distance between mirror points in the geomagnetic field may be 3×10^4 km, so that the transit time may be as much as 1 sec. Thus hydromagnetic waves with periods as long as 1 sec may cause I_L to vary.

In section 2 we make a rough estimate of the direction and rate of change of I_L and w_{\parallel} for hydromagnetic waves of a given amplitude ϵ and frequency ω . It follows, of course, that the wave frequency ω is small compared with the cyclotron frequency of trapped electrons and of the protons trapped in the inner belt. Thus the first invariant I_n is preserved, where

$$I_n = w_{\perp}^2/B \quad (2)$$

where w_{\perp} represents the particle velocity perpendicular to the field of density B .

2. PARTICLE DIFFUSION WHEN LONGITUDINAL INVARIANT IS VIOLATED

A. Individual Particle Motion

The essential feature of a hydromagnetic wave sweeping across the mirror point of a charged particle in the geomagnetic field is its compression of the field in the vicinity of the mirror point. Consider the motion of a particle along a line of force in the z direction in a slowly varying magnetic field of density $B(z, t)$. Then from the guiding center approximation the particle acceleration¹ is

$$\frac{d^2 z}{dt^2} = -\frac{w_n^2}{2B} \frac{\partial B}{\partial z} \quad (3)$$

¹ Since our calculations are nonrelativistic they do not recognize the mass changes that will accumulate through repeated scattering of electrons with energies initially greater than a few hundred kev. Our results are therefore only qualitatively correct for these higher energies.

The transverse particle velocity w_n is subject to the invariant condition (2), so that, if $w_n = w_0$ at a position and time where $B(z, t) = B_0$, we have

$$\frac{d^2 z}{dt^2} = -\frac{w_0^2}{2B_0} \frac{\partial B}{\partial z}$$

Without loss of generality we may write $\partial B/\partial z$ as

$$\frac{\partial B}{\partial z} = \frac{B_0}{a} f(z, t)$$

where a is the scale of variation of B in the z direction. Then expanding in ascending powers of z we have

$$\frac{d^2 z}{dt^2} = -\frac{w_0^2}{2a} \left[f(0, t) + \left. \frac{\partial f}{\partial z} \right|_{z=0} z + \dots \right]$$

As a first approximation we drop all but the first term in the expansion, obtaining

$$\frac{d^2 z}{dt^2} = -\frac{w_0^2}{2a} f(0, t) \quad (4)$$

The field configuration is shown in Figure 1. The approximation reduces the hydromagnetic wave to essentially a uniform compression. It neglects the motion of the wave crest along the lines of force and thereby omits the higher probability of a head-on reflection as compared with an overtaking one. Hence the approximation will yield a lower limit to the particle acceleration and diffusion.

Assuming the field compression to be the result of a hydromagnetic wave of amplitude ϵ , frequency ω , and phase δ , we let

$$f(0, t) = 1 + \epsilon \sin(\omega t - \delta) \quad (5)$$

Then, if $dz/dt = w_{s0}$ and $z = 0$ when $t = 0$, (4) may be integrated to give

$$\begin{aligned} \frac{dz}{dt} &= w_{s0} - \frac{w_{n0}^2}{2a} t \\ &+ \frac{w_{n0}^2 \epsilon}{2a\omega} [\cos(\omega t - \delta) - \cos \delta] \end{aligned} \quad (6)$$

and

$$\begin{aligned} z &= w_{s0} t - \frac{w_{n0}^2}{4a} t^2 \\ &+ \frac{w_{n0}^2 \epsilon}{2a\omega^2} [\sin(\omega t - \delta) - \omega t \cos \delta + \sin \delta] \end{aligned} \quad (7)$$

The particle enters the region $z \geq 0$ of hydromagnetic wave compression when $t = 0$. The

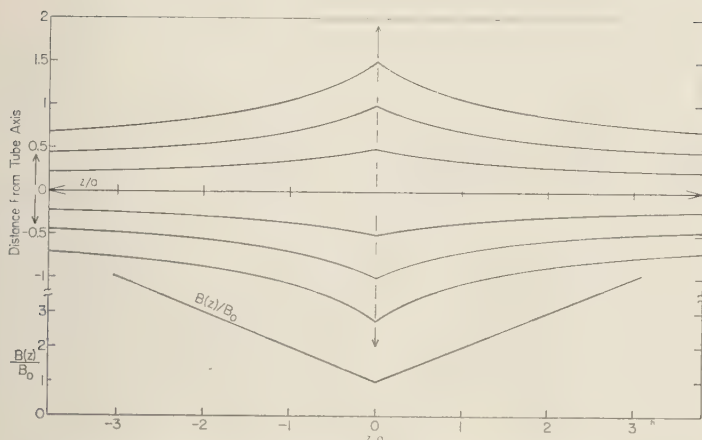


Fig. 1. A map of the lines of force of the field with axial symmetry, in which $B(z) = B_0(1 + z/a)$ shown in the lower curve. The field is taken to be along the z axis, with π representing radial distance measured from the axis. The charged particles under consideration are supposed to oscillate across the $z = 0$ plane, mirroring in the stronger field to the right and left. The simple model (equation 4) for the hydromagnetic waves is equivalent to a uniform compression perpendicular to the z axis of the field independently in each region $z > 0$ and $z < 0$.

particle is reflected at time t_n , given by the root of

$$0 = w_{s0} - \frac{w_{n0}^2}{2a} t_n + \frac{w_{n0}^2 \epsilon}{2a\omega} \cdot [\cos(\omega t_n - \delta) - \cos \delta] \quad (8)$$

from a position $z_n (>0)$, and returns to $z = 0$ at time t given by the root of

$$0 = w_{s0} t - \frac{w_{n0}^2}{4a} t^2 + \frac{w_{n0}^2 \epsilon}{2a\omega^2} [\sin(\omega t - \delta) - \omega t \cos \delta + \sin \delta] \quad (9)$$

at which time the particle velocity may be computed from (6) with the value of t determined from (9). The velocity will in general be different from the initial speed, and the difference will be a function of ϵ , ω , and δ . It will be supposed that the phase of the wave is independent of the particle motion, and therefore random. It is required to compute the change in particle velocity averaged over δ . We restrict our calculations to sufficiently low values of ω that $\omega t < 1$ as the particle returns to $z = 0$, so that we may expand the root of (9) in ascending powers of ω ,

$$t = \sum_{n=0}^{\infty} f_n \omega^n$$

and substitute into (9). Equating to zero the coefficients of each power of ω , we obtain

$$\begin{aligned} f_0 &= \frac{4aw_{s0}}{w_{n0}^2(1 - \epsilon \sin \delta)} \\ f_1 &= -\frac{16\epsilon a^2 w_{s0}^2 \cos \delta}{3w_{n0}^4(1 - \epsilon \sin \delta)^3} \\ f_2 &= -\frac{16a^3 w_{s0}^3 \epsilon}{3w_{n0}^6(1 - \epsilon \sin \delta)^5} \cdot \left[\sin \delta - \epsilon \left(1 + \frac{5}{3} \cos^2 \delta \right) \right] \end{aligned}$$

The velocity of the particle upon returning to $z = 0$ is, then,

$$\begin{aligned} \frac{dz}{dt} &= -w_{s0} \left\{ 1 + \frac{4a\omega w_{s0} \epsilon \cos \delta}{3w_{n0}^2(1 - \epsilon \sin \delta)^2} \right. \\ &\quad \left. + \frac{8a^2 \omega^2 w_{s0}^2 \epsilon}{3w_{n0}^4(1 - \epsilon \sin \delta)^4} \right\} \\ &\quad \cdot [\sin \delta - \epsilon(1 + \frac{1}{3} \cos^2 \delta)] \end{aligned}$$

The change in speed from the initial value of w_{s0} is

$$\begin{aligned} \Delta w_{s0} &= w_{s0} \frac{4a\omega w_{s0} \epsilon}{3w_{n0}^2} \\ &\quad \cdot \left\{ \frac{\cos \delta}{(1 - \epsilon \sin \delta)^2} + \frac{2a\omega w_{s0}}{w_{n0}^2(1 - \epsilon \sin \delta)^4} \right. \\ &\quad \left. \cdot [\sin \delta - \epsilon(1 + \frac{1}{3} \cos^2 \delta)] \right\} \end{aligned}$$

The time of initial arrival $t = 0$ of the particle at $z = 0$ is taken to be independent of the phase δ of the hydromagnetic wave. Averaging over δ gives

$$\langle \Delta w_s \rangle \equiv \frac{1}{2\pi} \int_0^{2\pi} d\delta \Delta w_s = w_{s0} \frac{4a^2 \omega^2 w_{s0}^2 \epsilon}{3\pi w_{n0}^4} \cdot \int_0^{2\pi} d\delta \frac{[\sin \delta - \epsilon(1 + \frac{1}{3} \cos^2 \delta)]}{(1 - \epsilon \sin \delta)^4}$$

Assuming that $\epsilon \ll 1$ yields

$$\langle \Delta w_s \rangle \cong \frac{20}{9} w_{s0} \frac{a^2 \omega^2 w_{s0}^2}{w_{n0}^4} \epsilon^2 + 0(\epsilon^3)$$

Similarly, remembering that $\omega t \cong \omega f_0$, we have

$$\begin{aligned} \langle (\Delta w_s)^2 \rangle &= \frac{1}{2\pi} \int_0^{2\pi} d\delta (\Delta w_s)^2 \\ &\cong \frac{8}{9} w_{s0}^2 \frac{a^2 \omega^2 w_{s0}^2 \epsilon^2}{w_{n0}^4} \\ &\quad \cdot [1 + 0(\omega^2 f_0^2)] + 0(\epsilon^3) \end{aligned}$$

The mean and mean square velocity changes per unit time are these expressions divided by f_0 , or

$$\langle \Delta w_s \rangle_\tau = 5w_{s0}^2 a \omega^2 \epsilon^2 / 9w_{n0}^2 \quad (10)$$

$$\langle (\Delta w_s)^2 \rangle_\tau = 2w_{s0}^3 a \omega^2 \epsilon^2 / 9w_{n0}^2. \quad (11)$$

B. Particle Distribution

i. General equations. The particle distribution ψ over longitudinal velocity $u \equiv w_{s0}$ after a time τ may be computed from the Fokker-Planck equation

$$\begin{aligned} \frac{\partial \psi}{\partial \tau} &= \frac{1}{2} \frac{\partial^2}{\partial u^2} [\psi \langle (\Delta w_s)^2 \rangle_\tau] \\ &\quad - \frac{\partial}{\partial u} [\psi \langle \Delta w_s \rangle_\tau] \end{aligned} \quad (12)$$

with the assumption that the hydromagnetic waves are uncorrelated between consecutive passages. This is not an altogether valid assumption when $\omega t < 1$, but to the order in ϵ that we are considering the effective scattering after the passage of many waves is not altered. It requires only a larger number of particle reflections before the wave phase δ distribution may be considered random. In terms of the dimensionless variables,

$$s \equiv \partial \omega^2 \epsilon^2 \tau / 9w_{n0} \quad (13)$$

$$\xi \equiv w_{s0} / w_{n0} \quad (14)$$

(12) may be rewritten with the aid of (10) and (11) to be

$$\frac{\partial \psi}{\partial s} = \frac{\partial^2}{\partial \xi^2} (\xi^3 \psi) - 5 \frac{\partial}{\partial \xi} (\xi^2 \psi) \quad (15)$$

ii. Idealized model. To demonstrate the general diffusion properties resulting from hydromagnetic waves we first adopt the simple model that $z = 0$ represents the equatorial plane of the geomagnetic field and $z = \infty$ represents the terrestrial atmosphere where particles are lost by diffusion, as shown in Figure 1. It will then be a simple matter to demonstrate the diffusive migration of particles by introducing small bunches of particles at various points. Following the treatment of this illustrative case we will go on to models whose boundary restraints more closely relate to the circumstances obtained in the geomagnetic field.

We assume symmetry of the static geomagnetic field, the hydromagnetic wave intensity, and the particle distribution about the geomagnetic dipole axis and about the equatorial plane. We neglect radial diffusion due to sudden commencements, as previously computed [Parker, 1960]. Our boundary conditions are that ψ vanish at $\xi = \infty$ and that there be no particle flux approaching $\xi = 0$, i.e.,

$$0 = (\partial / \partial \xi) (\xi^3 \psi) - 5\xi^2 \psi \quad (16)$$

at $\xi = 0$.

The general solution to (15) which satisfies the boundary conditions at $\xi = 0$ and $\xi = \infty$ is

$$\psi(s, \xi) = \int_0^\infty d\Omega \Omega F(\Omega) \exp\left(-\frac{\Omega^2 s}{4}\right) J_4\left(\frac{\Omega}{\xi^{1/2}}\right)$$

where $F(\Omega)$ is an arbitrary function of Ω . In terms of the initial distribution $\psi(0, \xi)$ we have

$$F(\Omega) = \frac{1}{2} \int_0^\infty \frac{d\xi}{\xi^2} \psi(0, \xi) J_4\left(\frac{\Omega}{\xi^{1/2}}\right)$$

by the usual Fourier-Bessel inversion theorem, and hence

$$\begin{aligned} \psi(s, \xi) &= \frac{1}{2} \int_0^\infty \frac{d\mu}{\mu} \psi(0, \mu) \\ &\quad \cdot \int_0^\infty d\Omega \Omega \exp\left(-\frac{\Omega^2 s}{4}\right) J_4\left(\frac{\Omega}{\xi^{1/2}}\right) J_4\left(\frac{\Omega}{\mu^{1/2}}\right) \\ &= \frac{1}{s} \exp\left(-\frac{1}{s\xi}\right) \int_0^\infty \frac{d\mu}{\mu^2} \psi(0, \mu) \\ &\quad \cdot \exp\left(-\frac{1}{\mu s}\right) I_4\left(\frac{2}{s\mu^{1/2}\xi^{1/2}}\right) \end{aligned} \quad (17)$$

If a delta function distribution of N particles is introduced at $\xi = \xi_0$ when $s = 0$, then

$$\psi(0, \xi, \xi_0) = (N/w_{n0}) \delta(\xi - \xi_0) \quad (18)$$

and

$$\psi(s, \xi, \xi_0) = \frac{N}{w_{n0}\xi_0^2 s} \cdot \exp \left[-\frac{1}{s} \left(\frac{1}{\xi} + \frac{1}{\xi_0} \right) \right] I_4 \left(\frac{2}{s\xi_0^{1/2}\xi^{1/2}} \right) \quad (19)$$

The particle distribution, for sufficiently large values of time that $s\xi_0 \gg 1$, is given by the asymptotic form

$$\psi(s, \xi, \xi_0) \sim \frac{N}{24w_{n0}\xi_0^4 s^5 \xi^2} \exp \left(-\frac{1}{\xi s} \right) \quad (20)$$

which is valid for all values of ξ sufficiently large that ψ is nonnegligible. The distribution is a single wave (similar to that discussed in connection with violation of the third invariant) whose maximum density is at ξ_{\max} ,

$$\xi_{\max} = 1/2s \quad (21)$$

approaching the origin with a velocity proportional to $1/s^2$. The total number of particles in the wave is n ,

$$n \equiv \int_0^\infty du \psi(s, u, \xi_0) \sim N/(24\xi_0^4 s^4) \quad (22)$$

which diminishes to zero like s^{-4} . The particles are not conserved, because the flux at $\xi = \infty$ is nonvanishing for finite s . The flux is, in fact,

$$\begin{aligned} \text{Flux} &= -\frac{1}{2} \frac{\partial}{\partial u} [\psi \langle (\Delta w_s)^2 \rangle_\tau] + \psi \langle \Delta w_s \rangle, \\ &= \frac{a\omega^2 \epsilon^2}{9} \left[2\xi^2 \psi - \xi^3 \frac{\partial \psi}{\partial \xi} \right] \end{aligned}$$

With the asymptotic form (20) we obtain

$$\text{Flux} \sim \frac{a\omega^2 \epsilon^2 N}{54w_{n0}\xi_0^4 s^5} \exp \left(-\frac{1}{\xi s} \right) \left(1 - \frac{1}{4\xi s} \right)$$

in the limit as $\xi \rightarrow \infty$ we have

$$\text{Flux} \sim \frac{a\omega^2 \epsilon^2 N}{54w_{n0}\xi_0^4 s^5}$$

so that after a time τ the flux carries away the n particles remaining

$$\int_t^\infty d\tau \text{ Flux} = \frac{N}{24\xi_0^4 s^4} = n$$

We see then that the particles leak out of the outer side of the particle wave, at the same time that the wave drifts toward $\xi = 0$ as given by (21). This is qualitatively similar to the radial diffusion due to magnetic-storm violation of the third invariant [Parker, 1960].

If we introduce particles at ξ_0 at a steady rate of N/sec , the resulting stationary particle distribution $\Psi(\xi, \xi_0)$ is given by

$$\begin{aligned} \Psi(\xi, \xi_0) &= \int_{-\infty}^\tau dq \psi(\tau - q, \xi, \xi_0) \\ &= \frac{9w_{n0}}{a\omega^2 \epsilon^2} \int_0^\infty ds \psi(s, \xi) \end{aligned} \quad (23)$$

where ψ is the distribution (19) for a single bunch of N particles. Then from Watson [1958], who uses Barne's notation for the associated Legendre function, we have

$$\begin{aligned} \Psi(\xi, \xi_0) &= \frac{9N2^{1/2}}{a\omega^2 \epsilon^2 \xi_0^2 \pi^{1/2}} \\ &\quad \cdot \frac{Q_{7/2}^{-1/2}(\cosh \alpha) \sinh^{1/2} \alpha}{\sin 4\pi} \end{aligned}$$

where

$$\cosh \alpha = \frac{\xi + \xi_0}{2(\xi\xi_0)^{1/2}}$$

Then, since [Hobson, 1955]

$$\begin{aligned} \frac{Q_{7/2}^{-1/2}(x)}{\sin 4\pi} &= -\frac{\pi^{1/2}}{2^{13/2} x^4 (x^2 - 1)^{1/4}} \\ &\quad \cdot F \left(\frac{5}{2}, 2; 5; \frac{1}{x^2} \right) \\ &= -\frac{\pi^{1/2}}{2^{6/2} (x^2 - 1)^{1/4} [x + (x^2 - 1)^{1/2}]^4} \end{aligned}$$

we have

$$\Psi(\xi, \xi_0) = \frac{9N}{4a\omega^2 \epsilon^2 \xi_0^2} \left(\frac{\xi_0}{\xi} \right)^2 \quad (24)$$

for $\xi > \xi_0$. For $\xi < \xi_0$ we choose the opposite sign for $(x^2 - 1)^{1/2}$ in $Q_{7/2}^{-1/2}$ and obtain

$$\Psi(\xi, \xi_0) = \frac{9N}{4a\omega^2 \epsilon^2 \xi_0^2} \left(\frac{\xi}{\xi_0} \right)^2 \quad (25)$$

The result may be obtained directly from (12) by putting $\partial\psi/\partial\tau = 0$ and requiring that the

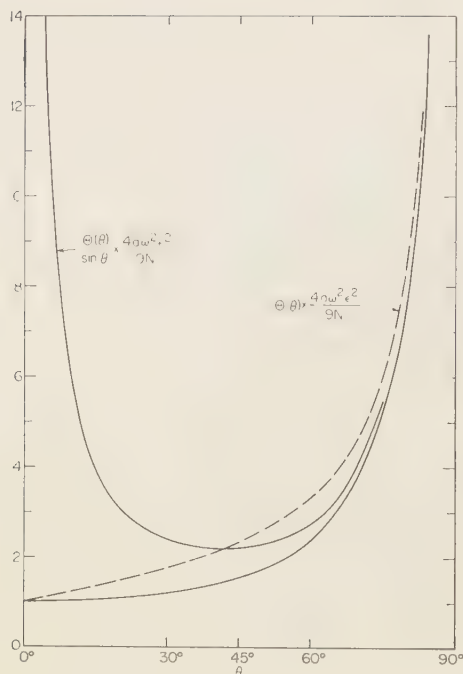


Fig. 2. Plot of the total number of particles $\Theta(\theta)$ per unit pitch angle while crossing $z = 0$, and of the total number of particles $\Theta(\theta)/(\sin \theta)$ per unit solid angle while crossing $z = 0$. The broken line represents $1 + \tan \theta$, which we use as a rough approximation to $\Theta(\theta)$.

total flux be N/sec in $\xi > \xi_0$ and zero in $\xi < \xi_0$. The total number of particles N_t is

$$\begin{aligned} N_t &\equiv w_{n0} \int_0^\infty d\xi \Psi(\xi, \xi_0) \\ &= \frac{3Nw_{n0}}{a\omega^2 \epsilon^2 \xi_0} \end{aligned} \quad (26)$$

so that the mean life is

$$T = \frac{N_t}{N} = \frac{3w_{n0}}{a\omega^2 \epsilon^2 \xi_0} \quad (27)$$

Now, to construct an example which may have some relevance to the Van Allen belt, we inject particles into $(\xi_0, \xi_0 + d\xi_0)$ at a rate $f(\xi_0) N d\xi_0$. The resulting distribution is

$$\Phi(\xi) = \int_0^\infty d\xi_0 f(\xi_0) \Psi(\xi, \xi_0) \quad (28)$$

As an example suppose that particles are introduced isotropically at the equatorial plane, so that their distribution in pitch angle θ is $\sin \theta$. Since

$$\xi = \cot \theta$$

it follows that

$$f(\xi) = \sin \theta \frac{d\theta}{d\xi} = \frac{1}{(1 + \xi^2)^{3/2}}$$

Putting (24) and (25) into (28), we obtain

$$\begin{aligned} \Phi(\xi) &= \frac{6N}{a\omega^2 \epsilon^2} \\ &\cdot \left[\xi^2 + \frac{(1 + \xi^2)^{1/2}(1 - 2\xi^2)}{2\xi} \right] \end{aligned} \quad (29)$$

The distribution over pitch angle, $\Theta(\theta)$ of all the particles crossing $z = 0$ is

$$\begin{aligned} \Theta(\theta) &= \Phi(\xi) (d\xi/d\theta) w_{n0} \\ &= \frac{3Nw_{n0}(1 + 2 \cos \theta)}{a\omega^2 \epsilon^2 \cos \theta (1 + \cos \theta)^2} \end{aligned} \quad (30)$$

which is plotted in Figure 2.

The divergence at $\theta = \pi/2$ is of the form

$$\Theta(\theta) \sim \frac{3Nw_{n0}}{a\omega^2 \epsilon^2} \tan \theta \quad (31)$$

and will be discussed in terms of the total particle density later. The nonvanishing of $\Theta(\theta)$ at $\theta = 0$ does not imply a divergence in the particle density, because $\Theta(\theta)$ is the number of particles everywhere along the field with pitch angle θ when crossing $z = 0$. As may be seen by taking $B_1 \rightarrow \infty$ in (41), the density per unit volume is finite.

Now consider the case where an atmosphere stops all particles with pitch angle less than θ_1 .

iii. *Atmospheric model.* Suppose that we require $\psi = 0$ for $\xi \leq \xi_1$, because particles for which $\xi > \xi_1$ would mirror below the 'top' of the atmosphere and so be lost. Then $\psi(s, \xi)$ is of the form

$$\psi(s, \xi) = \sum_{n=1}^{\infty} A_n \exp\left(-\frac{\Omega_n^2 s}{4}\right) J_4\left(\frac{\Omega_n}{\xi^{1/2}}\right) \quad (32)$$

where the Ω_n are the roots of

$$J_4(\Omega_n/\xi_1^{1/2}) = 0$$

The functions analogous to (19), (24), (25), and (28) are readily computed in a manner analogous to the calculations in article *ii*. The function of principal interest is the steady-state solution Ψ resulting from a steady introduction at $\xi_0 (< \xi_1)$ at a rate N/sec , which is readily shown to be

$$\Psi(\xi, \xi_0) = \frac{9N}{4a\omega^2 \epsilon^2 \xi_1^2} \times \begin{cases} \left[\left(\frac{\xi_1}{\xi_0} \right)^2 - \left(\frac{\xi_0}{\xi_1} \right)^2 \right] \left(\frac{\xi}{\xi_0} \right)^2 & \text{for } \xi < \xi_0 \\ \left[\left(\frac{\xi_1}{\xi} \right)^2 - \left(\frac{\xi}{\xi_1} \right)^2 \right] & \text{for } \xi_0 < \xi < \xi_1 \\ 0 & \text{for } \xi > \xi_1 \end{cases}$$

If we introduce particles into $\xi < \xi_1$, with an isotropic distribution at a rate $N/\Delta\pi$ per second per steradian, then the distribution over ξ is

$$\begin{aligned} \Psi(\xi) &= \frac{9N}{4a\omega^2 \epsilon^2 \xi_1^2} \left\{ \int_0^\xi \frac{d\xi_0}{(1 + \xi_0^2)^{3/2}} \right. \\ &\quad \cdot \left[\left(\frac{\xi_1}{\xi} \right)^2 - \left(\frac{\xi}{\xi_1} \right)^2 \right] + \int_\xi^{\xi_1} \frac{d\xi_0}{(1 + \xi_0^2)^{3/2}} \\ &\quad \cdot \left[\left(\frac{\xi_1}{\xi_0} \right)^2 - \left(\frac{\xi_0}{\xi_1} \right)^2 \right] \left(\frac{\xi}{\xi_0} \right)^2 \Big\} \\ &= \frac{3N}{a\omega^2 \epsilon^2} \left\{ \frac{\xi^2(2\xi_1^2 + 1)(\xi_1^2 - 1)}{\xi_1^3(1 + \xi_1^2)^{1/2}} \right. \\ &\quad \left. + \frac{(1 - 2\xi^2)(1 + \xi^2)^{1/2}}{\xi} \right\} \end{aligned} \quad (33)$$

It is obvious that when $\xi_1 \gg 1$ this expression reduces to our earlier expression (29) for all values of ξ . Hence, when $\xi_1 \gg 1$, the principal change is to cut off the distribution (29) at ξ_1 , or at θ_1 , where

$$\theta_1 \cong 1/\xi_1$$

The expression (30) is valid for $\theta < \theta_1$ and is plotted in Figure 2. The number of particles per unit solid angle is $\Theta(\theta)/2\pi \sin \theta$, which is also shown in Figure 2.

To calculate the particle density we consider the flux of particles across $z = 0$ with pitch angle ϑ in the interval $(\theta, \theta + d\theta)$. Elsewhere along the line of force the pitch angle ϑ of these particles is related to θ by (2), so that

$$\sin^2 \vartheta = \sin^2 \theta (B/B_0) \quad (34)$$

if B_0 is the field density at $z = 0$. With the approximation used in (4) we note that

$$B = B_0(1 + z/a) \quad (35)$$

The number of particles per unit volume in $(\theta, \theta + d\theta)$ at $z = 0$ is denoted by $F(\theta) d\theta$. Then, if each particle passes $z = 0$ twice every f_0 seconds with a velocity w_{z0} , and if the cross-sectional area of the field is A_0 at $z = 0$, we have

$$F(\theta) = \frac{2\Theta(\theta)}{A_0 w_{z0} f_0} = \frac{\Theta(\theta)}{2a A_0 \xi^2} \quad (36)$$

neglecting terms $O(\epsilon^2)$.

If we consider the flux of such particles along a flux tube of cross section A , then, with

$$AB = A_0 B_0$$

we have

$$A_0 w_{z0} F(\theta) d\theta = A w_z H(\vartheta, z) d\vartheta$$

where $H(\vartheta, B)$ is the distribution over pitch angles ϑ at B ; at $B = B_0$ we have $\vartheta = \theta$. It follows that

$$\begin{aligned} H(\vartheta, B) &= (B/B_0)^{1/2} F(\theta) \\ &= \frac{1}{2a A_0} \left(\frac{B}{B_0} \right)^{1/2} \frac{\Theta[\theta(\vartheta)]}{\cot^2 \theta(\vartheta)} \end{aligned} \quad (37)$$

The particle density is, then,

$$N(B) = \int_{\arcsin(B/B_0)^{1/2}}^{\pi/2} d\vartheta H(\vartheta, B) \quad (38)$$

Far down the tube where $B \gg B_0$ it is the small values of θ that contribute; all larger values of θ have already been mirrored and turned back. Thus

$$\Theta(\theta) \sim \frac{9N w_{z0}}{4a\omega^2 \epsilon^2} \quad (39)$$

On the other hand, near $B = B_0$ it is the very large number near $\theta = \pi/2$ (see equation 31) that contribute most of the density, yielding

$$\Theta(\theta) \sim \frac{3N w_{z0}}{a\omega^2 \epsilon^2} \tan \theta \quad (40)$$

The sum of these two asymptotic expressions is a rough approximation to (33) (for large ξ_1), as may be seen from the broken line in Figure 2. Thus we compute the particle density $N_1(B)$

from (39), which is the principal density when $B \gg B_0$,

$$N_1(B) = \frac{9Nw_{n0}}{8A_0a^2\omega^2\epsilon} \left(\frac{B}{B_0}\right)^{1/2} \left\{ -\left[\frac{\pi}{2} - \arcsin\left(\frac{B}{B_1}\right)^{1/2}\right] + \frac{1}{(1 - B_0/B)^{1/2}} \cdot \left[\frac{\pi}{2} - \arcsin\left(\frac{B/B_0 - 1}{B_1/B_0 - 1}\right)^{1/2}\right] \right\} \quad (41)$$

As $B \rightarrow B_1 \gg B_0$, we let $B = B_1(1 - \delta)$, obtaining

$$N_1(B) \sim \frac{9Nw_{n0}}{8A_0a^2\omega^2\epsilon} \delta^{1/2} \left(\frac{B_0}{B_1}\right)^{1/2}$$

When $B \rightarrow B_0$ we let $B = B_0(1 + \Delta)$, obtaining

$$N_1(B) \sim \left(\frac{\pi}{2\Delta^{1/2}} - \frac{\pi}{2}\right) \frac{9Nw_{n0}}{8A_0a^2\omega^2\epsilon}$$

We compute the density $N_2(B)$ from (40), which is the principal density when $B \cong B_0$,

$$N_2(B) = \frac{3Nw_{n0}}{2A_0a^2\omega^2\epsilon} \left\{ \frac{(1 - B/B_1)^{1/2}}{(1 - B_0/B)(1 - B_0/B_1)^{1/2}} - \left(\frac{B}{B_0}\right)^{1/2} \ln \left[\frac{(1 - B/B_1)^{1/2} + (B/B_0)^{1/2}(1 - B_0/B_1)^{1/2}}{(B/B_0 - 1)^{1/2}} \right] \right\}. \quad (42)$$

As $B \rightarrow B_1 \gg B_0$ we again let $B = B_1(1 - \delta)$, obtaining

$$N_2(B) \sim \frac{3Nw_{n0}}{2A_0a^2\omega^2\epsilon} \frac{B_0}{B_1} \delta^{1/2}$$

As $B \rightarrow B_0$ we let $B = B_0(1 + \Delta)$, obtaining the divergent form

$$N_2(B) \sim \frac{3Nw_{n0}}{2A_0a^2\omega^2\epsilon} \left\{ \frac{1}{\Delta} - \frac{1}{2} \ln \frac{1}{\Delta} \right\}$$

The sum of (41) and (42) is a rough approximation to $N(B)$ everywhere,

$$N(B) \approx N_1(B) + N_2(B) \quad (43)$$

We note that both N_1 and N_2 , and therefore N , diverge as $B \rightarrow B_0$. The reason for this is that Δw_s , on which the diffusion depends, vanishes there in our oversimplified model, (4).

Yet, by insisting that an isotropic distribution is continually introduced at $z = 0$, we are constantly putting in particles which mirror at $B = B_0$, i.e., $\theta = \pi/2$, which pile up to infinite density before they can escape. This is obviously the fault of our artificial model, which is avoided in the next example by the simple expedient of not continually adding particles at $\theta = \pi/2$. Adding an isotropic distribution at $z > 0$ would suffice, and the reader may, if he wishes, fit the solution of the next example on to the solution of this example to avoid the divergence at $B = B_0$.

What is of principal interest in the present example, in which there is a continual flux of particles toward smaller pitch angles and lower mirror points, is that

$$N(B) \sim N_1(B)$$

at large B , and, as may be seen from Figure 1, for the special case that $B_1 = 100B_0$, $N(B)$ decreases monotonically with increasing B . This is in sharp contrast to the next example where we assume no net flux.

iv. Cutoff model. Suppose that the hydro magnetic wave amplitude diminishes with in-

creasing field density so that the flux into the atmosphere is relatively small. We may achieve a rough approximation to this case with our present model by supposing $f(z, t)$ to be a step function. We suppose that there are no hydro magnetic waves where $B > B_2$, so that only particles with mirror points above B_2 experience the passage of waves during their mirroring. It follows that diffusion goes rapidly to zero as $\xi = \xi_2$, where

$$1 + \xi_2^2 = B_2/B_0$$

The system is closed off at ξ_2 , so that there is no net loss. The initial number of particles is preserved. Our boundary conditions in $B_0 < B < B_2$ are simply the requirement of zero flux at both $\xi = 0$ and $\xi = \xi_2$. Then $\psi(s, \xi)$ is of the form (32), where the Ω_n are now determined by the condition that

$$0 = \frac{\Omega_n}{\xi_2^{1/2}} J_4' \left(\frac{\Omega_n}{\xi_2^{1/2}} \right) + 4 J_4 \left(\frac{\Omega_n}{\xi_2^{1/2}} \right) \quad (44)$$

there is no net flux out of the region $\xi < \xi_0$, so that, if N particles are introduced with $\theta > \theta_2$, they will eventually take up the stationary distribution

$$\Phi(\xi) = \frac{3N}{w_{n0}\xi_2^3} \xi^2 \quad (45)$$

to compute the particle density per unit volume. Note from (37) that

$$\begin{aligned} H(\vartheta, B) &= \frac{1}{2aA_0} \left(\frac{B}{B_0} \right)^{1/2} \frac{\Phi(\xi)w_{n0}}{\xi^2} \frac{d\xi}{d\vartheta} \\ &= \frac{3N}{2aA_0\xi_2^3} \left(\frac{B}{B_0} \right)^{3/2} \frac{1}{\sin^2 \vartheta} \end{aligned}$$

thus it follows that

$$N(B) = \frac{3N}{2aA_0} \frac{B/B_2}{(1 - B_0/B_2)} \left(\frac{1 - B/B_2}{1 - B_0/B_2} \right)^{1/2} \quad (46)$$

particles/cm³

where $B \geq B_2$.

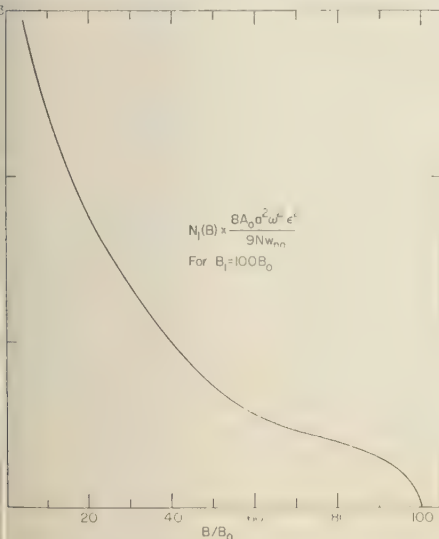


Fig. 3. The particles per unit volume $N_1(B)$ when particles are introduced isotropically at $B = B_0$ and absorbed at $B = B_1$ for the special case that $B_1 = 100B_0$. This density is the principal density for $B \gg B_0$ and decreases rapidly with increasing B .

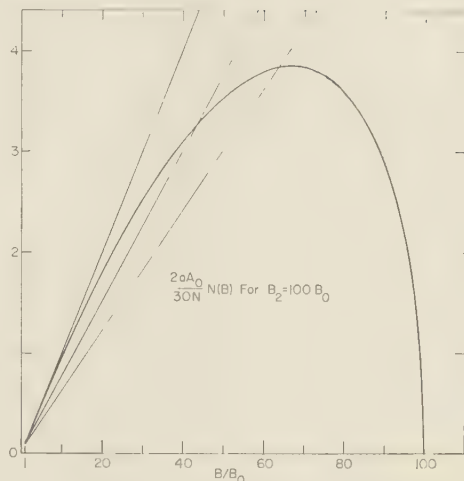


Fig. 4. The total particles per unit volume $N(B)$ when diffusion terminates at $B_2 = 100B_0$ without absorption. The density increases with increasing B all the way to $65B_0$.

$N(B)$ is plotted in Figure 4 for the special case that $B_2 = 100B_0$. It is interesting to note that $N(B)$ varies approximately linearly with B from $B = B_0$ to $B = 60B_0$. In contrast to the previous case, $N(B)$ increases with B until very close to $B = B_2$, where N is required to go to zero by the boundary conditions.

3. TENTATIVE GEOMAGNETIC MODEL

We now turn to the problem of applying the formal results of section 2 to the charged particles trapped in the geomagnetic field, particularly in the outer Van Allen radiation zone where large relative hydromagnetic wave amplitudes are expected. The first question that arises is whether the hydromagnetic waves in the geomagnetic field are of sufficient amplitude to significantly affect the electron distribution in the lifetime, conventionally of the order of a few years, of the individual electrons.

A. Estimated Hydromagnetic Amplitude

We have pointed out [Parker, 1958] that the outer geomagnetic field is unstable to the solar wind blowing against and across it, so that we expect wave amplitudes of $\Delta B \cong B$ at some distance of the order of 6 earth's radii, where $B \cong 10^{-3}$ gauss. The frequency of these waves is expected to be of the same order of magnitude

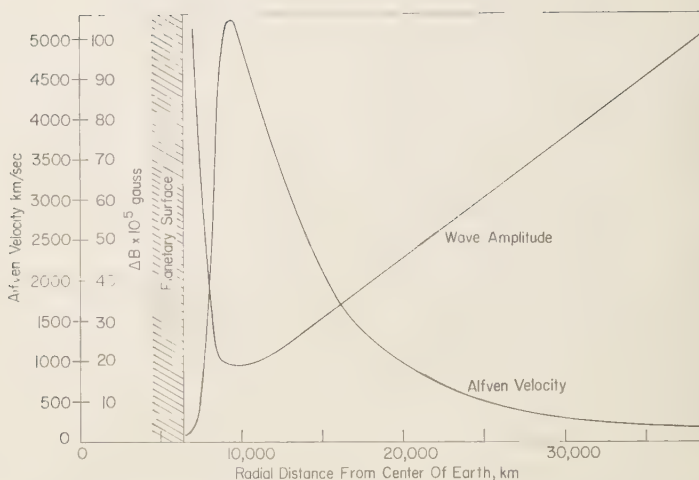


Fig. 5. The hydromagnetic wave velocity C as a function of radial distance from the center of the earth, and the hydromagnetic wave amplitude ΔB deduced with the simple assumption of constant of energy flux. The amplitude was taken to be 10^{-3} gauss at 6 earth's radii.

as the ion cyclotron frequency, or of the order of 1 cps. To estimate the amplitude which propagates closer to earth we make the simple assumption that the energy flux carried by the waves is of constant density, so that if C is the Alfvén velocity we have $\Delta B \alpha C^{-1/2}$ [Dungey, 1955]. With $\Delta B = 10^{-3}$ gauss at a radial distance of 6 earth's radii on a quiet day, ΔB has elsewhere the values shown in Figure 5, which are to be compared with the much higher estimates for active periods [Dessler, 1958]. This estimate neglects refraction, which depends upon the initial wave form and direction.² Nor does the estimate take into account reflection in the rapid velocity change below 10^4 km. The figure suggests that $\Delta B \approx 10^{-4}$ gauss is a conservative order-of-magnitude estimate of the wave amplitude in the outer Van Allen radiation zone.

It should be noted for future reference that the rapid decrease in the Alfvén velocity below a radial distance of 10^4 km is a consequence of the rapidly increasing atmospheric density. Somewhere below this level, at an altitude of 10^3 km or so, is the effective 'top' of the atmosphere, below which trapped particle lives become very short because of the high collision rate.

² Some examples of refraction may be found in Dessler, Francis, and Parker [1960], from which the values of C were taken.

B. Estimated Diffusion Time

Equation 27 gives a characteristic diffusion time of T . The transit time between mirror points is, to lowest order in ϵ ,

$$f_0 \cong 4a\xi_0/w_{n0}$$

so that (27) may be rewritten

$$T \cong f_0 \left(\frac{12}{\epsilon^2 \omega^2 f_0^2} \right)$$

In order that a hydromagnetic wave be effective in violating the longitudinal invariant, its period must not be very much greater than the order of magnitude of f_0 . On the other hand, our calculations are not quantitatively correct when $\omega f_0 \gg 1$ because of the assumption that $\omega t < 1$ in our evaluation of the roots of (9). As there is little observational evidence for the existence of such high-frequency waves $\omega f_0 \gg 1$, we shall pursue them no further in the present calculation. It follows, then, that with $\omega f_0 \lesssim 1$

$$T \geq (12/\epsilon^2)f_0$$

where ϵ is now the relative amplitude, $\Delta B/B_0$, of all the hydromagnetic disturbances satisfying $\omega f_0 \lesssim 1$. Since the transit time f_0 is inversely proportional to the particle velocity, it follows that the diffusion time is smaller for particles of higher energy, unless of course ϵ should be con-

derably smaller at the necessary higher wave frequencies.

Noting that f_0 is of the order of 1 sec for 0-key electrons, we see that a wave amplitude $\omega \geq 1$ radian/sec) of 10^{-4} gauss at 5000 km where $B \cong 0.1$ gauss yields $\epsilon = 10^{-3}$ and a diffusion time of only 4 months, which is to be compared with our order-of-magnitude estimate of 1 month in section 1. Thus we conclude that violation of the longitudinal invariant plays an important role in limiting the life and setting the distribution along the lines of force of the electrons in the outer Van Allen radiation zone. It is presumably more effective for mirror altitudes above $0(10^3)$ km than Coulomb scattering.

5. Distribution along the Lines of Force

To illustrate some possible applications of the formal results computed in this paper consider the atmospheric model, section 2, B, *iii*, in which the hydromagnetic waves propagate all the way into the atmosphere. In Figure 6 we plot $N_1(B)$ as a function of latitude for the numerical value $B_1 = 100B_0$, which corresponds to the line of force from latitude $\pm 62^\circ$, crossing the equatorial plane at 4.64 earth's radii. The

density decreases monotonically to zero with increasing geomagnetic latitude and decreasing altitude. There is a net diffusive flux downward along the lines of force into the atmosphere. Out of general interest we plot in the same figure the electron density (at 10⁻⁶-ev energies) observed by Fan, Meyer, and Simpson (unpublished) from Explorer VI. The density vanishes below an altitude of 10^3 km because of the high collision rate with atmospheric particles.

The atmospheric model is to be contrasted with the cutoff model, section 2, B, *iv*, in which the hydromagnetic waves do not extend into the 'top' of the atmosphere and there is no loss of particles. The electron density is plotted as a function of geomagnetic latitude in Figure 7 from (46) with $B_2 = 100B_0$. Note how closely the density follows $1/r^2$, shown by the light lines. The density increases inward, in contrast to the atmospheric model in which the density decreases rapidly as one approaches earth.

These two cases together illustrate the effects on the density distribution to be expected from hydromagnetic waves at the mirror points violating the longitudinal invariant. To apply the models to a particular particle energy in the

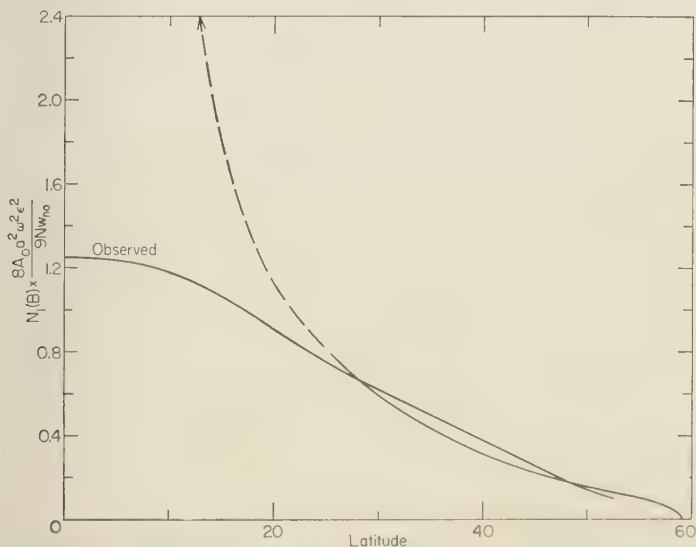


Fig. 6. The electron density along a geomagnetic line of force, from (41) for the case that the hydromagnetic waves propagate into the dense atmosphere. We let $B_1 = 100B_0$, which corresponds to the line of force from latitude $\pm 62^\circ$, crossing the equatorial plane at 4.64 earth's radii. The broken part of the curve is of little significance because it represents the artificial divergence at zero latitude introduced by oversimplification in the model.

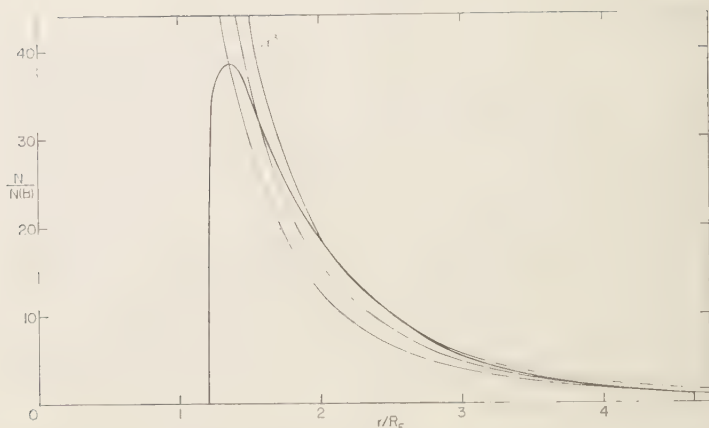


Fig. 7. The electron density along a geomagnetic line of force, from (46) for the case that the hydromagnetic waves are reflected before reaching the dense atmosphere. We let $B_2 = 100B_0$, which corresponds to a line of force from latitude $\pm 62^\circ$, crossing the equatorial plane at 4.64 earth's radii. The light lines represent r^{-3} for purposes of comparison.

geomagnetic field will require a knowledge of hydromagnetic wave spectrum, and a knowledge of the depth into the atmosphere, which begins to appear at 4000 km, to which hydromagnetic waves of a given frequency will propagate. Deeply penetrating waves cause the particles to be lost by collision, and give a density decreasing downward.

D. Particle Acceleration

With the formal calculations carried out in this paper and in the previous paper [Parker, 1960] it is now possible to establish some limitations on accelerating mechanisms that might contribute to the maintenance of the outer Van Allen radiation zone, and for the sudden enhancement following the active phase of a geomagnetic storm [Fan, Meyer, and Simpson, 1960]. The energy of a charged particle q in a hydromagnetic field ($\mathbf{E} = -\mathbf{v} \times \mathbf{B}/c$) can be increased only through some form of the Fermi mechanism, in which the field and plasma motion \mathbf{v} works against the Lorentz force ($q/c)(\mathbf{w} \times \mathbf{B})$ on the particle. This is easily seen from the equation of motion for the particle velocity \mathbf{w} ,

$$\frac{d}{dt} \left(\frac{1}{2} M w^2 \right) = M \mathbf{w} \cdot \frac{d\mathbf{w}}{dt} \\ = q \mathbf{w} \cdot (\mathbf{E} + \mathbf{w} \times \mathbf{B}/c) = \frac{q}{c} \mathbf{v} \cdot \mathbf{w} \times \mathbf{B}$$

An irreversible energy increase of a trapped

particle involves, of necessity, the violation of one of the three adiabatic invariants of the particle motion.

Now in the previous paper [Parker, 1960] we investigated violation of the third invariant by large-scale intermittent compression of the geomagnetic field. In the present paper we consider violation of the second or longitudinal invariant by hydromagnetic waves near the mirror point. In both cases we supposed the field changes to be sufficiently slow as to preserve the first invariant, $w_\perp^2/B = \text{constant}$. And in both cases we found that particle loss by diffusion is so rapid that no net particle energy gain occurs. For violation of the third invariant, the particles remaining trapped move inward in the geomagnetic field so that the individual particle energy $\langle E \rangle$ increases like $1/r^3$. But particles leak out the field into interplanetary space so fast that the number of particles remaining decreases like $1/\langle E \rangle^{15/4}$, and their total energy like $1/\langle E \rangle^{11/4}$. There results a rapid loss of both particles and total particle energy. Violation of the second invariant leads to a similar conclusion, except that the particles remaining migrate toward lower energies (see equation 21) while the bulk leak down the field into the atmosphere.

Neither of these models yields a net particle acceleration that might account for the enhanced electron density in the outer radiation belt. We were to assume that some kind of acceleration were necessary, which way might we turn? T

basic failing in the acceleration models so far is the large diffusive particle loss that appears simultaneously with the acceleration. There does not seem to be any simple remedy in the case of the longitudinal invariant acceleration discussed in the present paper. Increasing the energy along the field lowers the mirror points, with eventual loss by collision in the atmosphere. On the other hand, a very simple modification is possible in the case of violation of the third invariant [Parker, 1960]. Our calculations showed that the rapid leakage out of the geomagnetic field into interplanetary space arises from the fact that the scattering, for the sudden-commencement magnetic field compression, increases very rapidly with radial distance from the earth. The mean square displacement per compression of the field is proportional to r^0 . Suppose, therefore, that in addition to the sudden commencement of geomagnetic storms there are other hydromagnetic disturbances of smaller scale that are capable of violating the third invariant, as suggested by Kellogg [1959]. Is there a spatial distribution of such disturbances that can accelerate electrons, in keeping with (2), without sending them into interplanetary space by diffusion? The answer is obviously in the affirmative, we can find a hydromagnetic disturbance

- capable of violating the third invariant and
- localized inside the geomagnetic field.

For if a disturbance is localized inside the geomagnetic field, and is not found in the outermost regions of the field, electrons cannot diffuse outward beyond the extent of the disturbance. Electrons can diffuse inward as far as the disturbance extends, increasing their energy like $1/r^3$ according to (2).

As a simple example consider the electrons confined to the equatorial plane of the geomagnetic field. If their density per unit area is $n(r, t)$, then in terms of the mean square displacement $\langle(\Delta r)^2\rangle$ per unit disturbance n we have something like

$$\frac{\partial \phi}{\partial n} \cong \frac{1}{r} \frac{\partial}{\partial r} \left[r \langle(\Delta r)^2\rangle \frac{\partial \phi}{\partial r} \right]$$

if the disturbances are confined to some broad interval such that $a < r < b$ and such that

$$\langle(\Delta r)^2\rangle \cong \begin{cases} h^2 & \text{in } a < r < b \\ 0 & \text{otherwise} \end{cases}$$

then it is readily shown that

$$\begin{aligned} \phi(r, n) = & \frac{2}{b^2 - a^2} \int_a^b dr r \phi(r, 0) \\ & + 2 \sum_{\nu=1}^{\infty} \frac{\left[\int_a^b dr r Z_0(k_\nu, r) \phi(r, 0) \right]}{b^2 Z_0^2(k_\nu, b) - a^2 Z_0^2(k_\nu, a)} \\ & \times Z_0(k_\nu, r) \exp(-k_\nu^2 h^2 n) \end{aligned}$$

where

$$Z_\nu(kr) \equiv Y_1(ka) J_\nu(kr) - J_1(ka) Y_\nu(kr)$$

and k_ν is the ν th root of

$$Z_1(k, b) = 0$$

Thus, for instance, if we introduce N particles at $r = b$, then after many hydromagnetic disturbances we have a uniform distribution

$$\phi(r, n) \sim \frac{N}{\pi(b^2 - a^2)}$$

with a final total energy equal to $2(b/a)/(1 + a/b)$ times the initial total energy. Thus, if $a \ll b$, there is a large energy increase, by a factor of approximately $2b/a$.

It is possible, then, to achieve a large increase in particle energy through (2) by hydromagnetic violation of the third invariant. It is only necessary to postulate a localized region of hydromagnetic disturbances so that there is little or no loss by scattering from the region of hydromagnetic activity.

On the other hand, the acceleration is not unlimited. Each particle may have its energy increased by whatever factor B increases during its diffusion (because equation 2 is inviolate). Thus to produce 100-keV particles at, say, 3 earth's radii, we must begin with the equivalent of 10 keV at 6.5 radii. Particles cannot be accelerated at a given location from small to large energies.

Further, the necessary assumption of localized hydromagnetic disturbances, which do not extend out through the geomagnetic field to interplanetary space, is perhaps a little artificial. And limited scattering of accelerated motion perpendicular to the field into the direction along the field by these same hydromagnetic disturbances is a further necessary assumption. Thus, altogether, it appears that hydromagnetic acceleration by violation of the second and third invariants of the particle motion is possible but, at least for the moment, unappealing.

What then are the alternatives? As we have

already remarked, irreversible acceleration requires violation of one or more of the three adiabatic invariants of the motion of the charged particle trapped in the geomagnetic field. If violation of the second and third invariants is not suitable, alone, then we require violation of the first as well. Hydromagnetic frequencies and wave numbers are limited to the ion cyclotron frequency and radius of gyration. Thus hydromagnetic fields cannot violate the first invariant of the electrons (with which we are principally concerned at the moment). At higher frequencies where the first invariant can be violated we have the whistler electromagnetic waves, then waves near the plasma frequency, and finally radio waves. Such high-frequency fields as these are the alternatives to the hydromagnetic field.

It is interesting to note that on rather different grounds, viz. the lack of displacement of the Argus electrons and the protons of the inner belt during a magnetic storm, Kellogg [1960] some time ago suggested that it is the higher-frequency electromagnetic fields that are responsible for the acceleration of the electrons.

In conclusion, then, if there is to be an electron-accelerating mechanism in the outer Van Allen, the acceleration must proceed more rapidly than diffusion, or there is no net energy gain. Electromagnetic frequencies above the ion cyclotron frequency need to be investigated carefully and quantitatively, because they hold promise of reduced scattering in proportion to the energy increase when the first invariant (equation 2) is violated. A recent note by Herlofson [1960] gives a qualitative discussion of such electron scattering and diffusion.

Acknowledgments. I should like to express my gratitude to Dr. A. J. Dessler of the Missiles and Space Division of Lockheed Aircraft Corporation for stimulating discussion and many valuable suggestions in the preparation of this paper, and to Professor J. A. Simpson of the University of Chicago for helpful comments in the presentation.

This research is supported by the Office of Scientific Research, Air Research and Development Command, contract AF 18(600)-666, and the National Aeronautics and Space Administration under grant NASA-NsG-96-60.

REFERENCES

- Arnoldy, R. L., R. A. Hoffmann, and J. R. Winckler, Observations of the Van Allen radiation regions during August and September 1959, part 1, *J. Geophys. Research*, **65**, 1361-1376, 1960.
- Coleman, P. J., C. P. Sonett, D. L. Judge, and E. J. Smith, Some preliminary results of the Pioneer V magnetometer experiment, *J. Geophys. Research*, **65**, 1856-1857, 1960.
- Dessler, A. J., Large-amplitude hydromagnetic waves above the ionosphere, *J. Geophys. Research*, **63**, 507-511, 1958.
- Dessler, A. J., W. E. Francis, and E. N. Parker, Geomagnetic storm sudden-commencement times, *J. Geophys. Research*, **65**, 2715-2719, 1960.
- Dungey, J. W., Electrodynamics of the outer atmosphere, *Proc. Ionosphere Conf. Phys. Soc. London*, p. 229, 1955.
- Dungey, J. W., *Cosmic Electrodynamics*, pp. 151, 152, Cambridge University Press, 1958.
- Fan, C. Y., P. Meyer, and J. A. Simpson, Trapped and cosmic radiation measurements from Explorer VI, *Proc. First Intern. Space Sci. Symposium*, North Holland Publishing Co., Amsterdam, 1960.
- Fermi, E., On the origin of cosmic radiation, *Phys. Rev.*, **75**, 1169, 1949.
- Herlofson, N., Diffusion of particles in the earth's radiation belts, *Phys. Rev. Letters*, **5**, 414, 1960.
- Hobson, E. W., *The Theory of Spherical and Ellipsoidal Harmonics*, pp. 195, 196, Chelsea, New York, 1955.
- Kellogg, P. J., Van Allen radiation of solar origin, *Nature*, **183**, 1295-1297, 1959.
- Kellogg, P. J., Electrons of the Van Allen radiation, *J. Geophys. Research*, **65**, 2705-2713, 1960.
- Northrup, T. G., and E. Teller, Stability of the adiabatic motion of charged particles in the earth's magnetic field, *Univ. Calif. Lawrence Radiation Lab.*, Livermore, UCRL-5615, 1959.
- Parker, E. N., Interaction of the solar wind with the geomagnetic field, *Phys. Fluids*, **1**, 171, 1958.
- Parker, E. N., Geomagnetic fluctuations and the form of the outer zone of the Van Allen radiation belt, *J. Geophys. Research*, **65**, 3117-3130, 1960.
- Singer, S. F., (Abstract) *Bull. Am. Phys. Soc.*, [2], **1**, 229, 1956.
- Sonett, C. P., E. J. Smith, and A. R. Sims, Surveys of the distant geomagnetic field: Pioneer I and Explorer VI, *Proc. First Intern. Space Sci. Symposium*, North Holland Publishing Co., Amsterdam, 1960.
- Vernov, S. N., and A. E. Chudakov, Terrestrial corpuscular radiation and cosmic rays, *Proc. First Intern. Space Sci. Symposium*, North Holland Publishing Co., Amsterdam, 1960.
- Vernov, S. N., A. E. Chudakov, A. I. Lebedinsky, and I. P. Ivanenko, Composition of the earth's corpuscular radiation and possible mechanism of its origination, *Proc. Moscow Cosmic Ray Conf.*, **3**, 46, Moscow, 1960.
- Watson, G. N., *Theory of Bessel Functions*, 2d ed. p. 388, Cambridge University Press, 1958.
- Wentworth, R. C., W. M. MacDonald, and S. F. Singer, Lifetimes of trapped radiation belt particles determined by Coulomb scattering, *Phys. Fluids*, **2**, 499, 1959.

(Manuscript received December 1, 1960;
revised December 22, 1960.)

Equation of a Charged Particle Shell in a Perturbed Dipole Field

RALPH H. PENNINGTON

*Headquarters, Defense Atomic Support Agency
Washington, D. C.*

Abstract. The earth's magnetic field is considered to be described as a dipole perturbed by the addition of higher-order poles of small magnitude, an equation is given for the shell generated by the motion of a trapped, charged particle. The equation obtained is shown to be in agreement with the shell measured by satellite 1958 ϵ following the high-altitude nuclear detonation of September 6, 1958. Magnetic field coefficients in various coordinate systems are given.

The shape of the natural Van Allen belts and the artificially produced electron shells caused by the nuclear detonations of the Argus experiment, in August and September of 1958, can be approximately described by treating the earth's magnetic field as a simple dipole. The shape for such a shell is roughly that of an axially symmetric surface obtained by rotating a single field line about the dipole axis. If the pole field is described by the scalar potential

$$V = M \cos \theta / r^2 \quad (1)$$

on the surface is

$$r = c \sin^2 \theta \quad (2)$$

If the field is not axially symmetric, it has been shown [Chew, Goldberger, and Low, 1955] that a charged particle will remain near the surface made up of field lines satisfying the condition

$$\int_{T_1}^{T_2} (1 - B/B_T)^{1/2} dl = \text{constant} \quad (3)$$

where the integral is taken along a field line from one turning point T_1 of the charged particle to the other turning point T_2 , and B_T is the field strength at the turning points. Vestine and Sibley [1959] have shown by machine computation, using a 48-term expansion for the earth's magnetic field, that such a condition can be used to compute the auroral isochasms. In this paper an approximate analytical equation for the shell and its earth intercept is presented. The derivations are omitted [Pennington, to be published].

Since the earth's field is approximately a

dipole, the condition (3) can be applied to first order in a perturbation theory treatment to obtain an explicit equation for the surface. Let the potential function for the earth's field be described by the customary expression

$$V = a \sum_{n=1}^{\infty} \sum_{m=0}^n (a/r)^{n+1} (g_n^m \cos m\phi + h_n^m \sin m\phi) P_n^m(\theta) \quad (4)$$

where the $P_n^m(\theta)$ are orthogonal polynomials defined by Schmidt [Chapman and Bartels, 1940]. If all the g_n^m and h_n^m except g_1^0 are assumed to be of order ϵ , and (3) is satisfied to first order in ϵ , along field lines described to first order in ϵ , one obtains for the equation of the surface

$$r = (c/g_1^0) \sin^2 \theta \sum_{n=1}^{\infty} \sum_{m=0}^n (a/c)^{n-1} \cdot [V_n^m(\theta) - \alpha_n^m] (g_n^m \cos m\phi + h_n^m \sin m\phi) \quad (5)$$

where

$$V_1^0(\theta) = 1, \quad V_n^m(\theta) = \int_{\pi/2}^{\theta} \csc^{2n} \theta [(n+1) \cdot \sin \theta P_n^m(\theta) + 2 \cos \theta \frac{d}{d\theta} P_n^m(\theta)] d\theta \quad (6)$$

for other n, m . Table 1 gives these functions for $n < 4$. The constants α_n^m depend only on the value of the mirror point colatitude θ_T . The dependence is a rather complex one, being given by the relations

$$\alpha_1^0 = 0, \quad \alpha_n^m = [K_1(n, m) + K_2(n, m) + K_3(n, m)]/K_4 \quad \text{for other } n, m, \quad (7)$$

TABLE 1. $V_n^m(\theta)$ As Defined by Equation 6

n	m	$V_n^m(\theta)$
1	0	1
1	1	$-2 \cot \theta$
2	0	$3/2 \cot \theta \csc \theta$
2	1	$(3)^{-1/2} (3 \csc \theta - 2 \csc^3 \theta - 1)$
2	2	$[(3)^{1/2}/2] [-2 \cot \theta \csc \theta + \ln (\csc \theta - \cot \theta)]$
3	0	$[1/2] (4 \csc^4 \theta - 5 \csc^2 \theta + 1)$
3	1	$[-(6)^{1/2}/10] \cot \theta (4 \csc^4 \theta - 13 \csc^2 \theta - 1)$
3	2	$[(15)^{1/2}/2] (-\csc^4 \theta + \csc^2 \theta)$
3	3	$[-(10)^{1/2}/2] \cot \theta (\csc^2 \theta + 1)$

where

$$K_1(n, m) = \int_{\theta_T}^{\pi - \theta_T} [(1 + 3 \cos^2 \theta)/(1 - \beta)]^{1/2} \cdot (2 + \beta) V_n^m(\theta) \sin \theta \, d\theta \quad (8)$$

$$K_2(n, m) = \int_{\theta_T}^{\pi - \theta_T} \csc^{2n-3} \theta [(1 + 3 \cos^2 \theta) \cdot (1 - \beta)]^{-1/2} (2 - 3\beta) \left[2(n + 1) \cos \theta P_n^m(\theta) - \sin \theta \frac{d}{d\theta} P_n^m(\theta) \right] d\theta \quad (9)$$

$$K_3(n, m) = \int_{\theta_T}^{\pi - \theta_T} 2 \csc^{2n-2} \theta [(1 + 3 \cos^2 \theta) \cdot (1 - \beta)]^{1/2} \frac{d}{d\theta} P_n^m(\theta) \, d\theta \quad (10)$$

$$K_4 = \int_{\theta_T}^{\pi - \theta_T} [(1 + 3 \cos^2 \theta)/(1 - \beta)]^{1/2} \cdot \sin \theta (2 + \beta) \, d\theta \quad (11)$$

where

TABLE 2. Values of $\alpha_2^1, \alpha_3^0, \alpha_3^2$

θ_T	α_2^1	α_3^0	α_3^2
15°	-.90	-1.50	-5.00
30°	-.64	.237	-1.76
35°	-.62	.397	-1.50
40°	-.61	.490	-1.32
45°	-.59	.543	-1.19
50°	-.60	.539	-1.05
55°	-.59	.532	-.944
60°	-.58	.530	-.882
75°	-.58	.528	-.720

$$\beta = (\sin^6 \theta_T / \sin^6 \theta)$$

$$\cdot [(1 + 3 \cos^2 \theta)/(1 + 3 \cos^2 \theta_T)]^{1/2} \quad (12)$$

Values for the first three nonzero alphas ($\alpha_2^1, \alpha_3^0, \alpha_3^2$) for various values of θ_T are given in Table 2.

The intersection of the surface given by equation 5 with the surface of the earth can be obtained by setting $r = a$ in (5) and solving for θ in terms of ϕ . To first order in the magnetic field coefficients

$$\theta_0 = \sin^{-1} (a/c)^{1/2}$$

$$\theta = \theta_0 - (\tan \theta_0 / 2 g_1^0) \sum_{n=1}^{\infty} \sum_{m=0}^n (\sin \theta_0)^{2n-2} \cdot [V_n^m(\theta_0) - \alpha_n^m] (g_n^m \cos m\phi + h_n^m \sin m\phi) \quad (13)$$

where the prime on the summation sign is to indicate that the term corresponding to $m = 0, n = 1$ is missing. Equation 13 gives two traces for θ , corresponding to the first and second quadrant values of the arc sine.

TABLE 3. Finch-Leaton Coefficients (cgs) for the Earth's Magnetic Field (1955)

Coefficient	Geographic Coordinates	Centered, Tilted Dipole (Geomagnetic) Coordinates*	Offset, Tilted Dipole Coordinates
g_1^0	-.3055	-.3120	-.3120
g_1^1	-.0277	0	0
h_1^1	.0590	0	0
g_2^0	-.0152	-.0049	0
g_2^1	.0303	.0288	0
h_2^1	-.0190	.0214	0
g_2^2	.0158	-.0198	-.0198
h_2^2	.0024	.0026	.0025
g_3^0	.0118	.0080	.0059
g_3^1	-.0191	-.0115	-.0115
h_3^1	-.0045	-.0165	-.0179
g_3^2	.0126	-.0108	-.0098
h_3^2	.0029	.0110	.0136
g_3^3	.0091	-.0057	-.0089
h_3^3	-.0009	-.0055	-.0071

* Best-fitting centered dipole, chosen to make g_1^1 and h_1^1 equal to zero. The axis is tilted 11.7° toward a geographic longitude of 69.0°W. Geomagnetic longitude of geographic pole is 180°.

Best-fitting offset dipole, chosen to make $g_1^1, h_1^1, g_2^0, g_2^1$, and h_2^1 equal to zero. The origin is displaced by 411.4 km on the line from the center of the earth toward a point at 150.8°E, 15.6°N, and tilted as for the centered case.

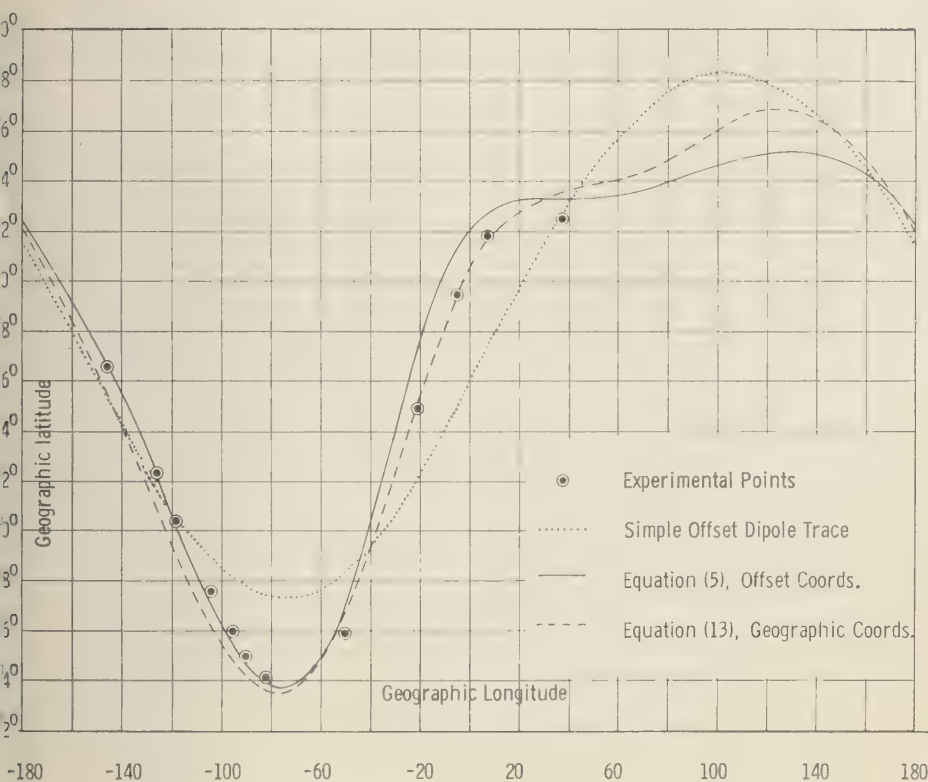


Fig. 1. Earth trace of Argus III shell.

In determining the first-order perturbation of the integral 3, use is made of the fact that the departure of the mirror point colatitude from the constant zero-order value θ_T is small. In geographic coordinates this assumption is not very good, since the 11° tilt of the earth's magnetic axis with respect to its geographic axis introduces a sizeable variation of 11° in the mirror point colatitude. For latitudes of 45° or less, the error is not serious. For higher latitudes, however, (5) and (13) are more accurate if used in a coordinate system based on a tilted dipole axis. Table 3 shows values for g_n^m and h_n^m in geographic coordinates for the year 1955 by Finch and Leaton. Also shown are values based on the best centered, tilted dipole and also values based on the best offset, tilted dipole. Equation (5) applies in either system, but equation 13 applies only in an earth-centered system.

Figure 1 shows a comparison of (5) and (13)

with experimental data. The experimental points are earth projections along field lines of intercepts of the Argus III shell by the Explorer IV satellite [Van Allen, McIlwain, and Ludwig, 1959]. These points have been projected from satellite altitudes of 1000 to 2000 km, and may be subject to latitude error of the order of 1° . The dotted line is the earth trace which would be obtained if the earth's field were a pure dipole field, based on the best possible offset dipole. The solid line is from (5), where terms through $n = 3$, average mirror point latitude of 45° , and the g_n^m and h_n^m for an offset dipole coordinate system are used. This equation was solved simultaneously with that of the earth's surface by computer. The dashed line is from (13), where terms through $n = 3$, $\theta_0 = 42.7^\circ$, and geographic values of the g_n^m and h_n^m are used. On the exaggerated latitude scale the differences are quite apparent. The perturbation

theory treatment appears to give definite improvement over the best dipole approximation, and even the simple calculation according to (13) gives fair accuracy.

Acknowledgment. The assistance of Pfc Bryan L. Blackburn, Pfc Paul Dunne, and Mr. William Ruhsam in the performance of the numerical computations is gratefully acknowledged.

REFERENCES

Chapman, S., and J. Bartels, *Geomagnetism*, vol. II, Clarendon Press, Oxford, 1940.

Chew, G. F., M. L. Goldberger, and F. E. Low, A adiabatic invariant for motion along the magnet lines of force, *Los Alamos Rept. LA-2055 T-76* September 1955.

Pennington, R. H., Argus shell equations, to be published.

Van Allen, J. A., C. E. McIlwain, and G. H. Ludwig, Satellite observations of electrons artificially injected into the geomagnetic field, *J. Geophys. Research*, 64, 877-891, 1959.

Vestine, E. H., and W. L. Sibley, Remarks on auroral isochasms, *J. Geophys. Research*, 64, 1338-1339, 1959.

(Manuscript received August 22, 1960.)

Theory of Auroral Morphology

J. W. KERN AND E. H. VESTINE

*Engineering Division, The RAND Corporation
Santa Monica, California*

Abstract. A new theory of auroral morphology based on the production of instabilities in electron sheets is developed. It is found that the theory predicts a longer duration of homogeneous auroral arcs in the early evening and a shorter duration during morning hours. Observed transitions from glow to homogeneous arcs to ray arcs and draperies are also predicted. An especially interesting feature is the lowering of mirror points accompanying development of brighter features of a display. The theory also achieves encouraging success in explaining horizontal and vertical luminous wave-progressions found in flaming aurora.

1. INTRODUCTION

Theories of the aurora [Störmer, 1955; Chapman and Ferraro, 1940; Alfvén, 1950; Chamberlain, 1957, 1960] ascribe auroral forms to energetic charged particles moving in the geomagnetic field. Existing theories do not profess to explain the sequence of events or the various auroral forms appearing in visually observed aurora. Consequently, a theory of auroral morphology has been completely wanting. In the present paper a preliminary outline of such a theory is set forth.

A typical sequence in the appearance of auroral forms has often been remarked [Stagg, 1935]. The usual physical sequence is from glow to homogeneous arc, to ray arc, to rays with some tensification before a final breakup of the display occurs. Later the same night the sequence may be repeated. There is, therefore, a more or less typical morphology of the aurora.

The present theory attempts to explain this sequence on the basis of the stability of groupings of energetic charged auroral particles moving in the geomagnetic field. Also considered are related phenomena, such as the polar electrojets of geomagnetism.

GENERAL FEATURE OF AURORAL MORPHOLOGY

According to Stagg [1934], in latitudes near or just south of the auroral zone, a typical display then begins with a glow in the northern sky persisting from minutes to an hour or so. The equatorward region of glow then gradually develops a brightening edge that intensifies into a homogeneous auroral arc. This homogeneous arc then extends nearly from horizon to horizon, its

greatest height being roughly above the magnetic meridian. This arc persists without much fluctuation in intensity perhaps for 15 minutes, and, more rarely, even for several hours. A transition then occurs, and some irregularities or flutes along the arc may develop, and within a minute or so a transition to a ray arc occurs. The base of the ray arc is usually at a higher level than the homogeneous auroral arc, so that it appears in the low F region, whereas the homogeneous arc usually has its base in the E region. Exceptions do occur, and rays sometimes penetrate levels as low as 60 km or so. The ray arc is less stable, and it soon breaks up, perhaps with a transient increase in extent and brightness as curtains or draperies. The latter then become dissipated until only shreds of the display may remain as isolated pulsating patches [Stagg, 1934; Vestine, 1944; Störmer, 1955].

More complex situations often occur, many forms appearing simultaneously and at times covering the entire sky. There may also be isolated, thin auroral arcs at height 200 km that extend weakly across the sky for a period of minutes to an hour or so [Störmer, 1955; Vestine, 1943]. Isolated red auroral arcs at heights 400 km and above are also known in middle latitudes [Elvey, 1957; Roach, 1960].

3. THE POLAR ELECTROJETS OF GEOMAGNETISM

During magnetic storms, which may occur 10 to 20 times or so a year, and during many lesser periods of disturbances known as magnetic bays, there appear in auroral regions electrojets located within the low ionosphere closely associated with auroral displays. A strong nighttime electrojet

occurs between local midnight and dawn, with an intense jet of current flowing westward along the auroral zone. A weaker eastward-directed electrojet can often be noted in the afternoon. The current system for a particular bay grows in intensity with time to a maximum and then diminishes over a period of a few hours. There may be more than one such intensification during a 24-hour period. An interesting feature is the tendency for bays to recur at 24-hour intervals for several nights running, a new theory which will be discussed in subsequent papers.

In recent articles it has been suggested that trapped radiation, moving in accord with predictions based on adiabatic invariants of the particle motion, might form the two electrojets [Vestine, 1960; Chamberlain, Kern, and Vestine, 1960]. Although it was suggested that the charged particles responsible were of solar origin, these could without loss of generality be regarded as generated within the geomagnetic field by interactions with solar streams carrying magnetic fields.

A recent suggestion is that geomagnetically trapped particles, when accelerated, drift in longitude about the polar cap along spirals and thus might give rise to a more or less meridional electric field driving the nighttime polar electrojet [Chamberlain, Kern, and Vestine, 1960]. A feature of this explanation is that the Hall conductivity, with a magnitude about ten times that of the conductivity across the geomagnetic field, would dominate in the low ionosphere. The recent studies of auroral arcs and polar electrojets by Akasofu (private communication) have indicated that a meridional electric field may drive the nighttime polar electrojet. The aurora and the electrojet are more or less closely associated phenomena [Heppner, 1954]; accordingly, it is of interest to consider interrelated mechanisms [Chamberlain, Kern, and Vestine, 1960]. These may predict features expected in the aurora and in the polar electrojets. In particular, it is perhaps constructive to begin by imagining that in the high ionosphere a down-coming filament of trapped radiation, aligned vertically along the geomagnetic field, arrives at the nighttime electrojet to give rise to an auroral arc. This will next be considered.

If the particle flux producing an auroral display consists of trapped electrons and protons, those not immediately absorbed will drift—electrons to

the east and protons to the west—with velocities near the mirror points given approximately by

$$v_d = \frac{3E}{Ber}$$

where E is the energy of the particle, B the magnetic field, e the electronic charge, and r the distance from the earth's center [Christofilos, 1959]. The initial filament a kilometer or so wide aligned along the geomagnetic field, will produce drift of protons as a thin arc to the west, and electrons to the east.

One possibility is that charges may accumulate near mirror points within the atmosphere, producing electric fields with associated current flows in the ionosphere. For accelerated particles the charge separation on the night side may give a meridional electric field in the ionosphere. In this event, a situation favorable to generation of the nighttime electrojet may arise.

The details of the electric-field distribution that could give rise to the polar electrojet system during magnetic bays are unknown. The eastward-directed electrojet, flowing in the low ionosphere on the early evening side, can be driven by an electric field from west to east in the low ionosphere, where the electrical conductivity has been enhanced during the day, with conductivity augmented by the penetration of auroral particles during an auroral display. At a slightly higher level, the electric field during the electrojet would be more effective if applied in a poleward direction. If it be supposed that the west-to-east electric field at lower levels is the more important, this electric field E , or its motor effect, will tend to cause the trapped radiation producing the jet to drift poleward also.

In the case of the early-morning electrojet, an electric field directed from pole to equator locally is regarded as the more likely driving force, since the Hall electric conductivity within the E region is greater than that for current flow parallel to the electric field and across the geomagnetic field.

4. STABILITY OF HOMOGENEOUS AURORAL ARCS

Students of mirror machines and plasma physics have learned a few facts about the stability of trapped radiation [Kruskal and Schwarzschild, 1954; Post, 1956; Rosenbluth, 1960; Rosenbluth and Longmire, 1957]. It is, of course, not necessarily known that auroral morphology arises as an analogous consequence of plasma

stabilities arising from radiation trapped in the magnetic field. An auroral arc, once formed, however, provides a region of increased particle flux that should spread rapidly eastward (or westward) to extend the arc, as noted previously. If homogeneous auroral arcs appear simultaneously in both northern and southern hemispheres, defined by geomagnetic field lines, the base of the arc in either hemisphere may be described as anchored within electrically conducting levels of the ionosphere. If, as supposed here, there is connection of an auroral arc in the northern hemisphere via geomagnetic field lines with an arc in the southern hemisphere, physical experience with mirror machines leads to the expectation that it is only a question of time until fluted irregularities in auroral formations will appear [Kruskal and Schwarzschild, 1954], but the greater the E -region conductivity, the faster this time should be. These flutes grow rapidly and the display breaks up. The importance of the application of these theoretical concepts to the great natural phenomenon of the aurora seems to have been suggested only recently [Vestine and Sibley, 1960].

It has already been remarked that for polar electrojets in the low ionosphere associated with auroral displays, the Hall electric conductivity in the region of current flow is probably about ten times the cross conductivity. Consequently, the electrojets are likely to be driven by nearly meridional electric fields, regarded as arising between drifting proton and electron sheets oriented more or less vertically and east-west. Attention here will be confined to the sheet closest to the equator. This will here be identified, tentatively, as having a homogeneous auroral arc at its base, in which any minute irregularities could grow exponentially with time, in accordance with the principles and methods developed by Kruskal and Schwarzschild in their classic paper and by Rosenbluth and Longmire [1957].

First, the stability of an idealized homogeneous auroral arc will be investigated. The main assumption is that a northern auroral zone arc sustained by geomagnetically trapped particles. The region of particle incidence is taken as a thin sheet oriented roughly east-west in a surface of constant integral invariant (parallel to geomagnetic field lines) and connected via the magnetic field with a similar arc in the southern hemisphere. An initial supply of trapped electrons

penetrating beneath the ionosphere will drift east, and any protons, west, with separation of the charges. This will occur both in the northern and southern hemispheres. The width in latitude 1 and length L of field lines joining the northern and southern hemispheres may be of the order of, say, 400 km and 10^6 km, respectively. The ionospheric circuit, as in mirror machine studies, will comprise resistance R , over-all capacitance C , and a current I .

If flutes involving charge irregularities are formed on a longitudinal sheet of incident particles, such as the diamagnetic sheet of section 4, perturbation electric fields will appear in the plane of the incident-particle sheet. Such perturbation electric fields will produce drift normal to the plane of the sheet. Thus if the incident-particle sheet is represented by the xz plane, drift may occur in the y direction such that $\dot{y} = E'/B$ where \dot{y} is the drift velocity, E' is the perturbation electric field, and B the local magnetic field. It is assumed that collisions can be neglected, as in the case in the F region.

Writing δ for the distance between equivalent perturbations in the x direction (east-west), the perturbation electric field E' can be replaced by equivalent potential perturbations $V' = B\delta\dot{y}$. Now the east-west drift of particles inside the sheet provides a westward-directed current $I = 2L\rho\bar{v}_d\dot{y}$, where y is the north-south sheet thickness, L is the length of a field line connecting arcs in the northern and southern hemispheres, ρ is the space charge density (given by $n_e e = -n_i e$), and \bar{v}_d is an average transverse drift velocity for the particles moving in Störmer orbits along the magnetic field lines. This current links the regions of charge density variation.

A circuit equation for the perturbation voltage V' can therefore be written

$$\dot{V}' + \frac{V'}{CR} - \frac{I}{C} = 0 \quad (1)$$

noting the resistance $R = \delta/\sigma_1 A$, where σ_1 is the transverse electric conductivity, and A is the cross-sectional area of the part of the incident-particle sheet of finite thickness within the ionosphere; the cross section is that imagined obtained by a vertical slice taken roughly in the north-south direction. Then

$$\sigma_1 A B R \dot{y} + (\sigma_1 A B / C) \dot{y} - (2L\rho\bar{v}_d / C) y = 0 \quad (2)$$

so that

$$y = \alpha [\exp(4L\rho\bar{v}_d/\sigma_1 AB)t - \exp(-2\sigma_1 A/C)t] \quad (3)$$

where α is a constant. It can be shown that the second term, under the circumstances, rapidly decays, so that y grows exponentially with the time at a rate that is less when the resistance $1/\sigma_1 A$ is less.

An early evening homogeneous auroral arc often lasts about 15 minutes (~ 1000 seconds) before breaking up. During the morning hours, however, the direct conductivity appearing in equation 3 may be reduced by a factor of 10 or more. Thus (3) predicts increased rates of perturbation buildup during morning hours. *Störmer* [1955] gives observational data indicating that morning displays tend to be more transitory in character than those appearing earlier in the evening.

A characteristic time constant for a perturbation buildup from equation 3 can be calculated. The time for an e -fold increase of y is given by

$$\tau = \sigma_1 AB/4L\rho\bar{v}_d \quad (4)$$

Taking $\sigma_1 = 10^{-14}$, $A = 2 \text{ km} \times 50 \text{ km}$, $B = 0.4$, $L = 10^6 \text{ km}$, $\bar{v}_d = 10^{-3} \text{ km/sec}$ (for, say, 6 kev electrons), and $\rho = ne = 10^2 \times 1.6 \times 10^{-20} \text{ emu/cm}^2$, we obtain from equation 4, $\tau = 600 \text{ sec}$. This seems compatible with observed durations of homogeneous auroral arcs. It should be noted that this requires a continuous supply of 6-kev electrons, since nearly all particles of this energy will be absorbed at auroral levels, without reflection [Welch and Whitaker, 1959].

The homogeneous auroral arc is usually replaced by a ray arc, with the lower end of the illumination or rays in the low F region. At this level σ_1 is considerably less than in the E region, say by a factor of 10, so that the time constant τ is less, or perhaps 60 seconds. For draperies the height of the base may be even higher, so that breakup of the displays may occur with an even shorter time constant. It may also be remarked that auroral rays penetrating to levels below 80 km, where the electric conductivity is also relatively small, seem to have a short duration. The short-circuiting properties of the electrically conducting atmosphere therefore seem to exert an important stabilizing influence by reducing the local electric field irregularities that tend to

grow and disrupt the displays. Consequently, the transition sequence in auroral forms and, in particular, the time of ending of auroral forms, seem dependent on the stability of displays, which in turn tends to be greater when disrupting electric fields can be short-circuited by a good electrical conductor.

5. GENERATION OF AN AURORAL ARC BY GEOMAGNETICALLY TRAPPED RADIATION

A broadly distributed auroral glow, perhaps associated with incoming protons, often precedes a brighter auroral display within the glow itself. The glow is often followed in a limited region by an intensification of illumination that may be caused by a local influx of charged particles. This possibly means there is drainage of trapped particles due to a local lowering of the mirror point of incident radiation in the brighter region. This brightening region may develop on the equatorward edge of the glow. The cause of such mirror point depression is not known. One suggested mechanism is that solar streams locally stretch or compress geomagnetic field lines, so that particles may drift equatorward, near midnight, to lower mirror-point heights when certain invariants of the particle motion are conserved [Vestine, 1960]. Once established, such an auroral form, limited in extent, will probably have a lifetime closely related to the local electric conductivity which short-circuits any electric field irregularities in the display [Vestine and Sibley, 1960]. As mentioned above, this may explain why auroral displays in the early morning appear to be shorter in duration than in early evening; in fact, in the evening, the auroral glow preceding the brighter form may suggest buildup in the electric conductivity permitting a longer display lifetime. This lifetime may be affected by the events in the local irregularity or ridge in an east-west direction referred to above. Thus a discharge to lower levels, through secondary effects of electric and magnetic fields set up in the region, may cause growth or accentuation of the discharge to lower reaches of the ionosphere. This may arise as a consequence of local acceleration of the trapped particles, promoting increased flux penetration to auroral levels. The factors leading to the transition from glow to the first indications of a homogeneous auroral arc are, of course, obscure, and as yet quite unknown. Since such transitions often occur, certain

ectrical and magnetic effects associated with the production of the first bright segment of the homogeneous auroral arc will be considered here. In fact, this observed feature of a brightening edge of illumination of the glow on the low mirror-point equatorward side would be expected rather as a result of a slight acceleration of the particles or of equatorward migration of a glow produced by trapped radiation.

Diamagnetic sheet mechanism. If charged particles can be supplied to a region at auroral heights at such a rate that a net space charge is built up, associated electric and magnetic fields will arise. Drift of particles at right angles to the electric field of the space charge distribution, and to the ambient magnetic field, leads to induced magnetic-field intensities on the interior of the charge distribution. Such a polarization distribution may occur at the base of a homogeneous auroral arc.

It is therefore of considerable interest to estimate the magnetic field B within the interior of a simple charge distribution, maintained by continuous supply of incident particles, and to try to assess the implications for auroral morphology.

An increase of trapped-particle flux density due to an injection event over a given longitude will be regarded as the source of incident particles. To permit growth of a space charge, the flux must consist predominantly of particles of one sign (for example, electrons). The over-all space charge distribution is, to some extent, neutralized by small motions of charges in the surrounding partly ionized upper atmosphere.

The space charge distribution considered here is oriented in a surface of constant integral variant

$$I = \int_{B_m}^{B_m^*} \sqrt{1 - B/B_m} \, dl$$

the geomagnetic field B [Vestine and Sibley, 1960]. Such a surface will be elongated approximately along lines of geomagnetic latitude. The thickness of the sheet will be taken as small compared to its longitudinal extent. Suitable reference axes are provided by taking the origin at right-handed Cartesian coordinates at the top of the sheet with the z axis downward; the y axis normal to the sheet, and the x axis internal to the sheet and horizontal. For purposes of comparison with the orientation of an auroral

arc due to incident electrons in the northern hemisphere, z is in the direction of the geomagnetic field, x is to the east and tangent to the mirror-point curve for particles of fixed energy drifting along a curve of constant integral invariant [Vestine and Sibley, 1960].

Suppose that the incident flux is sufficient to maintain a space charge distribution ρ such that $\rho(x, z) = \text{constant}$ and $\rho(y)$ is given by $\rho = \rho_0 \cos(\pi/b)y$, where b is the thickness of the charge distribution and the distribution is symmetric about the plane $y = 0$. The particle drift velocity magnitude v is approximately equal to E/B ; this drift will be in the x direction, the approximation being very good in the F region, and fairly good down to upper reaches of the E region, where the collisional frequency becomes comparable with the spiral frequency of electrons.

From Poisson's equation

$$\nabla^2 V = \frac{d^2 V}{dy^2} = -4\pi c^2 \rho_0 \cos(\pi/b)y = -\frac{dE}{dy} \quad (5)$$

where V is the electric potential, c the velocity of light, and b the thickness of the sheet. Thus

$$E = 4c^2 \rho_0 b \sin(\pi/b)y \quad (6)$$

may provide a useful approximation of physical interest. Since the distribution is symmetric about $y = 0$, and the charge-drift direction is opposite on either side of this plane, the magnetic field produced by the moving charges opposes the original ambient field B_0 inside the charge distribution. This decrease in the magnetic field lowers the mirror points for trapped radiation mirroring inside the charge distribution.

The magnetic field decrease dB , due to current flow in a sheet of thickness dy , at a distance y from the center of the charge distribution, is approximately (except near end points) $dB = 2\pi \rho v dy = 2\pi \rho (E/B)dy$, or roughly $2\pi (\rho/B_0) E dy$; if B_0 is the field in the absence of the currents, the field decrease due to these currents is small compared with B_0 . Noting that v reverses on crossing the plane $y = 0$, the field on the central plane of the charge sheet $B(0)$ can be written

$$B(0) = B_0 - \frac{8c^2 \rho_0^2 b^2}{B_0} \quad (7)$$

Consideration of the contribution of regions $(-y, y)$ and $(-b/2, y)$, $(y, b/2)$ leads readily to the change in field as a function of y

$$\Delta B(y) = -(8c^2 \rho_0^2 b^2 / B_0) \cos^2 (\pi/b)y \quad (8)$$

Thus B is reduced inside the sheet. For this reason, the particle flux increases, since particles mirroring at higher altitudes (lower field intensities) can now penetrate the region. Hence ρ_0 increases, and b decreases, so this theory may provide some insight respecting the remarkable thinness often remarked in auroral arcs. The effect is reminiscent of the pinch effect in charged particle beams, but here the effect is due to lowering of mirror points [Bennett, 1934]. It is not known whether or not transitions in auroral form from a diffuse glow over a broad area to a thin arc can be explained using this mechanism. More detailed study is desirable on this point. In the meantime, however, the reduction of b and increase in ρ_0 clearly predicted by the foregoing analysis, are in encouraging agreement with observation.

The space charge density used above can be considered in a dynamic sense as the number of particles per cubic centimeter times the particle charge. The contribution to n depends upon source, upon particles mirroring in a given region, and upon particles traversing the region [Welch and Whitaker, 1959]; also included are particles coming to rest in the region as a result of inelastic collision processes. In the case of an isotropic 6-keV electron flux of the order of 5×10^{10} particles $\text{cm}^{-2} \text{sec}^{-1} \text{steradian}^{-1}$ [McIlwain, 1960], n is about $10^7/\text{cm}^3$. ΔB is very sensitive to the thickness b . However, for $b = 4 \text{ km}$, $B_0 = 0.450$, and $n = 10^7$, then $\Delta B = -8c^2 e^2 n^2 b^2 / B_0$, so $\Delta B = -0.0074 \text{ gauss} = -740 \gamma$. This corresponds to a change in mirror-point altitude $(0.0074/0.450)r_0 = 110 \text{ km}$, permitting deeper penetration of incident-particle flux. Since $\Delta B \sim 4\pi b \sigma_2 E = 4\pi n e v b \sigma_2 / \sigma_1$, where σ_2 is the Hall conductivity, when the flux $n e v \sim \sigma_1 E$ (the loss), a homogeneous arc may be lowered to maximum σ_2/σ_1 , at height about 110 km.

The observable effect of the diamagnetic sheet mechanism would be a transition from a quiescent broad glow pattern to a thin auroral arc with ionization drifting at high velocity parallel to the arc surface and normal to the geomagnetic field. For space-charge distributions due to electron flux, the drift will be opposite that for protons.

The composition of the incident flux may therefore be expected to contribute to drifts in auroral rays, which may in part explain observational data on drift of ionization at auroral altitudes [Nichols, 1957] as well as frequently observed visible drifts in aurora [Becken and Maehlum, 1960]. The broad features of the present diamagnetic sheet may be identified with the auroral arcs and their morphology. In particular, it will be instructive to consider the stability of such auroral arcs in another way and to consider whether evidence of such instability exists. This we will discuss next, neglecting other features of the diamagnetic sheet, such as the fact that the mirror point of the down-coming spiraling radiation arc is supposed within the electrically conducting ionosphere, so that the space charges rapidly dissipate. It will be assumed, however, that the rate of supply of charge is adequate to maintain the system.

6. DEVELOPMENT AND STABILITY OF DRAPERIES AND RAY ARCS

If the diamagnetic sheet model described above in (4) and (5) is assumed, electron-beam theory may be of special interest in interpreting features of ray and drapery structures that develop from an initial homogeneous auroral arc. Of such beam investigations, the experimental studies by Webster [1955], Kyhl and Webster [1956], and Cutler [1956] show instability patterns in sheet electron beams extremely suggestive of auroral behavior. Alfvén [1950] suggested this application of electrodynamics to drapery structures, but theoretical interest has apparently been centered around electron-beam tube development. Pierce [1956] and Kyhl and Webster [1956] treat the problem of the hollow cylindrical electron beam developing stability criteria.

The following treatment aims to apply and extend the theory in connection with the sheet beam described in (4). It is first shown that elementary considerations of a thin-sheet beam aligned along the geomagnetic field, lead to a plausible explanation of observed sheet-beam instability. If there is an electric field due to the space charge of the beam, drift motion of the electrons in the crossed electric and magnetic fields will lead to growth of any charge density perturbation.

The general effect of an electric field perturbing

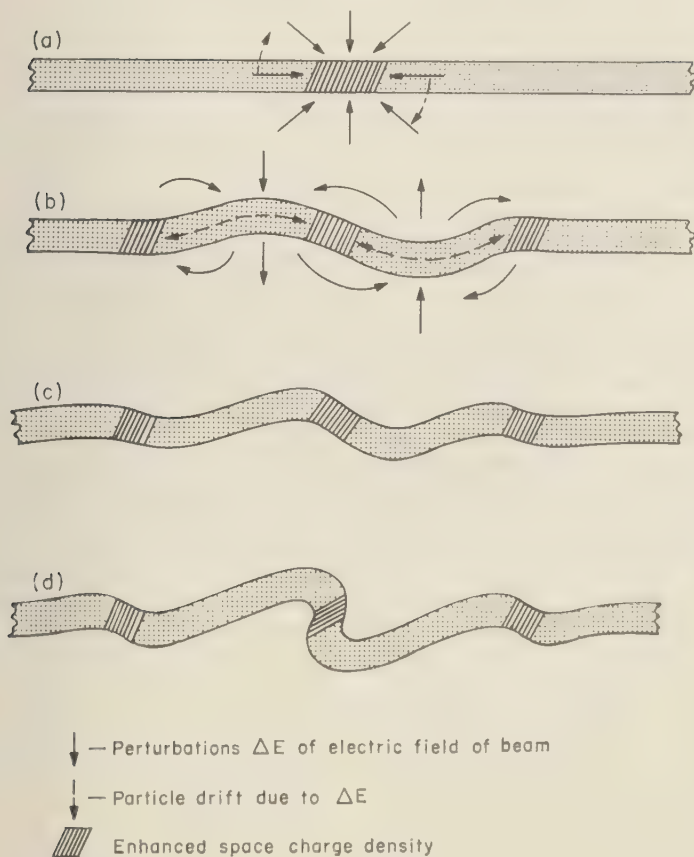


Fig. 1. Mechanism of disturbance buildup in thin auroral arc.

on due to a charge perturbation is illustrated in Figure 1 as a drift motion caused by the field perturbation. It is seen that the drift distorts the sheet beam into an 'S' curve. This leads to a further perturbation of the electric field. As a consequence, the drift motion enhances the original charge perturbation, and charge perturbations propagate along the beam at right angles to the magnetic field. The progression of this distortion leads ultimately to vortical regions of high-particle flux, connected by thin filaments [Kyhl and Webster, 1956].

Early stages of this process can be identified with auroral rays involving distortions of a sheet beam of incident particles [Alfvén, 1950].

Consider the theory of a sheet beam of the kind indicated in (4), for reasons of theoretical

convenience being supposed of zero thickness. Any waves associated with finite beam thickness are therefore neglected. A periodic boundary condition is obtained by specifying $n + 1$ regions of variation for the sheet length $n\delta$ where δ is the distance separating regions of variation.

Suitable solutions giving the perturbations or displacements in a plane sheet auroral arc which vary with time and distance in the x direction (direction of east-west drift motion) and z direction (direction of downward particle propagation along the geomagnetic field B) are conveniently regarded as a product of typical terms

$$e^{i\omega t} e^{-i\beta z} e^{-i\gamma x}$$

where $\gamma = 1/\delta$, with δ real [Pierce, 1956]. Let

$$W = \omega - \beta u_0 - \gamma u_1$$

where u_0 and u_1 are the average particle velocities in the z and x directions, respectively.

The equations of motion are

$$\begin{aligned}\ddot{x} &= iW\dot{x} = \frac{e}{m} \frac{\partial V}{\partial x} + \omega_c \dot{y} \\ \ddot{y} &= iW\dot{y} = \frac{e}{m} \frac{\partial V}{\partial y} - \omega_c \dot{x} \\ \ddot{z} &= iW\dot{z} = \frac{e}{m} \frac{\partial V}{\partial z}\end{aligned}\quad (9)$$

where e/m is taken as positive and $\omega_c = Be/m$ is the spiral or gyro frequency.

The equation of continuity must be satisfied for particle flow within the auroral arc. That is, the divergence of the current density is equal to the negative of the time rate of change of the charge density in the arc. Let ρ be the charge density of the auroral sheet of thickness b and ρ_0 the average value of ρ . Then

$$i\omega\rho = i\beta(\rho u_0 + \rho_0 \dot{z}) + i\gamma(\rho u_1 + \rho_0 \dot{x}) \quad (10)$$

and

$$\rho = (\beta\rho_0/W)\dot{z} + (\gamma\rho_0/W)\dot{x}, \quad (11)$$

with ρ_0 negative. Consequently the fluctuations in charge density depend both on frequency and displacement velocity. Following Pierce [1956], if B_z is the magnitude of the magnetic field at the surface of the beam, and u_1 the drift velocity, the surface electric field E_y is $-\partial V/\partial y = u_1 B_z$.

The potential due to the thin auroral arc of thickness b will be assumed to be of the form

$$\begin{aligned}V_1 e^{-ky} - (\alpha b\rho_0/\epsilon)y, & \quad y > 0 \\ V_2 e^{ky} + (1 - \alpha)(b\rho_0/\epsilon)y, & \quad y < 0\end{aligned}\quad (12)$$

where α is a constant, and ϵ the dielectric constant.

From Poisson's equation $k^2 = \beta^2 + \gamma^2$, and there must also result the relation

$$V_1 - V_2 = (b\rho_0/\epsilon)y \quad (13)$$

where y is a small displacement in the y direction. From Gauss's theorem, to the first order,

$$-k(V_1 + V_2) = (b\rho_0/\epsilon) \quad (14)$$

Hence

$$V_1 + V_2 = \frac{1}{k} \frac{\beta b\rho_0}{W} \dot{z} + \frac{\gamma b\rho_0}{W} \dot{x} \quad (15)$$

Thus

$$\begin{aligned}-\frac{\partial V}{\partial y} &= -\frac{k}{2}(V_1 - V_2) = -\frac{k b\rho_0}{\epsilon} y \\ -\frac{\partial V}{\partial z} &= i(\beta^2 u_1 B/kW)\dot{z} + i(\beta\gamma u_1 B/kW)\dot{x} \\ -\frac{\partial V}{\partial x} &= i(\beta\gamma u_1 B/kW)\dot{z} + i(\gamma^2 u_1 B/kW)\dot{x}\end{aligned}\quad (16)$$

Substituting the above in the equations of motion (9) and eliminating velocities (together with $k^2 = \beta^2 + \gamma^2$) yields

$$\begin{aligned}(W^2 - ku_1\omega_c)(W^2 + ku_1\omega_c) \\ = \omega_c[W^2 - (\beta^2/k)u_1\omega_c]\end{aligned}\quad (17)$$

In cases of physical interest in connection with aurora

$$1/4 \gg k^2 u_1^2 / \omega_c^2 - \beta^2 u_1 / k\omega_c \quad (18)$$

hence

$$W = \pm\omega_c \left[1 + \frac{k^2 u_1^2}{\omega_c^2} - \frac{\beta^2 u_1}{k\omega_c} \right]^{1/2} \quad (19a)$$

$$W = \pm i\omega_c \left[\frac{k^2 u_1^2}{\omega_c^2} - \frac{\beta^2 u_1}{k\omega_c} \right]^{1/2} \quad (19b)$$

Equation 19a gives, very nearly, $W = \pm\omega$, which is of no physical interest in the present context. Equation 19b represents the condition for growing waves when

$$k^3 u_1 > \beta^2 \omega_c \quad (20)$$

Now

$$W - \omega = \beta u_0 - \gamma u_1 = \omega - \beta u_0 - u_1/\gamma$$

For stationary waves $\omega = 0$, and

$$\beta = -\frac{1}{\delta} \frac{u_1}{u_0} \pm i\omega_c \left[\frac{k^2 u_1^2}{\omega_c^2} - \frac{\beta^2 u_1}{k\omega_c} \right]^{1/2} \quad (21)$$

The wavelength of such waves propagating in the z direction will be

$$L = -(Re\beta)^{-1} = \delta u_0 / u_1 \quad (22)$$

The time constant for buildup in the z direction is given by

$$\tau = -(Im\beta)^{-1} = \frac{1}{\omega_c} \left[\frac{k^2 u_1^2}{\omega_c^2} - \frac{\beta^2 u_1}{k\omega_c} \right]^{-1/2} \quad (23)$$

where it is assumed that $Re\beta \gg Im\beta$, and β^2 taken as real. We find that τ can also be written

$$\tau = \frac{1}{ku_1} \left(1 - \frac{\beta^2 \omega_c}{k^3 u_1} \right)^{-1/2} \quad (24)$$

Setting $-\beta = (u_1/\delta u_0)$ as an approximation, and with $\gamma \gg \beta$, we have $L \gg \delta$ and $k \cong \gamma = 1/\delta$. This implies

$$\tau = \frac{\delta}{u_1} \left[1 - \frac{\delta u_1 \omega_c}{u_0^2} \right]^{-1/2} \quad (25)$$

For the earth's field at auroral heights, take $B = 0.45$, so that $\omega_c = 8 \times 10^6 \text{ sec}^{-1}$, $= 3 \times 10^6 \text{ cm}$ (from observations), and suppose $u_1 = 6 \times 10^4 \text{ cm/sec}$ (for ionization drift velocities) within a typical fluted auroral structure. Thus instabilities will develop in a time $\tau = (1 - 1.44 \times 10^{17}/u_0^2)^{-1/2}$, if $u_0^2 > 15 \times 10^{16}$, or $u_0 \gtrsim 4 \times 10^8 \text{ cm/sec}$. This corresponds to electron energies of about 40 ev.

The diamagnetic sheet mechanism of 4 shows that u_1 is determined by the space-charge distribution, and observed values of u_1 suggest values of E smaller than the model value. For a given structure (δ and b given) u_0 will have an upper limit for stability which depends upon electron mobilities, and thus is related to the conductivity at auroral altitudes.

Since in a diamagnetic sheet the electric driving force yielding the drift velocity u_1 increases with increasing charge density ρ , decreased conductivity reduces the loss of ρ with time, or tends to enhance u_1 with time. From equation 25, since the growth time τ is shortened when u_1 is increased, decreased electric conductivity leads to increased instability of the spray. This accords with various experimental observations of electron beams [Cutler, 1956].

It is also interesting to note from (25), that u_0^2 must exceed $\delta u_1 u_1$ in order that τ be real, thereby promoting growth of instabilities. Consequently the stability is sensitive to increase in the incoming particle velocity u_0 .

From the foregoing, we see that elementary considerations of electron-beam theory predict perturbations of a thin auroral arc. The first stage in perturbation growth resembles very closely auroral drapery structures. Perturbation growth proceeds to raylike patterning in which the charge distribution as indicated by experiment [Kiyhl and Webster, 1956; Cutler, 1956] is critical about magnetic field lines. Because of higher mirror points of the remaining particles, the base of a ray arc is higher than in a homogeneous arc.

7. COMPARISON WITH OBSERVATION

Auroral features before and after midnight. It has frequently been remarked that homogeneous auroral arcs of longer duration are a feature of the hours before magnetic midnight and that displays thereafter are more transitory and fleeting in space and duration. Since the ionosphere decreases in electric conductivity during the night, the theory of stability of homogeneous auroral arcs would appear to predict this outstanding feature of auroral morphology.

Radar observations of auroral drift. Investigations of auroral reflections using HF and VHF radar [Nichols, 1957; Unwin, 1959; Lyon and Kavadas, 1958; Bullough and Kaiser, 1957] indicate motion of reflecting regions, westward before magnetic midnight and eastward after magnetic midnight. These data were obtained using antennas with broad radiation patterns. Leadabrand, Presnell, Berg, and Dyce [1959], using UHF narrow beam-width radar, have obtained Doppler-shift patterns indicating predominantly westerly drift motions, independent of time of day, with average velocities of 500 m/sec. These UHF data gave similar results for both diffuse and discrete auroral forms. The diamagnetic sheet mechanism, developed above, predicts drift directions within auroral forms due to incident electrons observed to the north, corresponding to those inferred by Leadabrand, Presnell, Berg, and Dyce [1959] but with opposite results for the poleward side of the diamagnetic sheet.

Leadabrand and his co-workers further found that east-west echo drift of the reflecting region aggregate was not systematic (although the 500-m/sec Doppler-shift drift was predominantly westward), with eastward or westward drifts equally likely. Diffuse auroral echoes rarely exhibited any motion, and most of the time they appeared to come from the underside of a layer extending as much as 800 km in magnetic latitude and 500 km east-west at about 90- to 110-km altitude (lower in the north). Discrete echoes were usually reflected from the same region as the diffuse. The discrete echoes corresponded to auroral arcs along lines of geomagnetic latitude. The motion of the sheet as a whole, as inferred from the diamagnetic sheet mechanism, would be controlled by the broad pattern of local electric and magnetic fields arising from

ionospheric current systems, as *Nichols* [1957] has suggested.

It may well be that many features of auroral drift motions are explained by the diamagnetic sheet model, since it moves readily in response to variations in incident-particle flux, to the local electric fields, and to magnetic gradients associated with ionospheric current systems. The latter may play a part in the formation of pairs of homogeneous auroral arcs joined at one end [*Vestine*, 1960]. The high east-to-west UHF Doppler-shift drifts of *Leadabrand*, *Presnell*, *Berg*, and *Dyce* [1959] can be interpreted on the basis of the drift velocities internal to the sheet. Observational data such as those of *Kim* and *Currie* [1958] do not afford indications of the drift velocities internal to the sheet.

Observations of auroral form transitions. *Stofregen*, *Derblom*, and *Omholt* [1960], reporting on studies of *D*-region ionization during auroras in northern Sweden, find that such ionization is closely associated with sudden increases in auroral visual intensity. They infer that both primary electrons of energy in excess of 100 kev and secondary X rays contribute to *D*-region ionization. They ascribe such high energy radiation to leakage from the Van Allen belts [*Arnoldy*, *Hoffman*, and *Winckler*, 1960]. The auroral forms preceding the sudden intensity increases were typically G, HA, HB, and R moving slowly toward lower latitudes. Auroral intensity increased slowly and smoothly for about 1/2 to 2 hours, then suddenly increased in intensity to a high value. Following the sudden increase, the auroras were much brighter, varying rapidly in visual intensity, and covered great parts of the sky, moving south. Red color appeared, followed by pulsating forms ('flaming aurora'). It is noted that the observations seem to accord well with the present theory, the increased brightness and pulsations being predicted as a manifestation of instability before breakup. The diamagnetic sheet mechanism offers a possible means of tapping high mirror-point trapped radiation, accentuating the brightness and hastening the breakup.

Observations of pulsating or flaming aurora. Oscillatory phenomena are commonly observed in auroral displays. The most spectacular are described as so-called 'flaming aurora' which usually develop immediately preceding the end of displays. Other modes of pulsation have been

reported, however. *Geddes* [1939] reports three pulsating arcs in which waves were observed traveling along the arcs following one another at intervals of about 10 seconds. The phenomena immediately preceded the RA phase and stopped before development of RA. Using the results of the electron beam instability theory we would deduce drift velocities of $u_1 = \delta/\tau$, where δ is the separation of regions of charge density perturbation and $\tau = 10$ sec as given by *Geddes*' observations. Suppose $\delta = 5$ km, the separation of elements of the developed R, then $u_1 = 5 \times 10^4$ cm/sec. This is in agreement with drift velocities obtained from radar Doppler shift measurements.

These results for flaming aurora (F), with vertical propagation of waves, as described in the *Photographic Atlas of Auroral Forms* [1939] are predicted by the present theory for auroral morphology. According to *Elvey* (private communication), he and his co-workers have also considered the flaming aurora as a manifestation of plasma instabilities.

In the unusual flaming aurora observed by *Geddes* [1939] in New Zealand, the wave moment involved the progress of a bright HA from a southern elevation of 15° to 50° in about $1/2$ second, followed by subsequent sequences of similar arcs. If a distance of 300 km is taken from observer to HA, the distance traversed about 200 km. This gives a wavelength L of about 400 km (peak intensity to peak intensity) with a period τ of $1/2$ second for buildup of the disturbance. It would therefore be inferred that incident-particle velocity $u_0 = L/\tau$ is about 10^8 cm/sec. This corresponds to electron energy somewhat less than the 6 kev reported by *McIlwain* [1960] from direct measurements in bright HA.

Vestine [1944] reports a vertically propagating wave display. In a flaming aurora associated with HB, the wavelength L determined from the data is about 25 km with period τ of about 0.002 second (observed over a span of about 12 waves). This gives the incident particle velocity u_0 as about 1.2×10^9 cm/sec, in fair correspondence to *McIlwain*'s [1960] direct electron energy measurements. Near the end of the display, the wavelength had about doubled, the period was about half the original, and the HB had disappeared. Using the electron beam instability theory, we would predict that the

incident-particle velocity u_0 is about 4 times the original, or about 10^{10} cm/sec. This corresponds to electron energies of about 100 keV as inferred by Stoffregen, Derblom, and Omholt [1960] in their D -region ionization studies.

Acknowledgment. This paper is based on research sponsored by the National Aeronautics and Space Administration under contract NAS5-276.

REFERENCES

- Alfvén, H., *Cosmical Electrodynamics*, Oxford University Press, 237 pp., 1950.
- Arnoldy, R. L., R. A. Hoffman, and J. R. Winckler, Observations of the Van Allen radiation regions during August and September, 1959, part I, *J. Geophys. Research*, **65**, 1361-1376, 1960.
- Breen, J., and B. Maehlum, Drift measurements at Kjeller on the ionospheric F region, *J. Geophys. Research*, **65**, 1485-88, 1960.
- Chapman, W. H., Magnetically self-focusing streams, *Phys. Research*, **45**, 890-897, 1934.
- Cullen, K., and T. R. Kaiser, Radio reflections from aurora, III, the association with geomagnetic phenomena, *J. Atmospheric and Terrest. Phys.*, **11** (3-4), 237-254, 1957.
- Hamberlain, J. W., On a possible velocity dispersion of auroral protons, *Astrophys. J.*, **126**, 245-252, 1957.
- Hamberlain, J. W., *Physics of the Aurora and Airglow*, Academic Press, New York, chapter 7, 1960.
- Hamberlain, J. W., J. Kern, and E. H. Vestine, Some consequences of local acceleration of auroral primaries, *J. Geophys. Research*, **65**, 2535-2537, 1960.
- Hapman, S., and V. C. A. Ferraro, cited in Chapman, S., and J. Bartels, *Geomagnetism*, 2 vols., Clarendon Press, Oxford, 1940.
- Hristofilos, N., The Argus experiment, *J. Geophys. Research*, **64**, 869-875, 1959.
- Utler, C. C., Instability in hollow and strip electron beams, *J. Appl. Phys.*, **27**, 1028-1029, 1956.
- Ivey, C. T., Problems in auroral morphology, *Proc. Nat. Acad. Sci.*, **43**, 63-75, 1957.
- Edwards, M., Some characteristics of auroras in New Zealand, *Terrest. Magnetism and Atmospheric Elec.*, **44**, 189-193, 1939.
- Eppner, J. P., Time sequences and spatial relations in auroral activity during magnetic bays at College, Alaska, *J. Geophys. Research*, **59**, 329-338, 1954.
- Kim, J. S., and B. W. Currie, Horizontal movements of aurora, *Can. J. Phys.*, **36**, 160-170, 1958.
- Ruskal, M., and M. Schwarzschild, Some instabilities of a completely ionized plasma, *Proc. R. Soc. London, A*, **223**, 348-360, 1954.
- Yih, R. L., and H. F. Webster, Breakup of hollow cylindrical electron beams, *IRE Trans. on Electron Devices*, **ED-3**, 172-183, 1956.
- Radabrand, R. L., R. I. Presnell, M. R. Berg, and R. B. Dyce, Doppler investigations of the radar aurora at 400 Mc/s, *J. Geophys. Research*, **64**, 1197-1203, 1959.
- Lyon, G. F., and A. Kavadas, Horizontal motions in radar echoes from aurora, *Can. J. Phys.*, **36**, 1661-1671, 1958.
- McIlwain, C. E., Direct measurements of particles producing visible aurora, doctoral dissertation, Graduate College of the State University of Iowa, 59 pp. + figures, 1960.
- Nichols, B., Auroral ionization and magnetic disturbances, *Proc. IRE*, **47** (2), 245-254, 1959.
- Nichols, B., Drift motions of auroral ionization, *J. Atmospheric and Terrest. Phys.*, **11** (3-4), 292-293, 1957.
- Photographic Atlas of Auroral Forms*, Internat. Union Geod. Geophys., Oslo, 1930.
- Pierce, J. R., Instability of hollow beams, *IRE Trans. on Electron Devices*, **ED-3**, 183-189, 1956.
- Post, R. F., Controlled fusion research, *Rev. Mod. Phys.*, **28**, 338-362, 1956.
- Rosenbluth, M. N., Plasma physics, *Physics Today*, **13**, no. 8, 27-30, 1960.
- Rosenbluth, M. N., and C. L. Longmire, Stability of plasmas confined by magnetic fields, *Ann. Phys.*, **1**, 120-140, 1957.
- Stagg, J. M., Some general characteristics of aurora at Fort Rae, N.W. Canada, 1932-33, The British National Committee for the Polar Year, 1932-33, Royal Society, London, 6 pp., 1935.
- Stagg, J. M., *British Polar Year Expedition, Fort Rae, N.W. Canada, 1932-33*, Vol. 1, Royal Society, London, 1937.
- Stoffregen, W., H. Derblom, and A. Omholt, Some characteristics of the D -region ionization during auroral activity, *J. Geophys. Research*, **65**, 1699-1704, 1960.
- Störmer, C., *The Polar Aurora*, Clarendon Press, 403 pp., Oxford, 1955.
- Unwin, R. S., Movement of auroral echoes and the magnetic disturbance current system, *Nature*, **183** (4667), 1044-1045, 1959.
- Vestine, E. H., Preliminary summary, auroral observations, Meanook, Canada, December 1, 1932 to June 30, 1933, *Terrest. Magnetism and Atmospheric Elec.*, **49**, 25-36, 1944.
- Vestine, E. H., Remarkable auroral forms, Meanook Observatory, Polar Year, 1932-33, *Terrest. Magnetism and Atmospheric Elec.*, **48**, 233-236, 1943.
- Vestine, E. H., and W. L. Sibley, The geomagnetic field in space, ring currents, and auroral iso-chasms, *J. Geophys. Research*, **65**, 1967-1979, 1960.
- Vestine, E. H., Polar auroral, geomagnetic, and ionospheric disturbances, *J. Geophys. Research*, **65**, 360-362, 1960.
- Webster, H. F., Breakup of hollow electron beams, *J. Appl. Phys.*, **26**, 1386-1387, 1955.
- Welch, J. A., and W. A. Whitaker, Theory of geomagnetically trapped electrons from an artificial source, *J. Geophys. Research*, **64**, 909-922, 1959.

The Relationship between Unique Geomagnetic and Auroral Events¹

Y. SOBOUTI

*Yerkes Observatory, University of Chicago
Williams Bay, Wisconsin*

Abstract. From magnetic data obtained at eleven Canadian stations, the ionospheric current patterns in the auroral zone, during several magnetic storms, have been sketched and the predominant current patterns determined for each phase of an 'average' storm. It is found that the auroral displays tend to occur along current lines.

A high correlation is found between the geomagnetic latitudes of the southern extents of auroral displays and the most southerly current lines. When these two sets of data are plotted against a 'storm-phase,' a southward shift of the aurora is seen to accompany the southward motion of ionospheric currents.

INTRODUCTION

An attempt is made, in this paper, to relate individual auroral displays to their simultaneously occurring geomagnetic storms. Following the often quoted concept that the ionospheric currents responsible for magnetic storms are associated with auroras, the data on a number of simultaneous auroras and magnetic storms have been studied to find the dominant patterns of the ionospheric overhead currents.

The magnetic data have been obtained from five permanent observatories and six temporary magnetic stations in Canada (see Figs. 4 and 5) that were operating during the IGY (1957-1958). The distribution of the stations covers a fairly wide range of latitude, including the auroral zone and part of the polar cap, which are of great geomagnetic interest.

Visual auroral observations were made at more than 300 stations distributed all over Canada (*Canadian National Committee for the IGY*, 1959). The National Research Council of Canada has made one map for each hour of the night during the IGY. Each map contains the auroral information (approximate location, type, color, and brightness, as estimated by observers) from 5 minutes before to 5 minutes after the specified hour on the map.

The analysis is based on data obtained during 20 days, each characterized by the fact that five or more Canadian all-sky camera stations were

operating and 75 per cent or more of these showed auroras. These days are: October 1, 20, 21, 1957; November 24, 25, 27, 29, 1957; December 1, 11, 12, 13, 30, 1957; January 13, 1958; and April 15, 16, 17, 18, 19, 21, 24, 1958.

The selection of days was made on the basis of auroral observations only, without reference to the magnetic activity. It later developed, however, that 10 of these days were internationally geomagnetically disturbed (5 days in each month), 7 days were immediately before or after the 5 disturbed days, 3 others had moderate magnetic activity, and none were among the 10 internationally quiet days [see 'Geomagnetic and Solar Data,' *J. Geophys. Research*, 63, 1958].

REPRESENTATION OF MAGNETIC DISTURBANCES

The magnetic data on 5 international quiet days were used to determine the reference line on the magnetograms. The size of a given disturbance was measured as the average departure from the reference line, in 15-minute intervals, for the dark hours. Measurements were taken on three components, either X , Y , and Z or H , D , and Z . The total horizontal disturbance force and its azimuth were then calculated and plotted against Greenwich Mean Time, along with the vertical component of the disturbance (Fig. 1). One chart was made for each of the 20 days and contains the disturbance field for the five permanent observatories only. These diagrams give a vivid description of the magnetic storm over the range of latitude covered by the stations, and facilitate the sketching of the patterns of the overhead

¹ This work is based on a thesis for the M.A. degree submitted to the Department of Physics at the University of Toronto.

ionospheric currents presumed to be responsible for the disturbance field.

In a statistical sense, at Resolute Bay (geomagnetic latitude 83.2°N) the activity is low. Variations in the field components are slow and take place without any rapid changes. The horizontal component of the disturbance field, starting from the southwest, rotates clockwise and increases very slowly in intensity. Once it reaches northwest, the rotation becomes still

slower and within 4 to 6 hours the horizontal component approaches the north, or occasionally reaches the northeast. (It should be noted that Fig. 1 is only a sample and might differ, in some respects, from these general statements.) The vertical component Z , which is usually downward at evening hours, decays gradually and becomes upward after midnight. The low intensity of the Z component, together with its very slow variations, might serve as an indication

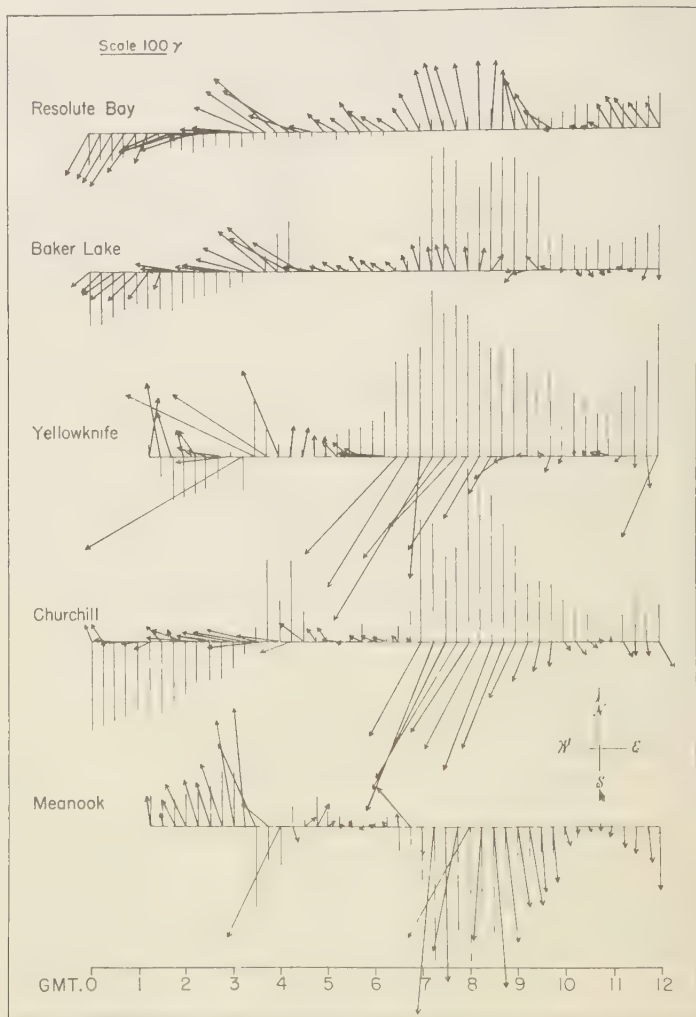


Fig. 1. Horizontal component (arrows) and vertical component (straight lines) of the geomagnetic disturbance field, April 15, 1958.

that the overhead currents can be approximated better by sheet currents than linear ones.

At Baker Lake (geomagnetic latitude 73.0°N) the behavior of a storm is more or less similar to that at Resolute Bay, except that (a) the variations in both the H and Z components are more rapid, and (b) the intensity of the Z component is larger. These differences might indicate either narrower sheets of ionospheric currents, or sharp bending of current lines in this region, or both.

At Yellowknife (geomagnetic latitude 69.1°N) and Churchill (geomagnetic latitude 68.4°N) the disturbance is most intense. The storm begins with an increase in the H component (first phase) which decays after a while and grows again negatively (main phase). During the main phase, the disturbance is more intense and lasts much longer than in the first phase. The Z component is downward during evening hours, upward for the rest of the night, and is remarkably large.

Meenook (geomagnetic latitude 62°N) has the typical characteristics of a low-latitude station. There is a distinct positive phase in the H component which is followed by an intense negative main phase. The intensity and rapid fluctuations of the H component are comparable to those at Yellowknife and Churchill, but the Z component is less active. It remains mostly downward except during the first phase.

The hypothetical ionospheric current system that would produce these magnetic disturbances would have the following general characteristics: at latitudes such as that of Meenook, just outside the auroral zone, the currents are more intense and concentrated in narrower sheets than they are in the polar-cap region (Resolute Bay and Baker Lake). In the inner portion of the auroral zone, at Yellowknife and Churchill, the large Z component suggests still narrower sheets of currents, probably accompanied by sharp bendings above these stations. However, the abnormal behavior of the Z component within the auroral zone is not well understood, and even circular or semicircular currents (which give the highest Z and lowest H components) fail to explain its peculiar activity.

The magnetic disturbance vectors, for all seven stations, are shown on the auroral maps (see Figs. 4 and 5) with slight modifications. It was mentioned above that each auroral map contains only the information from 5 minutes before to 5 minutes after the specified hour on the map.

To keep the magnetic and auroral data consistent, measurements of the disturbance field were selected for the same intervals as the auroral data. Further, the highest values (rather than the averages) of the disturbance, during these intervals, have been used.

DETERMINATION OF THE CURRENT SYSTEMS

If the currents producing the magnetic changes are actually located in the ionosphere, the E layer is the most likely region in which they might exist. Vestine [1960], in a discussion of magnetic storms, has concluded that there must be polar electric currents, flowing near or within the E region, that give rise to magnetic storms. Ratcliffe and Weekes [1960] have shown that, at places not too near the equator, the ionosphere is highly conducting between about 90 and 140 km (wherein the dynamo region supposedly lies). They also have stated that the calculated dynamo currents, arising from the tidal motion of air, are of the same order as currents deduced from geomagnetic data. Vegard and Krogness [1920] found an average height of 107.9 km for the lower borders of 1927 auroral displays. They also have shown that the mean distance from the lower border to the maximum luminosity (which presumably corresponds to the center of the current lines) is about 6 to 9 km. Weaver and Skinner [1960], assuming that the ionization within an auroral arc is proportional to the auroral light intensity, have calculated the approximate conductivity of the ionosphere within an auroral arc. They concluded that the maximum conductivity during an active auroral period occurs at a height of about 105 km.

In view of these considerations, an average height of 110 km seems appropriate for ionospheric overhead currents. Figures 2 and 3 illustrate the means used to locate the currents. In Figure 2 the horizontal and vertical components of the magnetic field of sheet currents of various widths are plotted against the distance from the center of those currents. The width of the sheets, $2W$, ranges from 0 to 600 km. In Figure 3, the ratio of Z/H is plotted against the distance. It is apparent that, at distances exceeding about 400 km, the magnetic effects of sheet currents are comparable to those of the linear one.

On the basis of the preceding discussion of the behavior of the disturbance fields at different

stations, the following widths were assumed for the current sheets: 300 km for the southern stations, Meanook, Saskatoon, Flin Flon, The Pas, and Winnipeg; 200–300 km for the auroral zone stations, Bird, Churchill, Yellowknife, Ennadai Lake, and Baker Lake; 500 km and over for the polar-cap station, Resolute Bay.

From the ratio Z/H at any station, the curves of Figure 3, and the right-hand rule, the hypothetical current may be located for any observation of the magnetic disturbance. At the southern stations, a correction was made for the effect of the neighboring current, by means of the curves

of Figure 2. (The correction was usually small, of the order of a few tens of kilometers.) Inside the auroral zone, however, because of the abnormal behavior of the Z component, the correction did not prove to be useful and seemed to result in more spurious current patterns.

No correction was made for the induced underground currents. The effect of an induced current is to reduce the Z and enhance the H component. Since in the present problem the height of the current is assumed to be fixed, the apparent current thus determined would be closer to the station than the real one. In any event, the

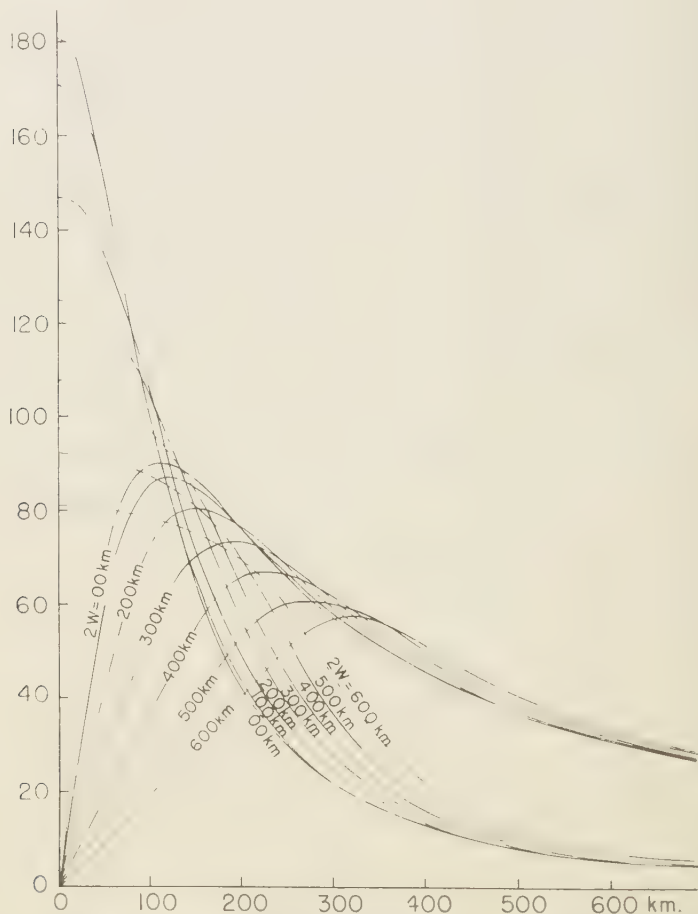


Fig. 2. Horizontal component (H) and vertical component (Z) of the magnetic field of sheet currents plotted against the distance from the center of the sheets. The sheets are assumed to have a width of $2H$ and to be at a height of 110 km. The scale of the magnetic field is arbitrary and we have used only the relative field intensities of the currents.

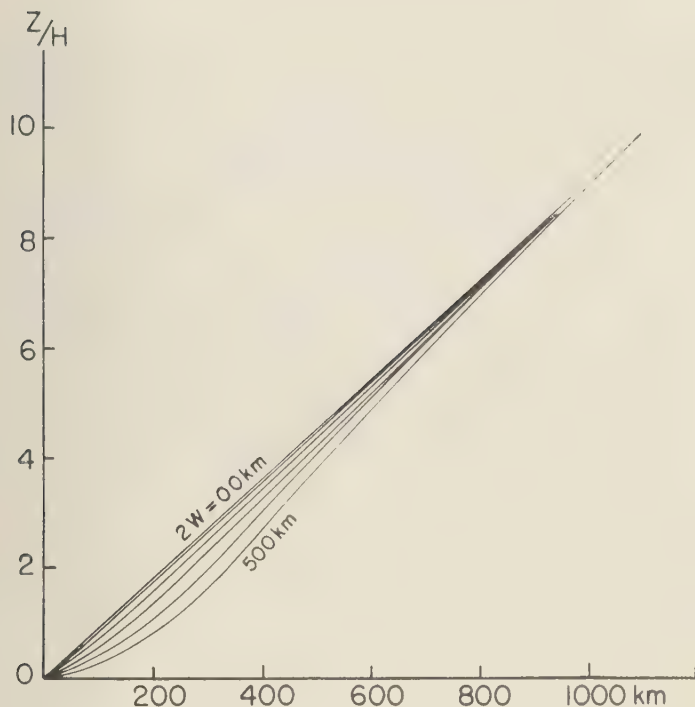


Fig. 3. Ratio Z/H of sheet currents plotted against the distance from the center of the sheets. The sheets are assumed to have a width of $2W$ and to be at a height of 110 km.

duced earth currents probably do not have a serious effect on the results of this analysis. Even if the induced currents contribute one-third of the total disturbance field, they would produce only a small displacement of the ionospheric current patterns, and the shape of the patterns would remain unaltered.

DISCUSSION AND CONCLUSIONS

In this section we discuss the overhead current patterns and their relation to auroral displays. We present a few sample maps of the superimposed magnetic and auroral data pertinent to several storms and then explain their principal features. Finally, we discuss the correlation of the southern boundaries of the overhead currents with those of the auroral displays during several storms.

(a) *Overhead current patterns and auroras.* As a typical example, two current patterns of April 5, 1958, are given in Figure 4. Before discussing

these patterns, let us briefly outline the magnetic activity on this particular night (see Fig. 1).

A storm begins to develop slightly before 0100 GMT, with a distinct positive phase (horizontal component), at Meanook, Churchill, and Yellowknife. (It should be noted that at high latitudes—Baker Lake and higher—the morphology of a storm is different from that at lower latitudes, and the distinction of positive and negative phase is for middle and low latitudes only.) The transition to a negative, main phase takes place around 0330, but after a short while this main phase is interrupted by a superposition of the positive phase of a new storm. The latter lasts for a few hours and in turn is followed by a well defined, strong main phase, which lasts until dawn.

The auroral maps and the current patterns corresponding to the positive phase of these storms are not presented here. These patterns, however, were characterized at southern stations by eastward currents that bent northward around

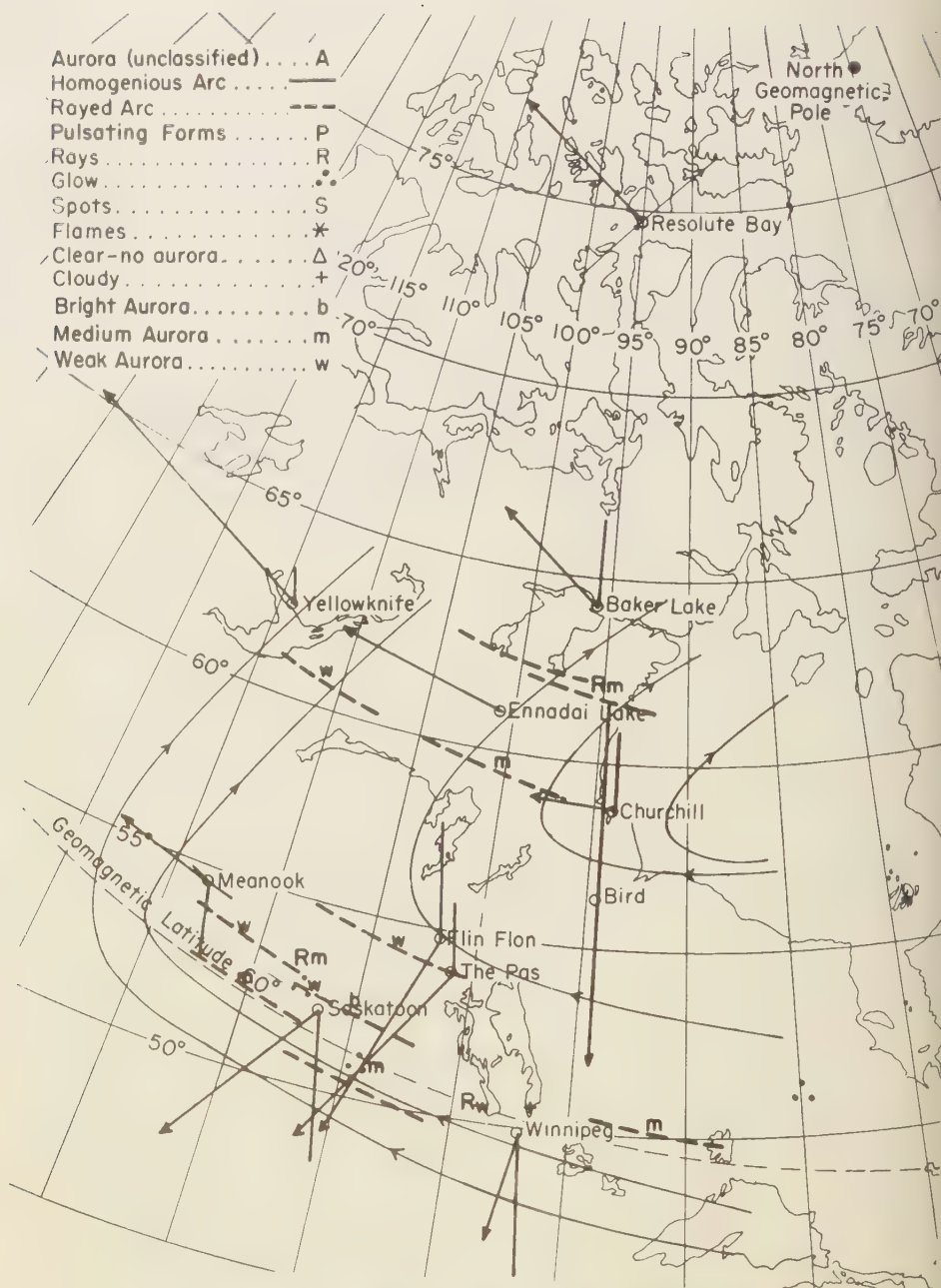


Fig. 4a. Auroral plotting map, 0400 GMT, April 15, 1958. The arrow originating from each station represents the total horizontal component of the magnetic disturbance field, the straight line represents the magnitude of the vertical component. The thin lines across meridional lines represent the ionospheric current paths.

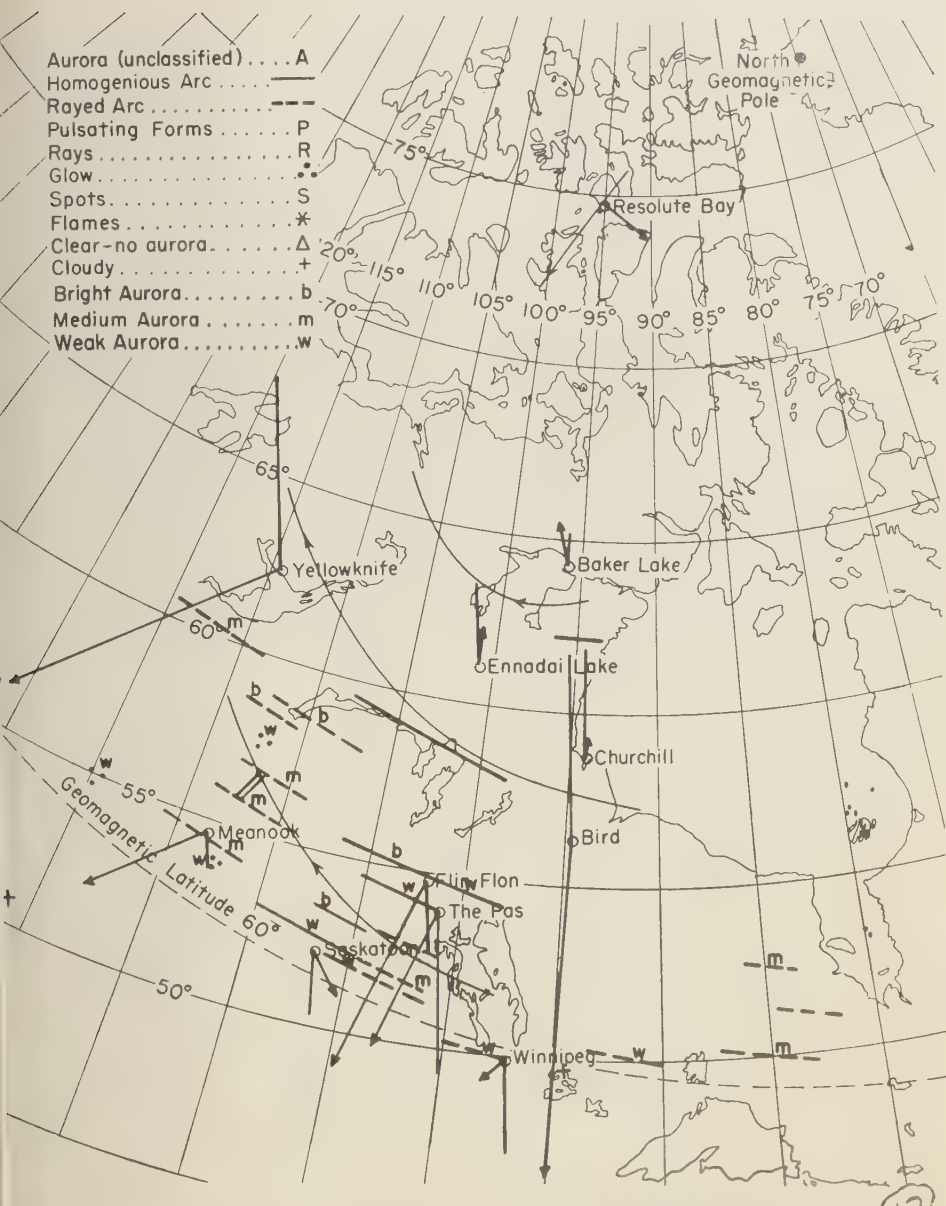


Fig. 4b. Auroral plotting map, 0700 GMT, April 15, 1958. (See legend for Figure 4a.)

Churchill and Bird. The auroral activity was low during the positive phases of the storms.

Figures 4a and 4b correspond to the main phase of the storm, characterized by intense southward H components at lower latitude stations. The earlier eastward currents are now replaced by currents flowing westward; at higher latitudes they flow either northeast or northwest. The displays occur quite frequently and extend over the more northerly stations. A more detailed discussion of the maps of Figure 4 is presented in the following section.

(b) *Superimposed maps.* An inspection of all the patterns at different locations and times, and under various degrees of magnetic activity, revealed that auroras, as a whole, tend to be aligned along the current path. (The alignment of the entire pattern of auroral activity may be different from the direction of orientation of a particular auroral arc or band, which was arbitrarily drawn always along a parallel of geomagnetic latitude.) This statement may be verified by comparing Figures 4a and 4b.

In Figure 4a, the auroras extend east-west over the southern stations, and run from southwest to northeast from Meanook and Saskatoon to Yellowknife and Baker Lake. These two directions happen to be the simultaneous directions of the current lines. In Figure 4b, however, there are no auroras over Churchill, Ennadai Lake, and Baker Lake; instead the auroras extend northwest from Saskatoon and The Pas to Yellowknife, which is again the direction of the ionospheric currents. To show this tendency of the aurora to occur along the current patterns in a more striking fashion, a series of superimposed maps (Fig. 5) was made as follows.

The 7 days of April 1958 were selected for this purpose, as the morphologies of the magnetic storms on these nights resemble each other. The maps were inspected, and those having approximately the same distribution of the horizontal disturbance vectors (in direction) were superimposed upon one another. Then all magnetic vectors, current paths, and auroral displays were copied on a blank overlay map. Because the magnetic storms on different nights have different durations, the above procedure does not superimpose maps of equal 'storm-time.' Instead, we may say that it superimposes maps at the same 'storm-phase,' where *phase* signifies a particular distribution of the horizontal disturbance vectors

during the development of a storm. According to this definition, all storms belonging to a specified phase will have the same pattern of activity.

These superimposed maps illustrate characteristics that tend to recur in different storms. Figure 5a corresponds to the positive phases of the storms. Associated with the low magnetic activity during these phases, few auroras are observed and most of these occur over the southern stations and show a very slight extension toward Churchill. The contrast between the auroral and current patterns of Figures 5b and 5c, both of which correspond to the negative phases of the storms, is striking. In Figure 5b both currents and auroras extend from Winnipeg, Saskatoon, and Meanook to Yellowknife, whereas in Figure 5c neither currents nor the auroras show an extension from Meanook to Yellowknife. On both maps the region of Ennadai Lake, Baker Lake, and higher latitudes is clear. Incidentally, the information presented in Figures 5a, 5b, and 5c is less than one-tenth of the total data used in this analysis. This tendency of auroras to occur along current paths was maintained throughout all the data and appears to be statistically significant.

A divergence of current sheets, and consequently a reduction of the current density in higher latitudes, is apparent in Figures 5a, 5b, and 5c, and appears to be associated with the scarcity of auroral displays in these regions.

(c) *Low-latitude boundaries of ionospheric currents and auroras.* An auroral display has a rather sharp boundary at its low-latitude extension, whereas its activity diminishes gradually to the north. Hence, the southern limit of a display is much more distinct than the northern limit.

Magnetic storms, and, therefore, ionospheric currents, show this same feature. At their southern limit, the intensities of auroral-zone currents decrease abruptly, while on the northern side, at latitudes as high as that of Resolute Bay, the storm still has a moderate activity.

In order to see whether there is any correlation between the southern limits of auroras and overhead currents, a special analysis was made for Meanook, Saskatoon, and Winnipeg, which are located in the southern part of the auroral zone. (On quiet days the southern boundary of a disturbance may move northward as high as Flin Flon and The Pas.) Geomagnetic latitudes of the central line of the most southerly current

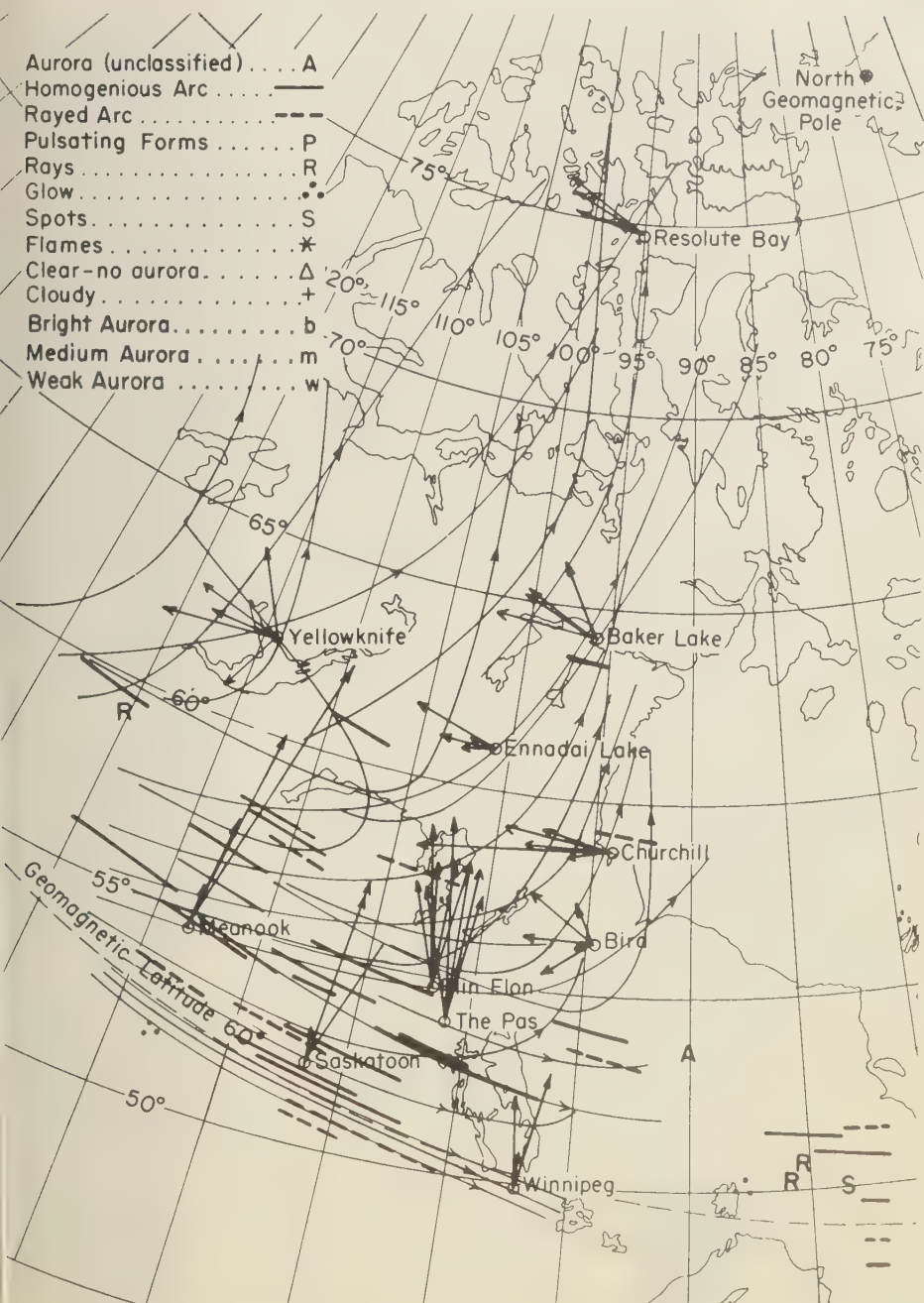


Fig. 5a. Auroral plotting map, constructed by superimposing the 5 maps of 0300 April 15, 0500 April 16, 0400 April 17, 0400 April 19, and 0100 April 24, 1958. (See legend for Figure 4a.)

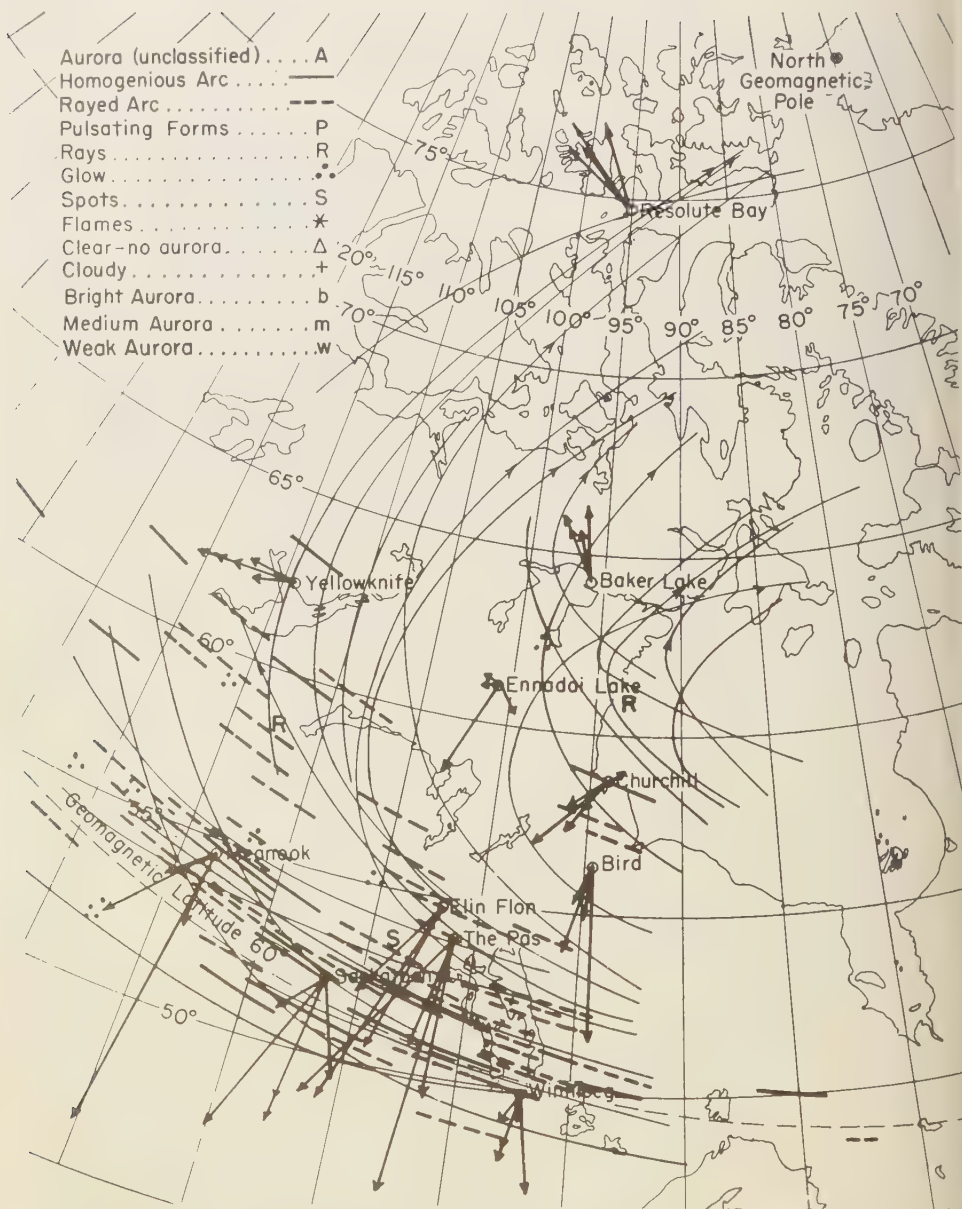


Fig. 5b. Auroral plotting map, constructed by superimposing the 5 maps of 0800 April 16, 0700 April 17, 0700 April 18, 0700 April 19, and 0800 April 24, 1958. (See legend for Figure 4a.)

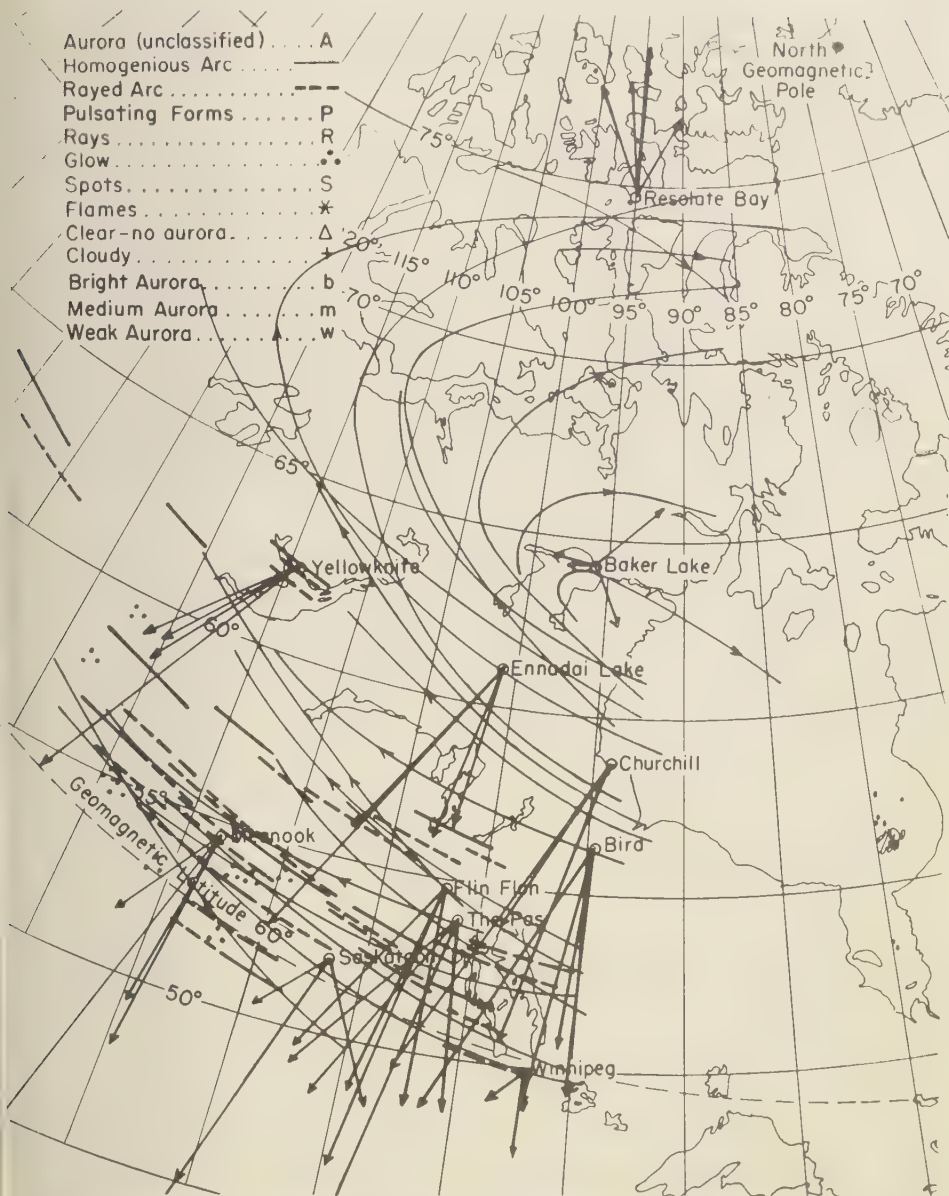


Fig. 5c. Auroral plotting map, constructed by superimposing the 4 maps of 1000 April 16, 0900 April 17, 1100 April 18, and 1000 April 19, 1958. (See legend for Figure 4a.)

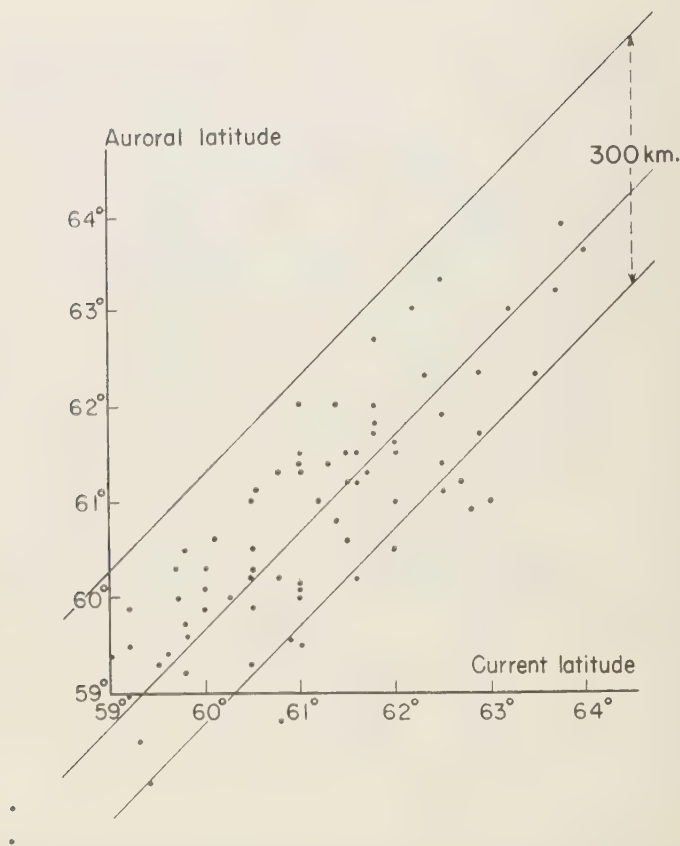


Fig. 6. Geomagnetic latitude of the most southern auroral displays plotted against the geomagnetic latitude of the most southern ionospheric current—April 15, 16, 17, 18, 19, 21, and 24, 1958.

sheets and those of the most southerly auroral displays in the vicinity of these southern stations were measured, with an accuracy of about 0.2° , by overlaying a 'geomagnetic coordinate grid' on the maps. The two sets of auroral and current latitudes thus obtained were compared in two ways.

First, correlation coefficient, $r = 0.85$, was found between the auroral and current latitudes. The 95 per cent confidence limits of r were 0.77 and 0.90.

Indeed, existence of a high correlation is seen from Figure 6, in which the auroral latitudes are plotted against current latitudes. The elongated shape of the cloud of points, along a line inclined at 45° to the axes indicates a high cor-

relation between the two sets of data. This high correlation between the latitudes of currents and auroras on the southern extension of activity suggests that auroras and currents are indeed coincident in time and place.

In view of this evidence a linear relation of the form $Y = X + a$ was assumed between the latitudes of the most southerly current sheet and auroras. From the data of Figure 6, it was found that $a = -0.32^\circ = -36$ km. The line $Y = X - 0.32^\circ$, together with the limits of 300-km wide hypothetical current sheet, are plotted in Figure 6. The intercept 36 km to the south places an average southern limit for the auroras within this current sheet. However, the 'average' limit has little significance: first, because

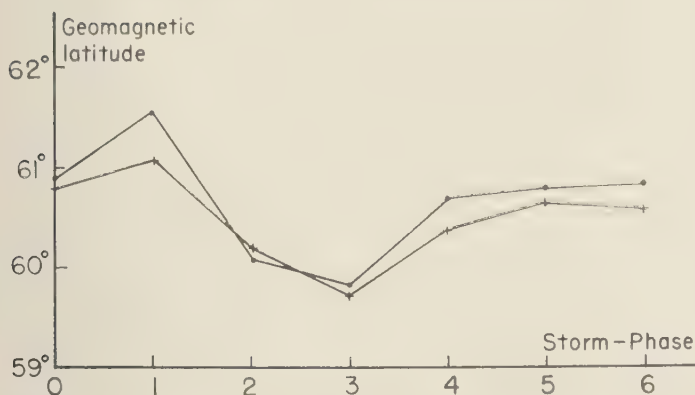


Fig. 7. Geomagnetic latitude of the most southern ionospheric currents and auroral displays at the southern boundary of the auroral zone, plotted against the storm-phase. Averaged data on April 15, 16, 17, 18, 19, 21, and 24, 1958. (·) current latitude, (+) auroral latitude. The duration of all phases (0-6) is roughly 6 hours.

of a fairly large spread of data of Figure 6 around this line and, second, because of a probable displacement of the current patterns caused by neglecting the magnetic effects of the induced earth currents. It should be emphasized here that the width of the currents may not be inferred from this 36-km intercept.

The second comparison of the current and auroral latitudes was made as follows: the two sets of latitudes of the most southerly currents and auroras were classified according to their corresponding 'storm-phase' (as defined above). The averages of all data having the same storm-phase are plotted against storm-phase in Figure 7. The outstanding features of this graph are:

(a) The graph of auroral latitudes is parallel to that of current latitudes; i.e., the auroras tend to appear within the sheets of ionospheric currents.

(b) The southward shift of the current system of the auroral zone is clearly demonstrated in Figure 7. During the positive phase of the storm (0 and 1 on the graph), currents and auroras both have high latitudes. As the storm develops and reaches its most intense negative phase (2 and 3 on the graph) currents and auroras move southward and again gradually back to north, as the storm decays and vanishes.

Acknowledgments. I wish to extend my sincere thanks to Dr. E. R. Niblett, Dr. M. G. Rochester,

and Professor J. T. Wilson for their supervision and encouragement in the course of this research while I was studying at the University of Toronto. Also, thanks are given to Dr. L. Wallace for reading the manuscript and for his helpful suggestions. The assistance of the Dominion Observatory of Canada, in providing the magnetic data, and of the National Research Council of Canada, in providing the auroral data, are gratefully acknowledged.

The preparation of this paper was supported in part by Geophysics Research Directorate of the Air Force Cambridge Research Center, Air Research and Development Command, under Contract AF19(604)-3044 with the University of Chicago.

REFERENCES

- Canadian National Committee for the IGY, *Report on the Canadian Program for the International Geophysical Year*, NRC, Canada, 1959.
- Geomagnetic and solar data, *J. Geophys. Research*, **63**, 416, 829, 1958.
- Ratcliffe, J. A., and K. Weekes, *The ionosphere, Physics of the Upper Atmosphere*, edited by J. A. Ratcliffe, 377-470, Academic Press, New York and London, 1960.
- Vegard, L., and O. Krogness, *The position in space of the aurora polaris*, *Geophys. Publ.*, **1**, No. 1, 1920.
- Vestine, E. H., *The upper atmosphere and geomagnetism, Physics of the Upper Atmosphere*, edited by J. A. Ratcliffe, 471-512, Academic Press, New York and London, 1960.
- Weaver, J. T., and R. Skinner, *A theory of ionospheric currents associated with aurorae II*, *Can. J. Phys.*, **38**, 1104-1114, 1960.

(Manuscript received January 3, 1961.)

Influence of Sunspots on Geomagnetic Disturbance

FRED WARD AND RALPH SHAPIRO

*Geophysics Research Directorate, Air Force Research Division
Laurence G. Hanscom Field
Bedford, Massachusetts*

Abstract. The hypothesis that the ejection of solar corpuscles is influenced by interactions of 'active region' magnetic fields is tested empirically. The results do not support the hypothesis.

INTRODUCTION

The twin problem of understanding and predicting geomagnetic disturbances continues to be the subject of considerable study. The sun has received the most attention in this connection in view of the fact that the geomagnetic disturbance field has 11-year and 27-day quasi-periodic variations.

Most empirical attempts to date have implicitly assumed that the effect of a particular solar parameter on the geomagnetic field would not be unduly influenced by another coexisting solar parameter. A study by *Pecker and Roberts* [1955], however, attributed recurrent 'M region' geomagnetic disturbances to the arrival at the earth of solar corpuscles that have been gathered into beams by the deflecting action of coronal-region fields. These fields, presumably magnetic, were associated with centers of heightened solar activity. They attempt to explain, by their hypothesis, some results for the period 1952-1953, and some earlier results by *Allen* [1944] and by others that showed a definite diminution in certain types of recurrent geomagnetic disturbances approximately 3 days after central meridian passage (CMP) of active centers on the sun.

The essence of the Pecker-Roberts hypothesis is that combinations of active centers, if distributed on the solar disk in a prescribed manner, can, by the interaction of their magnetic fields, focus the continually generated corpuscles into streams that reach the earth. By allowing combinations of active centers to be responsible for the recurrent storms, not only are Allen's results explained, but also the lack of association of these storms with any specific solar feature is understandable.

In view of the limited success of the earlier

attempts to explain recurrent geomagnetic disturbances on the basis of individual solar features, an extensive test of the Pecker-Roberts hypothesis, with its novel use of interactions between solar parameters, is felt to be long overdue. The main purpose of this note is to present the results of a reasonably thorough test of this hypothesis. In the course of this examination, other mechanisms of a similar nature were also investigated.

SUNSPOT DATA

There is a long and consistent record of sunspot data from which positional information can be obtained. Sunspot positions, although not necessarily corresponding exactly to the 'active regions' of Pecker and Roberts, should specify their locations to a high degree of approximation. Furthermore, the sizes of the sunspot groups should, to a first approximation, indicate the intensity of their magnetic fields [*Kiepenheuer*, 1953].

Sunspot position and area data for the period January 1, 1936, to December 31, 1947, were extracted from the Greenwich Photoheliographic Results. Greenwich publishes the solar latitude, longitude, and whole spot area in millionths of the visible hemisphere (corrected for foreshortening) for each sunspot group, and the longitude of the central meridian for each day of the year.

The 360 degrees of solar longitude were divided into fifty-six half-lunes as shown in Figure 1. The total sunspot area in each of the twenty-eight half-lunes of the visible disk was computed for each day of the 12-year period. The total area of a spot group was assigned to the semilune in which its center was situated. Separation into northern and southern semilunes was made on the basis of solar latitude without correction for the 7-degree tilt of the solar axis.

Table 1 contains the total spot area for each

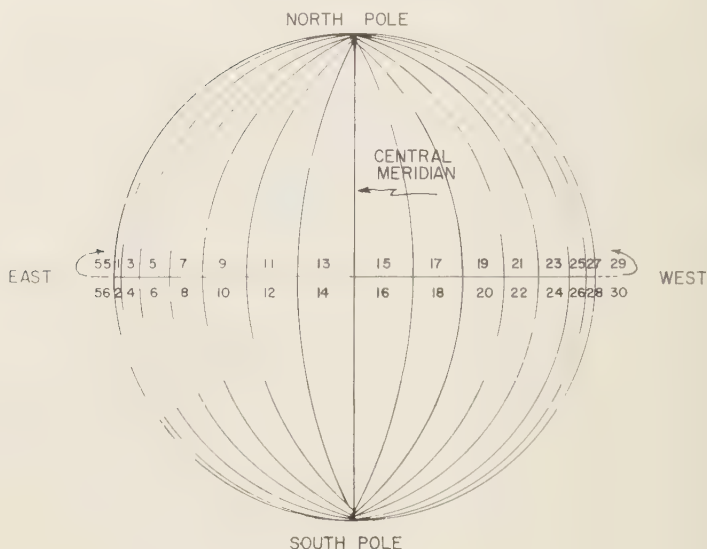


Fig. 1. Numbering system for the division of the solar surface into lunes and semi-lunes.

semilune for the 12-year period. There are large discrepancies between the lunes near the edge and those toward the center of the disk. This is true in spite of the geometric correction for foreshortening which is applied in the original Greenwich data. It is obvious from this data that there are serious observational difficulties near the limbs. A further correction was therefore applied to the total area data in each semilune as shown in Table 2.

The data for the invisible face were linearly interpolated from semilunes 27 and 1 for the northern hemisphere and from semilunes 28 and 2 for the southern hemisphere. The result of this calculation yielded the twice-corrected sunspot areas in each of 56 semilunes for each day of the 12-year period from January 16, 1936, through December 16, 1947. The total areas by semilunes (both visible and invisible faces) for this period are shown in Table 3. The first and last 15 days are missing because of the interpolation routine. The trend of the values across the invisible face is due to the linear interpolation scheme, and merely reflects the different sums on the two-edge lunes of the visible face.

RESULTS

A set of experiments was designed to test the Pecker-Roberts hypothesis, as well as other ideas

based on distributions of solar magnetic fields, by selecting key days on which the solar conditions were appropriate and performing superposed epoch analyses on the geomagnetic character figure C_t . Appropriate conditions were defined in various ways, depending on the spot area, number of areas of sufficient size, distance between appropriate groups, phase of the sunspot cycle and whether the pairs of spots were in the same or opposite hemisphere.

There were many days on which a considerable number of semilunes contained spots. There was frequently a range of more than two orders of magnitude in the spot areas on any one day. An arbitrary filtering of spots was therefore performed for the purpose of reducing the difference between the extreme spot areas on a particular day. At the same time it reduced the total number of occupied semilunes, and hence reduced the computational complexity.

The filtering procedure operated as follows. For each day the lune with the largest total area (sum of north and south) was selected. Each lune in which the total was equal to or greater than one-quarter of the largest value was also chosen. The midpoint between consecutive pairs of occupied lunes was determined. If any one of these midpoints fell on the central meridian line, or in either lune adjacent to it, that day was

TABLE 1. The Total Spot Areas for the Twelve-Year Period
($\times 10^{-6}$ of the Visible Hemisphere)

Semilune Number	Total Area	Total Area	Total Area
1	65990		
2	68940	134930	
27	71270		285910
28	79710	150980	
3	150060		
4	163120	313180	
25	182510		680530
26	184840	367350	
5	179660		
6	185790	365450	
23	192590		740630
24	182590	375180	
7	176990		
8	198690	375680	
21	202400		768210
22	190130	392530	
9	199600		
10	216510	416110	
19	219530		838780
20	203140	422670	
11	203700		
12	220480	424180	
17	215100		854850
18	215570	430670	
13	215830		
14	217520	433350	
15	211230		860440
16	215860	427090	

TABLE 2. Correction Factors

Semilune Number	Total Area Multiplied by
1, 2, 27, 28	3.0
3, 4, 25, 26	1.3
5, 6, 23, 24	1.2
7, 8, 21, 22	1.1
9-20	1.0

selected as a key day. Although this admits the possibility of two consecutive key days, this occurred in less than 11 per cent of the cases.

For this group of key days the following data were tabulated: the date, the largest sunspot area and its location (lune), the number of lunes whose area was equal to or greater than one-fourth of the largest, the area total of each of the two lunes whose midpoint is on or near the

TABLE 3. Total Areas After Statistical Correction ($\times 10^{-6}$ of the Visible Hemisphere)

Semilune Number	Total Area	Semilune Number	Total Area	Semilune Number	Total Area
1	197970	29	212754	1 + 2	404790
2	206820	30	236634	3 + 4	407134
3	195078	31	212608	5 + 6	438540
4	212056	32	234378	7 + 8	413248
5	215592	33	211338	9 + 10	416110
6	222948	34	232122	11 + 12	424180
7	194689	35	210224	13 + 14	433350
8	218559	36	229866	15 + 16	427090
9	199600	37	209110	17 + 18	430670
10	216510	38	227990	19 + 20	422670
11	203700	39	207996	21 + 22	431783
12	220480	40	225810	23 + 24	450216
13	215830	41	206882	25 + 26	477555
14	217520	42	224988	27 + 28	452940
15	211230	43	205768	29 + 30	449388
16	215860	44	222630	31 + 32	446986
17	215100	45	204654	33 + 34	443460
18	215570	46	220380	35 + 36	440090
19	219530	47	203540	37 + 38	437100
20	203140	48	218300	39 + 40	433806
21	222640	49	202426	41 + 42	431870
22	209143	50	216016	43 + 44	428398
23	231108	51	201312	45 + 46	425034
24	219108	52	213684	47 + 48	421840
25	237263	53	200198	49 + 50	418442
26	240292	54	211384	51 + 52	414996
27	213810	55	199084	53 + 54	411582
28	239130	56	209102	55 + 56	408186

central meridian, the spacing (number of lunes) between this pair of lunes. In addition to this set of key days, another set exists where the second largest lune-area was not at least equal to one-quarter of the largest, and the largest was in the

lune either side of the central meridian. In the following experiments various stratifications of the data were attempted. The degree of stratification was determined by the amount of data.

Figure 2 shows the mean value of C_i preceding

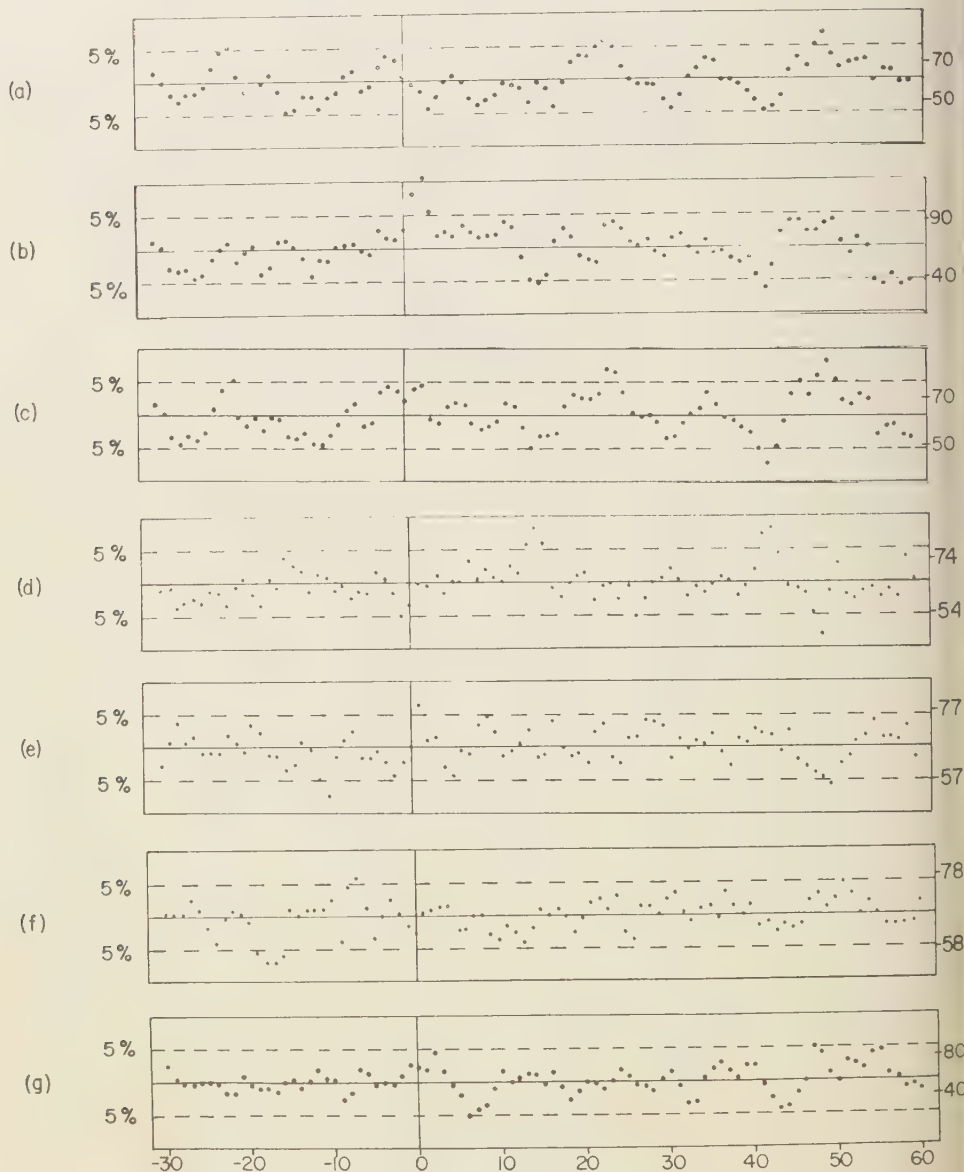


Fig. 2. *a-g*, superposed epoch analyses of C_i around selected key days.

and following the key days selected according to the criteria outlined in Table 4. Table 4 lists all the experiments attempted.

The first column in Table 4 is the figure designation where applicable. Dashes indicate that

the results of the experiment are not presented. The second column shows groupings according to the number of 'large groups' on the sun on any one day. For example, '3' indicates that there are two spot areas at least equal to one-quarter the

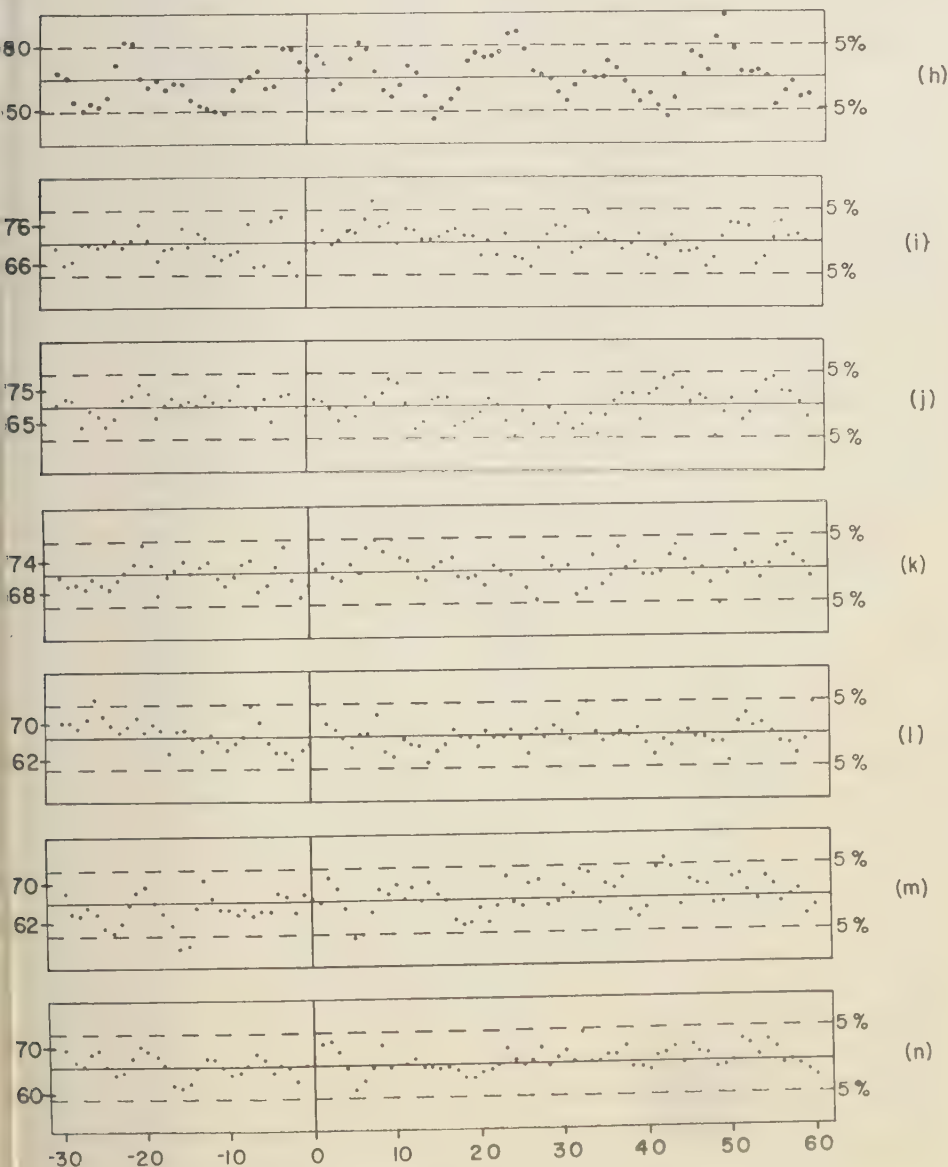


Fig. 2. (Cont.) h - n , superposed epoch analyses of C_i around selected key days.

largest spot area. Column three indicates the years from which the data were selected for the particular experiment. 'N' refers to years of non-recurrent disturbance, 1936-1938 and 1945-1947. 'R' refers to years of recurrent disturbance, 1939-1944. Column four classifies the experiment by the size of the largest spot area. Column five gives the location of the matching pair ('visible face' includes the instances where one lune is at the edge of the visible face and the other lune at the opposite edge of the invisible face). Column

six gives information on a set of experiments in which the classification was based upon the occurrence of pairs of spots in opposite (O) hemispheres (north or south) or in the same hemisphere (S). The last column gives the number of key days in each experiment.

The particular selection of experiments attempted was a result of compromising completeness with the labor involved. It is apparent from the results presented in Figure 2 that further stratification is unwarranted.

TABLE 4. Listing of Experiments

Figure Designation	Number of Lunes on a day with area $\geq 1/4$ largest area	Years	Largest Area (10^{-6} of visible hemisphere)	Location of Matching Lunes	Location of Pairs (hemisphere)	Number of Key Days
2a	1	All	<1000	36
2b	1	"	≥ 1000	13
2c	1	"	All	49
...	2	"	<1000	Visible face	...	22
...	2	"	<1000	Invisible face	...	19
...	2	"	≥ 1000	Visible face	...	11
...	2	"	≥ 1000	Invisible face	...	14
2d	2	"	All	Both faces	...	66
...	3	"	<1000	" "	...	53
...	3	"	≥ 1000	" "	...	36
2e	3	"	All	" "	...	89
...	4	"	<1000	" "	...	58
...	4	"	≥ 1000	" "	...	48
2f	4	"	All	" "	...	106
...	5	"	<1000	" "	...	56
...	5	"	≥ 1000	" "	...	30
...	5	"	All	" "	...	86
...	6	"	<1000	" "	...	43
...	6	"	≥ 1000	" "	...	28
...	6	"	All	" "	...	71
...	7	"	<1000	" "	...	29
...	7	"	≥ 1000	" "	...	28
...	7	"	All	" "	...	57
...	8	"	<1000	" "	...	17
...	9	"	<1000	" "	...	9
...	10-14	"	<1000	" "	...	6
...	8	"	≥ 1000	" "	...	6
...	9	"	≥ 1000	" "	...	10
...	10-14	"	≥ 1000	" "	...	4
...	8-14	"	All	" "	...	52
2g	1	N	"	11
2h	1	R	"	38
2i	2-14	R	"	...	O	103
2j	2-14	R	"	...	S	86
2k	2-14	R	"	...	All	189
2l	2-14	N	"	...	O	157
2m	2-14	N	"	...	S	181
2n	2-14	N	"	...	All	338

Each part of Figure 2 is constructed as follows. The mean is indicated by a solid horizontal line flanked by two dashed horizontal lines indicating the approximate 5 per cent confidence limits ($2\frac{1}{2}$ per cent on either side) for the departure of each value from the population mean as determined by Student's *t*-test. It should be noted that the spacing between the confidence limits has been standardized. It is therefore possible to compare the various parts of Figure 2 even though the number of key days is variable. An absolute scale of C_i ($\times 100$) is indicated in the margin.

Sunspot area, spacing between spot groups, and number of spot groups. Figures 2a-2f are a selection from the larger group of experiments (Table 4) that were designed to determine whether spot sizes, the spacing between spot groups, and the number of groups on the disk were related to geomagnetic disturbance. Figure 2b confirms the well known result [Newton, 1949] that geomagnetic disturbance increases following central meridian passage (CMP) of very large sunspots.

It should be noted in Figures 2a-2f that there are scattered maxima and minima that exceed the 5 per cent confidence limits, and that these show a pronounced tendency for 27-day recurrence. This is to be expected since C_i has a strong 27-day period.

The Pecker-Roberts hypothesis predicts an increase in geomagnetic disturbance near CMP of the midpoint between two active regions. Verification of the hypothesis requires high values near or immediately following day zero in Figures 2d, 2e, and 2f (2, 3 and 4 large sunspot groups on the sun respectively). No consistently high values are apparent in these figures. Furthermore the number of values that exceed the confidence limits throughout the entire range of these figures is approximately equal to that expected by chance.

Recurrent and nonrecurrent magnetic storms. Since recurrent and nonrecurrent magnetic storms may reflect substantially different mechanisms for the ejection of solar corpuscles, some of the results are presented separately for each type of storm. The phase of the sunspot cycle offers a simple and effective way of differentiating between recurrent and nonrecurrent storms. The nonrecurrent storm years are 1936-1938 and 1945-1947, and the recurrent storm years are

1939-1944. The sample of key days was further subdivided into cases where there was only one lune with a large total spot area (no others greater than or equal to $\frac{1}{4}$ of this), and all others.

The results for the single large sunspot group for nonrecurrent and recurrent years are shown in Figures 2g and 2h, respectively. The principal difference between Figures 2g and 2h is the pronounced tendency for a 27-day oscillation in the recurrent years.

The results for the remaining cases of the nonrecurrent and recurrent years are shown in Figures 2i and 2k, respectively. It should be recalled that only those cases are included where the midpoint between pairs of sunspots groups falls on or adjacent to the central meridian, and the sunspot areas are at least equal to one-quarter of the largest. It is apparent from these figures that a stratification on the basis of the recurrence tendency of magnetic storms does not alter the negative results shown in Figures 2d, 2e, and 2f.

Strictly speaking, the Pecker-Roberts analysis was based only on pairs of 'active regions' in opposite hemispheres (north-south) of the sun. In order to test this effect, the data in Figures 2k and 2n, were each divided into two halves according to whether the lune area totals were contributed mainly by semilunes in the same or opposite hemisphere. The results for the recurrent years (Fig. 2k) are shown in Figure 2i (opposite hemisphere) and Figure 2j (same hemisphere). Similarly, the results for the nonrecurrent years (Fig. 2n) are shown in Figure 2l and 2m. Because of the selection of key days, Figure 2i should most closely resemble the results of Pecker and Roberts. Neither this figure nor any of the others, however, show any evidence favorable to the Pecker-Roberts hypothesis.

CONCLUSIONS

A number of experiments were performed to determine whether certain characteristics of sunspots, acting singly or in combination, are related to the earth's magnetic field. The results of all of the experiments except one were negative. This one experiment, which tested the effect of large sunspots around CMP, merely confirmed a well known result. All other factors tested, including the spacing between spot groups, number of spot groups on the disk, area of spot groups, phase of the sunspot cycle, and the

location of pairs of spots with respect to the solar equator showed no relationship to the geomagnetic field. One must conclude therefore that the Pecker-Roberts hypothesis, as well as others based on combinations of the magnetic fields of sunspots, offers little hope for explaining magnetic storminess.

REFERENCES

Allen, C. W., Relation between magnetic storms and solar activity, *Monthly Notices Roy. Astron. Soc.*, 104, 13-21, 1944.

Kiepenheuer, K. O., Solar activity, in *The Sun*, edited by G. P. Kuiper, University of Chicago Press, Chicago, chapter 6, 1953.

Newton, H. W., Observational aspects of the sunspot-geomagnetic storm relationships, *Monthly Notices Roy. Astron. Soc., Geophys. Suppl.*, 5, 322-335, 1949.

Pecker, J. C., and W. O. Roberts, Solar corpuscles responsible for geomagnetic disturbances, *J. Geophys. Research*, 60, 33-44, 1955.

(Manuscript received November 12, 1960;
revised December 27, 1960.)

Low-Latitude and High-Latitude Geomagnetic Agitation

E. R. HOPE

Defence Research Board of Canada, Ottawa, Ontario

Abstract. At high latitudes there are statistical *morning*, *afternoon*, and *night* maxima of geomagnetic agitation (irregular disturbance or activity), the complicated distribution and seasonal behavior of which can be explained only in terms of patterned corpuscular bombardment. At subequatorial latitudes there are *noon*, *afternoon*, and *night* maxima, of which only the last two are related to the corresponding high-latitude maxima; the noon maximum, which differs in character from the others, represents a locally generated (Sq) agitation, presumably due to direct solar radiation. Since the afternoon and night maxima are traceable continuously from auroral through middle to low latitudes, and since their respective seasonal variations are everywhere the same, they may be explained as agitation transported from high to low latitudes by an ionospheric current system resembling (and probably identical with) the SD circulation. If so, this circulation is a physical reality, not an analytical construct; the SD currents must flow at their own level, independently of the Dst and Sq circulations. Besides the SD and Sq components of current-transported agitation, there is also a Dst component which, so far as identified, represents pulsative compressions of the geomagnetic field. Sudden commencements have SD, Sq, and Dst components largely analogous to those of agitation.

The importance of geomagnetic agitation (irregular disturbance of the geomagnetic field) is, in the first place, its association with the corpuscular bombardment of the upper atmosphere, and consequently with corpuscular effects such as radio-wave absorption and blackout, phenomena of technological as well as scientific interest. In the second place, the study of agitation and of related phenomena will yield essential information on the ionospheric electric current systems and the exospheric mechanisms of magnetic storms.

In this paper we shall discuss the complicated earth-surface distribution of agitation and of sudden-commencement pulses (which are, for our immediate purposes, the most important related phenomena). In particular we shall deal with agitation in the middle and the low latitudes and its relationships with high-latitude agitation—relationships that have never been elucidated. High-latitude agitation itself will not be fully discussed; it will be the subject of a later paper.

DESCRIPTION OF THE PROBLEM

§1. Geomagnetic agitation is the chaotic residue that must remain in the variometer trace of each geomagnetic element after subtraction of the so-called regular variations. This low-frequency magnetic noise is employed as a general measure of geomagnetic activity but has been

much less studied than the regular variations, even though in the high latitudes its amplitude may be greater than that of the regular variations by a factor of 10 or more [Nikol'ski, 1947, p. 148].

The above-mentioned association with corpuscular bombardment is indicated by many features, the most obvious of which are the existence of a near-midnight diurnal maximum of agitation on the side of the earth away from the sun, and the existence of a great zonal maximum of agitation in the auroral zone [Stagg, 1935a, Fig. 1B; Wallis, 1931]. But not all agitation is due to corpuscular bombardment. From the recent work of Bobrov [1959b, 1960] it appears that low-latitude agitation includes compression pulses in the geomagnetic field, produced by corpuscular clouds or condensations impacting upon the exterior field, without necessarily being precipitated upon the ionosphere. On the other hand, not all corpuscular precipitation causes agitation: there is now ample evidence of a pole-cap bombardment, with particles of almost cosmic-ray velocities, that is often unaccompanied by any magnetic effect [Shapley and Knecht 1958; Hakura, Takenoshita, and Otsuki, 1958; Obayashi and Hakura, 1960]. Agitation thus promises to have value not only as an index to the distribution of the corpuscular bombardment but also as a discriminator between different sorts of bombardment. The relationships are extremely

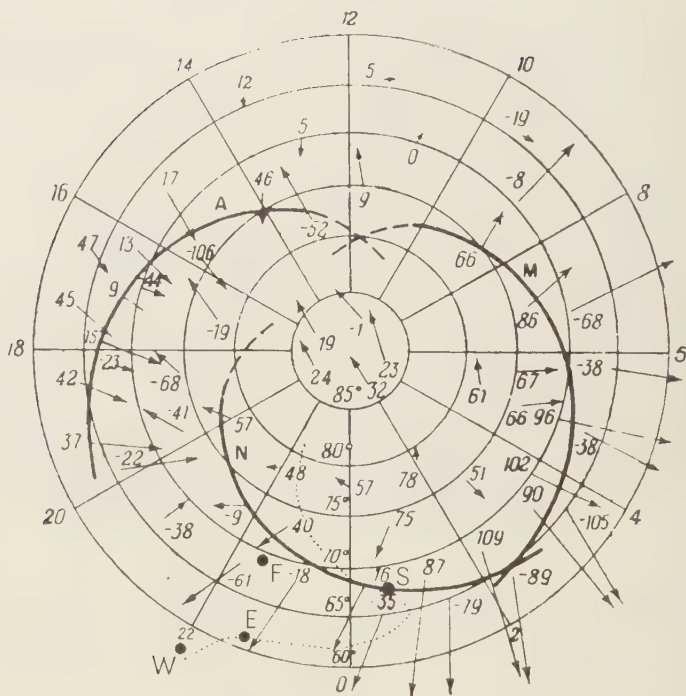


Fig. 1. Loci of morning (*M*), night (*N*), and afternoon (*A*) maxima of ΔH and of geomagnetic agitation, in geomagnetic time (AT) versus 'auroral' latitude. From Burdo [1957]. We have added the dotted line, which represents the locus of night agitation as found by Mayaud (see §§4, 5). Locus *M* is identical with Nikol'ski's morning spiral of agitation, aurora, and ionospheric absorption. The plot in geomagnetic time is approximately valid as a plot in geomagnetic longitude. (This statement also applies to Figs. 5 and 6.) "Auroral" latitude is an adjusted geomagnetic latitude: the auroral maximum zone is arbitrarily taken as 70°N , and latitudes are measured north and south from this line.

complicated, however, and our understanding of them is still vague.

In the high latitudes, geomagnetic agitation statistically exhibits three diurnal peaks, the loci of which form, in geomagnetic latitude and geomagnetic local time, the pattern of Figure 1. They may be designated as the morning, afternoon, and night maxima.¹ The three peaks appear well separated in the curves for some stations

¹ There is also a fourth diurnal peak, the 'axis maximum' [Hope, 1954], which is not a local time but a Universal Time phenomenon, connected with the diurnally varying inclination of the geomagnetic axis with respect to the sun. We shall not be able to discuss it here, but note that a similar phenomenon is discovered in the distribution of high-latitude sporadic-*E* ionization [Penndorf and Coroniti, 1958].

(Fig. 2), but it is more usual for them to overlap in one way or another. The most general case is a diurnal curve with two maxima [Chapman and Bartels, 1940, p. 389]. For this reason the existence of a high-latitude afternoon maximum was only recently demonstrated [see Nikol'ski, 1958; Fel'dshtein, 1960], though such a maximum has long been recognized at cisauroral latitudes (Fig. 3).

One reason for the overlaps is the convergence of the occurrence times of the three maxima toward midnight in auroral latitudes, as in Figure 1. This, however, is by no means the whole story. Figure 1 represents average positions of the loci which undoubtedly have considerable independent variations with longitude [Hope, 1956; Nikol'ski, 1951, pp. 24, 25; Nikol'ski, 194

. 158-159]. Generally speaking, these variations determine the overlaps [Nikol'ski, 1958, p. 2].

In the middle latitudes, agitation is less intense, an order of magnitude than in the auroral zone. The morning maximum disappears (though the trace of it is still visible in the Yakutsk curve, Fig. 3). The typical middle-latitude agitation curve has a wide-spreading winter-equinoctial night maximum that tends to swallow up the summer-equinoctial afternoon maximum. The latter usually appears only as a shoulder peak or plateau on the side of the night maximum, as at Yakutsk in Figure 3. At the longitudes of Yakutsk and Sluck, however, the afternoon peak is well separated from the night peak.

In the low latitudes agitation again increases sharply toward the geomagnetic equator [Stagg, 1955a, Fig. 1B]. Once more it has three distinct statistical maxima: at noon, in the afternoon, and near midnight (Fig. 4a).

Our task is essentially to relate these different agitation regimes.

2. We follow Mayaud [1955, 1956] in using the term *agitation* (rather than *irregular disturbance* or *activity*), because a specific term seems needed to distinguish local irregular disturbance from the general or planet-wide magnetic disturbance level or activity level. Agitation, then, will mean *local* irregular disturbance within the band of frequencies that is recorded by ordinary magnetic variometers [see Chapman and Bartels, 1940, pp. 48, 385-389, 887], in particular when the said disturbance is directly expressed, in gammas, as the hourly (or other) range or amplitude of fluctuation, after subtraction of the regular variations, but without adjustments intended to secure a generalized index [cf. Bartels, Heck, and Johnston, 1939, p. 417, §9]. Agitation is thus the proper quantity to study in connection with the earth-surface distribution pattern of irregular disturbance.

Nevertheless, the available modern data are usually in terms of the K index, which, with proper allowances for its nature, is usable as an agitation characteristic. Mayaud introduced the procedure of working back from the K index to recover the original gamma values of agitation. Agitation is most efficiently measured as an hourly range (amplitude), in the horizontal component (r_H^γ) or in the vertical component (r_V^γ). It is commonly it is measured in the total vector

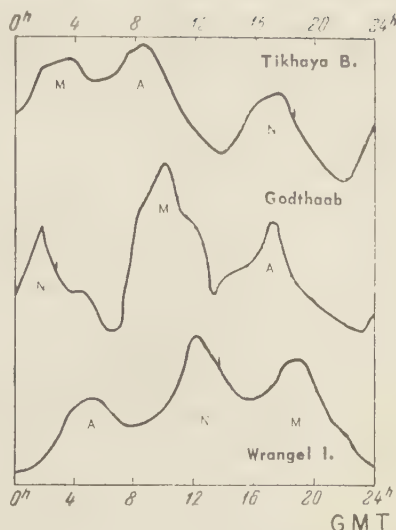


Fig. 2. Geomagnetic agitation (r_H) in the high arctic latitudes: examples of triple-peaked diurnal variation curves; peaks corresponding to loci M, N, A of Fig. 1. From Nikol'ski [1958]. Local geomagnetic midnight is marked on each curve by a vertical tick. Though the seasonal variations are not shown here, the night agitation on N is winter-equinoctial, whereas the morning and afternoon agitations on M and A are summer-equinoctial. See Fel'dshtein [1960, p. 8 and Fig. 1]. For a similar triple-peaked curve from Antarctica, exhibiting the seasonal variations, see MacDowall [1959, Fig. 2].

F of the geomagnetic field (e.g., the characteristic $Hr_H + Zr_Z$ used by Stagg; compare Chapman and Bartels [1940, p. 361]). Often, where more suitable data were lacking, the range of declination (r_D^γ) has been employed. The measure r_D is just as satisfactory as any other for local comparisons or for qualitative intercomparisons between stations; Nikol'ski [1951, pp. 14-15] took pains to prove this by combining the hourly ranges to produce 3-hourly values and comparing them with the local K index. For quantitative purposes, however, r_D is unsuitable, particularly in the high latitudes. It suffices to point out that at many such stations the disturbance vector, which for any pulse of analyzable size tends to lie in the geomagnetic meridian [Kalashnikov and Zybin, 1960, Fig. 4] will at the same time lie in or close to the local magnetic meridian and thus be ineffective in deviating the needle, whereas at other stations the disturbance vector will be

acting at a large angle to the local magnetic vector. Nikol'ski's finding, however, proves that at any given station the components of agitation in and across the meridian are more or less proportionate.

In the higher latitudes, agitation measured in H , Z , or F gives similar diurnal curves (see Stagg's diagram, reproduced by Chapman and Bartels [1940], p. 388); in the lower latitudes, we shall note significant differences between agita-

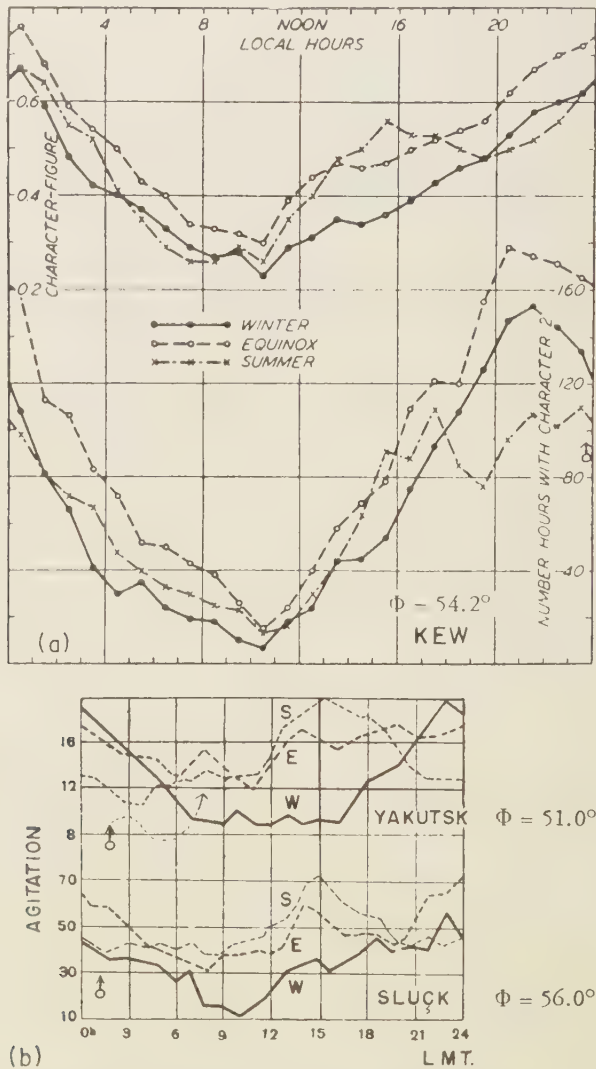
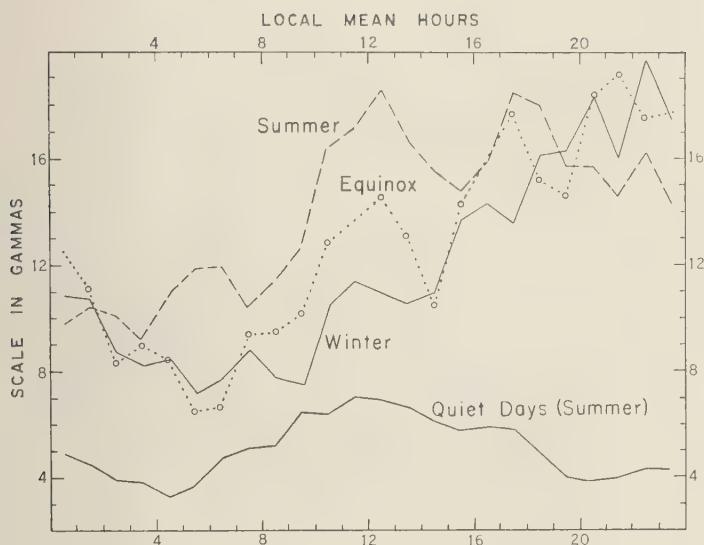
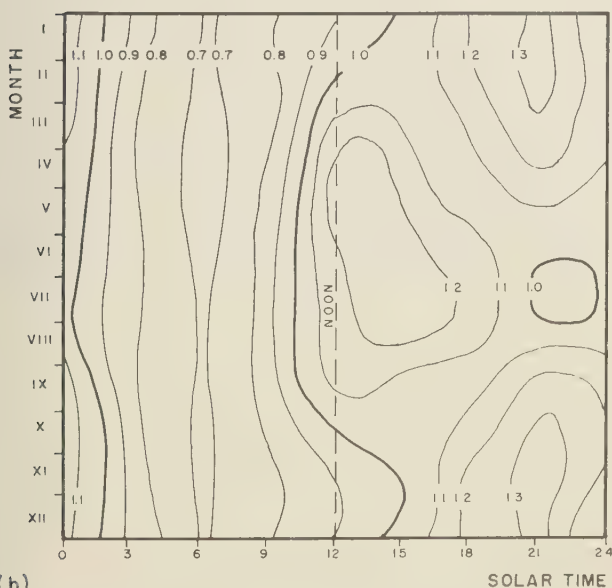


Fig. 3. Agitation in the higher middle latitudes; diurnal variation by seasons. The night maximum is winter-equinoctial; the afternoon maximum is summer-equinoctial. (a) Upper curves: hourly character figures for Kew Observatory, 1913-1923. Lower curves: number of hours with character figure 2. From Chapman and Bartels [1940], after Stagg [1926]. (b) Agitation at Yakutsk and Pavlovsk-Sluck, 1936-1943; diurnal curves for summer (S), equinoxes (E), and winter (W). From Nikol'ski [1951].



(a)



(b)

Fig. 4. Agitation in the low and lower-middle latitudes. (a) Diurnal variation of τ_H at Bombay, $\Phi = 9.5^\circ\text{N}$, for 1923–1933. After Narayanaswami [1941]. Seasonal curves for days of character 2 (disturbed); for comparison, the quiet-days curve (character 0 and 1) for summer only. The night maximum is winter-equinoctial; the afternoon and noon maxima are summer-equinoctial. The same three diurnal maxima, at 12–13, 17–18, and 23–24 hr LT, respectively, are exhibited by the geomagnetic ‘spasms’ investigated by van Bemmelen [1899, table on p. 120] at Batavia, $\Phi = 18.0^\circ\text{S}$. (b) Isopleths of relative geomagnetic activity (K index) at Tashkent-Keles, $\Phi = 32.4^\circ\text{N}$, for 1941 and 1943. From Kozik [1950]. The night maximum is winter-equinoctial; the noon and afternoon maxima (blended together because of the poor resolution afforded by the 3-hourly K index) are summer-equinoctial.

tion in H and in Z , implying that it would be expedient to study the two quantities independently. Thus for our purposes the K index, which is based on whichever one of three geomagnetic elements happens to be most disturbed in each 3-hour period, could advantageously be replaced by separate K indices for H and for Z . (Moreover, agitation data ought to be separately compiled for polar storms and world-wide storms, for sudden-commencement storms and M-type storms, in view of the fundamental character of these distinctions.)

The r symbols (r_H , r_Z ...) appear nowadays to be accepted in the sense of *hourly* ranges. The 3-hourly K index is a very rough one indeed where study of the diurnal variation is concerned [Fe'ld'shtein, 1960] and its nonlinearity sometimes produces discrepant results in computation [Kozik, 1950]. A 15-minute index (Q index) has recently been introduced, which may, for instance, be useful for tracing the coherent extents of agitation pulses in latitude and longitude without recourse to direct comparison of the variograms [cf. Bobrov, 1959b, 1960]. The curves of Q are perhaps too accidented for easy visual appraising of the diurnal variations; for this purpose the hourly ranges seem best suited and are adequate. A comparison of the K , r , and Q measures and their serviceability has been made by Fe'ld'shtein [1960, Figs. 1 and 2].

Toward the equator the amplitude of agitation is of the same order as that of the regular diurnal variations of the geomagnetic field; thus, during hours when the diurnal variation curve is steep, an uncorrected range measurement may be merely a segment of the variation curve and not a measure of agitation at all [Narayanaswami, 1941]. For this reason much of the earlier agitation data, not corrected in the manner of Narayanaswami or in the manner of the K index, must be regarded with suspicion. Kozik [1950], at Tashkent, finds it essential to remove the Sq variation from at least the quiet-day agitation curves; at higher disturbance levels it is not so important. But in the middle latitudes Hasegawa's effect [Chapman and Bartels, 1940, p. 238] creates a practical difficulty in removing Sq, so that spurious peaks may be introduced into the medium-intensity diurnal variation of the K index [Giorgi and Molina, 1956, pp. 180, 192]. In the high latitudes agitation so much exceeds the

regular variations that the influence of the latter may be ignored [Chapman and Bartels, p. 3].

HIGH-LATITUDE AGITATION

§3. The regular variations (Sq, SD, L, Dst) of the geomagnetic field are explainable as the magnetic effect of electric currents flowing beyond the ionosphere. In the irregular variations (that is, agitation) a great part of the disturbance must likewise be the magnetic effect of overhead electric currents. This is quite evident for agitation in the auroral zone and its vicinity.

The cause of bay disturbances has long been identified as an ionospheric circulation of the type, with an intense linear current or electric field in the auroral zone. In a typical magnetic bay the linear current, flowing at E -region heights, in a band about 400 km wide, may extend for 1000 km or more along the auroral zone [Pudovkin, 1960], and the duration of the phenomenon is of the order of an hour or two. Now from the background of geomagnetic agitation Bobrov [1959b] has isolated certain major fluctuations, or agitation peaks, which he shows to be due to linear filaments of electric current extending for distances of 100 to 300 km along the parallel of geomagnetic latitude and having a decay time of the order of 15 minutes. The mechanism of the Bobrov agitation pulses is therefore precisely the same as that of a bay, though on a smaller geographic scale and of shorter duration. The presumption is that this mechanism is general and that the chaotic, minor-scale background agitation is similarly formed, namely, by magnetic fluctuations due to intensity variations of the overhead currents and to positional shifts of current filaments.

Of course, the possibility of contributory mechanisms, not involving overhead currents, cannot be ruled out. A type of low-latitude agitation identified by Bobrov [1959b, 1960] seems to be due to compression pulses in the geomagnetic field, and Alfvén waves associated with these compression pulses may contribute to polar-region agitation (Bobrov). Inductive, hydromagnetic or field-distorting effects of solar ion clouds striking or passing the earth have been suggested by various authors [e.g., Briunelli, 1954; Warren, 1959]; passing ion clouds seem indeed to have been directly detected [Kraus and Crone, 1960]. Nevertheless, the evidence for the role of

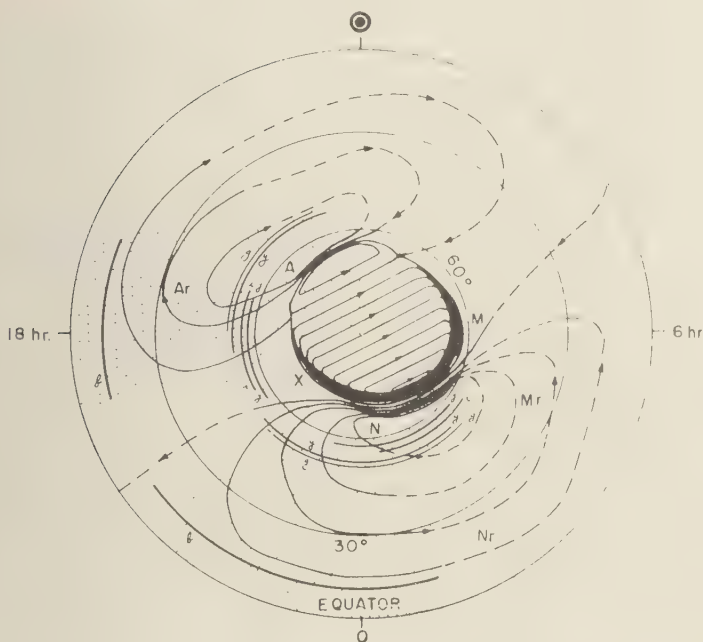


Fig. 5. SD current system, with the distributions (schematically indicated by the stippled bands) of afternoon and night agitation and of certain associated phenomena. In geomagnetic time and geomagnetic latitude (ΔT , Φ). The current system as shown was derived for geomagnetic bays [Silsbee and Vestine, 1942], but is generally accepted as an approximation of SD of geomagnetic storms. *Geomagnetic agitation*. Arcs b : afternoon and night maxima of agitation at Bombay, from Figure 4a. Arcs y : same at Yakutsk, from Figure 3b. *Radio aurora*. Arcs i , j : diurnal maxima of radioauroral echoes as observed from Ithaca and Jodrell Bank, Figure 8. *Sudden commencements and sudden impulses*. Arcs g : diurnal SC + SI maxima at Greenwich and Abinger, from Figure 9. Note similarity to arcs y .

eric currents and current filaments is overwhelming. In this connection see Pudovkin [1956, 1960], Fel'dshtein and Kurdina [1958]; Alek-drov, Pudovkin, and Yanovski, [1959]. Linear currents and current filaments, in the auroral zone, have been found to flow in the bases of auroral arcs [Heppner, 1954].²

At subauroral latitudes, agitation pulses, even of duration as short as 10 seconds to 2 minutes, exhibit a characteristic rotation of the vector in the horizontal plane [Kalashnikov and others, 1960], behavior reminiscent of the vector of magnetic-bay and storm disturbances [Fukushima, 1953, pp. 308-309; Chapman and Bartels, 1940, pp. 314-317]. This rotation would seem to be an important test for agitation theories. A motion of disturbance source is indicated. It may be that, when a current filament forms in the atmosphere, it undergoes a whiplike motion, conceivably due to its

Let us then confine our attention, for the moment, to agitation produced by overhead currents, regardless of other possible forms.

There is no reason to suppose that the ionospheric currents or current filaments producing geomagnetic agitation are distinct from the currents causing the regular magnetic variations. That is, geomagnetic agitation probably reflects agitation or turbulence in the current sheets and electrojets of, for instance, the SD circulation of Figure 5. If we assume that the pattern of this

reaction with the geomagnetic field. Whiplike motions of current-filaments may no doubt under favorable circumstances develop into oscillations (geomagnetic pulsations of auroral-zone type). Oscillations of the edge of a radio aurora, in slant range, have been described by McKinley and Millman [1953].

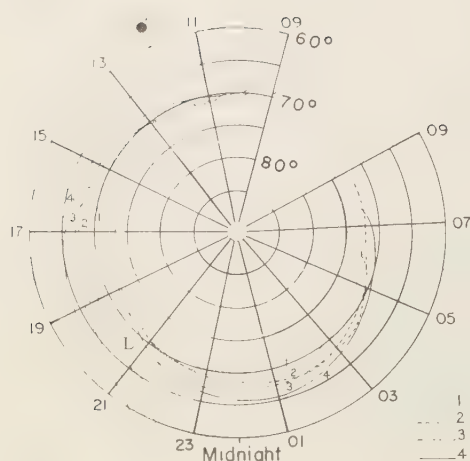


Fig. 6. Loci of maximum intensity of auroral-zone electric currents (electrojets), as observed on geomagnetic meridian $\Lambda = 120^\circ$, for different ranges of storminess (1, 2, 3, 4): mean picture for ΔH and ΔZ fields. After Harang [1946]. Plotted in geomagnetic time and geomagnetic latitude ($\Delta T, \Phi$).

SD circulation depends on a patterned enhancement of ionospheric conductivity due to corpuscular bombardment of the auroral zone and pole cap [Fukushima, 1953; Obayashi and Jacobs, 1957], the powerful high-latitude agitation may be due to fluctuations in the intensity and distribution of the bombardment. Thus one may say that agitation is generated by the corpuscular bombardment. But, be it noted, the bombardment and resulting ionization could not alone produce agitation in the geomagnetic field. An electric current is necessary. When an electric current—driven, let us say, by atmospheric dynamo forces, by implanted electric charges, or by electric fields—is threading its way through an area of chaotic and fluctuating atmospheric ionization, it must be fluctuating and irregular. The chaotic ionization itself will not produce any magnetic effect in the absence of a current flowing through the area.

A corollary to this argument is that agitation may be transported by the overhead electric currents, even beyond the foci of corpuscular bombardment where it is generated. Figure 5 suggests that auroral-zone agitation may indeed be transported to the low latitudes by certain parts of the SD circulation. But we shall consider

this point later: for the moment let us demonstrate our proposition in the auroral zone.

Burdo [1957] found the high-latitude loci of maximum ΔH (maximum diurnal departure of the horizontal component from its day-to-day mean) and the loci of maximum agitation to be so nearly identical that it was superfluous to chart them separately. That is to say, the three spiral loci of Figure 1 represent statistical diurnal maxima both of overhead current and of agitation: the distribution of maximum agitation corresponds to the statistical centers of intensity of the auroral electrojets. Compare Figures 1, 3, and 6.

The arrows in Figure 1 represent the ΔZ vectors at various stations and times; we see that they are normal to the loci. The numbers placed against the sources of the arrows indicate the size of the corresponding ΔZ vectors, which are seen to change sign from one side to the other of the loci. This means that the currents producing the variations ΔH and ΔZ flow along the loci. Their direction is westward on M and L and eastward on A —the directions of the electrojets in Figures 5 and 6.

Inevitably Figure 1 suggests that agitation may be no more than an accompaniment of overhead currents or electrojets; that N is the continuation of M , the combined locus $M + N$ being no more than the average trace of the night jet; that agitation is merely a function of overhead current density. If so, there is no reason at all to invoke corpuscular bombardment as the source of agitation; agitation is simply the noise of the electrojets.

Such an explanation, however, is untenable. To demonstrate this there is rather convincing evidence, though no full account of it can be given here. For the time being the following considerations must suffice.

(a) Nikol'ski [1947, p. 153] found a poor correlation between occurrences of night and morning agitation, indicating that the night and morning outputs of agitation (on loci N and M) are independent and their excitation independent.

(b) The night agitation, on locus N , differs in seasonal behavior from the morning agitation on M [Stagg, 1935b, Fig. 3; Nikol'ski, 1938; Maynard, 1956, Fig. 3], being in the first case *winter-equinoctial* and in the second *summer-equinoctial*. (We note, incidentally, that this cannot be explained by a daylight-dark effect, or the like.)

According to both Mayaud's and Burdo's loci in Fig. 1, the transition point between the two curves is near 02 hr of the night.) On the afternoon side of the night maximum the behavior in changes: the agitation of locus *A* is, like morning agitation, summer-equinoctial, as Figure 3 shows.

(c) Burdo [1957, p. 4 of translation] mentions that, although the diurnal maxima of ΔH and of ΔI closely coincide in position (on loci *M*, *N*, and *A* of Fig. 1), nevertheless the relative intensities of the ΔH maxima and agitation maxima are markedly different. That is to say, agitation is not directly related to the current intensity. Here again it is unlikely that a daylight-dark effect is involved. The daytime *E* layer may indeed partly shield agitation from the earth-surface observer (§10), but for the high-latitude observer such an effect on the intensity of agitation could scarcely be unaccompanied by a seasonal displacement of the loci, the apparent centers of intensity. No such displacement occurs. On the contrary, the times of the maxima are remarkably stable. See for instance the morning maximum at Godhavn and Sodankylä as shown in Mayaud [1956, Fig. 3]; see the afternoon maximum in our Fig. 3. The displacements that do occur are as often as not contrary to a daylight-dark effect.)

(d) At some longitudes (particularly in the Siberian sector: cf. *Nikol'ski* [1951], p. 21) locus *A* intersects the auroral zone. That is, the morning maximum of agitation is detected at auroral latitudes, as in the Yakutsk summer curve of Figure 3b, namely, at 7 to 8 hr LMT at geomagnetic latitude 51°. Exceptionally, however, the mean center of intensity of the morning agitation is here far south of the center of intensity of the electrojet as shown in Figure 6. See further in §4.)

In general it seems that since corpuscular bombardment provides the only consistent explanation of the auroral zone, of certain forms of aurora itself, of the statistical positions of the auroral electrojets, of polar absorption and blackout of polar sporadic-*E* ionization, and of other phenomena at auroral latitudes, it would be unrealistic to deny the bombardment any role in creating agitation.

The three loci of Figure 1 can indeed be correctly identified as sites of corpuscular bombardment, provided that one grants a connection

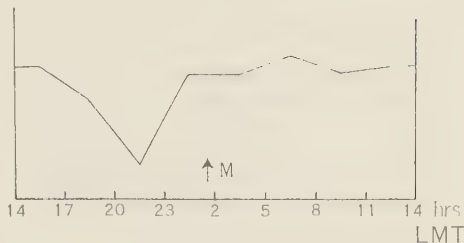


Fig. 7. Diurnal variation of ionospheric absorption (cosmic radio noise, 3-hourly index) for College, Alaska, $\Phi = 64.5^\circ$, Feb. 15 to April 5, 1955. From *Little and Leinbach* [1958, Fig. 19]. The sharp minimum in the evening is verified also for Point Barrow (op. cit., p. 347). A similar minimum is very prominent in *MacDowell's* [1959, Fig. 3] diurnal curves of blackout and of the local *Q* index at Halley Bay in Antarctica, at a geomagnetic latitude (65.8° S) comparable to that of College.

between corpuscular bombardment and ionospheric absorption in the auroral zone. In Figure 7 we reproduce, from *Little and Leinbach* [1958 Fig. 19], a mean diurnal curve of absorption at College, Alaska. This station, at geomagnetic latitude 64.5° N, passes diurnally across the gap between loci *A* and *N* of Figure 1, or, what is the same thing, the gap *L* between the parallel portions of the evening electrojet paths of Figure 6. Obviously the passage over the gap is marked by a sharp decline in the elsewhere almost level auroral-zone absorption curve. The gap in the 'electrojet auroral zone' is statistically associated with a diurnally recurring lull in the corpuscular bombardment that causes the absorption. This implies dependence of the loci (electrojets and agitation) on the bombardment.

§4. *The precise shape of the night locus.* Mayaud, utilizing the difference in the seasonal behavior of the night and morning agitation, extracted the night agitation and was able to chart its locus (its statistical center line of intensity) in more detail than Burdo. He found the diurnal peaks of intensity of the night maximum at different latitudes to be distributed along the dotted curve in Figure 1. (Mayaud's original locus [Mayaud, 1956, Fig. 4] was in terms of magnetic dip; this we have converted to geomagnetic latitude. We have not, however, attempted to adjust it to the 'auroral' latitudes of Fig. 1.)

According to Mayaud, then, the center of intensity of the winter-equinoctial night agitation

has a shape compellingly reminiscent of Cyrano de Bergerac's nose. This configuration is not so strange once we recognize it as a double-branched, diverging curve, corresponding to the divergent SD current paths at N - X in Figure 5. *The winter-equinoctial agitation appears to be transported by the currents which issue from the western end of the auroral night electrojet, turning north over the pole cap and south into the lower latitudes.*

But here, of course, the direction of the currents is conventional; actually there are electronic and ionic currents in opposite directions. We must picture the mechanism as follows.

In the auroral zone there is a rather large region of winter-equinoctial corpuscular bombardment, centered near midnight. The SD currents flowing through this disturbed region are thereby modulated and broken into shifting filaments; that is, geomagnetic agitation is generated. The disturbance, though present throughout the whole area of the night bombardment, nevertheless appears most strongly along the centers of current intensity, the two branches of Mayaud's locus.

To the east of the area of night disturbance the electrojet does not carry any winter-equinoctial agitation; the two branches of Mayaud's locus end at ~ 1 hr ΔT (the tip of Cyrano's nose). Eastward of here the electrojet carries agitation, but it is the summer-equinoctial agitation of the morning maximum, which is generated on the morning side of the auroral zone. It is, of course, on the basis of this very difference that Mayaud's locus is derived.

On the same basis we can, it seems, reject an idea that Figure 1 might otherwise suggest: namely, that either the upper branch of Mayaud's night agitation locus (= Burdo's locus N) or the lower branch of Mayaud's locus is the continuation of the morning agitation locus M . This could not be so unless it were supposed that the agitation changed (at about 02 hr) from summer-equinoctial at one end of the combined locus to winter-equinoctial at the other end.

We have already noted that at some longitudes the morning maximum is detectable at sub-auroral latitudes, as in the Yakutsk curve of Figure 3. Locus M must therefore cut through the auroral zone; it does not proceed toward the apex of Mayaud's night locus. The occurrence time of the Yakutsk morning maximum, ~ 7.5 hr LT, is remote from that of the night maximum.

So too at other stations in this region: for instance Sagastyr ($\Phi = 62.2^\circ$), where the two peaks are at 6-7 hr LT and 1-2 hr LT [Nikol'ski, 193 §10]. Here, in the auroral zone, there is a distinct lull between the night and morning agitation maxima. True, at most longitudes the morning peak, in the vicinity of the auroral zone, comes close to the night peak and merges with it, but at Yakutsk and Sagastyr the separation is quite clear.

§5. There is little doubt about the shape of Mayaud's night agitation locus as shown in Figure 1, because independently of Mayaud's derivation the said shape was anticipated by Nikol'ski [1938], and it is also implicit in the data of Stagg [1935b].

Stagg [1935b, p. 302] found that the local time of the night agitation maximum varied quasilinearly between $69^\circ N$ and $55^\circ N$ of geomagnetic latitude: thus, Fort Rae, 24 hr; Sodankylä, 21 hr; Eskdalemuir, 21.5 hr; Wilhelmshafen, slightly before 21 hr. Had he converted his local (mean solar) times to geomagnetic local time (ΔT), he would have observed a more complicated relationship; in fact, he would have glimpsed Cyrano's nose.

	Agitation Peak, hr ΔT	Geo- magnetic Latitude	'Auroral' Latitude
Fort Rae	~ 22.5	69.0°	$\sim 69^\circ$
Sodankylä	~ 0.6	63.8°	~ 67.5
Eskdalemuir	~ 22.6	58.5°	~ 61.5
Wilhelmshafen	~ 22.0	54.5°	~ 57.5

Perhaps, if Stagg did derive these figures, he simply concluded that geomagnetic time had no relevance to the problem. For comparison he may have plotted Stagg's four points at F , S , E , and W in Figure 1 (in terms of the 'auroral' latitudes used by Burdo).

Nikol'ski agreed with Stagg that the night maximum of agitation shifted to later hours with increasing geomagnetic latitude, but he observed that north of $\Phi \approx 70^\circ$ the trend reverses: the maximum retreats again to earlier hours. This statement will be found in conclusion 2 at the end of Nikol'ski's [1938] paper. He thus anticipated Mayaud, though Mayaud's result is, of course, based on much more extensive data.

§6. We have rejected the idea that locus N in Figure 1, or either branch of Mayaud's locus might be the continuation of the morning agitation locus M . On the other hand it does seem possible that

Mayaud supposes, the afternoon locus A is a continuation of M on the other side of the minimum. The agitation on both M and A is summer-equinoctial; moreover, *Nikol'ski* [1951, 1958] found a high correlation (0.87) between occurrences of the (Tikhaya Bay) morning and (Akutsk) afternoon agitations, in contrast to the poor correlation (above-mentioned) between morning and night agitations. Yet, if M and A are the same locus, the excitation cannot be continuous along it; there must be a gap, as Figure 1 shows. (The gap will be broader than that in Fig. 7, where the activity on locus N is included.) It seems that there are, on locus $M + A$, concentrations of intensity suggesting concentrations on a Störmer spiral of proton precipitation [Störmer, 1955, Fig. 177].

The picture is therefore, tentatively, as follows. Locus $M + A$ is the site of a summer-equinoctial excitation, presumably a corpuscular bombardment. Possibly $M + A$ is a somewhat eccentric quasi-Störmer proton spiral, that is, the form given by a Störmer spiral in a distorted and partially restricted geomagnetic field [Obayashi and Hakura, 1960, Fig. 8]. On this quasi-Störmer spiral there may be, as in Störmer's Figure 177, concentrations of the corpuscular bombardment, with gaps or lulls between them. The night excitation between Störmer's second and third concentrations seems to be especially prominent in the quasi-Störmer spiral; it corresponds to the hiatus between M and A in Figure 1. The hiatus is partly filled in (Fig. 7) by the independent correlative bombardment responsible for the night excitation maximum, the locus of which is shown on Figure N by Burdo and as the dotted curve (Fig. 7) by Mayaud. The night bombardment is winter-equinoctial in character, and its occurrences are well correlated with those of the summer-equinoctial bombardment on locus $M + A$.

The above picture differs from that recently suggested by *Nikol'ski* [1957; 1960a, b]. *Nikol'ski* is at present attempting to account for all the seasonal maxima of agitation (and at all latitudes) in terms of the concentrations on a single Störmer spiral. In doing so he abandons his own important thesis of the different seasonal characteristics, and presumably different excitations, of night and morning maxima [*Nikol'ski*, 1947]. On the other hand, regard the night excitation of geomagnetic disturbance as a phenomenon distinct from the excitation on the quasi-Störmer

spiral. *Nikol'ski's* discovery of the spiral immediately suggested to us [*Hope*, 1954] that there were separate 'polar' (Störmerian) and 'equatorial' (neutral stream) mechanisms of corpuscular precipitation. Evidence has been accumulating that this view is essentially correct [see *Obayashi and Hakura*, 1960, p. 34 and Fig. 24].

It now appears that the 'equatorial' mechanism is connected with the outer part of the outer van Allen radiation belt. The corpuscles involved are probably van Allen electrons, precipitated, however, by an interaction with the low-energy solar proton streams, such as will explain the concentration of auroral-zone excitation near midnight and its winter-equinoctial character. The 'polar' mechanism is of course the quasi-Störmer bombardment of high-energy protons (possibly supplemented by a secondary precipitation of Van Allen particles). The high-energy solar flux may include (a) protons arriving directly from the sun and (b) protons transported from the sun in the magnetic fields of the low-energy particle clouds (T. Obayashi, private discussion).

§7. Though we cannot adequately discuss the matter here, our picture—a winter-equinoctial night excitation filling in a gap in a morning-afternoon spiral of summer-equinoctial excitation—is reflected in a whole series of phenomena. *Rees and Reid* [1959] have traced a diurnal variation in the latitude of the auroral hydrogen emission, the mean locus of which would coincide very well with the eccentric path of $M + A$ in Figure 1. A midnight gap in the hydrogen emission was observed by *Montalbetti and Vallance Jones* [1957, p. 46]; the hydrogen emission disappears with the incidence of the midnight auroral breakup and is resumed in the morning hours [Veller, 1958; Galperin, 1959, p. 58]. A similar midnight gap was observed by *Barbier* [1958, Fig. 11] in the middle-latitude type A red aurora, which thus also would seem to be located on $M + A$.

According to *Galperin* [1959, p. 61], there is an almost 100 per cent association between the auroral hydrogen emission and (one type of) radioauroral reflections; this proton radio aurora [cf. *Rees and Reid*, 1959] corresponds to the 'diffuse' type of radio aurora distinguished by *Presnell, Leadabrand, Peterson, Dyce, Schlobohm, and Berg* [1959] and to the 'S-reflexions' described by *Forsyth, Green, and Mah* [1960]. It is a morning

and afternoon phenomenon (Forsyth), and is probably on $M + A$. Presnell's Figure 12 shows that, as observed from College, Alaska ($\Phi = 64.5^\circ\text{N}$), the diffuse radio aurora has afternoon and morning maxima of occurrence centered at ~ 17 hr and ~ 6 hr AT. As reported from Kiruna ($\Phi = 65.8^\circ$) these occurrence maxima are at 14–18 hr and 5–8 hr AT [Egelund, Hultqvist, and Ortner, 1960], with a lull of activity between them. (The College and Kiruna radio-auroral peaks may be compared with the two peaks of visible aurora that are observed higher on the pole cap; for instance, see Landolt's occurrence-frequency curve for aurora at South Pole Station, exhibiting maxima at 18.5 and 6 hr AT [Malville, 1959, Fig. 2].) Allowing for radio reflection geometry and aspect relationships which must modify the distribution plot for stations at different latitudes, and allowing also for differences of distribution with longitude (§1), it seems that the diffuse radio aurora may be identified with loci M and A .

The midnight gap between the afternoon and morning diffuse radio aurora is filled in by a different, 'discrete' radio aurora,³ which is predominantly a night phenomenon with its occurrence peak at 21–23 hr AT; see Figure 5 of Presnell, Leadabrand, Peterson, Dyce, Schlobohm, and Berg [1959]. It corresponds to the 'A-reflexions' described by Forsyth *et al.*, and its association with the night magnetic activity in the auroral zone is clear; so also is its association with the visible night aurora [Forsyth, Green, and Mah, 1960, Fig. 2].

Forsyth's A reflections were received from formations located between $\Phi = 55^\circ(?)$ and $\Phi = 75^\circ$. In this interval there was, with increasing latitude, a regression of occurrence time from 1.5 to 21.5 hr LT, a regression that places the reflecting formations on the night agitation locus N —or on the northern branch of Mayaud's locus—in our Figure 1; see Forsyth, Green, and Mah [1960, Fig. 4]. (We shall enlarge upon this point in a subsequent paper.)

The discrete night radio aurora seems to be winter-equinoctial [Presnell, Leadabrand, Peter-

son, Dyce, Schlobohm, and Berg, 1959, pp. 11, 1185] like the night agitation. The diffuse morning and afternoon echoes have been observed throughout the year, but it is not improbable that they will be found to have a summer-equinoctial variation, like that of morning and afternoon agitation.

Recapitulating, let us trace the behavior of radio aurora with increasing latitude. Observed from Jodrell Bank and Ithaca, the diurnal variation has afternoon and early morning peaks (Fig. 8i). Between the peaks there is some night activity, but the dayside activity level is vanishingly low. The two peaks may be explained by reflecting aurora on the southern ends of loci M and A , on either side of the night gap. At these stations (and at the radio frequencies in question) the discrete night radio aurora fills the gap is not strongly recorded, but at Saskatoon, closer to the auroral zone, the reflection geometry becomes more favorable, as at College, and a powerful night or night + afternoon peak is reported (Fig. 8ii). Still farther poleward at Kiruna the night activity almost disappears from between the afternoon and morning peaks [Egelund, Hultqvist and Ortner, 1960]; evidently most of the night aurora is reflected at too high an angle to be observed.

In the present paper we have no intention of discussing the complicated distribution of visible aurora, but one especially relevant feature may be mentioned. The boundary of southern extent of weak visible aurora exhibits two lobes [Davies and Kimball, 1960, Fig. 8 and p. 10], lying on either side of midnight and obviously corresponding to the maxima of radio aurora in Figure 8i. For strong aurora, however, there is a single lobe; the night maximum expands and effaces the double-lobed contour.

Two analogous lobes appear in one of Heppner [1954, Fig. 12] standard auroral progressions at College, Alaska, and it is to them that Lyon and Kavadas [1958, p. 1669] refer in connection with radar-auroral echoes.

LOW-LATITUDE AGITATION

§8. The notion suggested by Figure 5, namely the transport of geomagnetic agitation from high to low latitudes by parts of the SD current system, offers no difficulty in principle. Auroral zone agitation being so much more powerful than that of all other latitudes, it could well

³ One may no doubt explain the difference of character (but, of course, not the distribution of the aurora) in terms of the presence or absence of sunlight at E -layer levels, as Presnell, Leadabrand, Peterson, Dyce, Schlobohm, and Berg [1959, p. 1183] suggest.

regarded as the major source for the whole globe, and the decline of Stagg's intensity curve from the auroral zone is, except for a small zonal maximum at the equator, quite consonant with the idea of transport. It is reasonably evident that sudden commencement pulses (§15) are carried in part by a current system resembling SD; the transport of agitation pulses by SD should therefore be possible.

At Bombay there are three diurnal maxima of agitation; they appear in the disturbed-days curves for all seasons, and are detectable even in

the quiet-days curve (Fig. 4a). Two of them, the morning and afternoon low-latitude maxima, are traceable all through the middle latitudes from the auroral zone. The third maximum, centered near noon, is not traceable through the middle latitudes; it has nothing to do with the high-latitude morning maximum or with any feature of the high-latitude diurnal progression.

Figure 4a shows that at Bombay the transported night agitation still retains its *winter-equinoctial* character, as in the auroral zone, or as at Kew, Yakutsk, and Sluck in the upper

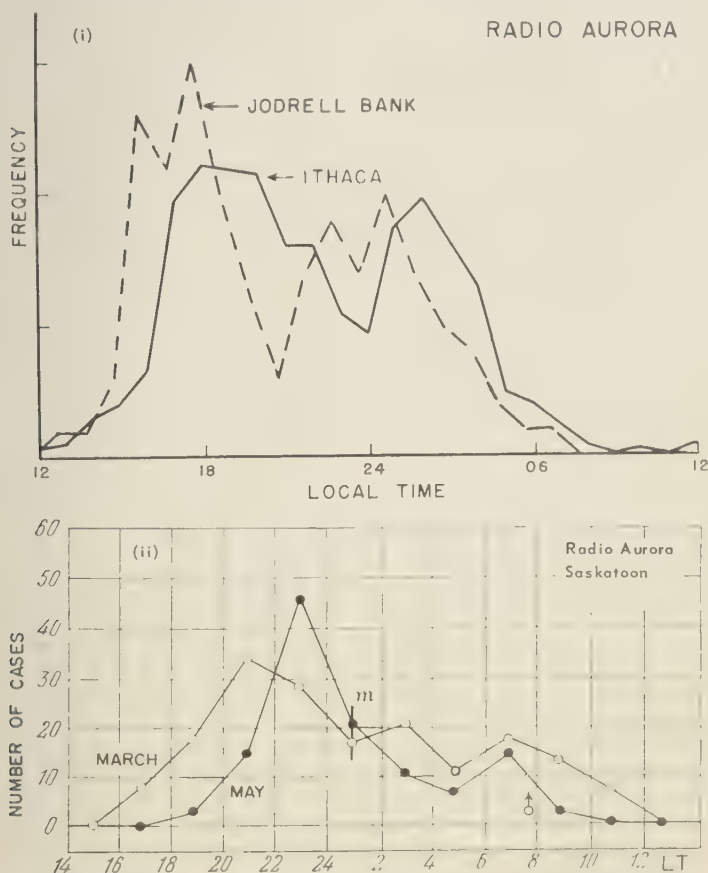


Fig. 8. Diurnal variation of radio aurora. (i) Ithaca, N. Y. 50-Mc/s transmission from Cedar Rapids by way of reflections from aurora at $\Phi = 58^\circ$, 1952-1954. Local time is shown for mid-point of path. Jodrell Bank. Diurnal variation of 72-Mc/s echoes from aurora at $\Phi = 59-60^\circ$, 1949-1953. Local time is shown for average longitude of reflecting region. The curves, which are normalized to include the same area, are from Kaiser [1955]; after Kaiser and Ballough [1955], Booker, Gartlein, and Nichols [1955], and R. Dyce. (ii) Saskatoon, 56-Mc/s radio auroral echoes, Feb. 23 to April 9 and May 5 to May 30, 1952, according to Carra, Forsyth, and Vauter [1953]. The echoes are from $\Phi = 66^\circ$. Compare also Lyon and Kawadas [1958, Fig. 2].

middle latitudes (Fig. 3), or as at Tashkent in the lower middle latitudes (Fig. 4b). The afternoon agitation at Bombay is *summer-equinoctial* as in the auroral zone, and it is summer-equinoctial throughout the middle latitudes (Figs. 3, 4b).

Arcs y and b are plotted in Figure 5 as representative of the night and afternoon agitation maxima in the middle and subequatorial latitudes. Similar arcs could be plotted for Tashkent, but only in an imprecise and awkward fashion, because of the poor resolution of the 3-hourly K index and the blending of the noon and afternoon maxima (Fig. 4b). This difficulty is common in the available agitation data for these latitudes (see for example *Bartels, Heck, and Johnston* [1939, Fig. F]; *Giorgi and Molina* [1956, Fig. 2], but the existence of the maxima and of their seasonal variations, as we have described them, is quite clear.

The low-latitude noon agitation maximum is evidently a local phenomenon, generated at the center of the sunlit hemisphere, no doubt by a direct, linearly arriving solar radiation. Nevertheless the radiation in question is not the steady thermal radiation of the sun, because the noon maximum is a magnetic disturbance phenomenon, as is shown by the difference between the disturbed-days and quiet-days curves of Figure 4a. Nor can this maximum be any kind of atmospheric or 'meteorological' phenomenon. (By the same token the afternoon agitation is a magnetic disturbance phenomenon; it cannot, for instance, be connected with the afternoon tropical thunderstorm activity that produces electromagnetic noise at higher frequencies.)

The small zonal maximum of agitation at the equator [*Stagg*, 1935a, Fig. 1B] no doubt represents the locally generated noon agitation (together with some contribution from Bobrov's compression pulses, §13).

The center of intensity of the noon agitation must oscillate back and forth across the equator with the sun. Consequently its seasonal variation, at Bombay and everywhere in the middle latitudes, is of the same summer-equinoctial type as the afternoon agitation [cf. *Narayanaswami*, 1941, Fig. 5], and often the two maxima, as in Figure 4b, are not separated.

The noon maximum of agitation extends its effects, with diminishing intensity, from the equator to the middle latitudes [*Mascart*, 1900, pp. 299, 301]. As far north as Tashkent ($\Phi = 32.5^\circ$)

it is stronger, in summer, than the night maximum; this explains why at Tashkent the principal diurnal peak of agitation is alternately at ~ 2 hr LT in winter and around noon in summer [Kozik, 1950, Table 1]. Kozik emphasizes that this is not a positional shift of a single peak but an alternating development of two stationary peaks.

It is reasonable to suppose that the noon agitation is carried by the dayside electric currents of the Sq system. Agitation, like the Sq variation exhibits a marked noonday enhancement at the equator (at Huancayo: see *Bartels, Heck, and Johnston* [1939, Fig. F]; compare *Chapman and Bartels* [1940, p. 213 and Fig. 4]).

Finally, we note, in the summer and equinoctial disturbed-days curves of Figure 4a, a small morning peak of agitation. This peak, if real might represent a dawn effect, perhaps the analog of the photodetachment effect at E -layer sunrise discussed by *Chatterjee* [1953] in connection with meteor E_s at Calcutta; see also *Presnell, Leadabrand, Peterson, Dyce, Schlobohm, and Berg* [1959, p. 1189]. If so, the photodetachment must depend on some prior change in the night ionosphere produced by magnetic disturbance, since the Bombay dawn peak does not appear in the quiet-days agitation curve.

§9. From *Narayanaswami's* data it appears that at Bombay there is, between the noon agitation on the one hand and the night agitation on the other, a radical difference of character, a difference that supports our thesis that low latitude noon agitation is locally generated whereas the afternoon and night agitations are imported.

The night maximum of agitation at Bombay shows up almost exclusively in the H component of the geomagnetic field, leaving the Z component nearly unperturbed [*Narayanaswami*, 1941, p. 161 and Fig. 9]. This can only mean that the night agitation at equatorial latitudes is transported by a uniform, far-extending horizontal current sheet.⁴ In contrast, the noon maximum of agitation at Bombay appears just as intense,

⁴ Van Bemmelen, investigating a certain class of geomagnetic pulsations at Batavia, found them to be very scarce in the Z component, and of course he likewise concluded that they were transported by a horizontal current sheet (*Van Bemmelen* [1900, pp. 83, 87]; see also *Chapman and Bartels* [1940, p. 352]).

Z as in H , the disturbing currents being momentous and turbulent, as might be expected in a locally generated agitation.

The Bombay afternoon maximum is partly overlapped by the noon agitation, but if it could be freed of this contamination its behavior would, it seems, be the same as that of the night maximum. That is to say, the afternoon agitation like the night agitation is transported by a smoothing current sheet. Even with the contamination the afternoon agitation is far stronger in H than in Z ; see Narayanaswami's Figure 9.

Accordingly, we find, in Narayanaswami's Figure 9, that the diurnal curves of agitation in H and Z are strikingly different, the H curve having three maxima but the Z curve only one, at noon. This difference is uniquely a characteristic of low-latitude agitation. Nothing of the sort is found in the high latitudes, where, as we have shown, there is little to choose between H and Z for measuring agitation: the diurnal curve of variation is the same in both components [Chapman and Bartels, 1940, p. 388; Narayanaswami, 1941, p. 161].

The Bombay difference between the maxima also appears at Tashkent, and it accounts for a phenomenon noted by Kozik [1950] that would be very puzzling to explain otherwise. At Tashkent, Kozik found that agitation measured as a percentage of the H component has an evening maximum in the yearly mean whereas agitation measured by the K index has its maximum at noon in the yearly mean. This means that in the H component the afternoon and night agitation, carried by smooth current sheets, outweighs the noon agitation, but in the K index, which is based on Z as well as on H , the noon agitation has the lead.

The picture may be summarized as follows. In the high latitudes where they are generated, the afternoon and morning agitations are carried by turbulent and filamented overhead currents, and therefore appear equally in H and Z . As they progress toward the equator, the turbulent streams subside into smooth current sheets, which affect only the H component. The agitation carried by such current sheets is in the form of density variations only (§3), and is therefore coherent at points along the stream. This explains the correlation found by Lawrie [1959] between magnetic fluctuations (of duration 30 seconds to 5 minutes) at Lovö and at stations on a line

extending meridionally to Tamanrasset (geomagnetic latitudes 58.1° to 26°). In the middle and low latitudes the noon agitation enters the picture. The electric currents transporting it are everywhere turbulent, presumably as a result of turbulent ionospheric conditions in the sunlit hemisphere at the level where these currents flow. The noon agitation consequently appears in both Z and H .

The practical conclusion can be drawn that the systematic recording and comparative study of agitation in H and in Z would be worth while. Of course the amount of agitation in Z does not depend on the character of the overhead currents alone, but also on the local distribution of ground conductivity [Duffus, Shand, and Wright, 1960]. The ratio of Z agitation to H agitation will vary from place to place. Nevertheless, at any one place a diurnal variation of the ratio, as at Bombay and Tashkent, will be indicative of the overhead conditions.

§10. Next is the question of how agitation may appear to be transported only in the night and afternoon parts of the low-latitude SD circulation (Fig. 5). Why is agitation not transported over the whole of this circulation? The easiest answer is that the two great low-latitude SD circuits are the statistical summation of many elementary loops, much narrower in longitude, as shown, for example, by Fukushima [1953, p. 328]. Only the elementary loops that pass through the night and afternoon auroral-zone foci of agitation pick up and transport the disturbance to the lower latitudes. The agitation carried by these momentary and fluctuating elementary loops is statistically concentrated in the stippled areas of Figure 5.

It is much to be doubted, however, that this is a full explanation. The morning agitation on locus A of Figure 1 does not appear to be picked up or transported by the elementary current loops passing through auroral latitudes in this vicinity. It seems we shall have to postulate some difference between the daytime and the nighttime ionosphere: perhaps the daytime E layer has a shielding effect. (We do not, of course, conclude that night ionospheric conduction involves noise, while day conduction is not noisy; this would not allow for the equatorial noon maximum, nor would it explain the different seasonal variations of the low-latitude maxima.)

The mechanism of ionospheric conduction is

undoubtedly complicated, involving not only elementary loops but also traveling electric vortices [Chapman and Bartels, 1940, pp. 311–314; Wiese, 1955; Burkhart and Selzer, 1955]. It must also involve both electronic and ionic drifts. Radio and radar observations, revealing the direction of *electron* motion, show (real or apparent?) east-west drifts at subauroral latitudes that statistically are in the expected direction, that is, contrary to the statistical streamline directions of Figure 5 [e.g., Kaiser, 1955]. These observations, however, probably relate only to the lowest level of *E*-layer conduction, while at greater altitudes the conduction transverse to the geomagnetic field will be ionic [Chapman and Bartels, 1940, pp. 535–538; Ben'kova, 1953, ch. 8, §2; Bless, Gartlein, Kimball, and Sprague, 1959, pp. 951–952]. The SD circulation may indeed involve both the *F* layer and the *E* layer, as argued by Ben'kova; there are many, even if tenuous, indications that this is not an idea to be dismissed. Middle-latitude visible aurora is high aurora (or, from the opposite point of view, the base of the visible aurora is depressed in the auroral zone, which may be regarded as a deep trough or canyon in an auroral plain). It is possible that the SD circulation is similarly distributed in altitude, concentrating at ~ 100 km in the night auroral zone but diffusing or rising to heights of 160 to 400 km or more in subauroral latitudes [Ben'kova, 1953, ch. 5, §§2, 7; ch. 6, §2]. Though at low latitudes the existence of *E*-layer electric currents, probably belonging to Sq, has been demonstrated [Cahill, 1959], on the other hand the mechanism of at least the lunar geomagnetic variation appears to operate at *F* levels [Raja Rao, 1959].

If the SD return circuits do flow higher than the *E* layer, it renders more probable a shielding of the transported agitation by the daytime *E* layer, as suggested above.

Narayanaswami [1941, p. 162] observed that the Bombay agitation maxima were related in some way to the *E*-layer and *F*-layer ionization. It is an interesting possibility that the paths of the low-latitude SD circuits of Figure 5, and therefore the positions of the afternoon and night maxima of agitation, may be decided not so much by atmospheric dynamo geometry as by low-latitude ionization pattern. The daily mean distribution of electron densities at Talara, Peru (summer of 1957), showed, at all levels of the

ionosphere, broad daytime and nighttime maxima, separated by relatively narrow minima centered at ~ 6 hr and ~ 20 hr LT [IGY Bull. 16, 1958, Fig. 3 and p. 1020]. This pattern is explained in terms of daytime solar irradiation and nighttime compression (contraction) of the ionosphere. The minima correspond fairly well with the nodal points of the two low-latitude circuits of Figure 5. It seems reasonable that the SD return circuits should be located within the two broad maxima of low-latitude ionospheric ionization.

Bemmelen [1899, pp. 120–121 and table] observed that the diurnal occurrence-frequency of his geomagnetic 'spasms' at Batavia showed narrow minima at sunrise (6–8 hrs LT) and sunset (18–19 hrs LT).

Interesting also is the fact that audiofrequency geomagnetic noise transmission is channeled in a similar pattern: Goldberg [1956], in Oregon, observed minima at 07 and 21–22 hr, in reasonable agreement with the Talara ionization-minima and with the nodes of Figure 5.

In the middle latitudes the distribution of airglow, of visible and invisible aurora, and of associated ionospheric phenomena is complex to a degree unsuspected a few years ago [Roach, 1958; Barbier, 1958; Roach and Marovich, 1959; Trojickaya and Mel'nikova, 1959]. In particular there seems to be a band of cisauroral excitation exhibiting a remote control by activity in the auroral zone. Divari [1947] reported fluctuations of the general sky brightness at Alma Ata in synchrony with aurora on the northern horizon. Dufay and Dufay [1947] found the behavior of certain lines in the night sky spectrum to depend on aurora in the north. Mednikova [1948] observed, overhead at Moscow, the formation of an ionized layer higher than the *F*₂ layer, presumably a corpuscular effect, which was inevitably accompanied by aurora visible in the north; it could indeed be regarded as a practical harbinger of aurora at Moscow. Warwick [1958] found the overhead ionization at Boulder, Colorado, to be strongly correlated with the intensity of ionization in an auroral arc hundreds of miles to the north. The picture suggests a corpuscular bombardment, consisting of radiation drained from the relatively empty space between the inner and outer van Allen belts (Roach and Marovich) but diurnally modulated by some reaction or relationship with the solar corpuscular irruption.

that produce the aurora in the auroral zone (compare §6). The ionization caused by this diurnally modulated bombardment may be part of the channeling mechanism for the low-latitude D circuits.

Connected with the cisauroral zone of high red aurora (Barbier; Roach and Marovich) there might be, in the middle latitudes, some zonal distortion of the geomagnetic storm variation. Afanas'yeva and Kalinin [1952] found, at $\approx 50-55^\circ$, an apparent maximum of the periodic or storm-time variation Dst, separated from the auroral-zone Dst maximum by a pronounced minimum at $\Phi \approx 55-60^\circ$. These authors explain the minimum as a zonal cancellation effect due to opposing components of the Dst circulation at *E*-layer (auroral) and *F*-layer (red auroral) heights. There is, however, reason to believe that the auroral-zone maximum represents only a pseudo-Dst (§14), in which event the configuration reported by Afanas'yeva and Kalinin needs to be re-examined. Sugiura [1955, Fig. 5 and p. 70] found the range of SD(*H*) to be smaller at geomagnetic latitude 52° than at either 42° or 59° . But this is explainable as an SD analog of Hasegawa's effect (§2); that is, the eyes' of the two SD circuits (Fig. 5) may fluctuate in latitude from north to south of $\Phi = 52^\circ$, so that in the *X* component of *H* there is a statistical cancellation.

§11. Let us now consider a proof that the afternoon and night low-latitude agitations are in fact transported by the currents of the SD system.

At auroral latitudes the direction of the SD currents (the electrojets and the current filaments of which they are compounded) is east-west, and in agreement with this it is observed that the agitation vector statistically lies in the geomagnetic meridian. In the low latitudes also the direction of the agitation vector is meridional [Bartels, Heck, and Johnston, 1939, p. 421 and Fig. C], corresponding to the east-west flow of the SD (and Sq) currents. In the middle latitudes, however, where the direction of the SD currents is meridional, the agitation picture changes in conformity. At Gibilmanna in Sicily ($\Phi = 38.5^\circ$) we find that the east-west component of agitation is strong [Giorgi and Molina, 1956, Fig. 6, curve D], and that it exhibits large afternoon and night peaks. This is in striking agreement with our picture of agitation transported by the SD

currents, and indeed most strongly by the night and afternoon parts of the SD system, as in Figure 5.

In the diurnal curve of the north-south agitation component at Gibilmanna (labeled *H* in Giorgi and Molina's Fig. 6) the highest peak in the curve is around noon, which agrees with the idea that the noon agitation is transported by the *Sq* currents, the direction of which, in the vicinity of noon, is east-west [Chapman and Bartels, 1940, p. 229].

§12. Gibilmanna appears to be situated at a favorable latitude for revealing the meridional SD transport of agitation. A more usual report from the middle latitudes is that the agitation vector has no preferred azimuth [e.g., Bartels, Heck, and Johnston, 1939, p. 421]. That is to say, the effects of N-S and E-W currents, carrying agitation, are superimposed.

At Gibilmanna the SD and Sq components of agitation are separable because each is concentrated in a different part of the day. In the higher middle latitudes, however, this separation is obscured by the remote influence of the auroral electrojets. The electrojets are so powerful that to a considerable distance their magnetic influence dominates over that of the electric currents directly overhead. Fel'dshtein and Kurdina [1960] have demonstrated, from the relationships between ΔH and ΔZ , that such is the case with magnetic variation in a broad band to the north of the electrojets, and the same principle is basic in Stagg's [1935c, Fig. 4] study of the aspects of the currents producing magnetic disturbance at stations between geomagnetic latitudes 52° and 60° . The remote influence will extend far into the middle latitudes because of the storm-time expansion (dilatation) of the auroral electrojet zone. Bobrov [1960, §3] compiled statistics for the number of bay-producing E-W current filaments passing *directly overhead*, and found that these outriders of the auroral electrojets were distributed, with declining frequency, over a distance of 1200 km south of the auroral maximum zone, the number falling only at Leningrad to zero.

Thus at Borok ($\Phi = 53.0^\circ$), Kalashnikov and Zybin [1960] find that the vector of agitation pulses is predominantly in the geomagnetic meridian (corresponding to E-W current filaments). Nevertheless at these latitudes the southward SD currents (Fig. 5) are contributing

their quota of agitation, as may be seen from the range volumes for stations such as Sitka at $\Phi = 60.0^\circ$ [Bartels, Heck, and Johnston, 1939]. Possibly at $\Phi \approx 50^\circ$ [Bobrov, 1959b, §2] the effect of the electrojets takes second place to that of the overhead SD and Sq currents.

THE DST COMPONENT OF AGITATION AND OF VARIATION

§13. We have identified SD and Sq components of agitation; it is natural to inquire whether there is not also a Dst component of agitation, carried by the Dst current system (or systems) of magnetic storms. One would assume that this must be so, in view of the important Dst component not only in the storm variation but also in storm sudden commencements (§15). A plausible index to the amount of Dst agitation would be the height of the morning minimum in the low-latitude agitation curves (Fig. 4; Bartels, Heck, and Johnston [1939, Fig. F]; Giorgi and Molina [1956, Fig. 2]), in particular the height of this minimum for the N-S component of agitation [Giorgi and Molina, 1956, Fig. 6H], since the Dst currents are by definition directed along the parallels of geomagnetic latitude.

The Dst variation in the initial phase of storms takes the form of an augmentation of H , the greater part of which is probably not due to any atmospheric electric circulation. It is believed to represent a compression of the geomagnetic field by the approaching storm blast of solar corpuscles. The compression, which amounts to a transfer of energy from the moving particles to the earth's field, is describable as an eddy-current magnetic effect:⁵ a surge of electric current, eastward along the geomagnetic equator and closed through the higher latitudes,⁶ is

⁵ Though compression of a magnetic field may at times be conveniently visualized as a mechanical effect, it is of course always electromagnetic.

⁶ It may be suggested that, as the corpuscular stream enfolds the earth, the westward return currents of the eddies shown by Chapman and Bartels [1940, p. 860] will flip over the terrestrial poles and close the eastward circuit around the equator, thus equalizing the initial-phase compression on the night and day sides. At the point where the outer bounds of the geomagnetic field and the face of the corpuscular stream first interpenetrate, electrons and positive ions in the face are accelerated west and east; the magnetic field of this eastward surge of electric current, added to the earth's field, cancels the interpenetration, and

induced in the face of the arrested corpuscular stream [Chapman and Bartels, 1940, pp. 860-861]. Nevertheless there is evidence that the initial phase does also involve electric currents within the ionosphere [Vestine, 1953], though it is open to question whether these do not really belong to SD or to a disturbed Sq rather than to Dst (§14).

Dst in the main phase of storms takes the form of a slowly decaying depression of the H component, which is, or includes, the magnetic effect of a westward exospheric ring current. At least one such ring current has been directly detected by Soviet and United States space probes [Dolginov and Pushkov, 1959; Sonett, Smith, Judge, and Coleman, 1960].

Now, geomagnetic agitation may well include a Dst component owing to ordinary variations or filamentations in the Dst currents as described, but concerning this we have no evidence to discuss. On the other hand, the existence of a virtual Dst agitation, in the form of compression pulses in the geomagnetic field, has been demonstrated by Bobrov [1959b, 1960]. It is in general associated with magnetic storms and is observable in the zone between $\Phi \approx 50^\circ\text{N}$ and $\Phi \approx 50^\circ\text{S}$. Bobrov calls it *symphasic agitation*, because it is made up of pulses that are simultaneous and in phase over great distances in longitude. For example, the symphasic disturbance shown in Bobrov's [1959b] Figure 3 was registered over 263° of the earth's equatorial circumference, from 7 hr LT through morning, afternoon, and evening to past midnight.

in effect the earth's field is compressed by the advancing stream. The sideways-accelerated particles will retain a forward component of motion and will enfold the earth on either side. The eastward equatorial stream of Chapman's eddy system (p. 860) will thus be elongated and wrapped half way or more around the globe, after which the eddy current will be closed equatorially, by the shortest path (since the exosphere is not a vacuum), rather than through higher latitudes as shown by Chapman. This initial-phase eastward ring current may decay rather slowly, but, as Chapman points out (p. 867), the initial-phase effect is soon canceled by the westward ring current of the main phase, an entirely different phenomenon. (Chapman's classical explanation [p. 868] of the main-phase ring current must now, it would seem, be superseded by a van Allen belt drift mechanism, and the westward ring current, or currents, will almost certainly be of crescentic cross section.)

All the characteristics of Bobrov's symphasic agitation indicate that it is due to relatively small solar ion clouds or concentrations within the storm blast, the impacts of which cause brief compressions of the geomagnetic field, associated, no doubt, with *localized* eddy currents within the face of the stream. Symphasic pulses were never observed to extend completely around the equatorial zone. Always there is a gap, where the pulse, if propagated as a wave around the globe, does not penetrate. Indeed, according to Bobrov there may be, at different longitudes, two or more simultaneously existing regions of disturbance, each symphasic but independently so.

The magnetic vector of symphasic pulses is always northward (corresponding to a field compression and never a rarefaction). The Z and D components of the low-latitude surface field are meanwhile little disturbed and generally exhibit no coherent pattern. The recovery from a symphasic pulse is slower than the initial rise, and it is nonoscillatory (which suggests a damping effect of the ionosphere).

During magnetic storms symphasic disturbance occurs both in the initial phase and in the main phase. Thus during the initial storm compression and also during the ring current and slow recovery stages of the storm the exterior geomagnetic field is buffeted by minor clouds or concentrations of the solar corpuscular emission.

§14. If SD transport of agitation does indeed account for the pattern of Figure 5, the SD circulation is a physical reality and it must flow independently of any Dst circulation. That is, SD and Dst are at different levels, for a mixing of the two would destroy the pattern. Likewise if the noon agitation is carried by Sq, the Sq circulation is real and separate; otherwise the patterns of Figure 4 would be lost.

Now, so far as Dst corresponds to exospheric eddy currents and ring currents, the postulate of a separate level for the Dst circulation is nothing new. Nevertheless in principle this kind of evidence is important, for in the original derivation and definition of Sq, Dst, and SD (Chapman and Bartels, 1940, chapters VII and X) there is nothing to indicate whether, or to what extent, these variations correspond to real electric current systems within or beyond the ionosphere. Nor is it possible to say whether each system, ionospheric or exospheric, is itself simple or complex.

The magnetic disturbance field, which includes the SD and Dst variations, is defined as the difference between the quiet-day field Sq and the observed field; it is obtained by direct subtraction. So long as Sq is an analytical concept there is nothing to be said against the procedure; but, immediately we refer Sq to a real electric circulation, it is implied that that circulation is totally unaffected by magnetic disturbance. This is highly improbable. (Compare, for instance, the amounts of quiet-day and disturbed-day agitation associable with Sq in Fig. 4a.) More likely we have a 'storm Sq' variation, which, being a *terminological contradiction*, we cannot recognize; part of it is assigned to SD and part to Dst. On the other hand, Sq is measured for the 5 quietest days of the month; not for absolutely quiet conditions; therefore it will contain part of the disturbance field. For instance, the complicated Sq field shown by Obayashi and Jacobs [1957, Fig. 13] is almost certainly a combination of Sq and a residual polar SD, the latter being the almost permanent pole-cap disturbance on which Bobrov [1960] insists. On *absolutely quiet* days the polar field loses its complexity and tends to assimilate itself to the Sq field in lower latitudes; a quite regular Sq field will then represent the variation even over the polar regions [Nagata and Mizuno, 1955; cf. Chapman and Bartels, 1940, pp. 290-291].

We have seen that corresponding to the exospheric initial-phase Dst compression of the geomagnetic field there is Bobrov's symphasic compression-pulse agitation. Now Bobrov shows that the compression-pulse agitation diminishes from the equator and is no longer distinguishable beyond geomagnetic latitude $\pm 50^\circ$. So too the compression Dst of the storm initial phase diminishes with latitude and in the auroral zone and above is no longer detected; this may be seen from Sugiura's [1955] Figures 4b and 11, where the Dst variation of H , taken around geomagnetic latitudes 65° and 80° , does not exhibit the initial-phase increase that is characteristic of Dst in the lower latitudes. These facts support each other and indicate the same thing: namely, that a compression of the exterior field, whether the major compression of the storm initial phase or the minor pulses of Bobrov's symphasic agitation, can pass downward through the equatorial ionosphere but cannot much affect the surface field in the high latitudes where the

lines of force are nearly perpendicular to the ionosphere.

The high-latitude loss of the initial phase has been ascribed to obscuration by the random auroral-zone disturbance, but this does not seem to be a satisfactory explanation. It is a fundamental assumption of the analysis that random disturbance may be removed by averaging.

Moreover, there is evidence that the main-phase Dst, that is, the true equatorial Dst which is the magnetic effect of the ring current, likewise decreases monotonically with latitude and is small in the auroral zone. That is to say, the supposed secondary maximum of Dst in the auroral zone [Chapman and Bartels, 1940, p. 308] is Dst by definition only, and has nothing to do with the true equatorial Dst or with the ring current. In Chapman's theory the only function of this secondary zonal maximum was to account for the different strength of the westward and eastward electrojets; the main-phase Dst would add to one and subtract from the other. There is, however, no reason why the electrojets should not be unequal of themselves, as in polar storms or bays. It is possible, although the situation is not yet clear, that the auroral zone *pseudo-Dst* is no more than the summation, around the auroral zone, of the magnetic effects of these unequal electrojets. (Just such a pseudo-Dst effect occurs also in sudden commencements, for we observe that the zonal maxima in this case [Obayashi and Jacobs, 1957, Fig. 9] do not coincide with the auroral zone, but extend between $\Phi = 40^\circ$ and 70° , which is roughly the latitude extent of the SD-like currents of the sudden commencement circulation; see §15.)

Even before the war it had been discovered by A. P. Nikol'ski that in the quiet intervals of geomagnetic storms at high latitudes the horizontal component H of the geomagnetic field returns to exactly the same values as on quiet days [Nikol'ski, 1947, Table 2 and Fig. 24]. Now the depression of H due to the ring current—that is, the main-phase Dst—cannot behave like this; it is a slowly decaying phenomenon, corresponding to the slow decay of the ring current. Therefore if this true equatorial Dst had a secondary maximum in the auroral zone it would be impossible for H to return to quiet-day values during the quiet intervals of storms in the episodic manner observed by Nikol'ski.

What has been defined as Dst in the auroral

zone must in terms of real electric circulations be part of SD; like SD it is of a fluctuating and episodic character.

Of course the *mean* SD activity does decline with the decline of a magnetic storm and so is mimetic of Dst. We note that Vestine [1953] spoke of a polar part of the storm field which 'simulated the storm-time variation'; see also Lewis [1955], p. 132. Birkeland long ago observed that the effect of equatorial storms was of little importance at polar stations.

Few people were inclined to believe Nikol'ski's observations. His discussion of the storm-time variation [Nikol'ski, 1947, pp. 167–169, 148; 1951, pp. 12–13] seems to have been interpreted as a rejection of the whole theory of ionospheric electric currents, at least as a cause of high-latitude magnetic variation. This was unfortunate for his facts. No verification of them was attempted until 1953 (in the West, none at all). Finally Ben'kova [1953, ch. 2, §2; ch. 3, §§1, 2] took up the matter. Her result was failure to detect any real secondary zonal maximum of Dst in the auroral zone; she found Dst to decline smoothly from the equator and to be imperceptible at geomagnetic latitude 70° . [Cf. Dungey, 1958, p. 133.] Nevertheless Ben'kova still questioned Nikol'ski's findings and suggested, since quiet intervals are rare in world-wide storms, that what Nikol'ski had actually selected from the data were quiet intervals in *polar* storms. But Burdo [1957] disposed of this notion by showing that world-wide and polar storms were identical as regards the behavior of H in quiet intervals. Although he too seems to have started out with every intention of disproving Nikol'ski's findings, he thus ended by confirming them entirely.

What is more, Burdo showed that not only H but also Z and D , in the quiet intervals of storms, return to their quiet-day values. This is a remarkable point, since it appears to mean that the effect of the ring current (if we accept the ring-current theory of the main phase) cannot be figured as a simple superimposition of fields, with the screening effect of the ionosphere neglected. As in the initial-phase compression, and in the equatorial compression-pulse agitation, the main-phase ring current can modify the surface field at the equator but does not greatly affect any element of the high-latitude field.

SUDDEN COMMENCEMENTS AND SUDDEN IMPULSES

§15. The sudden commencements (SC's) of magnetic storms, together with the sudden impulses (SI's) that imitate SC's but are not followed by storms, exhibit a local-time variation of occurrence frequency which, in the middle latitudes, resembles the diurnal variation of geomagnetic agitation. Compare Figures 9 and 3a, b; compare Figure 9 with *Giorgi and Molina's* [1956] Figure 6, curve H. The agreement is also exhibited in our Figure 5, where arcs *g* represent the afternoon and night maxima in Newton's long series of SC + SI statistics for Greenwich and Abinger (Fig. 9). The natural conclusion is that the sudden-commencement pulse is a surge of a current system resembling SD, which carries agitation in the middle latitudes.

The existence of a diurnal variation of SC's was unexpected, since a great many data indicate that the pulses are a world-wide phenomenon. Yet the reality of Newton's variation can scarcely be doubted. A similar variation was found by *Rodés* [1932] for 'abrupt jumps' (presumably SC's plus SI's) in the geomagnetic trace at the Ebro. More decisive, because of the difference of longitude, is *Sugiura's* curve (Fig. 9) for SC occurrence frequency at Cheltenham, closely agreeing with that of Newton.

The consistency of the data is best seen from

Table 1, where we have listed the positions of the two principal minima of the SC or SI diurnal variations reported by several authors. These minima may be taken as corresponding to the dead points or stagnant nodes of a current system like the middle- and low-latitude part of the SD circulation in Figure 5. (Compare the Talara ionization-minima, §10.)

It should therefore be no surprise that a model current system for sudden commencements, a model containing an SD-like component and effectively explaining the diurnal variation of the pulse, has recently been constructed by *Obayashi and Jacobs* [1957, Figs. 4, 5, 8].

We should note at once, however, that in spite of the evident similarities between the SD-like part—let us call it SD(c)—of Obayashi and Jacobs' model and the magnetic storm or magnetic bay SD circulation of Figure 5, there is also the radical difference that SD(c) has no concentrated auroral-zone electrojets. SD(c) has a cross-polar current sheet with more or less the same orientation as in Figure 5 (though with considerable variation of phasing in the individual SC events; compare Obayashi and Jacobs Figs. 7 and 8b). The circulation is closed through two middle-latitude circuits which, lacking auroral-zone concentrations, spread far out over the subauroral latitudes. They probably spread farther than appears from Obayashi and Jacobs' diagrams, for the magnetic effect of SD(c) is

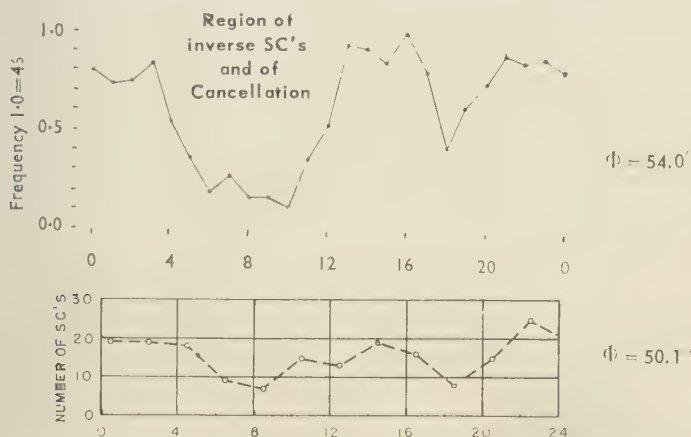


Fig. 9. *Upper curve:* hourly occurrence frequency of all SC's and SI's recorded at Greenwich and Abinger, 1879-1944, in local (Greenwich) time. From *Newton* [1948]. *Lower curve:* diurnal variation of occurrence frequency, at Cheltenham (Md.), of SC's observed conjointly at Cheltenham, Huancayo, and Watheroo, 1922-1946, 75th West Meridian Mean Time. From *Sugiura* [1953].

TABLE 1. Times of Diurnal Minima, SC's and SI's

				Nodal Minima, Centered at		Secondary or Uncertain Minima at	
				8	18 hr GMT	15	1 hr
Newton	1874-1944	Greenwich and Abinger	SC + SI, frequency	8	18 hr GMT	15	1 hr
Rodés	1905-1931	The Ebro	SC + SI, frequency	8	18-20 hr GMT	13	0 hr
Sugiura	1922-1946	Cheltenham, Md.	SC, frequency	8	18-19 hr LT	12.5	0 hr
Jacobs and Obayashi	1946-1953	Agincourt (Toronto)	SC, frequency	~9	~24 hr LT	15	hr
			SI, frequency	~9	~24 hr LT		
Berishvili	1933-1945	Tiflis	SC, amplitude	6	22 hr LT	17	hr

certainly manifested as far south as geomagnetic latitude $\sim 35^\circ$ [Matsushita, 1960, Figs. 2 and 7]. These SD(c) circuits thus resemble, in distribution though not in direction, the low-latitude return circuits of Figure 5 rather than the electrojets. Though the extraordinary agreement between arcs g and γ in Figure 5 reflects the similar positioning of the two middle-latitude loops, the directions of current in these loops, as between our Figure 5 and Obayashi and Jacobs' Figures 7 and 8*b*, are reversed. See also Obayashi and Jacobs' Figure 13.

The absence of sudden-commencement electrojets is most interesting. The SD(c) surge currents must flow at a level where they are not much affected by the auroral-zone ionization. (The auroral zone and its activity, though emphasized during magnetic storms, is of course a constant

feature of the ionospheric landscape.) Apparently the sudden-commencement circulation leaps over the auroral 'trough' of §10 and does not descend into it.

The Dst(c) circulation in Obayashi and Jacobs' model, analogous to Dst of magnetic storms but of relatively greater importance, is dominant in the lower latitudes, and, since this circulation is along the parallels of latitude, we should expect no low-latitude diurnal variation of SC's. This proves to be more or less true as far as low-latitude SC occurrences are concerned [Ferraro, Parkinson, and Unthank, 1951, Fig. 3], and the diurnal occurrence curve continues to be flat even at the latitude of Tiflis, as our Figure 10 shows. But the Tiflis curve of SC amplitudes (Fig. 10) is very different. Here we see narrow afternoon and night peaks, analogous to those of agitation and indicating the presence of the SD(c) component. The daytime level of amplitudes is depressed, and the general reason for this depression, as suggested by the parallel with agitation, may be one (or both) of those given in §10. Either the pulses carried by the overhead currents are partially shielded from earth-surface observation by the daytime E layer, or they are generated with greatest intensity in the afternoon and night auroral zone and are propagated with greatest intensity from these points by elementary loops of current concealed within the general SD(c) circulation diagram. (Heppner [1954, 1955] at College, Alaska, noted that storm sudden commencements had a diurnal maximum of occurrence near the midnight transition point between the eastward and westward SD auroral electrojets.)

In the upper middle latitudes where the

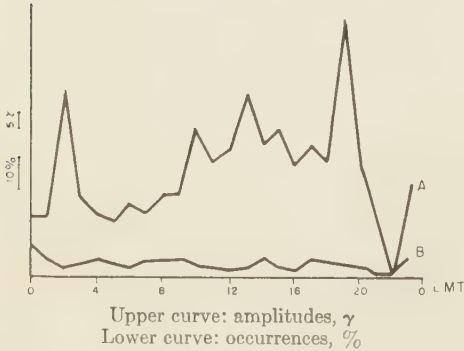


Fig. 10. Diurnal variation of SC amplitudes and frequencies, 1933-1945, at Tiflis (Dusheti and Karsani Magnetic Observatories, $\Phi = 36.7^\circ$ and 36.4°); hourly values. From Berishvili [1947].

fluence of SD(c) is still stronger, the narrow afternoon and night amplitude peaks are faintly reflected even in the occurrence curves (Fig. 9). The reason is undoubtedly that, where the amplitudes are greater, fewer pulses are missed from the count.

At these latitudes, however, there is an even more powerful effect that reduces the amplitude of the main SC pulse in a region on the morning side of the globe, and consequently, through losses from the count, produces a sag in the diurnal occurrence curves. This effect is a cancellation of pulses. In the model circulation [Obayashi and Jacobs, 1957, Fig. 7 or Fig. 8b] it is seen that during the main sudden commencement pulse the SD(c) and Dst(c) currents, on the morning side, flow in opposite directions. The resulting pulses are thus enfeebled. Or if not so much enfeebled, they may be distorted to such an extent that they escape recognition as SC's (Sugiura, private communication). Compare Forbush and Vestine [1955, p. 309].

This cancellation effect takes a notable bite out of the Greenwich-Abinger occurrence curve of Figure 9; at Cheltenham, as we see, its influence is less. In the amplitude curve the morning depression may be seen at the latitude of Tiflis (Fig. 10).

The result of the cancellation is to deepen and widen the morning nodal minimum as in Figure 9. It would be a mistake to suppose, however, that it creates the morning minimum. Table 1 shows that there are *two* persistent minima, conjugates at local time (~ 8 AM and ~ 8 PM). The morning minimum, though broadened by the cancellation, is an independent nodal effect and a counterpart to the evening nodal minimum, which is not similarly broadened (Figs. 9 and 10).

§16. Obayashi and Jacobs' model accounts very well for the observed similarities between the diurnal variations of SC's and of agitation, but its fact alone is not a sufficient demonstration of our case. Inasmuch as we are contemplating a similarity of mechanisms, it seems necessary to show that the SC model is consistent with the whole picture that we have drawn.

It is therefore interesting to observe that the SC model includes, in addition to SD(c) and Dst(c), also an Sq(c) component [Obayashi and Jacobs, 1957, Fig. 5; Matsushita, 1960, Fig. 7]. That is, it has the same three components that we have distinguished in the agitation mechanism.

And, again in agreement with the agitation picture, SD(c) and Sq(c) obviously correspond to ionospheric electric circulations, whereas Dst(c) probably does not. Dst(c) has the same northward H vector as Dst of the storm initial phase; if the latter is exospheric and the result of a compression of the geomagnetic field by the arrested solar corpuscular storm blast, Dst(c) very likely corresponds to a preliminary pulse of the same compression, due to the initial impact of the corpuscular front or a shock wave accompanying the front (Singer and others). Of course we cannot definitely rule out the possibility that Dst(c) is complex, involving also ionospheric electric currents. Nevertheless, so long as we do not have to provide a secondary zonal maximum of Dst(c) at auroral latitudes (§14) there does not seem to be any requirement for ionospheric Dst(c) currents. The entire atmospheric part of a sudden-commencement disturbance can probably be assigned to SD(c) or to a perturbed Sq.

The facts as a whole appear to be consistent with the thesis that Dst(c) is exospheric, a compression-pulse or storm-front eddy-current effect. The H vector of Dst(c) is unidirectional and northward. At low or middle latitudes the behavior of the Z component of SC's, according to Matsushita [1960, p. 1431], displays no particular distribution pattern, though it will be consistent at a given station, suggesting that it is decided merely by local idiosyncrasies of ground conductivity. Finally, the Dst(c) pulse is believed to propagate as a wave around the equator.

Incidentally we note that in the meridional direction the sudden commencement probably involves *two* waves, one in Dst(c) and the other in SD(c), analogous to the equatorial and polar waves of magnetic variation demonstrated by Fukushima and Abe [1958] in the initial phase of the great magnetic storm of February 11, 1958. In Japan the two initial-phase waves were of equal intensity at about $\Phi = 30^\circ\text{N}$, with the polar component predominating north of there and the equatorial component predominating to the south. The wave from the north, which no doubt belongs to the early-developing SD circulation [Fukushima, 1953, pp. 378, 380], preceded the wave from the south. So too, though in a shorter time scale, SC's are always first observed in the high latitudes [Williams, 1960; Benioff,

1960]. Apparently the SD(c) circulation is not static but expands equatorward during the pulse.

§17. In Obayashi and Jacobs' model, the Dst(c) surge currents flow in the eastward direction. The Sq(c) surge currents flow eastward along the midday part of the equator and (if the pulses are in phase) will add to Dst(c). This reinforcement, affecting the pulse count, will explain the slight midday excess of low-latitude SC occurrences noted by Moos at Bombay in 1910 [cf. *Ferraro, Parkinson, and Unthank*, 1951, p. 178; *Berishvili*, 1957]. Moreover Sq(c) will doubtless have an equatorial enhancement like that of the ordinary Sq [*Chapman and Bartels*, 1940, p. 212]; this will account for the equatorial enhancement of sudden commencements [*Sugiura*, 1953] and no doubt also for the statistical connections with Sq and with the storm initial phase, as demonstrated by *Forbush and Vestine* [1955, pp. 310-314].

The Sq(c) circulation, like that of the ordinary Sq, is essentially an eddy on the day side of the globe, closing westward through latitudes above $\sim 30^\circ$ [compare *Obayashi and Jacobs*, 1957, Fig. 5; *Chapman and Bartels*, 1940, p. 229]. The midday sudden-commencement activity corresponding to this Sq(c) eddy shows up in the diurnal curve of SC amplitudes at Tiflis (Fig. 10), separated from the late afternoon maximum by a slight lull. The same thing is perhaps detectable in the Greenwich and Cheltenham occurrence curves (Fig. 9). We note also the subsidiary minimum in the vicinity of 16 hr (\pm) in Table 1.

The Sq(c) surge might perhaps be a secondary, atmospheric effect of Dst(c): the ordinary Sq circulation is abruptly disturbed by the Dst(c) compression pulse in the ionosphere.⁷ The Sq(c) and Dst(c) pulses would thus always be in phase. (Possibly the same effect contributes, on a pulse-for-pulse basis, to the Sq component of geomagnetic agitation, the compression pulses here being those of the Bobrov symphasic disturbance.)

At Agincourt near Toronto, *Jacobs and Obayashi* [1956, Fig. 2] found that SC's and SI's of small amplitude had a midday maximum, in

⁷ The mechanism could be somewhat more complicated, for according to *Matsushita* [1960, p. 1427] the initial negative stroke of the (infrequent) low-latitude SC's also exhibits the equatorial enhancement. See §19.

startling contrast to the afternoon maximum of the larger pulses. The midday peak is so outstanding that the only evident explanation is a greater strength of the Sq(c) pulse, during small SC's, as compared with either the Dst(c) or the SD(c) pulse. Now this could happen if, as we have suggested, Sq(c) is an atmospheric effect and the Dst(c) compression: at times when the Dst(c) and SD(c) pulses at the earth's surface are weak, the Dst(c) compression pulse at the level of the ionosphere might yet be strong enough to energize the Sq(c) surge.

At the latitude of Agincourt the direction of the Sq(c) surge current is westward and the Sq(c) pulse is negative in *H*. (*Jacobs and Obayashi's* statistics include, but do not distinguish, negative pulses.) Thus between Sq(c), Dst(c), and SD(c) cancellation phenomena are no doubt to be expected in this neighborhood [see *Obayashi and Jacobs*, 1957, Fig. 5], though of course, only so far as the pulses are in phase.

§18. We have seen the important morning pulse-cancellation effect in the diurnal variation curves of sudden commencements (§15). This mechanism should be examined in detail, since it may offer instructive analogies for the study of geomagnetic agitation.

It might appear that the addition laws of sudden commencements and of agitation are basically different: pulses may cancel, but chaotic disturbance can, in general, only add. The distinction is not so absolute, however. On the one hand it is found that at least the onset of a sudden commencement has an oscillatory fin structure, with the oscillations extending over the first or rising half⁸ of the main SC pulse [*Matsushita*, 1960, p. 1426 and Fig. 5; *Benioff*, 1960, Fig. 27]. The fine-structure addition law may therefore be partly of the chaotic type. And should we on the other hand come to investigate the fine structure of agitation—for instance to trace the coherence and earth-surface distribution of individual agitation pulses in the manner of *Lawrie* [1959] and *Bobrov*—local cancellations and reinforcements of pulses may be a factor impossible to disregard.

In *Obayashi and Jacobs' sudden-commencement model*, the SD(c) circulation has bot

⁸ It is interesting that geomagnetic pulsations characteristically accompany the first half of a geomagnetic bay, but not the second (declining) half.

reverse and normal surges.⁹ A typical sudden commencement begins with a reverse SD(c) surge, followed by the normal surge. The reverse SD(c) slightly leads the main or Dst(c) pulse; it produces the initial reversed stroke of SC* and inverted SC* events. *Obayashi and Jacobs* [1957] have attempted to explain the reverse and normal SD(c) surges in terms of corpuscularly enhanced ionospheric conductivity over the pole caps and atmospheric dynamo effects at two different altitudes.

The normal SD(c) surge, in the upper middle latitudes, is more or less simultaneous with the Dst(c) surge, and, since these two oppose each other on the morning side of the globe, the cancellation effect of §15 occurs. At higher latitudes (e.g., at subauroral stations like College and Sitka) where the Dst(c) pulse is weak, it may be obliterated by the contrary SD(c) pulse, and the result is an inverted or negative sudden commencement [*Obayashi and Jacobs*, 1957, Fig. 6; *Jacobs and Obayashi*, 1956, p. 879].

Because of its characteristic lead, the reverse SD(c) pulse, which is contrary to Dst(c) on the afternoon side of the globe, does not produce any cancellation phenomena: there is no afternoon bite out of the diurnal curves, nor is there any broadening of the evening nodal minimum (Fig. 9, Fig. 10). The afternoon effect of the reverse SD(c) is to produce (in *H*) the negative leading stroke of the SC* or, in Matsushita's [1960] notation, -SC event. SC* or -SC events occur in the region, centered in the afternoon, that is marked by crosses in Matsushita's Figure 2. Compare the principal peak of SC*'s in *Newton's* [1948] Figure 5A and in *Jacobs and Obayashi's* [1956] Figure 1. On the morning side of the globe, the reverse SD(c) may add a positive leading stroke to the above-mentioned inverse sudden commencement, to produce an inverted SC*; these events correspond to the small morning

peak of SC* occurrences in *Newton's* Figure 5A and in *Jacobs and Obayashi's* Figure 1.

The normal SD(c) surge, though basically in phase with the Dst(c) surge, seems often to lag somewhat behind, with the result that a negative stroke may appear *after* the main sudden-commencement pulse in *H*. This phenomenon, in Matsushita's notation, is an SC⁻, and of course it occurs in the same region as the morning cancellation effect of Figure 9; compare the dotted region in Matsushita's Figure 2.

From Matsushita's description (p. 1425) it is clear that a given SC can exhibit negative strokes in *H* both before and after the main positive Dst(c) pulse, but the two negative strokes are then observed in different local-time regions. In other words, the phenomenon may really be described as -SC⁻, but it is observed as -SC in the afternoon region and as SC⁻ in the morning region of Matsushita's diagram. The preceding negative stroke is due to the reverse SD(c); the following negative stroke is due to the normal SD(c).

§19. Such is the fundamental mechanism, aside from Sq(c) effects, of Obayashi and Jacobs' model. Let us now consider two seeming anomalies.

(a) As we have indicated, -SC's produced in the manner described can occur only in the afternoon. Yet Matsushita in his Figure 2 shows the -SC region at the higher latitudes ($\Phi = 50-70^\circ$) extending almost around the globe, in a band crossing the SC⁻ region. This might be due to large positional fluctuations of the reverse SD(c) current system, but such a theory will not account for the restriction to the higher latitudes. Another possible explanation is that the reverse SD(c) surge is at times absent, with the result that the normal SD(c) surge occurs earlier and may slightly lead Dst(c) instead of lagging. -SC's may thus be produced on the *morning* side of the globe, for it is in the morning that the normal SD(c) is counter to Dst(c). These morning -SC's will no doubt occur mainly in the high latitudes because of the double wave effect mentioned in the last paragraph of §16: with decreasing latitude Dst(c) swallows up the slight lead of the normal SD(c).

Thus Matsushita's almost circumglobal distribution is explained by the morning -SC's added to the ordinary afternoon -SC's, the

⁹ It is interesting that Matsushita [1960, Fig. 9] reports an unusual reversed magnetic bay, with the directions of the electrojets and low-latitude circuits just the opposite of those in our Figure 5. It may of course turn out that the electrojets are not correctly shown by Matsushita; that the reality is either an episodic expansion of the auroral electrojets to extraordinarily low latitudes, or an extraordinarily late bay disturbance of afternoon type, which would indeed practically amount to a reversal of the SD circulation.

former being due to early normal SD(c) pulses and the latter to the reverse SD(c) pulses.

(b) *Matsushita* [1960, p. 1424] reports that -SC's are occasionally observed in the very low latitudes. They occur, however, on the daytime side of the globe, between 7 and 18 hr LT, that is, in a sector not corresponding to either the -SC or the SC- region of the higher latitudes. In fact, the sector would appear to be that of the daytime Sq(c) circulation. Furthermore, the *negative pulse* of the low-latitude -SC's exhibits the equatorial enhancement characteristic of Sq and Sq(c). All this suggests an interaction, inductive or otherwise, between the SD(c) and Sq(c) current systems, such that a negative pulse from SD(c) gets through, via Sq(c), to the equator.

§20. In view of the efficacy of Obayashi and Jacobs' model in accounting for the behavior of SC's, we must note with uneasiness that we cannot satisfactorily explain an apparently fundamental difference of behavior between SC's and SI's. In the middle latitudes SC and SI occurrences exhibit practically the same diurnal variation, of SD(c) type; see for example *Jacobs and Obayashi* [1956], Figure 1. At the equator, where the Dst(c) circulation dominates, we should expect (aside from the small Sq(c) noon effect) a flat diurnal curve of occurrences (§15). This expectation is met for SC's but not for SI's. *Ferraro et al.* show that at low latitudes the diurnal curve of SC occurrences is almost flat. It continues to be flat even at the altitude of Tifis (Fig. 10). SI's, on the contrary, exhibit the SD(c)-type variation even at the lowest latitudes. This may be seen in Figures 4 and 6 of *Ferraro, Parkinson, and Unthank* [1951], where the smoothed mean curve of SI occurrences for six predominantly equatorial stations—the same stations that showed a flat SC occurrence curve—has well-marked minima at ~ 8 and ~ 20 hr LT.

It seems possible that the statistics for sub-equatorial SI's may include two categories of pulses: one which has the same mechanism as SC's, and another of different origin which, like van Bemmelen's *geomagnetic spasms* (§10) imitates the SD(c) diurnal variation.

CONCLUSIONS

1. The transport of agitation is of course the principal thesis of this paper. It will account for (a) the strange shape of the night agitation locus (Cyranov's nose) and (b) the distribution and

seasonal behavior of the night and morning agitations throughout the middle and low latitudes. A powerful item of supporting evidence is the different character of agitation as between *H* and *Z* in the three low-latitude diurnal maxima (§9).

2. Systematic comparison of the horizontal and vertical components of geomagnetic agitation may be expected to yield useful results (§9).

3. Geomagnetic agitation has two identifiable causes. By far the more important is a chaotic corpuscular bombardment of the ionosphere. The other is brief equatorial compressions of the exterior geomagnetic field by the impact of solar corpuscular clouds (§13).

4. Part of the complicated distribution of high-latitude agitation may be explained in terms of a quasi-Störmer mechanism of spiral corpuscular precipitation (§6).

5. The distribution of radio-reflecting aurora matches that of high-latitude agitation (§7). The distribution of the auroral hydrogen emission appears to match that of the morning and afternoon agitations (§7).

6. The mechanism proposed by Obayashi and Jacobs provides an excellent explanation for the behavior of SC's and for certain resemblances between the distributions of SC's and of agitation.

7. The Sq(c) component of SC's may be a secondary, atmospheric effect of the Dst(c) compression pulse (§17).

8. There may be inductive or other coupling between the Sq(c) and SD(c) circulations (§19) and thus presumably also between the Sq and SD circulations.

Acknowledgments. We thank the Defence Research Board of Canada for permission to publish. To the various authors named in the legends of the figures we are grateful for the use we have made of their diagrams and data. For permission to reproduce this material and for other assistance we are indebted to the Oxford University Press and Pergamon Press, to the Editors of this journal, and to those of the *Monthly Notices of the Royal Astronomical Society*, the *Proceedings of the IRE*, and the *Canadian Journal of Physics*.

REFERENCES

- Afanasyeva, V. I., and Yu. D. Kalinin, A peculiarity in the geographic distribution of the magnetic storm field (in Russian), *Doklady Akad. Nauk SSSR*, 82 (3), 379-380, 1952.
 Aleksandrov, B. A., M. I. Pudovkin, and B. M. Yanovskiy, The magnetic field of magnetic dis-

- turbance in the arctic and antarctic, *Magnitno-ionosfernyye vozmushcheniya* [Magnetospheric Disturbances], Acad. Sci. Press, Moscow, 1959. (Translation to appear in vol. X of the *Ann. IGY*, Pergamon Press.)
- Barbier, D., L'Activité aurorale aux basses latitudes, *Ann. Géophys.*, 14 (3), 334-355, 1958.
- Bartels, J., N. H. Heck, and H. F. Johnston, The three-hour-range index measuring geomagnetic activity, *Terrest. Magnetism and Atmospheric Elec.*, 44 (4), 411-454, 1939.
- Benioff, H., Observations of geomagnetic fluctuations in the period range 0.3 to 120 seconds, *J. Geophys. Research*, 65 (5), 1413-1422, 1960.
- Ben'kova, N. P., Magnetic storms and electric current systems, *Tr. N-I. Inst. Zemnogo Magnitizma* [Tr. Research Inst. Terr. Magn.], no. 10 (20), Leningrad, 1953. Translation ATIC-262920 F-TS-8974/V.
- Berishvili, G. P., Contributions to the study of the principal characteristics of magnetic storms with sudden commencements, *Tr. Inst. Geophys., Georgian Acad. Sci.*, 16, 40-51, 1957. Defence Research Board of Canada translation T 332 R.¹⁰
- Bless, R. C., C. W. Gartlein, D. S. Kimball, and G. Sprague, Auroras, magnetic bays, and protons, *J. Geophys. Research*, 64 (8), 949-953, 1959.
- Bobrov, M. S., The estimation of some parameters expressing the inhomogeneity of solar corpuscular streams (in Russian), *Astron. Zhur.*, 36 (4), 601-615, 1959a.
- Bobrov, M. S., A study of solar corpuscular streams based on world-wide geomagnetic disturbances observed during the IGY (in Russian), *Astron. Zhur.*, 36 (6), 1028-1036, 1959b.
- Bobrov, M. S., Types of irregular geomagnetic disturbances and mechanism of the influence of solar corpuscular streams on the outer atmosphere (in Russian), *Astron. Zhur.*, 37 (3), 410-424, 1960.
- Booker, H. G., C. W. Gartlein, and B. Nichols, Interpretations of radio reflections from the aurora, *J. Geophys. Research*, 60 (1), 1-22, 1955.
- Briunelli, B. Ye., Possible cause of the disturbance daily variation S_D of the geomagnetic field, *Doklady Akad. Nauk SSSR*, 99 (5), 741-743, 1954. DRB translation T 166 R.
- Burdo, O. A., Re certain laws of magnetic disturbance in the high latitudes, *Fizika Solnechnykh Korpuskulyarnykh Potokov i ikh Vozeistviye na Verkhniyu Atmosferu Zemli* (Physics of the Solar Corpuscular Streams and Their Action upon the Upper Atmosphere of the Earth), USSR Academy of Sciences Press, Moscow, 1957. DRB translation T 321 R.
- Burkhart, K., and E. Selzer, Analyse de la variation de forme sinusoïdale sur la déclinaison magnétique du 11 avril 1954, *Ann. géophys.*, 11 (3), 353-368, 1955.
- Cahill, L. J., Investigation of the equatorial electrojet by rocket magnetometer, *J. Geophys. Research*, 64 (5), 489-503, 1959.
- Chapman, S., and J. Bartels, *Geomagnetism*, Clarendon Press, Oxford, 1940.
- Chatterjee, B., Nature and origin of sporadic-E regions as observed at different hours (over Calcutta), *J. Atmospheric and Terrest. Phys.*, 3 (5), 229-238, 1953.
- Currie, B. W., P. A. Forsyth, and F. E. Vawter, Radio reflections from aurora, *J. Geophys. Research*, 58 (2), 179-200, 1953.
- Davies, T. N., and D. S. Kimball, Incidence of auroras and their north-south motions in the northern auroral zone, *Univ. Alaska Geophys. Inst. Sci. Rept.* 4, January 1960.
- Divari, N. B., The aurora of September 22, 1946, and its effect on the night sky luminescence, *Meteorologiya i Hidrologiya*, no. 6, 85-88, 1947. DRB translation T 254 R.
- Dolginov, S. Sh., and N. V. Pushkov, Results of measurements of geomagnetic field made by space probe (in Russian), *Doklady Akad. Nauk SSSR*, 129 (1), 77-80, 1959.
- Dufay, M., and J. Dufay, Les bandes négatives de l'azote dans le spectre du ciel crépusculaire, *Compt. rend.*, 224 (26), 1834-1836, 1947.
- Duffus, H. J., J. A. Shand, and C. S. Wright, Influence of geological features on very low frequency geomagnetic fluctuations, *Nature*, 186 (4719), 141-142, 1960.
- Dungey, J. W., *Cosmic Electrodynamics*, Cambridge University Press, 1958.
- Egelund, A., B. Hultqvist, and J. Ortner, A daytime maximum of oblique auroral reflexions observed in the auroral zone, *Nature*, 185, (4712), 519, 1960.
- Fel'dshtein, Ya. I., The Dickson Island and Cape Cheliuskin Q-indices of magnetic activity, *Vozmushcheniya Elektromagnitnogo Polia Zemli* (Disturbances of the Terrestrial Electromagnetic Field), 5-15, Acad. Sci. Press, Moscow, 1960. DRB translation T 347 R.
- Fel'dshtein, Ya. I., and Ye. I. Kurdina, Magnetic variations in the region of the auroral zone, *Problemy Arktiki*, no. 3, 53-59, 1958. DRB translation T 318 R.
- Fel'dshtein, Ya. I., and Ye. I. Kurdina, Magnetic variation inside the principal auroral zone, *Problemy Arktiki i Antarkitiki*, no. 3, 118-119, 1960. DRB translation T 342 R.
- Ferraro, V. C. A., W. C. Parkinson, and H. W. Unthank, Sudden commencements and sudden impulses in geomagnetism; their hourly frequency at Cheltenham (Md.), Tucson, San Juan, Huancayo and Watheroo, *J. Geophys. Research*, 56 (2), 177-195, 1951.
- Forbush, S. E., and E. H. Vestine, Daytime enhancements of size of sudden commencements and initial phase of magnetic storms at Huancayo, *J. Geophys. Research*, 60 (3), 299-316, 1955.

¹⁰ All DRB translations here mentioned have been deposited in the Library of the National Research Council, Sussex Street, Ottawa, and in a number of other libraries, from which photocopies may be obtained.

- Forsyth, P. A., F. D. Green, and W. Mah, The distribution of radio-aurora in central Canada, *Can. J. Phys.*, **38** (6), 770-778, 1960.
- Fukushima, N., Polar magnetic storms and geomagnetic bays, *J. Fac. Sci. Univ. Tokyo*, section II, part V, vol. 8, 291-412, 1953.
- Fukushima, N., and S. Abe, The initial phase of the magnetic storm of February 11, 1958, *Rept. Ionosphere Research Japan*, **12** (1), 44-49, 1958.
- Galperin, G. I., Hydrogen emission and two types of auroral spectra, *Planetary and Space Sci.*, **1** (1), 57-62, 1959.
- Giorgi, M., and F. Molina, Sugli indici *K* per il 1955 dell'osservatorio magnetico di Gibilmanna (Sicilia), *Ann. geofis. Rome*, **9** (2), 179-194, 1956.
- Goldberg, P. A., Electromagnetic phenomena of natural origin in the 1.0-150 c/s band, *Nature*, **177** (4522), 1219-1220, 1956.
- Hakura, Y., Y. Takenoshita, and T. Otsuki, Polar blackouts associated with severe geomagnetic storms on September 13, 1957, and February 11, 1958, *Rept. Ionosphere Research Japan*, **12**, (4), 459-468, 1958.
- Harang, L., The mean field of disturbance of polar geomagnetic storms, *Terrest. Magnetism and Atmospheric Elec.*, **51** (3), 353-380, 1946.
- Heppner, J. P., A study of relationships between the aurora borealis and the geomagnetic disturbances caused by electric currents in the ionosphere, Thesis, California Institute of Technology, 1954. Republished (by permission) as Defence Research Board of Canada publication DR 135.
- Heppner, J. P., Note on the occurrence of worldwide s.s.c.'s during the onset of negative bays at College, Alaska, *J. Geophys. Research*, **60** (1), 29-32, 1955.
- Hope, E. R., A new picture of magnetic disturbance in the high latitudes, *Defence Research Board of Canada Publ.*, T 165 R, 1954.
- Hope, E. R., Spiral patterning of solar corpuscular precipitation, *Nature*, **177**, (4508), 571-572, 1956.
- IGY Bull. 16, U. S. Natl. Acad. Sci., Ionospheric electric density in height profiles, *Trans. Am. Geophys. Union*, **39** (5), 1018-1021, 1958.
- Jacobs, J. A., and T. Obayashi, The diurnal behavior of sudden commencements of magnetic storms at Agincourt, *Can. J. Phys.*, **34** (8), 876-883, 1956.
- Kaiser, T. R., Radio investigations of aurorae and related phenomena, *The Airglow and the Aurora*, Pergamon Press, London, 1955.
- Kaiser, T. R., and K. Bullough, Radio echoes from aurorae, *Ann. géophys.*, **11** (3), 279-283, 1955.
- Kalashnikov, A. G., and K. Yu. Zybin, Some results from observations of the horizontal-component variation-vector of the geomagnetic field (in Russian), *Izvest. Akad. Nauk SSSR, Ser. Geofiz.*, no. 2, 236-242, 1960.
- Kozik, S. M., Diurnal curves of geomagnetic activity at Tashkent, *Tr. Tashkent. Geofiz. Obs.*, no. 4 (5), 3-9, 1950. Translation ATIC-262921, F-TS-8975/V.
- Kraus, J. D., and W. Reed Crone, Apparent observation of solar corpuscular clouds by direct continuous-wave reflexion, *Nature*, **184** (4691), 965-966, 1959.
- Lawrie, J., Rapid fluctuations during magnetic disturbance, *J. Atmospheric and Terrest. Phys.*, **17** (1/2), 145-149, 1959.
- Lewis, R. P. W., The geomagnetic post-perturbation effect, *J. Atmospheric and Terrest. Phys.*, **6** (2/3), 129-133, 1955.
- Little, C. G., and H. Leinbach, Some measurements of high-latitude ionospheric absorption using extraterrestrial radio waves, *Proc. IRE*, **46** (1), 334-348, 1958.
- Lyon, G. F., and A. Kavadas, Horizontal motions in radar echoes from aurora, *Can. J. Phys.*, **36** (12), 1661-1671, 1958.
- MacDowall, J., Geomagnetic activity at Halley Bay, on disturbed days, *Nature*, **184**, (4698), 1543-1545, 1959.
- Malville, J. M., Antarctic auroral observations, Ellsworth Station, 1957, *J. Geophys. Research*, **64** (10), 1389-1393, 1959.
- Mascart, E., *Traité de magnétisme terrestre*, Paris, 1900.
- Matsushita, S., Studies on sudden commencements of geomagnetic storms using IGY data from United States stations, *J. Geophys. Research*, **65** (5), 1423-1435, 1960.
- Mayaud, P.-N., *Terre Adélie 1951-1952*, fasc. II, Expéditions polaires françaises, Résultats scientifiques, IV, 2, Paris, 1955.
- Mayaud, P.-N., Activité magnétique dans les régions polaires, Rapports scientifiques des expéditions polaires françaises, *Ann. géophys.*, **12**, fasc. 1, 84-101, 1956.
- McKinley, D. W. R., and P. M. Millman, Long-duration echoes from aurora, meteors and ionospheric back-scatter, *Can. J. Phys.*, **31** (2), 171-181, 1953.
- Mednikova, N. V., Ionospheric disturbances of a special type, *Doklady Akad. Nauk SSSR*, **59** (3), 475-478, 1948. NRL translation 187.
- Montalbetti, R., and A. Vallance Jones, H_e emissions during aurorae over west-central Canada, *J. Atmospheric and Terrest. Phys.*, **11** (1), 43-50, 1957.
- Nagata, T., and H. Mizuno, S_e field in the polar region on absolutely quiet days, *J. Geomag. Geoelect. (Japan)*, **7** (3), 69-74, 1955.
- Narayanaswami, R., The daily variation of irregular disturbances of the earth's magnetic field at Bombay, *Terrest. Magnetism and Atmospheric Elec.*, **46** (2), 147-162, 1941.
- Newton, H. W., 'Sudden commencements' in the Greenwich magnetic records (1879-1944) and related sunspot data, *Monthly Notices Roy. Astron. Soc., Geophys. Suppl.*, **5** (6), 160-185, 1948.
- Nikol'ski, A. P., The diurnal variation of magnetic disturbance in the high latitudes, *Problemy Arktiki*, no. 4, 5-43, 1938, Translation available

- from SLA Translations Pool, John Crerar Library, Chicago.
- Nikol'ski, A. P., Dual laws of the course of magnetic disturbance and the nature of mean regular variations, *Terrest. Magnetism and Atmospheric Elec.*, 52 (2), 147-173, 1947.
- Nikol'ski, A. P., Magnitnyye Vozmushcheniya v Arktike [Magnetic Disturbance in the Arctic] (in Russian), *Tr. Arkhticheskogo N.-I. Instituta*, 36, 1951.
- Nikol'ski, A. P., Magnetic disturbance in the circumpolar region and the existence of a second zone of enhanced disturbance-intensity, *Fizika Solnechnykh Korpuskulirnykh Potokov i ikh Vozdeistviye na Verkhniyu Atmosferu Zemli*, Moscow, 1957. Am. Meteorol. Soc. translation T-RC-13⁺.
- Nikol'ski, A. P., Magnetic disturbance in the circumpolar region of the Arctic, *Problemy Severa*, no. 1, 116-132, 1958. Translation available from National Research Council, Ottawa.
- Nikol'ski, A. P., Latitude and longitude dependences of mean level of geomagnetic activity (in Russian), *Problemy Arktiki i Antarkтики*, no. 3, 85-91, 1960a.
- Nikol'ski, A. P., Planetary distribution of mean level of magnetic-ionospheric disturbance (in Russian), *Tr. AANII* [Tr. Arctic and Antarctic Research Institute of the Northern Sea-Route Authority], 223 (3), 5-19, 1960b.
- Obayashi, T., and Y. Hakura, Enhanced ionization in the polar ionosphere caused by solar corpuscular emissions, *Rept. Ionosphere and Space Research Japan*, 14 (1), 1-40, 1960.
- Obayashi, T., and J. A. Jacobs, Sudden commencements of magnetic storms and atmospheric dynamo action, *J. Geophys. Research*, 62 (4), 589-616, 1957.
- Örendorf, R., and S. Coroniti, Polar E_s , *J. Geophys. Research*, 63 (4), 789-802, 1958.
- Presnell, R. I., R. L. Leadabrand, A. M. Peterson, R. B. Dyce, J. S. Schlobohm, and M. R. Berg, VHF and UHF radar observations of the aurora at College, Alaska, *J. Geophys. Research*, 64 (9), 1179-1190, 1959.
- Rudovkin, I. M., Magnetic variations in the high latitudes, *Izvest. Akad. Nauk SSSR, Ser. Geofiz.*, no. 7, 835-837, 1956. DRB translation T 233 R.
- Rudovkin, M. I., Origins of bay disturbances (in Russian), *Izvest. Akad. Nauk, Ser. Geofiz.*, no. 3, 484-487, 1960.
- Śaṭja Rao, K. S., On the seat of the L currents causing geomagnetic tides, *J. Geophys. Research*, 64 (3), 384-385, 1959.
- Tees, M. H., and G. C. Reid, The aurora, the radiation belt and the solar wind: a unifying hypothesis, *Nature*, 184 (4685), 539-560, 1959.
- Teach, F. E., The night airglow, *Geophysics and the IGY*, Am. Geophys. Union Monograph 2 (Publ. 590), 97-101, 1958.
- Teach, F. E., and E. Marovich, A monochromatic low-latitude aurora, *J. Research NBS*, 36D (3), 297-301, 1959.
- Todés, L., Período diurno, anual y secular en las perturbaciones súbitas del campo magnético terrestre, *Terrest. Magnetism and Atmospheric Elec.*, 37 (3), 273-277, 1932. DRB translation T 1 Sp.
- Shapley, A. H., and R. W. Knecht, Solar cosmic effects on February 23-25, 1956, observed by ionospheric soundings network, *Natl. Bur. Standards Rept. 5596*, 1958.
- Silsbee, H. C., and E. H. Vestine, Geomagnetic bays, their frequency and current-systems, *Terrest. Magnetism and Atmospheric Elec.*, 47 (3), 195-208, 1942.
- Sonett, C. P., E. J. Smith, D. L. Judge, and P. J. Coleman, Jr., Current systems in the vestigial geomagnetic field: Explorer VI, *Phys. Rev. Letters*, 4 (4), 161-163, 1960.
- Stagg, J. M., Hourly character-figures of magnetic disturbance at Kew Observatory, Richmond, 1913-1923, *Meteorol. Office (London) Geophys. Mem.* 32, 1926.
- Stagg, J. M., Numerical character-figures of magnetic disturbance in relation to geomagnetic latitude, *Terrest. Magnetism and Atmospheric Elec.*, 40 (3), 255-260, 1935a.
- Stagg, J. M., The diurnal variation of magnetic disturbance in the high latitudes, *Proc. Royal Soc. London, A* 149 (867), 298-311, 1935b.
- Stagg, J. M., Aspects of the current system producing magnetic disturbance, *Proc. Royal Soc. London, A* 152 (876), 277-298, 1935c.
- Störmer, C., *The Polar Aurora*, Clarendon Press, Oxford, 1955.
- Sugiura, M., The solar diurnal variation in the amplitude of sudden commencements of magnetic storms at the geomagnetic equator, *J. Geophys. Research*, 58 (6), 558-559, 1953.
- Sugiura, M., A study on the morphology of magnetic storms, *Univ. Alaska Geophys. Inst. Sci. Rept.* 1, 1955.
- Troyickaya, V. A., and M. V. Mel'nikova, Characteristic intervals [episodes] of oscillations of diminishing period (10-1 sec) in the geomagnetic field and their connection with phenomena in the upper atmosphere (in Russian), *Doklady Akad. Nauk SSSR*, 128 (5), 917-920, 1959.
- van Bemmelen, W., *Spasmen in de aardmagnetische krachten te Batavia*, 115-125, Akad. Wetenschappen, Amsterdam, Verslag Gewone Vergadering Wis- en Natuurkundige Afd., 1899.
- van Bemmelen, W., Erdmagnetische Pulsationen, *Natuurk. Tijdschr. Ned. Indië*, 62, 71-89, 1903.
- Veller, A. E., Hydrogen emission at the final stage of the aurora, *Ann. geophys.*, 14 (3), 323-325, 1958.
- Vestine, E. H., The immediate source of the field of magnetic storms, *J. Geophys. Research*, 58 (6), 560-562, 1953.
- Wallis, W. F., The geographical distribution of magnetic disturbance, *Terrest. Magnetism and Atmospheric Elec.*, 36 (1), 15-22, 1931.
- Warwick, J. M., Absorption of cosmic radio noise during the great aurora of 11 February, 1958, *Science*, 127 (3305), 1047-1048, 1958.
- Warwick, J. M., Some remarks on the interaction

- of solar plasma and the geomagnetic field, *J. Geophys. Research*, 64 (4), 389-396, 1959.
- Wiese, H., Die ionosphärischen Stromwirbel erdmagnetischer Baistörungen, *Gerlands Beitr. Geophys.*, 65 (1), 70-85, 1955.
- Williams, V. L., The simultaneity of sudden commencements of magnetic storms, *J. Geophys. Research*, 65 (1), 85-92, 1960.
- (Manuscript received November 29, 1960;
revised December 28, 1960.)

Some Properties of Radio Waves Reflected from the Moon and Their Relation to the Lunar Surface

TOR HAGFORS

Radioscience Laboratory, Stanford University, Stanford, California

Abstract. This report presents a theoretical discussion of the statistical properties of radio waves reflected from the moon. The discussion is based on the assumption of a large number of scattering areas simultaneously contributing to the signal. The properties of the echoes are usually described in terms of pulse broadening or by means of an average-power pulse response when very short pulses are transmitted. Here it is shown that the same type of information can be obtained by studying the correlation of complex amplitudes of two sine waves reflected from the moon at frequencies separated by $\Delta\omega$. By studying this correlation as a function of $\Delta\omega$ it is possible to compute the power pulse response of the earth-moon-earth propagation circuit. It is suggested that this method will prove particularly useful in the study of the surface properties of more distant targets such as the planets. It is also shown how the correlation technique can be extended to a two-dimensional mapping of a rotating rough body. The properties of the echoes returned from the moon are related here to a crude statistical model of the lunar surface roughness. This model is shown to lead to a satisfactory account for the semispecular component of the return from the moon if a large-scale structure with rms slopes of 1/20 to 1/10 are assumed.

INTRODUCTION

The lunar surface as seen through a powerful telescope appears to be rough and rocky. There are also large plains ('seas') which appear to be fairly smooth, having gentle slopes and isolated hills, and which are sometimes traversed by clefts. The large plains are often more or less completely surrounded by mountain borders with a precipitous face toward the plain and with less steep slopes on the other side. The diameter of some of the numerous craterlike depressions may exceed 100 miles. The mountains may be as much as 30,000 feet high. Signs of erosion are apparent in many places, and there may have been gigantic landslides here and there [Moore and Wilkins, 1958]. Surface temperature measurements made by study of meter and centimeter waves emanating from the moon indicate that the surface material has a low thermal conductivity [Pawsey and Bracewell, 1955], suggesting that a large part of the lunar surface may be covered by some lustlike substance.

Whereas the moon appears almost uniformly bright in the visual and infrared frequency range, only a limited region round the point nearest to the earth reflects well both meter and centimeter radio waves [Evans, Evans, and Thompson, 1959; Hey and Hughes, 1959; Yaplee and others, 1959]. Only with the most powerful present-day radars

is it possible to obtain weak echoes from near the limb [Pettengill, 1960; Leadabrand and others, 1960].

Both the visual picture of the moon and the experimental evidence obtained by radar studies show that a large number of independently scattering areas contribute to the total echo signal. Because of this, and because of the relative motion of the earth and the moon, the returned signals may be expected to fade in a noise-like manner, which is indeed observed [Evans, Evans, and Thompson, 1959; Hey and Hughes, 1959].

The presence of a large number of reflecting areas over the moon's surface evidently imposes on any returned signal certain bandwidth limitations. From the point of view of terrestrial radio communication using the moon as a passive reflector, it appears to be desirable to arrive at some statistical description of the propagation circuit. Conversely, the statistical properties of the signal are closely connected with the nature of the lunar surface. A study of the statistical properties of signals returned from the moon is therefore of interest for at least two reasons: it makes possible an evaluation of various modulation techniques in lunar communication, and it may reveal some interesting data on the structure of the lunar surface. In this report we shall discuss various expected statistical properties of

radio signals returned from the moon, assuming, where not otherwise specified, that the entire moon is within the beams of the transmitting and of the receiving antennas. The propagation circuit will be described in terms of an equivalent two-port electrical network. The properties of this network, of course, can only be given in rather general terms. In particular we note that, owing to the libration of the moon, the network parameters must vary with time. This network description will, incidentally, show how continuous-wave and pulse techniques for exploring the lunar surface are basically equivalent. An attempt is made to compute from a particular lunar model the properties of the returned signal. Finally, some of the results of the theoretical studies of this report are discussed in view of currently available experimental data on lunar echoes.

THE PROPAGATION CIRCUIT AS A TWO-PORT NETWORK

Since the idea of regarding a propagation circuit as a two-port network is by no means new, we shall here only introduce the concept by means of a simple example.

Let an antenna be situated in a semi-infinite space in front of an infinite, plane, perfect reflector. When a continuous sine wave is transmitted, the ratio of received and transmitted complex voltage at the antenna terminals is given by

$$\frac{e_{\text{received}}}{e_{\text{transmitted}}} = S(\omega) \exp [-2ikd] \quad (1)$$

where $k = \omega/c$, ω being the angular frequency, c the speed of light in the space in front of the reflector, and d the distance between antenna and reflector. The transmitting and receiving are done by the same antenna, and the transmitter and receiver may be imagined to be isolated by an ideal directional coupler. The quantity $S(\omega)$ is some amplitude function, determined by the transmission loss and by the antenna characteristics, and varies relatively slowly with frequency.

For the network the equivalent equation is

$$\frac{e_{\text{out}}}{e_{\text{in}}} = G(\omega) = A(\omega) \exp [-i\Phi(\omega)] \quad (2)$$

where $G(\omega)$ is the transfer function and where $A(\omega)$ is some slowly varying function of fre-

quency. The propagation circuit and the network are seen to be equivalent, provided that

$$A(\omega) = S(\omega) \quad \text{and} \quad \Phi(\omega) = 2kd$$

GENERAL PROPERTIES OF THE EQUIVALENT NETWORK WHEN THE REFLECTOR IS ROUGH

We shall in this section consider a network equivalent to a rough reflecting surface. The problem will be dealt with in two steps. In the first subsection the rough surface will be considered stationary with respect to the transmitter-receiver antenna. This means that the parameters of the network will not vary with time. In general, however, as in the case of moon echoes, the reflecting surface may either be changing or moving relative to the antenna, and the transfer function of the network must vary with time. This more general case is dealt with in the subsequent subsection.

Stationary reflector. The transfer function $G(\omega)$ for one particular rough surface at a mean distance d may be expressed as

$$G(\omega) = A(\omega) \exp \left\{ -i \left[\frac{2d}{c} \omega + \phi(\omega) \right] \right\} \quad (3)$$

where $\phi(\omega)$ and $A(\omega)$ are some kind of irregular function of frequency. If, in the actual propagation circuit, the signal originates in a fairly large number of reflecting areas, the transfer function may be thought of as a sum of phasors, as follows:

$$G(\omega) = \sum_k A_k(\omega) \exp [-i\omega\tau_k(\omega)] \quad (4)$$

Alternatively, we may put

$$\begin{aligned} A(\omega) \exp [-i\phi(\omega)] &= \exp [i\omega\tau_0] \sum_k A_k(\omega) \exp [-i\omega\tau_k(\omega)] \\ &= \sum_k A_k(\omega) \exp [i\omega(\tau_0 - \tau_k)] \end{aligned} \quad (5)$$

where $\tau_0 = 2d/c$. If τ_0 (and d) has been properly chosen, the systematic rotation of the various phasors with frequency will have been removed and the phasor $A(\omega) \exp [-i\phi(\omega)]$ therefore will not rotate in any preferred sense with a change in frequency.

From the above description we may conclude that the real and imaginary parts of the phasor $A(\omega) \exp [-i\phi(\omega)]$, in accordance with the central limit theorem, are gaussian-distributed with identical standard deviations and with mean

equal to zero. This statement is probably strictly true when we regard an ensemble of phasors corresponding to an ensemble of realizations of the rough reflector. For the time being we shall assume that the statistical properties of the transfer function are independent of frequency. An ensemble average may therefore be replaced by an average over frequency.

Let us compare our gaussian phasor with a more familiar type of phasor. Rice [1944 and 1945] has shown that a gaussian noise signal of small relative bandwidth may be represented as

$$f(t) = R(t) \cos [\omega_0 t + \Phi(t)] \quad (6)$$

where $R(t)$ and $\Phi(t)$ are slowly varying random functions of time. Apart from the uninteresting harmonic oscillation the noise signal may be described by the phasor $R(t) \exp [i\Phi(t)]$. We see that the variation with time here corresponds to the variation with frequency above. In particular we note that the mean noise frequency of Rice, ω_0 , corresponds to the mean time delay τ_0 of our equivalent network.

In the case of gaussian noise signals we know that all the statistical properties of the signal are determined either by the frequency power spectrum or by the autocorrelation function. We therefore inquire what the equivalent quantities are in the case of the random transfer function of our network.

The response to a δ pulse of a general network is known as the impulse response of the network and is given in terms of the transfer function in the following way:

$$W(\tau) = \frac{1}{2\pi} \int_{-\infty}^{+\infty} G(\omega) \exp(i\omega\tau) d\omega \quad (7)$$

This assumes, of course, that the integral exists. Unfortunately, in the present case where $G(\omega)$ extends throughout an infinite frequency range, this integral does not exist. To begin with, we must therefore limit the frequency range so that $|\omega| \leq \Omega$. The response to this modified pulse is then given by

$$W_\Omega(\tau) = \frac{1}{2\pi} \int_{-\Omega}^{+\Omega} G(\omega) \exp(i\omega\tau) d\omega \quad (8)$$

and the power in the pulse by

$$\langle W_\Omega(\tau)^2 \rangle = \left(\frac{1}{2\pi} \right)^2 \int_{-\Omega}^{+\Omega} \int_{-\Omega}^{+\Omega} G(\omega) G(\omega') \exp[i\tau(\omega + \omega')] d\omega d\omega' \quad (9)$$

We now take an ensemble average of this

$$\langle W_\Omega(\tau)^2 \rangle_{av} = \left(\frac{1}{2\pi} \right)^2 \int_{-\Omega}^{+\Omega} \int_{-\Omega}^{+\Omega} \langle G(\omega) G(\omega') \rangle_{av} \exp[i\tau(\omega + \omega')] d\omega d\omega' \quad (10)$$

Owing to the assumptions made above about the transfer function, it can be shown that $\langle G(\omega) G(\omega') \rangle_{av}$ is appreciably different from zero only when $\omega \approx -\omega'$. We therefore put $\omega' = -\omega + \Delta\omega$, and introduce as new variables ω and $\Delta\omega$. This results in

$$\langle W_\Omega(\tau)^2 \rangle_{av} = \left(\frac{1}{2\pi} \right)^2 \int_{-\Omega}^{+\Omega} \int_{-\infty}^{+\infty} d\omega d(\Delta\omega) \cdot \langle |G(\omega)|^2 \rangle_{av} R(\Delta\omega) \exp(i\Delta\omega\tau) \quad (11)$$

Here we have defined

$$\langle G^*(\omega) G(\omega + \Delta\omega) \rangle_{av} = \langle |G(\omega)|^2 \rangle_{av} R(\Delta\omega) \quad (12)$$

Because of the assumptions made, both $\langle |G(\omega)|^2 \rangle_{av}$ and $R(\Delta\omega)$ are independent of frequency. Therefore

$$\langle W_\Omega(\tau)^2 \rangle_{av} = \left(\frac{1}{2\pi} \right)^2 2\Omega \langle |G(\omega)|^2 \rangle_{av} \cdot \int_{-\infty}^{+\infty} R(\Delta\omega) \exp(i\Delta\omega\tau) d(\Delta\omega) \quad (13)$$

Dividing both sides of this by $2\Omega/2\pi \langle |G(\omega)|^2 \rangle_{av}$, we find

$$\lim_{\Omega \rightarrow \infty} \frac{\langle W_\Omega(\tau)^2 \rangle_{av} \pi}{\langle |G(\omega)|^2 \rangle_{av} \Omega} = \left(\frac{1}{2\pi} \right) \cdot \int_{-\infty}^{+\infty} R(\Delta\omega) \exp(i\Delta\omega\tau) d(\Delta\omega) \quad (14)$$

This limit we may define as a 'delay spectrum' $D(\tau)$

$$D(\tau) = \lim_{\Omega \rightarrow \infty} \frac{\langle W_\Omega(\tau)^2 \rangle_{av} \pi}{\langle |G(\omega)|^2 \rangle_{av} \Omega} \quad (15)$$

We therefore end up with

$$D(\tau) = \left(\frac{1}{2\pi} \right) \int_{-\infty}^{+\infty} \exp(i\Delta\omega\tau) R(\Delta\omega) d(\Delta\omega) \quad (16)$$

and

$$R(\Delta\omega) = \int_{-\infty}^{+\infty} D(\tau) \exp(-i\Delta\omega\tau) d\tau \quad (17)$$

For the idealized model of $G(\omega)$ considered above we therefore see that the delay spectrum $D(\tau)$ and the correlation coefficient $R(\Delta\omega)$ are Fourier transforms. The equivalent quantities in noise theory, of course, are the power spectrum $w(f)$ and the correlation function $\rho(\tau)$ [Rice, 1944]. Similar analogies with noise theory have been obtained by J. A. Ratcliffe in ionospheric physics in connection with the relation between an angular power spectrum and the complex correlation over a radiating source [Ratcliffe, 1956].

It is easy to imagine that $R(\Delta\omega)$ is an observable quantity in practice, but we would like to know whether the delay spectrum $D(\tau)$ is in any way related to the pulse shape when a high-frequency pulse of limited bandwidth is applied to the equivalent network.

In order to decide this let us apply a pulse of spectrum $S(\omega)$ to the equivalent network. The response to this pulse will be

$$W(\tau) = \left(\frac{1}{2\pi}\right) \int_{-\infty}^{+\infty} S(\omega) G(\omega) \exp(i\omega\tau) d\omega \quad (18)$$

and the apparent power response averaged

$$\begin{aligned} \langle W(\tau)^2 \rangle_{av} &= \left(\frac{1}{2\pi}\right)^2 \\ &\cdot \int_{-\infty}^{+\infty} d\omega \int_{-\infty}^{+\infty} d(\Delta\omega) S^*(\omega) S(\omega + \Delta\omega) \\ &\cdot \langle |G(\omega)|^2 \rangle_{av} R(\Delta\omega) \exp(i\Delta\omega\tau) \end{aligned} \quad (19)$$

To get a general idea of the problem we consider only two extreme cases. In the first, the bandwidth of the applied pulse is very much larger than the range over which $R(\Delta\omega)$ is different from zero. In this case:

$$\begin{aligned} \langle W(\tau)^2 \rangle_{av} &\approx \left(\frac{1}{2\pi}\right)^2 \int_{-\infty}^{+\infty} d\omega |S(\omega)|^2 \\ &\cdot \langle |G(\omega)|^2 \rangle_{av} \int_{-\infty}^{+\infty} R(\Delta\omega) \exp(i\Delta\omega\tau) d(\Delta\omega) \\ &= \text{constant} \int_{-\infty}^{+\infty} R(\Delta\omega) \exp(i\Delta\omega\tau) d(\Delta\omega) \end{aligned} \quad (20)$$

The apparent delay spectrum is thus proportional to the actual delay spectrum.

The other extreme case corresponds to a very

narrow band pulse. One finds

$$\begin{aligned} \langle W(\tau)^2 \rangle_{av} &\approx \left(\frac{1}{2\pi}\right)^2 \int_{-\infty}^{+\infty} d\omega \langle |G(\omega)|^2 \rangle_{av} \\ &\int_{-\infty}^{+\infty} S^*(\omega) S(\omega + \Delta\omega) \exp(i\Delta\omega\tau) d(\Delta\omega) \end{aligned} \quad (21)$$

and the apparent delay spectrum is entirely determined by the properties of the applied pulse.

We note that in order to determine the degree of pulse distortion it is sufficient to know the correlation function $R(\Delta\omega)$.

There still is one point to be considered. The initial assumptions regarded the statistical properties of $G(\omega)$ as completely independent of frequency.

This is known not to be true of reflections from the moon, since at meter and centimeter wavelengths the energy appears to be returned mainly from only a fraction of the moon's visible disk, whereas in the visual wavelength region the moon is almost uniformly bright. This means that the correlation function $R(\Delta\omega)$ depends on frequency. But if the statistical properties of $G(\omega)$ remain essentially constant over a frequency range very much larger than the range over which $R(\Delta\omega)$ differs from zero, the concepts of delay spectrum and frequency correlation may be applied, and the results translated from noise theory may be used as an approximation.

Nonstationary reflector. Observations show that the rapid fading of signals returned from the moon is due to lunar libration. This means that the properties of the propagation circuit are changing with time, and we would consequently like to make our equivalent network change with time in a similar way.

We therefore attempt to describe this time variation as follows. The pulse response will be assumed to change with time of observation. This means that the pulse response will no longer be determined only by the time interval elapsed since the application of the δ pulse at the input of the network but also by the actual time of observation. Therefore, let $W(\tau, t)$ denote the response at time t to an impulse applied at a time $t - \tau$. We would like to express the fading properties of the network in terms of some correlation function such as

$$R(T, \tau) = \frac{\langle W(\tau, t) W(\tau, t + T) \rangle_{av}}{\langle W(\tau)^2 \rangle_{av}} \quad (22)$$

This quantity is probably not very useful in practice, because we can never apply a true pulse but only some short pulse with a spectrum centered on a carrier frequency ω_0 . The correlation function we would measure would almost certainly depend on the frequency ω_0 . This means that we could not hope to measure the above quantity.

An alternative description of the time-varying network could probably be obtained by measuring the correlation function

$$\rho(T, \Delta\omega) = \frac{\langle G^*(\omega, t) G(\omega + \Delta\omega, t + T) \rangle_{av}}{\langle |G(\omega)|^2 \rangle_{av}} \quad (23)$$

Since the speed of fading is proportional to frequency one would expect that $R(T, \Delta\omega)$ is essentially a function of $\Delta\omega$ and ωT . This expectation, of course, has to be checked by experiment. If the assumption holds true, however, measurements in one particular frequency range would give information about the signal properties over a wide frequency range. It also appears that the type of correlation function introduced above is suitable for studying the fading characteristics of a demodulated signal communicated to the moon.

If the speed of fading is very high, it may not be possible to measure $R(T, \Delta\omega)$, because it may be that a spectral line in the process of reflection will be smeared out over a range of frequencies in excess of the range over which $R(\Delta\omega)$ is different from zero. This is most likely to happen at frequencies well above those usually employed in radar systems.

A new method for mapping the source of radar echoes from rotating targets without angular resolution has recently been proposed [Green, 1960] and used [Pettingill, 1960] to map the reflectivity over the lunar surface. It is based on the fact that energy received from a certain range interval d originates in a circular ring on the moon's disk whereas energy received with a Doppler shift f_D originates in a certain strip parallel to the projection of the axis of rotation in a plane perpendicular to the line of sight. Hence, by measuring returned energy versus delay and Doppler displacement, it is possible to obtain a two-dimensional picture of the reflectivity across the lunar disk.

Since the rate of change of our equivalent net-

work, as described by T in the correlation function, is related to the Doppler spread f_D , and the frequency of modulation $\Delta\omega$ is related to the delay τ , we may not be surprised to find that the 'target function' $\sigma(\tau, f_D)$ [Green, 1960], which describes energy as a function of Doppler frequency and delay, is actually related to our correlation function $R(\Delta\omega, T)$.

In order to see this we proceed as follows: The pulse response at a delay τ observed at a time t is

$$W_a(\tau, t) = \frac{1}{2\pi} \int_{-\infty}^{+\infty} G(\omega, t) \exp(i\omega\tau) d\omega \quad (24)$$

and

$$\begin{aligned} W_a(\tau, t + T) \\ = \frac{1}{2\pi} \int_{-\infty}^{+\infty} G(\omega, t + T) \exp(i\omega\tau) d\omega \end{aligned} \quad (25)$$

The autocorrelation of the pulse response at the delay τ hence becomes proportional to

$$\begin{aligned} \rho(\tau, T) &\sim \langle W_a(\tau, t) W_a(\tau, t + T) \rangle_{av} \\ &\sim \int_{-\infty}^{+\infty} R(\Delta\omega, T) \exp(i\Delta\omega\tau) d(\Delta\omega) \end{aligned} \quad (26)$$

In accordance with noise theory the power spectrum and the autocorrelation function are related by means of a Fourier relationship, so that we finally end up with

$$\begin{aligned} \sigma(\tau, f_D) &\sim \int_{-\infty}^{+\infty} \int_{-\infty}^{+\infty} R(\Delta\omega, T) \\ &\cdot \exp[i\Delta\omega\tau - 2\pi f_D T] d(\Delta\omega) dT \end{aligned} \quad (27)$$

and the desired relationship is established.

In order to see how $R(\Delta\omega, T)$ may be related to the properties of the lunar surface, or the surface of some other celestial body, we proceed, in the next section, to derive an expression for this correlation function for a particularly simple model.

REFLECTION FROM A MODEL MOON

We shall here deduce the correlation function $R(T, \Delta\omega)$, assuming certain statistical knowledge about the moon's surface roughness and taking into account the known rate of libration of the moon. We shall make only a crude analysis based on the Huygens-Kirchhoff principle. In the next section the results of this analysis will be com-

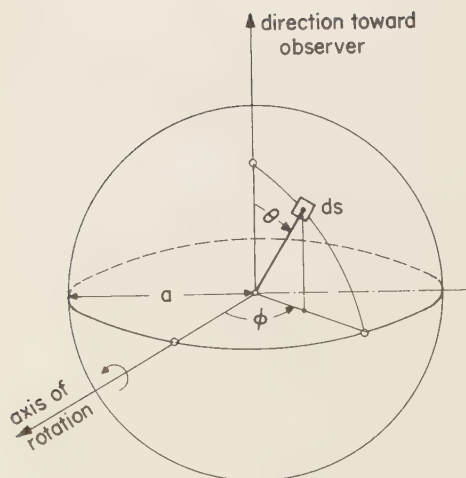


Fig. 1. Geometry and notations.

pared with certain observational data in an attempt to determine some of the parameters introduced in the analysis.

If the field at a distance R from the transmitter equals E_0/R , then from Huygens-Kirchhoff principle it follows that the returned field is equal to

$$E_p(\omega, t) = \frac{kE_0}{2\pi i} \int_{\text{surface}} \frac{\exp[-2ikR(t)]}{R^2} dS_n \quad (28)$$

The reflection coefficient is here put equal to unity. This does not make any difference to the statistical properties of the returned waves. By means of this expression we form the product

$$E_p^*(\omega, t)E_p(\omega + \Delta\omega, t + T)$$

and take an ensemble average over these products. Let this average be denoted by $\langle I \rangle_{av}$. After considerable simplifications we obtain

$$\begin{aligned} \langle I \rangle_{av} &\sim \exp[-2i \Delta k R_0] \\ &\cdot \int dS \frac{L^2}{4(h_m k)^2} \exp[-L^2 \tan^2 \theta / 4h_m^2] \\ &\cdot \exp[2i(kv_z T \sin \theta - \Delta k a \{1 - \cos \theta\})] \quad (29) \end{aligned}$$

In order to arrive at this result it was assumed that the lunar surface is rough so that over the surface the radius of the moon deviates from its mean value a by an amount h which varies from

point to point. It was further assumed that the height deviations at neighboring points are correlated

$$\langle h_1 \cdot h_2 \rangle_{av} = h_m^2 \rho(r)$$

and that the correlation function is of the form

$$\rho(r) = \exp(-r^2/L^2) \quad (30)$$

where r is the distance between the points where the height deviations are measured. The apparent angular velocity of the moon is Ω , the mean distance to the moon is R_0 , and the velocity v_x given by

$$v_x = a\Omega \sin \phi$$

The purely geometrical quantities involved are shown in Figure 1. It was also assumed that

$$h_m/\lambda \gg 1 \quad (h_m/L)^2 > 1/4ka$$

The first of these inequalities states that the rms height deviations are greater than the wavelength. The second inequality requires that the rms slope on the moon is greater than the wavelength divided by the linear extent of the central Fresnel zone.

We should keep in mind that this does not take into account the very small structure on the moon. This is not important at the present stage of the development, since we base our calculation on the Huygens-Kirchhoff principle, which already is known to be unsuitable for dealing with small-scale structure. We may therefore expect that our result will only account for the reflections originating in areas on the moon near the point that is closest to the observer.

It is interesting to note that $\langle I \rangle_{av}$ actually takes the form of a two-dimensional Fourier transform. To see this we have only to introduce new variables in the final double integral over θ and ϕ as follows:

$$\tau = (2a/c)(1 - \cos \theta) = \text{delay}$$

$$\begin{aligned} f_D &= \pi^{-1}kv_z \sin \theta = \pi^{-1}ka\Omega \sin \phi \sin \theta \\ &= \text{Doppler shift} \end{aligned}$$

We may hence write

$$\begin{aligned} \langle I \rangle_{av} &\sim \iint d\tau df_D \sigma(\tau, f_D) \\ &\cdot \exp[-i(\Delta\omega - 2\pi f_D T)] \quad (31) \end{aligned}$$

and this is in complete agreement with the previous results obtained from a general argumentation (see equation 27).

Putting $dS = a^2 \sin \theta \, d\theta \, d\phi$ and integrating over ϕ , we obtain

$$\begin{aligned} \langle I \rangle_{av} &\sim \exp(-2i \Delta k R_0) \\ &\cdot \int \sin \theta \, d\theta J_0(2ak\Omega T \sin \theta) \\ &\cdot \exp[-2i \Delta ka(1 - \cos \theta)] \\ &\cdot \exp[-L^2 \tan^2 \theta / 4h_m^2] \quad (32) \end{aligned}$$

where J_0 denotes a Bessel function of the first kind of order zero. If we put $T = 0$ here, and introduce the delay as new variable in the same way as above, we obtain expressions in complete agreement with earlier formulas. The delay spectrum is therefore of the form

$$D(\tau) \sim \exp[-L^2 \tan^2 \theta(\tau) / 4h_m^2] \quad (33)$$

At this stage we take the opportunity to make correction for the previous neglect of the small-scale structure by adding a term $F(\theta)$ to be determined from experimental results:

$$\begin{aligned} \langle I \rangle_{av} &\sim \exp(-2i \Delta k R_0) \\ &\cdot \int \sin \theta \, d\theta J_0(2ak\Omega T \sin \theta) \\ &\cdot \exp[-2i \Delta ka(1 - \cos \theta)] \\ &\cdot [\exp(-L^2 \tan^2 \theta / 4h_m^2) + F(\theta)] \quad (34) \end{aligned}$$

Under the further assumption that $L/h_m > 1$, the first term may be determined quite accurately [Reddy and others, 1955]. The second term must be left until the delay spectrum can be determined from experiments. We therefore end with

$$\begin{aligned} (\Delta\omega, T) &\sim \frac{\exp\{-(a\Omega kT)^2 / [(L/2h_m)^2 + ia\Delta k]\}}{[(L/2h_m)^2 + ia\Delta k]} + R_2 \\ &\quad (35) \end{aligned}$$

COMPARISON WITH EXPERIMENTAL DATA

Probably the most reliable measurement yet available of the delay spectrum of the moon has recently been presented by Pettengill [1960] from observations at 440 Mc/s. It was shown that the fall of the echo (power) follows a $\cos^2 \theta$ law.

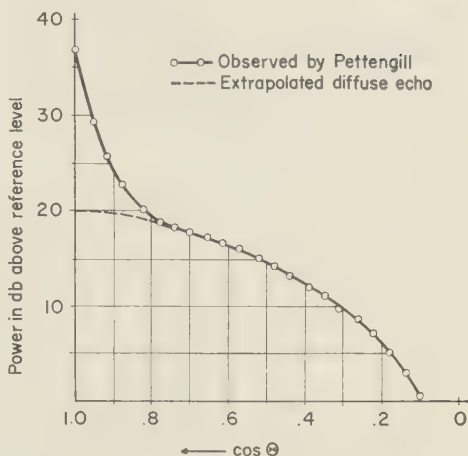


Fig. 2. Observed delay spectrum [Pettengill, 1960].

From Pettengill's diagram of power versus $\cos \theta$, which is replotted in our Figure 2, it appears that the delay spectrum is of the form (note that $\cos \theta = 1 - cr/2a$)

$$\begin{aligned} f(\theta) &= \exp(-L^2 \tan^2 \theta / 4h_m^2) \\ &\quad + \cos^2 \theta / 35 \quad (36) \end{aligned}$$

Because a pulse width of 500μ was used it may be that the initial sharp pulse should be somewhat higher and sharper than indicated. We shall, however, use Pettengill's result as an approximation to the delay spectrum. Doing this, we obtain from the shape of the initial pulse

$$L/h_m \approx 10$$

Let us next consider the results of Evans, Evans, and Thompson [1959], who studied the autocorrelation function of signals returned from the moon at 120 Mc/s. From the previous section, putting $F(\theta)$ equal to $(\cos \theta)^2/35$ as suggested by Pettengill's results, we obtain

$$\begin{aligned} R(T) &\sim (2h_m/L)^2 \exp[-(2akh_m\Omega T)^2 / L^2] \\ &\quad + (1/35) \int \sin \theta \, d\theta \\ &\quad \cdot J_0(2ak\Omega T \sin \theta) \cos^2 \theta \quad (37) \end{aligned}$$

To bring our result in agreement with that of Evans we substitute as follows:

$$ak\Omega/\pi = f_m = \text{maximum Doppler}$$

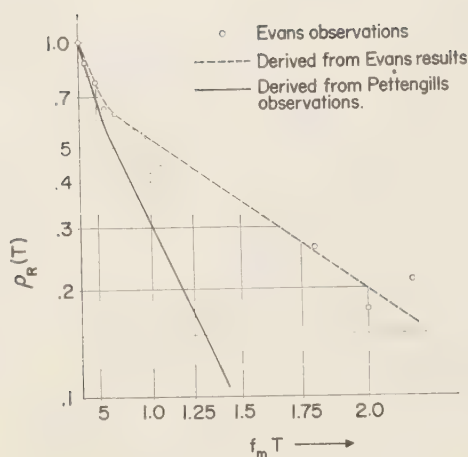


Fig. 3. Autocorrelation of lunar signal [Evans, Evans, and Thompson, 1959].

With this substitution we obtain

$$R(T) \cong 0.81 \exp [-0.4(f_m T)^2] + \begin{cases} 0.19[1 - 4(f_m T)^2] & f_m T < 0.3 \\ 0 & f_m T > 0.7 \end{cases} \quad (38)$$

The autocorrelation of the envelope, which is actually what Evans measured, is approximately given by the square of this,

$$\rho_R(T) \approx R(T)^2$$

Figure 3 shows a plot of Evans' results together with the correlation function deduced from Pettengill's results. The agreement is obviously poor. The broken line in the same diagram shows an attempt to fit a function of the general type suggested by Pettengill's work to the results of Evans. The autocorrelation function thus derived is given by

$$R(T) \cong 0.84 \exp [-0.166(f_m T)^2] + \begin{cases} 0.16[1 - 4(f_m T)^2] & f_m T < 0.3 \\ 0 & f_m T > 0.7 \end{cases} \quad (39)$$

From this it appears that the ratio of powers in the specular and the diffuse components is in agreement, but that Evans' results, interpreted in this manner, seem to indicate a sharper initial

pulse than is found by Pettengill.¹ Evans' results appear to show that

$$(L/h_m) \approx 15$$

Let us finally consider briefly the data presented by Hey and Hughes based on measurements at 3000 Mc/s using 5- μ pulses. Only the initial pulse was studied. The shape of this gives

$$(L/h_m) \approx 18$$

This shape of the initial 'average' pulse, therefore, does not seem to change very significantly with frequency. From the data available at present it is not possible to guess how the diffuse component varies with frequency.

From this discussion it appears that more experimental data must be collected and properly interpreted before a complete understanding of the nature of the lunar surface as a reflector of radio waves can be gained. It is suggested that some of the concepts introduced above may be useful in this work.

CONCLUSION

In this report we have shown that the properties of the semispecular reflection from the moon may be described by means of a large-scale irregular surface structure on the moon with slopes of the order of 1/20 to 1/10. The diffuse part of the echo, which we have not here attempted to relate to the structure of the lunar surface, is presumably due to a small-scale roughness superimposed on the large-scale structure.

The methods developed for dealing with the statistical properties of echoes returned from the moon may well find application in other types of propagation circuits with randomly varying parameters. It was shown that for such circuits information about the average-power pulse

¹ After the paper was submitted Evans kindly drew my attention to recent unpublished results obtained by Pettengill using 100- μ pulses. These results show that the initial pulse is indeed much sharper than that shown in Figure 2. With these new results there is very good agreement between continuous-wave and pulse techniques when the are compared as in Figure 2.

Also, these recent results appear to show that the initial pulse is of the form $\exp(-\alpha \cdot \theta)$ rather than the gaussian form arrived at above. This discrepancy may be removed by a different choice of the correlation function (30).

response can be obtained by studying the phase and amplitude relationship of two carriers at a time, these being separated by a frequency difference $\Delta\omega$. Expressions were given for the average-power pulse response in terms of the correlation of the complex amplitudes of the two carriers $R(\Delta\omega)$.

It may be that the methods of measurement described offer certain advantages over ordinary pulse methods because all the available power may be concentrated in two spectral lines rather than being spread out over a wide spectrum. The returned signal power per unit bandwidth will therefore be much higher in a two-frequency experiment than in a pulse experiment, and the detection of the signal will accordingly be much easier. This may be particularly important in radar studies of the surface properties of planets where the returned power is very marginal indeed.

It is interesting that there is a close analogy between interferometric techniques and the correlation method described above. When using an interferometer each antenna spacing gives information on one Fourier component of the distribution of illumination over the source. Similarly, each modulation frequency in the correlation technique gives one Fourier component of the power pulse response of the target. The pencil-beam scanning of a target to obtain the distribution of illumination corresponds to the examination of the target response by means of very short transmitted pulses.

For rotating bodies the two-frequency method may be extended to a two-dimensional mapping of the surface in much the same manner as proposed by Green [1960] with pulse techniques.

The description of a propagation circuit by means of correlation function $R(\Delta\omega, T)$ also appears to be well suited for a discussion of the effect of the circuit randomness on the modulation of a transmitted signal.

Acknowledgments. The present investigation was originally suggested by Professor V. R. Eshleman in connection with the measurement of cislunar electron density by means of moon echoes [Eshleman, Gallagher, and Barthle, 1960]. It is a pleasure to acknowledge the benefit of several discussions

with Dr. Eshleman as well as with Dr. P. B. Gallagher during the course of the work.

The work was supported by the Electronics Research Directorate of the Air Force Cambridge Research Laboratory, Bedford, Massachusetts, under contract AF-19(604)2193.

The author is on leave from the Norwegian Defence Research Establishment, Kjeller, Norway, and his study has been supported in part by a grant from the Royal Norwegian Council for Scientific and Industrial Research.

REFERENCES

- Erdelyi, A., and others, *Higher Transcendental Functions*, vol. 3, p. 50, McGraw-Hill Book Co., New York, 1955.
- Eshleman, V. R., P. B. Gallagher, and R. C. Barthle, Radar methods of measuring the cislunar electron density, *J. Geophys. Research*, 65 (10), 3079-3086, 1960.
- Evans, J. V., S. Evans, and J. H. Thompson, The rapid fading of moon echoes at 100 Mc/s, paper 2, *Paris Symposium on Radio Astronomy*, edited by R. N. Bracewell, Stanford University Press, Stanford, 1959.
- Green, P., Detection techniques for interplanetary radar observations, *MIT Lincoln Lab. Group Rept.*, pp. 34-84, 1960.
- Hey, J. S., and V. A. Hughes, Radar observations of the moon at 10 cm wavelength, paper 3, *Paris Symposium on Radio Astronomy*, edited by R. N. Bracewell, Stanford University Press, Stanford, 1959.
- Leadabrand, R. L., and others, Radio frequency scattering from the surface of the moon, *Proc. IRE*, 48, 932, 1960.
- Moore, P., and H. P. Wilkins, *The Moon*, Faber and Faber, London, 1958.
- Pawsey, J. L., and R. N. Bracewell, *Radio Astronomy*, chapter 8, Clarendon Press, Oxford, 1955.
- Pettengill, G. H., Measurement of lunar reflectivity using the Millstone radar, *Proc. IRE*, 48, 933, 1960.
- Ratcliffe, J. A., Some aspects of diffraction theory and their application to the ionosphere, *Phys. Soc. Repts. Progr. in Phys.*, 19, 188, 1956.
- Rice, S. O., Mathematical analysis of random noise, *Bell System Tech. J.*, 23, 282, 1944; 24, 46, 1945.
- Yaplee, B. S., and others, A lunar radar study at 10 cm wavelength, paper 4, *Paris Symposium on Radio Astronomy*, edited by R. N. Bracewell, University Press, Stanford, 1959.

(Manuscript received September 16, 1960;
revised December 20, 1960.)

Daytime and Nighttime Atmospheric Properties Derived from Rocket and Satellite Observations

H. K. KALLMANN-BIJL¹

University of California, Los Angeles, California

Abstract. Upper air densities obtained by means of rockets and satellites in the region from 100 to about 800 km are presented. Variations of densities from day to night become apparent around 200 ± 30 km; the effect increases with altitude. Pressures and scale heights are derived from densities, and preliminary mean, and daytime and nighttime values are obtained. From the variation of scale height with altitude, regions of constant temperature and of variable molecular weight have been determined. It has been found that the mean temperature at about 300 km is approximately 1400°K, and that it stays constant above that altitude.

Two hours after noon, at about 350 km, the temperature rises to approximately 1800°K. Shortly after midnight, the temperature drops to about 1050°K and stays approximately constant above 250 km. A change in slope of the density curve in the ionosphere is indicated from satellite observations. It is shown that, as a result of this, the scale height in the *F* and *E* regions has a pattern comparable to the electron density pattern in these regions. The possibility of a solar activity effect on densities is discussed.

Introduction. For more than 10 years the atmosphere has been studied by means of rockets and for more than 3 years by means of satellites and space probes. Observations by means of rockets [Horowitz and LaGow, 1957; 1958; 1959] show upper atmosphere densities that indicate nearly as well as possible latitude and seasonal variations. Satellite observations indicate monthly [Jacchia, 1959], day-to-night [Jacchia, 1959; Priester and Martin, 1959], and also yearly [King-Hele and Walker, 1960a] variations. Monthly and daytime and nighttime variations have been compared by Jacchia [1959; 1960] and by Martin and Priester [1960], with the variation of the decimeter radiation coming from the sun. Daytime and nighttime variations have been observed by Paetzold [1960] and by Groves [1960]. The correlation that has been found suggests long- and short-term solar effects on the atmosphere. The long-term yearly variations probably are due to the changing activity of the sun over approximately an 11-year period; actually the period may vary anywhere from 8 to 13 years. The short-term effect is indicated by the variation of density correlated with the solar decimeter radiation.

It seems too early to reach any definite conclusion about the many new observations

that have been obtained by means of rockets and satellites, observations that are often difficult to interpret and to correlate with existing knowledge. An attempt has been made to determine pressure, scale height, and temperature in certain regions of the atmosphere, on the basis of presently available data.

Density observations. The densities derived from rocket and satellite observations for the region between 100 and 300 km are shown in Figure 1. It may be noted that the data obtained in 1951 by Horowitz and LaGow [1957] were taken in a year of relatively low solar activity, whereas the data obtained in 1957 [Horowitz and LaGow, 1958] were taken during maximum solar activity. If a comparison is made of the densities labeled 1958 and 1957, for the same latitude, there is found a decrease of about 20 ± 5 per cent during that year; the decrease is smaller at lower altitudes. If this is assumed to be the yearly decrease in density from high to low solar activity, we arrive at the following results: the density at 180 km in 1957 was 8.9×10^{-13} gm/cm³ [Horowitz and LaGow, 1958]; working backward, a decrease of 20 per cent per year gives a density of 2.33×10^{-13} gm/cm³ in 1951. The observed density [Horowitz and LaGow, 1957] was 2.3×10^{-13} gm/cm³. At 100 km the density was 7.2×10^{-10} in 1957 [Horowitz and LaGow, 1958]; a decrease of 16 per cent per year gives a density of 2.6×10^{-10}

¹ This paper was presented at the XII General Assembly International Union of Geodesy and Geophysics, July 26–August 6, 1960, in Helsinki.

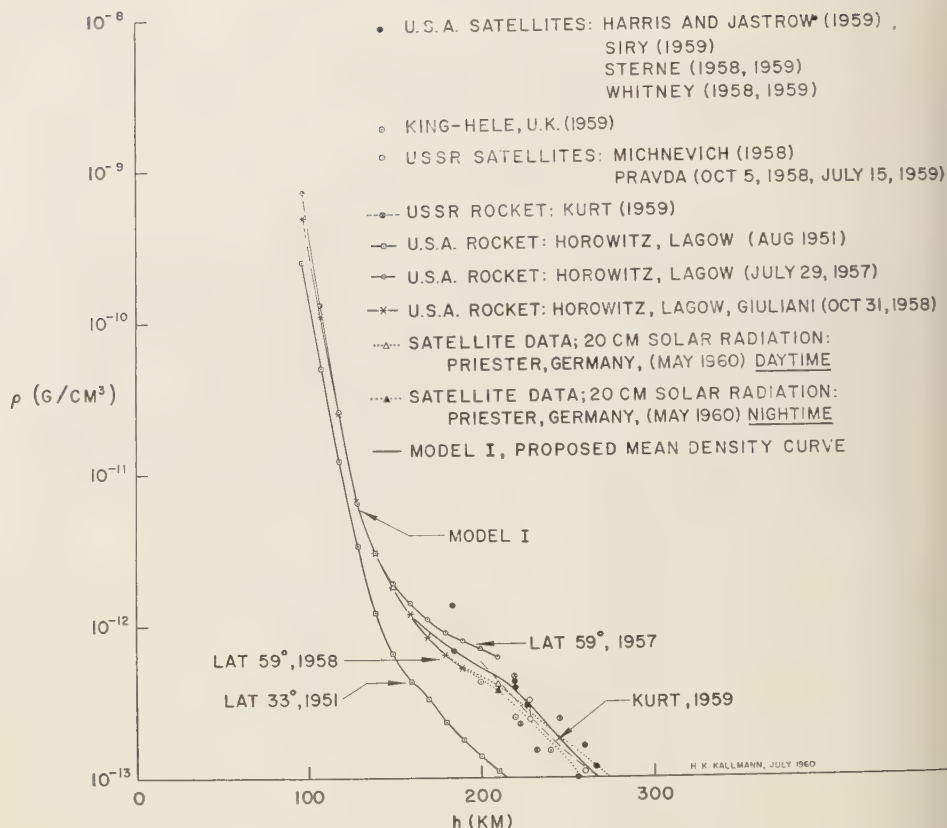


Fig. 1. Variable densities derived from rocket and satellite observations, 100–300 km.

gm/cm³ in 1951. The observed density was 2.5×10^{-10} gm/cm³ [Horowitz and LaGow, 1959]. The agreement of these results may be coincidental, because the year of lowest solar activity was 1954.

Comparing day-to-day records from year to year, we may find a similar activity for one particular day; this, however, would not exclude the presence of an over-all yearly effect on the density. King-Hele and Walker [1960a] find from their evaluation of satellite data a decrease in density from 1957–58 to 1960 of about 20 per cent. This also would indicate an over-all solar-cycle effect. It would be most desirable to separate these yearly, latitudinal, seasonal and solar cycle effects and their importance at various altitudes. This has not been done successfully so far.

For clarity Figure 1 has been redrawn to some

extent in Figure 2, showing only densities obtained by means of rockets in October 1958 [Horowitz, LaGow, and Giuliani, 1959], and densities derived from satellite observations mostly during 1958–59, in order to reduce a possible solar cycle effect.

Figure 3 shows the densities derived from rocket and satellite data in the region between 300 and about 800 km. The mean density here is based on rocket data obtained in 1958 [Horowitz and LaGow, 1959] and on satellite data obtained in 1958–1959. The satellite data are taken from Harris and Jastrow [1958, 1959], Siry [1959], Whitney [1959], and King-Hele [1959]. The daytime and nighttime values are taken from Priester, Martin, and Kramp [1960]. They have been reduced to a standard value of solar activity measured by the 20-cm radiation. This remarkable daytime and nighttime effect, which has been

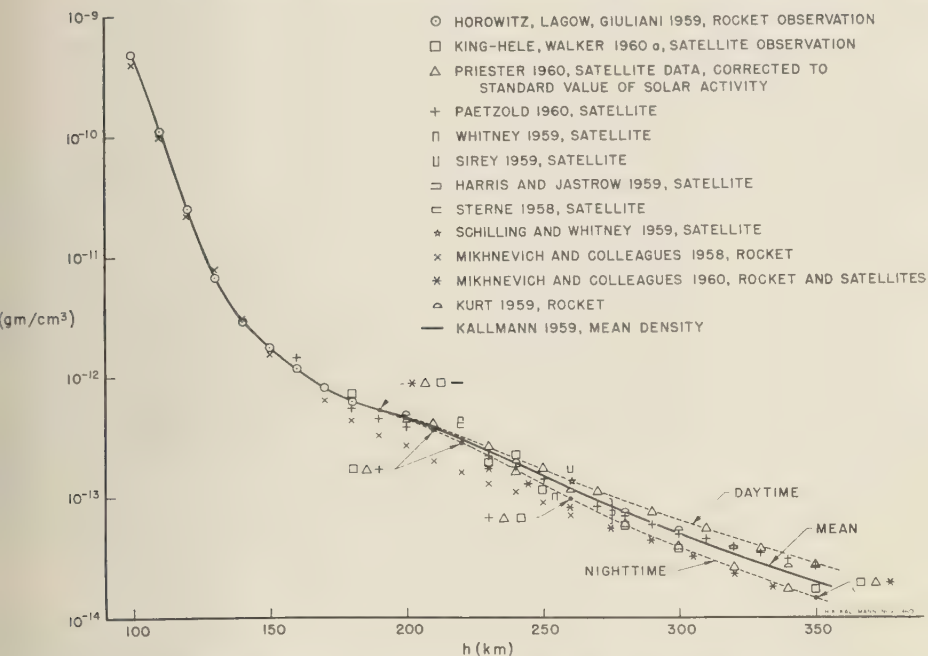


Fig. 2. Variable densities derived from rocket and satellite observations, 100-350 km.

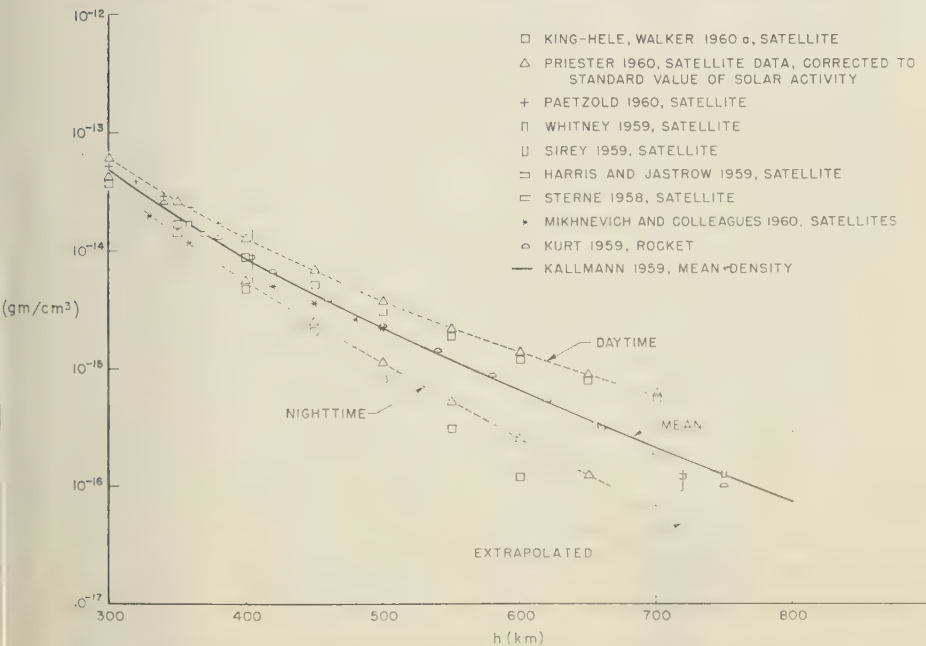


Fig. 3. Variable densities derived from rocket and satellite observations, 300-800 km.

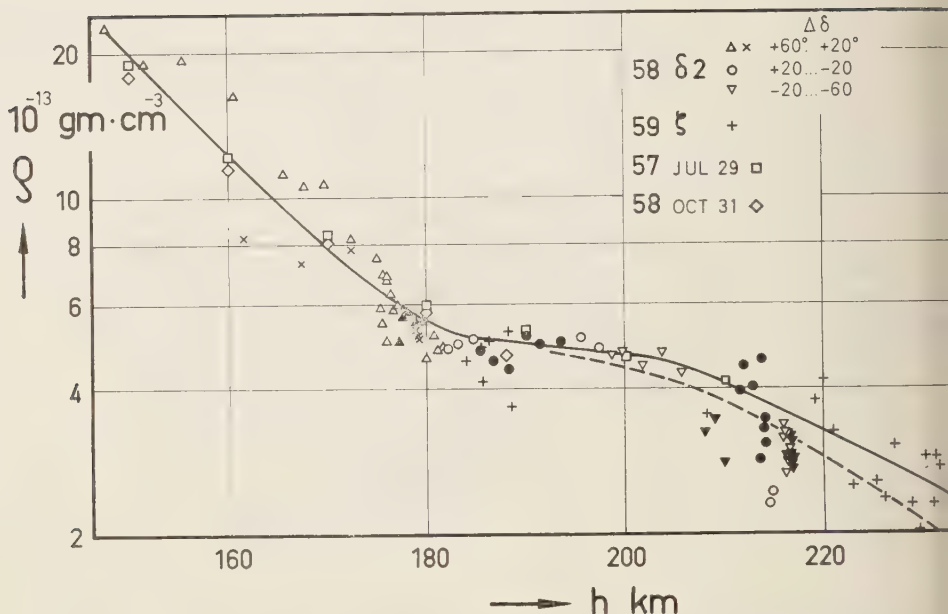


Fig. 4. Atmospheric densities at altitudes 150–230 km above the earth ellipsoid. The solid line refers to 14 hr local time, the dotted line to 6 hr local time. The results were obtained from the satellites 1958 $\delta 2$, 1959 ζ , and the rocket launchings of July 29, 1957, and October 31, 1958. The results from 1958 $\delta 2$ are subdivided into three groups according to their $\Delta\delta$ -values ($\Delta\delta = \delta_\pi - \delta_\odot$) (where δ is declination, π is perigee, \odot is sun). Open symbols give daytime values (8–20 hr T.L.T.); filled symbols give nighttime values (20–8 hr).

—From W. Priester and H. A. Martin, *Nature*, vol. 188, 201, 1960; reproduced by courtesy of *Nature*, London.

observed by *Jacchia* [1960], *Priester and Martin* [1960], and *King-Hele* [1960b], increases with altitude. The absolute magnitude of the daytime and nighttime densities varies, as pointed out by *King-Hele and Walker* [1960a]. Therefore, the data shown in Figures 2 and 3 are approximate values and show only the possible variations that may occur between day and night. The densities labeled 'daytime' have been observed about 2 hours after midday, and the densities labeled 'nighttime' have been observed 2 hours after midnight.

The densities published by *Michnerich, Denilin, Repner, and Sokolov* [1960] are the results of rocket and satellite observations. Above 200 km, these data are based on magnetometer readings, which are converted into densities by assuming a molecular weight.

The method of ejecting sodium from an altitude of about 430 km and observing its interaction and expansion in the atmosphere has

been used by *Kurt* [1959]. He points out that this method gives reliable results in the region between 200 and about 650 km. But here again a molecular weight has to be assumed for evaluating the data.

The densities shown in Figure 2 in the region between 150 and 250 km do not quite follow a smooth exponential curve, as was usually assumed. A change in slope in density in the ionosphere implies a change in slope of temperature, i.e., a temperature inversion, or temperature pattern in the ionosphere. This possibility has been pointed out first by *Kallmann* [1959] in January 1959. A change in slope in densities has been observed by *Priester, Martin, and Kramp* [1960a] and is illustrated in Figure 2 [Priester and Martin, 1960b]. Similar observations have been made by *King-Hele and Walker* [1960] by *Groves* [1960] and by *Paetzold* [1960].

An explanation of this phenomenon may be found in the preferred absorption of the He⁺ li-

304 Å in the F_1 region and the absorption of the helium line at 584 Å at altitudes between 300 and 500 km; the second line is barely detectable at 210 km, according to the observations by *Antreger, Damon, Heroux, and Hall* [1960]. More observations and knowledge about the composition and the chemical and photochemical reactions that take place in the atmosphere are necessary to come to final conclusions.

Pressure and scale height. For the density curves shown in Figures 2 and 3, mean, daytime, and nighttime, the corresponding pressures have been calculated from the hydrostatic equation. The method outlined by *Kallmann* [1959] has been used. The numerical integration has been carried out from the top of the atmosphere downward. This implies assuming a boundary value for pressure at the top of the atmosphere.

Calculations for various pressures, varying by powers of 10, have been performed, and it can be seen that the assumed boundary values have negligible effect on the results below an altitude of about 600 km. Thus, below about 600 km, the pressure corresponds to the adopted density curves. The results are shown in Figure 5.

The scale height has been computed from the ratio of pressure to density. The results show that the variations of scale height with altitude in the region between 500 and 600 km, for all three density curves, are so small that they can be attributed only to the variation of gravity with altitude. Thus, it is concluded that the temperature and the mean molecular weight are nearly constant above 550 ± 50 km. On the basis of these findings, the pressure p_0 at the top of the atmosphere, in this case at 800 km, has been

TABLE 1. Variable Densities and Scale Heights

Altitude, km	Mean Values			Daytime		Nighttime	
	Density, gm/cm ⁻³	Pressure, dynes/cm ⁻²	Scale Height, km	ρ , gm/cm ⁻³	H, km	ρ , gm/cm ⁻³	H, km
800	7.4×10^{-17}	5.33×10^{-7}	93.13	2.64×10^{-16}	119.3	1.83×10^{-17}	73.2
700	2.12×10^{-16}	1.53×10^{-6}	90.5	5.90×10^{-16}	115.9	6.28×10^{-17}	71.1
600	6.56×10^{-16}	4.73×10^{-6}	88.0	1.40×10^{-15}	112.6	2.55×10^{-16}	69.2
550	1.21×10^{-15}	8.45×10^{-6}	84.2	2.25×10^{-15}	108.5	5.35×10^{-16}	68.2
500	2.26×10^{-15}	1.54×10^{-5}	81.2	3.80×10^{-15}	101.7	1.14×10^{-15}	66.1
450	4.36×10^{-15}	2.89×10^{-5}	77.6	6.86×10^{-15}	92.8	2.49×10^{-15}	64.3
400	8.69×10^{-15}	5.59×10^{-5}	74.1	1.29×10^{-14}	85.3	5.57×10^{-15}	62.0
350	1.95×10^{-14}	1.14×10^{-4}	66.4	2.64×10^{-14}	76.3	1.40×10^{-14}	56.5
300	4.99×10^{-14}	2.56×10^{-4}	57.3	6.34×10^{-14}	63.8	3.78×10^{-14}	51.6
280	7.44×10^{-14}	3.65×10^{-4}	54.6	9.17×10^{-14}	60.5	5.72×10^{-14}	50.1
260	1.18×10^{-13}	5.35×10^{-4}	50.1	1.36×10^{-13}	56.8	9.63×10^{-14}	45.1
240	1.93×10^{-13}	8.14×10^{-4}	46.3	2.09×10^{-13}	53.0	1.67×10^{-13}	41.0
230	2.43×10^{-13}	1.00×10^{-3}	45.2	2.61×10^{-13}	51.4	2.20×10^{-13}	39.9
220	3.09×10^{-13}	1.26×10^{-3}	44.7	3.23×10^{-13}	50.3	2.86×10^{-13}	39.4
210	3.84×10^{-13}	1.58×10^{-3}	44.8	3.95×10^{-13}	50.1	3.62×10^{-13}	40.0
200	4.59×10^{-13}	1.97×10^{-3}	46.5	4.68×10^{-13}	51.4	4.45×10^{-13}	41.5
190	5.42×10^{-13}	2.43×10^{-3}	48.5	5.42×10^{-13}	53.6	5.32×10^{-13}	43.7
180	6.42×10^{-13}	2.97×10^{-3}	50.0	6.42×10^{-13}	54.2	6.43×10^{-13}	45.1
170	8.29×10^{-13}	3.64×10^{-3}	47.3	8.29×10^{-13}	50.6	8.28×10^{-13}	43.6
160	1.19×10^{-12}	4.58×10^{-3}	41.1	1.19×10^{-12}	43.4	1.19×10^{-12}	38.6
150	1.77×10^{-12}	5.94×10^{-3}	35.7	1.77×10^{-12}	37.3	1.77×10^{-12}	34.0
140	3.04×10^{-12}	8.11×10^{-3}	28.4	3.04×10^{-12}	29.3	3.04×10^{-12}	27.4
130	6.70×10^{-12}	1.24×10^{-2}	19.6	6.70×10^{-12}	20.0	6.70×10^{-12}	19.1
120	2.46×10^{-11}	2.49×10^{-2}	10.7	2.46×10^{-11}	10.8	2.46×10^{-11}	10.6
110	1.16×10^{-10}	8.02×10^{-2}	7.29	1.16×10^{-10}	7.31	1.16×10^{-10}	7.26
108	1.59×10^{-10}	1.06×10^{-1}	7.05	1.59×10^{-10}	7.05	1.59×10^{-10}	7.05
106	2.16×10^{-10}	1.41×10^{-1}	6.91	2.16×10^{-10}	6.92	2.16×10^{-10}	6.90
104	2.89×10^{-10}	1.89×10^{-1}	6.90	2.89×10^{-10}	6.90	2.89×10^{-10}	6.90
102	3.77×10^{-10}	2.52×10^{-1}	7.03	3.77×10^{-10}	7.03	3.77×10^{-10}	7.03
100	4.80×10^{-10}	3.33×10^{-1}	7.30	4.80×10^{-10}	7.30	4.80×10^{-10}	7.30

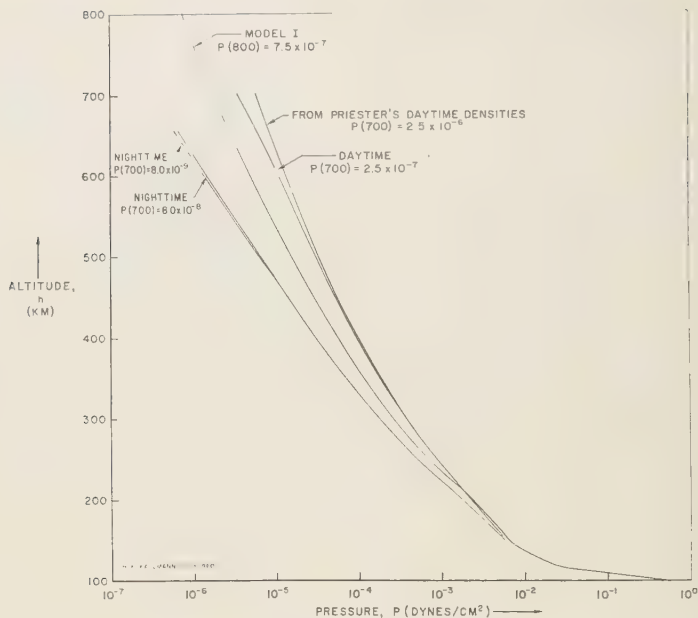


Fig. 5. Pressure derived from density data.

determined more accurately from the relation:

$$\frac{dH}{H} = -\frac{dg}{g} \quad (1a)$$

$$p_0 = H_0 \rho_0 g_0 \quad (1b)$$

With a more accurate boundary value for pressure at 800 km, pressures and scale heights, calculated from the densities, have been repeated. The numerical integration has been carried out in small height intervals (2 km) on electronic computing equipment.

Mean daytime and nighttime densities shown in Figures 2 and 3, and calculated pressures and scale heights are shown in Table 1. The scale heights are shown in Figure 6.

Molecular weight and temperature. In the region between 300 ± 50 and 550 ± 50 km, the scale-height gradient is still small in comparison with the gradient in the ionosphere between 100 and 200 km. Therefore, we may assume that the change in scale height with altitude is primarily due to the change in molecular weight, and that the temperature stays constant above 300 ± 50 km. Thus the molecular weight in the region between 300 ± 50 and

550 ± 50 km has been calculated from the relation

$$\frac{dH}{H} = -\frac{dM}{M} - \frac{dg}{g} \quad (2)$$

where M is the molecular weight.

The measurements of ion concentrations allow an estimate of the composition and molecular weight at various regions in the atmosphere, in particular at the high altitudes. *Newell* [1966] has summarized the results obtained by means of rockets in the United States. The results show a gradual change from molecular to atomic oxygen ions with increasing altitudes from 100 to 200 and 250 km, a changing amount of nitric oxide, and a variation of all of these constituents from day to night. *Poloskov* [1960] reports about the data obtained in the USSR. Molecular ions of nitrogen, oxygen, and nitric oxide have been detected up to 400 and 500 km. Their relative abundance with respect to atomic oxygen ion decreases with altitude. Above 500 km only atomic oxygen ions ($M = 16$) and very small amounts of atomic nitrogen ion ($M = 14$) have been observed. Therefore, on the average,

TABLE 2. Day- and Nighttime Temperature and Molecular Weight

Height, km	Mean		Daytime		Nighttime	
	M	T, °K	M	T, °K	M	T, °K
00	16	1389	16.5	1828	15.5	1055
↓	↓	↓	↓	↓	↓	↓
50	16		16.50		15.50	
100	16.85		17.76		15.62	
150	17.37		19.19		15.96	
200	17.92		20.57		16.31	
250	19.71		22.65		17.64	
300	22.50		23.48	1828		
350	23.46	1389			19.02	
400						
450					22.43	
500					23.46	1055

molecular weight of 16 may be expected at high altitudes above 500 km.

If most of the heating takes place in the ionosphere, the hot air may rise during midday. This causes an increase in density during the day; it may also cause a slight increase in molecular weight during the night. Because of the arguments given above, it has been assumed that $M = 16 \pm 0.5$ at about 800 km. Then $M \cong 23$ at 500 km during the day, and has the same value at 250 km at night. The results obtained from equation 2 and the boundary values assumed, discussed above, are shown in Table 2. From scale height and molecular weight the temperature has been determined at 800 km.

These results may be compared with a daytime temperature of 2000°K and a nighttime temperature of about 1000°K , obtained by *King-Hele and Walker* [1960a] and temperatures ranging from 1180°K , 1580°K , 1640°K , and 2030°K for our model atmospheres presented by *Nicolet* [1960a]. *Jastrow and Kyle* [1961], arrive at a mean temperature of 1494°K and a nighttime temperature of 1014°K at 800 kilometers. The regions of constant temperatures above the F region have been pointed out on the basis of theory by *Thomson* [1958] and *Nicolet* [1960b].

Conclusion. It has been shown that the solar

cycle effect may cause a yearly effect on the upper air density. Around 200 ± 20 km, the density may rise by about 20 per cent per year with increasing solar activity. Around 100 km the effect may be only 15 per cent or less.

From daytime and nighttime densities, pressures and scale heights have been obtained. From the change in scale height with altitude it has been deduced that there are regions of constant temperatures which vary from day to night. On the basis of the daytime and nighttime densities adopted here, it has been shown that the mean and daytime temperatures may not change appreciably above 350 km. The nighttime temperature apparently stays constant above 250 km.

From the values obtained for scale heights in the region between 100 and 300 km, it must be concluded that the temperature in the ionosphere has a pattern similar to the pattern of the

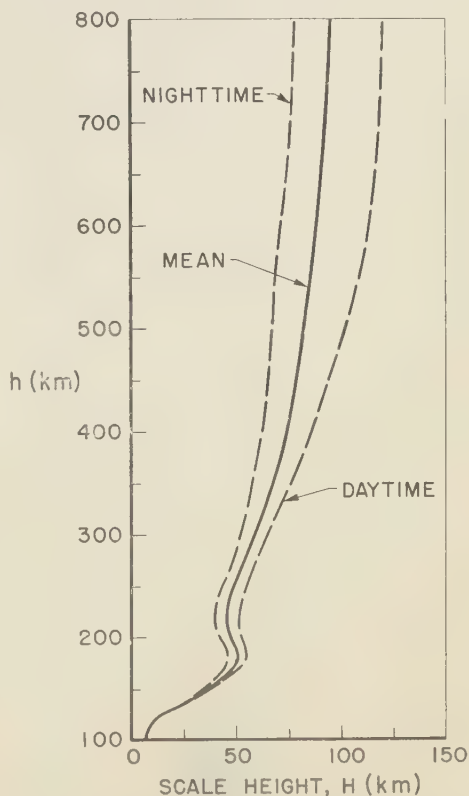


Fig. 6. Daytime and nighttime scale heights derived from rocket and satellite data.

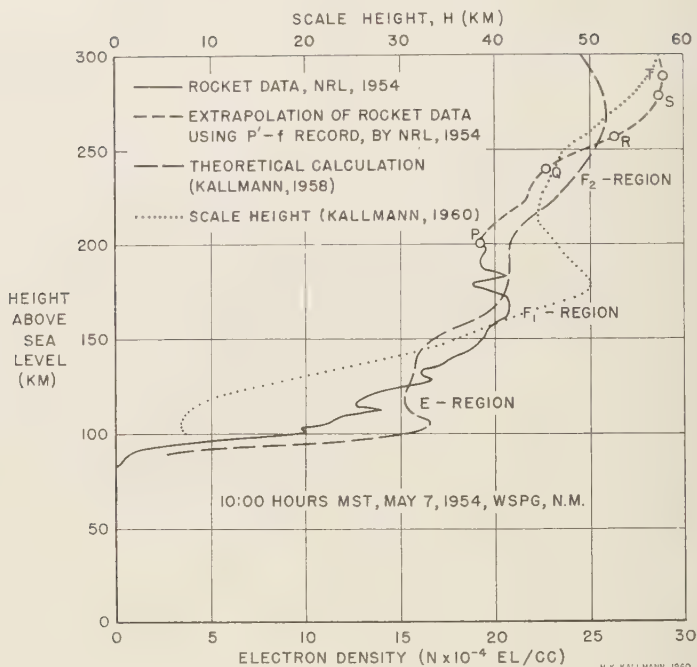


Fig. 7. Rocket data and theoretically calculated electron densities.

electron densities. It can be seen from Table 1 that the scale height shows a slight pattern in the E region, between 100 and 110 km, and another pattern in the F_1 region. The temperature maximum in the F_1 region is probably around 180 km, and the minimum is probably around 210 km. Because of the large heat conduction to be expected at higher altitudes, as deduced by Nicolet [1960a, b], a change in direction of the slope of the scale height might not be expected in the F_2 region.

Figure 7 shows the electron densities obtained by Seddon, Pickar, and Jackson [1954] by means of rockets, the calculated electron densities based on theory [Kallmann, 1958], and the superimposed scale height, derived from the mean density curve shown in Figure 2 and tabulated in Table 1.

The numerical values given in Tables 1 and 2, and the scale height shown in Figure 7, are only indicative and show a general pattern the atmosphere may assume from day to night, a pattern which has been arrived at from density data obtained from rocket and satellite observations.

Acknowledgment. I am grateful to Mr. William

Sibley, Computer Science Department of RAND Corporation, who supervised the calculations. The calculations were done on the IBM-709. Work for this paper was supported by the RAND Corporation, Santa Monica, California.

REFERENCES

- Groves, G. V., Polar and diurnal variations of electron densities from 190 to 280 km, as derived from the orbits of Discoverer satellites, University College, London, November 1960.
- Harris, I., and R. Jastrow, An interim atmosphere derived from rocket and satellite data, *Planets and Space Sci.*, 1, 20-26, 1959.
- Harris, I., and R. Jastrow, Density determination based on the Explorer and Vanguard satellites, *Science*, 128, 420, 1958.
- Hinteregger, H. E., K. R. Damon, L. Heroux, and L. A. Hall, Telemetering monochromator measurements of solar 304A radiation and its attenuation in the upper atmosphere, *Space Research*, edited by H. K. Kallmann-Bijl, North Holland Publishing Co., Amsterdam, pp. 615-627, 1960.
- Horowitz, R., and H. E. LaGow, Upper air pressure and density measurements from 90 to 220 kilometers with the Viking 7 rocket, *J. Geophys. Research*, 62, 57-77, 1957.
- Horowitz, R., and H. E. LaGow, Summer-d auroral-zone atmospheric-structure measurements

- from 100 to 210 kilometers, *J. Geophys. Research*, **63**, 757-772, 1958.
- Browitz, R., H. E. LaGow, and J. F. Giuliani, Fall-day auroral zone atmospheric structure measurements from 100 to 188 km, *J. Geophys. Research*, **64**, 2287-2294, 1959.
- Cecchia, L. G., Two atmospheric effects in the orbital acceleration of artificial satellites, *Nature*, **183**, 526, 1959.
- Cecchia, L. G., Solar effects on the acceleration of artificial satellites, *Special Report No. 29*, Smithsonian Institution, Cambridge, Massachusetts, September 1959.
- Cecchia, L. G., A variable atmospheric-density model from satellite accelerations, *Special Report No. 39*, Smithsonian Institution, Cambridge, Mass, March 1960.
- Costrow, R., and L. Kyle, The upper atmosphere in *Handbook of Astronautical Engineering*, McGraw-Hill Book Co., to be published, 1961.
- Johnson, F., Temperatures in the high atmosphere, *Ann. Geophys.*, **14**, 94-108, 1958.
- Kallmann, H. K., Un nouveau modèle, d'ionosphère, *La Météorologie*, **4**, 52, 235-244, 1958.
- Kallmann, H. K., A preliminary model atmosphere based on rocket and satellite data, *J. Geophys. Research*, **64**, 615-623, 1959.
- Kling-Hele, D. G., Density of the atmosphere at heights between 200 km and 400 km, from analysis of artificial satellite orbits, *Nature*, **183**, 1224-1227, 1959.
- Kling-Hele, D. G., and D. M. C. Walker, Atmospheric densities at heights of 180-700 km, Royal Aircraft Establishment, Farnborough, England, July, 1960. Paper presented at the Symposium on Aeronomy organized by the International Association of Geomagnetism and Aeronomy, Copenhagen, 19-22, July 1960a.
- Kling-Hele, D. G., and D. M. C. Walker, Upper-atmosphere density and its dependence on the sun, *Nature*, **186**, 928, 1960b.
- Kling-Hele, V. G., Determining the density of the neutral component of the ionosphere, *Izvestiya Vysshikh Uchebnykh Zavedeniy—Radiofizika*, **v. 2**, No. 6, 1007-1009, 1959.
- Kling-Hele, H. A., and W. Priest, Measurement of solar and diurnal effects in the high atmosphere by artificial satellites, *Nature*, London, **185**, 600, 1960.
- Kling-Hele, V. V., On pressure and density of atmosphere, VCSAGI held in Moscow July-August 1958.
- Kling-Hele, V. V., B. S. Denilin, A. I. Repnev, V. A. Sokolov, Some results of the determination of the structural parameters of the atmosphere using the third Soviet artificial earth satellite (published translation), *ARS Journal*, **30**, 407-413, 1960.
- Newell, H., The upper atmosphere studied by rockets and satellites, *Physics of the Upper Atmosphere*, edited by J. A. Ratcliffe, Academic Press, New York and London, pp. 73-132, 1960.
- Nicolet, M., The properties and constitution of the upper atmosphere, *Physics of the Upper Atmosphere*, edited by J. A. Ratcliffe, Academic Press, New York and London, pp. 17-71, 1960a.
- Nicolet, M., Les variations de la densité et du transport de chaleur par conduction dans l'atmosphère supérieure, *Space Research*, edited by H. K. Kallmann-Bijl, North Holland Publishing Co., Amsterdam, 46-89, 1960b.
- Paetzold, H. K., Die Luftdichte in der Irdischen Ionosphäre und Exosphäre, Technische Hochschule Muenchen, October 1960.
- Poloskov, S. M., Upper atmosphere structure parameters according to data obtained from USSR rockets and satellites during IGY, *Space Research*, edited by H. K. Kallmann-Bijl, North Holland Publishing Co., Amsterdam, 95-116, 1960.
- Priester, W., and H. Martin, Solar und Tageszeitliche Effekte in der Hochatmosphäre aus Beobachtungen an Kunstlichen Erdsatelliten, *Mitteilungen der Universitäts, Sternwarte Bonn*, Nr. 29, December 1959.
- Priester, W., H. A. Martin, and K. Kramp, Modell der Hochatmosphäre mit Temperaturinversion in der F1-Schicht, berechnet aus Satellitenbeobachtungen, *Mitteilungen der Universitäts, Sternwarte Bonn* Nr. 34, May 1960.
- Priester, W., and H. A. Martin, Temperature Inversion in the F1-layer, *Nature*, **188**, 200-202, 1960.
- Schilling, G. F., and C. A. Whitney, Derivation and analysis of atmospheric density from observations of Satellite 1958e, *Planetary and Space Sci.*, **1**, 136, 1959.
- Seddon, J. C., A. D. Pickar, and J. A. Jackson, Continuous electron density measurements up to 200 km, *J. Geophys. Research*, **59**, 513-524, 1954.
- Siry, J. W., Satellite orbits and atmospheric densities at altitudes up to 750 km obtained from the Vanguard orbit determination program, *Planetary and Space Sci.*, **1**, 184, 1959.
- Sterne, T. E., The density of the upper atmosphere, *Special Report No. 11*, Smithsonian Institution, March 1958.
- Whitney, W., The structure of the high atmosphere, *Special Report No. 21*, Smithsonian Institution, February 1959.

(Manuscript received November 21, 1960.)

A Subtropical Convergence Line of the South Pacific A Case Study Using Meteorological Satellite Data

LESTER F. HUBERT

*U. S. Weather Bureau
Washington, D. C.*

Abstract. A subtropical convergence line in the southwest Pacific some 2000 miles long has been recorded by television pictures of Tiros I on May 11 and 12, 1960. The standard meteorological data have been analyzed and compared with the pictorial data. It is shown that although this synoptic system was vigorous and well documented by the pictures, its existence and extent cannot be delineated by standard meteorological observations. The tropical area pictured is shown to contain no vigorous disturbances and the value of such pictures to the tropical analyst is discussed.

INTRODUCTION

The origin, dynamics, and even description of tropical disturbances are incompletely known, but it is generally agreed by tropical meteorologists that lines and areas of convergence lying completely within a homogeneous air mass exist in the lower troposphere. Examples of such systems are the easterly waves studied by Riehl (1954), the equatorial waves described by Palmer (1952), and the intertropical convergence zone (ITCZ) which has received continued attention ever since polar front enthusiasts attempted to apply the air mass model at the equator. In addition to the traveling disturbances in the tropics and subtropics, there exists a system previously identified as a convergence line, a shear zone, or even a stationary front. Indeed, it is sometimes possible to trace such a line of convergence back to a true polar front from mid-latitudes, but having traveled many days over a warm ocean it no longer represents an air mass boundary [see Riehl, 1954, chapter 10]. Despite incomplete frontolysis, a band of cloudiness and frequently an accompanying line of shear retain their identities for several days. Such systems are significant since it is clear they are perpetuated long after the potential energy of the old air mass has been dissipated, thereby posing an interesting question of the dynamics of its maintenance after the potential energy is consumed. Furthermore, since they often become quasi-stationary, these systems may remain detected for long periods because they do not sweep across reporting stations as do the waves and vortices, and for that reason have been

incompletely described and largely neglected insofar as theoretical study is concerned. The study presented here considers such a quasi-stationary convergence line in the southwest Pacific, studied by use of the television pictures from the meteorological satellite, Tiros I.

TIROS I—METEOROLOGICAL SATELLITE

A satellite carrying two television cameras was launched April 1, 1960, under the auspices of the National Aeronautics and Space Administration. The cameras were mounted so that both their optical axes were parallel to the spin-axis of the vehicle. The payload was spin-stabilized, changing its orientation in space only slowly [Bandein and Manger, 1960]. Since the earth rotates about 25° during the 99-minute satellite period, pictures may be taken along swathes about 1500 nautical miles apart on the northbound or southbound part of a pass. The combination of the earth's rotation rate with the satellite period and the fact that Tiros is spin-stabilized permits photographing the same part of the earth's surface at 24-hour intervals. Such a potential is particularly useful for the application of these data to meteorological analysis because the time change of synoptic systems is an important diagnostic element.

One camera with a wide-angle lens encompassed a field of view just over 100° object space angle while the second camera viewed about 14°. Since the field of view of each camera was scanned by the same number of television raster lines, the 'resolution' of the longer focal length system is an order of magnitude greater than the

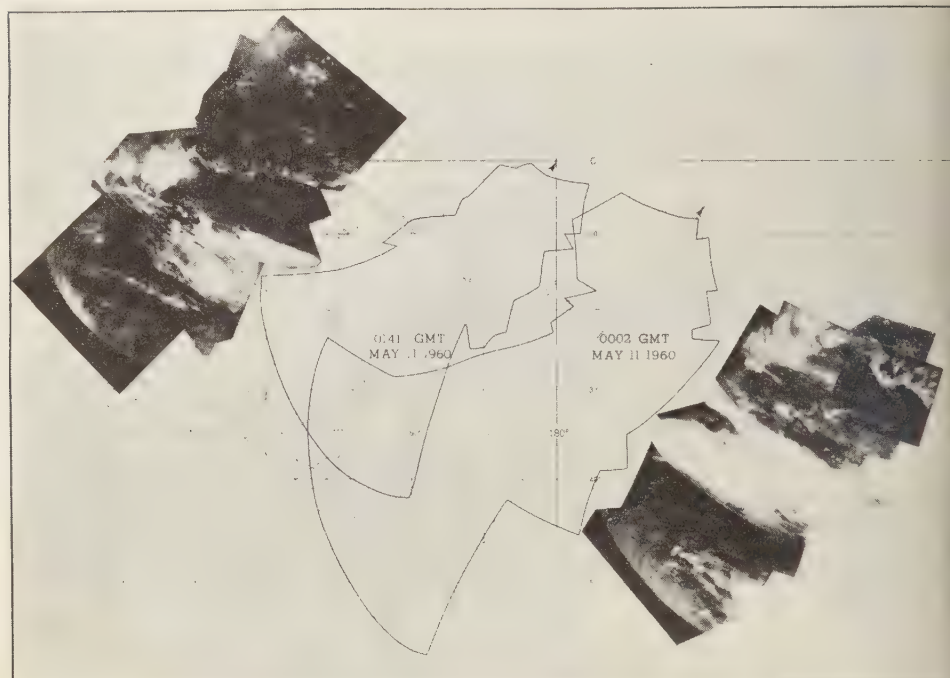


Fig. 1a. Composite of pictures taken near 0000 GMT, May 11, 1960. Dotted lines show satellite track; irregular outlines indicate boundary of pictured area.

short focus system. In the mode of operation where pictures are stored on tape for later transmission, both cameras take simultaneous pictures at 30-second intervals.

During the second week of May, Tiros cameras were directed earthward in favorable picture-taking conditions (of angle and illumination) approximately between latitudes 40°S and 20°N . On May 11 and 12 pictures were obtained covering the area shown in Figure 1. Trajectories of the satellite subpoint are shown along with the time of each pass across latitude 25°S . On each pass the satellite was moving toward the northeast and the cameras were viewing back along the track toward the southwest. The strip composites (Fig. 1) represent the photographic coverage obtained on each of the four passes over the area.

CASE STUDY OF A CONVERGENCE LINE

Photographic data. Two frames from each of the four passes (Fig. 1) are shown in Figures 2-9 with geographical grids superimposed. Each

picture requires its own grid, which must be computed for that particular camera position in space and orientation of the optical axis. Even small errors in these parameters produce uncertainties in the placement of the grids upon the pictures, so precise location of any detail (within a few miles) cannot be expected. It is estimated that the accuracy of locating features on the pictures by reference to the superimposed grid is ± 50 nautical miles at distances halfway to the horizon.

The outstanding synoptic feature that appears in the pictures is a broad, solid band of cloud having an average width of about 300 nautical miles and extending from the Solomon Islands in the southwest Pacific nearly 2000 miles toward the southeast (see Fig. 10). It is not possible, in general, to identify cloud genus (e.g., stratocumulus vs. altocumulus) at great distances on the wide-angle pictures, but the narrow-angle pictures are usually adequate to distinguish between cumuliform and stratiform clouds. Comparison of these higher resolution pictures with simul-

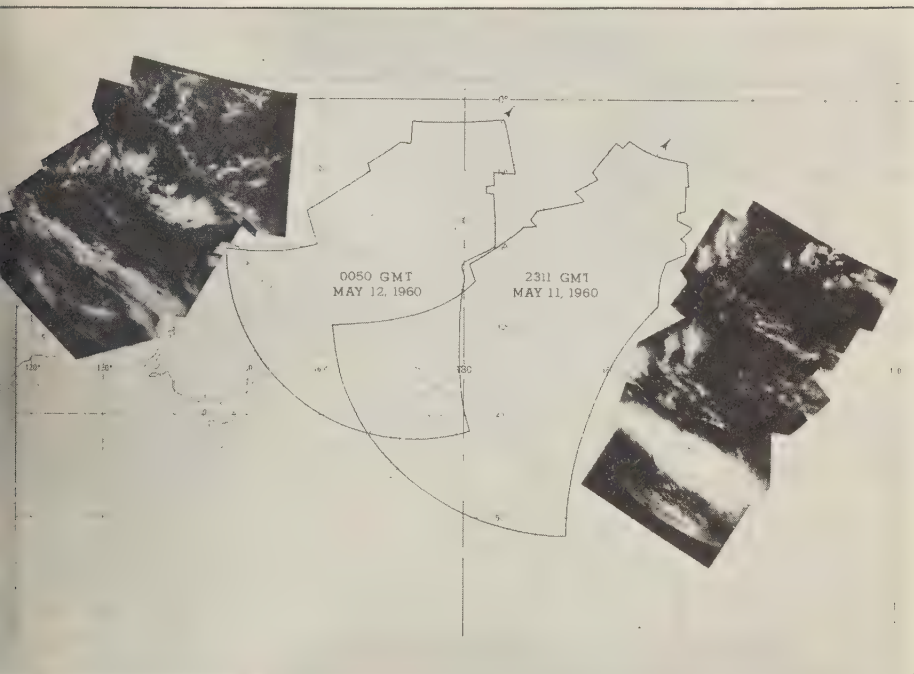


Fig. 1b. Composite of pictures taken near 0000 GMT, May 12, 1960. Dotted lines show satellite track; irregular outlines indicate boundary of pictured area.

neous wide-angle pictures shows that separate elements of cumuliform clouds produce a grey, unulated texture on the wide-angle pictures. The size of the cloud elements and the size of the clear spaces between clouds approach the limit of resolution of the television system. Figure 5 includes a narrow-angle picture illustrating the difference in resolution of the two cameras as well as the relative areas covered. Notice in the lower right portion of the small wide-angle picture clouds of cumulus appearance can be distinguished while the same portion of the large field picture shows only irregular grey shade. Similar areas can be found on most other pictures, for example, Figure 4, in the portion surrounding the intersection 12°S , 170°E . The pictures therefore indicate that the major cloud band is a solid overcast with cumulus clouds on the edges, thereby suggesting that the band is composed of buildup and merged cumulus or multilayered clouds. The surface reports confirm this. It is also clear from surface reports that cumulus clouds existed over portions of the region

but, for the most part, they cannot be identified from the wide-angle pictures—see, for example, Figure 8, 13°S , 177°W where cirrus is reported (Fig. 11b). On the other hand, the narrow-angle pictures frequently show feather-edged, tenuous patches that might be cirrus, low stratus, or even fog. An example of this is shown in the small field picture of Figure 5. The isolated patch indicated near the center has the tenuous character on its left edge and, occurring as it does in tropical air with cumulus clouds, it is quite probably Cirrus Nothus.

In order to incorporate this type of satellite data into meteorological analysis it is necessary to transpose perspective-distorted cloud pictures onto a map projection similar to that used for mapping and analyzing standard meteorological data. The difficulty of using pictures directly is illustrated by the strip composites of Figure 1. Because of the enormous change of slant range from the horizon to the field directly beneath the camera, the smaller patches of clouds near the camera are exaggerated while the major cloud

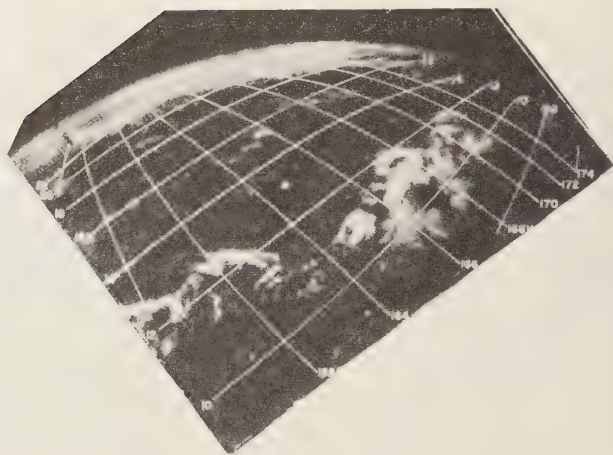


Fig. 2. Individual frame showing weak convergence clouds in tropics and major cloud band on horizon. Picture taken at 0009 GMT, May 11, 1960.

bands at great distance are minimized. Figure 10 is a schematic representation of the pictured clouds from the four passes (Figure 1) in which two shades are used to differentiate the highly reflective clouds from those that are a more dull grey on the photographs. The type of cloud schematic map illustrated here is capable of showing only the large-scale features, and it is obvious that the meteorologist must refer to the

photographs to gain a true appreciation of the cloud fields.

Analysis of standard data. In this portion of the South Pacific many surface reports are available, but the tropical analyst must be cautious in evaluating the conflicting evidence of individual observations because the synoptic system produce subtle changes that are easily masked by local effects and small inaccuracies. Fo

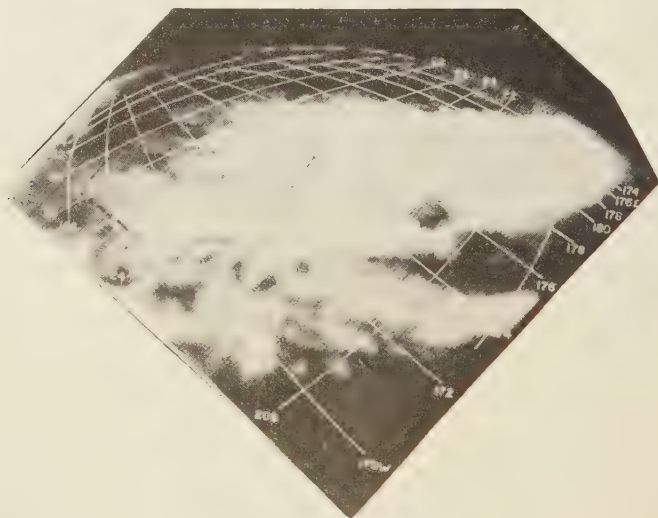


Fig. 3. Individual frame showing cloudless corridor of anticyclone (19°S , 176°W) cutting into northern edge of major cloud band. Picture taken at 0005 GMT, May 11, 1960.

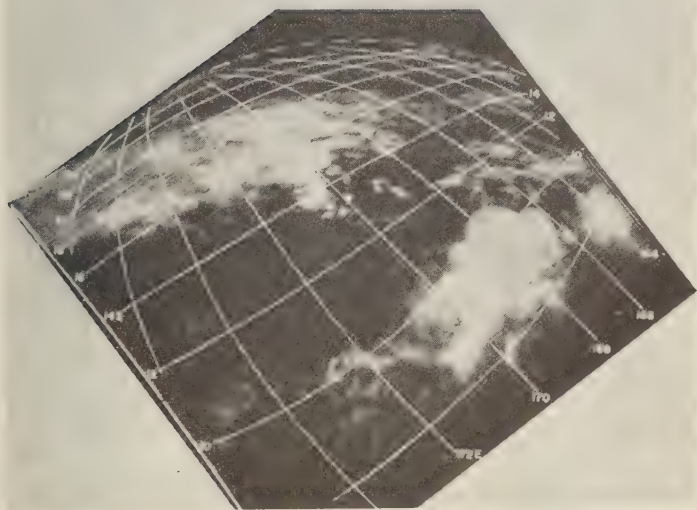


Fig. 4. Individual frame showing western end of major cloud band and weaker convergence clouds at 10°S . Taken at 0150 GMT, May 11, 1960.

For example, significant weather-producing systems are often shown only by a small change in wind direction and an increased cloudiness and precipitation, but every sizable island has local and diurnal effects that produce changes of equal magnitude [Palmer, Wise, Stempson, and Duncan, 1955]. Ship reports, of course, are not affected by terrain, but small wind changes are not efficiently observed from a moving ship.

The cloud-reporting code is inadequate in the tropics to differentiate local cumulus and showers from those of a disturbed situation. The clue to synoptic disturbances provided by surface observations is a larger-than-normal amount of middle cloudiness at a group of stations. In this event the surface observations do confirm large amounts

of middle clouds in the region of the main cloud band, but it is not possible to deduce from those observations that a continuous band existed. Surface pressure analysis by itself is inadequate to delineate synoptic systems before they have reached great intensity, so streamline analyses of the surface wind reports have been made and are shown in Figures 11a and 11b.

The analyses of Figure 11 were made from surface observations, independent of the photographic data. Six-hourly maps for May 10, 11 and 12, 1960 were analyzed to exploit time continuity, and manuscript maps for this area, furnished by the Weather Bureau Airport Station at Honolulu, Hawaii, were available to show changes over longer periods. Most of the islands

in this region are of rugged volcanic character, and consequently all have local effects that create serious problems in surface streamline analysis. It will be noticed that some of the wind reports do not fit the analyses. In every case where a choice has been made between conflicting evidence, it has been done by reviewing the station's location relative to terrain [Ramage, 1959], considering time continuity, and making the most reasonable meteorological choice. For example, the surface west wind reported at Nandi (17.6°S , 177.6°E) appears to be a local wind signifying no large-scale synoptic feature in the low troposphere—an opinion based partly on the fact that this station is downwind from 4000 ft peaks and

partly because pilot balloon data show easterlies from 2000 to 9000 ft at the first map time and light and variable winds up to 7000 ft at the second map time.

One of the important uses of streamline analysis in the lower troposphere is to indicate areas of divergence and thereby vertical motion. Divergence is, of course, dependent upon speed as well as directional divergence. Figure 11 shows no speed field because the data are inadequate to yield a definitive isotach analysis. It has been shown, however, that in the tropics frequently there is correlation between directional divergence in the low troposphere and total horizontal divergence [Palmer, Wise, Stempson, and Dunca

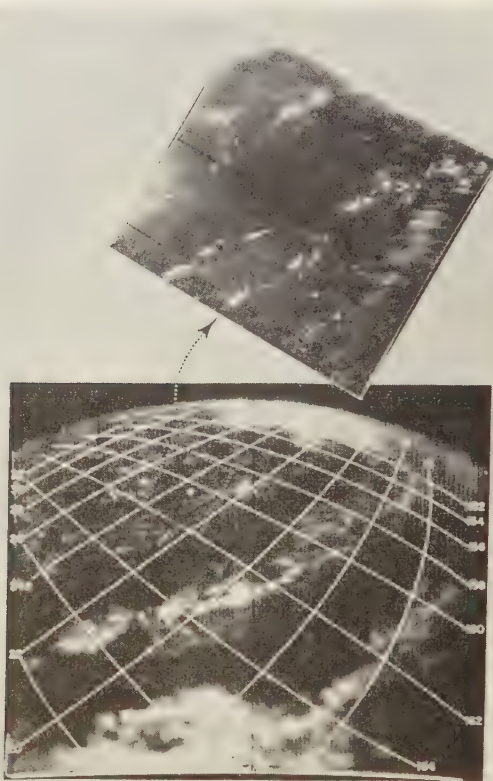


Fig. 5. Individual frame showing cloud pattern in anticyclone from New Caledonia in left foreground to Australia on horizon. Dotted outline in large picture indicates coverage of narrow field picture (above). Pictures taken at 0145 GMT, May 11, 1960.

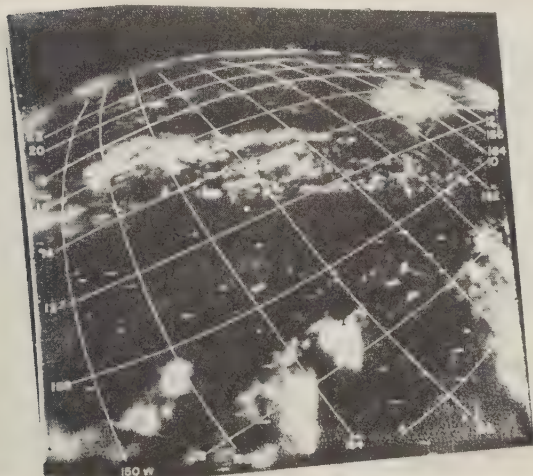


Fig. 6. Individual frame showing weak convergence clouds in tropical South Pacific. Picture taken at 2317 GMT, May 11, 1960.

55], so that the streamline pattern is of some use by itself in indicating probable lines of convergence for comparison with the pictured cloud band. Directional convergence is implied by the analyses of Figure 11 along the asymptote emanating from the col at 180° longitude. It can be shown that two principal asymptotes must

intersect in a col (neutral point), one being the locus of converging streamlines, the other the locus of diverging streamlines [Palmer, Wise, Stempson, and Duncan, 1955]. The convergent asymptote is indicated by the double-weight streamline through the col near the date line in Figures 11a and 11b, and these asymptotes are

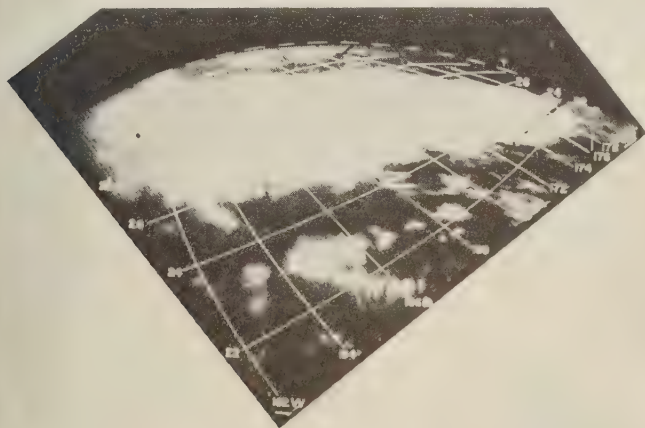


Fig. 7. Individual frame showing western portion of major cloud band. Picture taken at 2313 GMT, May 11, 1960.

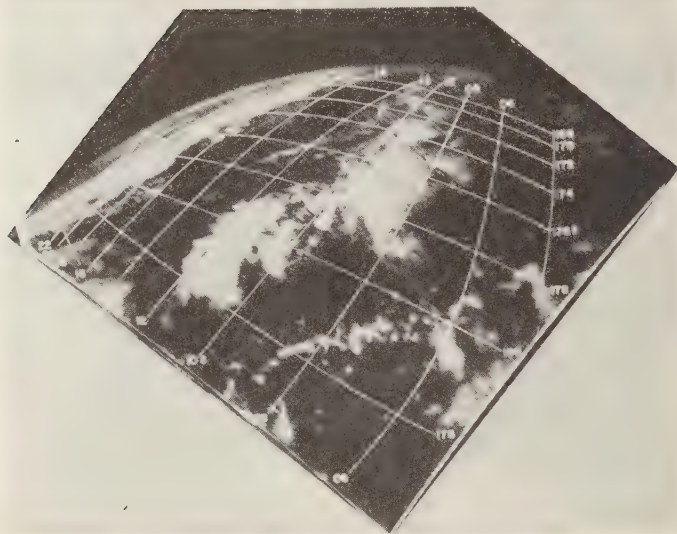


Fig. 8. Individual frame showing tropical convergence line near 10°S and major cloud band on horizon. Picture taken at 0057 GMT, May 12, 1960.

also shown in Figure 10 by the heavy lines through the major cloud band.

If we now examine the pattern of streamline convergence for correlation with the major cloud band, we can see some agreement. In general the cloud band follows the convergence asymptotes emanating from the col at 180° . Furthermore, the portion of that asymptote southeast of the col moved poleward during the 24 hours shown, and the cloud band in that region also moved south. Meanwhile the asymptote extending toward the northwest showed little displacement and the cloud band here was also stationary.

The small anticyclone that moved from 174°W to 180° in this interval is well documented so that it is clear that it moved along the cloud band without any great effect on the total sky cover. Apparently a corridor of little cloudiness extended from the cell center toward the northwest shown by the shading in Figure 10a and in the right foreground of Figure 3, and 24 hours later a break is shown in the solid band at 21°S , 178°W in Figure 8. It is significant to notice that this cell *was not* the typical subtropical anticyclone, that is, a slow-moving large-scale high; rather it was small and moved downstream in the trades at a speed typical of disturbances in

the easterlies (10 to 12 kt). It is therefore likely that this small cell was quite shallow and produced divergence and downward motion only in the low troposphere. If this were true it would suppress the low cloudiness with little effect on the middle clouds that are seen from above. Indeed, there is a hint of this from the report in the cell at 0000 GMT, May 11 at 19° and 21°S and at 0000 GMT, May 12 at 21°S , where only one to two-tenths of low clouds are reported beneath the middle clouds. In addition, an upper wind sounding at 21°S , 175°W at 2300 GMT May 11 shows the wind backing from southwest through south and east between the surface and 4000 ft, strengthening the deduction that the circulation was very shallow.

During its evolution, if the cloud band was initially associated with a polar front, it was quite likely a line of cyclonic vorticity, because of the shear and sharp cyclonic curvature of the air motion that characterizes frontal zones. The air mass difference across a front decreases and finally disappears during its slow movement over the warm ocean, and in the tropical phase frequently only the cyclonic shear remains, thereby giving rise to its identification as a shear line. Finally even the shear must dissipate; there

it seems reasonable to examine the shear along the cloud band (in so far as it is reflected in surface data), attempting to obtain an estimate of the phase of evolution shown in the figures from a frontal zone, to a shear line, to a line of weakening convergence.

Were the isotach field available, the vorticity along the cloud band could be computed with reasonable accuracy. In the absence of an adequate speed field, however, the following procedure was adopted in an effort to examine this feature. The surface pressure field was analyzed at intervals of 1 mb (not shown) and the pressure gradient measured on either side of the cloud band at intervals of 180 nautical miles along its length, with the exception of the southeastern extremity where no data were available. Using the relation between average geostrophic and average actual wind speed at low latitudes, after *Adams*, [1953], the shear across the cloud band was computed and the results are shown in Figure 12. Although the shear above the friction layer thus determined must be regarded only as a crude indication, the similarity between the curves of Figure 12, representing the beginning and end of a 24-hour period suggests that the sense of the shear may be revealed. Figure 12 shows that not only is the cyclonic shear small—

even at its maximum of 7 kt per 180 nautical miles (7 kt per 180 nautical miles = 10^{-6} sec $^{-1}$)—but the sign reverses so that anticyclonic shear extends from the col southeastward.

The point of this is to show there is a suggestion, at least, that this line of convergence retained its vigor for the interval pictured here even though its evolution had passed through the frontal phase and even, perhaps, well through the shear line phase. Further, at this stage it appears to follow the motion of the convergent asymptote between subtropical anticyclones, an indication that its future depends critically upon the convergence between flow in the equatorward limb of the anticyclones and the trade wind easterlies.

Upper air observation. The upper air data are an order of magnitude less dense than the surface coverage so upper air analyses have not been made, but some comment can be made relative to the upper-air circulation in the vicinity of the few reports available. The single wind observation near the small high cell has already been mentioned; no radiosonde observation was taken at this station.

Upper wind observations in the equatorial and tropical regions, at Nauru Island (0.5°S, 167°E) at Guadalcanal (9°S, 170°E) and at Bora Bora

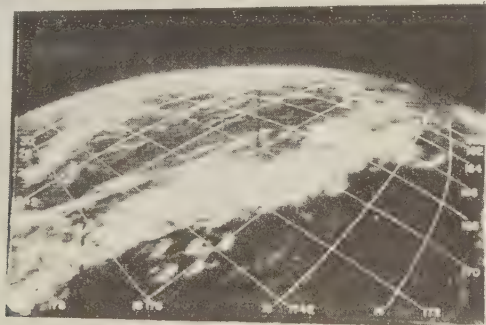


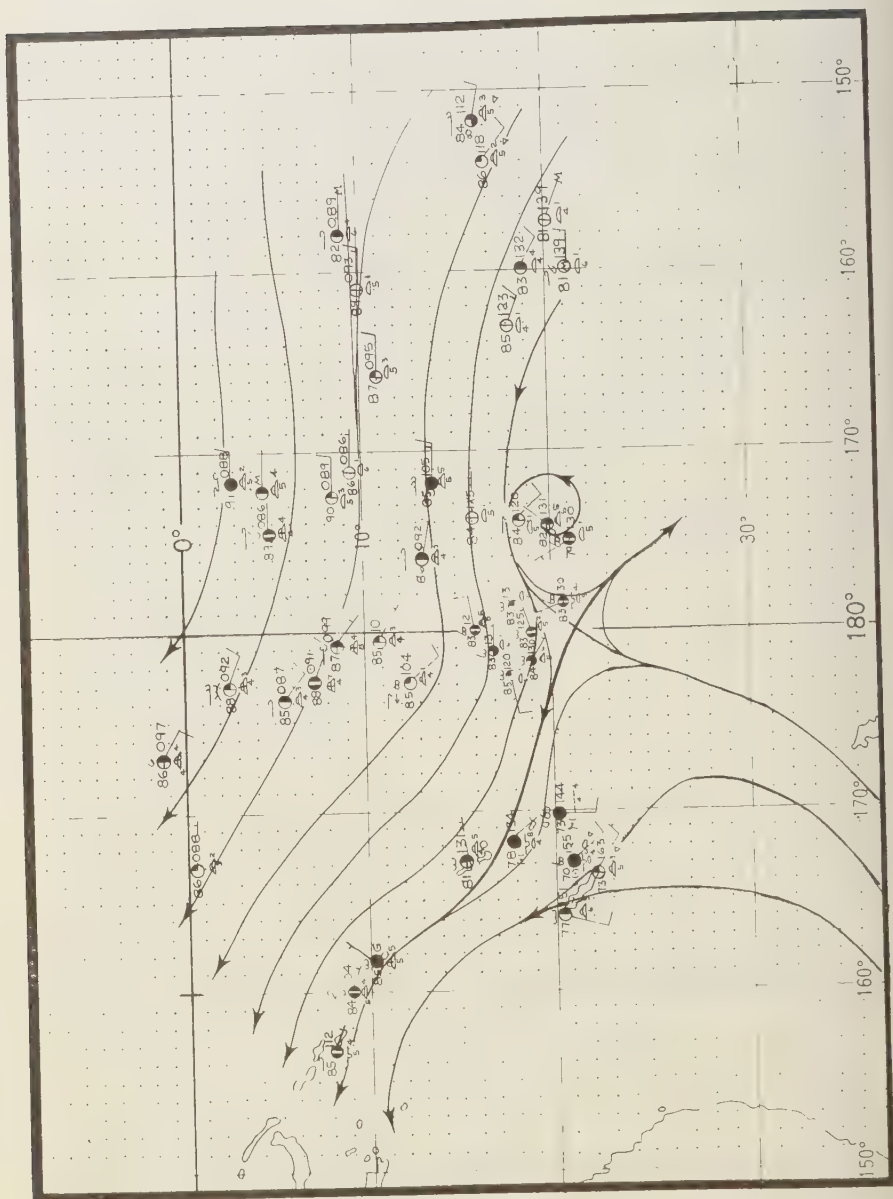
Fig. 9. Individual frame showing western end of major cloud band and cloud covered eastern Australia on horizon. Picture taken at 0054 GMT, May 12, 1960.



Fig. 10a. Schematic representation cloud coverage derived from pictures taken near 0000 GMT, May 11, 1960. Light and dark gray areas represent bright and dark cloud areas, respectively. The dark gray areas are the same as the dark gray areas in the schematic representation of the cloud coverage derived from Figure 11a.



Figure 10b. Schematic representation of cloud coverage derived from pictures taken near 0000 GMT, May 12, 1960. Light and dark grey areas represent bright and dull cloud areas of pictures. Heavy dark line in cloud area is the convergence asymptote transferred from Figure 11b.



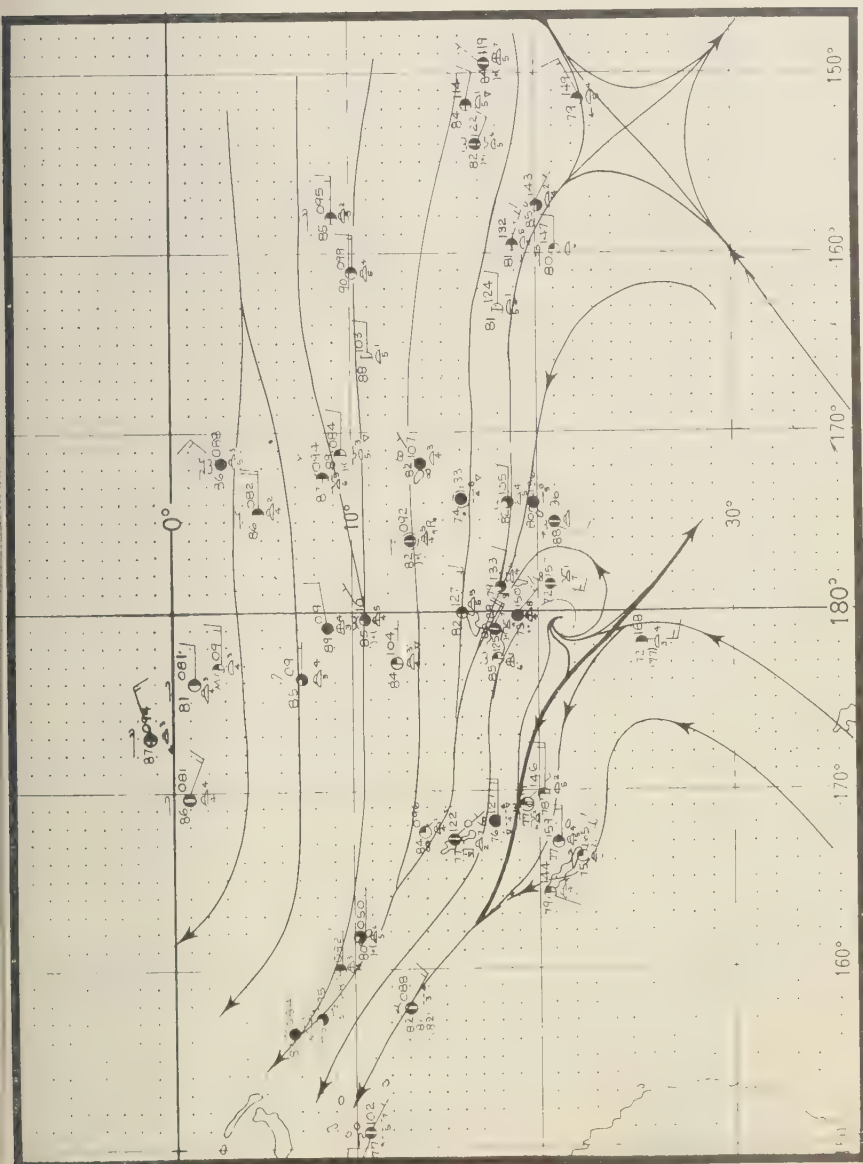


Fig. 11b. Surface streamline analysis for 0000 GMT, May 12, 1960.

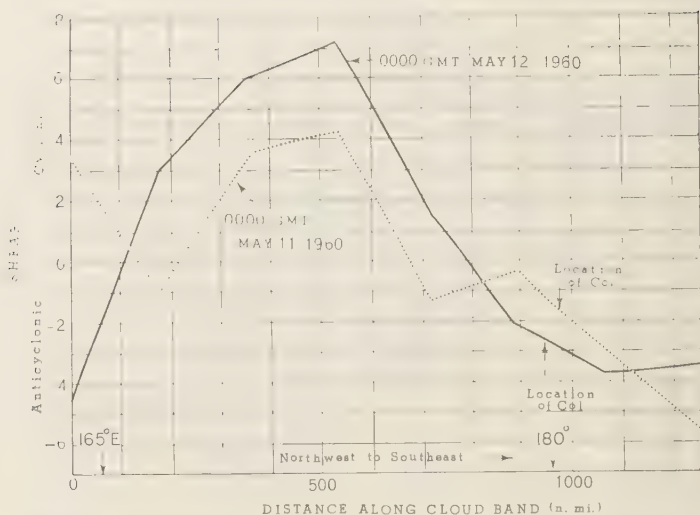


Fig. 12. Computed shear across major cloud band in units of knots per 180 nautical miles; positions of col shown for beginning and end of May 11, 1960.

(16°S, 152°W) all show typical trade wind flow with easterlies throughout the low and middle troposphere. Of this group only Guadalcanal has a radiosonde and this shows a typical trade wind layer overlain with deep easterlies, and a moist layer from the surface to about 12,000 ft. The great distance between stations leaves ample room for undetected perturbations and the winds are cited only to point out that the nonperturbed surface flow in the vicinity of those stations is confirmed by the upper air observations.

Two wind reports that were taken on opposite sides of the major cloud band are interesting because they detect flow directed toward the cloud band from opposite sides, in the layer between the surface and about 7000 ft. The pibal taken at 15°S, 167°E indicates light winds, northeast, just north of the band, and at 22°S, 166°E the winds are all south of east. Again the latitudinal span of 7 degrees between these observations may contain a complicated circulation pattern; one can only point out that the data do not conflict with the convergence asymptote shown on the surface analysis.

The only other upper-air data available in the area of interest are radiosonde and wind observations at Nandi (17.6°S and 177.6°E). It has already been mentioned that the layer from 2000

to 7000 ft contained east winds, but the winds changed to westerlies at greater height; at about 10,000 ft at the beginning of this 24-hr period at 8,000 ft at 1200 GMT, and at 3,000 ft during the last 6 hours of the 11th. Because a trough line extending from higher latitudes moved over Nandi during this interval, and because the westerlies increased with height, it is quite certain that these were midlatitude westerlies overlying the very shallow easterlies at the surface. No doubt clouds were associated with this potential trough but no good pictures were obtained of the high latitude portion of the trough.

TIROS PICTURES AS COMPLEMENTARY METEOROLOGICAL DATA

The pictures presented here show features not discussed up to this point that illustrate the potential of satellite data in synoptic analysis. An intermittent zone of increased cloudiness is visible on Figures 2, 4, 6 and 8 from 10°S to 12°S indicating a line of weak convergence roughly parallel to the major subtropical band to the south, a feature only vaguely indicated by the surface data. The tropical analyst would note this weak convergence at this map time and forecast no extreme weather for the pictured area in the near future.

When any one wind report shows a significant deflection from east in the trade wind region, the tropical analyst must scrutinize all evidence in an attempt to explain it. This evidence consists of the past record, indicating whether the cause might be a sea breeze or other local effect, the reputation of that particular station for reliability, and the previous weather analysis of the stream area to see if a wave may have been developing unnoticed. In cases like this even the negative information of pictures showing no well-developed waves is useful because the 'detective work' is enormously eased. An example of this occurred during the analysis of the map series necessary to produce Figures 11a and 11b. On 00 GMT, May 10, the surface wind at Christmas Island (2°N , 158°W) was south; 20 kt and 12 hours later it had returned to southeast. Because the map series was being analyzed independently of the pictures, considerable time was spent in attempting to account for this wind shift by a strong disturbance extending both north and south of the equator, extrapolating its position downstream to see if appropriate wind changes at other stations verified a traveling disturbance. Finally, with no other changes occurring downstream, it was concluded that no significant disturbance had moved into the disturbed area, and Figures 11a and 11b show uniform easterlies in the tropical area east of 10°W . Turning then to the pictures, a brief inspection verified the absence of an intense wave (see Figs. 2 and 8). Use of the pictures during the analysis would have eased the analyst's chore and lent confidence to the final result.

Because the camera was viewing well above the horizon while the satellite was south of 30°S , pictures of the higher latitudes are less satisfactory than pictures of the tropics. Nevertheless some excellent pictures of the patterns within the subtropical anticyclone were obtained. The area near the horizon in the westernmost strip composite of Figure 1a and the individual frame in Figure 5 show a curved pattern of clouds curving from left to right toward Australia on the horizon. This pattern delineates the northern limb of an anticyclone that was shown on the Australian coded analysis. According to that source, a high was centered at 30°S , 158°E , at 0500 GMT, May 11, 1960.

These pictures of clouds in the anticyclone are

of interest because a large number of vortex patterns so prominent in the Tiros data are associated with cyclones where the low-level convergence produces copious cloudiness that arranges itself in the characteristic spiral patterns. Here, however, is anticyclonic circulation that is undoubtedly producing surface divergence and subsidence, yet there are sufficient clouds (probably no more than a few tenths) to show this curved pattern. Purely from meteorological reasoning one can be moderately confident that the cloudiness is suppressed cumulus limited by an inversion or by a dry stable layer.

SUMMARY

This study has shown that a dense network of surface observations (by tropical standards) provided only a tentative indication of lines of convergence in the low troposphere. Based only on surface cloud data the presence of disturbed weather near the major convergence line was suggested, but it was not possible to delineate a continuous band of clouds and thereby a continuous convergence line. Furthermore, efforts to detect a line of vorticity failed to show a significant magnitude of cyclonic shear along the convergence line. One might therefore conclude that the evolution of the system producing the major cloud band had passed through the frontal stage and even the shear line characteristic was dissipating. In any event, an excellent surface data network in the tropics is not adequate to describe the quasi-stationary type of system studied here because the effect on the field of horizontal motion is so small that it is virtually undetectable when the systems are quasi-stationary. The standard data must be complemented by more complete cloud observations such as those provided by satellite observations. The pictures provided by the four passes showed nearly 2000 miles of a vigorous band of middle and low clouds that apparently maintained its position over the main convergence asymptote at the surface, a very good pictorial evidence of a persistent line of convergence.

Acknowledgements. This work has been carried out in the Meteorological Satellite Laboratory of the U. S. Weather Bureau and was made possible only by the use of the Computation Section and other supporting facilities in that laboratory. The

work is supported by the National Aeronautics and Space Administration.

REFERENCES

- Bandeem, W. R., and W. P. Manger, Angular motion of the spin axis of the Tiros I meteorological satellite due to magnetic and gravitational torques, *J. Geophys. Research*, 65, 2992-2995, 1960.
- Jordan, C. L., Comparison between observed and geostrophic winds. *Quart. J., Roy. Meteorol. Soc.*, 79, 153-156, 1953.
- Palmer, C. E., Tropical meteorology, *Quart. J., Roy. Meteorol. Soc.*, 78, 126-163, 1952.
- Palmer, C. E., C. W. Wise, L. J. Stempson, and G. H. Duncan, The practical aspects of tropical meteorology, *Air Force Surveys in Geophysics* no. 76, 195 pp., 1955.
- Ramage, C. S., Notes on the meteorology of the tropical Pacific and Southeast Asia, *report to Geophysics Research Directorate, Contract No. AF 19(604)-1942*, University of Hawaii, 174 pp., 1959.
- Riehl, H., *Tropical Meteorology*, McGraw-Hill Book Co., New York, 392 pp., 1954.

(Manuscript received December 12, 1960.)

Evidence of a Downward-Propagating, Annual Wind Reversal in the Equatorial Stratosphere¹

RICHARD J. REED, WILLIAM J. CAMPBELL,
LOWELL A. RASMUSSEN, AND DALE G. ROGERS

*Department of Meteorology and Climatology
University of Washington
Seattle 5, Washington*

Abstract. Stratospheric wind data for Canton Island (3°S) and Nairobi, Kenya (2°S), reveal that during the period July 1955–February 1960 alternate bands of easterly and westerly winds progressed downward from the highest level of observation (30 km) at intervals of approximately 1 year, suggesting the presence of a 2-year zonal wind oscillation in the equatorial stratosphere. The bands circle the entire globe, reach their greatest strength near 25 km, are about 10 km deep at intermediate levels, move downward at about 1 km per month, and weaken and become erratic near the tropopause. On the basis of ozone measurements it is argued that the downward propagation represents a wave motion, not a mass transport. The periodic appearance of westerly momentum at the equator suggests the presence of disturbances in the tropical stratosphere which transport momentum in a preferred manner.

INTRODUCTION

On the basis of the fragmentary observational data then available, Palmer [1954] characterized the stratospheric circulation of the equatorial region by two zonal currents of great persistence: the Berson westerlies and the Krakatoa easterlies. The westerlies, first discovered in central Africa by Von Berson, were pictured as a 'thread' of steady west winds, encircling the globe in a narrow belt lying within about 7° of the equator. Their base was stated to lie near 20 km and their top to vary in height from month to month and from year to year, an upper figure of 27 km being given.

The easterly current, first manifested by the read of dust from the volcanic eruption of Krakatoa, was described by Palmer as being confined mainly to the zone between 15°N and 5°S and prevalent at all longitudes from which data were available. In the vertical the easterlies are believed to extend from the vicinity of 10 km to 40 km and above, and a figure of 30 m sec⁻¹ was given for their average strength.

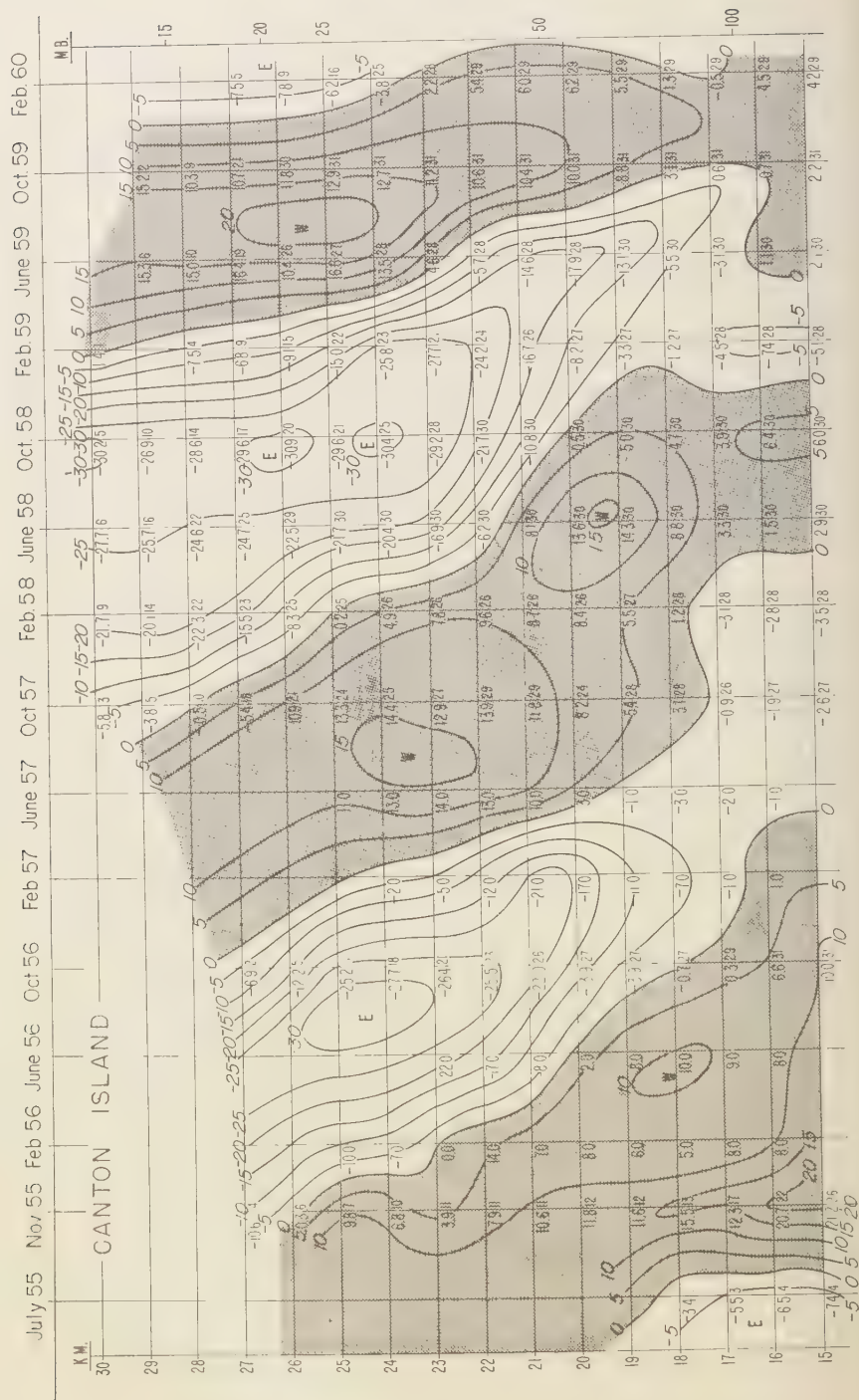
The year-to-year variation in the height of the westerlies has been confirmed in a recent study of Viezee [1958], based on wind data for

a 2-year period from nine stations in the equatorial Pacific. A particularly striking example of inter-annual changes has been presented by McCreary [1959]. On the basis of monthly wind averages for Christmas Island (2°N, 157°W) he has demonstrated that westerly winds which were present near 30 km in October 1956 gradually lowered and were replaced by easterlies in late 1957. During 1958 the easterlies strengthened and progressed downward, while the westerlies weakened and diminished in depth.

McCreary regarded the initial westerlies near 30 km as a different phenomenon from the Berson westerlies and spoke of the wind regime of the year 1958, in which westerlies near 20 km were surmounted by easterlies at higher levels, as being closer to the 'accepted normal.' However he qualified his remarks with the statement that 'there is insufficient data for the equatorial stratosphere to warrant an estimation as to which year is more nearly normal.'

The picture shown by McCreary's limited data of successive bands of westerlies and easterlies lowering from the highest levels of observation at an interval of about 1 year is sufficiently different from Palmer's preliminary description of the equatorial circulation to merit investigation over a longer period of time and at other localities. In the present study wind data for selected months during a 56-month period at

¹ Contribution No. 57, Department of Meteorology and Climatology, University of Washington, Seattle.



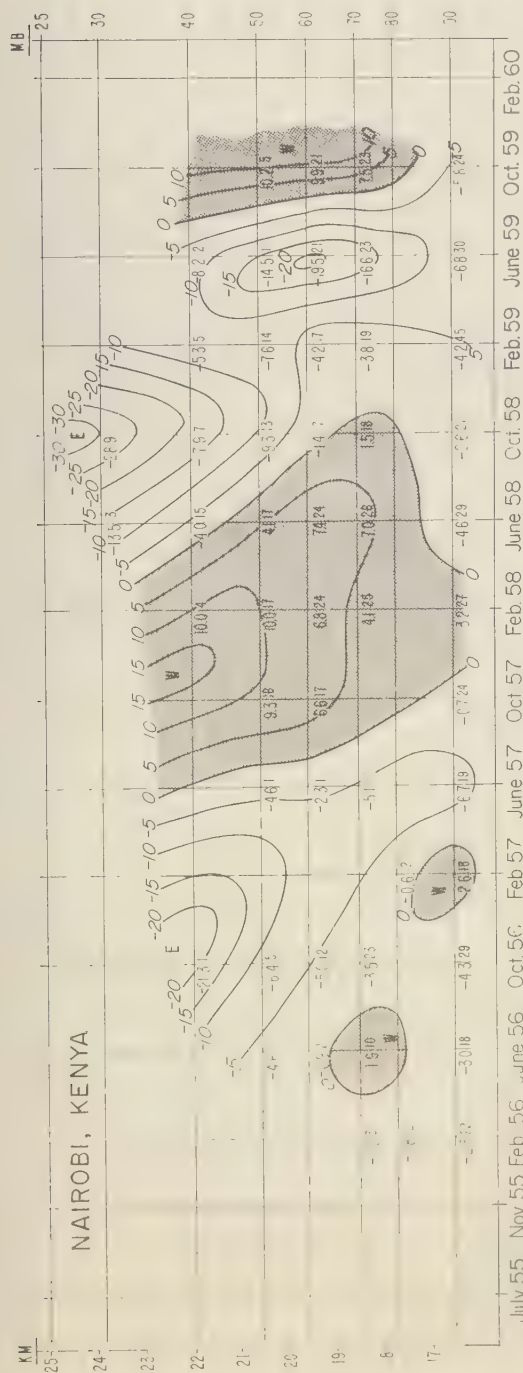


Fig. 1. Time-height sections of mean monthly zonal wind components for Canton Island and Nairobi, Kenya. Wind speeds are in meters per second and are plotted to the left of the verticals. The number of observations entering into each mean is shown to the right.

Canton Island (3°S, 172°W) in the Pacific Ocean and during a 45-month period at Nairobi, Kenya, are examined, and it is demonstrated that descending alternate bands of easterlies and westerlies were present also at these stations, that the yearly wind reversal occurred throughout the extended period of record, and that the phase of the reversal was the same at these two stations as at Christmas Island.

DATA ANALYZED

Average monthly zonal wind components were computed generally at intervals of 4 months for the period July 1955 to February 1960 at Canton Island and the period February 1956 to October 1959 at Nairobi. Winds for Canton Island were taken from the *Northern Hemisphere Data Tabulations* [U. S. Department of Commerce 1955-1960], the report for 0000 UT or 0300 UT, supplemented by the report for 1200 UT or 1500 UT when the latter reached to greater altitudes, being used to obtain monthly averages for each kilometer between 15 and 30 km, inclusive. Average values for February and June, 1956 and 1957, were read from graphs presented by *Viezee* [1958].

Microfilm copies of the daily wind soundings at Nairobi were kindly supplied by the Director of the East African Meteorological Department. Stratospheric wind data were recorded on the film at 10-mb intervals, and the averages have been determined for the levels provided. When more than one sounding was available for the day, the 1200 UT report was used, if sent. Otherwise the 0000 UT or 0600 UT report was substituted.

The mean monthly zonal winds in meters per second are entered in Figure 1 along with the number of observations used in computing each average. Smoothed isopleths of zonal wind component have been drawn in order to afford a visual representation of the wind variations.

OBSERVED CHARACTERISTICS OF THE WIND OSCILLATION

Examination of Figure 1 reveals the following main features of the equatorial stratospheric wind oscillation. The description applies only to the years under investigation, and no claim is made as to its past or future validity.

1. The zonal wind component in the equatorial

stratosphere undergoes an annual reversal, period of approximately 2 years being required for the wind at a particular level to describe complete oscillation from easterly to westerly and back.

2. The easterly and westerly currents descend at a rate of about 1 km/month. Upon approaching the tropopause, they generally weaken and become diffuse and irregular.

3. At intermediate levels the currents are about 10 km deep. At the top and bottom of the layers the depths are quite variable.

4. The westerly and to a lesser degree the easterly currents appear to attain their maximum intensity near 25 km.

5. Above the 50-mb level (21 km), easterlies are more frequent than westerlies and are generally of greater strength. The predominance of the easterlies with increasing altitude is brought out by Table 1. All averages were computed over complete wind cycles.

TABLE 1. Mean Zonal Wind at Various Heights in the Equatorial Stratosphere Obtained by Averaging over Complete Wind Cycles in Figure 1. (Easterly, east to west, winds negative)

Height, km	16	18	20	22	24	26	28
Wind speed, m sec ⁻¹	2.8	2.0	0.8	-3.9	-4.8	-5.0	-7.0

6. The currents are of global extent. This statement is based on comparison of the analyses for Canton Island and Nairobi and on data presented by *Viezee* [1958] which indicate that during 1956 and 1957 the depicted wind regime prevailed at all stations in the equatorial Pacific between 155°W and 155°E.

Corresponding monthly averages of meridional wind components and 50-mb temperatures were also computed for Canton Island. Meridional components were of the order of 1 to 2 m sec⁻¹, rarely exceeding 5 m sec⁻¹, and along any vertical were alternately north and south in layers about 2-km deep. The monthly mean 50-mb temperature varied by as much as 10°C in an apparently irregular fashion. Neither the meridional components nor the 50-mb temperatures were related in any obvious way to the zonal

wind patterns, though it is possible that more careful analysis might reveal some relationships.

THEORETICAL COMMENTS

In view of the relatively short period of record and the limited information on spatial variations, it would seem premature at this time to attempt a complete theoretical explanation of the motions depicted in Figure 1. However, it is not too early to comment on certain theoretical aspects of the problem.

The downward propagation of the currents. This is almost certainly a wave motion in which the mass transport is more likely to be upward than downward. The basis for this assertion is the finding by Dütsch [1959] and others that ozone concentrations between 15 and 26 km in equatorial Africa are below the amounts required by photochemical theory. If the air currents were settling bodily, the opposite would be the case.

The presence of westerlies on the equator. It is difficult on the basis of any simple circulation scheme involving the motion of rings of air to account for the appearance of a ring of westerly winds at or near the equator. Zonal rings acquire westerly momentum in moving horizontally to the equator, and rather small meridional displacements lead to the generation of substantial easterlies [Haurwitz, 1941]. Inward shrinking of an equatorial ring from great heights could produce westerlies of the observed magnitude, but the argument of the previous paragraph rules out this possibility.

It seems necessary to resort to disturbed motions which transport momentum in a preferred manner to explain the formation and maintenance of the equatorial westerlies. Just as it is now known that the westerly jet stream of middle latitudes is maintained in part by the eddy flux of momentum associated with synoptic or large-scale disturbances, it is conceivable that the equatorial westerlies are manifestations of high-level tropical disturbances which have the property of transporting westerly momentum into a narrow belt about the equator. There are, in fact, clear indications of disturbed motions in the tropical stratosphere on daily 50-mb and 25-mb charts published in connection with the International Geophysical Year [Behr, Jacobs, Petzoldt, Scherhag, and Warnecke, 1960a,b]. Work is currently in progress to measure the

eddy flux of momentum at stations in the tropical and equatorial Pacific during various portions of the wind cycle.

Perhaps pertinent to the problem of the Berson westerlies is a somewhat analogous feature of the oceanic circulation: the equatorial undercurrent or Cromwell Current [Knauss, 1960]. The geometrical similarity between the oceanic and atmospheric currents suggests certain dynamic similarities, the most obvious of which is the absence or near absence of the Coriolis force. On the other hand there is at least one major difference between the two phenomena. The Cromwell Current derives its momentum [Charney, 1960] from east-west pressure differences which are established by the effect of the trade winds in redistributing water mass. The Berson westerlies encircle the globe and consequently cannot experience any net pressure force in the east-west direction. The only possible source of momentum would seem to be the Reynolds stresses associated with stratospheric disturbances.

Acknowledgment. We wish to thank the Director of the East African Meteorological Department for providing wind data for Nairobi.

REFERENCES

- Behr, K., I. Jacobs, K. Petzoldt, R. Scherhag, and G. Warnecke, Tägliche Höhenkarten der 50 mbar Fläche für das Internationale Geophysikalische Jahr 1958, Teil I, *Meteorologische Abhandl.*, 12, 1960.
- Behr, K., I. Jacobs, K. Petzoldt, R. Scherhag and G. Warnecke, Tägliche Höhenkarten der 25 mbar Fläche für das Internationale Geophysikalische Jahr 1958, Teil I, *Meteorologische Abhandl.*, 10, 1960.
- Charney, J. G., Non-linear theory of the wind-driven homogenous layer near the equator, *Deep-Sea Research*, 6, 303, 1960.
- Dütsch, H. U., Vertical ozone distribution over Arosa, *Final Rept., contract AF 61 (514)-905*, Lichtklimatisches Observatorium, Arosa, 1959.
- Haurwitz, B., *Dynamic Meteorology*, McGraw-Hill Book Co., New York, 1941.
- Knauss, J. A., Measurements of the Cromwell Current, *Deep-Sea Research*, 6, 265, 1960.
- McCreary, F. E., Stratospheric winds over the tropical Pacific Ocean. Paper presented at Minneapolis Meeting of American Meteorological Society, 1959.
- Palmer, C. E., The general circulation between 200 mb and 10 mb over the equatorial Pacific, *Weather*, 9, 341, 1954.

U. S. Department of Commerce, *Northern Hemisphere Data Tabulations*, 1955-1960.

Vieze, W., The mean circulation of the equatorial stratosphere, *Final Rept., contract AF 19 (604)-2134*, Univ. Calif., Inst. Geophys., Los Angeles, 1958.

(Manuscript received November 9, 1960.)

Note added in proof. Since the foregoing article was submitted for publication, an article entitled

'Notes on the wind flow at 50 mb in tropical and sub-tropical regions in January 1957 and January 1958' by R. A. Ebdon has appeared in the October 1960 issue of the *Quarterly Journal of the Royal Meteorological Society*. This article reveals that the annual stratospheric wind reversal at Canton Island extended back at least to January 1954, so that it is now possible to delineate, from the present results and the results of Ebdon's paper, eight successive annual wind reversals.

Analysis of a Falling-Sphere Experiment for Measurement of Upper-Atmosphere Density and Wind Velocity

J. OTTERMAN,¹ I. J. SATTINGER, AND D. F. SMITH²

*Institute of Science and Technology
The University of Michigan, Ann Arbor, Michigan*

Abstract. A method is described by which upper-air density and wind velocity might be determined by measuring the drag acceleration of a falling sphere by means of accelerometers mounted on an inertial platform carried within the sphere. An investigation was made to determine the size, weight, and accuracy of available inertial platforms. An analysis based on this information shows that air density and wind velocity can be measured by this method up to altitudes of at least 150 km and 120 km, respectively. The error in air-density measurement would be 20 per cent or less, and the wind-velocity error would be 10 m/sec or less.

Introduction. A proposed experiment for measuring air density and wind velocity at high altitudes is described. The measurement of density and wind velocity would be accomplished by measuring the drag acceleration of a falling sphere, ejected from a high-altitude rocket, by means of accelerometers mounted on an inertial platform carried in the sphere. The techniques for carrying out the experiment are briefly described.

A variety of methods have been used by other investigators for obtaining information on air density. [Whipple, 1952; Frieland, Katzenstein, and Zatzick, 1956]. A rocket technique which has been successfully used for determining air density involves the measurement of the drag acceleration of a falling sphere. In the experiment currently being carried out [Jones and Bartman, 1956; Jones, Fischbach, and Petersen, 1958], the magnitude of drag acceleration acting on the sphere is measured by a transit-time accelerometer. The experiment provides information about the magnitude of the drag acceleration; however, no information is obtained on the direction of acceleration. Thus, the telemetered signals do not provide direct information about the trajectory of the missile or of the ejected sphere, and wind-velocity determination is not possible. The range of the experiment is 90 km [Jones, Fischbach, and Petersen, 1958].

In spite of the great advances in research techniques, the density of the upper atmosphere has not been sufficiently determined. Thus, different researchers report measurements of atmospheric density at 100-km altitude which differ by a factor of 4 [Nicolet, 1959].

Wind velocity has been determined by observing the motions of meteor trails [Whipple, 1952; Robertson, Liddy, and Elford, 1953]. Information about winds at an altitude of about 80 km can be obtained by observing the movements of noctilucent clouds [Ludlam, 1957]; this technique is limited to high geographic latitudes. Wind direction and velocity have been measured by observing artificial sodium clouds [Edwards, 1958], chaff [Smith, 1958], and the propagation of sound from grenades [Stroud, Bandedeen, Nordberg, Bartman, Otterman, and Titus, 1958] after these materials have been released from rockets at high altitudes. Of the three methods, only the range of the sodium-cloud method extends somewhat above 100 km.

At present, the wind information up to altitudes of 100 km is rather incomplete, and above 100 km it is very scanty. The atmospheric motions above altitudes of 100 km are of great current scientific interest; this knowledge is important theoretically because the theory of atmospheric motions affects our understanding of the atmosphere as a whole, and important practically because atmospheric motions affect radio communications and radio astronomy. Hines [1959], in his article on motions in the ionosphere, lists almost 70 references, practically all recent, dealing with various aspects of this

¹ Present affiliation: ITT Laboratories, Nutley, New Jersey; located at Bell Telephone Laboratories, Whippany, New Jersey.

² Present affiliation: Stromberg-Carlson, Inc., Rochester, New York.

problem. The opening sentence of his conclusions reads: 'Perhaps the most immediate conclusion that can be drawn from all these remarks is that a very great deal has yet to be learned about motions in the ionosphere.'

Experimental procedure. To measure drag acceleration, an inertial platform similar to those used for the guidance of ballistic missiles is mounted in the sphere. The inertial platform contains three accelerometers which measure acceleration along three mutually perpendicular axes which are fixed with respect to inertial space.

A rocket carrying an inflatable sphere is fired into the upper atmosphere; inside the uninflated sphere is the inertial platform. At an altitude of approximately 80 km this instrumentation system is ejected from the rocket, and the folded container is inflated to form a sphere with the inertial platform at its center, the total system weighing about 120 pounds. The sphere continues on a trajectory which is, except for the drag, a free-fall trajectory. Its peak altitude should be about 250 km or higher.

The accelerometer data of thrust and drag accelerations are telemetered throughout the flight to the ground, where they can be recorded and subsequently converted by means of an electronic computer into data on the velocity and position of the rocket and, subsequent to the ejection, of the sphere. The computation involves the integration of the measured acceleration of the rocket and the sphere due to thrust and drag, their computed acceleration due to gravity, and conversion from an inertial system of coordinates to an earth-fixed system of coordinates. Values of the components of acceleration, velocity, and position in earth-fixed coordinates can then be used to determine air density and wind velocity as a function of altitude. The basic equations are derived in the following section.

The inertial-platform consists of a four-gimbal stabilized platform, a group of electronic circuits for controlling the platform and operating the gyros and accelerometers, and the necessary power supply. The over-all dimensions and weight of the inertial-platform equipment influence the size of the rocket required to send the sphere into the upper atmosphere. In addition, size and weight affect the area-to-mass ratio of the falling sphere and hence the sensitivity of the experiment. The assumed weight of the inertial-platform system, including the batteries and the

transmitter, is about 80 pounds. The platform is approximately 10 inches in diameter and 10 inches long. Smaller inertial platform systems are currently under development. The accuracy of the accelerometers and the gyros of the inertial platform determine the obtainable accuracy of the experiment.

The proposed sphere is collapsible, being made of 2.5-mil Mylar. The instruments are mounted in one of three telescoping tubes which are 6 feet long when collapsed and extend to the sphere diameter of 12 feet when the sphere is inflated. The inflated sphere will have an internal pressure of 2 inches of water and will collapse when the stagnation-point pressure is above this value. Since the stagnation-point pressure will not exceed the internal pressure above 80 km, the sphere will remain inflated in the region where measurements are desired and at altitudes which will provide a check point for the accuracy of the density determination. Spheres based on this design have worked successfully in actual firings [Jones, 1953].

Basic equations for the experiment. A set of equations can be written describing the forces and motions of the falling sphere subsequent to its ejection and inflation. From the equations air density and wind velocity can be calculated. The following notation is used.

a_e, a_n, a_z = East, North, and Up components of \vec{a} , the drag- and thrust-acceleration vector in the earth-coordinate system.

v_e, v_n, v_z = East, North, and Up components of \vec{v} , the sphere velocity vector in the earth-coordinate system.

c_e, c_n, c_z = East, North, and Up components of \vec{c} , the sphere velocity vector relative to the ambient air in the earth-coordinate system.

w_e, w_n, w_z = East, North, and Up components of \vec{w} , the velocity vector of wind in the earth-coordinate system.

If the aerodynamic forces caused by the spinning of the sphere are neglected, the basic drag equation in vector form is

$$\vec{a} = -\frac{C_d \rho A}{2m} |\vec{c}| \vec{c} \quad (1)$$

where C_d is the coefficient of drag, ρ the density of the air, A the cross section of the sphere, and

its mass. The coefficient of drag, C_d , generally depends on the Mach number and the Reynolds number, but it varies rather slowly in most of the range of interest.

In terms of the magnitude of drag acceleration, (1) becomes

$$(a_e^2 + a_n^2 + a_z^2)^{1/2} = \bar{a}$$

$$= \frac{C_d \rho A}{2m} (c_e^2 + c_n^2 + c_z^2) \quad (2)$$

From (1) it follows that the drag acceleration and the velocity of the sphere relative to the ambient air are collinear (and in the opposite direction). Thus, the following equations hold:

$$c_e = c_z(a_e/a_z) \quad (3)$$

and

$$c_n = c_z(a_n/a_z) \quad (4)$$

If (2), (3), and (4) are combined,

$$\rho = \frac{2ma_z}{C_d A c_z^2 [1 + (a_e/a_z)^2 + (a_n/a_z)^2]^{1/2}} \quad (5)$$

The wind-component equations are

$$w_e = v_e - c_e = v_e - c_z(a_e/a_z) \quad (6)$$

$$w_n = v_n - c_n = v_n - c_z(a_n/a_z) \quad (7)$$

and

$$w_z = v_z - c_z \quad (8)$$

In (5) through (8), v_e , v_n , v_z and a_e , a_n , a_z are trajectory data which are derived from the outputs of the three mutually perpendicular accelerometers contained in the inertial platform.

Equations 5 through 8 contain seven unknowns: c_e , c_n , c_z , w_e , w_n , w_z , and ρ . Thus a solution is impossible solely on the upleg or solely on the downleg without some additional assumption. We propose to use the assumption of zero vertical winds, the same assumption that is currently being used in the data reduction of the grenade experiment for the determination of upper-atmosphere temperature and wind characteristics [Stroud, Bandeen, Nordberg, Bartman, Otterman, and Titus, 1958].

$$w_z = 0 \quad (9)$$

Several alternative approaches are possible. If one assumes that the density and wind conditions are constant in the time interval between

the upleg and downleg (this time interval will be about 10 minutes), there are for each altitude point 12 equations (i.e., two sets of equations 5-8) with 10 unknowns: c_e , c_n , c_z , w_e , w_n , w_z , ρ , and c_e' , c_n' , c_z' , where c_e , c_n , c_z refer to the upleg only and c_e' , c_n' , and c_z' to the downleg only. This set of equations is overdeterminate and can be solved for the best fit in w_e , w_n , w_z , and ρ . As another alternative, it can be assumed that the horizontal winds w_e and w_n do not remain constant. Then two additional unknowns, w_e' and w_n' , appear, and there is a system of equations with 12 unknowns. This upleg and downleg data reduction, of course, is possible only at altitudes higher than that at which the sphere is ejected.

Conclusions. Analysis of expected errors indicates that the proposed experiment promises to yield relatively accurate data about atmospheric density up to at least 150 km and data about horizontal winds up to at least 120 km [Otterman, Sattinger, and Smith, 1960]. The error in air-density measurement is expected to be 20 per cent or less, and the wind-velocity error 10 m/sec or less. On the basis of this study, it appears that the proposed experiment would add substantially to existing knowledge of the upper atmosphere.

Acknowledgment. The research reported in this paper was supported by the Geophysics Research Directorate of the Air Force Cambridge Research Center, Air Research and Development Command, under contract AF 19(604)-5205.

REFERENCES

- Edwards, H. D., Emission from a sodium cloud artificially produced by means of a rocket (Abstract), *Bull. Am. Meteorol. Soc.*, 39, 436, 1958.
- Frieland, S. S., J. Katzenstein, and M. R. Zatzick, Pulsed searchlighting the atmosphere, *J. Geophys. Research*, 61, 415-434, 1956.
- Hines, C. O., Motions in the ionosphere, *Proc. IRE*, 47, 176-186, 1959.
- Jones, L. M., Atmospheric phenomena at high altitudes, *Quart. Progr. Repts. 3-6*, contract DA-36-039-sc-15443, Eng. Research Inst., Univ. Mich., Ann Arbor, Michigan, 1 July 1952-30 June 1953.
- Jones, L. M., and F. L. Bartman, A simplified falling sphere method for upper-air density, *AFCRCTN-56-497 (ASTIA 101 328)*, Eng. Research Inst., Univ. Mich., Ann Arbor, Michigan, 1956.
- Jones, L. M., F. F. Fischbach, and T. W. Peterson, Seasonal and latitude variation in upper-air density, *IGY Rocket Rept. Ser. 1*, National Academy of Science, 47-57, 1958.
- Kallmann, H. K., A preliminary model atmosphere

- based on rocket and satellite data, *J. Geophys. Research*, 64, 615-623, 1959.
- Ludlam, F. H., Noctilucent clouds, *Tellus*, 9, 341, 1957.
- Nicolet, M., The constitution and composition of the upper atmosphere, *Proc. IRE*, 47, 142-147, 1959.
- Otterman, J., I. J. Sattinger, and D. F. Smith, Analysis of a falling-sphere experiment for measurement of upper-atmosphere density and wind velocity, *Rept. 2873-5-F*, Willow Run Labs., Univ. Mich., Ann Arbor, Michigan, 1960.
- Robertson, D. S., D. T. Liddy, and W. G. Elford, Measurements of winds in the upper atmosphere by means of drifting meteor trails, *J. Atmospheric Terrest. Phys.*, 4, 255, 1953.
- Smith, L. B., Measurement of winds between 100 and 30,000 feet by use of chaff rockets (Abstract), *Bull. Am. Meteorol. Soc.*, 39, 436, 1958.
- Stroud, W. G., W. R. Bandeen, W. Nordberg, F. L. Bartman, J. Otterman, and P. Titus, Temperatures and winds in the Arctic as obtained by the grenade experiment, *IGY Rocket Rept. Ser. 1*, National Academy of Sciences, 58-79, 1958.
- Whipple, F. L., Exploration of the upper atmosphere by meteoric techniques, in *Advances in Geophysics*, edited by H. E. Landsberg, Academic Press, New York, vol. I, p. 119, 1952.

(Manuscript received August 26, 1960;
revised December 15, 1960.)

Technique for Introducing Low-Density Space Charge into the Atmosphere

B. VONNEGUT, K. MAYNARD,¹ W. G. SYKES, AND C. B. MOORE

*Arthur D. Little, Inc.
Cambridge, Massachusetts*

Abstract. A technique for modifying the natural fair-weather electric field over large areas by the introduction of artificially produced space charge is described. The apparatus consists of a fine horizontal wire supported on insulators and maintained at a high voltage by a d-c power supply. With a 0.013-cm-diameter wire 4.5 km long and 4 m high maintained at 12 kv of negative polarity a corona current of about 1 ma flows, and the normal fair-weather electric field is reversed for a distance of 10 km or more downwind. The experimental observations are in fair agreement with a simple theory.

INTRODUCTION

During the period 1953-1956, under the sponsorship of the U. S. Signal Corps, our laboratory carried out experiments on the production of artificially produced space charge. These experiments had as their goal the modification or dispersal of fogs by electrical means. Although the few experiments on natural fogs were inconclusive, the research led to the development of techniques for producing significant modification of the natural fair-weather electric field over any square kilometers. We have subsequently employed variations of these techniques in research reported elsewhere [Vonnegut and Moore, 1959]. Now that our initial work has been declassified, it appears worth while to describe our original experiments.

Two techniques for introducing space charge to the free atmosphere were devised; one produces a rather low concentration of charge over a large area, and the other produces a very high concentration over a small area. The former method is the subject of this paper; the latter will be described in a forthcoming report.

EXPERIMENTAL CONSIDERATIONS

The main purpose of the space-charge generating equipment was to provide a simple and economical method of creating electric fields over tens of square kilometers. In the laboratory and the industrial Cottrell precipitator, it is quite simple to make electric fields of any desired

intensity by applying a potential difference between two parallel metallic plates. In the free atmosphere, this technique becomes prohibitively expensive because of the vastly larger dimensions. An alternative and far less expensive method of creating and maintaining electric fields in the atmosphere is to support the free charge in the atmosphere itself. A simple way to do this is to release free charge into the air and allow the wind to carry it away.

If one is to create electric fields over large areas, the charges must remain in the atmosphere as long as possible. Important factors determining the persistence of free charge in the atmosphere are the mobility of the charge carriers and their settling rate under the influence of gravity. They must not move rapidly in the electric field that they produce, and they must not fall out under the influence of gravity.

Fast ions (singly charged gas molecules) can readily be produced by point discharge and would be excellent charge carriers were it not for their high mobility ($1 \text{ cm sec}^{-1} \text{ per } v \text{ cm}^{-1}$). It is clear that in the absence of appreciable rate of ascent of the air, these ions would move rapidly to the ground and disappear. If the charge is to persist, it must be carried in the form of large ions of low mobility. This can be accomplished readily if the charge is attached to aerosol particles that provide enough drag to reduce the mobility by several orders of magnitude. Of course the aerosol particles must be so small that their rate of fall under the influence of gravity will be negligible.

The foregoing considerations indicate that an effective space-charge generator for atmospheric

¹ Present address: White Face Mountain Authority, Wilmington, New York.

experiments is in essence a device for producing large amounts of unipolarly charged aerosols. There are two possible approaches in designing such a device: one is to make an aerosol generator provided with an electrical charging system; the other is to utilize naturally occurring atmospheric aerosols and impart the electric charge to these. The technique to be described here is of the latter sort; not only are naturally occurring aerosol particles used but also the natural wind is used to carry the particles through the charging apparatus and out into the atmosphere. This system has some disadvantages:

1. The naturally occurring aerosols used to carry the charge are subject to wide variations in size and concentration.
2. The concentration of aerosol particles in the atmosphere is normally far lower than that which can be achieved readily with an aerosol generator.
3. The output of the apparatus varies widely because of the variability in both the direction and the speed of natural winds.

These disadvantages, serious though they may sometimes be, are largely compensated for by the simplicity and economy of the technique.

PRINCIPLE OF OPERATION

The apparatus consists of two parts. The first is a fine, stainless steel wire 0.01 to 0.05 cm in diameter, supported on insulators, and stretched horizontally above the ground. The second is a d-c power supply that maintains the wire at a potential at which a corona current will flow from

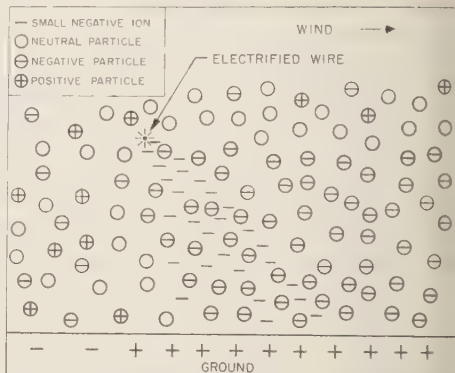


Fig. 2. Electrical charging of nuclei passing under the wire.

the wire to the air. Corona discharge at the wire releases positively or negatively charged gas molecules, depending on the polarity of the high voltage power supply.

Some idea of the operation of the wire can be obtained from the idealized representation shown in Figures 1 and 2. (In these drawings the wire is represented as negative; the situation would be much the same if it were positive, except that the sign of the charges would be reversed.)

If there is a horizontal wind flowing normal to the wire and if there are few if any nuclei, the situation when we view the wire end-on is shown in Figure 1. The charge released by the wire induces an equal and opposite charge on the ground beneath, and the resultant electrostatic attraction moves the charge rapidly to the ground. Thus, few charges would remain in the atmosphere more than a few hundred meters downwind.

If appreciable numbers of small particles are suspended in the air, the situation is quite different (Fig. 2). The fast ions released from the wire rapidly become attached to aerosol particles carried with the wind under the wire. Normally before these natural aerosol particles pass under the wire, they may carry either a positive or a negative charge or they may be electrically neutral. As they pass under the wire the neutral particles acquire a single elementary negative charge, and the positive particles acquire two elementary negative charges. Therefore, downwind most of the particles are carrying unipolar elementary charges.

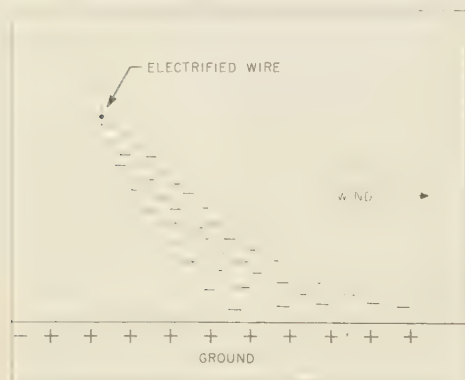


Fig. 1. Behavior of fast ions released from the wire when there is a low aerosol concentration.

THEORY OF OPERATION

Rate of charge release from the wire. It is necessary that the wire have a fairly high potential relative to its surroundings in order to emit charge into the atmosphere at a significant rate. At low potentials the only way that charge can flow is by conduction through the atmosphere. Since the air is a very poor conductor of electricity, the rate of flow of charge by this mechanism is exceedingly small.

When the wire is raised to a critical voltage V_c above its surroundings, an ionization process suddenly takes place in the air about it that increases its conductivity and permits much larger currents to flow. For a detailed description of this process, corona discharge, the reader is referred to *Cobine* [1958] and *Loeb* [1955].

Above the critical potential the current increases very rapidly with increasing voltage. Under the conditions of our experiments the corona current density flowing from the wire is so low we are justified in assuming that at steady state the potential difference between the wire and its surroundings is a constant, V_c .

The potential of the wire is determined by the potential of the power supply to which it is connected. The potential of the environment of the wire² is determined by the natural fair weather potential gradient and by the potential gradient that is produced by the space charge that is being released. Since the space charge released by the wire opposes the corona discharge process by increasing the potential of the wire's environment, the rate of release of charge is limited by the rate that the charge moves away from the wire.

We can derive a simple mathematical expression for the current flowing from the wire if we make the simplifying assumption illustrated in Figures 3 and 4, that the charge leaving the wire is carried downwind in a thin horizontal sheet. The potential of the environment of the wire is determined by the height of the wire h , the fair weather electrical potential gradient G_{fw} , and the potential gradient G_{sc} that arises from the charge

² We define the term 'potential of the environment' to mean the potential the wire would assume if it were suddenly disconnected from the power supply and the ground, if all charge at its surface were removed, and if the distribution of space charge previously released from it remained unchanged.

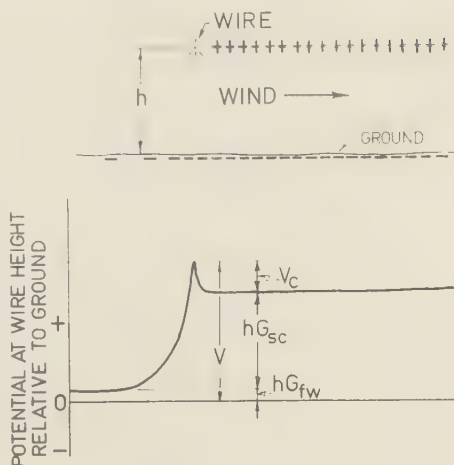


Fig. 3. Potential with respect to ground at wire height when positive charge is being emitted.

produced by the wire. If the wire is maintained at a potential V , with respect to ground, then V_c is equal to the difference between the potential of the wire and its environment, or

$$V_c = V - hG_{fw} - hG_{sc} \quad (1)$$

This relationship is shown graphically in Figures 3 and 4, which indicate schematically the electrical potential at the height of the wire

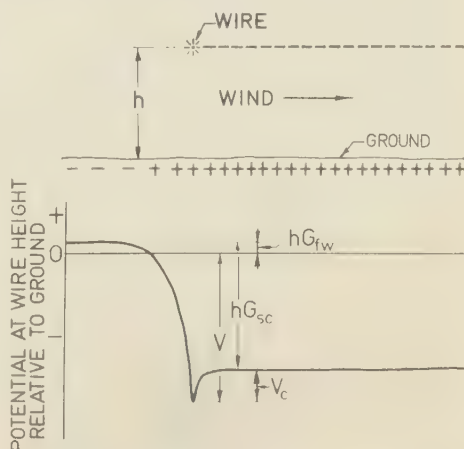


Fig. 4. Potential with respect to ground at wire height when negative charge is being emitted.

upwind and downwind when it is releasing positive and then negative charge.

If σ is the density at the earth's surface of charge produced by the wire, the potential gradient G_{sc} resulting from this charge is given by the solution of Poisson's equation for a pair of parallel plates with surface charge density σ . We have, therefore,

$$G_{sc} = 4\pi\sigma \quad (2)$$

If we designate the wind speed by w and its angle with respect to the wire by θ , then the rate of flow of charge downwind from a unit length of wire is given by

$$I = \sigma w \sin \theta \quad (3)$$

By substituting (2) and (3) into (1) and rearranging, we obtain

$$I = \frac{(V - V_c - hG_{fw})w \sin \theta}{4\pi h} \quad (4)$$

Charging of natural aerosol particles passing beneath the wire. Although in the foregoing discussion some indication has been given of the rate of charge release from the wire as a function of wind speed and potential, we have not dealt with the problem of the persistence of the charge in the air. For the charge to remain in the atmosphere for any length of time, the fast ions released from the wire must quickly become attached to suspended aerosol particles. When this happens, as we have said, the mobility of the charge carriers is decreased and their downward velocity under the influence of electrical forces becomes very small. Although equation 4 indicates that one might put out unlimited amounts of charge by using a high potential or a very low wire, this charge would be largely wasted, for it would disappear very rapidly. It is evident that the effective output from the wire is limited by the flux of natural aerosol particles available to carry the charge.

A rigorous theoretical treatment of the charging of aerosols is difficult, for it depends on the electric field and the fast-ion flux, both of which vary in a complicated way. Near the wire both the field and the fast-ion current are very high, so here those natural aerosol particles larger than about 0.1 micron will accept many elementary charges according to the *Ladenburg* [1930] relation. Away from the wire, where the field and the

current density are small, most aerosol particles will accept only single elementary charges. Since the region of high charging near the wire is of limited extent and since the numerical preponderance of aerosol particles usually consists of very small Aitken nuclei that will accept only single charges, we are justified in neglecting the rather few large particles that acquire high charges near the wire. Accordingly, we shall make the simplifying assumptions that only a single elementary charge is carried on each particle and that the concentration of particles is essentially the concentration of Aitken nuclei.

With these assumptions the maximum rate of output of charge in the form of large, low-mobility ions, which we shall designate as I_m , is limited by the flux of Aitken nuclei under the wire. If N denotes the number of nuclei per cm^3 , then

$$I_m = e h N w \sin \theta \quad (5)$$

where e is the electronic charge.

The condition for the optimum performance of the wire exists when just enough current flows to give each aerosol particle a single elementary charge. We can determine the conditions for this by combining (4) and (5):

$$e h N w \sin \theta = \frac{(V - V_c - hG_{fw})w \sin \theta}{4\pi h} \quad (6)$$

or

$$V = 4h^2 N e + V_c + hG_{fw} \quad (7)$$

It can be seen from this that since the potential required for the wire varies as the square of its height, effective use of a high wire requires a power supply of very high voltage.

Theoretically, by using a high enough wire maintained at an appropriately high potential, one can produce enough space charge to make any desired electric field. Practically, the intensity of the fields one can produce is severely limited by point discharge from the surface below the charge layer. Over usual land surface—with trees, other vegetation, and man-made structures—point discharge begins when the field, exceeds about 10 or 20 v cm^{-1} . Because point discharge produces large quantities of fast ions that neutralize the space charge rapidly, it is not possible to maintain fields in excess of this value over any appreciable area. Since a field of 20

1 cm^{-1} is equivalent to a surface charge density of 10^7 elementary charges cm^{-2} , with a concentration of 10^4 charged condensation nuclei cm^{-3} , one could achieve this limiting field with a wire about 10 m high and a power supply delivering 15 to 30 kv.

The threshold for point discharge over water or over smooth, structureless land surfaces (a desert or a snow-covered plain) is undoubtedly much higher. Here it should be possible to maintain much higher fields with a higher wire and much higher voltages.

We are encouraged to believe that the foregoing, simple theoretical treatment has some validity. It will be shown later that there is fair agreement between it and the experimentally determined flux of space charge. As we shall see, because of leakage currents, the current flowing from the power supply to the wire can be many times larger than the flux of charge carried downwind.

In concluding this discussion of the theory of the rate of space charge production from the wire, it is worth while to review the assumptions that were made and to recognize their limitations.

First, it has been assumed that the air passing under the wire is moving only horizontally and that the vertical motions are negligible. Actually, the vertical motions are probably quite large at times, because of convection and turbulence. In this case even fast ions unattached to aerosol particles may be carried up in the air.

A second assumption is that the field at the wire resulting from the space charge can be computed on the basis that the charge is in a thin horizontal sheet of infinite horizontal extent. The space charge obviously has a more complicated distribution, because of ion migration and atmospheric turbulence. Furthermore, since almost all the charge is downwind, the wire is at the edge of the charge layer and the potential at the wire is somewhat less than was assumed.

A third assumption is that the charge is carried solely on small Aitken nuclei, each of which accepts only a single elementary charge. Under many conditions there is undoubtedly a high concentration of larger particles that will carry appreciable quantities of charge.

A fourth assumption is that fast ions and aerosol particles combine until the supply of one or the other is completely exhausted. Undoubtedly the reaction is incomplete; even when there is an

excess of fast ions, it is possible that many aerosol particles can pass beneath the wire without acquiring charge and, conversely, even when there is an excess of aerosol particles, many fast ions might move to the ground without ever encountering one.

EXPERIMENTAL OBSERVATIONS

Our earliest experiments with the fine-wire method were carried out in 1953 in front of our laboratory on Memorial Drive in downtown Cambridge. Here we used a wire about 15 m long and 2 m high and found that we could cause appreciable perturbations in the gradient for several hundred meters downwind. The following year we conducted experiments with a wire 200 m long erected on masts on the roof of the Acorn Park laboratory in West Cambridge. When we released negative space charge at the rate of about 100 microamps, we were able to follow the plume for several kilometers downwind.

Another series of experiments with the fine-wire technique was carried out at Mt. Washington, New Hampshire. We erected a line 1 km long in the form of an arc about 200 m below the summit. The conditions for this experiment were difficult, with winds of about 20 m sec^{-1} , but we were able to reverse the electric potential gradient over the summit, and we detected clouds of space charge blowing by. During these tests the air had a very low concentration of condensation nuclei, of the order of 10^3 cm^{-3} , so the perturbations we could produce in the electric field were small in comparison with those in other experiments.

The most extensive and best instrumented of our early experiments was carried out during the summer of 1955. We installed a .013-cm-diameter stainless steel wire 4.5 km long near the shore line at Duxbury Beach, Massachusetts. The wire was supported about 4 m above the ground by polystyrene insulators 30 cm long which were attached to existing wooden telephone poles. A d-c power supply capable of giving a negative potential of about 15 kv and a current of a little over 1 ma was used to electrify the wire.

The experimental points in Figure 5 show the relationship between the applied voltage and the current flowing to the wire on June 30 when there was a wind of about 2.3 m sec^{-1} blowing normal to the wire.

We made several experiments during fair-weather conditions to determine the extent of the

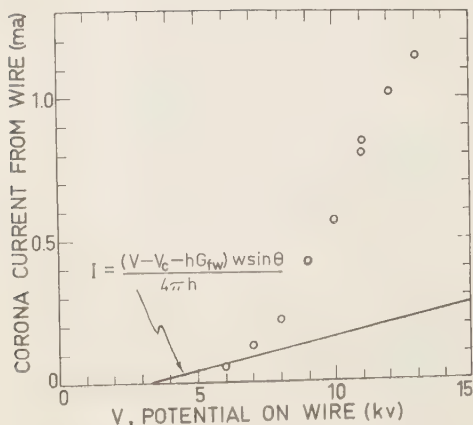


Fig. 5. Points show observed currents flowing to wire as a function of applied voltage on June 30, 1955. Straight line shows theoretical space charge flux computed from equation 8.

atmospheric electrical perturbations that could be caused by the apparatus. We found that beneath the wire and immediately downwind of it there was a significant alteration of the potential gradient, amounting to 10 v cm^{-1} or more. Upwind of the wire the perturbation dropped off very rapidly. With a wind of a few meters per

second the effect of the wire could not be detected upwind for more than about 100 m, and beyond this distance the gradient had the normal fair-weather value.

With a steady offshore breeze, when the space charge produced by the wire was carried out to sea, it was possible to follow the dispersal of the charge into the atmosphere by potential-gradient measurements over the water. These determinations were made from a power boat equipped with a radioactive probe and a vacuum-tube electrometer. We obtained the data by steering a zigzag course under the plume of charge.

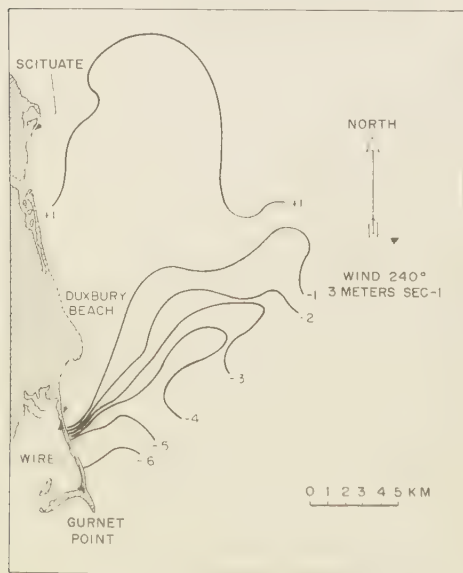


Fig. 6. Potential gradient downwind of wire June 30, 1955.

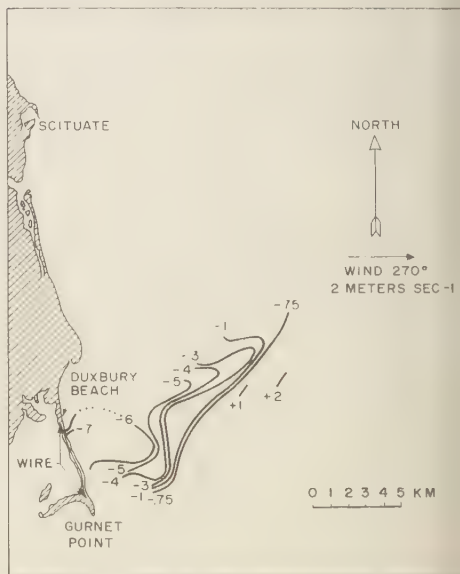


Fig. 7. Potential gradient downwind of wire July 1, 1955.

It should be recognized that because it required about four hours in each experiment to make the electrical measurements from the boat, the figures indicate not an instantaneous distribution but only an approximation. At the shoreline where air heated over the warm land suddenly passes out over the much cooler ocean, the air trajectories are certainly quite variable in space and time. Instead of moving out to sea in a simple orderly fashion, the charge will probably follow a complicated path. Not only will it move in varying horizontal directions but there will very likely be areas of convergence and divergence

caused by vertical motions. These will increase or decrease the depth of the charged air layer and hereby cause regions of enhanced or diminished field perturbations.

Figure 6 shows that on June 30 the potential gradient was reversed for a distance of 14 km or more downwind. Note that although the wind at the wire was almost directly out of the west, the plume appears to have been carried somewhat to the north.

Figure 7 shows a similar aberration of the electric field on July 1, with the reversal extending for approximately 18 km—in this case in accordance with the wind direction observed at the wire.

DISCUSSION

We find that the measured current flowing from the power supply to the electrified wire is considerably larger than the theoretical flux of space charge from the wire computed according to equation 4. If we put equation 4 in convenient, practical units we obtain

$$I = l \frac{(V - V_c - hG_{fw})w \sin \theta}{h} \times 9 \times 10^{-7} \quad (8)$$

where

w is the wind speed in meters sec⁻¹.

l is the length of the wire in km.

h is the height of the wire in cm.

V is the potential of the power supply in volts.

I is the space charge flux flowing downwind from the wire in amperes.

V_c is the critical corona potential in volts.

G_{fw} is the fair weather gradient in volts cm⁻¹.

The straight line plotted in Figure 5 shows the theoretical space charge current on June 30 as a function of space charge plotted from equation 8. The value of 4 kv used for V_c was experimentally determined in the laboratory. Although the observed and theoretical values are in fair agreement at lower potentials, the current at the operating potential of the line (13 kv) is about an order of magnitude larger than the predicted value for the space charge current.

We believe that this difference is caused by a corona leakage current. The measured gradient a few meters downwind of the line was of the order of 20 v/cm. It can be computed from this

using Poisson's equation that the flux of charge moving downwind from the line is only of the order of 2×10^{-4} amperes. This necessarily means that only a small fraction of the current flowing to the wire is being carried off into the atmosphere and that most of the charge fed to the wire is flowing rapidly to ground.

The conduction of charge from the wire directly to ground can occur by leakage through the insulators used to support the wire or by a fast ion current flowing from the wire to the supporting poles. One would expect that a leakage current flowing through the insulators would be ohmic in character. Since our data show a negligible current flow until the potential of the wire exceeds about 5 kv, we believe that the primary leakage is occurring as a fast ion current that flows between the wire and the grounded supporting poles.

From the distribution of the potential gradient downwind and from the wind velocity, one can compute, using Poisson's relation, the flux of charge that is being carried by the wind. Unfortunately, the gradient patterns in Figures 6 and 7 are incomplete, so that it is impossible to make this computation rigorously. One can, however, make a guess about the form of the missing portions of the pattern. We have made such estimates and found that on both days the flux of charge approximately 3.5 km downwind of the wire was of the order of 10^{-4} amperes.

The pattern of the decrease of potential gradient downwind suggests that the charge emitted from the wire is being lost by conduction to the surface. Our measurements of atmospheric conductivity show that the electrical relaxation time was of the order of 10^3 seconds. The decay of the electrical perturbation with distance is about what one would expect on the basis of this rate of charge leakage with time.

Rough estimates of the concentration of condensation nuclei made with a simple beer-can type of apparatus [Vonnegut, 1949] indicate that the air passing under the wire had 10^4 to 10^5 nuclei cm⁻³. With a wind speed of several meters sec⁻¹, the flux of nuclei under the wire amounted to 10^{15} to 10^{16} nuclei sec⁻¹. This would be adequate, if each nucleus carried one elementary charge, to carry a current of 10^{-4} to 10^{-3} amperes. It appears that an adequate concentration of natural nuclei existed to carry the observed flux of space charge.

CONCLUSIONS

The results of the experiments outlined above show that with relatively simple equipment and very modest expenditure of electrical energy it is possible to introduce into the atmosphere sufficient quantities of electric charge to cause significant changes in the fair-weather electric field over many square kilometers.

This technique should be of value in field experiments involving fair-weather atmospheric electrical phenomena and the effect of electricity on cloud and fog behavior, and in micrometeorological studies of air motion and trajectories.

Acknowledgments. We wish to express our appreciation to the U. S. Signal Corps for its support of this research under contracts DA 36-039-SG42585 and DA 36-039-SG64569. We are also grateful to the U. S. Coast Guard for allowing us to put our high voltage line on its telephone poles. We are glad to acknowledge our debt to Dr. A. G. Emslie

of this laboratory for his invaluable counsel and help throughout this work.

REFERENCES

- Cobine, J. S., *Gaseous Conductors*, Dover Publications, New York (606 pp.), 258-261, 1958.
Ladenburg, R., Untersuchungen über die physikalischen Vorgänge bei der sogenannten elektrischen Gasreinigung, *Ann. Physik*, 4, 5863-5897, 1930.
Loeb, L. B., *Basic Processes of Gaseous Electronics*, University of California Press (1028 pp.), 1955.
Vonnegut, B., A continuous recording condensation nuclei meter, *Proc. First Natl. Air Pollution Symposium*, sponsored by Stanford Research Institute, 36-43, 1949.
Vonnegut, B., and C. B. Moore, Preliminary attempts to influence convective electrification in cumulus clouds, *Recent Advances in Atmospheric Electricity*, Pergamon Press, London (631 pp., 317-331, 1959).

(Manuscript received October 14, 1960;
revised December 7, 1960.)

Calculations of Cloud Electrification Based on a General Charge-Separation Mechanism

J. D. SARTOR

*Planetary Sciences Department, The RAND Corporation
Santa Monica, California*

Abstract. Using recent solutions for the electrostatic and hydrodynamic two-body problems of the fields and forces between freely falling spheres in an electrostatic field, quantitative computations are made of the effectiveness of a general theory of cloud electrification that considers all particles in a cloud to be polarized by the electrostatic field of the atmosphere, and rebounding encounters to result in the transfer of charge in the direction required to increase the existing fields. The calculations employing observed cloud- and rain-drop size distributions give electrostatic fields of the magnitude observed in the time required for the development of a thunderstorm.

INTRODUCTION

Recent electrostatic and hydrodynamic solutions to the two-body problem of the fields and forces between freely falling spheres in uniform electrostatic fields allow quantitative computations of the effectiveness of a general theory of cloud electrification that considers all particles in a cloud to be polarized by the electrostatic field of the atmosphere, and rebounding encounters to result in the transfer of charge in the direction required to increase the existing fields.

The theory results from studying a laboratory model of freely falling cloud droplets in an electrostatic field [Sartor, 1954]. The basis of the theory was the observation that, when two originally uncharged droplets falling freely in the presence of an electrostatic field collided but failed to coalesce, the larger droplet acquired a net charge opposite in sign to that on the lower charged plate used to produce the field. The difficulty of simultaneously modeling the electrical, dynamic, and interfacial forces left in doubt the applicability of this observation to the atmosphere. The theory therefore could not be substantiated on the basis of the experiment alone. To support the theory it is necessary:

1. To demonstrate that the trajectory of a smaller droplet with respect to the larger of a pair of colliding cloud droplets is asymmetrical and causes the droplets to separate after the smaller has made a close approach to the underside of the larger. (Such a trajectory ensures that the charge transferred is in the direction proposed in the cloud-electrification theory.)

2. To demonstrate a charge-transfer mechanism for colliding droplets and compute the amount of charge transferred.

3. To show quantitatively that the cloud-electrification theory is capable of explaining the observed fields in clouds.

It is now possible to provide substantiating evidence for each of the three items above.

RELATIVE TRAJECTORY

Using the forces obtained from the Davis [1960] solution to the two-body electrostatic problem and those derived from calculations by Hoeking [1959] of the hydrodynamic interaction of two spheres, Sartor [1960] computed the relative trajectory of two cloud droplets in an electrostatic field by a step-by-step integration process on the IBM-704.

The relative trajectory of a small falling droplet with respect to a larger one for hydrodynamic forces only is shown in Figure 1. The pair of droplets, shown here at the point of least separation, have a zero collision efficiency despite the fact that the underside of the larger droplet is approached very closely by the smaller droplet. The droplets reach a minimum separation at a point well on the underside of the larger droplet. Following this closest approach, the separation of the droplets continuously increases as the smaller drop moves past the upper side of the larger. This behavior is characteristic of relative trajectories over a wide range of initial horizontal separations between any two cloud or rain drops. Trajectories of the very large drops may differ because of irregularities in the trajectory due to

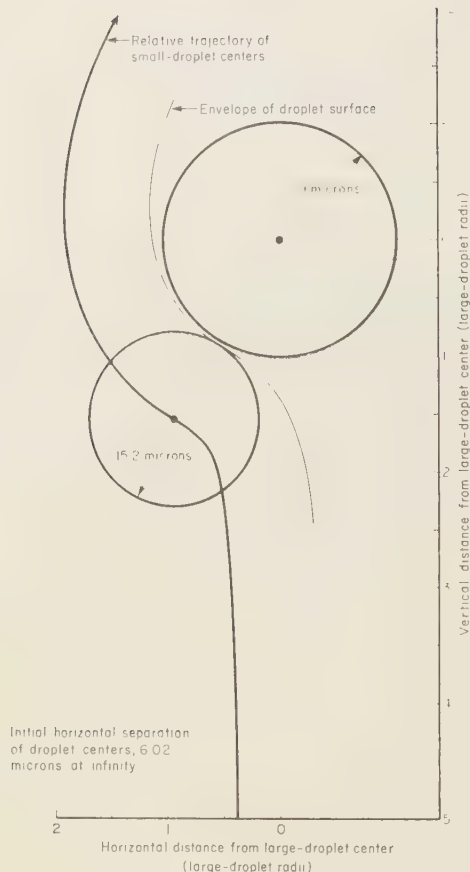


Fig. 1. Free-fall relative trajectory of a small droplet with respect to a larger one.

oscillations in the shape of the drops as well as the reverse flow in the wake of the large drops. However, the relatively rare interactions between the very large drops are masked by the vastly more common interactions of the type described in this paper.

COLLIDING CLOUD DROPS IN AN ELECTROSTATIC FIELD

In support of the charge-transfer mechanism, a study of the electrostatic field between the near surfaces of two cloud drops approaching in an electrostatic field was initiated in 1956. The results for two equal drops in a uniform field parallel to the line of their centers was reported by Sartor [1957]. Earlier this year, the problem

was solved in all generality by a RAND colleague, M. H. Davis [1960]. These computations showed that the field and the local force between the near surfaces increases indefinitely as the separation decreases.

Figure 2 shows what happens to a uniform electrostatic field when two uncharged cloud drops are introduced so that they line up with the field. The cloud drops for this purpose are essentially conductors and are therefore polarized as shown in the figure. As the two droplets approach, the field between their near surfaces becomes more and more concentrated because of the imaging of the charges on the one droplet in the other. For example, the solution to this electrostatic problem by Davis [1960] shows that when the drop surfaces are 0.1 radius apart, the ambient field is enhanced 14 times at the droplet surfaces. The enhancement as a function of separation becomes 92 at .01 radius, 690 at .001 radius and 5600 at .0001 radius. As observed in the laboratory [Sartor, 1954], when the droplets come sufficiently close together, charge is transferred. There are a variety of possible mechanisms for this transfer, depending on the final separation, the field, and the size of the droplets. When the droplets touch without coalescing, the mechanism is conduction. On close approach the near surfaces may be deformed slightly outward by the strong local field between them, creating an unstable situation that further enhances the field to the point of discharge between the droplets or shearing off of a portion of one droplet and depositing it on the other.

The electrical interaction between two cloud droplets during their close passage is illustrated in Figure 3 in which the trajectory of the smaller droplet is shown with respect to the center of the larger. The field E_0 of Figure 3 is in the direction of the atmospheric field. As the smaller droplet approaches the larger, both are polarized as shown for the drop illustrated in the lowest position, but are initially uncharged. Those that collide, but pass on, transfer charges so that the larger drop becomes negatively and the smaller one positively charged. Those drops that coalesce instead of bouncing subsequently aid the process as will be evident later, both because of their increased size and their terminal velocities.

Now let us consider a large number of droplet interactions. After each interaction producing a charge transfer, there is one relatively small

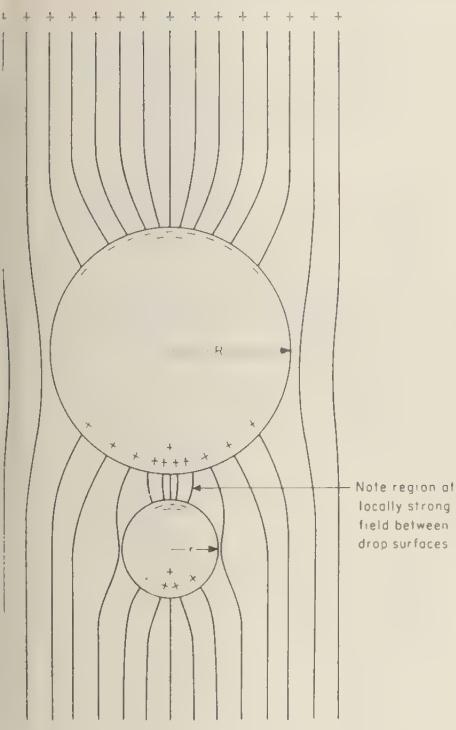


Fig. 2. Schematic showing effect of two uncharged cloud droplets on a uniform electrostatic field.

droplet with net positive charge and one relatively larger droplet with a net negative charge. Because of their differential settling velocity, a virtual current is produced. Some of the larger droplets will, after a while, coalesce with droplets smaller than themselves and thereby grow. The larger droplets tend to acquire charges of opposite sign to the smaller; consequently the charge-transfer process aids droplet growth, and charge transfer between these larger droplets will be greater because of their increased size. The larger droplets, in the presence of an electrostatic field, tend to absorb smaller droplets (through coalescence) and electrons (through collision) while continuing to build the field as a consequence of their greater fall velocity. Thus the larger cloud droplet acts like an electrostatic sponge, by acquiring both electric charge and water as the result of collisions with smaller cloud droplets.

As a cloud-charging mechanism, the process is probably considerably more efficient when the cloud particles are in the solid state as ice crystals, graupel, and hail. The decreased fall velocity due to the larger surface-to-mass ratio of the ice forms is far outweighed by their rapidity of growth, larger dimensions, and lower coalescence efficiency following collision. In what has been said previously and in that which follows, however, liquid elements are considered almost exclusively. First, cloud-charging mechanisms must be capable of explaining the warm-cloud lightning observed by Foster [1950] and by Moore, Vonnegut, Stein, and Survilas [1960]. But, more importantly for the purposes of this paper, the hydrodynamic and electrostatic theory as well as actual cloud measurements are more

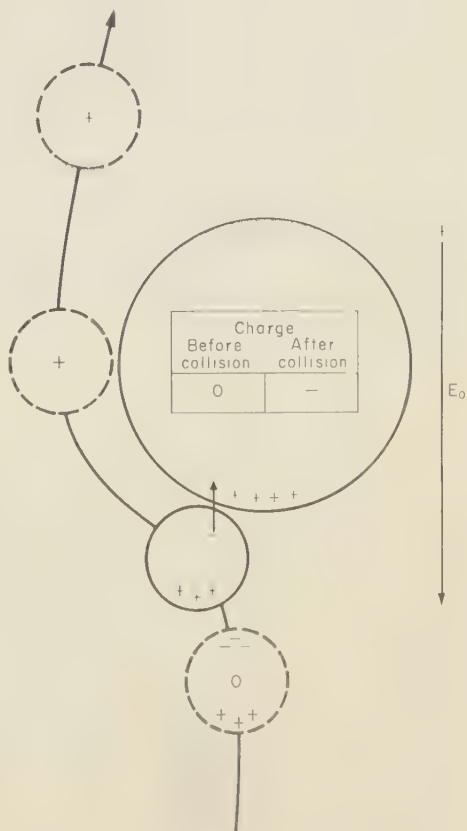


Fig. 3. Electrical action between cloud droplets during a close passage.

appropriately applied to cloud drops which for theoretical purposes may be considered spheres over a great range of sizes.

Quantitative considerations. The magnitude of the charge transferred between droplets colliding in line with the field is

$$q_0 E r^2$$

where E is the ambient electrostatic field, r the small drop radius, and q_0 is the charge-transfer coefficient. Table 1 lists a few typical values of q_0 , given by Davis [1960], as a function of the ratio of the radius of the large drop R to that of the small drop r . It can be seen from Table 1

TABLE 1

R/r	q_0 esu
1	5.5×10^{-3}
2	7.0×10^{-3}
5	8.8×10^{-3}
10	9.9×10^{-3}
100	10.8×10^{-3}

that the value of q_0 depends weakly on the ratio of the radii of the large and small drops. Using expression (1) for the charge transfer in a cloud containing the electrostatic field E , one can show that the rate of charge transfer between droplets per unit volume, $\partial \rho / \partial t$, is given by

$$\frac{\partial \rho}{\partial t} = n_i N_j \pi R_i^2 (V_i - v_i) \epsilon_{ij} E q_0 r_i^2 \quad (2)$$

where n_i refers to the concentration of drops in the i th size interval; N_j refers to the concentration of drops in the j th ($j > i$) size interval; R_i and r_i are, respectively, the radii of the larger and smaller drops corresponding to the concentration N_i and n_i ; V_i and v_i refer similarly to their terminal velocities; ϵ_{ij} is the percentage of the interacting droplets which subsequently separate.

Let us integrate this equation over an interval of time for which the variation of any of the elements is small. In this case, if at $t = 0$ the charge density (charges of both signs separated by the droplets in a unit volume) ρ , due to this cause, is zero,

$$\pm \rho = \mp [n_i N_j \pi R_i^2 (V_i - v_i) \epsilon_{ij} q_0 r_i^2] E t \quad (3)$$

The reversal of sign is due to the fact that charge is transferred in the opposite direction to that of $(V_j - v_i)$. The expression within the brackets we define as the charge separation coefficient Q_{ij} . Thus we can write

$$\pm \rho_{ij} = \mp Q_{ij} E t \quad \text{esu} \quad (4)$$

Let us assume that somewhere in the cloud the charges effectively form a parallel plate condenser that has a capacity per unit area of $C = 1/(4\pi H)$, where H is the separation. If σ is the surface-charge density on this hypothetical condenser and ϕ the potential difference between the plates,

$$\sigma = \phi C = \frac{\phi}{4\pi H} = \frac{-E}{4\pi}$$

where E is the electrostatic field. But associating plus charges with small droplets and minus charges with larger drops, the rate of growth of the electric field in the cloud is

$$\left(\frac{dE}{dt} \right)_{,,} = -4\pi \left(\frac{d\sigma}{dt} \right)_{,,} = -4\pi \rho_{ij} (V_i - v_i) - \lambda E$$

where λ is the specific conductivity in the cloud. Introducing ρ_{ij} from equation 4 and summing over all the droplet pairs, we have

$$\frac{dE}{dt} = 8\pi^2 \sum_i^K \sum_j^K n_i N_j r_i^2 R_j^2 (V_i - v_i)^2 \cdot \epsilon_{ij} q_0 E t - \lambda E \quad \text{esu} \quad (5)$$

Continuing to consider the droplet distribution as fixed and integrating, we obtain

$$\frac{E}{E_0} = \exp \left[4\pi^2 \sum_{j=1}^K \sum_{i=1}^K n_i N_j r_i^2 R_j^2 (V_i - v_i)^2 \cdot \epsilon_{ij} q_0 E t^2 - \lambda t \right] \quad \text{esu} \quad (6)$$

where E_0 is the field at the initial time $t = 0$.

QUANTITATIVE RESULTS

The equation for the enhancement of the field (6), was derived with the assumption that the droplet distribution and λ do not vary with time. In order that computations made with this equation apply to a cloud, we will start the computations after a period of time has elapsed sufficient to produce drops of the size used in the

computations. The growth of the field due to differential ionic migrations at the cloud boundary observed by *Moore, Vonnegut, and Botka* [1958] in the early stages of cumulus development may be accounted for later by using their values for the initial field. We are now saying that in order to obtain an order-of-magnitude approximation of the proposed cloud electrification process, we will make the following four simplifications:

1. Time in equation 6 starts after the first 15 or 20 minutes in order that the drops have time to grow appreciably.
2. The drop size distributions are fixed, thus n_i , N_i , r_i , R_i , and $(V_i - v_i)$ are constant and
 - a. The smaller cloud drop distribution agrees with that given by *Diem* [1948] and *Weickmann and aufm Kampe* [1953]. See Table 2.

TABLE 2

Cloud Drop Distribution after Diem (1948) and Weickmann and aufm Kampe (1953)		Raindrop Distribution after Blanchard (1953) Sample No. 27, Thunderstorm	
$n \times 10^4$	$n \text{ cm}^{-3}$	$R \text{ cm} \times 10$	$N \text{ cm}^{-3} \times 10^3$
2.5	150	0.05	11.2
5.0	550	0.15	0.68
7.5	250	0.25	0.23
10.0	50	0.35	0.055
12.5	30	0.45	0.120
15.0	20	0.55	0.066
		0.65	0.065
		0.75	0.044
		0.85	0.034
		0.95	0.050
		1.05	0.036
		1.15	0.017
		1.25	0.027
		1.35	0.010
		1.45	0.005

- b. The large drop distribution is taken directly from *Blanchard* [1953] and is his sample no. 27, a thunderstorm situation. See Table 2.
3. The value for q_0 is chosen to have the constant value 10^{-2} esu, since, as shown by Table 1, its total variation is small.
4. The efficiency of drop separation, ϵ_{ij} , is averaged over time and drop size. The results

will be displayed parametrically with $\overline{\epsilon_{ij}}$ equal to 0.008, 0.04, 0.1, 0.2, 0.3, and 0.5.

The cloud- and rain-drop distributions chosen are among the most favorable for the growth of the field; however, they do refer to cumulus and cumulonimbus clouds, the electrical activity of which we will attempt to demonstrate. The remaining approximations are more conservative. Because of the lack of measurements in the intermediate range, a portion of the drop size distribution is left out with the resultant loss of its contribution to the electrification. The early electrification due to conductivity difference inside and outside of the cloud is incorporated by taking an observed value of the field some minutes after the cloud has formed. All in all the net result of all approximations should be to provide a realistic or slightly conservative view of the field enhancement process.

Table 2 gives the actual values of the cloud parameters used in the computations. The results are shown in Figure 4, in which the abscissa is time and the ordinate is the ratio of the field at any time to the initial field. In applying the data from this graph one must always remember that the time employed here is the time elapsed since the ambient electrostatic field in the cloud was E_0 . Thus, for example, with an average droplet separation efficiency of 0.1, an initial field of the

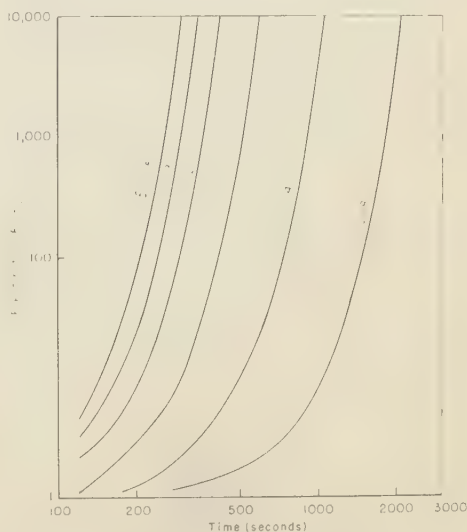


Fig. 4. Increase of field ratio with time for six droplet-separation efficiencies.

order of 1 volt/cm becomes a field of the order of 1000 volts/cm after an elapse of time of approximately $8\frac{1}{2}$ minutes. One thousand volts per centimeter is a large value for a field in clouds, even for thunderstorms. The period of $8\frac{1}{2}$ minutes is about right for the time, when it is recalled that it takes 15 to 20 minutes to form the drop distribution used in the calculations. The initial field after 15 to 20 minutes is probably more likely of the order of 10 volts/cm than 1 volt/cm because of the boundary charging effect, observed by *Moore, Vonnegut, and Botka* [1958]. If this is the case, the field of 1000 volts/cm will be reached after approximately 7 minutes instead of $8\frac{1}{2}$ minutes.

DISCUSSION OF RESULTS

Different values of the charge-interaction efficiency give widely different results in terms of the growth of the field. Little information is available, however, on the value of the charge-interaction efficiency that is directly applicable to clouds, although a recent paper by *Goyer, McDonald, Baer, and Braham* [1960] gives some values of the coalescence efficiency of 600- to 790-micron diameter drops for drops around 100 microns in electrostatic fields of varying strength. The charge-interaction efficiency will be equal to or greater than one minus the coalescence efficiency.

Charge-interaction efficiencies derived from the Goyer, McDonald, Baer and Braham data are shown in Table 3; they may be too small, in moderate-to-strong fields, due to droplets that fail to collide but come close enough for corona or arc discharge between them. On the other

hand, the efficiencies may be high, since the observed coalescence efficiencies were obtained in a range of ambient humidity of 50 per cent. In any event, values for the charge-interaction efficiency used in these calculations appear reasonable.

If the coalescence efficiency does increase with increasing humidity, as demonstrated in the laboratory by *Prokhorov* [1954], an interesting side light appears. Since a smaller coalescence efficiency (larger charge-interaction efficiency) provides more charge-separation encounters, those clouds with the greatest amount of entrainment of environmental air are favored (all other things being equal) for strong electric fields. In this way, swelling cumulus clouds, with their violent mixing and with roots in the lower moist layers but growth into drier upper levels, are favored for electrical activity. They are favored according to the theory for other reasons also. The rapid cooling of the air in the stronger updrafts favors the activation of a large number of nuclei giving greater droplet concentrations of droplets N_i and n_i . Strong vertical accelerations of the air and great depth of cloud allow adequate separation of charge due to differential settling of the drops through a distance equal to the product of the maximum drop velocity difference $(V_i - v_i)_{\max}$ and the total time. In the earlier sample, $(V_i - v_i)_{\max} = 980$ cm/sec, so that these charges are separated by almost 5 kilometers after $8\frac{1}{2}$ minutes.

It may be noted that below the main negative charge center in a thunderstorm, i.e., between the negative center and its positive image at the surface, encounters between particles will provide a negative charge for the smaller and a positive charge for the larger. The existing field is enhanced again and the observed positive rain and positively charged region in the center of the heaviest precipitation zone is provided for by the theory.

DISCUSSION OF CHARGE TRANSFER PROCESS

The proposed charge-separation and cloud electrification process is quite general. Employment of the exact solution for the field between two spheres provides analytical substantiation of the existence of a charge-transfer mechanism as well as precise calculations of its magnitude. The theory encompasses solid as well as liquid cloud elements. To the extent that collision

TABLE 3. Charge-Interaction Efficiencies Estimated by Taking One Minus the Coalescence Efficiency Given by *Goyer, McDonald, Baer, and Braham* [1960] in Their Table 1

Field strength volts/cm	Charge-interaction efficiency [1 - (coalescence efficiency)]
0.0	.706
3.1	.665
15.4	.113
38.4	.047
923.0	*

* No collision or coalescence obtained due to strong like charges acquired by induction when drops are produced in this high field.

hout combination occurs between the cloud particles in an electrostatic field, the mechanism must appear in all clouds. In fact, the arrangement of charges on individual cloud elements and all configuration of charge areas should be largely dominated by this process, although free charges may be provided by other processes such as freezing, melting, condensation, evaporation, fusion, or collision with ions.

Phillips and Kinzer [1958], with reference to their observations of a rather heterogeneous distribution of charges, object that 'no accepted electrification mechanism is capable of producing such a charge mixture.' Their objection does not apply to the present theory. It is an essential consequence of the present theory that a mixture of charges appears throughout the major portion of the cloud except where lightning discharges, the cloud boundary phenomena, or other mechanisms provide restricted regions of unipolar charge of considerable intensity.

This general theory may be thought of as containing, as special cases, the theories of Elster and Geitel [1913] and of Müller-Hildebrand [1954]. Elster and Geitel considered that the cloud drop simply pick up charge from collisions with the relatively much larger but polarized rain drop. Müller-Hildebrand invoked collision between ice crystals and graupel polarized by an electrostatic field. Whereas the other theories consider special particles and size groups or one phase only, the present theory considers collisions between cloud elements of all physical states and relative sizes and permits quantitative computations for spherical particles. Either the Elster and Geitel theory or that of Müller-Hildebrand could provide a part, or possibly most, of the observed electrification when the special conditions required by them are met within the cloud.

The cloud electrification hypothesis of Wilson [1929] is, in a less direct way, a special case of a more general theory. By considering the ions and very small charged droplets, the theoretical derivations of Davis [1960] and Sartor [1960] for droplet pairs are applicable to the polarized droplets and ions invoked by the Wilson theory. The effect of the Wilson theory was determined to be small compared with the contribution due to the droplet pairs used and therefore was neglected. The effect of the dynamic motions in the cloud has not been included. These larger scale motions are assumed to act alike on all of the cloud

particles and although gross translations occur, the relative electrical distributions are thought of as being unaffected. The vertical upward accelerations will be effective in increasing the rate of separation of the smaller and larger droplets. Incorporating the effect of the acceleration would increase the rate at which the electrostatic field grows so that here again the estimates made are conservative.

CONCLUSIONS

The proposed cloud-electrification mechanism is capable of producing charges of the magnitude observed in clouds, and, by using reasonable approximations for drop distributions in clouds, it can produce electrical fields in clouds which are of the order of magnitude of those observed in thunderstorms within the period of time in which they are known to form. The mechanism is applicable to both ice and water clouds when the shape of the particles is properly accounted for.

Acknowledgments. I would like to express my appreciation for many rewarding discussions with Dr. John W. Kern and Dr. M. H. Davis on the nature and application of the electrical aspects of the theory.

REFERENCES

- Blanchard, Duncan C., Rain-drop size in Hawaiian, rains, *J. Meteorol.*, **10**, 457-473, 1953.
- Davis, M. H., The forces between two spheres in a uniform field, to be published as *RM-2607*, The RAND Corporation, Santa Monica, Calif., 1960.
- Diem, M., Messungen der Grosse von Wolkenelementen, II, *Met. Rundschau*, **1**, 261-273, 1948.
- Elster, I., and H. Geitel, Zur Influenztheorie der Niederschlags Elektrizität, *Phys. Z.*, **14**, 1287, 1913.
- Foster, H., An unusual observation of lightning, *Bul. Am. Meteorol. Soc.*, **31**, 140-141, 1950.
- Goyer, G. G., J. E. McDonald, F. Baer, and R. R. Braham, Effects of electric fields on water-droplet coalescence, *J. Meteorol.*, **17**, 442-445, 1960.
- Hocking, L. M., The collision efficiency of small drops, *Quart. J. Roy. Meteorol. Soc.*, **85**, 44-50, 1959.
- Moore, C. B., B. Vonnegut, B. A. Stein, and J. J. Survilas, Observations of electrification and lightning in warm clouds, *J. Geophys. Research*, **65**, 1907-1910, 1960.
- Moore, C. B., Bernard Vonnegut, and Alexander T. Botka, Results of an experiment to determine initial precedence of organized electrification and precipitation in thunderstorms, *Recent Advances in Electricity*, Pergamon Press, New York, 1958.
- Müller-Hildebrand, D., Charge generation in thun-

- derstorms by collision of ice crystals with graupel, falling through a vertical electric field, *Tellus*, 6 (4), 367, 1954.
- Phillips, B. B., and G. D. Kinzer, Measurements of the size and electrification of droplets in cumuloform clouds, *J. Meteorol.*, 15, 369-374, 1958.
- Prokhorov, P. S., The effects of humidity deficit on coagulation processes and the coalescence of liquid drops, *Discussions of the Faraday Society*, No. 18, 41-51, The Faraday Society, Aberdeen University Press Ltd., Aberdeen, 1954.
- Sartor, D., A laboratory investigation of collision efficiencies, coalescence and electrical charging of simulated cloud droplets, *J. Meteorol.*, 11, 91-103, 1954.
- Sartor, J. D., The mutual attraction of cloud droplets in the electrostatic field of the atmosphere, *The RAND Corporation, P-1824*, Santa Monica, Calif., 1957.
- Sartor, D., Some electrostatic cloud-droplet collision efficiencies, *J. Geophys. Research*, 65, 1953-1957, 1960.
- Weickmann, H. K., and H. J. aufm Kampe, Physical properties of clouds, *J. Meteorol.*, 10, 204-211, 1953.
- Wilson, C. T. R., Some thunderstorm problems, *Franklin Institute J.*, 208, 1-12, 1929.

(Manuscript received December 19, 1960.)

Effects of Wind-Induced Advection on Sea Surface Temperature

L. E. EBER

*U. S. Bureau of Commercial Fisheries
Biological Laboratory, Stanford, California*

Abstract. Wind-induced advection is one of the mechanisms through which conditions in the surface layer of the ocean can be affected by atmospheric fluctuations. An attempt was made to assess the relative importance of this mechanism in the northeast portion of the Pacific Ocean for two periods, fall 1957 and winter 1957-1958. Sea conditions were represented by sea surface temperatures averaged over the middle 10 days of each month and by anomalies of these 10-day means from long-term monthly normals. Anomalous sea temperature advection was determined by using surface water displacements computed solely from monthly mean geostrophic wind anomalies. Observed sea temperature anomaly changes within each of the two seasons were then compared with the computed advective sea temperature anomalies. Good agreement was found for the winter period and poor agreement for the fall period. The results for the winter period (but not for the fall period) showed a stronger correlation between computed advective and observed sea temperature anomalies than was found earlier by Namias for the same two cases. The principal modification to Namias's procedure which was made in the present study involved an attempt to take into account the initial state. It was concluded that advection may have had a dominant effect on sea surface temperature in the winter case, but was subordinate to other processes during the fall case.

Introduction. Large-scale anomalies of substantial magnitude are known to occur in monthly and seasonal mean distributions of sea surface temperature. Empirical evidence has pointed to the existence of an interrelationship between sea surface temperature and the surface wind, but the relative importance of various wind-connected mechanisms, such as advection or upwelling, has not been conclusively established.

Namias [1959] attempted to clarify the role of wind-induced advection in the production of sea temperature anomalies by comparing observed anomalies in the northeast Pacific with independent estimates of wind-induced advective anomalies. His procedure is described in the paper cited. Briefly, it entails the computation of wind-induced displacements of surface water from monthly mean sea level pressure anomaly charts, using the geostrophic relation to determine wind from pressure, and Ekman's empirical formula relating wind speed to surface water current, expressed as follows:

$$v/w = 0.0127 / \sqrt{\sin \phi}$$

where v is the speed of the surface water current,

w is the wind speed, and ϕ is latitude. The direction of the surface wind drift was assumed to be 45° to the right of the wind.

By superimposing the displacement vectors onto the normal sea surface isotherms appropriate to the season, Namias obtained a computed seasonal temperature anomaly due to the advection of surface water by the anomalous wind.

Observed seasonal sea temperature anomalies were obtained from 10-day mean anomaly charts prepared by Bureau of Commercial Fisheries Biological Laboratory, Honolulu. The 10-day anomalies represent the deviations of temperatures, averaged over the middle 10 days of each month, from monthly normals published by the U. S. Hydrographic Office [1944].

Comparing the corresponding fields of observed and computed anomalies for several seasons during 1957, Namias found a small measure of agreement in the broad-scale patterns. Considering this outcome in view of the assumptions made in computing the advective changes, and the neglect of nonadvective processes, he concluded that effects other than simple surface

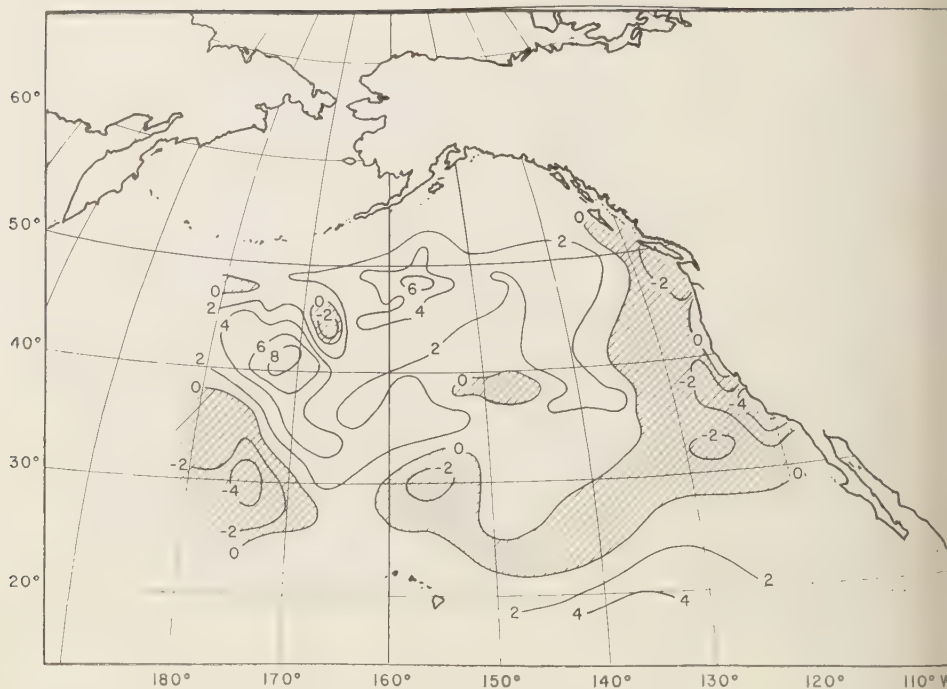


Fig. 1. Observed change of sea surface temperature anomalies ($^{\circ}\text{F}$) between September 11-20, 1957, and November 11-20, 1957.

advection must contribute significantly to the observed anomalies.¹

The strength of this conclusion, however, is weakened by the acknowledged fact that the computations were subject to stringent assumptions. If advection in the real ocean has a more dominant influence on sea temperatures than is indicated by Namias's results, the removal of one or more of these assumptions should reveal a closer agreement between computed and observed patterns.

Implicit in Namias's procedure is the assumption

¹ In a personal communication to the author, Namias has indicated that his latest studies suggest better agreement than he had expected between observed sea surface temperature anomalies and those computed by the above method when the period of averaging is a month rather than a season. Furthermore, he considers the sea surface temperature charts, currently prepared by the Bureau of Commercial Fisheries, which represent averages for full months rather than only for the central 10 days to be an obvious improvement for studies of this kind.

tion that the ocean current velocities were initially normal, and that the only deviation from normal occurring during the period of computations were those induced by the anomalous winds. As Namias noted, little can be done toward removing this assumption until our knowledge of the ocean currents is greatly augmented.

A further limitation inherent in his procedure also pointed out by him, is the assumption that sea temperatures were normal in the initial state. Since this condition is frequently not satisfied in the real ocean, a more realistic approach would be to determine the change in the anomaly of sea surface temperature, between the beginning and end of a period, for comparison with the computed effects of advection by anomalous winds.

Two of the seasons investigated by Namias (fall 1957 and winter 1957-1958) were characterized by substantial temperature anomalies at their onset, that is, in September 1957 and December 1957, respectively. In consequence of

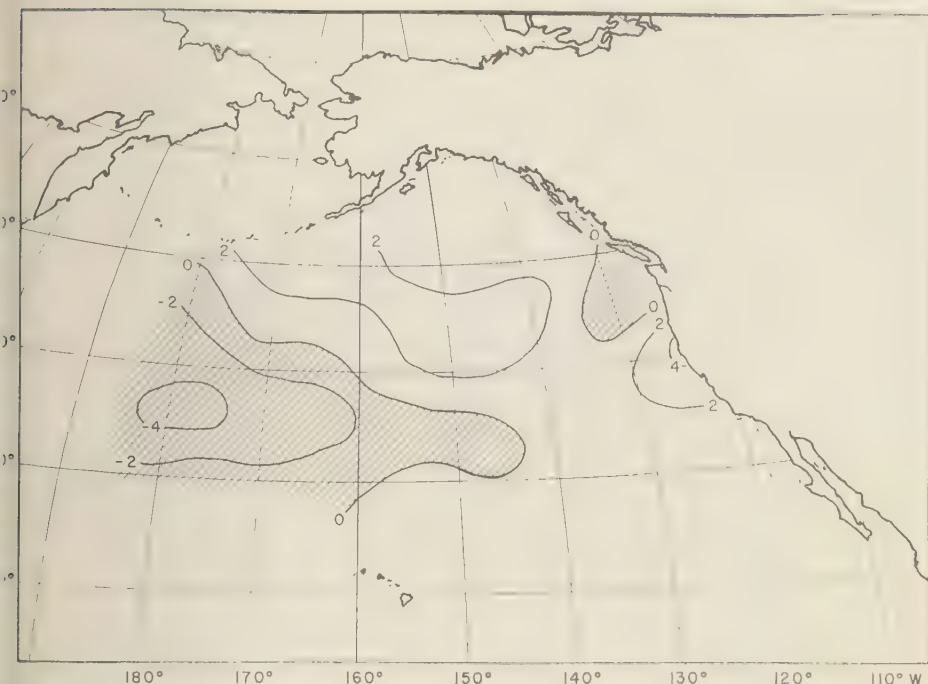


Fig. 2. Advective anomalies of sea surface temperature computed for the period September-October, 1957.

the considerations mentioned above, it appeared worthwhile to examine the within-season changes in the observed anomalies for these two cases to see whether they would reveal a closer correspondence with computed advective changes than the average seasonal anomalies.

Computation of observed and advective anomaly change. Observed anomaly changes were computed by graphical subtraction from the same source data that Namias used. For example, the difference between the anomaly charts for September 11-20 and October 11-20, 1957, was taken as the 1-month change from mid-September to mid-October. One-month anomaly changes were also computed for mid-October to mid-November, 1957; mid-December, 1957, to mid-January, 1958; and mid-January to mid-February, 1958.

Similarly, 2-month anomaly changes were obtained for mid-September to mid-November, 1957, representing the fall case, and for mid-September, 1957 to mid-February, 1958, representing the winter case.

Independent computations of anomalous wind-induced advective temperature changes were made by using a procedure analogous to that followed by Namias, that is, by determining surface water displacements from geostrophic wind data and Ekman's wind-water current relationship, and superimposing the results on isotherm charts to arrive at an estimate of temperature advection. The procedure differed from that of Namias in that the winds were derived from monthly, instead of seasonal, anomalies of sea level pressure and the isotherm charts used represented the particular months under investigation, rather than long-term normals.

Charts of computed advective anomaly change were prepared for the months of September, October, and December, 1957, and for January 1958. The charts for September and October, and similarly those for December and January, were combined to give charts of advective changes for 2-month periods.

Results. The monthly charts of anomaly

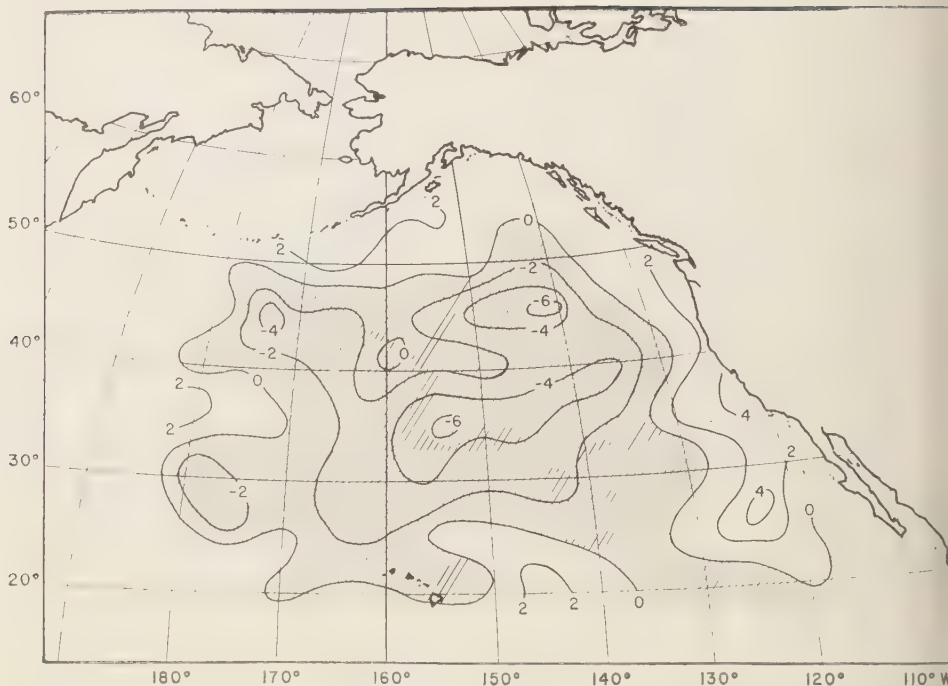


Fig. 3. Observed change of sea surface temperature anomalies between December 11-20, 1957, and February 11-20, 1958.

change are not reproduced and will be discussed only briefly. Since the observed charts represent approximately mid-month to mid-month intervals and since the advective charts represent calendar months, the respective periods of corresponding observed and advective changes overlap by 50 per cent at most. An examination of all such overlapping pairs without any consideration of lag, revealed little or no evidence of correlation. However, the month-to-month fluctuations in both sea temperature and pressure anomaly patterns were found to be large; hence the mismatching of periods may have obscured any relation between causal influences and effects.

The computed and observed anomaly changes for 2-month intervals are shown in Figures 1, 2, 3, and 4. Here a more critical comparison of computed and observed values can be made, since their respective periods have a 75 per cent overlap.

Examining first the charts for fall 1957, we

see a more complex pattern in the observed anomaly changes for mid-September to mid-November (Fig. 1) than in the advective changes for September-October (Fig. 2). Both charts show generally positive anomaly changes in the Gulf of Alaska and in the adjacent region southward to about 40°N. However, the anomalous warming in excess of 4°F which appears in Figure 1 between 45°-50°N, 155°-160°W does not occur in the chart for advective changes (Figure 2). Along the west coast of North America there is fair agreement in the region of British Columbia and Washington, but contradictory values occur farther south. In both charts regions of anomalous cooling appear to the northwest of Hawaii, with minima below -4°F. The centers of these minima, however, are displaced from each other by nearly 500 miles. The greatest discrepancy occurs south of the Aleutians near 40°N, 170°W, where Figure 1 shows anomalous warming of more than 8°F while the advective chart indicates cooling. The

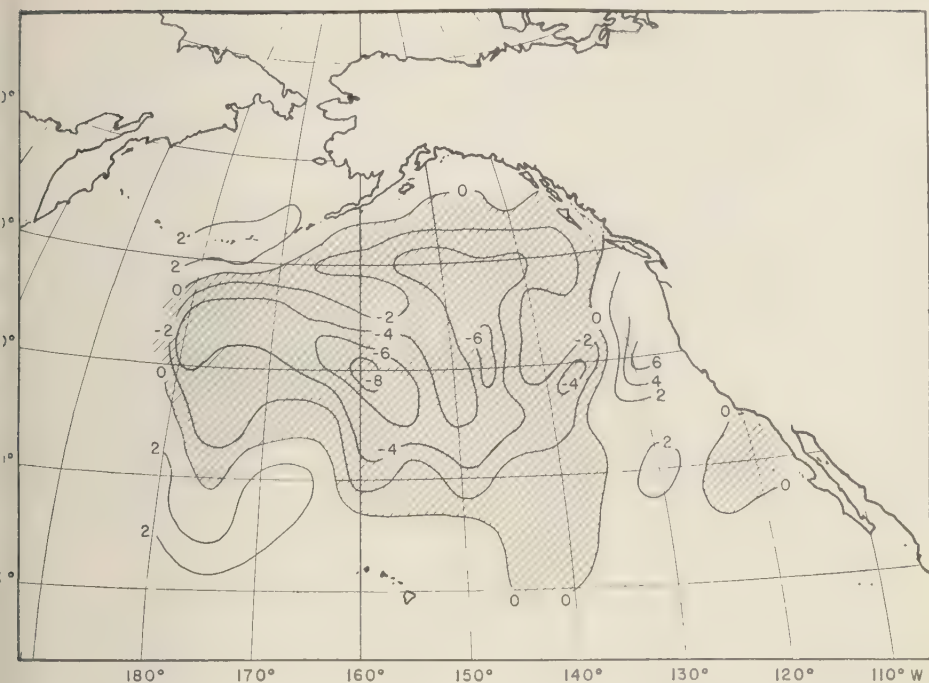


Fig. 4. Advective anomalies of sea surface temperature computed for the period December, 1957-January, 1958.

While suggestive similarities can be seen in the large-scale features of the two charts, the over-all agreement is rather poor.

Certainly, the argument for advection is not advanced in this case by substituting the within-season anomaly changes (Fig. 1) for the mean seasonal anomalies shown by Namias (Fig. 4 of his report). It should be mentioned that Namias's computed advective anomalies for fall 1957 (Fig. 14 of his report), although generally similar to Figure 2, indicate much greater cooling in the vicinity of 40°N, 170°W. Moreover, the distribution of negative advective anomalies shown on Namias's chart for this area appear to correspond to a similarly situated, although less intense, center of minimum values in his observed anomaly chart for the same season. However, the latter feature reflected a condition already present at the beginning of the season (Sept. 11-20) and might not be related to the average advection throughout the season.

The results for the winter of 1957-1958 are

quite different. The observed temperature anomaly changes over the interval December 11-20, 1957, to February 11-20, 1958 (Fig. 3), show a striking similarity in general pattern and magnitude to the advective changes computed for December 1957 and January 1958 (Fig. 4). Both charts show anomalous cooling over most of the region from 25° to 50°N and 135° to 175°W. Positive changes also prevail over most of the surrounding areas in both cases. Discrepancies can be seen in the small-scale features on the two charts, but these do not detract from the over-all likenesses to the extent found in the fall of 1957.

Again, when the results are compared with Namias's work, it can be stated that the computed advective anomaly patterns agree substantially better with the observed within-season anomaly changes (Fig. 3) than with the observed mean anomalies for winter 1957-1958 shown in Figure 5 of his report. The advective anomalies shown in Figure 4 for this case also agree well

with those computed by Namias for the winter season (Fig. 15 of his report).

Discussion. One might interpret these results as indicating that advection was a dominant factor during the winter but played a subordinate role to other influences during the fall. That such a hypothesis is at least tenable is suggested by a statistical study of monthly mean geostrophic wind components and sea surface temperatures observed at British Columbia shore stations. This work (to be published), based on a 19-year period, showed a significant correlation between wind and temperature anomalies in winter months but negligible correlation in late summer and early fall months.

One factor which may affect the relative effect on sea surface temperature of various mechanisms, at different times of the year, is the seasonal variation of thermal structure in the upper 100 meters or so of the sea. For example, intermittent wind mixing would be more likely to cause fluctuations of surface temperature in summer when the thermocline is typically shallow than in winter when a deep isothermal surface generally prevails.

Another aspect of the question which deserves closer scrutiny is the descriptive accuracy of the observed sea temperature anomalies. Some of the anomalous features found on the 10-day-mean charts used in the present study may be tran-

sient phenomena, possibly due to meandering currents, particularly in regions of strong horizontal temperature gradients. If the magnitude of such short-period fluctuations were large they would obscure the characterization month-to-month or longer-period fluctuations.

It is apparent that a quantitative account of anomalous temperature changes in the sea still lies ahead. However, promise of accelerated progress is offered by pending developments in instrumentation and new interest in oceanography. These can reasonably be expected to provide better information on the velocity and thermal structure in the upper layers of the sea as well as improved observational coverage for evaporation, precipitation, cloud cover and radiation, and more accurate determinations of momentum transfer due to wind stress. All these factors are probably significant in the formation of sea temperature anomalies.

REFERENCES

- Namias, Jerome, Recent seasonal interactions between North Pacific waters and the overlying atmospheric circulation, *J. Geophys. Research*, 64: 631-646, 1959.
U. S. Hydrographic Office, *World Atlas of Sea Surface Temperatures (H.O. 225) 2nd ed.*, 1944.

(Manuscript received October 14, 1960.)

The Principal Factors Influencing the Seasonal Oscillation of Sea Level

EUGENIE LISITZIN

*Institute of Marine Research
Helsinki, Finland*

AND

JUNE G. PATTULLO¹

*Scripps Institution of Oceanography
University of California, La Jolla, California*

Abstract. From the results of the tide gage data recorded during the IGY it is shown that the seasonal variation of sea level is mainly *isostatic*, at least in most oceanic areas of the Pacific. In low and subtropical latitudes the 'steric' term is predominant; in higher latitudes variation of air pressure is the more important factor. The boundary between the two zones runs approximately along the latitude of 40°–45°N.

INTRODUCTION

The improved distribution of tide gages in the Pacific Ocean during the International Geophysical Year has made it possible to give a comprehensive description of the seasonal variation of sea level [Pattullo, in press].² One is now able to compare these results with some of the factors which influence changes in sea level. We have selected for study two of these factors: variations of atmospheric pressure and changes in the specific volume of the water.

Both of these factors vary considerably with season. Furthermore the two terms considered together give the 'isostatic' portion of the change in sea level. At any depth below which seasonal variations in specific volume practically disappear, a pressure gage would indicate no seasonal variation in the total mass of water plus air. The *nonisostatic* portion of the observed variations of sea level therefore represents a seasonal change in the total fluid mass above the sea floor. The time variations in the horizontal distribution of total mass are of some interest in geophysics.

THE DATA

Atmospheric pressure. The distribution of air mass over the ocean varies markedly throughout the year. A small part of this change represents varying *total* mass over the oceans as the air moves, for example, over Siberia in the northern hemisphere in winter and over the oceans of this hemisphere during the warm season. This part cannot contribute materially to changes in level and must be eliminated from the computations. The water can be expected to respond to the local pressure changes as an 'inverted barometer,' standing at a low level when the atmospheric pressure is high, and vice versa. The effect is nearly 1-cm change in water level for each 1-mb change in atmospheric pressure; it has been discussed by numerous writers for different parts of the sea. In the Pacific, seasonal variations in air pressure are largest in the northerly parts of the ocean, with highest pressures in summer and lowest in winter. At Attu and Adak in the Aleutian chain it can be seen that the sea levels respond to these pressure changes almost as one-to-one mirror images (Fig. 1). Farther down the North American coast toward San Francisco, however, the air pressure changes diminish, and it is evident that sea level is not, in these latter cases, simply an inverted barometer.

The inverted barometer effect of seasonal changes in air pressure was computed by quarters

¹ Now affiliated with the Department of Oceanography, Oregon State College, Corvallis, Oregon.

² For the coast of Australia the sea level results of the IGY are presented by Hamon and Stacey [in press], and for the tide gages in the Soviet Union the preliminary results are given by Selitskaya [1959].

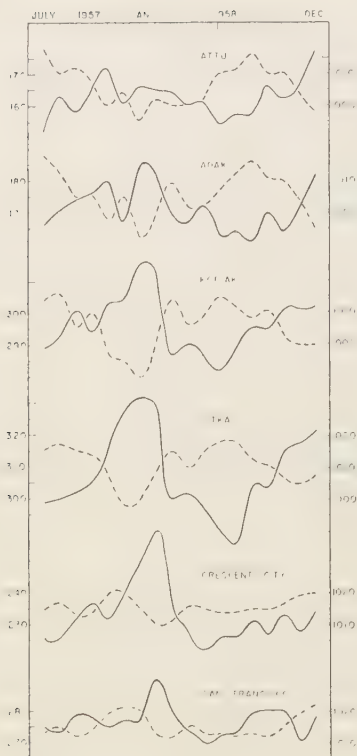


Fig. 1. Sea level in centimeters (solid lines), atmospheric pressure in millibars (dashed lines), at tide gages from the Aleutians to San Francisco. All values are monthly means for the period of IGY. Note that sea levels are measured above an arbitrary zero point that is different for each locality.

at a grid of points, with a 10° interval between the points, for all of the Pacific Ocean, from the average pressure charts given in the *Marine Atlas* [1953].

Specific volume. It has previously been shown by a number of writers that changes in the specific volume of the water are related to changes in recorded sea levels at some localities. A few examples of 'steric levels,' the deviation from mean annual sea level due to changes in specific volume of the water, are shown in Figure 2. Observed deviations from mean annual sea level, recorded from a nearby gage, are included for comparison. It is, of course, impossible as yet to measure temperature and salinity variations and sea level variations at exactly the same points.

The former must be done in deep water, and the latter at the coastline. In spite of this difficulty there is, in some cases, a good agreement between the recorded and the steric levels [Pattullo, Munk, Revelle, and Strong, 1955].

The curves shown in Figure 2 have been selected to illustrate the varying degree of agreement between the recorded and steric levels. The two are apparently very similar at Honolulu and remarkably dissimilar, for example, at Adak.

The Island Observatory Program during the IGY has made it possible to compute the steric term at a number of oceanic locations in addition to those given earlier by Pattullo, Munk, Revelle, and Strong [1955]. Quarterly averages of steric level deviations were calculated, using both IG

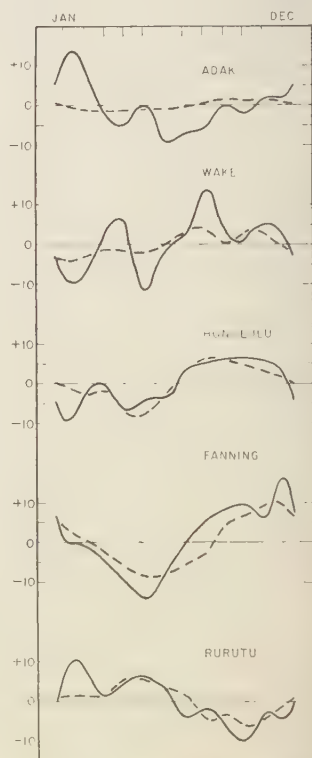


Fig. 2. Sea level in centimeters (solid lines), nearby steric levels in centimeters (dashed lines), for selected tide stations. Values are monthly deviations from annual means, determined from data collected during IGY, except at Adak, where earlier steric data are used (see Aleutians, Fig. 3).

and earlier data, and contour charts were constructed by approximately linear interpolation between available data. Owing to unfortunately large distances between the observational points in some regions the contours could be considered only approximate in position, of course. Nevertheless they showed quite distinctly that the seasonal deviations in steric levels are largest in low latitudes and become almost negligibly small at high latitudes, which is just the inverse of the effect of changes in air pressure. The locations of all steric data used are shown in Figure 3.

The isostatic term. The pressure and 'steric'

contributions have been summed to form the 'isostatic' variations in sea level. (The contour charts of steric level were read to provide values at the same grid points as were read for air pressure. Owing to lack of steric data the charts extend south only about to the latitude of New Zealand—30° to 40°S.)

The pressure and steric terms contribute in approximately equal amounts, but usually not in the same parts of the oceans. (One exception to this generality is in the area of Japan, where both terms contribute significantly [Miyazaki, 1955].) The pressure term is by far the more

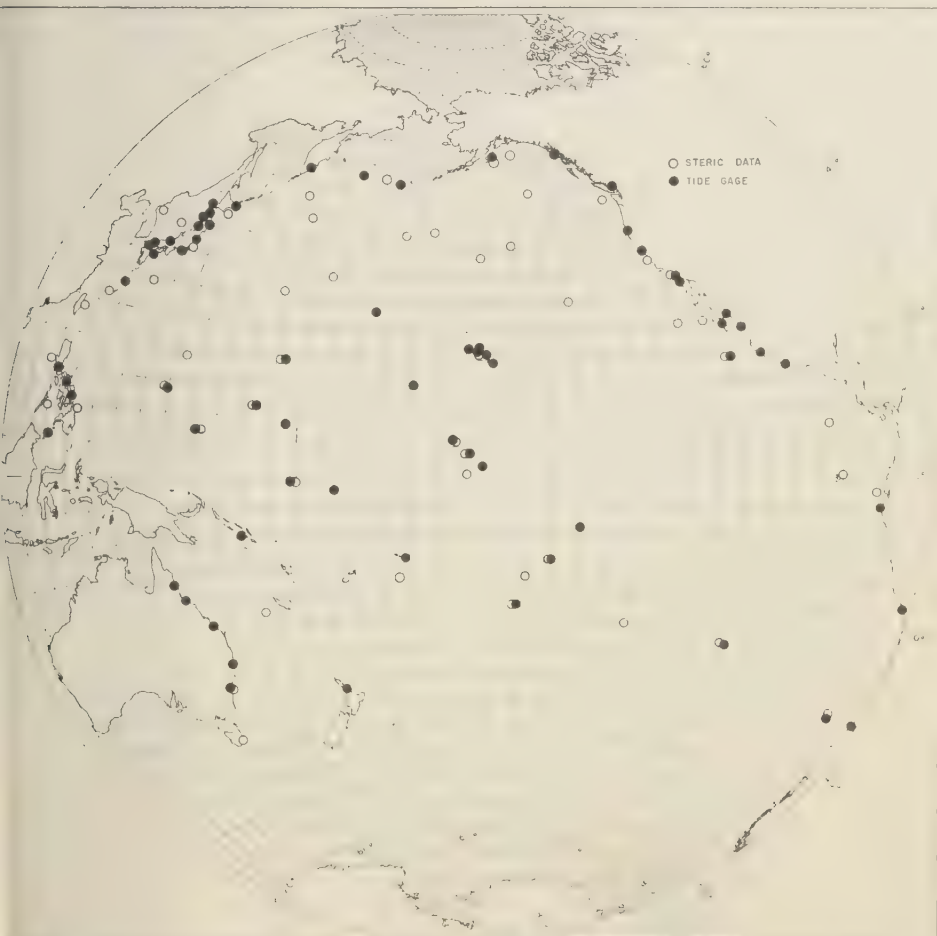


Fig. 3. Locations of tide gages (solid circles) and temperature and salinity data (open circles) used in this study.

important in the northern portion; the steric term prevails in low latitudes; the boundary between the two regions is, in the northern hemisphere, about 40° to 45°N . Owing to lack of steric data in the far south this boundary, if it exists, cannot be determined for the southern hemisphere.

THE RESULTS

Isostatic deviations. The combined effects of changes in specific volume and in air pressure are represented by the contours on Figures 4 through 7. These contours are *not* drawn to conform to the vertical numbers entered on these charts; the numbers represent observed deviations and will be discussed below.

The zero lines indicate the principal character of the seasonal oscillation. In March and September it is principally latitudinal; in June and December there is an additional longitudinal term. If we compare the maps for March and September with each other and leave out of consideration the more or less isolated and closed curves near mid-ocean, we note that the general features of the two months are the inverse of one another. In areas where we have positive data in March, we note negative deviations in September, and vice versa. The departures are, moreover, of the same magnitude. The inversion of the values is also characteristic of the months June and December, although the differences between the shapes of the particular corresponding curves are, for these months, more pronounced than for the former pair.

Recorded deviations. The numbers on the maps indicate the height of the recorded sea level, referred to the yearly average and given as the mean for February through April, May through July, etc. As it was impossible to enter all the recorded sea level data on the maps in restricted areas with a great number of tidal stations, such as Japan, a more or less arbitrary choice had to be made.

The locations of the tide gage stations used in this study are shown in Figure 3. Sea level records for most of the stations refer to the International Geophysical Year; the monthly means have been collected and published by the Permanent Service for Mean Sea Level [*Assoc. Océan. Phys.*, 1959]. To avoid leaving extensive areas with no data at all, means for earlier years were used at Vancouver, Talara, Matarani, Valparaiso, Samoa,

Guadalcanal, and Auckland [from *Pattullo, Munk, Revelle, and Strong*, 1955]. To mark their non-IGY origin, these data are given on the maps in parentheses.

Before we proceed to examine the results shown on the individual maps it should be noted that at least some of the discrepancies are due to the use of observational data which are not synoptic. Some of these effects can be determined, but most of them probably remain undetected.

Figure 4. February, March, April. As was mentioned earlier, the isostatic term is negative over most of the North Pacific and positive in the South Pacific, with largest absolute values of about -10 cm near Japan. The recorded values are, in general, in remarkably good agreement with these features except along certain coast lines. The greatest discrepancy occurs along the coast of Mexico, where we find a negligibly small isostatic term but large negative deviations. The recorded and isostatic deviations agree in sign along northeastern Australia and around Japan but the recorded deviations are appreciably larger. Finally, at the U. S.-Canadian border and at one tropical island (Kwajalein) the recorded values are positive while the isostatic ones are negative.

The last two of these discrepancies are probably due to inadequacies in the data being compared. Air pressure data from the IGY lead to positive isostatic deviations at the U. S.-Canadian border which agree with the positive deviations recorded during the same period of time. In the western tropical Pacific the steric computations showed large changes in magnitude and even in sign over relatively short distances and the 'smoothed' average pattern we have used probably cannot be expected to represent the details of the actual isostatic pattern during any one particular year.

However, the differences between the isostatic and the recorded amplitudes along the continental coasts appear to be well established and real and they probably reflect nonisostatic processes operative in these areas.

Figure 5. May, June, July. The principal feature of the average isostatic pattern during this season is a region of negative departure covering all of the central ocean from the Aleutians to about 20°S , and this is in good agreement with the sea level deviations as recorded during the IGY. As in the preceding season, recorded

values along Mexico are numerically larger than the isostatic ones, and gages in the Gulf of Alaska show larger negative deviations than the isostatic patterns suggest. Again, a few of the island stations do not conform either to the isostatic pattern or to the recorded deviations at other lands in the same area: Johnston with -9 cm and Wake with -4 cm are notable. As before, it seems probable that the discrepancies among the islands are due principally to the comparison of nonsynoptic data. For example, sea temperatures near Johnston were lower in June 1958 than during the years for which our average isostatic pattern was drawn. If these 1958 temperatures had been used to compute the steric level in this area, the isostatic deviation would have a larger negative value which would be in better agreement with the recorded value for IGY (1957-1958). Similarly, the air pressure pattern during the IGY was not identical with the average for this season, accounting for the discrepancy at Wake.

The discrepancies along Mexico and Alaska, however, probably represent nonisostatic deviations of sea level.

Figure 6. August, September, October. The results stated for the two preceding figures can, on the whole, be repeated in this case. The discrepancies are largest along the North American coast.

A long region having negative values centered along British Columbia is surely not in isostatic equilibrium; neither the pressure term nor the steric term had any appreciable value here during these months, but they would, in fact, lead to a small positive term as close to the coast as we can measure the steric values. Conversely, the values along Mexico are positive, but too large. In the Line Islands (Fanning $+7$ cm and Palmyra $+8$ cm) the discrepancies are large. Steric observations taken during IGY give values of -5 cm for Fanning and $+3$ cm for Palmyra; the smoothed isostatic contours for the area as a whole lead us to expect negative departures. Once more, the deviation at Johnston Island is so large, $+9$ cm, but this is in good agreement with an earlier 5-year recorded mean of $+7$ cm. The other pronounced discrepancy occurs at Guam, which has an IGY recorded departure of -7 cm, although both steric and recorded departures during earlier time periods were small—less than $+2$ cm in each case.

Figure 7. November, December, January. The

agreement is, on the whole, satisfactory. Kwajalein (-10 cm) and Moen (-9 cm) show the largest deviations. Apparently the real variability here is large.

This map shows an interesting feature in the Hawaiian Islands: a total difference from southeast to northwest of 3 cm on the main islands alone. This is a good indication that, at times, small-scale or local effects may be important even around mid-latitude island groups.

In the southern part of the ocean and along the South American coast, some of the values disagree in phase with the surroundings, but these values are numerically small. It is possible that the zonal zero line occupies a comparatively varying position, and large areas may show positive and negative values of the departures.

SUMMARY

Over the open oceans as a whole the recorded seasonal departures in sea level agree both in sign and in approximate magnitude with the isostatic departures computed from changes in air pressure and in water volume. We conclude that the large-scale variations in sea level are indeed isostatic, that is, that variations in total mass of air and water are small. Where barometric effects are large, as they are north of 40°N , there must be appreciable seasonal variation in the mass of water present, of course, while in low latitudes only the water volume, not the water mass, varies appreciably.

Isostatic conditions apparently do not prevail at least along certain parts of the continental coasts. The China Sea, northern Australia, British Columbia, and Mexico south of Baja California show the largest discrepancies. It is a curious fact that in most cases, but not in all, these discrepancies are of the same sign as the isostatic term; that is, the seasonal variations seem augmented by the local coastal conditions.

Large discrepancies frequently appear around the tropical islands. Some of these have apparently been introduced by the comparison of an average isostatic pattern with recorded values collected only during IGY. In this highly complex region small-scale effects cannot be neglected, even in the isostatic term. It may well be, also, that some of the recorded variations are not isostatic, and an explanation must be sought elsewhere.



Fig. 4. Contours represent the *isostatic* deviation from annual mean sea level, averaged over the months of February, March, and April (see text). Heavy solid lines indicate zero deviation, light solid lines positive deviations, dashed lines negative deviations. Contour interval 5 cm; each contour is labeled in inclined lettering. Vertical numbers show *recorded* deviations from annual mean sea level for the same months during IGY.



Fig. 5. Same as Figure 4 for May, June, and July.

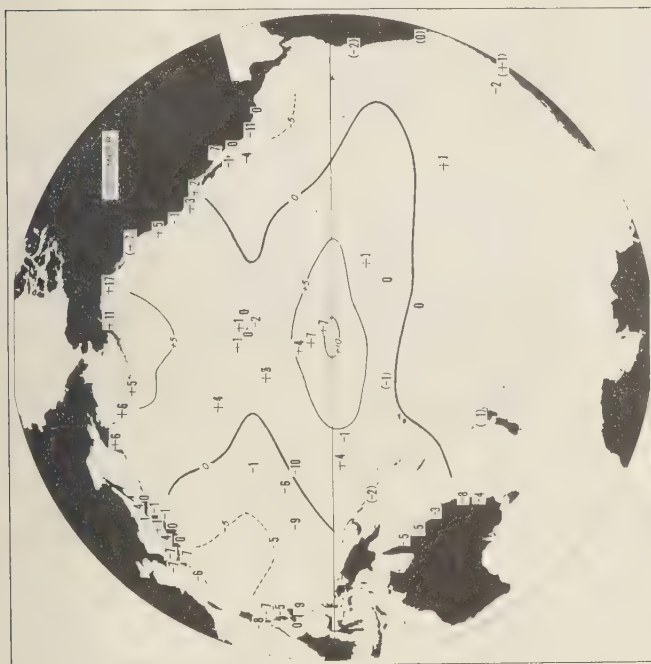


Fig. 7. Same as Figure 4 for November, December, and January.



Fig. 6. Same as Figure 4 for August, September, and October.

Acknowledgments. This paper represents the results of research carried out by the University of California under contract with the Office of Naval Research. Support was also received from the National Science Foundation, the U. S. State Department, and a Fulbright award to Dr. Lisitzin.

REFERENCES

- Association d'Océanographie Physique, Monthly and annual mean heights of sea level during the International Geophysical Year, 1957 and 1958 and unpublished data for earlier years. *Publ. Sci. No. 20*, 1959.
- Hamon, B. V., and F. D. Stacey, Sea Levels around Australia during the International Geophysical Year, *Australian J. Marine and Freshwater Research* (in press).
- Marine Atlas II (Morskoi Atlas II), Izdanie Morskogo General'nogo Shtaba, Moscow, 1953.
- Miyazaki, M., Seasonal variations of the sea level along the Japanese coasts, *Records Oceanog. Works Japan*, 2(3), 1-8, 1955.
- Pattullo, J. G., W. H. Munk, R. Revelle, and E. Strong, The seasonal oscillation in sea level, *J. Marine Research, Sears Foundation*, 14(1), 88-155, 1955.
- Pattullo, J. G., The seasonal variation in sea level in the Pacific Ocean during the International Geophysical Year, *J. Marine Research, Sears Foundation*, in press.
- Selitskaya, E. S., The study of the sea level variations, *Acad. Sci. d'URSS, Ann. Géophys. Intern., Bull. d'Information No. 7*, 60-64, Moscow, Russia, 1959.

(Manuscript received October 7, 1960;
revised December 15, 1960.)

Estimates of Vertical Motions and Meridional Heat Exchange in Gulf Stream Eddies, and a Comparison with Atmospheric Disturbances

CHESTER W. NEWTON

*The University of Chicago
Chicago, Illinois*

Abstract. On the basis of certain assumptions about the subsurface structure of the Gulf Stream eddy 'Edgar' (1950), computations were made of various properties of large-scale oceanic eddies by the methods employed in the study of atmospheric disturbances. It was found that during the formation of Edgar the southward flux through its neck in upper levels exceeded its rate of areal expansion, the reverse being true in lower levels. This implied general subsiding motions, reaching probable maximum mean values of 30×10^{-3} cm/sec at 600-meter depth. Indications are that descending motions were much stronger in the southern than in the northern part of the eddy. The heat exchange across the mean Gulf Stream, associated with the separation of one eddy from the main cold-water mass, was found to be about 200 to 400×10^{18} g-cal. A small annual number of eddies such as Edgar would be capable of transporting enough heat across the Stream to balance the loss of heat through the sea surface in the entire cold-water area west of Newfoundland. Horizontal and vertical mass transports in the Gulf Stream eddy, during the period of formation, were found to be comparable to those in a cold outbreak in the atmosphere.

INTRODUCTION

The tendency of the Gulf Stream to fluctuate markedly from its average location, and to form large warm and cold eddies, has aroused a great deal of interest in recent years. The first detailed description of such a disturbance came as a result of a multiple-ship survey (Operation Cabot) conducted in June 1950. *Iselin* [1950] drew attention to the similarity between such eddies (Fig. 1) in the ocean and 'cut-off lows' in the atmosphere, noting that in the development of a Gulf Stream meander 1 week corresponds to 1 day in an atmospheric jet-stream meander.

This analogy was discussed in some detail by *Rossby* [1951]. *Palmén* [1949] had found that an essential feature in the formation of cut-off lows is the sinking and low-level spreading of the central cold air, the generation of cyclonic vorticity in the cut-off low arising from a compensating convergence in upper levels. *Rossby* stated, 'If this system of vertical motions is essential to the evolution of meander loops in the atmosphere one can hardly avoid the conclusion that vertical motions, more specifically the sinking of cold water masses, must be of fundamental importance also to the meander formations observed in the Gulf Stream and to the maintenance of this current, which thus,

at least in part, would be driven by internal forces.'

With reference to the role of eddies such as Edgar in the cross-stream exchange of mass, heat, and salt in the upper layers, *Stommel* [1958] stated, 'A transfer of properties across the Gulf Stream on a scale smaller than that of these large eddies does not appear to be indicated.' As evidence for this statement, he cited the very detailed sections made by *Ford*, *Longard*, and *Banks* [1952]. These show that in locations far out in the open ocean a slender ribbon of fresh water and accompanying very strong concentrations of temperature gradient are observed; these could hardly have been preserved so far from the coast if there were appreciable small-scale diffusion across the Stream.

It is thus evident that a large part of the exchange across the Gulf Stream system must occur through the detachment of eddies and their gradual absorption in the water masses in which they become imbedded. It is my purpose in this paper to examine, with the aid of data from Operation Cabot, the orders of magnitude of the processes indicated above. The bulk of the data obtained in that survey pertained to the uppermost strata, and indirect methods will therefore be necessary if we are to infer the three-dimensional structure and

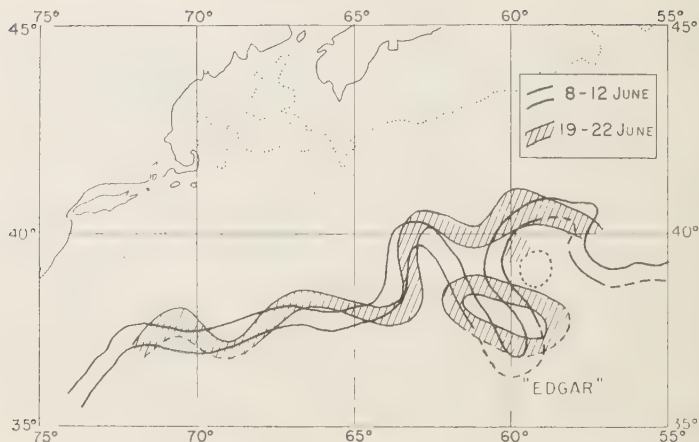


Fig. 1. Positions of the Gulf Stream during the first and last periods of Operation Cabot, after Fuglister and Worthington [1951].

broad-scale processes operative in the Gulf Stream eddy.

BROAD-SCALE STRUCTURES OF OCEANIC AND ATMOSPHERIC EDDIES

Since synoptic-aerological methods are used in the computations that follow, it is appropriate

to examine what likenesses exist between structures of oceanic and atmospheric currents. Comparisons in an earlier paper [Newton, 1959] show that, apart from a question of scale, there is a remarkable similarity in the basic features of the thermal and velocity structures of the two systems.

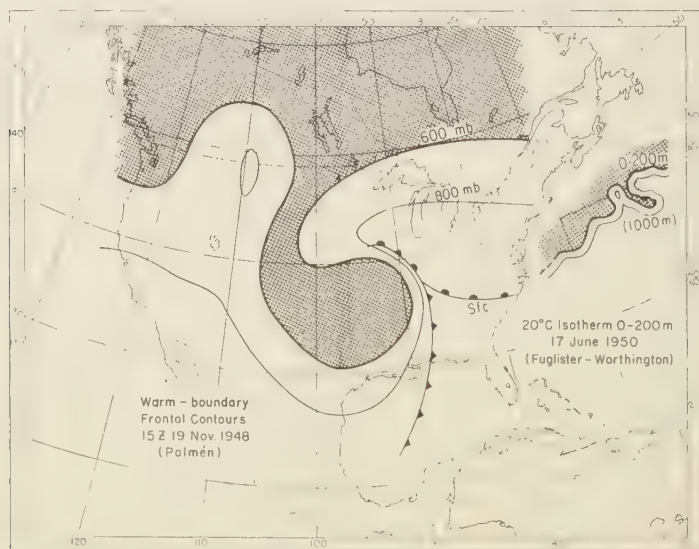


Fig. 2. Contours of the warm boundary of the polar front for a large-scale atmospheric eddy, compared with the configuration of the Gulf Stream front as observed in Operation Cabot. The thin line in the latter case is the 1000-m contour of the Gulf Stream front for an assumed slope of 1:75. After Palmén [1951a], and Fuglister and Worthington [1951].

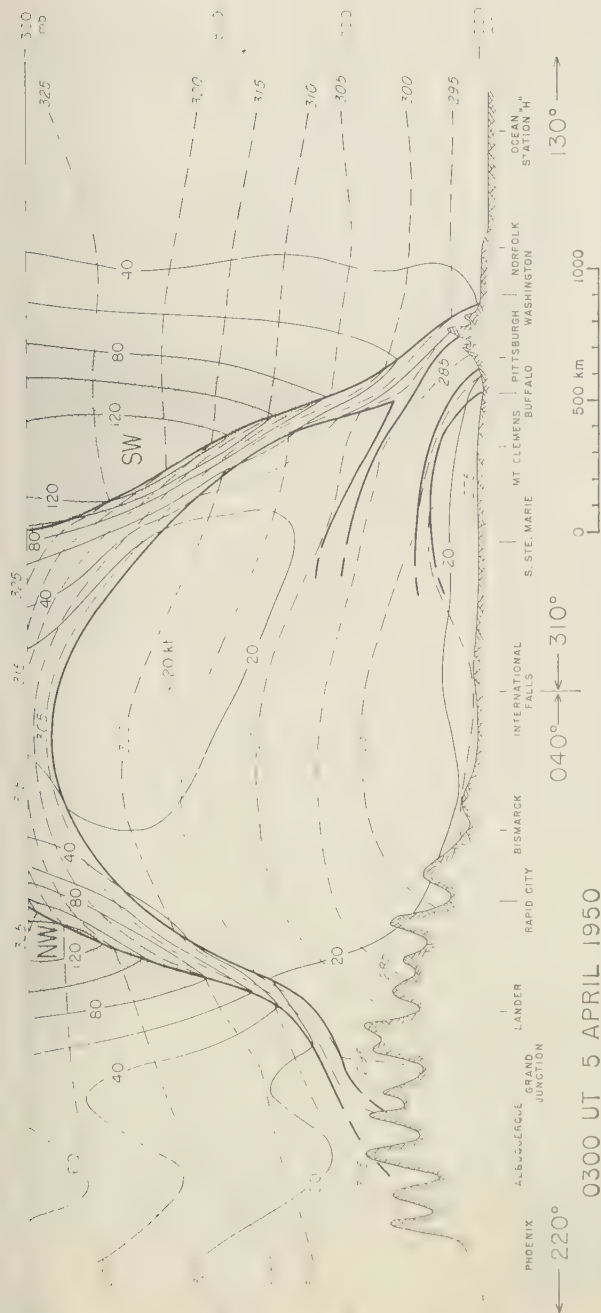


Fig. 3. Vertical cross section along the lines indicated in Figure 9. Heavy lines, boundaries of fronts or stable layers; dashed lines, isopleths of potential temperature ($^{\circ}\text{K}$); thin solid lines, isotachs in knots (2 knots \approx 1 m/sec). The jet stream is from NW in the left part and from SW in the right part of the figure, approximately normal to the section.

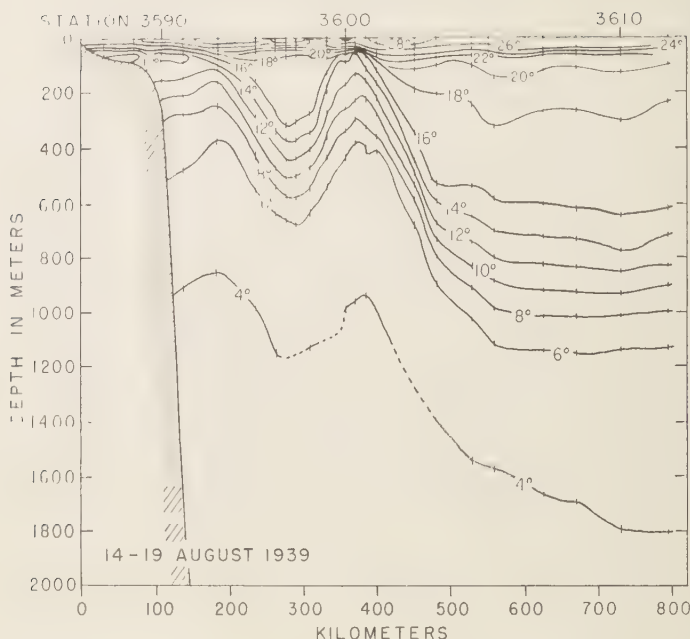


Fig. 4. Section through a cold eddy observed in August 1939, after *Iselin* [1940]. The slope of the cold-dome boundary, taken as that of a line drawn through the middle of the zone of strongest horizontal temperature gradient, is in this case about 1:120 on the right-hand side of the cold dome, down to 1000-m depth.

Figure 1 shows two positions of the Gulf Stream as observed in Operation Cabot. At the earlier time, a large meander was observed; ten days later the southern part of the cold-water tongue had cut off to form an isolated eddy, called 'Edgar' [*Fuglister and Worthington*, 1951]. A comparison of this cold-water tongue with an analogous feature on the atmospheric polar front is shown in Figure 2. The configuration of the Gulf Stream front in the general neighborhood of the eddy is remarkably similar to that of the atmospheric front; the dimensions differ in the approximate ratio 1:10.

Thermal structure. The thermal structure of a typical atmospheric trough is shown in Figure 3. [Potential temperature isopleths, shown in this section, are physically comparable to isotherms (or, more strictly, to isopycnals) in an oceanic section.] Noteworthy is the concentration of a large part of the available temperature contrast into a narrow frontal layer. Figure 3 illustrates a time when the polar front was distinct on all sides of this cold tongue.

Not enough deep hydrographic soundings were made for the structure of Edgar below the superficial layer to be ascertained. Apparently similar eddies have been traversed on other cruises, however; an example is shown in Figure 4. The proportionate depth and width of the baroclinic zone, relative to the total dimensions of the cold dome, appear greater than in the atmospheric case. A bathythermograph (BT) cross section in the upper 900-foot layer of an eddy observed in June 1947 [*Iselin and Fuglister*, 1948] shows a much more distinct concentration of isotherms in the horizontal than does Figure 4. The intensity of the polar front characteristically shows pronounced variations with time and location in atmospheric disturbances. Detailed BT sections by *Von Arx, Bumpus, and Richardson* [1955] suggest that this is also true of disturbances on the Gulf Stream front.

Velocity structures during eddy formation. It is characteristic of developing atmospheric troughs that the thermal concentration and the upper-tropospheric wind speed are much stronger on

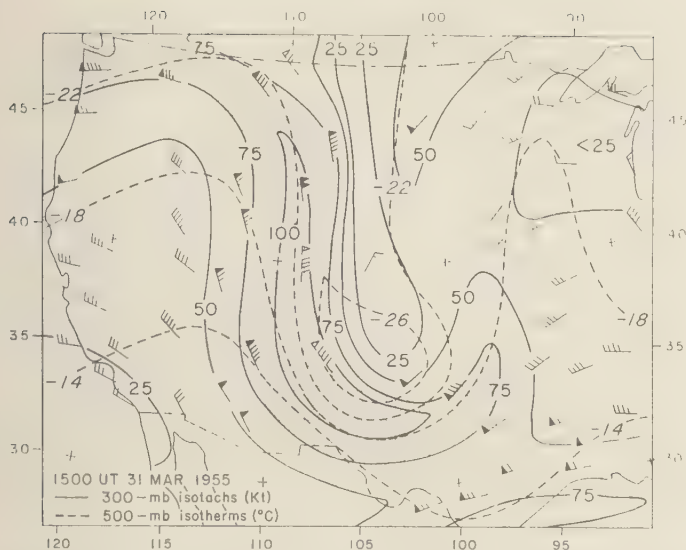


Fig. 5. Wind velocity distribution typical of the period of growth of a deep atmospheric trough, before formation of a cut-off low. Solid lines, isotachs (knots) at the 300-mb level (near level of maximum wind); dashed lines, isotherms at 500 mb, in the middle troposphere. Wind symbols: flag, 50 knots; full feather, 10 knots; dashed winds are at 1000 to 1500 m below 300-mb level.

the upstream than on the downstream sides. An example (for a case similar to that in Figure 5) is shown in Figure 5.

Fuglister and Worthington [1951] noted the same characteristic during the formation of Edgar. Figure 6 shows an analysis of the surface current speeds, superimposed on a skeleton of their analysis of the upper 200-meter isotherms, at three times during an 8-day period.¹ The greater concentration of isotherms and the presence of much stronger currents on the southwest than on the northeast side are particularly evident on the middle chart.

Growth in surface area of Edgar. Figure 7 shows six successive stages in the development of Edgar. At the time of discovery, the cold-water pendant was still connected to the main water mass, from which it split off around June 19. The sequence of events was quite similar to that in the formation of cut-off lows in the atmosphere [Palmén, 1949, 1951a].

¹ I am indebted to the Woods Hole Oceanographic Institution for permission to use the surface velocity data which did not appear on the published chart for the middle time.

With use of a planimeter, measurements were made of the area of cold water inside the 18° and 20°C isotherms, south of latitude 39° (the 'neck' in earlier stages). Although there is a great deal of scatter due to incomplete data for analysis on individual days, a progressive increase in area is clearly indicated (Fig. 8). Since conditions in the ocean are essentially adiabatic over such a short time period, if motions are horizontal the growth in area could be accounted for only by a net inflow of water through the neck of the cold-water pendant. The asymmetrical structure of the velocity field (Fig. 6; see also Von Arx [1951]) does suggest greater volume of southward than of northward flow through the neck. The required southward velocity, averaged across the whole width of the neck, would be of the order of 30 cm/sec between June 10 and 18.

THREE-DIMENSIONAL MOTIONS IN LARGE EDDIES

In view of the considerable similarity between thermal and current structures in atmosphere and ocean, it appears plausible that the general

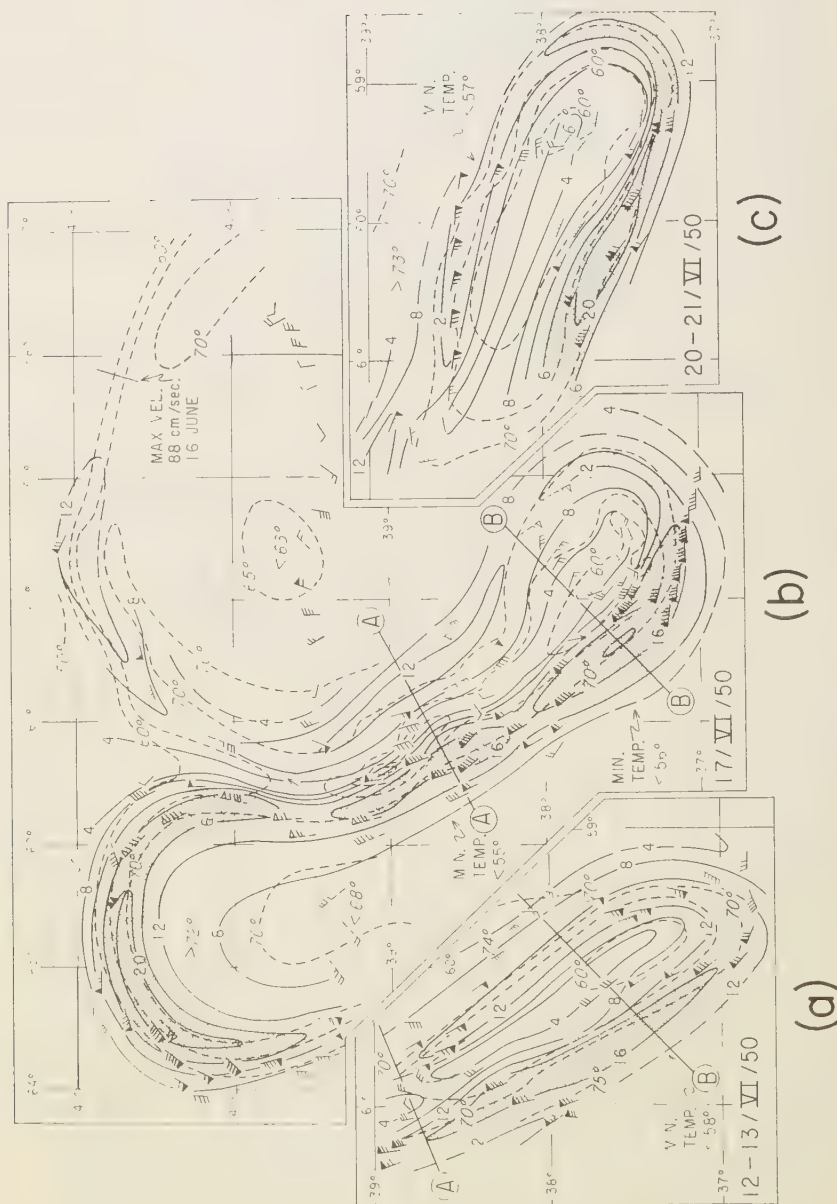


Fig. 6. Mean isotherms ($^{\circ}\text{F}$) in upper 200-m layer (short-dashed lines), after *Fuglister and Worthington* [1951]; and isobaths (decimeters/sec) of surface current speed, at three stages in the development of Gulf Stream eddy Edgar. Light stippling indicates current speed between 120 and 160 cm/sec; heavier stippling, speeds greater than 160 cm/sec. Velocity symbols: flag, 100 cm/sec; feather, 20 cm/sec. Where the symbols are dashed, they refer to observations made on June 16 or 18. The speeds shown are uncorrected GEK measurements, and should be multiplied by approximately 1.5 to obtain true surface current speeds. Transport computations referred to in text were made along sections A-A and B-B. Dates are approximately 1.5 days left of each figure.

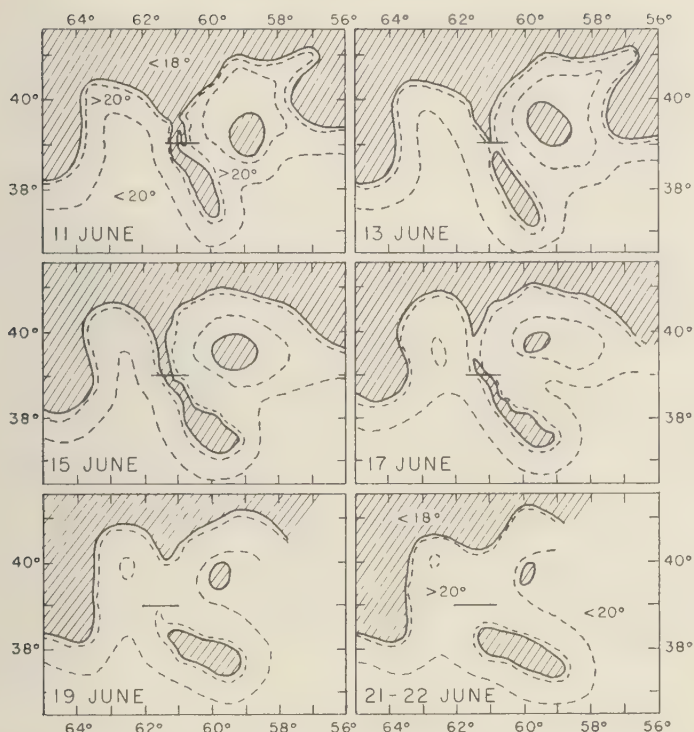


Fig. 7. Positions of 18°C (solid lines) and 20°C (dashed lines) isotherms in upper 200-m layer, at 2-day intervals from June 11 to 21, 1950. After Fuglister and Worthington [1951].

three-dimensional motions in oceanic eddies may themselves follow broadly the same pattern as that of an atmospheric eddy.

Palmén and Newton [1951] have made computations of the three-dimensional motions in a large-scale atmospheric cold outbreak. Figure 9 and the cross section in Figure 3 illustrate the general structure of the atmosphere. At the 500-mb level, a net southward flux of cold air was indicated through the 45° latitude parallel. However, successive frontal contour charts showed that, at that level, the area of the cold air south of this latitude did not increase. On the other hand, a vast increase in the area of cold air was observed at lower levels, an increase that could not be accounted for by the southward influx of air at the levels concerned.

Computations based on mass-continuity principles indicated general descent of the cold air, the strongest mean vertical velocity (near 500 mb) being -2.2 cm/sec. The mass budget was balanced in a manner which indicated that the

mass transfer across the polar-front surface was negligible. This is an essential assumption in the computations which follow for the Gulf

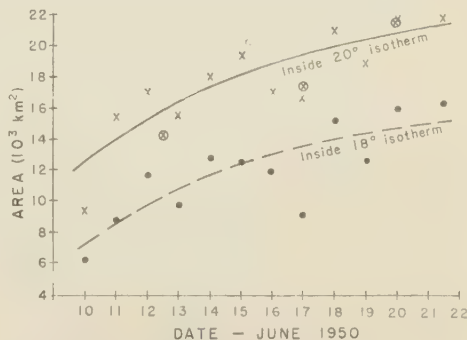


Fig. 8. Approximate areas inside cold-water tongue Edgar, south of 39° latitude, at successive times during its growth. Encircled crosses indicate areas inside 20°C isotherm at times shown in Figure 6, when observations were most complete.

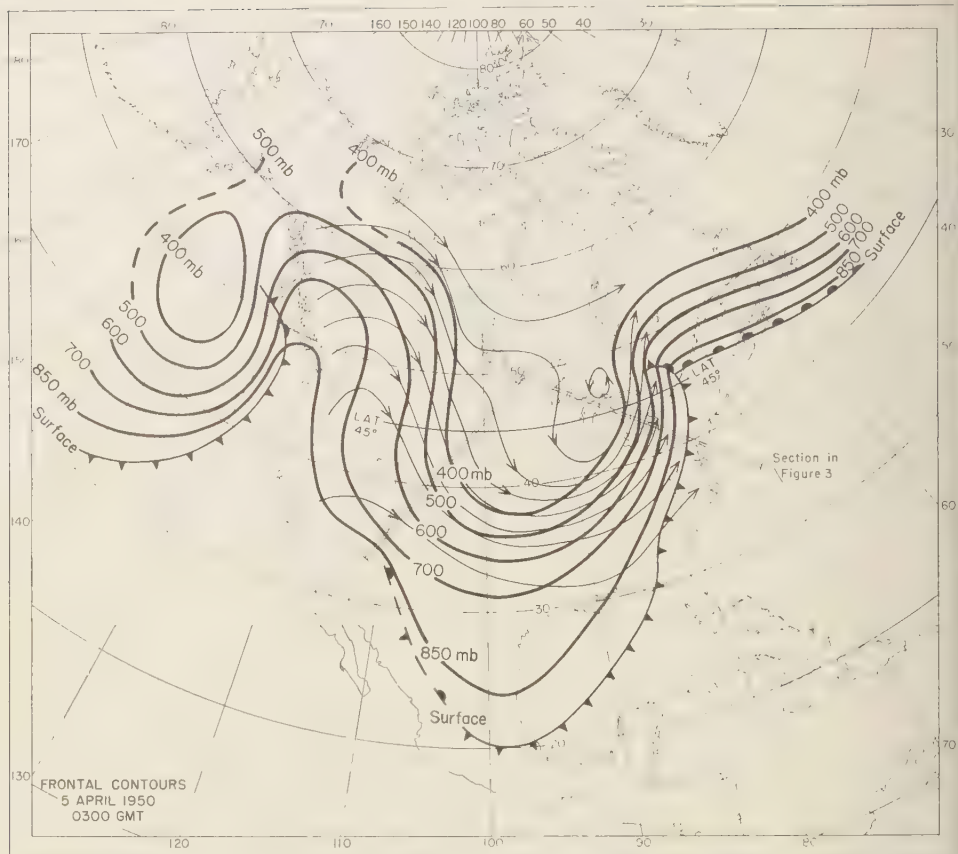


Fig. 9. Contours (heavy lines) of warm boundary of polar front, at 0300 UT, April 5, 1950. Thin lines with arrows are contours of the 500-mb surface, at 60-m intervals, corresponding approximately to transport lines [Palmén and Newton, 1951].

Stream eddy; these computations are based upon the indirect synoptic aerological methods employed in the study by Palmén and Newton.

Assumptions for analogous computations in Edgar. To make computations of this kind for the oceanic eddy, we must adopt several bold assumptions because of the lack of deep subsurface data. In most cases, these assumptions are prescribed by the general knowledge of current and thermal structure that has emerged from many different cruises. The derived quantitative values can only be regarded as indicating general magnitudes.

Preliminary computations for this paper were made before the spring 1960 Gulf Stream survey was carried out by Woods Hole Oceanographic

Institution. Having participated as an observer in the first part of that survey, I am aware that an eddy similar to Edgar was found, and I expect that succeeding cruises will have yielded much more adequate data for the study of eddy structure. Nevertheless, I believe that the attempt to make the indirect computations described below is justified because independent studies of these two cases may yield more information about eddy behavior than a study of one case alone.

As will be seen, the results obtained are sensitive to the first assumption below. Consequently, a range of possibilities, I, II, and III, will be considered. For the sake of consistency, different possibilities will also be considered in

ome of the other assumptions, but the range of these possibilities does not strongly influence the results.

Assumptions (a) through (c) concern, directly or indirectly, the continuity of mass within the cold tongue:

(a) The mass budget within the cold-water pendant is assumed to be balanced entirely above a level z_0 , variously taken at depths of (I) 1000 m, (II) 1500 m, or (III) 2000 m. That is, the vertical mass transport through this level, taken over the whole or a large portion of the area of the cold tongue, is assumed to be negligible. No convincing justification can be given for these choices; the proper choice must evolve from more complete observations.

(b) In the upper 200-m layer the 70°F (21°C) isotherm represents the warm-water boundary of the Gulf Stream front. Down to a depth of 1000 m the front has a slope of 1 : 75. This value is characteristic of the slope of the zone of strongest horizontal temperature gradient in most hydrographic sections (e.g., those of *Selvin* [1936]). Below 1000 m, the barocline zone is assumed to be vertical, as is also suggested by most deep sections.

(c) The axis of maximum current velocity lies on the warm-water boundary of the frontal or barocline zone defined above. This assumption is based partly on the fact that, when a distinct front is present, geomagnetic electrokinetograph (GEK) observations show this to be true at

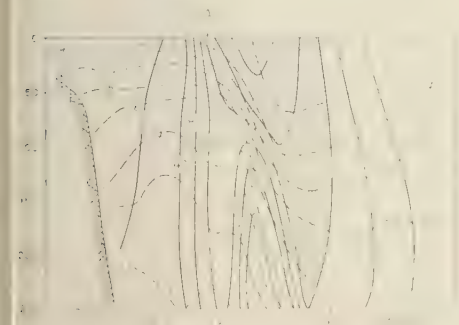


Fig. 10 Section across Gulf Stream south-east of Onslow Bay. Isotherms (dashed lines, °C), after *Von Arx, Bumpus, and Richardson* [1955]. Isotachs (solid lines, cm/sec) of current speed normal to section were computed from corrected GEK measurements at the surface with the assumption of a geostrophic decay with depth [*Newton, 1959*].

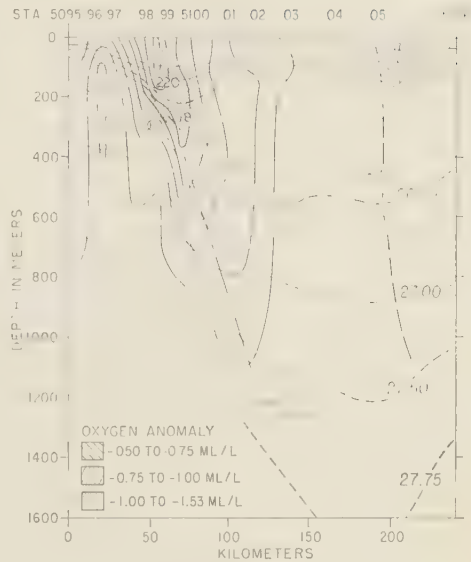


Fig. 11. Section along a NW-SE line near 37°N, 70°W, in August 1953, showing isopycnals (dashed lines) and isotachs (solid lines, cm/sec). After *Richards and Redfield* [1955].

the surface, and the geostrophic decay with depth indicates that it is also true at least down to 250 m (Fig. 10). This general type of current structure is evident in some deep sections (e.g., Fig. 11), although other sections indicate that the axis of strongest current is more nearly vertical. The differences in current structure shown in such sections, although perhaps real in some cases, appear in others to result largely from uncertainty as to the exact interpretation of isotherm structure arising from the appreciable distance (and time) between successive observations. Direct measurements with the bathypitotometer [*Malkus, 1953; Malkus and Johnson, 1954*] made by ships near the surface current axis have shown a rapid decay of velocity with depth. These observations would be consistent with Figure 11 but not with a structure showing a current with a vertical axis.

The essence of this assumption is that, if it is granted, the warm-water boundary of the frontal or barocline zone is a surface across which no appreciable transfer of mass is likely to occur. This follows because an abrupt change of potential vorticity would be required for water to pass from the cyclonic-shear side to the anti-

cyclonic-shear side of the current, or vice versa.² Moreover, such a transfer would require first an increase and then a decrease of the kinetic energy of a water element, which appears unlikely for an element traveling consistently either down or up the pressure gradient in crossing the current.

The remaining assumptions concern the flux of water into the cold tongue through a vertical section dividing it from the main cold-water mass:

(d) The surface inflow is given by the GEK measurements (Figs. 6a, 6b) corrected by a 'k-factor' of 1.5. This factor represents the ratio of actual current speed to the speed indicated by GEK measurements. The value chosen is a mean of the average values of 1.6 in cyclonic bends and 1.4 in anticyclonic bends of the Stream, determined by *Von Arx* [1952] for this cruise.

(e) At level z_0 , defined under assumption (a), the mean inflow velocity into the cold tongue, through a section *A* or *B* across it (Figs. 6a, 6b), is zero. This depends on the choice of the level of no motion. 1000 m is almost certainly too shallow, and has been included as an extreme assumption (I). In computations from hydrographic data, 2000 m (assumption III) appears to be the popular choice. On the basis of current measurements at great depths off the Carolina coast, *Swallow and Worthington* [1957] suggested that the level of no motion in that area probably lies between 1500 and 2000 m.

(f) At 1000-m depth, the mean inflow velocity through a section across the cold tongue is either (I) zero, (II) 5 per cent, or (III) 10 per cent of the surface inflow velocity. Assumption (I) is considered to be an extreme condition, (III) is typical of hydrographic sections (based on level of no motion at 2000 m), and (II) is a compromise.

(g) The vertical profile of the mean horizontal velocity through a given section is represented by a smooth curve without discontinuities in the vertical shear. The vertical shear has the

² With adiabatic motions, the potential vorticity Q/H is a conservative property [see *Stommel*, 1958]. Here Q is the absolute vorticity and H the vertical thickness of a water column. Considering, for example, the layer between the 26.50 and 27.00 isopycnals in Figure 11, a column crossing from the left to the right side of the current would undergo a decrease of absolute vorticity, which would be inconsistent with the vertical stretching implied by increased thickness of this layer toward the right.

minimum possible value consistent with the earlier assumptions. These statements are purely heuristic.

Results of the computations in Edgar. Computations of the mass budget were made for the 4½-day period between June 12–13 (Fig. 6a) and June 17 (Fig. 6b). These were based upon the southward flux of water through sections *A* and *B*, indicated on these figures, and upon changes of the areas included within the assumed frontal contours.

The rate of increase of the area *A* within the cold tongue south of a given section through horizontal advection would be

$$(\delta A / \delta t)_a = \bar{v}_n L \quad (1)$$

where \bar{v}_n is the mean velocity into the tongue (component normal to section *A* or *B*) over the length L between the frontal contours at the level concerned. The observed change in area at the corresponding level will be denoted by $(\delta A / \delta t)_o$. The total change in the volume V above a given level z is

$$\frac{\delta V}{\delta t} = \int_z^0 \frac{\delta A}{\delta t} \delta z \quad (2)$$

Under assumption (c), if variations in density are neglected, mass continuity requires that above the assumed level z_0 of no net vertical transport, the advective and actual volume changes be equal, or that

$$\int_{z_0}^0 \left(\frac{\delta A}{\delta t} \right)_o \delta z = \int_{z_0}^0 \left(\frac{\delta A}{\delta t} \right)_a \delta z \quad (3)$$

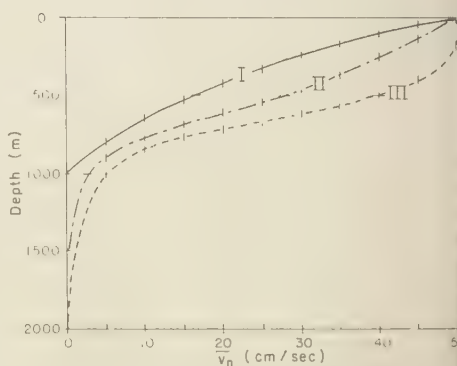


Fig. 12. Mean velocity of flow into Edgar at various depths through section *A* across the neck, determined as described in text.

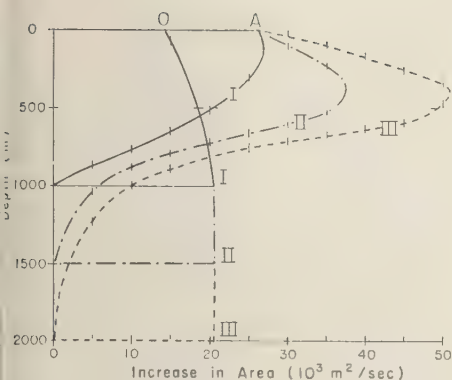


Fig. 13. 'Observed' (O) and horizontal advective (A) increases in area of Edgar during period of growth, for various assumptions as described in text. Solid lines (I) indicate area-change profiles when level of no vertical motion is taken at 1000 m; dashed-dotted lines (II) when taken at 1500 m; and dashed lines (III) when taken at 2000 m.

At the surface, \bar{v}_n was determined directly from the velocity profile given by the corrected TEK observations. Mean values (weighted for length L) were used for the times of Figures 6a and 6b, at which times complete sections were available. Since the sections do not coincide with lines of observations, values of \bar{v}_n were taken from the analyzed velocity fields.

At depth z_0 , \bar{v}_n was taken as zero according to assumption (e), and at 1000 m \bar{v}_n was defined by assumption (f). This fixed two or three points in the vertical profile of the mean inflow velocity. The profile was then drawn, by trial and error, in such a manner that equation 3 was satisfied.

The resulting velocity profiles are shown in Figure 12 for section A. The corresponding vertical profiles of the influx at various depths are shown in Figure 13. For any particular assumption, I, II, or III, there appears to be little leeway in the manner in which the \bar{v}_n profile can reasonably be drawn, and the exact shape of this profile does not appear to influence in any significant way the results which follow.

In any of the three cases, Figure 13 shows that, in the upper strata above some level located between depths of 550 and 850 m, the horizontal influx through section A exceeded the observed increase of area within the cold tongue. Below this level, the observed area increase

exceeded that to be expected from horizontal advection. It is seen, however, that the differences between advective and actual change of area, and thus the volume of water accumulated in the upper strata through horizontal motions, differ considerably in the three possibilities, I, II, and III, which were considered.

Continuity requires that the amount of mass accumulated above a particular level be removed by downward motions through that level. With negligible error, the ocean can be regarded as being homogeneous, so that at any level z ,

$$\bar{v} A(z) = - \int_z^0 \left[\left(\frac{\delta A}{\delta t} \right)_a - \left(\frac{\delta A}{\delta t} \right)_0 \right] dz \quad (4)$$

From this condition, it is possible to compute the mean vertical velocity \bar{v} at each level. The results for the entire cold tongue southeast of section A are shown in Table 1.

The strongest mean vertical velocity, for the three possibilities considered, was found to be -10 , -22 , or -34×10^{-3} cm/sec at mean levels of nondivergence located respectively at depths of 400, 600, or 650 m. As was noted earlier, it is virtually certain that assumption I, which was put in as an extreme upper estimate for the level of no motion (1000 m), is unrealistic. Unless otherwise noted in the following discussion, the numerical values quoted will refer to a compromise between the values corresponding to assumptions II and III (level of no motion at 1500 to 2000 m). In this case, the level of nondivergence would be located at about half the depth of the total layer of strong disturbance of the mass field, i.e., half the depth of the base of the warm-water thermocline (Fig. 4).

For the atmospheric case referred to earlier, the strongest mean vertical motion, expressed in pressure units, was about 1.6×10^{-3} mb/sec. This compares with 28×10^{-3} mb/sec for the maximum mean vertical motion over the whole area of Edgar. Thus, in dynamically comparable units, the vertical motions in the oceanic eddy appear to be 1 order of magnitude stronger than those in the atmospheric disturbance, although in terms of linear vertical velocity they are about 1/100 as large.

Distribution of vertical motion in different parts of the cold tongue. Computations of the sort outlined above were made separately for the portion of the cold tongue southeast of section B (Fig. 6) and for the central portion between

TABLE 1. Computation of Average Vertical Velocity in Cold-Water Tongue 'Edgar,' Southeast of Section A across the Neck

Depth, m	Area of Cold Water, km ²	Total Downward Volume Transport,* m ³ /sec	Mean Vertical Velocity (cm/sec) under Assumption		
			I	II	III
0	1.8×10^4	0	0	0	0
200	2.7	3.1×10^4	-8×10^{-3}	-12×10^{-3}	-14×10^{-3}
400	3.7	7.0	-10	-19	-27
600	4.7	10.2	-9	-22	-34
800	5.7	10.9	-5	-19	-33
1000	6.9	8.7	0	-12	-25
1200	6.9	5.2	...	-8	-21
1400	6.9	1.6	...	-2	-17
1600	6.9	-12
1800	6.9	-6
2000	6.9	0

* Total downward volume transport over whole area is given for assumption II only.

sections A and B. These portions are roughly equal in size. Results of the computations appear in Table 2, for the compromise assumption II. The vertical motions obtained by use of the extreme assumptions I and III varied by a factor of about 3, in all cases.

In the southern half of the cold tongue, the average descending motions were 5 to 10 times stronger than those in the northern half. This distribution of vertical motions is in qualitative accord with typical conditions in an atmospheric cold outbreak. These are exemplified by Figure 14 in which descending motions are shown everywhere south of latitude 42° , while farther north

areas of descent are partially compensated by areas of ascent.

A check on the magnitude of the computed vertical motions. It is possible to provide an independent check on the order of magnitude of the vertical motions shown in Table 1. It should be expected that these values, which represent average conditions over a large disturbance, would be considerably larger than vertical motions associated with long-period mean conditions over an appreciable length of the Gulf Stream (in which variations associated with disturbances are averaged out), and considerably smaller than the vertical motions associated with a part of a wave system in an individual disturbance. In the atmosphere, vertical motions characteristic of restricted regions on the flanks of the jet stream are of the order of 10 cm/sec, compared with 2 cm/sec indicated earlier as the average vertical velocity over the entire area of a cold outbreak.

Von Arx [1951, 1952] evaluated the average horizontal shear on the flanks of the Gulf Stream for Operation Cabot, and the results are shown in Figure 15 for the cyclonic flank. For the corrected GEK measurements, the absolute vorticity varied between average values of about $4 \times 10^{-4} \text{ sec}^{-1}$ in troughs and about $2 \times 10^{-4} \text{ sec}^{-1}$ in ridges (inclusion of the curvature would increase the variation slightly). As Von Arx has indicated, the ratio between GEK and navigational current speeds is proportional

TABLE 2. Average Vertical Velocity in Different Portions of Edgar, According to Assumption II

Depth, m	Mean Vertical Velocity, cm/sec		
	Over Whole Area SE of Section A	In Region between A and B	In Region SE of Section B
0	0	0	0
200	-12×10^{-3}	-2×10^{-3}	-22×10^{-3}
400	-19	-3	-36
600	-22	-6	-38
800	-19	-7	-30
1000	-12	-4	-20
1200	-8	-2	-12
1400	-2	0	-4
1500	0	0	0

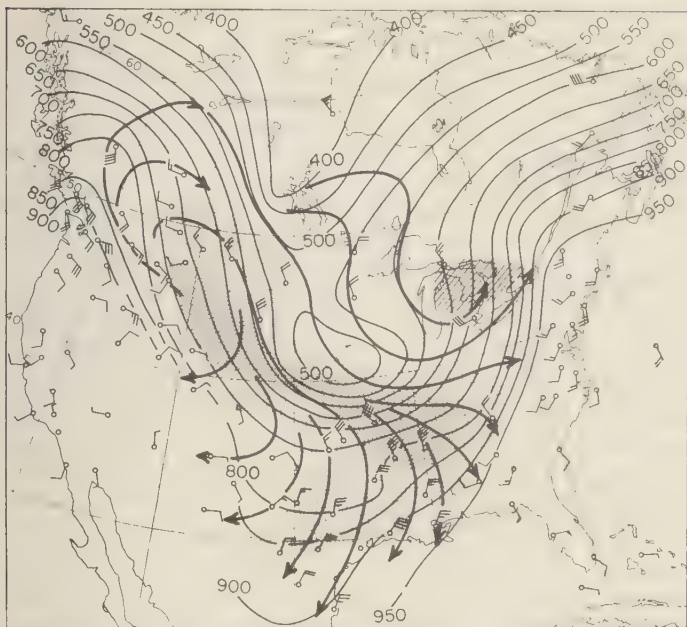


Fig. 14. Contours of isentropic surface 290°K at 0300 UT, April 5, 1950 (light solid lines, mb), and streamlines on that surface (heavy arrows). Vertical motion indicated by light stippling, descent at 50–100 mb/12 hr; by heavier stippling, more than 100 mb/12 hr; by hatching, ascent more than 50 mb/12 hr [Palmén and Newton, 1951].

to the depth of the current; since the 'k-factor' was found to be greater in cyclonic than in anticyclonic bends of the Stream, this indicates that the current was deeper in the cyclonic ends. As he further observed, 'Such an interpretation is consistent with an increase in cyclonic shear since vertical stretching and horizontal convergence of the flow [approaching] cyclonic curvatures would result in increased cyclonic vorticity on the left of the current maximum.'

According to the vorticity equation [see, for example, Petterssen, 1956], the divergence is

$$D = (-1/Q) (dQ/dt) \quad (5)$$

where Q is the absolute vorticity and D is the horizontal divergence. Equation 5 may be written

$$D = [-(v - c) Q] \left(\frac{\partial \phi}{\partial s} \right) \quad (6)$$

where v is the current speed, c is the phase velocity of the waves, and s denotes distance

along a streamline. On the average, the half-wavelength (for waves west of 63° longitude) was about 200 km, with a mean change of vorticity of about $2 \times 10^{-6} \text{ sec}^{-1}$ in this distance. Taking v as 150 cm/sec and c as 20 cm/sec,

$$|D| \approx 40 \times 10^{-7} \text{ sec}^{-1}$$

The vertical motion at the 200-m depth may be estimated from the continuity equation to be

$$|w_{200\text{m}}| = |D| \times 200\text{m} \approx 80 \times 10^{-3} \text{ cm/sec}$$

This value (probably an overestimate, since the divergence most likely decays with depth) is about 6 times as large as the mean vertical motion at 200 m computed for Edgar, approximately the ratio found in a similar comparison of atmospheric features. Thus it appears plausible that the vertical motions computed for Edgar are of the right order of magnitude.

Hela [1954] computed the divergence field in the western North Atlantic from charts of resultant surface currents. He found, on the average, horizontal divergence on the right

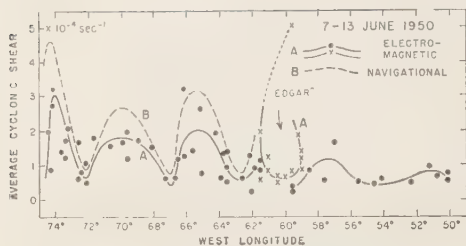


Fig. 15. Horizontal shear on cyclonic flank of Gulf Stream during Operation Cabot. West of longitude 62° , low values were observed in ridges and high values in troughs (cf. Fig. 1). After Von Arx [1952].

flank and convergence on the left flank of the mean Gulf Stream. If his results are assumed to be representative for the entire upper 200-m layer, the indicated maximum mean vertical motions would be around 3 to 10×10^{-3} cm/sec at 200-m depth.

It is thus seen that the values of vertical motion computed for Edgar are bracketed by values computed independently from other data and by other methods in a manner which would be expected from the space and time scales of the phenomena concerned.

It is not at all likely that the vertical velocity values in Tables 1 and 2 are representative of Gulf Stream eddies *after* their separation from the main Stream. If they were, the thermocline in such an eddy (cf. Fig. 4), sinking at 15 to 20 m/day, would evidently collapse to half its initial height (relative to warm-water isotherms) in 15 to 20 days. According to an estimate given below, eddies of this kind are not likely to form more often than once every 50 days, and they probably form much less often. The frequency

with which large distortions of the isotherm appear on hydrographic sections, and with which cold eddies appear at the surface, suggest that the lifetime of such disturbances must be longer than this.

Comparisons of horizontal and vertical mass transports. A schematic diagram of the mass budget for the cold-water tongue is shown in Figure 16. It will be noted that during this stage in the formation of the eddy, the net southward flux into the cold-water tongue was around 30 per cent of the volume transport characteristic of the Gulf Stream system.

For the average of assumptions II and III the greatest downward mass transport (near 800-m depth) was 1.5×10^{12} ton/day, compared with a horizontal inflow at the rate of 3.3×10^{12} ton/day through section A. For the atmospheric cold outbreak discussed earlier, the maximum downward transport was 4.7×10^{12} ton/day (at 740 mb) while the inflow through a section at latitude 45° was 8.3×10^{12} ton/day. Thus the oceanic and atmospheric eddies are comparable in the sense that in each case the maximum downward transport of mass took place at about half the rate of horizontal flow of mass into the cold-water or cold-air tongue.

As was noted by Palmén and Newton [1951] the computations given above correspond to an exceptionally strong outbreak of polar air. It appears safe to conclude from this fact, and from a comparison of the computed values, that the meridional mass exchange per day in a cold oceanic eddy is about the same as that in a typical atmospheric eddy.

The possible significance of the Gulf Stream eddy as an element in the thermohaline circulation may be appreciated from the fact that the vertical mass transport computed at 800-m depth amounts to 17×10^6 ton/sec, about 10 times the rate of formation of deep water by sinking in the North Atlantic according to Sverdrup [1943]. The sinking of the Gulf Stream eddy is, of course, presumably important mainly for the upper layers and only goes on at this rate part of the time.

HEAT EXCHANGE BY EDDIES

The bulk of the required latitudinal exchange of heat, momentum, and other properties in the atmospheric general circulation takes place in one manner or another, in eddies of the scale

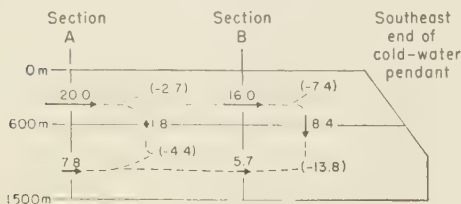


Fig. 16. A schematic vertical section along the axis of Edgar, showing computed horizontal and vertical volume transports in various parts of the eddy. Numbers in parentheses indicate volume expansion in the various portions. Units are 10^6 m³/sec.

of ordinary cyclones and larger [Palmén, 1951b; and others]. It is of some interest to examine the possible importance of eddies of the type of Edgar for the exchange of cold or warm water across the mean oceanic currents.

In the following, an estimate will be made of the amount of heat deficit in Edgar (relative to the surrounding water masses) after it was cut off from the main cold water mass. It is assumed that when such an eddy moves southward across the mean Gulf Stream, a mass of warm water, equivalent to that displaced by the cold eddy, is effectively transferred northward across the mean isotherms in the western ocean. The heat deficit can thus be regarded as a measure of the amount of heat transported across the mean isotherms as a result of the eddy formation.

In estimating the heat deficit in Edgar, a computation was made of the quantity

$$H = \int_{2000\text{ m}}^0 c \rho \Delta T(z) A(z) \delta z \quad (7)$$

ΔT being the difference between the heat content of the water within the eddy and an analogous body of water in the warm mass in which the eddy is imbedded. Here c is the specific heat, taken as 0.935 cal/g deg; ρ is the density, taken to have a mean value of 1.027 ton/m³; and $\Delta T(z)$ is the characteristic temperature difference across the Stream at a given depth z .

For lack of deep sounding data, ΔT was estimated from various published sections across the Gulf Stream. Values of ΔT taken from four sections in different seasons by Iselin [1936] are shown in Figure 17. With the exception of the surface layer, little seasonal variation is indicated. These values pertain to the Montauk-Bermuda section, considerably west of the location of Edgar, and may be somewhat an overestimate of the temperature contrast in the neighborhood of Edgar.

For heat computation purposes, the 65°F (18°C) isotherm, in the middle of the temperature gradient (Fig. 6c), was taken as defining the boundary of the eddy in the upper 200-m layer. By choosing the middle of the frontal zone as the reference for volume computations, an approximate true measure of ΔT at a given level is obtained, as is indicated schematically in the inset of Figure 17. As in the earlier computations, the center of the front was assumed to have a slope of 1:75 down to 1000-m depth,

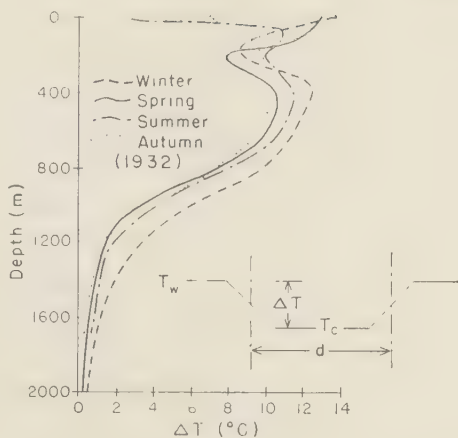


Fig. 17. Temperature differences across the Gulf Stream, taken from sections by Iselin [1936]. Inset shows schematic temperature profile across eddy; d indicates characteristic dimension utilized in mass computations (see text).

being vertical below that. For heat computation purposes, the exact depth to which the eddy extends (taken as 2000 m) is of little consequence, since the temperature difference between cold and warm water is small below about 1200 m.

The area of the cold water is plotted against depth in Figure 18a. Although the increase in area with depth may appear extreme, it is in line with that indicated by Figure 4. A section across the June 1947 eddy [Iselin and Fuglister, 1948] indicates an increase in width from 130 km at the surface to 260 km at a depth of 300 m, which would suggest an even more extreme variation of area with depth than is shown in Figure 18a.

A profile of ΔT was chosen (Fig. 18b) corresponding to the mean of the values in Figure 17 and utilizing for the upper 200-m layer the value of ΔT observed in Edgar. The difference in heat content between cold and warm water for various layers as derived from Figures 18a and 18b is plotted in Figure 18c. The total value of H evaluated from equation 7 is 384×10^{18} g cal. This can be regarded as the amount of heat exchanged across the mean position of the Stream as a result of the separation of one eddy.

Significance of eddies for meridional heat exchange. The over-all significance of Gulf Stream eddies as a mechanism for heat transfer

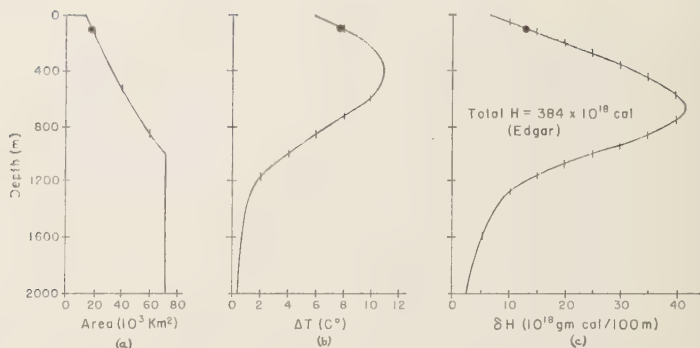


Fig. 18. Horizontal area of Edgar, assumed temperature difference across the Stream, and difference in heat content within 100-m layers, at various depths (see text).

cannot be evaluated until we know the number of such disturbances which form per year.

As an upper estimate of the rate of formation, it might be assumed that every large wave of the kind shown in Figure 1 eventually becomes unstable and forms an eddy. At the rate of movement of such waves as observed in Operation Cabot the waves would pass a given location at the rate of one about every 50 days. This would suggest a maximum of seven eddies per year.

If Edgar were typical and if the computed heat content is correct, seven eddies per year would be an unreasonably large number because this would imply an annual heat exchange of $50 \times 10^{20} \text{ cal}$, about the same as the total required meridional heat exchange across latitude 40° in both oceans [Sverdrup, 1955].

Professor S. Petterssen and Miss D. Bradbury have kindly allowed me access to some of their unpublished charts of the heat exchange (sensible and latent) between sea and atmosphere. These are based on averages of computations from daily maps, and are therefore more representative than earlier charts computed from monthly mean charts.

From their charts, I have computed the heat loss to the atmosphere over the region west of Cape Race, Newfoundland (53°W), from the coast south to the mean position of the Gulf Stream, an area of $1.5 \times 10^6 \text{ km}^2$. During the period December 1956 through February 1957, the average heat loss over this area was $0.42 \text{ cal/cm}^2 \text{ min}$, and in July 1958 it was $0.02 \text{ cal/cm}^2 \text{ min}$.

The annual variations shown by Sverdrup [1943] suggest that an average of these values should be nearly correct for obtaining an annual mean, giving $0.34 \times 10^{16} \text{ cal/min}$ heat loss to the atmosphere over the entire region. For this region, according to Sverdrup's charts, the radiation penetrating the ocean surface amounts to an annual area average of about $0.115 \text{ cal/cm}^2 \text{ min}$, giving $0.18 \times 10^{16} \text{ cal/min}$ radiative heat gain by the ocean.

From the above values it is found that, within the region considered, the ocean loses heat at a rate of approximately $840 \times 10^{18} \text{ cal/year}$. Cooling from continental runoff and from cold rain falling directly into the ocean is negligible, in comparison. Possible import by cold ocean currents south of Newfoundland has not been considered.

The amount of heat loss computed above is equivalent to the heat deficit in two to three Gulf Stream eddies (Fig. 18c). Thus, although the actual number of eddies per year is unknown and the heat content estimates are crude, it is hard to avoid the conclusion that the breaking off of large eddies in the Gulf Stream must be the principal mechanism for transporting heat between the central water mass and the slope water region of the western North Atlantic. Thus the synoptic-scale eddies in the Gulf Stream appear to play the same role as large-scale disturbances in the atmosphere.

CONCLUSION

The principal uncertainties in the above computations arise from the choice of a level of

vertical motion and of an assumed frontal slope. Aside from intuition and the general assumption that horizontal motions are small at a depth of 1500 to 2000 m, there is no basis for choice of a level of no vertical transport. The assumed frontal slope is based on the average conditions in available sections across the Stream, but it may reasonably be 50 per cent too large or too small.

If the frontal slope is too small, the computed horizontal motions are too small and the heat transport too large. On the basis of available knowledge of thermal structure, however, it appears reasonable to conclude that the computed heat deficit of the eddy is not off by more than 50 per cent, and that it amounts to 200×10^{18} cal. In this range, two to five eddies per year are enough to accomplish the required transfer of heat across the Gulf Stream. The fact that large eddies have been encountered often might suggest that an assumption of one per year, approaching the probable maximum frequency of formation from large waves in the Gulf Stream, is the most realistic. Heuristically, it might be most reasonable to suppose that eddy separation is most common in late winter and spring when the greatest need exists for heat transfer across the Stream.

The above findings support the conclusion reached by Stommel that large eddies play the major role in transfer of properties across the Gulf Stream, and the suggestion by Rossby that the basic behavior of such disturbances is analogous to that found in the atmosphere.

Acknowledgments. I am indebted to the Woods Hole Oceanographic Institution, and particularly Mr. L. V. Worthington, for giving me the opportunity to examine some of the results of Operation Abot and to reproduce unpublished observations from that survey. My gratitude is extended to Professor S. Petterssen and Miss D. L. Bradbury for allowing me to use some of their computations of sea-air heat exchange.

This research was supported by the Office of Naval Research contract Nonr 2121(10), NR 082-1, and the National Science Foundation grant SF-G6353.

REFERENCES

- rd, W. L., J. R. Longard, and R. E. Banks, On the nature, occurrence and origin of cold low salinity water along the edge of the Gulf Stream, *J. Marine Research, Sears Foundation*, 11, 281-293, 1952.
- nglister, F. C., and L. V. Worthington, Some results of a multiple ship survey of the Gulf Stream, *Tellus*, 3, 1-14, 1951.
- Hela, I., The surface current field in the western part of the North Atlantic, *Bull. Marine Sci. Gulf and Caribbean*, 3, 241-272, 1954.
- Iselin, C. O'D., A study of the circulation of the western North Atlantic, *Papers Phys. Oceanog. and Meteorol., Mass. Inst. Technol. and Woods Hole Oceanog. Inst.*, 4(4), 101 pp., 1936.
- Iselin, C. O'D., Preliminary report on long-period variations in the transport of the Gulf Stream System, *Papers Phys. Oceanog. and Meteorol., Mass. Inst. Technol. and Woods Hole Oceanog. Inst.*, 8(1), 40 pp., 1940.
- Iselin, C. O'D., Some common characteristics of the Gulf Stream and the atmospheric jet stream, *Trans. N. Y. Acad. Sci.*, 13, 84-86, 1950.
- Iselin, C. O'D., and F. C. Flugister, Some recent developments in the study of the Gulf Stream, *J. Marine Research, Sears Foundation*, 7, 317-329, 1948.
- Malkus, W. V. R., A recording bathypitotmeter, *J. Marine Research, Sears Foundation*, 12, 51-59, 1953.
- Malkus, W. V. R., and K. Johnson, A drift study of the Gulf Stream, *Tech. Rept., contract Nonr-769(00), (NR-083-069), Reference 54-67, Woods Hole Oceanog. Inst.*, 22 pp., 1954.
- Newton, C. W., Synoptic comparisons of jet stream and Gulf Stream systems, in *The Atmosphere and the Sea in Motion*, Rockefeller Inst. Press, New York, 288-304, 1959.
- Palmén, E., On the origin and structure of high-level cyclones south of the maximum westerlies, *Tellus*, 1(1), 22-31, 1949.
- Palmén, E., The aerology of extratropical disturbances, in *Compendium of Meteorology*, Am. Meteorol. Soc., Boston, 599-620, 1951a.
- Palmén, E., The role of atmospheric disturbances in the general circulation, *Quart. J. Roy. Meteorol. Soc.*, 77, 337-354, 1951b.
- Palmén, E., and C. W. Newton, On the three-dimensional motions in an outbreak of polar air, *J. Meteorol.*, 8, 25-39, 1951.
- Petterssen, S., *Weather Analysis and Forecasting*, vol. I, McGraw-Hill Book Co., New York, 428 pp. (see p. 321), 1956.
- Richards, F. A., and A. C. Redfield, Oxygen-density relationships in the western North Atlantic, *Deep-Sea Research*, 2, 182-199, 1955.
- Rossby C.-G., A comparison of current patterns in the atmosphere and in the ocean basins, *Union Geod. et Geophys. Intern., 9th Assembly, Assoc. de Météorol.*, Brussels, 9-31, 1951.
- Stommel, H., *The Gulf Stream*, Univ. Calif. Press, Los Angeles, 202 pp., 1958.
- Sverdrup, H. U., *Oceanography for Meteorologists*, Prentice-Hall, New York, 246 pp. (see pp. 172-173), 1943.
- Sverdrup, H. U., Discussion on the relationships between meteorology and oceanography, *J. Marine Research, Sears Foundation*, 14, 501-503, 1955.

- Swallow, J. C., and L. V. Worthington, Letter, *Nature*, 179, 1183-1184, 1957.
- Von Arx, W. S., Some measurements of the surface velocities of the Gulf Stream, *Tech. Rept., contract N6onr-27701 (NR-083-004)*, Reference 51-96, *Woods Hole Oceanog. Inst.*, 22 pp., 1951.
- Von Arx, W. S., Notes on the surface velocity profile and horizontal shear across the width of the Gulf Stream, *Tellus*, 4, 211-214, 1952.
- Von Arx, W. S., D. F. Bumpus, and W. S. Richardson, On the fine structure of the Gulf Stream front, *Deep-Sea Research*, 3, 46-65, 1955.

(Manuscript received September 12, 1960.)

Glaciological Regime at Little America Station, Antarctica

A. P. CRARY

*Arctic Institute of North America
Washington, D. C.*

Abstract. Factors affecting changes in the floating Ross Ice Shelf in the vicinity of the 1957-1958 IGY Little America Station are examined. From direct measurements, the amount of snow accumulation was 67 cm annually, or 26 cm ice equivalent. The principal horizontal strain rates, determined from repeated transit surveys, were 129 and 81×10^{-6} per year, with the minimum values in the approximate direction of motion. The maximum strain rate may be deduced from Weertman's formula for the creep of floating ice, using acceptable flow law constants. Vertical strain accompanying the horizontal strains should reduce the ice thickness by 54 cm/yr. From the known variations in ice shelf temperature with depth, 80 cm of melting at the ice-water interface is deduced. The net change for these factors would be an annual thinning of the ice shelf of 108 cm, equivalent to a decrease in surface elevations of 18 cm/yr. For the average surface slope in the Little America area of 65 cm/km, a forward ice shelf motion of 277 m/yr would be required, if elevations at fixed points remain constant with time. This velocity is comparable to that which has been deduced from the movement of Kainan Bay since it was first observed in 1912 by the Japanese Antarctic Expedition. Extrapolation of the creep rates and amounts of bottom melting south from the barrier edge give ice thinning that would result in somewhat higher ice movement values. Although the validity of the extrapolation to thicker ice is questionable, it appears likely that the ice west of Roosevelt Island is moving northward 3 to 4 times faster than the ice east of the island.

Introduction. In the period January 1957 to October 1958, a study was made of factors which affect the glaciological regime in the area of Little America Station in Antarctica. The pertinent information includes ice surface elevations and ice thicknesses, density and temperature throughout the shelf, accumulation of snow at the surface, oceanographic currents and temperatures, surface strain or creep as obtained from repeated surveys of a network of stakes, and absolute velocity of movement.

Little America Station, in January 1958, was at $78^{\circ}10'S$ and $162^{\circ}13'W$, about 4 km south of Kainan Bay on the northeastern side of the Ross Ice Shelf (Fig. 1). The station is north of the grounded ice of Roosevelt Island but about 50 km northeast of the Bay of Whales, the site of ice formation at the junction of the two branches of ice which flow around the island from the north. Kainan Bay, about 4 km wide and 3 km deep, is the northern part of a long rift, or tear, in the shelf, which runs about 15 km southward to the barrier edge. An east-west arm of this rift, known as Crevasse Valley, originates at the Kainan Bay rift about 1 km from the bay and extends for about 9 km to the east. The valley floors of these rifts, with minimum elevation of

about 15 meters, are hummocked and crevassed. Much of this deformation occurs when the elastic limit of the ice is exceeded by gravity or buoyant forces of the water and blocks of various sizes are displaced vertically. In the Little America area, there are also many small sinusoidal valleys, though none of these attains the depth of Crevasse Valley or the Kainan Bay rift. These smaller valleys are always connected with the rifts at one end, and, since the rifts are continually widening and lengthening, their movement into the shelf may be accompanied by the formation of the valleys. Since many of these rift and valley systems are normal to the direction of ice flow, it is to be expected that they would cause short-period deviations from the steady-state conditions.

Elevations. The elevations of the shelf ice above sea level were obtained by transit level survey from Kainan Bay to Little America Station and along the trail to Byrd Station for an additional 2.5 km. Other elevation observations include transit vertical angles between the stakes of the survey stake network, level survey along a 7-km seismic refraction line, and some altimetry surveys. The surface slope of the shelf ice, averaged over the 10-km distance from the

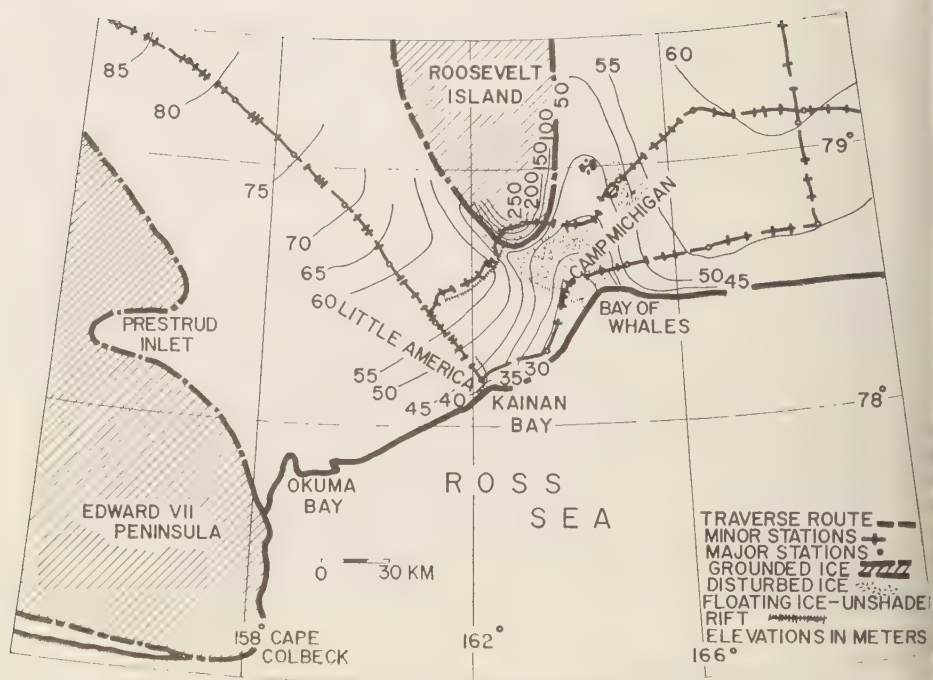


Fig. 1. Map of northeastern part of the Ross Ice Shelf, Antarctica.

barrier included in this study, is 65 cm/km, but the slope varies considerably over short distances. Along the Byrd trail southeast of the station, measured by altimetry survey on four different occasions, the average surface slope is about 45 cm/km toward the barrier. West of Roosevelt Island, the results of the Ross Ice Shelf traverse indicate a much smaller surface slope, and in the first 80 km from the barrier edge the increase in elevations is only 11 meters, an average of 14 cm/km.

Ice thickness. Values of ice thickness were obtained at about a dozen sites in the Little America area by seismic shooting. In addition, a deep hole was drilled at the station site within a few meters of the bottom of the ice by the Snow, Ice, and Permafrost Research Establishment (SIPRE) of the U. S. Army in late 1958 [Ragle, Hansen, Gow, and Palenau, 1960]. Crary [in press] computed a curve for ice thickness versus elevation from drill-hole densities and seismic soundings, and from this a ratio of about 6/1 at Little America is indicated. Thus the approximate 65-cm/km surface slope indicates a

thinning of the ice shelf of about 390 cm/k toward the barrier edge. If the shelf ice at a fixed geographic location does not change in thickness with time, the product of the surface slope and the absolute movement per year should equal the annual changes in elevation from thinning due to accumulation, ice creep effects, and bottom melting.

Accumulation. The record of accumulation snow on the shelf was obtained by routine measurements on about 100 stakes widely scattered over the Little America area. Figure 2 shows the results averaged by months, giving an annual accumulation of 67 cm of snow. However, there are some quite large variations in the record. Maximum accumulation occurs in April, May, and October; in November the wind actually scours snow from the surface. There is also variation in snow accumulation with distance from the barrier—40 cm at the barrier, 90 cm 20 km inland, and as low as 30 cm farther inland. The monthly accumulation for the few months in 1958 for which data are available is almost twice that of corresponding months in 1957.

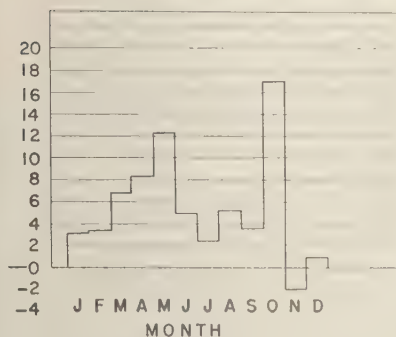


Fig. 2. Snow accumulation observed at Little America Station.

ten, in addition, there were local areas of normal accumulation, such as the northern ends of the rifts and valleys.

The variation of density with depth, taken in a total of 29 shallow-pit studies, has been used to obtain the ice or water equivalent of the ice of snow accumulation. The water equivalent of the accumulation was 24 g/yr. The annual addition to the thickness of the shelf should be the total weight divided by the maximum density of the shelf, or 26 cm.

Strain rate. The creep of the ice was obtained from a survey of a network of stakes covering an area about 9 km on a side, with center near Little America Station. The survey was based on the distance between two stakes approximately 3 km apart, obtained by chaining 14 times during the interval of approximately 600 days; during this period the distance increased by about 3 meters. The remaining survey was obtained

from angles of triangles, most of the angles being measured at 6-month intervals. All three angles of all triangles were obtained, and observations were repeated until the triangle closures were less than about 20 sec of angle. These values of angles were each plotted against time, and the values were interpolated or extrapolated as necessary to obtain angles for a beginning date of February 13, 1958, and for 600 days later. The strain values for lines that crossed either Crevasse Valley or the Kainan Bay rift were from 2 to 10 times as great as those not crossing these features. If these anomalous values are excluded, there is a definite maximum strain value approximately normal to the direction of flow. A least-squares solution was made for all lines of the triangles used in the survey, and the values of the horizontal strain were assumed to vary sinusoidally between maximum and minimum at the two principal horizontal strain rates 90° apart. Values of 129×10^{-5} and 81×10^{-5} per year were obtained, with the minimum values along true azimuths 135° and 315° .

Strain rates were also observed on a similar floating ice shelf during the Maudheim expedition of 1948–1952. These values, reported by *Swithinbank* [1958], are compared with the Little America results in Figure 3. For the Maudheim data, it was also necessary to exclude strain values for the lines across major valley systems. As at Little America, the minimum strain rate was parallel to the direction of probable ice flow, 160° and 340° . Values obtained for principal horizontal strain rates at Maudheim were 138×10^{-5} and 55×10^{-5} per year.

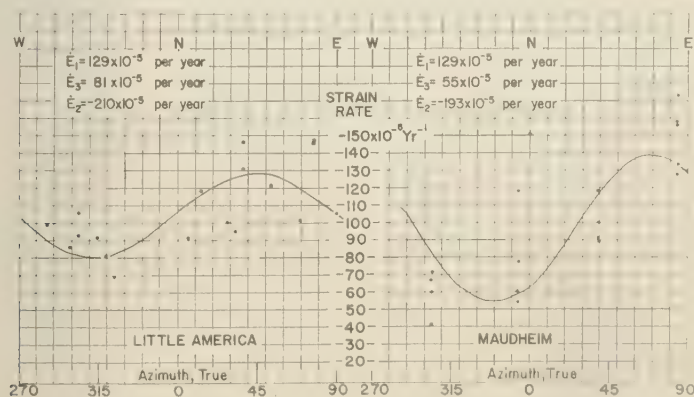


Fig. 3. Variation of horizontal strain rates with direction.

At the U. S. IGY Ellsworth Station, a network of stakes was surveyed [Aughenbaugh, Neuburg, and Walker, 1958]. The base line was chained three times, the last in October 1958, but the results are unfortunately not in accord. The results of the transit resurvey, combined with the base line distances obtained in March 1957 and in October 1958, show principal horizontal strain rates of 142×10^{-6} and 62×10^{-6} per year, with the minimum value in the directions 008° and 188° . Regardless of the possible error in base-line distance, the nearly 2 to 1 ratio of strain rates between directions normal to and parallel to the flow is again indicated.

Weertman [1957] has shown that the problem of the creep of a floating ice shelf is equivalent to that of a weightless material compressed by frictionless plates. If the power law relationship between strain rate and applied stress obtained in laboratory tests by Glen [1955] is used, Weertman's formula for the strain of floating ice free to flow in any horizontal direction is

$$\dot{\epsilon} = \frac{B}{2} \left\{ \frac{g \int_0^h \int_x^h \rho_i(g) dy dx - g/2\rho_w \left[\int_0^h \rho_i(y) dy \right]^2}{\left(\int_0^h \exp \left[-\frac{Q}{RT} + \frac{Q}{RT_m} \right] dy \right)^{1/n}} \right\}^n$$

where

$\dot{\epsilon}$ is the horizontal strain, which would be equal in all directions.

B , n , and Q are experimental constants of the flow law.

R is the gas constant, 1.9865 calories per degree-mole.

T and T_m are the ice temperatures and ice melting temperatures, respectively.

g is the acceleration of gravity.

h is the ice shelf thickness.

ρ_i and ρ_w are density values for the ice and for sea water, respectively. The required data on the temperature and density throughout the shelf are available at Little America from the SIPRE deep drill hole and at Maudheim from a drill hole about halfway through the shelf [Schytt, 1958]. The maximum principal horizontal strain rate found at Little America can be obtained by using the constants $B = .017$ $\text{yr}^{-1} \text{bar}^{-1}$, $n = 4.2$, and $Q = 21,500$ cal/mol .

For the Maudheim data the values $B = .017$ $\text{yr}^{-1} \text{bar}^{-1}$, $n = 4.2$, and $Q = 18,200$ cal/mol would give the observed maximum strain rate. These values of Q are lower than the original values given by Glen [1955] and somewhat higher than the values obtained for snow samples in the laboratory by Landauer [1955] and the values obtained by Nakaya [1958] for samples of ice from Greenland. However, observed values from Little America and Maudheim can also be obtained from Weertman's formula with other combinations of B , n , and Q values. It is interesting to note that the strain values for the Maudheim ice shelf are comparable to those found at Little America despite the thinner ice (190 m, compared with 257 m). The effect of ice thickness on the strain is offset by temperature values, which are about 5°C higher at the surface at Maudheim. The evaluation of the Ellsworth data has not been attempted because the length of the base line is uncertain and because the only density and temperature values

available are those taken to 60 meters in a deep pit, located at the bottom of a small valley where some anomalous ice conditions were found [Aughenbaugh, Neuburg, and Walker, 1958]. The formula for the flow of an ice shelf is simple, but many variations in temperature are to be found in the Antarctic. With additional observations it should be possible to determine the constants for the flow law.

Bottom melting. Melting of ice from the bottom of the shelf is the third major factor in the change of ice thickness, but the oceanographic observations obtained were insufficient to allow determination of this melting. Sverdrup [1958], examining this problem for the Maudheim ice shelf, showed that wind stresses were in the right direction to move water toward the shelf edge, but that this water descended on reaching the bare edge. Using observed temperatures and estimated velocities, Sverdrup was able to show that only 12 per cent of the potential melting in this water was needed to offset the accumulation of snow.

the entire ice shelf. Observations at Little America did not confirm the importance of wind-driven current; the average of a limited number of current values obtained at Kainan Bay was but 12 cm/sec from the south and east [Crary, 1958]. The potential temperatures of the water for melting purposes, and the possible volumes concerned, are sufficient to account for considerable bottom melting provided that the eddy diffusivity values under the shelf are large enough to cause a significant exchange of thermal energy. Certainly, the combinations of tidal currents, wind-driven currents, and dynamic currents near the edge of the shelf should result in considerable melting there, but direct information is not sufficient for an estimate to be made of the far back of the barrier this bottom melting can occur.

Observations at Little America of the temperature variations with depth through the ice and in the SIPRE drill hole and of variations throughout the year at shallow depth may be used indirectly to arrive at a figure for the bottom melting. At the surface the gradient is very small, but it becomes greater with depth and reaches a maximum at the bottom of the shelf. At [1958], studying similar temperature values obtained at Maudheim, has pointed out the

$$dh/dt = \frac{A}{p(h)} + \frac{h}{H} \left(M - \frac{A}{p(h)} \right) \quad (2)$$

where

A is the annual snow accumulation.

M is the amount of bottom melting per year.

p is the density, a function of the depth.

H is the ice thickness.

It is implied that the steady-state condition for a thinning ice shelf is one in which the temperature at any depth nH of the original shelf is equal to the temperature at any depth nH' of the shelf after thinning. Under this assumption the thinning of the ice by creep does not affect the temperature distribution. The error introduced by assuming no variation in temperature gradient due to the decrease in ice thickness (1 part in 257) is not significant.

If this value of vertical movement is used, the steady-state heat flow equation in one direction becomes

$$\frac{dT}{dh} \left[\frac{A}{p(h)} + \frac{h}{H} \left(M - \frac{A}{p(h)} \right) \right] = a(h) \frac{d^2 T}{dh^2} \quad (3)$$

where a , the thermal diffusivity, is also a function of the depth. The solution of this equation for the temperature values is given by

$$\frac{T_h - T_0}{T_H - T_0} = \frac{\int_0^h \exp \left\{ \int_0^h \left[\frac{A}{p(h)} + \frac{h}{H} \left(M - \frac{A}{p(h)} \right) \right] a^{-1}(h) dh \right\} dh}{\int_0^H \exp \left\{ \int_0^h \left[\frac{A}{p(h)} + \frac{h}{H} \left(M - \frac{A}{p(h)} \right) \right] a^{-1}(h) dh \right\} dh} \quad (4)$$

indications of the variations of gradient with regard to bottom melting. The alternative solution that the ice had been in a nearly isothermal condition at average air temperatures over land and had then moved out over the water but had not yet reached a steady-state condition, has been pointed out by [1960]. However, the necessary condition that the ice had originated on the ice shelf is questionable when the surface temperatures shown in Figure 1 are considered.

Theoretical solutions for shelf temperatures are computed by the method [Robin, 1955] in which the change of temperature with time is equated to the product of the temperature gradient and the vertical movement of the ice. This rate of movement for the ice shelf will be assumed to be

The values of density variations were obtained from the results of the SIPRE deep drill hole and averaged over 20-m intervals; the values of thermal diffusivity have been inferred from various sources, using as the maximum value 11.8×10^{-3} , the generally accepted value for ice. These values of density and diffusivity are shown in Figure 4. Figure 5 shows the results obtained by the numerical integration of equation 4, with a value of 24 grams for A , the accumulation, and values of 40, 60, and 80 cm for M . The curve for 80 cm of annual melting fits the observed ratios at the bottom of the ice, but values in the center of the shelf are nearer the curve for 60 cm of melting. Presumably, as the ice moves northward the boundary conditions change too fast

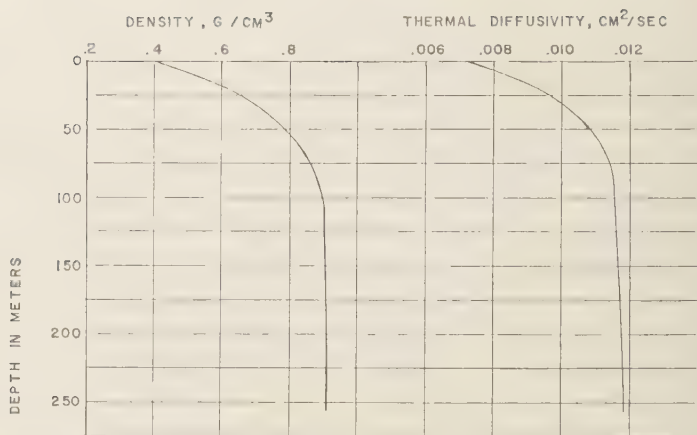


Fig. 4. Observed density values and assumed thermal diffusivity values in the ice shelf at Little America Station.

for the upward flow of heat to establish steady-state conditions.

Regime summary. The regime of the ice can be obtained from the amounts of accumulation, thinning by ice creep, and possible melting at the bottom. The results are given in Table 1. Thus, the ice at Little America loses 108 cm of its 257-meter thickness annually, and, from the thickness-elevation relation, this loss should represent a yearly decrease in elevation of 18 cm. From this value and the surface slope in the Little America area, 65 cm/km, the absolute velocity would have to be 277 m/yr if the ice

shelf were to remain unchanged with time. The fact that the barrier edge itself does not remain in the same position should not have a marked effect on the ice elevations at any fixed position, and the farther north the barrier extends, the thinner it should be at the edge.

Absolute movement. The most reliable value of the movement of the ice in the Little America area is obtained from comparison of the present location of Kainan Bay with that given in 1911 by the *Japanese Antarctic Expedition* [1958]. The average position for Little America, based on different determinations made during the I

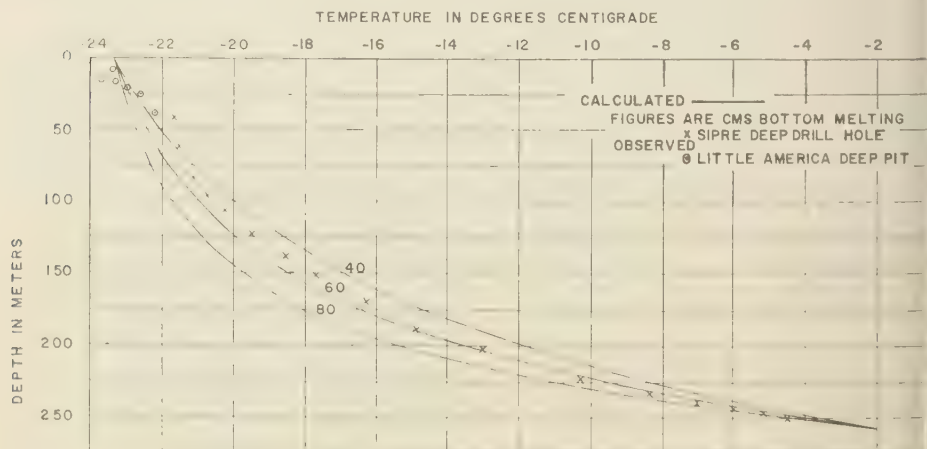


Fig. 5. Comparison of observed and theoretical ice shelf temperatures.

TABLE 1. Annual Changes of Thickness of Shelf Ice at Little America

	Ice-Thickness Change, cm	Water Equiva- lent, cm
Ice accumulation	+26	+24
Ice creep	-54	-46
Bottom melting	-80	-73
Net change	-108	-95

od, was extended to Kainan Bay from the survey network, and the total movement in 16 years was found to be 11.33 km in the direction N10°W. This gives an average velocity of 45 m/yr. A correction must also be made for amount of possible calving at the barrier edge. In 1957-1958 this amounted to 9 meters, and, if this figure is used, the velocity becomes 254 m/yr. In the comparison with the Japanese results it is assumed that the Japanese position is in the center of a line across the mouth of Kainan Bay. If it was 1 km inside the bay, the velocity would be 277 m/yr. Also the calving at the barrier could have been much larger, particularly if large portions of the ice have calved off en masse.

Ice regime inland. The extrapolation of the accumulation, creep rates, and melting at the bottom, to thicker ice away from the barrier, is highly subject to several possible errors, has been attempted in an effort to understand the significance of the difference in slope of the

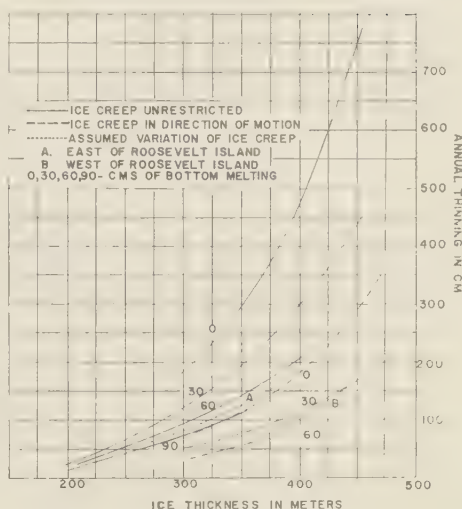


Fig. 6. Ice-shelf thinning versus ice thickness for various conditions of creep and bottom melting.

surface of the floating ice on either side of Roosevelt Island. The accumulation is assumed to decrease from a value of 26 cm at the barrier to 20 cm inland. At exposed areas such as Little America the ice creep is assumed to have movement directed only away from the exposed area. The bottom melting is assumed to decrease inland from 80 cm at the barrier. Figure 6 shows the variations of the thinning of the ice shelf by creep for various ice thicknesses and melting at

TABLE 2. Ice Budget, Averaged over a Two-Year Period

Thickness, m	Elev., m	Creep Loss, cm	Melt Loss, cm	Acc., cm	Net/yr, cm	Yrs/m	Avg	Years
East Side of Roosevelt Island								
257	44.6	-54	-80	+26	-108	0.93		
320	51.5	-100	-40	+24	-116	0.86	.90	57
400	60.2	-180	0	+20	-160	0.62	.62	59
								116
West Side of Roosevelt Island								
350	54.7	-41	-80	+26	-105	0.95	.88	44
400	60.2	-105	-40	+23	-122	0.82	.69	35
450	66.0	-169	-30	+20	-179	0.56		79

the bottom, the melting having considerable effect on the creep because of its effect on the temperatures of the shelf. The assumed conditions are represented by curve *A* for the area east of the island and curve *B* for the area west of the island, where the ice at the barrier edge is much thicker. Table 2 shows the ice regime for the two cases.

From the known elevations along the trail to the Byrd Station, east of Roosevelt Island, the ice thins from 400 to 257 meters in about 44 km, which would give an average velocity of 380 m/yr. West of the island, along the return route of the 1957-1958 traverse party, the elevations representing 450 to 350 meters of ice thickness are 102 km apart, indicating an average velocity of 1290 m/yr. Although the figures are subject to error in the extrapolation of ice creep and melting at the bottom, the ice on the west side must be moving considerably faster than the ice on the east.

This large difference in velocity on the two sides of the island can be inferred from other indirect evidence. *Ostenso and Bentley* [1959] have shown that the elevations along the trail to Byrd Station on the floating ice shelf drop, from a maximum, almost 20 meters before reaching the crevassed area marking the junction of the floating and grounded ice. Trail parties and tractor trains have passed over this crevassed junction for three consecutive years without finding major changes in the state of the crevassed area, a condition which could hardly be possible unless the movement is very slow. Also, *Crory* [1959] has given preliminary values of ice thickness for the Ross Ice Shelf which show that the nourishment for the shelf comes mainly from the part of Byrd Land southeast of the shelf. If the area east of Roosevelt Island receives its ice mainly from local accumulation, it would not have the forces to cause such high velocities as are inferred for the ice to the west of the island.

Acknowledgments. I wish to acknowledge the capable field assistance at Little America Station of Walter W. Boyd, Jr., Hugh Bennett, and William Cromie in 1957 and of Stephen den Hartog and Lyle McGinnis in 1958.

REFERENCES

- Aughenbaugh, N., Hugo Neuburg, and Paul Walker, Ellsworth Station glaciological and geological data, 1957-58, pp. 2-158, Rept. 825-1-Part I, Report of Ohio State University Research Foundation to IGY World Data Center A, Glaciology, American Geographical Society, New York, Oct. 1958.
- Crory, A. P., Oversnow traverses from IGY Little America Station, *IGY Bull.* 27, *Trans. Am. Geophys. Union*, 40, 311-315, 1959.
- Crory, A. P., Glaciological studies at Little America Station, Antarctica, *IGY Glaciol. Rept. Ser.*, 1, World Data Center A, Glaciology, American Geographical Society, New York, in press.
- Glen, J. W., The creep of polycrystalline ice, *Phil. Mag.*, 1, 349-362, 1955.
- Japanese Antarctic Expedition, Report of, *Antarctic Record*, vol. 4, Ministry of Education, Tokyo, Japan, July 1958.
- Landauer, J. K., Stress-strain relations in ice under uniaxial compression, *J. Appl. Phys.*, 26, 1493-1497, 1955.
- Nakaya, U., Visco-elastic properties of snow and ice in the Greenland Ice Cap, *Physics of the Movement of Ice*, Symposium of Chamorro Intern. Assoc. Sci. Hydrol., Publ. 47, 199-200, 1958.
- Ostenso, N. A., and C. R. Bentley, The problem of elevation control in Antarctica, and elevation control on the Marie Byrd Land traverses, 1957-1958, Group 4, *IGY Glaciol. Rept. Ser.*, 2, IGY World Data Center A, Glaciology, American Geographical Society, New York, July 1959.
- Ragle, R. H., B. L. Hansen, A. Gow, and R. Patenaude, Deep core drilling in the Ross Ice Shelf, Little America V, Antarctica, *Tech. Rept. 70*, U. S. Army Snow, Ice and Permafrost Research Establishment, Corps of Engineers, June 1960.
- Rubin, G. de Q., Ice movement and temperature distribution in glaciers and ice sheets, *J. Glaciol.*, 2, 523-533, 1955.
- Schytt, Valter, (C) The inner structure of the ice shelf at Maudheim as shown by core drilling, *Glaciology 2*, Norwegian-British-Swedish Antarctic Expedition, 1948-52; *Scientific Results*, vol. 4, Norsk Polarinstitut, Oslo, 1958.
- Sverdrup, H. U., The currents off the coast of Queen Maud Land, *Norsk Geograf. Tidsskr.* 14, 239, 1958.
- Swithinbank, Charles, (C) The movement of the ice shelf at Maudheim, pp. 81-84; *Glaciology*, Norwegian-British-Swedish Antarctic Expedition, 1948-52, *Scientific Results*, vol. 3, Norsk Polarinstitut, Oslo, 1958.
- Thiel, E. C., and N. A. Ostenso, The contact between the Ross Ice Shelf with the continental ice of Antarctica, *J. Glaciol.*, in press.
- Weertman, J., Deformation of floating ice shelves, *J. Glaciol.*, 3, 38-42, 1957.
- Wexler, H., Heating and melting of floating ice shelves, *J. Glaciol.*, 3, 626-646, 1960.

(Manuscript received October 31, 1960.)

Directional Properties and Phase Relations of the Magnetotelluric Fields at Austin, Texas

H. W. SMITH, L. D. PROVAZEK, AND F. X. BOSTICK, JR.

*Electrical Engineering Research Laboratory, University of Texas
Austin, Texas*

Abstract. Directional properties and phase relations of the variable electric and magnetic field components of selected data samples taken at Austin, Texas, are presented in the form of X - Y plots. Power density spectra of component signals are shown, and data recording and analysis techniques are described and illustrated for the selected data samples.

INTRODUCTION

Interest in the fluctuations of the so-called natural magnetotelluric field, i.e., the combined variable electric and magnetic fields of the earth, has shown a marked increase in recent years, as shown by Campbell [1959], Duffus and Shand [1958], and Seng [1954], and Maple [1959]. The measurements and analyses used to determine the directional properties and phase relations between components of magnetotelluric fields are described, and the results obtained from selected data samples taken during the months of June and July, 1960, at Austin, Texas are presented. The Electrical Engineering Research Laboratory of the University of Texas has recently completed the installation of a permanent magnetotelluric observation station on the grounds of the Balcones Research Center at Austin, Texas [30°23'N, 97°43'W]. Data and results obtained from this site are presented in the form of graphic recordings of the original and the filtered records, the power density spectra, and X - Y plots of selected electric and magnetic field components.

THE MEASURING SYSTEM

The details of this installation, including a complete description of the instrumentation and recording systems, have been published in report by Smith, Boothe, Fannin, and Bostick [1960], and only a brief summary of the salient features is included here. The system consists of four 1120-ft earth current lines, two each in the north-south (E_y) and east-west (E_x) directions. Maximum sensitivity on earth current systems is

approximately 3 mv/km for full-scale chart deflection. The north-south (H_y), east-west (H_x), and vertical (H_z) components of the magnetic field fluctuations are measured by a set of three mutually perpendicular air-core coils consisting of 15,000 turns of AWG28 insulated copper wire. The coil sensitivities are 47.4 $\mu\text{v}/\gamma/\text{sec}$, and the maximum sensitivity for the magnetic field variations is 1 γ for full-scale chart deflection. The frequency range extends from 0.005 to 1 cps for all components.

Esterline-Angus recorders are used to provide continuous measurement, and magnetic tape recorders are used to obtain selected samples up to 4 hours in duration. The latter are far superior in terms of dynamic amplitude and frequency range, freedom from noise, and ease of handling, and are used primarily for detailed analysis of short samples.

No great volume of data has yet been taken at this site, but sufficient observations have been made to indicate that the system is capable of producing high-quality records that will be suitable for detailed analysis. In the absence of a large quantity of observations, which will be available in the future, we decided to take a few selected data samples and perform some of the analyses within our present capabilities. We believe that the techniques used and the limited results obtained are of sufficient interest for presentation at this time.

DATA RECORDING

Two types of data are used in this analysis. The first type is concerned with the determination of the principal direction of the electric and magnetic field vectors at this location. These

data were obtained from recordings made by the direct application of the north-south and east-west components to an X-Y plotter.

The second type of data consists of a single set of recordings of approximately 1-hour duration of the north-south and east-west components of the earth current and magnetic field selected for a more detailed analysis. The original tapes were made with a seven-channel Ampex FR-100 magnetic tape recorder operating at a speed of $1\frac{7}{8}$ inches/sec. These tapes were then run at a playback speed of 30 inches/sec and re-recorded at $1\frac{7}{8}$ inches/sec on a second tape recorder. Final playback of the second set of tapes at 30 inches/sec gave a total speedup of 256. This process was necessary to put the frequency components of interest into the range of the filtering and analysis equipment, 1 cps to 5 kc/s. The samples chosen for this analysis appear to be typical of the signals for moderately 'quiet days' frequently referred to by investigators, having a more or less regular quasi-sinusoidal form in the frequency range near 0.06 cps. After a tape

speedup of 256, the original 1-hour recording compressed to approximately 14 seconds during playback, and the original bandwidth of 0.06 to 1 cps is shifted to the range from 1.28 to 256 cps.

DATA ANALYSIS

Graphic recordings taken from the 1-hour magnetic tape records to obtain the selected data sample are shown in Figure 1. Full chart sensitivities are 58.6 mv/km for the north-south and east-west components of the earth current at 10γ for the corresponding components of the magnetic field. Differences in the amplitudes of the components may be noted, but the general character of all of the signals is similar, particularly with regard to the prominent frequency component near 0.06 cps. The analyses used are briefly described as follows.

Power density spectra. Power density spectra of the four signal components, E_x , E_y , H_x , and H_y , of the original data were obtained from the power spectrum computer developed at the

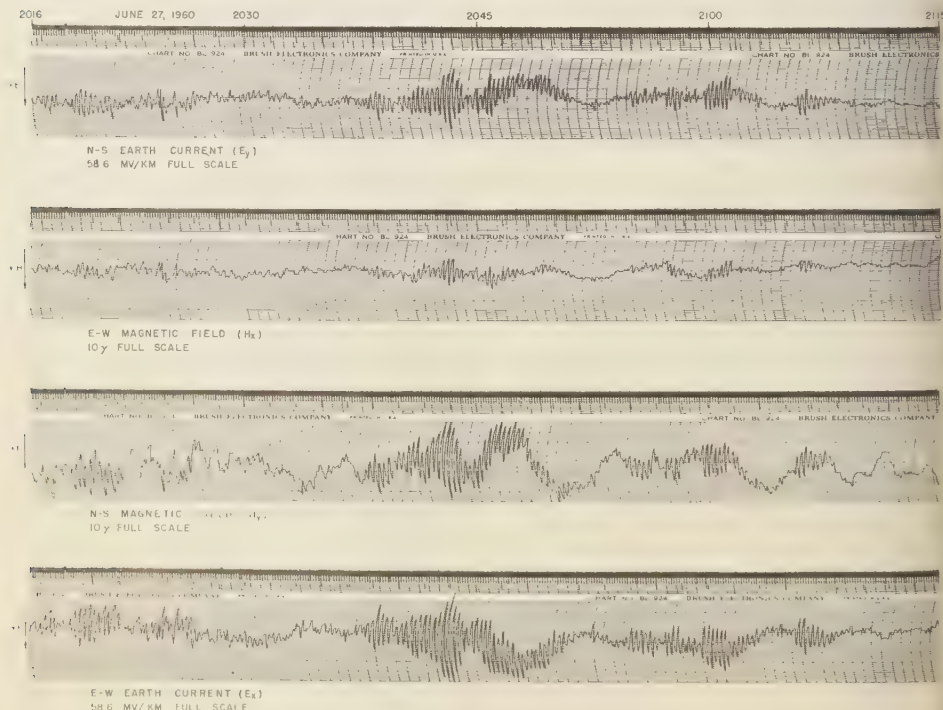


Fig. 1. Electric and magnetic field components.

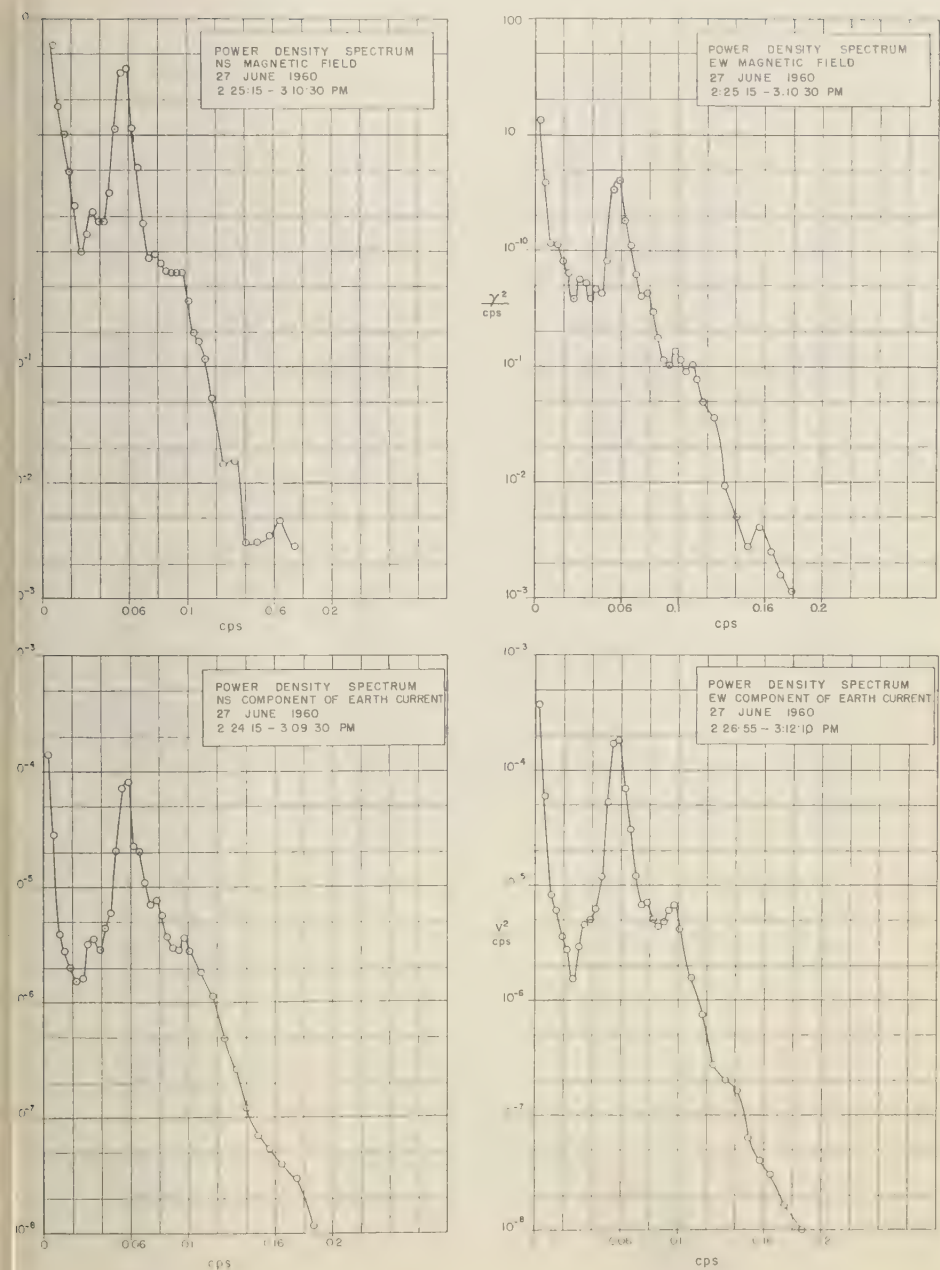


Fig. 2. Power spectra of electric and magnetic field components.

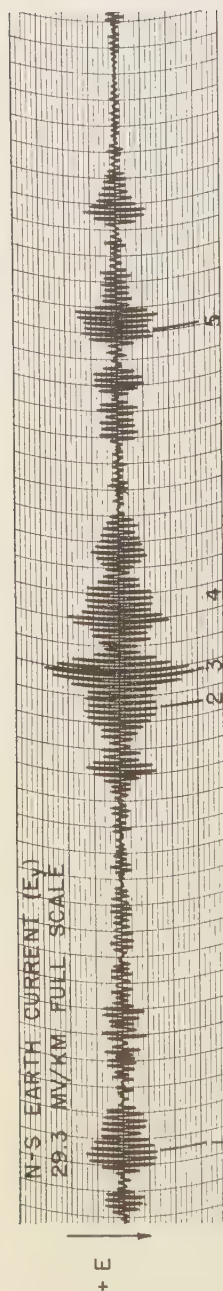
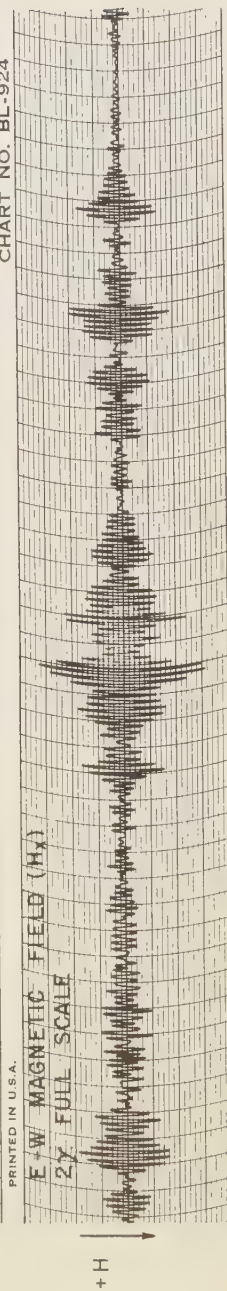
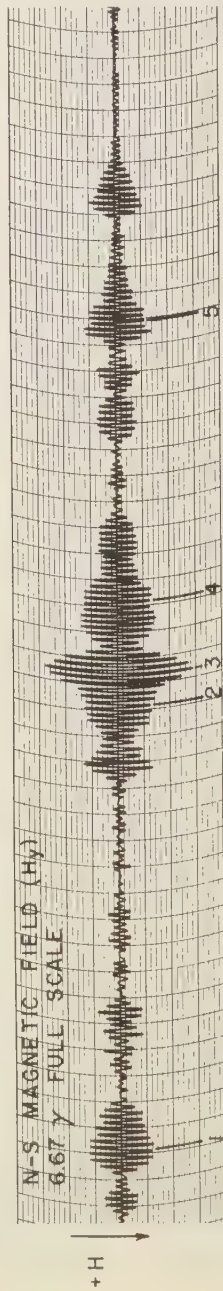


CHART NO. BL-924



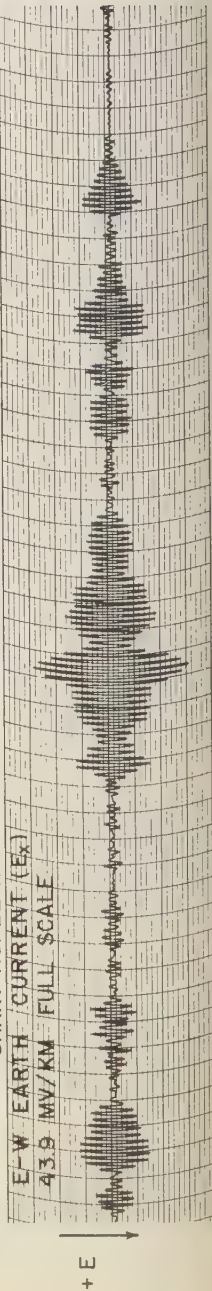
PRINTED IN U.S.A.



PRINTED IN U.S.A.

BRUSH ELECTRONICS COMPANY

CHART NO. BL-924



laboratory, *Smith, McClure, and Bostick* [1956]. Aside from the usual statistical considerations involved in the process of obtaining estimates of the power density spectrum [*Blackman and Key, 1958*], this computer has a dynamic range and accuracy that is sufficient for analysis of signals taken on magnetic tape recorders of the highest quality. These spectra (Fig. 2) were computed simply to determine the general frequency character of the signals and to compare the spectra of the individual components. Application of the power density spectra to the determination of the conductivity structure of

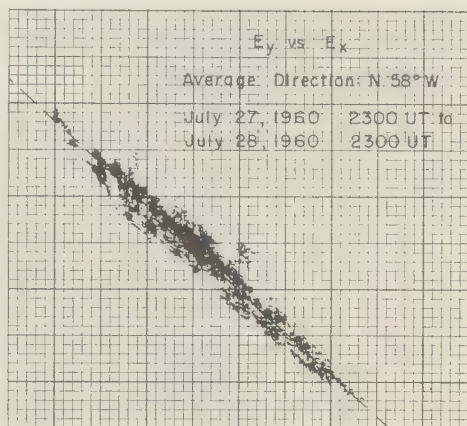


Fig. 4. Directional plot of the electric field.

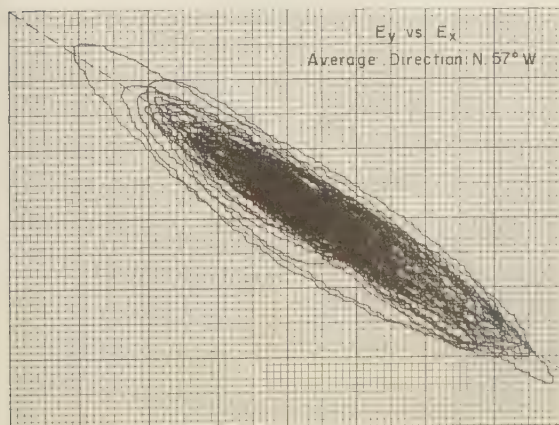
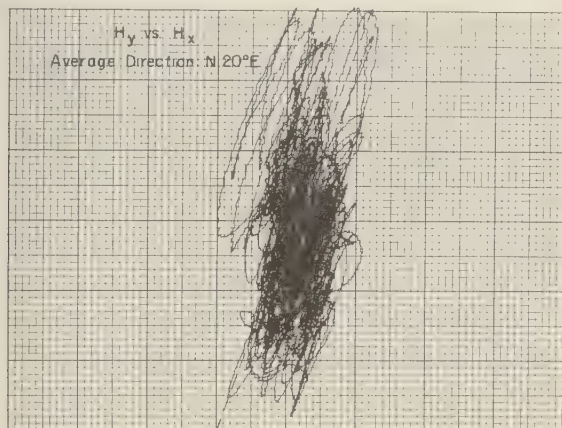


Fig. 5. Total electric and magnetic field directional plots for data shown in Figure 1.

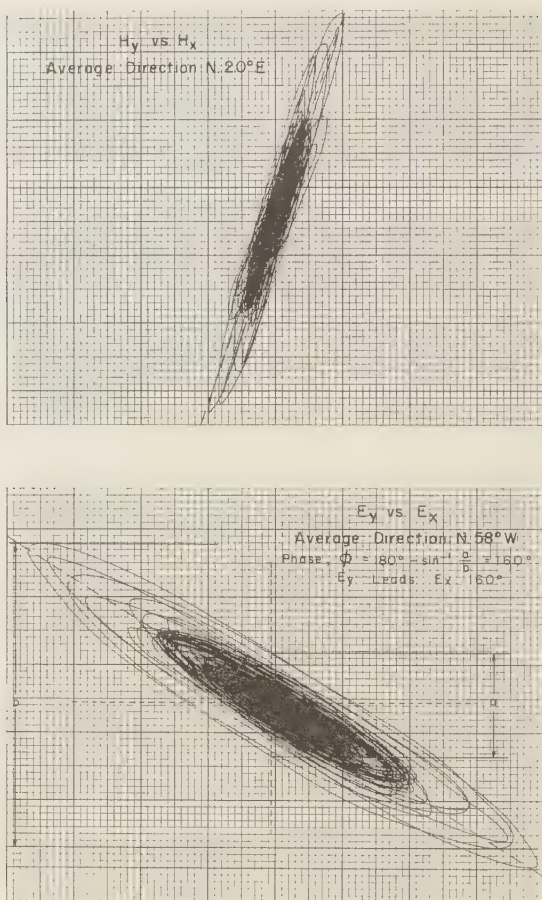


Fig. 6. X-Y plots of filtered electric and magnetic fields corresponding to data shown in Figure 3.

the earth, following *Cagniard* [1953], is in progress and will be reported later.

Narrow-band filtering. The original tape records used to produce Figure 1 were passed through a very narrow band filter having 3 db points at 0.05 and 0.0625 cps and skirts of 80 db/decade. This bandwidth was chosen to straddle the peak of the power density spectra shown in Figure 2. The filtered components are shown in Figure 3. Unequal component gains were used to bring out the striking similarity of all of the filtered signals.

Cross correlation functions. Cross correlation functions were computed for the E and H components of both the original and filtered records.

The maximum correlation obtained was 0.79 for the original records and 0.97 for the filtered records.

X-Y plots. With appropriate amplifiers and instrumentation, an X-Y plotter may be used to determine the direction of the total E and H vectors. The plotter may also be used to measure the phase between the total E and H signals and to measure the degree of elliptical polarization of these signals. The positive direction for the north-south fields (E_y and H_y) in all X-Y plots is along the vertical axis toward the top of the figure. Similarly, the positive direction for the east-west fields (E_x and H_x) is to the right along the horizontal axis. Thus, the top of the figure

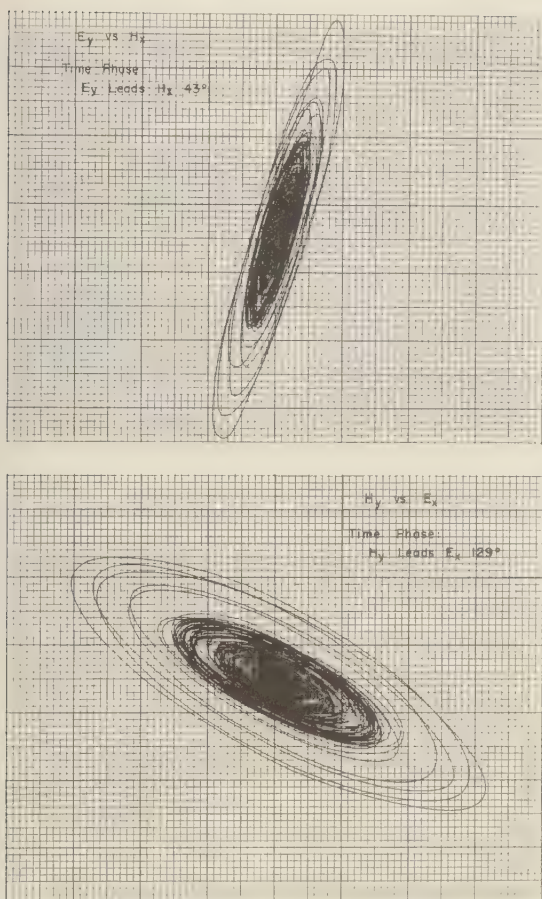


Fig. 7. X-Y plots of filtered components for data shown in Figure 3.

represents geographic north, with geographic east to the right in the usual convention. Figure 4 shows a typical directional plot of the total variable E field recorded at this location during a 24-hour period. The plots were made by applying the E_x and E_y components to the X-Y plotter on a regular sampling basis. For 1 minute out of every 12.5 minutes, the plotter was turned on. During this 1-minute period, 20 equally timed points representing the direction of the field were plotted. The origin of the coordinate axis corresponds to zero variable signal for both components. The dashed line represents the average directional trend over the 24-hour period.

Continuous X-Y plots of the total variable E

and H fields for the 1-hour sample recorded on magnetic tape are shown in Figure 5. The directional trend of the E field is clearly evident, but the trend of the H field is only vaguely discernable. Part of the difficulty results from the fact that the H_x component is so small that noise, equipment drift, and temperature changes become appreciable. Similar plots for the filtered components of Figure 3 are shown in Figure 6. The quality of the plots is seen to be much improved. Directional trends and the elliptical polarization of the E and H fields are now clearly evident. The average phase difference between the components can be measured as is indicated in Figure 6. Another type of plot made from the

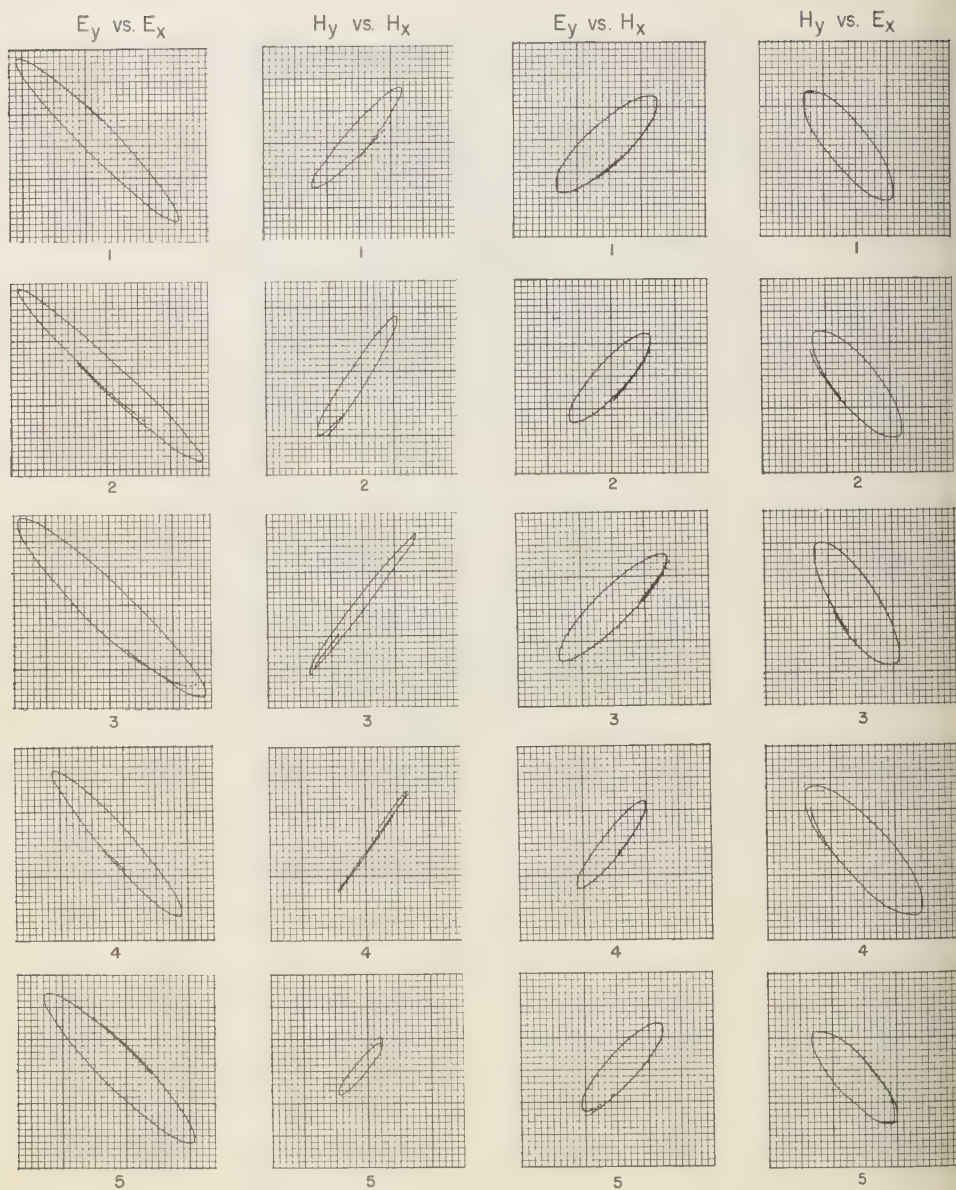


Fig. 8. Phase relations. Numbers below each ellipse correspond to times noted in Figure 3. (Refer to Table 1 for calculated phase for each ellipse.)

filtered records of Figure 3 is shown in Figure 7. These plots were obtained by applying the E_x and H_y and the E_y and H_x components to the X-Y plotter. These plots indicate the phase between E and H components.

Finally, individual cycles of the filtered data were applied to the X-Y recorder at the times indicated in Figure 3. The results are shown in Figure 8 for the following combinations of signal components: E_x and E_y , H_x and H_y , E_x and H_y , E_y and H_x .

RESULTS

The mean direction of the total variable E field for this location, determined from plots of the type shown in Figure 4, is N58°W. Variations in this direction as great as $\pm 9^\circ$ have been observed, although deviations of this magnitude from the mean are rare.

X-Y plots of the total H field over several hours have been inconsistent. Very few frequency drift in the equipment due to temperature changes coupled with the small signal level of the H_x component seem to be the principal cause of the poor results. However, the direction of the variable H field vector for the 1-hour sample is evident in the H -Y plot of Figure 5 and is clearly indicated as N20°E for the filtered component of Figure 6. In future study an attempt will be made to determine any directional variation in different frequency bands. It is interesting to note that the measured angle between the total E and H field vectors for the filtered components in Figure 6 is 78°.

The average phase relations between the various E and H field components are indicated in Figures 6 and 7. Variations in the phase relations for selected individual cycles of the filtered record are shown in Figure 8 and in Table 1. In this table, the phase relations between the E_y versus E_x and the H_y versus H_x components were calculated directly from the ellipses shown in Figure 8. In the case of the E_y versus H_x and the H_y versus E_x components, a phase difference correction of 14° was required to compensate for different phase shifts in the E and H measuring circuits at this narrow frequency band. Variations in the measured phase are reasonably small for all combinations except the H_x and H_y components. Again, we believe that the previously mentioned difficulties with the H components are responsible for this variation.

TABLE 1. Phase Relations for Figure 8

Components	Sample Time Corresponding to Figure 3					
	1	2	3	4	5	Avg.
E_y leads E_x	164°	168°	160°	162°	159°	163°
H_y leads H_x	21°	17°	8°	4°	20°	14°
E_y leads H_x	46°	44°	41°	38°	45°	43°
H_y leads E_x	131°	128°	127°	132°	129°	129°

CONCLUSIONS

The spectra and directional properties of a preliminary series of magnetotelluric recordings at this location have been obtained, and a number of interesting possibilities for further investigation have been indicated. The representativeness and absolute accuracy cannot be ascertained, however, until a new and extensive observation and analysis program has been completed and certain long-term instabilities in the magnetic field installation have been corrected. Although the analysis is not yet complete, measurements obtained on three additional days appear to have the same general character as the sample reported. This would indicate that this sample does not represent an isolated case. In particular, the application of narrow-band filtering of the signals at a number of different frequencies holds the greatest promise of yielding significant new data in the area.

Acknowledgment. The research reported here was supported by the Office of Naval Research under contract Nonr 375(01).

REFERENCES

- Blackman, R. B., and J. W. Tukey, *The Measurement of Power Spectra*, Dover Publications, New York, 1958.
- Boothe, R. R., B. M. Fannin, and F. X. Bostick, Jr., A geomagnetic micropulsation measuring system utilizing air-core coils as detectors, *Rept. 115, Elec. Engr. Research Lab., University of Texas*, August 1, 1960.
- Cagniard, L., Basic theory of the magnetotelluric method, *Geophysics*, 8, 605-635, 1953.
- Campbell, W. H., A study of micropulsations in the earth's magnetic field, *Inst. of Geophys., Sci. Rept. 1*, University of California, Los Angeles, April 1959.
- Duffus, H. J., and J. A. Shand, Some observations of geomagnetic micropulsations, *Can. J. Phys.*, 36, 1958.
- Dungey, J. W., Electrodynamics of the outer at-

- mosphere, *Ionospheric Research Lab., Sci. Rept. 69*, Pennsylvania State University, September 15, 1954.
- Maple, Elwood, Geomagnetic oscillations at middle latitudes, *J. Geophys. Research*, *64*, 1395-1425, 1959. (Additional references are to be found at the end of this article.)
- Smith, H. W., R. M. McClure, and F. X. Bostick, Jr., A power spectrum computer, *Rept. 86, Elec. Engr. Research Lab.*, University of Texas, November 15, 1956.

(Manuscript received November 17, 1960.)

The Record in the Meteorites

6. On the Chronology of the Early Solar System

GORDON G. GOLES AND EDWARD ANDERS

*Enrico Fermi Institute for Nuclear Studies and Department of Chemistry
University of Chicago
Chicago, Illinois*

Abstract. An attempt is made to account for the differences between the isotopic composition of terrestrial and meteoritic xenon reported by Reynolds. The two chief mechanisms proposed (other than the decay of I^{129} to Xe^{129}) are the production of $Xe^{131-136}$ by spontaneous fission of extinct nuclides in the earth, and the production of $Xe^{124-128}$ by nuclear spallation reactions in the early history of the solar nebula. About 9.6 per cent of the Xe^{136} in the earth's atmosphere appears to have arisen from the spontaneous fission of 76-million-year Pu^{244} , as proposed by Kuroda. The Pu^{244} - Xe^{136} decay interval of the earth is 290 m.y., and its I^{129} - Xe^{129} decay interval may be estimated as ≥ 210 m.y. Thus, the earth appears to be 100-200 m.y. younger than the meteorites. Possible errors in these determinations are discussed. A dating method, similar to the Pb^{207} - Pb^{206} method and based upon the two decay systems I^{129} - Xe^{129} and Pu^{244} - Xe^{136} , is proposed and the appropriate equations are given. The initial solar-system ratios of I^{129}/I^{127} and Pu^{244}/U^{238} , which can be determined by this method, would provide a crucial test of models of nucleosynthesis.

1. INTRODUCTION

In a previous paper [Goles and Anders, 1960, henceforth referred to as Paper 1] we reported iodine abundances in stone meteorites. From these, we calculated a set of 'I-Xe decay intervals,' the time elapsed between the isolation of the solar system and the cooling of several meteorites to temperatures low enough to retain radiogenic Xe^{129} from the decay of 16.4 m.y. I^{129} . In the present paper, we wish to offer comments of a more speculative nature on the isotopic anomalies of meteoritic xenon, on the age of the earth, and on the possible development of a new dating method.

2. NORMALIZATION AND 'SECONDARY ANOMALIES' OF METEORITIC XENON

Reynolds [1960a, 1960b] has pointed out that meteoritic xenon may differ from terrestrial xenon in two respects: it often, though not always, contains a large excess of Xe^{129} (the 'primary anomaly'), and it exhibits small 'secondary anomalies' in the relative abundances of the other xenon isotopes which, if they are observed at all, are consistent from one meteorite to another. For meteorites with a large excess of Xe^{129} , the choice of the isotope used as a basis for normalization (i.e., to define the amount of

the atmospheric xenon spectrum to be subtracted from the total meteoritic xenon) does not appreciably affect the estimate of the radiogenic Xe^{129} present. Reynolds normalized his data to Xe^{136} , thereby obtaining positive anomalies at all mass numbers. Kuroda [1960] has suggested that Xe^{136} is unsuitable for this purpose, since it can be produced by fission of heavy elements, and proposed that the shielded nuclide Xe^{130} be used instead.

This change in normalization has little effect on the decay intervals calculated for three of the meteorites listed in Table 2 of Paper 1. For the carbonaceous chondrite Murray, however, the difference between the two choices of normalization is quite large: under Kuroda's normalization, the radiogenic Xe^{129} content is decreased to $(-0.11 \pm 0.13 \times 10^{-9} \text{ cc STP/g, i.e., essentially zero, and the decay interval is increased to } \geq 150 \text{ m.y. In addition, the meteoritic xenon appears to be deficient in } Xe^{131,132,134,136}, \text{ and the positive secondary anomalies of } Xe^{124,126,128} \text{ in the meteoritic spectrum are decreased somewhat (Table 1). The differences between the results of these two normalization schemes are very important in the calculation of I-Xe decay intervals for Murray and other carbonaceous chondrites [Reynolds, 1960c, 1960d]; they are crucial in discussing the origin of the observed secondary$

TABLE 1. Relative Abundances of Xenon Isotopes*

Mass Num- bers	Normalized to Xe ¹³⁰			Normalized to Xe ¹³⁶		
	Murray	Richardton	Atmosphere	Murray	Richardton	Atmosphere
124	0.0295 ± 0.0006	0.034 ± 0.004	0.0236 ± 0.0001	0.0150 ± 0.0003	0.0171 ± 0.002	0.0108 ± 0.0001
126	0.027 ± 0.001	0.029 ± 0.001	0.0220 ± 0.0001	0.0137 ± 0.006	0.0145 ± 0.0005	0.0101 ± 0.0001
128	0.509	0.524	0.471 ± 0.002	0.258	0.263	0.216 ± 0.001
129	6.43 ± 0.06	8.97 ± 0.26	6.49 ± 0.03	3.28 ± 0.02	4.51 ± 0.09	2.98 ± 0.01
130	≡ 1.000	≡ 1.000	≡ 1.000	0.508 ± 0.04	0.50 ± 0.01	0.459 ± 0.002
131	5.02 ± 0.05	5.05 ± 0.14	5.20 ± 0.02	2.55 ± 0.02	2.54 ± 0.05	2.39 ± 0.01
132	6.12 ± 0.05	6.16 ± 0.17	6.60 ± 0.03	3.11 ± 0.02	3.10 ± 0.06	3.03 ± 0.01
134	2.33 ± 0.02	2.39 ± 0.07	2.56 ± 0.01	1.186 ± 0.008	1.20 ± 0.02	1.177 ± 0.003
136	1.97 ± 0.02	1.99 ± 0.06	2.177 ± 0.007	≡ 1.000	≡ 1.000	≡ 1.000

* Calculated from a similar table, normalized to Xe¹²⁹, supplied by Reynolds (private communication).

anomalies. Accordingly, we will treat this topic in some detail.

The deficiency in meteoritic Xe¹³¹⁻¹³⁶ noted above is best interpreted as an excess of these isotopes in the earth's atmosphere. Kuroda [1960], (and 'On the "extinct" transuranium elements,' to be published) attributes this excess to the spontaneous fission of Pu²⁴⁴ and Cm²⁴⁷; the effect is much more prominent in the earth's atmosphere because the xenon content per gram of the earth is quite low compared to the meteorites (3.8×10^{-13} g Xe/g compared with 6.1×10^{-12} g Xe/g for Richardton and 2.5×10^{-10} g Xe/g for Murray).¹ Indeed, it is reasonably certain that if 16-million-year I¹²⁹ was present in the early solar

system, then 76-million-year Pu²⁴⁴ also was present, in which event it cannot have failed to contribute to the heavy xenon isotopes by spontaneous fission. The magnitude of this contribution depends on the abundance of Pu²⁴⁴ at the time of the earth's formation. Although estimates of this abundance are sensitive to the choice of a model of nucleosynthesis and of the parameters used, all of which are somewhat indeterminate at present, it will be shown in a later section that even the most conservative estimate of the Pu²⁴⁴ abundance is more than ample to account for the observed anomalies. Accordingly, it would seem that Kuroda's normalization is to be preferred.

¹ The xenon content of the earth was estimated under the assumptions that atmospheric xenon represents the bulk of the earth's xenon, and that no significant amounts of radiogenic Xe¹²⁹ or Xe¹³⁶ are locked in the interior or dissolved in the oceans. It may readily be shown that the xenon in the hydrosphere comprises less than 10 per cent of the atmospheric xenon. According to Valentiner [1927], the distribution coefficient for xenon between aqueous and gas phases is 0.174 at 10°C, which we have assumed to be the mean temperature of the oceans. For an atmospheric xenon abundance of 8×10^{-8} by volume [Paneth, 1939] and a mass of the hydrosphere of 1.39×10^{24} g [Goldschmidt, 1954], the xenon content of the hydrosphere is 1.14×10^{14} g, which should be compared with 1.86×10^{15} g xenon in the atmosphere. We have used a value of 2.29×10^{16} g for the total terrestrial xenon, derived from data given by Goldschmidt [1954], and have thereby implicitly made what should be a liberal allowance for xenon in the hydrosphere and the crust. The assumption of essentially complete outgassing of the mantle will be discussed in a later section.

At first, it appears paradoxical that a carbonaceous chondrite such as Murray, with a large content of primordial noble gases, should have (under Kuroda's normalization) a greater decay interval than the bronzite chondrite Richardton. It should be recalled, however, that the I-Xe method indicates the time required for the cooling of the meteorites to temperatures low enough that radiogenic Xe¹²⁹ may be retained. Furthermore, the subsequent thermal history may greatly modify the apparent decay intervals obtained. Goles, Fish, and Anders [1960] have shown that environmental temperatures in meteoritic parent bodies and in the final, highly eccentric, meteoritic orbits were frequently high enough to cause appreciable diffusion losses of radiogenic Ar⁴⁰. It may be shown that such losses are likely to be more severe for carbonaceous chondrites, such as Murray. Reynolds [1960c] has reported an apparent K-Ar age for Murray of 2.9 aeons, and Stauffer [1960] has found similar low ages for four out of five carbonaceous

chondrite samples. Since these meteorites are undoubtedly much older, as indicated by their contents of primordial noble gases, these 'ages' should be interpreted as indicating severe diffusion losses of Ar^{40} . For Murray, a diffusion loss of about 83 per cent of the radiogenic Ar may be inferred using the model of *Goles, Fish, and Anders* [1960].

It remains to be demonstrated that radiogenic Xe^{129} in carbonaceous chondrites will be lost at least as easily as Ar^{40} . *Staufer* [1960] has shown that primordial and cosmogenic neon and primordial argon in the ornansite Lancé, a meteorite transitional between the carbonaceous chondrites and the hypersthene chondrites, are more strongly bound than is radiogenic Ar^{40} . Also, the Ar^{40} in Lancé diffuses ten times more rapidly at 950°K than does the Ar^{40} in bronzite and hypersthene chondrites.

The carbonaceous chondrites show evidence of the one-time action of liquid water [*DuFresne and Anders*, 1961], and since the alkalis in these meteorites are largely present in water soluble form, in contrast to other meteorites, it is not unlikely that the iodine also resides in a water-soluble phase. *Staufer's* experiment shows that this phase is highly permeable to argon, and it is not unreasonable to expect a high permeability for xenon as well. Thus, we would expect a large difference in the diffusion behavior of radiogenic Xe^{129} on one hand, and primordial xenon, which is probably locked in the silicate lattices, on the other. It would seem that most of the Xe^{129} could have been lost from Murray without greatly affecting the other xenon isotopes. Of course, the observed radiogenic Xe^{129} content should always be considered a lower limit to the true one, because of diffusion losses; in the case of Murray, such an error is likely to be especially serious. A similar argument may apply to the other carbonaceous chondrites studied by *Reynolds* [1960c, 1960d], which also display no excess Xe^{129} by the Xe^{130} normalization, and which have low K-Ar ages.

With Kuroda's normalization, the secondary anomalies of the meteoritic xenon spectra become easier to interpret. Kuroda has shown, using the *Suess* [1949] mass fractionation formula, that these anomalies are too large to have arisen by gravitational fractionation. Moreover, the observation that meteoritic krypton, which would be more strongly affected by mass fractionation,

shows no anomalies in isotopic composition [*Reynolds*, 1960b] would seem to rule out any such effect.

We have not been able to account for the secondary anomalies in the xenon isotopes in terms of a single cause. Accordingly, we shall propose three separate mechanisms. For the heavy isotopes $\text{Xe}^{131-136}$, spontaneous fission, as discussed above, would appear to be the most likely cause of the variation. Under this interpretation, the peak at mass 132 is somewhat puzzling, but until the spontaneous-fission yield curve of Pu^{244} becomes known, the possibility of a 'fine-structure' peak cannot be ruled out. The light isotopes $\text{Xe}^{124,126,128}$, on the other hand, are those likely to be produced in high yield by spallation of nuclides with $A \geq 129$. (Since nuclides on the neutron-poor side of the beta-stability line are greatly favored in spallation, the yield of Xe^{130} in such reactions would be appreciably lower than that of the lighter isotopes. Also, Xe^{130} is relatively abundant, so that a given level of spallation would result in a much smaller perturbation of this component. The use of this isotope as a normalization standard therefore seems justified.) In the case of Xe^{128} , and possibly of other isotopes, production by (n, γ) reactions on I^{127} , etc., could cause small additional changes in the xenon spectra, particularly if there had been an era of neutron capture in the solar nebula, after a partial fractionation of xenon.

The abundances of $\text{Xe}^{124,126}$ are only about 1/20 that of Xe^{128} , so they will be most strongly affected by a moderate level of spallation on nuclides of $A \geq 129$, and therefore can be used as an index for the intensity of these reactions. *Reynolds* [1960b] has convincingly argued that these abundance anomalies could not have been produced during the exposure of the meteoroid to cosmic rays. It therefore appears that the spallation reactions took place at a stage before the breakup of the meteoritic parent bodies. Because of the limited range of charged particles, such reactions must have occurred before the condensation of the parent bodies, i.e., in the early history of the solar nebula. *Cameron* [1960] and Fowler (private communication) have proposed a brief era of intense charged-particle acceleration in the last stages of the sun's formation, and *Gold* [1960] has argued that the high Li content of T-Tauri stars gives evidence for the

operation of such processes in newly formed stars. Such acceleration processes would depend critically on density and degree of ionization within the nebula, both of which would vary with distance from the sun. Reynolds' observation of positive secondary anomalies in meteoritic $\text{Xe}^{124,126,128}$ may well imply that the level of this nuclear activity was higher at 2-5 AU than at 1 AU, and that large-scale homogenization of the xenon isotopes did not take place.

If this were indeed the case, other elements in meteorites would be expected to display anomalies in their shielded isotopes comparable to the ~ 40 per cent excess reported for Xe^{124} and Xe^{126} . Such anomalies have not been observed for non-volatile elements [Brown, 1949; Schmitt, Mosen, Suffredini, Lasch, Sharp, and Olehy, 1960; Reed, Kigoshi, and Turkevich, 1960]. Although the absence of such anomalies in other elements should be further confirmed, it would seem from the data presently available that some unique factor, such as the volatility of xenon, must have been responsible for the exceptionally large effect in the case of this element. Perhaps these anomalies were produced after the fractionation of meteoritic xenon from the bulk of the solar system complement of xenon. One way in which this could have occurred is by charged-particle irradiation of grains in the early solar system. At some stage in the formation of the solar system, most of the nonvolatile fraction must have been present as grains, large enough to prevent free exchange between xenon formed in their interiors and that in the nebula, but small enough to act as a relatively 'thin' target to charged particles of perhaps 100-Mev energy. If the grains had retained, by adsorption, about 10^{-4} of the primordial xenon in the nebula (corresponding to somewhat more than the primordial xenon now observed in Murray), the transformation of a part-per-million of nuclides with $A \geq 129$ could have accounted for the observed secondary anomalies.

If this reasoning is correct, it is possible that a similar anomaly in meteoritic Kr^{78} could be detected. The effect in the case of krypton would be much smaller than for xenon, since the isotopic abundance of Kr^{78} is about four times that of Xe^{124} or Xe^{126} , and the primordial elemental abundance of krypton is more than ten times that of xenon. Note also that krypton in grains will exchange with the nebular gases more readily

than will xenon. Thus, even in the most favorable case, any contribution of spallation-produced Kr^{78} should be on the order of 1 per cent of the 'normal' Kr^{78} in the meteorite. An anomaly of this magnitude would be less than the errors reported in a preliminary study of meteoritic krypton by Reynolds [1960b], but it is in principle detectable.

The acceleration of charged particles in a nebula clearly requires fairly low densities and temperatures to minimize loss of energy to electrons or to the nebula as a whole. Fowler, Burbridge, and Burbridge [1955] have proposed a mechanism for the acceleration of charged particles in the atmospheres of magnetic A stars, at densities of 10^{-7} to 10^{-8} g/cm³ and temperatures on the order of 12,000°K. Under these conditions, energy losses by collisions with electrons become serious only when the dimensions of the regions of acceleration are on the order of 10^8 cm. The 'critical' density at which this mode of energy loss becomes serious is a function of temperature and of the size of the region; the latter, in turn, depends on the gradient of the magnetic field. Nevertheless, it is interesting to note that Urey [1958] has estimated densities in the solar nebula to be $\sim 10^{-6}$ g/cm³ at 1 AU, and $\sim 4.6 \times 10^{-8}$ g/cm³ in the region of the asteroidal belt. After the partial dissipation of the nebula, the densities will be still lower. Both this effect and the low temperatures in the nebula should help to compensate for the lower magnetic field strengths and greater dimensions of the regions of acceleration, which give rise to smaller field gradients than those discussed by Fowler, Burbridge, and Burbridge [1955]. One should also note that the efficiency required in the nebular acceleration mechanism is many orders of magnitude less than that postulated by Fowler and his co-workers.²

² If an era of charged-particle irradiation of grains was a feature of the history of the early solar system, then some neon and argon would have been produced also. The isotopic composition of this material would resemble that of the cosmic-ray produced noble gases in meteorites (e.g., $\text{Ar}^{36}/\text{Ar}^{38} \cong 0.6$, as opposed to ~ 5.4 in primordial argon). In the extreme case that these nuclides were retained to the same degree as the xenon isotopes, they might alter the apparent isotopic composition of primordial noble gases in meteorites by as much as a few per cent. This effect would be difficult to discern in the presence of cosmogenic argon and neon from the recent era of cosmic-ray exposure.

We have already noted that the difference between terrestrial and meteoritic $\text{Xe}^{124,126,128}$ may have been due to varying levels of charged-particle acceleration in different portions of the nebula. Another possible explanation is that the exchange of spallation-product xenon with the primordial xenon in the nebula was more effective at the relatively high temperatures prevailing at 1 AU than it was at 2-5 AU.

At present, it appears that all observed secondary anomalies are consistent from one meteorite to another, implying, by our model, that at some stage subsequent to the production of these anomalies, meteoritic xenon was homogenized, e.g., by mixing of the grains within the volume of the nebula sampled by the meteoritic parent bodies, or by diffusion within the parent bodies themselves. After this stage, diffusion losses (on both short and long time scales) and the addition of Xe^{129} changed the xenon content and over-all xenon spectra of various meteorites but did not affect the secondary anomalies.

3. THE AGE OF THE EARTH

The new meteoritic iodine abundances may be used to recalculate the I-Xe decay interval for the earth [Katcoff, Schaeffer, and Hastings, 1951; Suess and Brown, 1951; Reynolds, 1960b]. If we assume that the earth contains the same average concentration of iodine, ~ 65 ppb, as the bronzite and hypersthene chondrites studied previously (Paper 1), that the ratio $\text{I}^{129}/\text{I}^{127}$ at the time of the isolation of the solar system is given by $\tau_{129}/T = 2.37 \times 10^{-3}$ [Wasserburg, Fowler, and Hoyle, 1960], and that the earth's interior was efficiently outgassed during the first ~ 100 m.y. of its history, we obtain the graph for calculating I-Xe decay intervals shown in Figure 1. Even 170 m.y. after the isolation of the solar system, I^{129} is still abundant enough to produce all the Xe^{129} in the atmosphere. Values for the probable radiogenic component of atmospheric Xe^{129} , estimated on the basis of systematic trends in isotope ratios, range from ≤ 20 per cent [Katcoff, Schaeffer, and Hastings, 1951] to ~ 84 per cent [Cherdynstev, 1956]. These correspond to decay intervals of ≥ 210 m.y. and ~ 180 m.y. Even the shorter of these is distinctly greater than the decay intervals of Richardton and Indarch, the two meteorites discussed in our previous paper which do not appear to have lost Xe^{129} by diffusion.

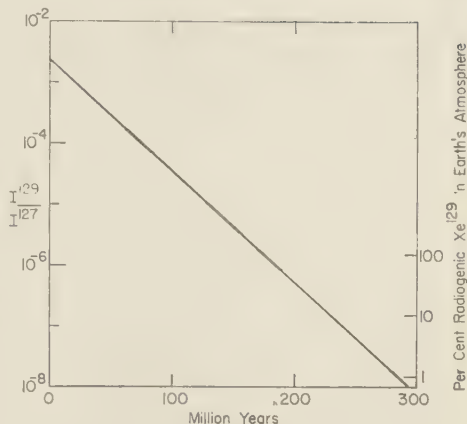


Fig. 1. Decay of I^{129} and its contribution to Xe^{129} in the earth's atmosphere. The ordinate on the left shows the proportion of I^{129} remaining at a given time after the isolation of the solar system. The ordinate on the right indicates the amount of radiogenic Xe^{129} produced subsequent to this time, expressed as a percentage of the Xe^{129} in the earth's atmosphere. Even for a decay interval as great as 170 m.y., the amount of I^{129} remaining would suffice to produce all of the Xe^{129} in the earth's atmosphere.

In this calculation, we have assumed an initial $\text{I}^{129}/\text{I}^{127}$ ratio of 2.37×10^{-3} , an average terrestrial iodine abundance of $6.5 \times 10^{-8}\text{g I}^{127}/\text{g}$ and a Xe^{129} abundance of $9.9 \times 10^{-14}\text{g Xe}^{129}/\text{g}$.

It does not seem possible to bring the decay intervals of these meteorites and the earth into agreement, except by postulating that the earth is depleted in iodine by a factor of more than one hundred relative to the chondrites, or that only crustal iodine, residing within 20 km of the surface, has ever contributed Xe^{129} to the atmosphere. The latter alternative compels one to assume that the subcrustal regions of the earth ceased to effuse Xe^{129} within a few million years after the earth's formation. In contrast, the data of Damon and Kulp [1958a] show that the Ar^{40} generated in the crust during 4.5 aeons accounts for no more than 78 per cent of the Ar^{40} now in the atmosphere. Thus at least 20 per cent of atmospheric Ar^{40} , equivalent to that produced in the mantle during the first 500 m.y. of the earth's history, must have been added from a source other than the crust. This argument based on material balance is strongly supported by

rate considerations: the present rate of effusion of Ar^{40} from the crust, if constant throughout the earth's history, can account for only 1 per cent of the Ar^{40} in the atmosphere [Damon and Kulp, 1958b]. In addition, the large amounts of 'trapped' helium and argon in ancient beryls imply a higher rate of outgassing in the past. One may also note that the $\text{Ar}^{40}/\text{Ar}^{36}$ ratios found in beryls and well gases are far greater than the atmospheric ratio, indicating that the nonradiogenic noble gases in the interior either are present in very small amounts or are held in such a way that their rate of escape is even smaller than that of Ar^{40} . It may be concluded, with a high degree of probability, that much higher rates of outgassing of both crust and mantle must have prevailed at some past stage. It is difficult to believe that the mantle should have become impermeable to xenon after a few million years, while presumably remaining permeable to argon for at least 500 m.y. after the formation of the earth.

An independent estimate of the interval between the isolation of the solar system and the retention of xenon by the earth may be made, using the $\text{Pu}^{244}\text{-Xe}^{136}$ decay. A value for the primordial ratio $\text{Xe}^{136}/\text{Xe}^{130}$ is required in this method. This ratio is probably that observed in the xenon from Murray, which could not have acquired more than about 1.1×10^{-11} cc STP/g of fission-produced Xe^{136} from Pu^{244} , even if it had begun to retain Xe immediately after the isolation of the solar system.³ This increment should be compared with the measured Xe^{136} content of Murray: 3.8×10^{-9} cc STP/g [Reynolds, 1960b]. Upon subtracting the Murray xenon spectrum from atmospheric xenon, one

³ Plutonium, like the other actinides, is likely to be tetraivalent in meteorites and would therefore be coherent with thorium. Since thorium and uranium are not significantly fractionated in meteorites, the present uranium content of about 1.5×10^{-8} g U/g in Murray can be used as an index for its maximum Pu^{244} content. The production ratio $\text{Pu}^{244}/\text{U}^{238}$, including progenitors of higher mass, is 0.963, according to Fowler and Hoyle [1960]. Assuming $T = 10^{10}$ years, and making appropriate corrections for decay, we find that the ratio of these two nuclides at the time of isolation of the solar system was about 2.1×10^{-2} . A fission yield of 6.0 per cent was assumed for the production of Xe^{136} in the 0.3 per cent spontaneous fission branch of Pu^{244} decay.

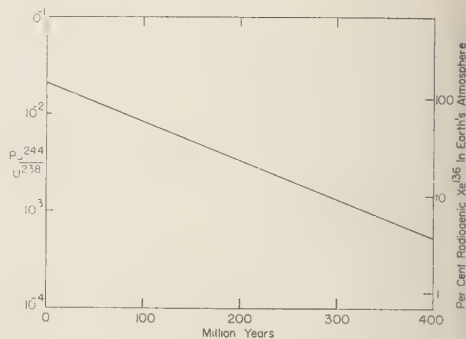


Fig. 2. Decay of Pu^{244} and its contribution to atmospheric Xe^{136} in the earth. If the radiogenic Xe^{136} content of the earth's atmosphere is 9.6 per cent (see text), then the earth formed 2.9×10^8 years after the cessation of nucleosynthesis, more than 10^8 years later than the meteorites.

The following parameters were used in this calculation: initial $\text{Pu}^{244}/\text{U}^{238}$ ratio = 2.1×10^{-2} ; Pu^{244} spontaneous fission yield at mass 136 = 6 per cent; initial U^{238} abundance in the earth = 2.34×10^{-8} g U^{238} /g; and Xe^{136} abundance = 3.5×10^{-14} g Xe^{136} /g.

finds that 9.6 per cent of the Xe^{136} in the earth's atmosphere is fission-produced, corresponding to a decay interval of 290 m.y. (Fig. 2).

It is somewhat surprising that the earth should have a decay interval nearly 200 m.y. longer than the meteorites. We may ask whether this difference could not be eliminated by a different choice of parameters. Indeed, when the normalization is carried out with respect to Xe^{128} , the apparent amount of fission-produced xenon in the atmosphere is doubled, and the Pu^{244} decay interval for the earth is hence shortened by 76 m.y. (A. G. W. Cameron, The formation of the sun and planets, to be published). Similarly, if the rate of nucleosyntheses is assumed to have decreased with time, the abundance of Pu^{244} and I^{129} at the time of isolation of the s.s. is lowered (Cameron, The formation of the sun and planets; Kuroda, On the 'extinct' transuranium elements). This will remove part but not all of the discrepancy, and we are thus forced to the conclusion that there is either a significant difference between the age of the earth and that of the meteorites, or that the extinct radionuclides in the early s.s. were not present in the abundances predicted by the model of Wasserburg, Fowler,

and Hoyle, 1960. The latter possibility will be taken up in section 4. For the moment, we shall assume that the earth's decay interval is indeed 290 m.y.

Reference to Figure 1 indicates that for an interval of this length, less than 1 per cent of the atmospheric Xe^{129} would be of radiogenic origin. If only 1 per cent of the earth's Xe^{129} is radiogenic, then the procedure used by Reynolds and ourselves of subtracting atmospheric Xe^{129} as if it were primordial is essentially justified. Also, the near-identity of $\text{Xe}^{129}/\text{Xe}^{130}$ ratios in the three carbonaceous chondrites studied (which, we have argued, have lost radiogenic Xe^{129} by diffusion) and in the earth becomes easier to understand. If an appreciable fraction of the Xe^{129} in any of these samples were radiogenic, it would be a most remarkable coincidence that the earth and the carbonaceous chondrites should have the same $\text{Xe}^{129}/\text{Xe}^{130}$ ratios, considering that their xenon contents per gram differ by a factor of 10^3 . If they were truly of the same age, then their iodine contents would have to differ fortuitously by the same factor (or proportionately less if part of the earth's xenon were locked up in the interior). On the other hand, if their ages were different, then an equally fortuitous balance of ages and iodine contents is required to produce identical $\text{Xe}^{129}/\text{Xe}^{130}$ ratios in objects with such strikingly different xenon contents. These difficulties can be avoided by assuming, as we have done, that diffusion losses and the late origin of the earth have insured the retention of only primordial Xe^{129} in the carbonaceous chondrites and the earth's atmosphere.

Nevertheless, it is difficult to dismiss Cherdyn'tsev's conclusion, based upon isotope systematics, that the atmosphere and, by an obvious extension, the carbonaceous chondrites contain 84 per cent radiogenic Xe^{129} .⁴ Sound as Cherdyn'tsev's interpolation may seem, his conclusion is open to all the objections above, so that a serious paradox exists. Any enrichment in radiogenic Xe^{129} common to terrestrial and meteoritic xenon must have taken place before the separa-

tion of terrestrial and meteoritic matter from each other. It is tempting to speculate that both types of xenon were enriched in Xe^{129} by some fractionation of iodine and xenon occurring before the segregation of their precursors from the solar nebula, or perhaps even before the isolation of the solar system itself. Until these problems are resolved, it is prudent to be very cautious in defining 'primordial' xenon; there may be many senses in which this term could be applied.

A tacit assumption of the preceding discussion has been that the I-Xe and Pu-Xe decay intervals of the earth should be identical. If the retention of Xe during the formation of the earth was primarily gravitational, then both Xe^{129} and Xe^{136} should have been held with virtually equal efficiency, and our assumption would be valid. We note, however, that the high xenon concentration in Murray casts serious doubts upon the hypothesis of gravitational retention of the noble gases [Russell and Menzel, 1933; Suess, 1949], at least as it applies to the meteorites. If the mechanism of xenon retention had been gravitational, the carbonaceous chondrites would have come from bodies much larger than the parent of Richardton, which in turn would have been larger than the earth. This hierarchy is in direct opposition to most of the other evidence [Fish, Goles, and Anders, 1960]. Instead, it seems reasonable to suppose that the initial retention of xenon was due to van der Waals adsorption on dust grains in the solar nebula. This mechanism would also provide a means of fractionating the noble gases, one from another. The differences in absorbability of the noble gases are known to be very great and are used in the laboratory for their separation. Ultimately, as Stauffer [1960] has shown, the noble gases found their way, by diffusion, by being trapped in growing grains, or otherwise, into the interiors of crystals, but this process does not require a large body capable of holding these elements gravitationally.

If retention of terrestrial xenon was also in part due to adsorption but at such low temperatures that the rate of exchange with the nebula was very small, no errors would be introduced into the I-Xe and Pu-Xe methods, and their results for the earth should agree, although the interpretation of this decay interval would be somewhat obscure. Temperatures in the solar nebula at 1 AU, however, might have been high

⁴ Cherdyn'tsev [1956] has compared the ratio of the abundance of Xe^{129} to the sum of the abundances of its shielded neighbors Xe^{128} and Xe^{130} with the ratios for similar isotopic triplets of Mo, Ru, Ba and Sm. For xenon, this ratio is 4.4, compared to a range of 0.6 to 0.9 for the other elements.

enough [Urey, 1952; Cameron, 1960] to cause some fractionation of xenon by reversible desorption. A more serious effect might have been due to diffusion losses of Xe^{129} and Xe^{136} from the precursors of the earth. In these bodies, presumably of kilometer to hundred-kilometer size, I^{129} and Pu^{244} were probably situated in minerals with different structures and diffusion parameters, at temperatures such that perceptible losses of xenon could occur. Clearly, in this event the apparent values of the two decay intervals need not agree, nor would they necessarily refer to the final stages of the earth's accretion.

At present, it appears that there are not enough data at hand to permit a satisfactory resolution of the questions raised. We may, however, note two additional points upon which these problems bear. If the earth is indeed almost 200 m.y. younger than the meteorites, then extinct radioactivities would have been of subordinate importance in its thermal history, a conclusion which would support Urey's [1952] arguments that the accumulation of the terrestrial planets was a low-temperature process. Also, once material from the moon becomes available, it will be most interesting to determine the isotopic composition of its xenon. Such measurements will establish the relative age of the moon, and may shed some light on the controversial question of its early thermal history.

4. THE $\text{Xe}^{129}\text{-Xe}^{136}$ METHOD

Fortunately, many of the problems discussed above may be attacked by the use of a dating method based upon the decay of both I^{129} and Pu^{244} to isotopes of the same element. (The system is closely analogous to the well-known $\text{Pb}^{207}/\text{Pb}^{206}$ method.) For an object containing radiogenic Xe^{129} , the following equation may be written:

$$\begin{aligned} \frac{\text{Xe}_r^{129}}{\text{Xe}^{130}} &= \frac{\text{Xe}^{129}}{\text{Xe}^{130}} - \frac{\text{Xe}_o^{129}}{\text{Xe}^{130}} = \frac{\text{I}_r^{129}}{\text{Xe}^{130}} \\ &= \frac{\text{I}^{127}}{\text{Xe}^{130}} \cdot \frac{\text{I}_o^{129}}{\text{I}^{127}} \cdot \exp(-\Delta t_1/\tau_{129}) \end{aligned} \quad (1)$$

where the elemental symbols represent abundances, while the subscript *r* refers to 'radiogenic,' *o* to 'primordial,' and *i* to the abundance at the

end of the decay interval Δt_1 , and where τ_{129} is the mean life of I^{129} . Solving for Δt_1 , we obtain:

$$\begin{aligned} \Delta t_1 &= \tau_{129} \left\{ \ln \frac{\text{I}^{127}}{\text{Xe}^{130}} + \ln \frac{\text{I}_o^{129}}{\text{I}^{127}} \right. \\ &\quad \left. - \ln \left[\frac{\text{Xe}^{129}}{\text{Xe}^{130}} - \frac{\text{Xe}_o^{129}}{\text{Xe}^{130}} \right] \right\} \end{aligned} \quad (2)$$

An exactly analogous expression may be obtained for Pu^{244} and Xe^{136} :

$$\begin{aligned} \Delta t_{\text{Pu}} &= \tau_{244} \left\{ \ln \frac{\text{U}^{238}}{\text{Xe}^{130}} + \ln \frac{\text{Pu}_o^{244}}{\text{U}^{238}} + \ln \beta \text{Y}_{136} \right. \\ &\quad \left. - \ln \left[\frac{\text{Xe}^{136}}{\text{Xe}^{130}} - \frac{\text{Xe}_o^{136}}{\text{Xe}^{130}} \right] \right\} \end{aligned} \quad (3)$$

where β is the fraction of decays by the spontaneous fission mode, and Y_{136} is the fission yield of Xe^{136} .

In equation 2, τ_{129} is known; I^{127} , Xe^{129} and Xe^{130} are measurable; $\text{I}_o^{129}/\text{I}^{127}$ and $\text{Xe}_o^{129}/\text{Xe}^{130}$ are unknown but assumed constant for any object formed within the solar system; and Δt_1 must be regarded as a variable from one case to another. Similar relations held for equation (3), although $\text{Pu}_o^{244}/\text{U}^{238}$ may not be strictly constant in some cases, owing to chemical fractionations. A very great simplification is possible if $\Delta t_1 = \Delta t_{\text{Pu}}$, i.e., if the object may be assumed to have retained both xenon isotopes with equal efficiency, as discussed above. In that event, each object contributes two equations with a total of five unknowns, four of which are constant from object to object. The problem becomes determinate with four such objects; with more than four objects the situation is overdetermined, thus providing a means of testing the initial assumptions.

There is an important requirement that each object must meet: it must contain a measurable increment of both radiogenic xenon isotopes. This requirement is most likely to be met by meteorites with higher-than-average U-Th and I contents, which acquired their textures at temperatures where the retention of primordial xenon was inefficient, and which resided in small bodies that cooled to temperatures such that radiogenic xenon retention began within not much more than 10^7 years. By these criteria, Murray is definitely unsuitable, while Richardson and Indarch are borderline cases because of

Acknowledgments. We are grateful for the helpful comments and critical advice provided by Professors Anthony L. Turkevich and Robert N. Clayton, and by Dr. George W. Reed. This work was supported in part by the U. S. Atomic Energy Commission.

Brown, H., A table of relative abundances of nuclear species, *Rev. Mod. Phys.*, **21**, 625, 1949.
Cameron, A.G.W., The origin of the solar system, *Proc. Highland Park Conf. on Nuclear Geology*, in press, 1960.

- Cherdyn'tsev, V. V., *Abundances of the chemical elements*, Moscow, USSR, 1956.
- Damon, P. E., and J. L. Kulp, Excess helium and argon in beryl and other minerals, *Am. Mineral.*, **43**, 433, 1958a.
- Damon, P. E., and J. L. Kulp, Inert gases and the evolution of the atmosphere, *Geochim. et Cosmochim. Acta*, **13**, 280, 1958b.
- DuFresne, E. R., and E. Anders, The record in the meteorites, 5, A thermometer mineral in the Mighei carbonaceous chondrite, *Geochim. et Cosmochim. Acta*, in press, 1961.
- Fish, R. A., G. G. Goles, and E. Anders, The record in the meteorites, 3, On the development of meteorites in asteroidal bodies, *Astrophys. J.*, **132**, 243, 1960.
- Fowler, W. A., G. R. Burbidge, and E. M. Burbidge, Nuclear reactions and element synthesis in the surfaces of stars, *Astrophys. J. Suppl.*, **2**, 167, 1955.
- Fowler, W. A., and F. Hoyle, Nuclear cosmochronology, *Annals of Physics*, **10**, 280, 1960.
- Gold, T., Abundance of lithium and origin of the solar system, *Astrophys. J.*, **132**, 274, 1960.
- Goldschmidt, V. M., *Geochemistry*, Oxford University Press, Oxford, 1954.
- Goles, G. G., and E. Anders, Iodine content of meteorites and their I^{129} -Xe 129 ages, *J. Geophys. Research*, **65**, 4181-4184, 1960.
- Goles, G. G., R. A. Fish, and E. Anders, The record in the meteorites, 1, The former environment of stone meteorites as deduced from K 40 -Ar 40 ages, *Geochim. et Cosmochim. Acta*, **19**, 177, 1960.
- Katochi, S., O. A. Schaeffer, and J. M. Hastings, Half-life of I^{129} and the age of the elements, *Phys. Rev.*, **82**, 688, 1951.
- Kohman, T. P., Chronology of nucleosynthesis and extinct natural radioactivity, *J. Chem. Ed.*, in press, 1960.
- Kuroda, P. K., Nuclear fission in the early history of the earth, *Nature*, **187**, 36, 1960.
- Paneth, F. A., The upper atmosphere, direct chemical investigation, *Quart. J. Roy. Meteorol. Soc.*, **65**, 303, 1939.
- Reed, G. W., K. Kigoshi, and A. Turkevich, Concentrations of some heavy elements in meteorites by activation analysis, *Geochim. et Cosmochim. Acta*, in press, 1960.
- Reynolds, J. H., Determination of the age of the elements, *Phys. Rev. Letters*, **4**, 8, 1960a.
- Reynolds, J. H., Isotopic composition of primordial xenon, *Phys. Rev. Letters*, **4**, 351, 1960b.
- Reynolds, J. H., Xenon in stone meteorites, *Proc. Highland Park Conf. on Nuclear Geology*, in press, 1960c.
- Reynolds, J. H., I-Xe dating of meteorites, *J. Geophys. Research*, **65**, 3843-3846, 1960d.
- Russell, H. N., and D. H. Menzel, The terrestrial abundance of the permanent gases, *Proc. Nat. Acad. Sci.*, **19**, 997, 1933.
- Schmitt, R. A., A. W. Mosen, C. S. Sufredini, J. E. Lash, R. A. Sharp, and D. A. Olehy, Abund-

- ances of the rare-earth elements, lanthanum through lutetium, in chondritic meteorites, *Nature*, 186, 863, 1960.
- Stauffer, H., Primordial argon and neon in carbonaceous chondrites and ureilites, *Geochim. et Cosmochim. Acta*, in press, 1960.
- Suess, H. E., Die Häufigkeit der Edelgase auf der Erde und im Kosmos, *J. Geol.*, 57, 600, 1949.
- Suess, H. E., and H. Brown, I^{129} and the age of the elements, *Phys. Rev.*, 83, 1254, 1951.
- Urey, H. C., *The Planets*, Yale University Press, New Haven, Conn., 1952.
- Urey, H. C., The early history of the solar system as indicated by the meteorites, *Proc. Chem. Soc. (London)*, 1958, 67, 1958.
- Valentiner, S., The solubility of the noble gases in water, *Z. Physik*, 42, 253, 1927.
- Wasserburg, G. J., W. A. Fowler, and F. Hoyle, The duration of nucleosynthesis, *Phys. Rev. Letters*, 4, 112, 1960.

(Manuscript received October 31, 1960;
revised December 22, 1960.)

Determination of Sedimentary Thickness in the Mexican Geosyncline by Rayleigh Wave Dispersion

D. H. SHURBET

*Seismological Observatory, Texas Technological College
Lubbock, Texas*

Abstract. Dispersion of short-period Rayleigh waves is studied in an effort to measure sedimentary rock thickness in the Mexican geosyncline. The measurement is approximate, but the study indicates uniformity of crustal structure over a very large area, including the Mexican geosyncline. Therefore the study suggests an economical method of measuring crustal thicknesses over the entire area. The study indicates that the average sedimentary thickness across the Mexican geosyncline is about 8 km.

Introduction. Observations made at Lubbock, Texas, of Rayleigh waves from earthquakes in the Gulf of California show that waves with periods less than about 15 sec have velocities much slower than are predicted by theoretical dispersion curves which do not take into account the surface sedimentary layers. *Oliver and Ewing* [1958] showed that the velocity of Rayleigh waves in this period range is strongly affected by sedimentary layers of average thickness. In this paper the measured dispersion of short-period Rayleigh waves is used to estimate the thickness of sedimentary rocks in continental areas where more direct evidence is lacking.

All records were from vertical-component seismographs ($T_0 = 10$ sec; $T_g = 90$ sec). The dispersion was measured by plotting, throughout the Rayleigh wave train, arrival times of successive peaks, troughs, or zeros against the serial numbers assigned to the waves. The slope of the resulting curve gives wave period, and the corresponding group velocity is easily calculated. These group velocities were then compared with theoretical dispersion curves for various models of crustal structure. The theoretical curves used in this paper were calculated by *Stoneley* [1955] for a model with two surface layers. In this report the two surface layers are treated as sedimentary layers over a granitic layer, as was done by *Oliver and Ewing* [1958]. Certainly, this two-layer crustal model is inadequate to give theoretical curves that will exactly compare with the measured dispersion, but *Oliver and Ewing* showed that semiquantitative information is thus available. Even this information is of some value for the Mexican region involved in this study.

Discussion. Table 1 gives U. S. Coast and Geodetic Survey information for the five earthquakes studied. The numbers assigned to the earthquakes in Table 1 indicate the geographical location of the epicenters on the map (Fig. 1). This map shows all Rayleigh wave paths from epicenters to Lubbock, and the division of the paths into segments according to surface features and known sedimentary history. From Lubbock toward the epicenters, the first approximately 413 km of each path crosses a West Texas-New Mexico area in which there has been considerable petroleum production. From various sources of information and data from petroleum producers it is known that the depth to Precambrian within this region varies because of different sedimentary and tectonic histories. However, the upper sediments are thick throughout the region, and for this paper it was estimated that the average thickness is about 3 km.

Beyond 413 km approximately 469 km of each path was considered in this investigation to cross the Mexican geosyncline. Sediments above Precambrian are believed to be very thick across this region, and the effects of the thick sediments should be observed in Rayleigh wave dispersion.

The portion of each path beyond the geosyncline region includes the Sierra Madre Occidental and a segment made up of the coastal plain region bordering the Gulf of California. The last segment of each path to the epicenter is made up of the Gulf of California.

For each path, the 413-km segment nearest Lubbock is assumed to be made up of two equally thick sedimentary layers above the granitic layer. The total thickness of the two layers is assumed

TABLE 1. U. S. Coast and Geodetic Survey Epicenter Information and Data for Equating Epicentral Distances to Lubbock, Texas

Earth- quake Number	Date	Time at Origin h m s	Epicenter		Total Distance to Lubbock, km	Kilometers to be Subtracted to Equate All Distances	Seconds to be Subtracted from Observed Travel Time to Equate Distances
			North Lat.	West Long.			
1	3/6/60	04 11 54	24	108	1219	144	55
2	3/31/60	19 56 14	26	110	1149	74	37
3	6/19/59	20 34 40	27½	111	1105	30	15
4	6/28/59	18 25 37	27½	112	1182	107	49
5	9/17/59	22 14 40	30½	114	1195	120	53

to be 3 km, which is average thickness above Precambrian in this area. The dispersion effect of this model is shown by the curve in Figure 2. The model is assumed to duplicate the true structure, and the travel time across this 413-km segment is calculated for waves of periods involved in the experiment.

This calculated travel time is subtracted from the total observed travel time with the result that, in effect, the 413-km segment nearest Lubbock is removed. Similarly, the effects of others of the segments can be removed from the ob-

served data. However, the other segments are not as well known as the one nearest Lubbock. Perhaps the least known and most important of the segments is the one that crosses the Mexican geosyncline. Therefore, approximate two-sedimentary-layer models were chosen to represent all segments except the one including the geosyncline. The effects of these models, according to dispersion curves shown in Figure 2, were subtracted from observed dispersion data, leaving the travel time, for waves of each period, across the geosyncline segment. The dispersion curves that were derived from these travel times were used to estimate sedimentary thickness across the Mexican geosyncline by comparison with theoretical dispersion curves (Fig. 2).

The approximate model chosen to represent the path segment made up of the Gulf of California consists of a liquid layer of water and sediments above a granitic layer 10 km thick. It was shown by Shurbet [1960] that the theoretical Rayleigh wave velocities over such a model, for short periods, are very low. A velocity of 1.0 km/sec was assumed for all wave periods involved.

The model for the Sierra Madre Occidental segment of each path consists of two layers of very thin sediments above the granitic rock, and a velocity of 2.95 km/sec is a good approximation for periods of waves considered. The errors introduced by assuming equal velocities across this segment are small. The theoretical Rayleigh wave dispersion curve for an earth model with no sediments and 35 km of granitic crust indicates that the variation of group velocity in the period range considered is only about 0.1 km/sec.

The segment made up of the coastal plain along

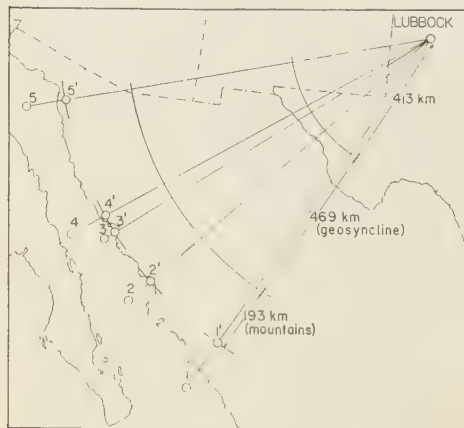


Fig. 1. Geographical location of epicenters. Numbers represent epicenters as designated in Table 1. The primed numbers represent the equating of epicentral distances to Lubbock. The arcs drawn with Lubbock as the center of the circle indicate the division of the Rayleigh wave paths into segments according to crustal structure. The length of each segment of a path is indicated in km.

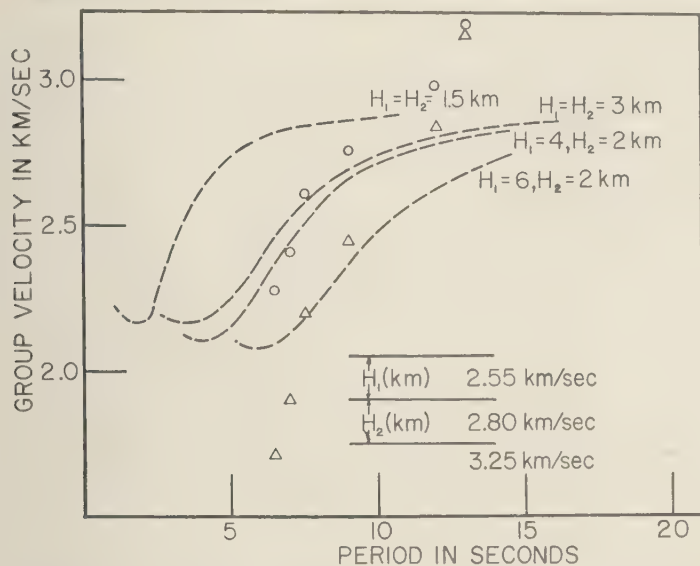


Fig. 2. Rayleigh wave dispersion curves. The dotted curves are theoretical dispersion curves as calculated by *Stoneley* [1955]. The crustal layer thickness is indicated for each curve, and the compressional wave velocities in the crustal model are shown near the bottom. The circular data points represent group velocities of Rayleigh waves calculated by dividing the equated epicentral distance by the adjusted total travel time. The triangle data points represent Rayleigh wave group velocities across the Mexican geosyncline as determined in the study.

the east margin of the Gulf of California was approximated by two sedimentary layers $1\frac{1}{2}$ km thick.

The observed data were first adjusted so that, for the investigation, all epicentral distances are equal (1075 km). The adjustments necessary to equate them are small. For all except earthquake 1 it was necessary only to subtract from the observed travel time for each trough, peak, or zero the time required for the wave to traverse a small segment of the Gulf of California at a velocity of 1.0 km/sec. For earthquake 1 it was also necessary to subtract the travel time of a segment of the coastal plain. These adjusted or equated epicenters are shown by primed numbers on the map (Fig. 1). Table 1 shows the amount of travel time involved in equating each epicentral distance to 1075 km. This simple adjustment of the epicentral distances simplified the analysis of the data.

With the epicentral distances equated in this way, a composite dispersion curve for all five earthquakes was easily obtained. The adjusted

travel time for each peak, trough, or zero read for each earthquake was plotted against wave number. The adjusted travel times for all readings are shown as Table 2, and the very close agreement of data from all earthquakes indicates that, although each path is complicated, all the paths must be very similar because the Rayleigh wave dispersion data are in such good agreement.

Presentation of data. Figure 2 shows theoretical dispersion curves as calculated by *Stoneley* [1955] for several crustal models of two sedimentary layers. The observed data, adjusted to equal epicentral distances, are shown as circles in Figure 2. The fact that the theoretical dispersion for 6 km of sediments and the observed dispersion agree for the shorter periods is taken to mean that the average sedimentary thickness over the entire length of the path is approximately 6 km. The fact that the observed velocities for longer periods are so much higher than the velocities predicted for the 6-km model is taken to mean that for this period range a crustal model including the higher-velocity basaltic material is

TABLE 2. Travel Times, in Seconds, of Peaks or Zeros from the Equated Epicenters to Lubbock (The equated epicenters are shown as primed numbers in Fig. 1. If the structure along each of the five paths is exactly the same, the travel times should be exactly the same.)

Earthquake Number				
1 (peaks)	2 (zeroes)	3 (zeroes)	4 (zeroes)	5 (zeroes)
	314			
	327½			
	331½			
339	339½			
	344½			
	349½			
353	355		353	355
	361½	361½	362	362½
364½		365		
	371½	372½	369	369
376		374½	374	374½
	377½	379½	379	380½
385	384	385	383	384½
			387	
		390½	390	389½
393	393½		394	393
	400½	399½	398	399
403			402	402½
	405½	405½	405	406
410	409	410½	409	409½
	413		412	
	417	415½		417
				419
420½	421½	422½	421	421½
	425½		424	
		427½	427	428½
430½	430½	430½	431½	431
				433½
	436½	435½	435	436½
438		438½	439	439½
	441			440½
	444	443½	443	443½
446	446½	446	446½	446½
	450	450½	449	450½
454	453½	453½	452½	453½
	457½	457½	455	456½
		460	458½	459½
462	461	464	462	
		466½	465	
468	467½		468	
		470½		
		473		
	475½			
478		477½		
		480½		
	481½			

more applicable. The predicted velocities for this model are near the observed velocities.

The calculated velocities for the 469-km segment across the Mexican geosyncline are shown as triangles in Figure 2. These data points, at periods of 7½ sec and 9 sec, fall close to the theoretical curve for a model made up of two sedimentary layers, the upper layer 6 km thick and the lower 2 km thick. For periods shorter than 7½ sec the triangles indicate velocities much lower than are predicted by any of the theoretical curves. These low velocities very probably indicate a surface layer velocity considerably lower than the velocities chosen for the models. The triangles indicate higher velocities than the theoretical curves predict for wave periods greater than 9 sec. This is again taken to indicate that a model including basaltic material is more nearly applicable for these longer periods.

Conclusions. This report does not directly yield quantitative information about sediment thickness in the Mexican geosyncline. However, it does illustrate a rather simple, economical method by which quantitative measurements could be made.

Since Rayleigh wave dispersion is so nearly the same along all the paths (Table 2), little variation in structure is indicated for all the wedge-shaped area between the paths of earthquakes 1 and 5 (Fig. 1), a structure profile for the wedge could be obtained, simply, by locating a few seismographs in easily accessible areas. The locations of seismographs need not be in a straight line, because the structure is similar along all paths. From the array of seismographs a reasonable measurement of sediments in the geosyncline should be obtainable for a fraction of the cost for measurements requiring field personnel.

REFERENCES

- Oliver, Jack, and M. Ewing, The effect of surficial sedimentary layers on continental surface waves, *Bull. Geol. Soc. Am.*, 48, 339-354, 1958.
 Shurbet, D. H., The effect of the Gulf of Mexico on Rayleigh wave dispersion, *J. Geophys. Research*, 65, 1251-1255, 1960.
 Stoneley, R., Rayleigh waves in a medium with two surface layers, *Monthly Notices Roy. Astron. Soc., Geophys. Suppl.*, 7, 71-75, 1955.

(Manuscript received August 4, 1960;
 revised November 26, 1960.)

Summary Report of Strong-Motion Measurements, Underground Nuclear Detonations

W. M. ADAMS AND R. G. PRESTON

*Lawrence Radiation Laboratory, University of California
Livermore, California*

P. L. FLANDERS AND D. C. SACHS¹

Stanford Research Institute, Menlo Park, California

W. R. PERRET

Sandia Corporation, Albuquerque, New Mexico

Abstract. Subsurface and surface motion measurements were made on six underground nuclear detonations in the Oak Springs tuff of Nevada Test Site in Operation Hardtack II: Shots Mars (~13 tons), Tamalpais (~77 tons), Neptune (~115 tons), Logan (~5 kt), Evans (~30 tons), and Blanca (~19 kt). Free-field peak radial acceleration decreased as the inverse third or fourth power of slant range, as for Rainier. Particle velocities attenuated at a rate between the inverse square and inverse cube. Maximum radial and tangential subsurface stress varied as the inverse cube of radial range. Observed peak strain suggested attenuation at a rate between inverse cube and inverse square of range. Maximum upheaval at Blanca surface zero was about 25.5 feet; ~2.5 feet at 750 feet radial range; and 1.5 feet at 910 feet. Reed gage spectra indicated a shift of maximum energy to lower frequencies with increasing ground range. All components of surface acceleration followed an empirical equation of the form

$$A(g) = 3.2 \times 10^6 W^{0.7} (kt) R^{-2} (ft)$$

All components of surface displacement did not follow a comparable relationship. Displacement is more precisely predicted than acceleration. The velocity of the tuff was determined to be 6200 ft/sec, with the velocity of the underlying dolomite 11,700 ft/sec. If a two-layer model for the crust beneath the Nevada Test Site is assumed, appropriate values for the thicknesses and velocities are 24 km and 5.69 km/sec for the top layer, and 36 km and 7.65 km/sec for the intermediate layer. The top of the mantle beginning at a depth of 60 km has a velocity of 8.12 km/sec and dips eastward.

INTRODUCTION

Scope of report. This report is a summary of shock-effects studies conducted as a part of Operation Hardtack, Phase II, underground tests of nuclear devices at the Nevada Test Site (NTS) during the fall of 1958. These studies are reported separately in more detail by the participating, performing agencies, the activities of which were organized into Program 26 and technically coordinated by the Lawrence Radiation Laboratory (LRL). See references at end of report.

There were six underground tests of nuclear devices in Operation Hardtack, Phase II, which were of interest to the shock-effects program. Shock-effects measurements were obtained for all

six of these tests. However, major programmatic efforts were limited to two of the events, Tamalpais and Evans. Locations of these test detonations are shown schematically in Figure 1. Yields for each event are given in Table 1.

The quantities measured, the component of the motion measured, the shot causing the motion, and the slant ranges over which the motion was observed are presented in Table 2.

Teloseismic data (Table A.18) are used only for travel times and direction of initial motion.

Historical background of underground nuclear shots. In September 1957, the United States successfully demonstrated a new technique for testing nuclear weapons underground. The Rainier shot of Operation Plumbbob showed that products of a nuclear device detonated at sufficient scaled depth beneath the ground surface

¹ D. C. Sachs is now at Aeronutronic, Inc., Newport Beach, California.



Fig. 1. General site plan showing Project 26.4 on-site seismograph stations.

TABLE 1. Shot Data, Underground Nuclear Detonations

Shot	Date (1958)	Time (UT)			Yield
		h	m	s	
Mars	Sept. 28	00	00	00.15	13.5 \pm 2.8 tons
Tamalpais	Oct. 8	22	00	00.13 \pm 0.01	77 \pm 10 tons
Neptune	Oct. 14	18	00	00.15	115 \pm 15 tons
Logan	Oct. 16	06	00	00.14 \pm 0.01	5.0 \pm 0.2 - 0.4 kt
Evans	Oct. 29	00	00	00.15 \pm 0.1	30 \pm 15 - 5 tons
Blanca	Oct. 30	15	00	00.15 \pm 0.1	19.2 \pm 1.5 kt

TABLE 2. Summary of Measurements

Measured Quantity	Component*	Shot	Instrument Environment	Slant Range, ft	Reference
Acceleration history	<i>V, R, T</i>	Tamalpais	Surface	2180-2222	<i>a</i>
	<i>V, R</i>	Tamalpais	Surface	1597-4925	<i>b</i>
	<i>V, R, T</i>	Logan	Surface	2621-17,060	<i>a</i>
	<i>V, R</i>	Evans	Surface	849-3701	<i>b</i>
	<i>V</i>	Evans	Boring	235-849	<i>b</i>
	<i>V</i>	Evans	Boring	190-850	<i>c</i>
	<i>V, R, T</i>	Evans	Surface	2235-18,075	<i>a</i>
	<i>V, R</i>	Evans	Surface	867-1136	<i>c</i>
	<i>V, R</i>	Blanca	Surface	3598-12,094	<i>b</i>
	<i>V</i>	Blanca	Boring	3392-3598	<i>b</i>
	<i>V</i>	Blanca	Boring	3411-3599	<i>c</i>
	<i>V, R</i>	Blanca	Surface	3736-4075	<i>c</i>
	<i>V, R, T</i>	Blanca	Surface	2679-13,311	<i>a</i>
	<i>V</i>	Evans	Boring	240-790	<i>c</i>
	<i>V</i>	Blanca	Boring	3421-3599	<i>c</i>
Strain history	<i>R</i>	Blanca	Surface	3599-4075	<i>c</i>
	Peak <i>R</i>	Blanca	Surface	1699-3888	<i>c</i>
Stress history	<i>R, T</i>	Tamalpais	Tunnel	100-425	<i>d</i>
Displacement history	<i>V, R, T</i>	Tamalpais	Surface	2180-45,771	<i>a</i>
	Peak <i>R</i>	Tamalpais	Tunnel	300 from GZ	<i>d</i>
	<i>V</i>	Neptune	Surface	356 from GZ	<i>e</i>
	<i>V</i>	Blanca	Surface	755 and 910 from GZ	<i>e</i>
	<i>V, R, T</i>	Logan	Surface	3527-47,057	<i>a</i>
	<i>V, R, T</i>	Evans	Surface	2235-47,109	<i>a</i>
	<i>V, R, T</i>	Blanca	Surface	2679-47,181	<i>a</i>

* *V* = vertical; *R* = radial, with respect to surface plane; and *T* = tangential.^a Carder, Cloud, Pearce and Murphy [1959].^b Perrett [1959].^c Swift, Sachs, and Wells [1959].^d Perkins and Thompson [1958].^e Morris and Schneiderhan [1959].

could be effectively contained in the locale of the test [Johnson, Pelsor, Preston, and Violet, 1958]. Shock effects of the Rainier shot were extensively measured and studied [Swift and Sachs, 1959; Perret, 1957; Carder, Cloud, Murphy, and Hershberger, 1958; Pieper, Tiemann, and Sivers, 1958; EG & G Inc., 1958]. A program of underground shock-effects studies was formulated for inclusion in the underground tests of nuclear devices scheduled as a part of Operation Hardtack, Phase II. This report covers results of efforts by several performing laboratories to obtain additional shock-effects data from the fall 1958 test series in Nevada.

It had been recommended, on the basis of Rainier results [Perret and Preston, 1958] that additional strong-motion data be obtained for different scaled depths of burial for yields differing substantially from that of Rainier (1.7 kt) and for rock media differing from volcanic tuff (the medium in which Rainier was detonated). An opportunity to carry out the first of these two recommendations was presented in Operation Hardtack, Phase II; and, accordingly, a shock-effects program was incorporated into the new test series.

As originally planned, shock measurements were to be obtained on Tamalpais and Evans shots, with maximum effort planned for the latter event. Predicted yields for these shots were 0.1 to 0.3 kt and about 6 kt, respectively. They were to be tested in new, separate drifts off the Rainier tunnel. It was thought that knowledge of shock effects could be improved in accuracy over the Rainier results. Tamalpais, of course, was of interest because it had a predicted yield 1 order of magnitude less than that of Rainier.

Theoretical background. Results from shock studies at Rainier [Perret, 1957] have indicated that initial peak radial accelerations within the rock medium relatively close to the detonation decayed with range from the detonation approximately as the inverse fourth power of the range. Conventionally, scaled transient shock parameters (peak radial accelerations, particle velocities and displacements) are functions of the scaled range $R/W^{1/3}$, where R is the radial range from the detonation point and W is the energy released by the detonations. Consistent with a dimensional analysis for a point-source release of energy, these parameters are related by the following expressions:

$$AW^{1/3} = k \left(\frac{R}{W^{1/3}} \right)^{-n} \quad (1)$$

for peak radial acceleration A .

$$V = k \left(\frac{R}{W^{1/3}} \right)^{-n} \quad (2)$$

for peak radial velocity V .

$$DW^{-1/3} = k \left(\frac{R}{W^{1/3}} \right)^{-n} \quad (3)$$

for peak displacement D .

In the above equations, the k 's are constants which differ for each parameter measured and are characteristic of the detonation medium. The n 's are not constants except for relatively short regions of scaled ranges where the shock is strong (but no longer supersonic) and the medium behaves elastically. Furthermore, since peak velocity and displacement are derivable by successive integrations of the acceleration with time, n is smaller for peak velocity and displacement. One further limitation in idealizing treatment of transient shock parameters is imposed by ordinary experimental and geometrical limitations: proximity of a free surface will cause overriding of outward moving shock by the reflected shock. Thus measurements of greatest interest for ideal treatment of experimental shock data are those obtained essentially in the free-field region. Values for the constant n are thought to be larger in the region where the medium behaves plastically (i.e., the shock is supersonic). At large scaled ranges, values of n may decrease to 1, even for the scaled peak acceleration. Point-source theory, however, has not been extended to this region. Experimentally, because of inhomogeneities in the medium, it is difficult to obtain definitive measurements at scaled ranges substantially beyond the region of 800 to 1000 feet.

Surface effects of the shock from an underground nuclear detonation are of interest as well as free-field effects near the explosion. At Rainier, integrated acceleration records [Swift and Sachs, 1959; Perret, 1957] and surface-motion photography [EG & G, Inc., 1958] clearly showed that the mesa above the detonation chamber was elevated momentarily about 1 foot. It then was in free-fall for 400 msec. Several separations in the layered rock occurred below the surface; and these stratified sections bottomed at successively later times as the surface was approached. This

effect is a form of spalling [Swift and Sachs, 1959]. It does not scale directly with the particle velocity because it depends upon tensile strength of the rock and geostatic pressure of the overburden, which are nonscaling properties. Undoubtedly, these observed parameters should be related to criteria for minimum depths for containment and maximum depths for cratering.

The wide ranges in static and dynamic responses of various soils (alluvium and rock) suggest that the proportions of energy of the shock partitioned into regions where the soils respond elastically will differ. Chaszeyka and Porzel [1958] have considered shock energy degradation theoretically for regions well inside the elastic range. Although literature on behavior of soils under static loads is extensive, literature on theory and experimental data for behavior of soils under dynamic loading is limited. Free-field shock data obtained from experimental measurements at underground detonations are, therefore, of considerable interest for developing an understanding of factors which influence shock attenuation in the elastic region. For example, a thorough understanding of factors which affect attenuation of shock within the free field would be an important corollary to any experiments designed to evaluate the detectability by seismic monitoring systems of underground detonations in various soils.

Seismic studies of the acceleration and displacement on the surface at distances greater than 1250 feet on Rainier indicated that the value of n was about 2 [Carder, Cloud, Murphy, and Hershberger, 1958]. It was necessary to remember, however, that such measurements should not be expected to follow a free-field rule because of the likely interface phenomena, reflection and refraction. It is desirable to correct for such effects and then analyze the data as free field; however, that is not possible for this preliminary summary. The empirical approach appears to be the only feasible one at present. At the close-in distances (3000- to 4000-ft radial range) where amplitude data are studied, the largest amplitude occurs in the direct wave which arrives after the first disturbance, a refraction through the underlying higher-velocity dolomite. It is the largest amplitude associated with the displacement or acceleration of the direct wave that is used for amplitude measurements.

In addition to studies of seismic effects, studies of the behavior of soils under shock loading from

an underground nuclear detonation are of interest for designing underground and surface structures for various applications. Transient shock data obtained from measurements in various media and conditions of detonations, when combined with limited, basic, structural-response data, may be used for predicting shock effects on underground protective shelters for personnel, on underground and surface targets, and on underground and surface structures installed in connection with exploiting nuclear explosives for industrial purposes.

INSTRUMENTATION AND SHOT LOCATIONS

Instrumentation for Program 26 projects was confined to Area 12 of Nevada Test Site with the exception of strong-motion and teleseismic instruments required for Project 26.4. Locations of on-site strong-motion stations for that project are indicated in Figure 1 on a map of the north end of NTS. A general site plan for Area 12, Figure 2, shows the position of the surface stations and vertical gage arrays of all Program 26 projects with respect to surface zeros of six of the Hardtack-II shots and of Rainier shot. Symbols designate the projects by which specific stations were used. Project 26.4 stations within Area 12 are indicated on both Figures 1 and 2.

A schematic elevation of Projects 26.1 and 26.2 instruments in the vertical borings above Evans is presented in Figure 3. Actual, as placed, instrument ranges are given as well as the gage code symbols which are used in presentation of the data in the section on results and discussion.

Instrument stations occupied by Projects 26.3 and 26.8 were in the U-12b tunnel or in side drifts from it. Those stations of both projects from which data were derived during the Tamalpais event are indicated in Figure 4. The Tamalpais drift, U-12b.02, is shown complete; all others are truncated beyond relevant portions.

Project 26.1—Stanford Research Institute (SRI) [Swift, Sachs, and Wells, 1959]. SRI measured vertical acceleration and velocity in a deep hole above Evans zero, horizontal and vertical acceleration on the mesa surface, and horizontal surface strain. The Evans instrumentation was reactivated for Blanca.

Vertical acceleration was measured in a deep hole (Sta. 1) above Evans zero at twelve vertical ranges from 200 to 800 feet (Fig. 3). Vertical and horizontal radial acceleration were measured at

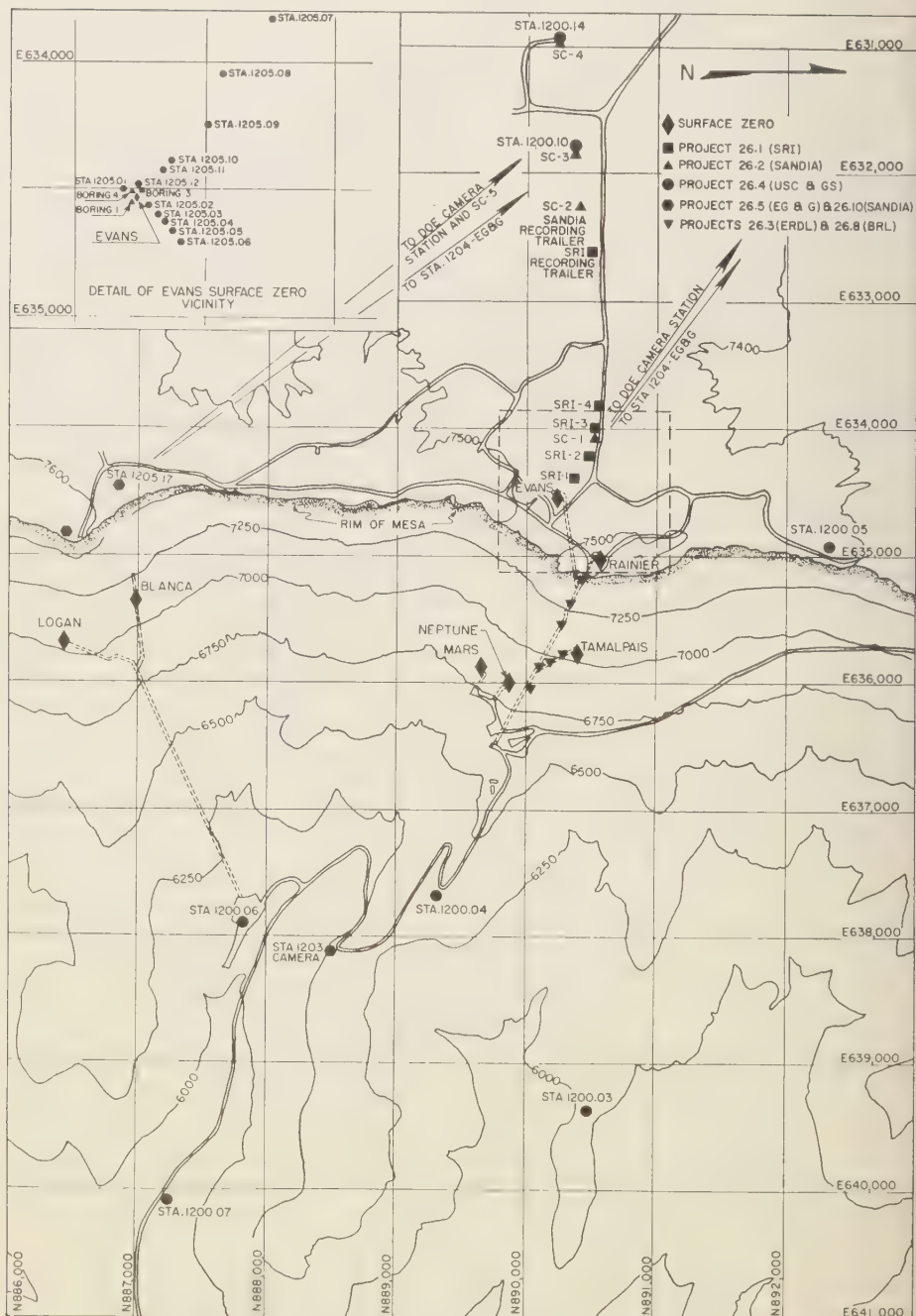


Fig. 2. Program 26 surface instrumentation plan, area 12.

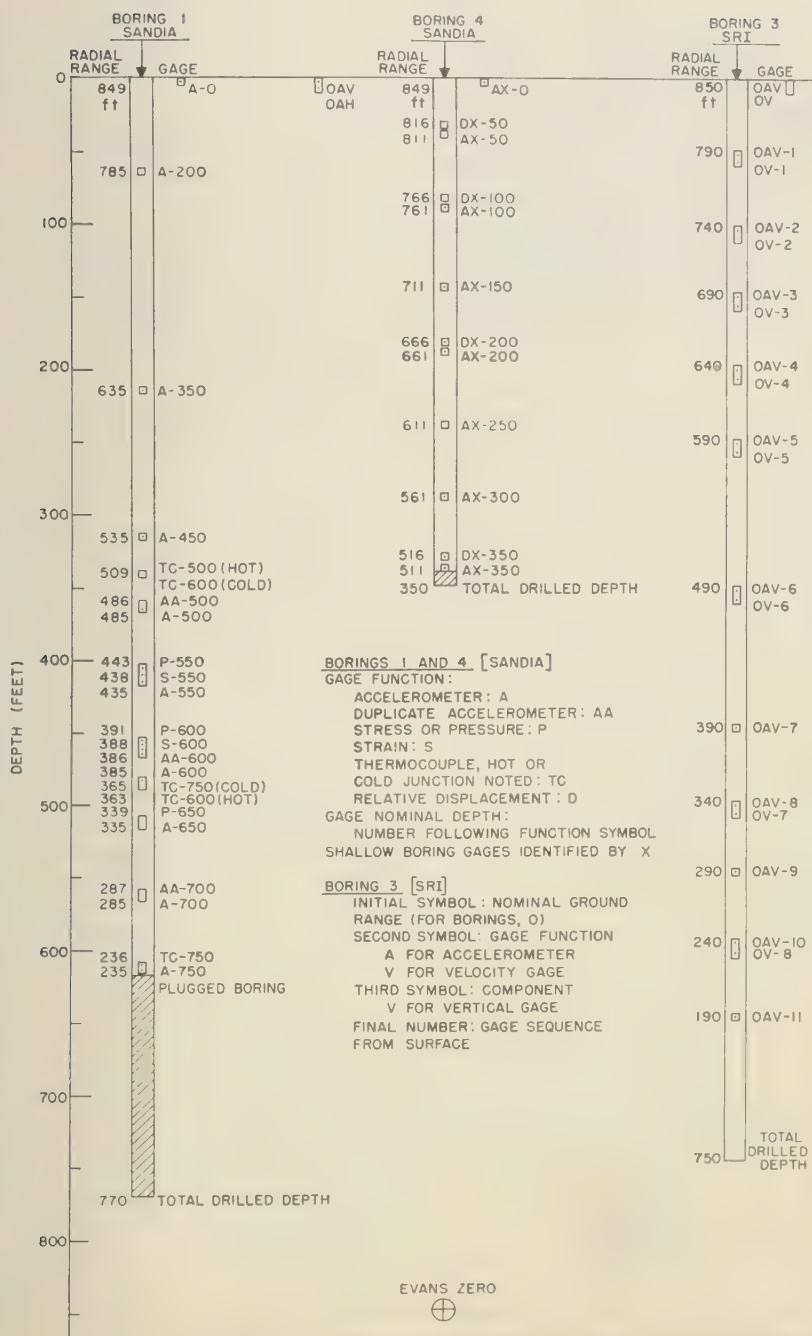


Fig. 3. Vertical boring gage arrays, Projects 26.1 and 26.2.

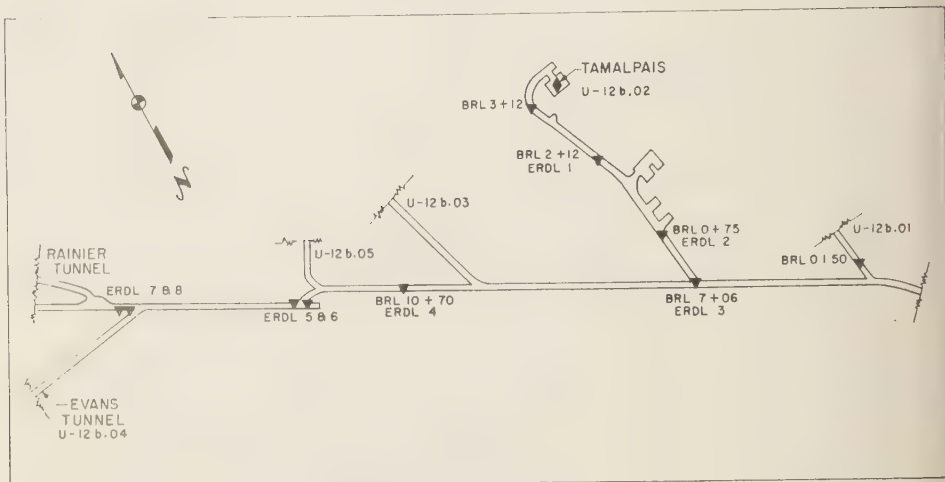


Fig. 4. Tunnel gage arrays, Projects 26.3 and 26.8.

four surface stations, 200, 400, 600, and 800 feet from surface zero (Fig. 2). Standard Wiancko variable reluctance accelerometers were used, those in the deep hole measuring in one direction

only, those on the surface measuring in two directions (two gages).

Particle velocity was measured at nine vertical ranges at Sta. 0 (Fig. 3) with a velocity gage of new design based on a principle not previously applied to effects tests. The velocity of a cylindrical plunger (a core of a linear variable differential transformer) falling through viscous fluid inside a cylindrical container of slightly larger diameter than the plunger is a direct function of the impressed acceleration (Fig. 5).

Surface strain was measured in two directions at surface zero and radially at 200, 400, 600, and 800 feet from surface zero (Fig. 2). Several strain measurements (cork-wire gages) were made at other locations on the mesa (Fig. 2).

Arrival times of the first ground motion were measured at five places on the mesa surface and at surface zero (Fig. 2).

Reed gage (Fig. 6) stations at several locations on the mesa, (Fig. 2), installed and operated by Space Technology Laboratories, recorded velocity response spectra [Halsey and Barton, 1959]. The reed gage is a completely self-contained, mechanical unit requiring no electronics or communication channels. It consists of a number of masses (mechanical reeds) attached to cantilever springs mounted on two sides of a vertical plate. Each reed has a characteristic natural frequency; these frequencies cover the range from ~ 3 to 300 cps. The gage is fastened to a concrete pad, and peal

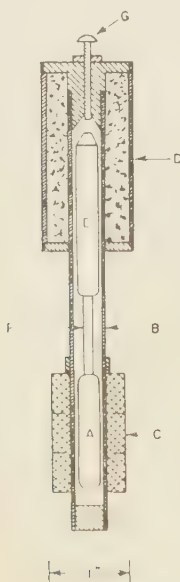


Fig. 5. Vertical velocity gage, SRI. A, steel core; B, nonmagnetic tube; C, differential transformer windings; D, solenoid; E, solenoid core; F, connecting rod; G, adjustment screw.

response to the motion input for each spring mass system is recorded by the mark of a stylus moving along a polished record plate upon which a thin carbon film is placed. The length of the marks (measure of displacement) is determined with a microscopic micrometer in the laboratory.

The recording system consisted of modified Wiancko oscillator-demodulator carrier systems with a few channels of a Consolidated carrier-amplifier system; all channels were recorded on Miller oscillographs.

Project 26.2—Sandia Corporation (SC) [Perret, 1959]. The radial acceleration on a vertical radius in two borings drilled from the mesa surface to depths of 750 and 350 feet above the Evans shot chamber was measured in Project 26.2. In addition, vertical and horizontal radial accelerations were measured on the mesa surface at several radial distances from Tamalpais, Evans, and Blanca surface zeros.

Accelerometers placed in two borings adjacent to Evans surface zero measured accelerations at 50-foot intervals in the lower 300 feet of the deep boring and in the upper 350-foot portion of the overburden over the Evans shot chamber (Fig. 3). Deep boring gages were at higher elevations than planned because of the difficulty in reaching the desired depth in the 750-foot boring, as indicated in Figure 3.

Vertical and horizontal (radial) surface accelerations were measured at three USC&GS stations, at Evans surface zero, and at the Sandia recording trailer (Fig. 2) on Tamalpais, Evans, and Blanca to provide backup for USC&GS strong-motion measurements (Project 26.4). A vertical accelerometer was installed at Doe station on Blanca (Fig. 2).

For very high ranges of acceleration (500 g or higher) Northam DP (A) 7-20 accelerometers (diaphragm fluid pressure gages adapted to acceleration measurement) were used [Perret, 1957]. For lower ranges of acceleration, Northam A-8 and Wiancko variable reluctance gages were used.

All transducers were operated through a Consolidated Engineering System D, 3-ke/sec carrier-amplifier system. The demodulated d-c output of the amplifiers was channeled through an Ampex FR-114 amplifier-recorder system at a center frequency of 54 kc/sec, with linear sideband capability of 40 per cent of center frequency.

Project 26.3—Engineer Research and Development Laboratories (ERDL) [Anthony, 1959]. In

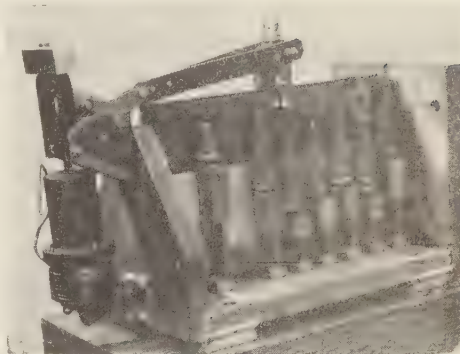


Fig. 6. Reed frequency spectrum gage, STL.

Project 26.3 it was planned to measure radial acceleration and strain in the medium surrounding the Evans shot. ERDL developmental strain gages were installed and tested on Tamalpais.

On Evans, in the U12b.02 tunnel, two accelerometers were installed at each of five stations at approximately 140 to 850 feet from the detonation point (Fig. 4). All but the two accelerometers closest to the Evans detonation point were Wiancko variable reluctance gages. The two other accelerometers were piezoelectric gages (developed by Columbia Research Laboratory).

At the same five stations in U12b.02 a minimum of two strain gages was installed. Strain-measuring instruments consisted of two SR-4 strain gages in a 'sandwich' configuration. At two stations which were expected to extend from the zone of crushing well into the zone of elastic response an additional strain gage was installed at a depth of 3 feet from the nearest free surface. With the exception of the latter, all Evans tunnel gages were placed at a minimum depth of 6 feet from the nearest free surface and oriented on a radius from the detonation point.

On Tamalpais, two ERDL strain gages were placed at four BRL stations, approximately 100 to 300 feet from the detonation point (Fig. 4), and fortunately the two most distant radial stations (ERDL) on Evans were oriented so that radial strain could be measured at these stations on Tamalpais.

All gages were set in cylinders of gypsum cement, and the cylinder was lowered into its hole. Residual strain in the medium was measured after the shot. Both oscillographic and magnetic tape recording were used on this project.

Project 26.4—U. S. Coast and Geodetic Survey (USC&GS) [Carter, Cloud, Pearce, and Murphy, 1959]. USC&GS measured surface acceleration and transient displacement (strong motion) on shots Tamalpais, Logan, Evans, and Blanca and at six stations within 240 km of the site. Reports and records of ground motion from established seismograph stations out to 3800 km from the site were also obtained.

Twelve strong-motion seismograph stations were located from 2000 to 50,000 feet from the zero sites (Fig. 1). Stations were selected so that the larger shots could be monitored from several directions and so that at least one station was located on each of the geologic formations in the area. Strong motion was recorded with standard, remotely controlled, optical mechanical seismographs. Established teleseismic stations were equipped with various seismographs.

Project 26.5—Edgerton, Germeshausen, and Grier, Inc., (EG&G) [Morris and Schneiderhan, 1959]. In Project 26.5 the objective was to measure photographically the transient vertical surface displacement on Evans, Blanca, and Neptune.

Two camera stations were located adjacent to the road between the portals of U12e and U12b tunnels (Fig. 2). Cameras viewed both the sloping face of the mesa and the tunnel portal, especially the area above each underground zero site. Four cameras were operated at each mesa slope station: two high-speed Mitchells (100 frames/sec) for ground zero coverage, one standard 35-mm camera (24 frames/sec) for general slope coverage, and one cloud camera (70 mm) for photography of the rising dust cloud. Fields of view approximately 600×800 feet and 1000×1500

feet were covered by Mitchells; other cameras had wider fields of view.

Surface upheaval was photographed from station 1204 on the mesa surface (Fig. 2), approximately 9000 feet from Blanca surface zero. Reference points for this photography were a series of lighted target towers (similar to those used on Rainier) on the mesa surface in the vicinity of Evans and Blanca surface zeros. Station 1204 cameras were four 35-mm high-speed Mitchells (100 frames/sec), a 35-mm Bell and Howell (12 frames/sec), and a Maurer at 1 frame/sec.

Project 26.8—Ballistic Research Laboratories (BRL) [Perkins and Thompson, 1958]. In Project 26.8 the objective was to measure acceleration, pressure, stress, and displacement in the tuff at various distances from Tamalpais. Owing to oscillator power supply failure, only stress and displacement measurements were successful.

Seven 8-foot holes were dug to house gage arrays in the floor of the U12b tunnel and U12b.02 drift at 40, 100, 170, 225, 300 (2 holes), and 425 feet from the Tamalpais detonation point. Variable reluctance Carlson-Wiancko stress gages were used to measure stress components in the tuff. Inertial displacement gages (Fig. 7) with a displacement range of 6 inches were constructed by Atlantic Research Corporation with Schaevitz linear variable differential transformers as transducing elements.

The length of the transformer core was increased by attaching a shaft, supported by ball bushings. When the base of the gage is displaced horizontally, the inertia of the shaft causes it to move with reference to its case a distance which, in the absence of friction, equals displacement of

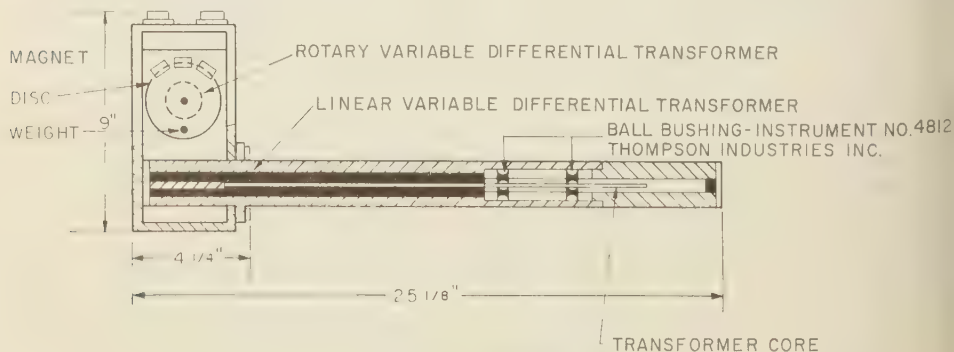


Fig. 7. Horizontal displacement gage, BRL.

the case. The gage is installed in the ground at an angle of about 2° to the horizontal so that the shaft will be at one end of its range (away from explosion point) and will return to that position if disturbed by the shock. The shaft will move relative to the case if the case is displaced away from the explosion with an acceleration greater than ~ 0.06 g. Corrections for effects of angle of inclination and for friction will not be large if the acceleration is large, but will be significant when the accelerations approach 0.06 g. A rotary variable-differential transformer incorporated in the gage with a pendulum attached to the shaft measures the inclination angle, a quantity important in installation and interpretation of results. Static laboratory tests showed the gage output to be linear with displacement to within ± 1 per cent.

At the close-in (40-foot) station a Statham unbounded gage was used to measure radial acceleration and a Wiancko variable reluctance gage was used to measure the transverse component. The latter type of gage was used at all other stations, as well, for measurement of radial acceleration.

Newly developed piezoelectric pressure transducers, designed by Atlantic Research Corporation, were used to measure pressure in the tuff close to the detonation point. For the transducer at the 40-foot station, the sensing element was a solid cylinder of lead metaniobate potted in Araldite 502 with a range of 10,000 psi. The transducer at the 100-foot station contained a sensing element of barium titanate and was considered adequate for the expected 500-psi pressure. These gages were encased in Hydrostone and grouted into place. The recording equipment was housed in a trailer 500 feet from the tunnel entrance.

Project 26.10—Sandia Corporation (SC) [Perret, 1959]. Project 26.10 was similar to Project 26.5 (EG&G). The displacement observations were obtained by photographing the same target arrays in the vicinity of Blanca and Evans surface zeros with equipment of greater resolution and more restrictive field of view.

At Doe camera station, 9550 feet northwest of Evans surface zero and 12,065 feet northwest of Blanca surface zero, three telescopes with long-ocul-length lenses were equipped with 35-mm Mitchell cameras. Under favorable atmospheric conditions, these telescopes can resolve 2 inches

at 10,000 feet with a lateral field of view of about 160 feet. Pitch-indicating gyro units at Doe station permitted correction of vertical target displacement for apparent displacement caused by the ground motion passing the foundation of the camera station.

RESULTS AND DISCUSSION

Data from strong-motion studies are treated by parameter (acceleration, velocity, displacement, and stress and strain) and by category—those derived from subsurface measurements and those derived from surface measurements. From these measurements propagation velocities have been determined and are discussed first, since they suggest some of the characteristics of the media in which the strong motion was measured.

Propagation velocity. Times of arrival for Tamalpais, Evans, and Blanca are plotted in Figure 8. Two general velocity ranges are apparent, about 6200 ft/sec for the nearer stations, typical of tuff, and about 11,700 ft/sec for the greater slant ranges.

At slant ranges less than 3000 feet first arrivals are assumed to travel entirely within tuff at an average velocity of 6200 ft/sec. The paths are generally direct, but inhomogeneities in the tuff evidently cause diversion from direct paths to some of the gages. The initial seismic pulse at all greater ranges traveled over minimum time paths through tuff to underlying dolomite, through dolomite to a point roughly beneath the gage station, and then upward through tuff to the gage. The velocity of 11,700 ft/sec defined by most of these data is characteristic of transit through dolomite. An anomalous group of data points from Blanca records imply arrivals at a velocity of 6200 ft/sec characteristic of tuff but at times which are too early by about 0.2 seconds for travel completely within tuff. These data are from the line of gages that was vertically above Evans zero, about 3300 feet north of Blanca zero. Evidently, first arrivals at these gages traveled over essentially identical refracted paths through dolomite and then traveled upward over paths of varying length within tuff to the gages. The travel times are thus characteristic of the dolomite path, but the transit times between gages of the vertical line are characteristic of travel through tuff. Travel-time data are consistent with a northward dip of the dolomite indicated by geologic investigations.

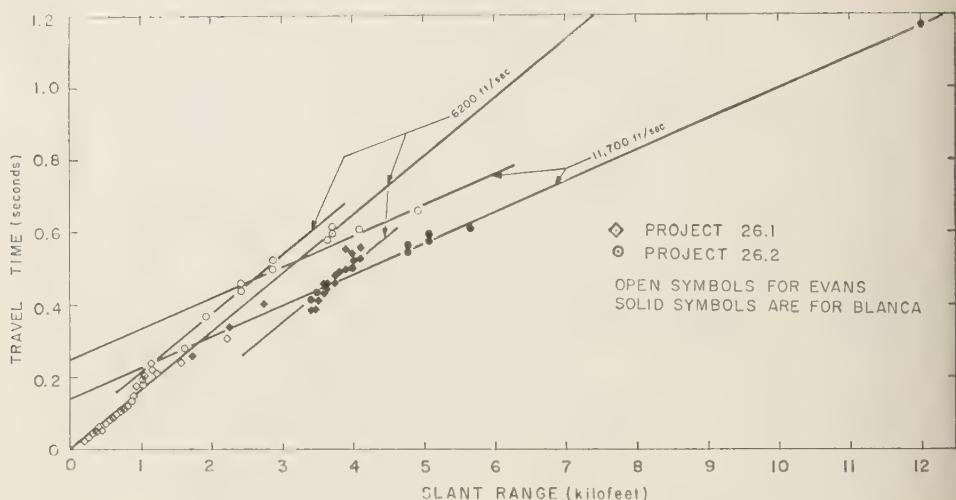


Fig. 8. Close-in travel-time curves, 200 to 12,000 feet, Projects 26.1 and 26.2.

Additional propagation velocity data are available from the first arrivals at the deep hole accelerometers and the preshot sonic log. Because of the very low amplitude acceleration records obtained on the Evans shot it is difficult to distinguish accurately the time of first signal arrival. For this reason, the sonic log is undoubtedly a more reliable measure of the vertical propagation velocities near the Evans deep borings.

Figure 9 shows the interval velocity profiles determined from the accelerometer data and the sonic log. It is evident that, although the interval velocity profiles for the deep holes obtained in the different borings are similar in general appearance, they differ in detail, particularly in the depth interval of 50 to 200 feet. The sonic log data show an abrupt increase in seismic velocity (approaching 13,000 ft/sec) between depths of 150 and 250 feet. Below 300-foot depths, sonic log data agree well with the calculations from interval velocities.

The average seismic velocities, computed from arrivals at geophones placed on the mesa at various distances from surface zero, all fell in the range 6400–7200 ft/sec. In this method of determining seismic velocity the presence of the high-velocity layer shown on the sonic log would usually not be detected.

Travel-time data from seismic stations op-

erated by the USC&GS (Table A.18) at ranges greater than 50 km and other data communicated privately by Prof. Frank Press of California Institute of Technology and by Dr. Carl F. Romney of Air Force Technical Application Center are plotted in Figure 10. Three straight lines, corresponding to two crustal layers are fitted to the observations. The one for epicentral distances

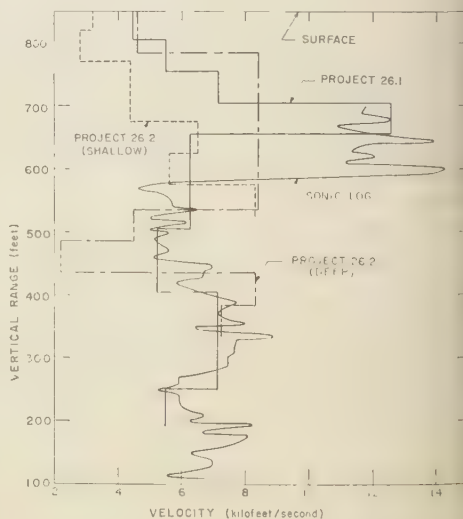


Fig. 9. Vertical profile of velocities.

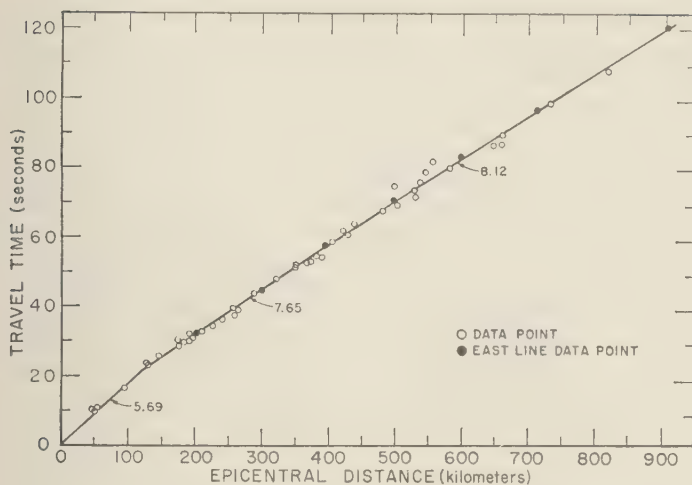


Fig. 10. Remote travel-time curves, 50 to 900 kilometers, Project 26.4.

from zero to 128 km indicates a velocity of 5.69 km/sec; the other from 128 km to 481 km, a velocity of 7.65 km/sec. The thicknesses can be computed to be 24 km for the 5.69-km/sec layer and 36 km for the 7.65-km/sec layer.

The velocity for the upper layer differs significantly from the results of *Carder and Bailey* [1958] who reported a corresponding velocity of 6.15 km/sec. The data in Figure 9 confirm the finding of a 7.66-km/sec stratum in the region by *Press* [1959]. The consistent late arrival at stations to the east, substantiated by a record from Salt Lake City [*Carder and Bailey*, 1958], indicates an eastward dip of the Mohorovicic discontinuity beneath NTS.

Acceleration. Vertical accelerations measured in the deep hole for Evans show almost identical waveforms independent of radial distance (Fig. 11): the first pulse is positive (acceleration away from the detonation point), followed by an almost equal negative pulse after which there is very little evidence of disturbance.

The behavior characteristics shown by these acceleration records from the same gages on Blanca are quite different (Fig. 11). Here the first pulse, although still upward, is seldom the maximum acceleration. Actually, it appears that in most cases the second positive and negative pulses are the largest. Also, at later times some low-frequency (about 2–5 cps) oscillations of acceleration appear. There are two anomalous pulses

at about 0.60 and 0.95 seconds in the A-200 record for Blanca which do not appear in any other records of this series. These pulses are presumed to be spurious electrical transients and

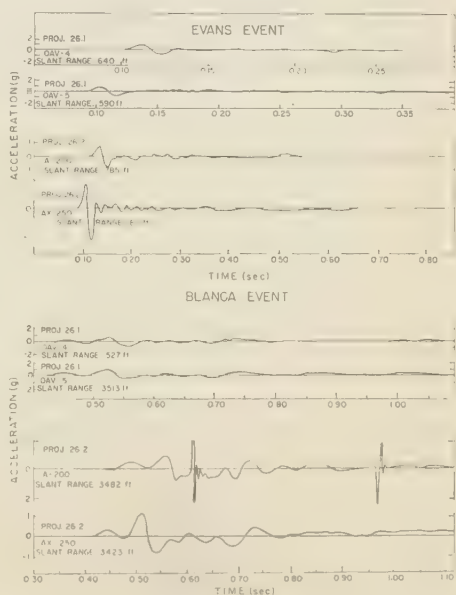


Fig. 11. Typical acceleration records from vertical instrument arrays, Evans and Blanca events, Projects 26.1 and 26.2.

not to be related to ground motion. These results are not surprising when one realizes that the shot-gage geometry on Blanca was vastly different from that on Evans. On Blanca, it would be expected that most of the energy would come to the array of gages in the vertical holes by rather indirect paths, due to refraction and reflection, because of the large distances involved. Blanca waveforms, showing a build-up to maximum accelerations at later times followed by low-frequency components, are characteristic of acceleration-time results obtained previously where refraction phenomena were pronounced [Carder, Cloud, Murphy, and Hershberger, 1958]. Because of the geometry, the deep gages in the vertical hole did not register very large amplitudes on Blanca; however, the values are measurable.

The characteristics of the Tamalpais waveforms change somewhat with increasing range, although the first acceleration pulse arriving at a station indicates motion up and out. The records show a gradual build-up of amplitude and larger peaks at late times, with the maxima occurring at later times at the more remote ranges. The predominant frequency appears to be about 5 cps. All this again points to the presence of a large proportion of refracted and reflected energy reaching these surface gages. Parenthetically, it should be recalled that the nearest surface gages on Tamalpais were somewhat farther (approximately 1300 feet) from the detonation point than they were on Evans.

Evans surface-level acceleration records are similar in form to those obtained on Tamalpais, but, unlike the latter, the Evans records show that the first acceleration peak is usually the maximum peak. Since this behavior is particularly characteristic of the shorter-range station gages, it gives further credence to the argument that energy arriving at the longer ranges suffers a good deal of refraction and/or reflection from the substrata known to exist in the test medium. Blanca records, as would be expected from the larger yield of this shot and the more distant ground ranges of the instrument stations, are much longer than those obtained on Evans. Again, evidence of refracted energy arriving at the surface-level gages is strong; at slant ranges of 1014 and 1136 feet there is a large pulse of energy which arrives at approximately 0.7 sec, long after the arrival of the first disturbance at each station. It is significant that this pulse ap-

pears to arrive at the more remote range earlier, and this is strong evidence that the energy was refracted owing to a higher-velocity subsurface formation.

This brief description of the main characteristics of the acceleration-time waveforms measured on Hardtack II underground shots indicates two principal precautions to be recognized in analysis:

1. Any acceleration-time measurements, particularly those taken on the surface, associated with an underground detonation are profoundly influenced by the stratification and faulting of the test medium. Therefore, one must realize that in other media the refracted and reflected energy might be more or less than was observed on the Rainier mesa at NTS.

2. The waveform characteristics and how they change with gage depth and distance from the detonation illustrate the inherent dangers involved in trying to choose a single number (i.e., the maximum acceleration) to describe the measurement. The first pulse can often be identified with the energy coming directly from the explosion (without reflection or refraction), but later peaks (from refracted energy) are sometimes larger than the first. It is not clear which maxima are most significant to the analysis of effects. Perhaps the particle velocity is a better parameter to use as a reference because it more closely approximates the form of the propagated stress wave.

In three projects radial acceleration data were obtained from within the rock. In the ERDL project report [Anthony, 1959] peak accelerations are quoted from two ranges recorded during the Tamalpais event (Table A.1). Both SRI and Sandia derived some data from vertical radius instrumentation above Evans [Swift, Sachs, and Wells, 1959; Perret, 1959; Tables A.2 and A.3]. Low-order yields from both events reduced reliability of the data, and, in preliminary analysis, only peak values are considered valid.

A logarithmic plot of peak acceleration versus range (Fig. 12) shows data trends and indicates a degree of scatter compatible with the low response from the unexpectedly low energy yield of Evans. The figure shows that, except for the measurements close to the detonation, the maximum upward and downward accelerations are approximately equal. Also, it is evident that the Sandia (26.2) data at close-in stations indicate

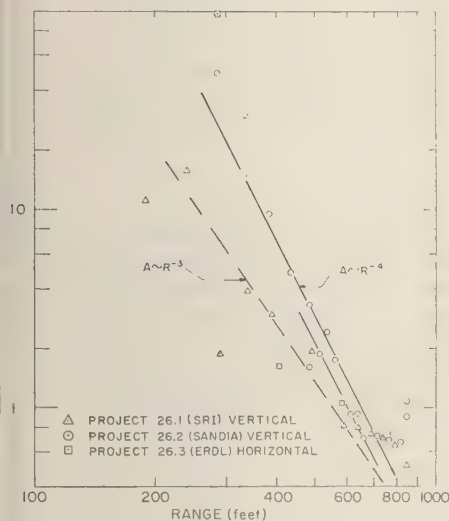


Fig. 12. Subsurface acceleration versus radial range, Projects 26.1, 26.2, and 26.3. Dashed symbols represent peak-to-peak observations. Corresponding half-values are plotted as solid symbols. Projects 26.1 and 26.2 data are for Evans. Project 26.3 data is for Tamalpais.

larger acceleration amplitudes than do the SRI (26.1) data.

Data indicate large scatter in the region of lowest range, as would be expected. In general, Project 26.1 data imply attenuation at a rate roughly comparable to the inverse cube of the range (dashed line, Fig. 12). Project 26.2 data from a parallel instrument array imply attenuation approximating the inverse fourth power of the range (solid line, Fig. 12). There is a possible trend toward inverse second- or even first-power attenuation in the vicinity of the 600-foot range, but scatter here and the apparent influence of the cap rock are too great to permit definition of such changes in trend. Caution should be used in comparing these data with the preliminary Rainier data because of saturation effects in the Rainier record peaks and low precision of the Evans records.

At depths of about 200 feet or more (ranges greater than 600 feet) the welded tuff cap rock and free surface influence data from both projects. Project 26.2 gages indicated enhanced peak accelerations near the free surface just as was found on the similarly placed gages in the Rainier test. However, this effect was not observed in Project

26.1 data, and strong free-surface influence and free-fall data were not as evident as they were for the near-surface gages during Rainier.

The maximum vertical accelerations measured in the Evans deep hole on Blanca (Tables A.4 and A.5), because of the geometry of the gage string with respect to the position of detonation, are confined to a slant-range interval of about 200 feet. As would be expected, the peak accelerations are relatively constant over this limited range. One should be cautious in making comparisons between the deep hole data for Evans and Blanca; for Evans, the principal path for the disturbance was directly from the detonation to the gages whereas for Blanca it is probable that a great deal of the energy arriving at the gages had been refracted or reflected from subsurface strata.

Project 26.3 horizontal-radius data in the tunnel (Table A.1) for Tamalpais fall in the vicinity of the Evans data in Figure 12; scatter and low gage response indicate only rough similarity in data at 600-foot range on vertical and horizontal radii from similar explosions.

The designations of peak acceleration for the vertical and radial surface-level measurements (Tables A.6 through A.12) have questionable value from the standpoint of data analysis (Fig. 13 and 14). Although Blanca and Tamalpais results appear to be fairly well behaved and indicate a reasonable variation with distance, the data from Evans are difficult to understand. At close-in ranges, the Evans peak acceleration data vary by more than a factor of 10 for a slant-range interval of only about 400 feet, which represents ground ranges from zero to 800 feet. One explanation for such behavior is that, whereas the gages closest to surface zero receive stress waves by rather direct paths from the detonation point, as the distances become larger the paths must necessarily approach the surface at more grazing angles. If there were a subsurface layer(s) possessing higher propagation velocity, it would be reasonable that at a certain grazing angle a good deal of the incident energy would be refracted by the layer, thereby decreasing the energy arriving at the surface gages above the layer. There is some evidence that such a high-velocity layer does exist in the test area (see the next section).

As was mentioned in the Introduction, peak surface acceleration is treated empirically and as

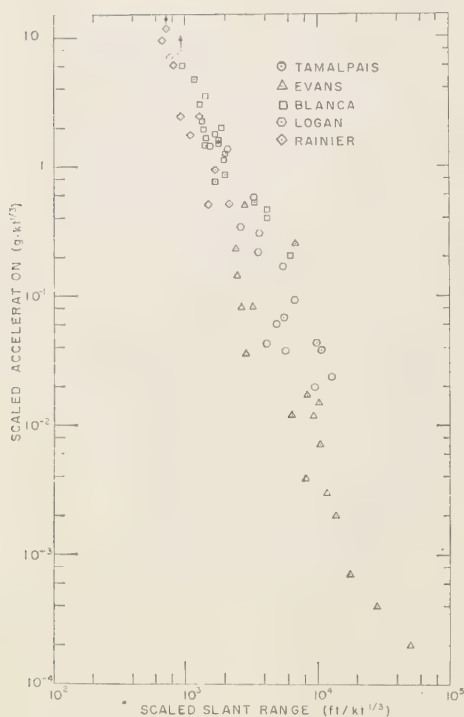


Fig. 13. Scaled vertical surface acceleration versus scaled slant range, Project 26.4.

a free-field phenomenon. The surface acceleration data from Operation Hardtack, Phase II, have been combined with those from Rainier of Operation Plumbbob and have been grouped according to the component of the motion observed—vertical, radial, or tangential. All suitable data from the reports in Table 2 have been used. The peak vertical surface acceleration data have been scaled according to equation 1 and are plotted in Figure 13 versus scaled slant range. Data for Evans at a scaled range of about 3000 feet show wide scatter. The Rainier point at about $7.5 \text{ g}/(\text{kt})^{1/3}$ is a minimum value, as is implied by the arrow directed to higher acceleration. Figure 14 is a similar graph for the scaled peak radial acceleration. The plotted data on both figures indicate a tendency for the scaled values from the higher-yield shots to be greater, but this is not definitely established.

By use of the empirical approach the data have been fitted by least squares to an equation of the form

$$A_{\text{peak}} = c_0' W^{c_1} R^{c_2} \quad (4)$$

written for purposes of computation as

$$\log A_{\text{peak}} = c_0 + c_1 \log W + c_2 \log R \quad (5)$$

where

$$c_0 = \log c_0' \quad (6)$$

and where A is peak acceleration in parts of gravity, W is the yield in kilotons, R is the slant range in feet, and c_0 , c_1 , and c_2 are the coefficients obtained in the best-fit procedure.

The resulting equations for the various components of motion are: vertical component of acceleration,

$$\log A_v = 6.46 + 0.70 \log W - 2.04 \log R \quad (7)$$

radial component of acceleration,

$$\log A_r = 6.65 + 0.69 \log W - 2.11 \log R \quad (8)$$

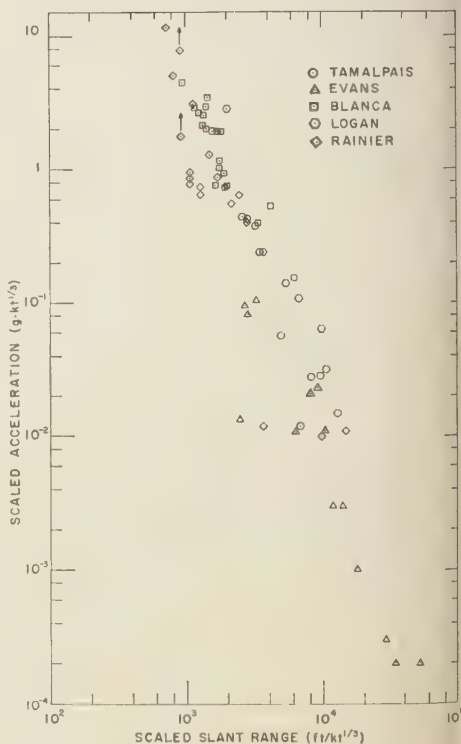


Fig. 14. Scaled radial surface acceleration versus scaled slant range, Project 26.4.

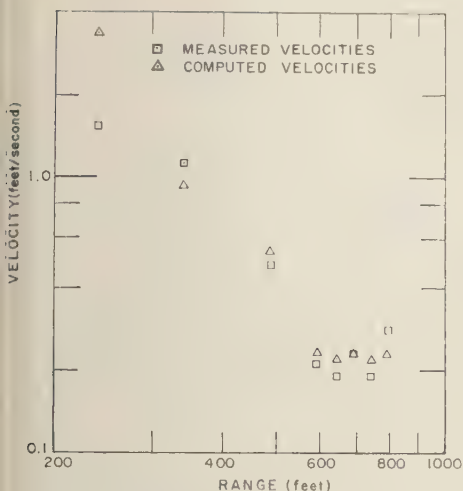


Fig. 15. Vertical particle velocity versus range, Evans event, Project 26.1.

and for the tangential component of acceleration, not included as a figure,

$$\log A_t = 6.52 + 0.67 \log W - 2.07 \log R. \quad (9)$$

The data are such that the third figure is not significant; but the surprising feature of the fitted curves is that they are so similar for all three components despite the interface and free surface effects that have been neglected. Furthermore, because of the complex geological structure and stratigraphy in the area, many stations were located on different types of rock. An equation satisfactory for all three components is

$$\log A = 6.5 + 0.7 \log W - 2.1 \log R \quad (10)$$

The values of c_1 definitely indicate a value of less than 0.75 while the values of c_2 indicate a value slightly greater than 2, say 2.07.

It is now possible to compare the coefficients obtained empirically with the free-field exponents of yield and range. Equation 1 may be written as

$$A = k \frac{W^{\frac{n-1}{3}}}{R^n} \quad (11)$$

Thus, if the exponent of the range is approximately 2, the exponent of the yield should be approximately $1/3$, according to the free-field assumption. This clearly is not in agreement with

the coefficients of yield in equations 7 through 9 which are about twice the exponent desired for the free-field condition. This example emphasizes the danger of assuming free-field conditions when they are not applicable. Such error is increased when magnified by extrapolation to yields several orders of magnitude greater than that of any existing experimental data.

Subsurface particle velocity. Peak particle velocities measured directly by Project 26.1 in the deep vertical boring (Tables A.13 and A.14) are compared in Figure 15 with similar peak values computed by integration (without adjustment) of acceleration time records obtained at the same depths during the Evans event. Computed values are in general greater, but differences except at the 240-foot range are relatively small. The particle velocity measurements were essentially a proof test of a new instrument. The results, of lower precision because of low input, indicate that the Stanford Research Institute velocity gage is a promising instrument.

In Figure 15 the attenuation of peak velocity is shown to be at a rate somewhere between the inverse square and inverse cube of range. At ranges greater than 600 feet the cap rock and free surface cause a reversal of trend similar to that observed for Project 26.2 accelerations.

Response spectrum is defined as the maximum response of a linear, single degree of freedom, spring mass system (reed gage), relative to the motion of the ground. Reed gage data (Table A.15) from a typical station on Blanca are plotted as vertical velocity spectrum versus frequency (Fig. 16) on a grid which facilitates determination of the vertical displacement spectrum and vertical acceleration spectrum. It should be noted that, although earth acceleration and displacement can be compared with the corresponding response spectra parameters, the earth particle velocity is quite different from the $\omega |x|$ parameter of the spectra, in which ω is the circular frequency in radians/sec and $|x|$ is absolute value of the maximum displacement of the spring mass system [Barton, 1957].

It was found that, as the ground range increases, the spectra shift to lower frequencies. If one compares the maximum value of the acceleration response spectra with the SRI-measured peak ground acceleration, a_{\max} , these comparisons indicate that the ratio $\omega |x|_{\max} / a_{\max}$ for Blanca ranges from about 2.5 to 3.5.

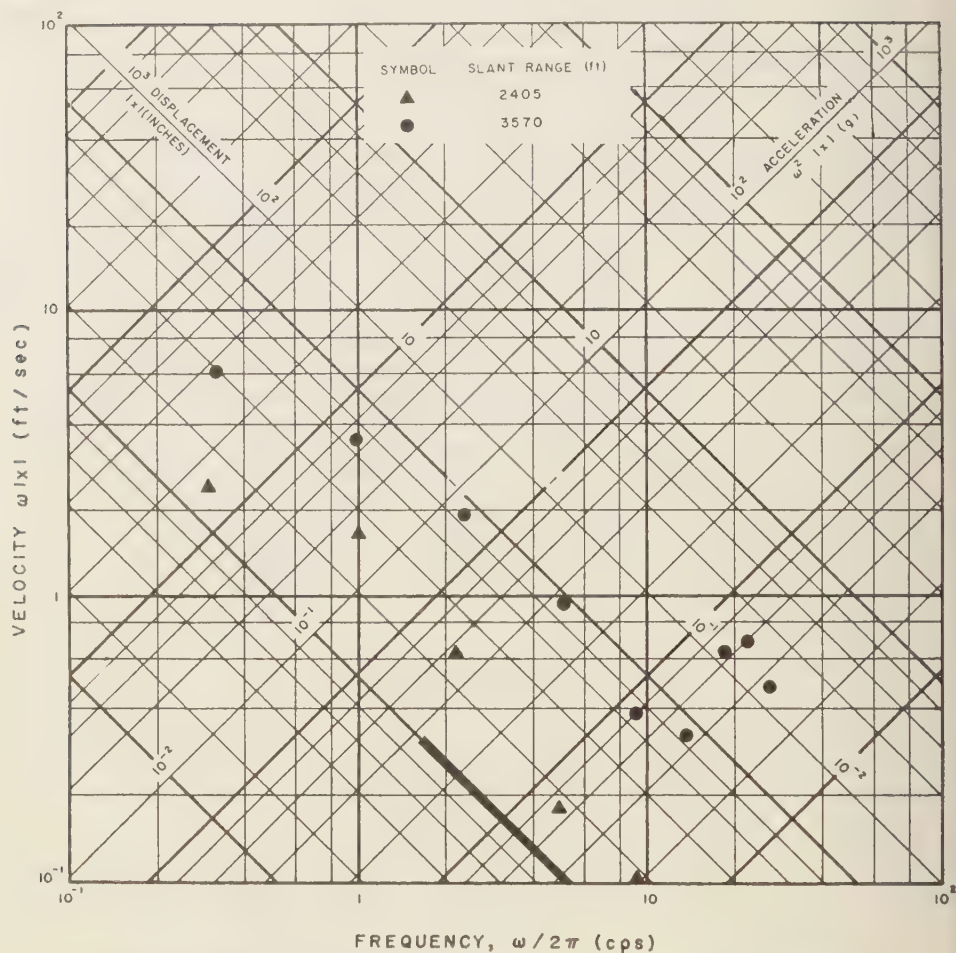


Fig. 16. Reed gage frequency spectrum, Blanca event at 2405 feet slant range, Project 26.1.

Displacement. Two BRL absolute displacement gages in the tunnel at 300 feet from Tamalpais and at azimuths which differed by about 80° gave peak displacements of 0.6 and 0.7 inch (Table A.16). Durations differed by a factor of 2, but this may not be a real function of the ground motion, since individual gage characteristics such as friction may exert a strong influence on the signal after peak displacement, particularly as the displacement approaches zero. These measurements were made at approximately the same scaled distance from Tamalpais as the Sandia gage, AHP-7, was from Rainier [Perret, 1957]. Integrated acceleration from the

Rainier gage gave peak displacement of about 2.4 inches. Displacements should scale as $D/W^{1/3}$, and comparison of the two scaled displacements (Tamalpais and Rainier) for the same scaled range shows agreement within a factor of 1.1 to 1.4.

Photographic analysis of ground surface motion above Evans indicated that vertical transient displacement was not greater than 2 inches.

At the mesa-top camera stations of Projects 26.5 and 26.10 the motion of two targets at 755 and 910 feet horizontal range from Blanca surface zero was observed, and at the Project 26.5 Station 1203-E motion on the mesa slope in the

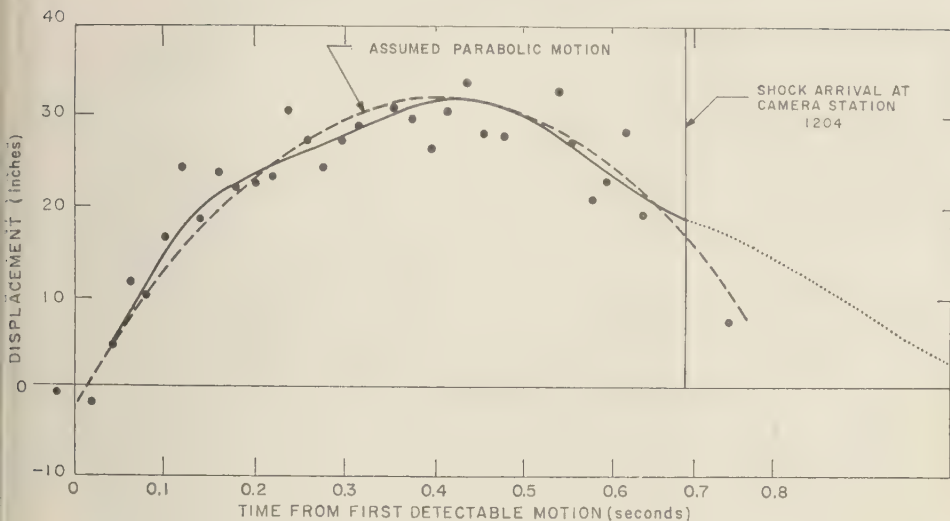


Fig. 17. Target vertical motion, Blanca event, Station 1205.18, Project 26.5.

immediate vicinity of surface zero was observed. There were no targets in the surface zero area, but it was possible to follow four specific points in the initial bulge area through maximum excursion before dust obscured them.

Project 26.5 data from Station 1205.18 (Fig. 17) at 755 feet horizontal range show a peak motion of approximately 30 inches at about 400 msec after start of motion. The solid curve represents a best fit to the observed points, and the dashed curve is an assumed parabolic representation based on expected free-fall characteristics for this motion. The approximate agreement between the two curves is reasonable. The more irregular curve is perhaps more realistic for target motion which involved considerable tilt induced by relative

motion of the two massive surface blocks which supported the target tower legs. Data for Station 1205.17 at a horizontal range of 910 feet (Fig. 18) show peak vertical displacement of about 20 inches at about 200 msec after start of motion.

Project 26.10 vertical motion data for Stations 1205.18 and 1205.17 (Fig. 19) include information extending over a period of about 8 seconds after detonation and a correction curve for vertical pitch of the camera station slab derived from a gyroscopic pitch indicator. Peak upward displacements are about 30 inches at horizontal range 755 feet and about 12 inches at 910 feet. Correction by subtraction of computed pitch does not remove all apparent target motion which has the pitch-motion characteristic. However, ex-

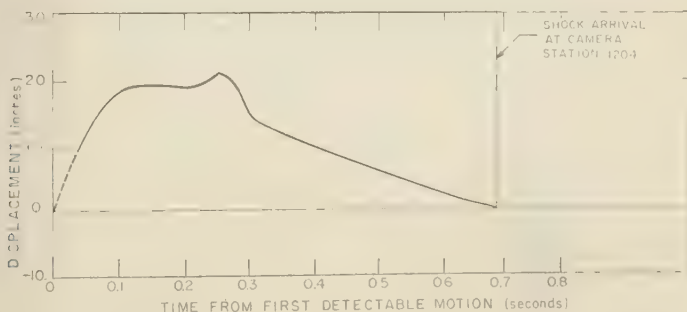


Fig. 18. Target vertical motion, Blanca event, Station 1205.17, Project 26.5.

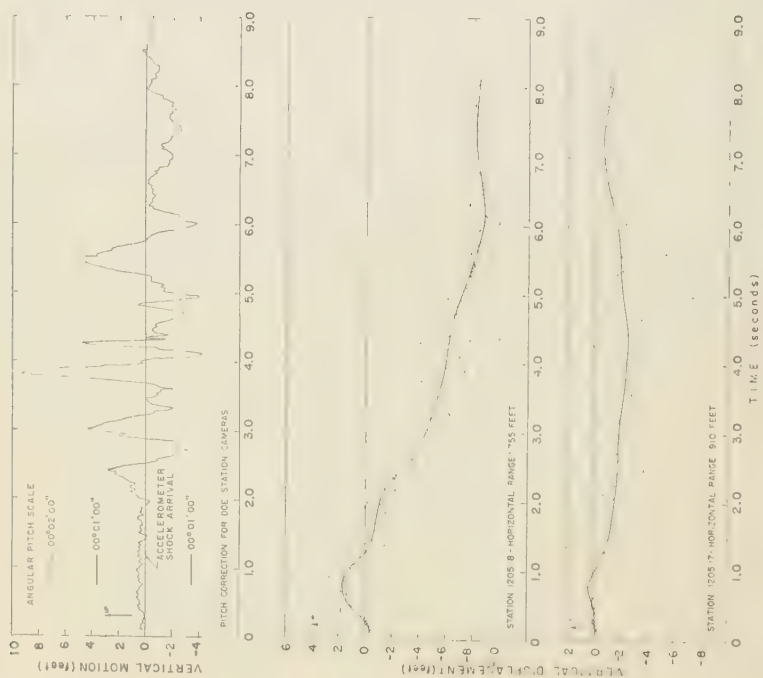


Fig. 19. Vertical motion of targets, Blanca event, Project 26.10.

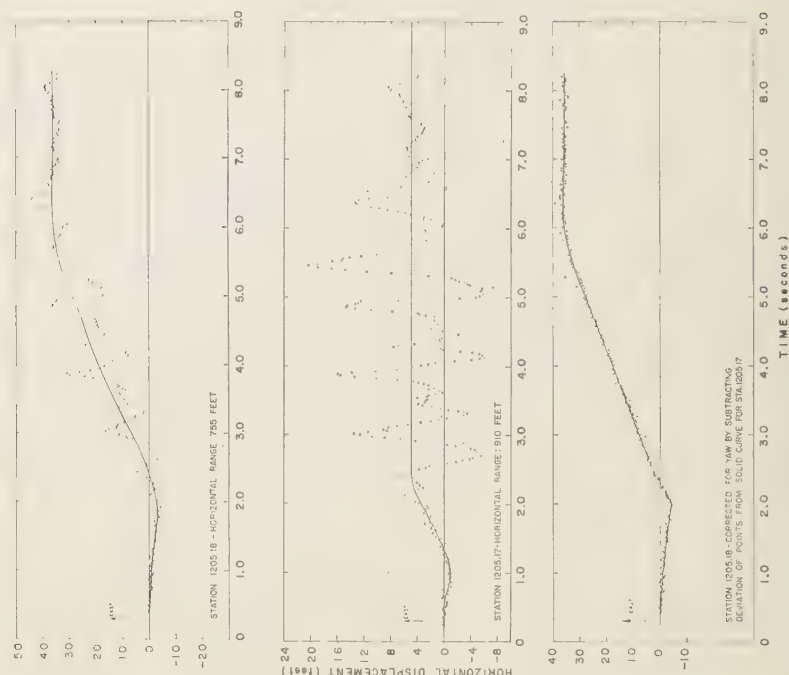


Fig. 20. Horizontal motion of targets, Blanca event, Project 26.10.

remely violent motion of unrealistically high rise times has been eliminated, and a reasonable approximation to real mass motion is represented by the solid curve. Extension of the record duration to 8 seconds has emphasized later motion of the targets, and general subsidence was indicated as the mesa rim caved away.

Horizontal motion of the targets along a line normal to the camera line of sight is plotted in Figure 20. The direction designated east is toward the mesa rim. Early motion is away from surface zero, but later portions of the film show motion dominated by subsidence toward the mesa slope. The third curve of Figure 20 represents subtraction of the more remote target data (Station 1205.17) from that of the closer target and eliminates the effect of camera-slab yaw from apparent horizontal motion of Station 1205.18.

Analysis of the EG&G film of the surface zero area on the slope above Blanca yielded the data presented in Figure 21. Of the four points followed in the analysis, three gave very similar results. Peak displacement was about 25.5 feet. The fourth point was evidently not within the limited region of maximum upheaval and has not been plotted in Figure 21.

Maximum velocities derived from the Blanca films are approximately 30 ft/sec directly above the explosion, and about 12 ft/sec at the mesa-top targets.

There appears to be no straightforward basis for scaling comparison of either peak displacements or velocities at surface zero from Rainier and Blanca. Overburden thickness was nearly the same for both events, but 1 order of magni-

tude difference in energy yield implies a scaled depth for Blanca less than half that for Rainier. This makes the accelerometer which was 370 feet above Rainier at nearly the same scaled range as the surface above Blanca. Peak velocity for that gage is about 6 ft/sec, which, with reflection doubling at the free surface, is still only 40 per cent of the estimated peak surface velocity over Blanca.

The treatment of the peak surface displacement data (see Tables A.7, A.9, A.10, A.12, and A.17) is similar to that of surface acceleration data. The data are analyzed empirically, and the results are compared with those for an assumed free field.

Peak surface displacement is fitted, by component, to an equation of the form

$$D_{\text{peak}} = c_0' W^{c_1} R^{c_2} \quad (12)$$

transformed for purposes of computation to

$$\log D_{\text{peak}} = c_0 + c_1 \log W + c_2 \log R \quad (13)$$

where

$$c_0 = \log c_0' \quad (14)$$

and where D is the peak displacement in centimeters, W is the yield in kilotons, R is the slant range in feet, and c_0 , c_1 , and c_2 are the coefficients obtained in the best-fit procedure. The following equations for the various components of the displacement result:

vertical component of displacement,

$$\log D_v = 3.46 + 0.69 \log W - 1.14 \log R \quad (15)$$

radial component of displacement,

$$\log D_r = 5.62 + 0.94 \log W - 1.68 \log R \quad (16)$$

and tangential component of displacement,

$$\log D_t = 5.73 + 0.82 \log W - 1.73 \log R \quad (17)$$

Again three figures are given, but only the first two are significant. The vertical component shows a value of exponent for range that is notably lower than either of the other two components of the displacement, and no general equation can be given. The exponent of the range, about 1.7 at most, is lower than values previously used or obtained [Carder, Cloud, Murphy and Hershberger, 1958].

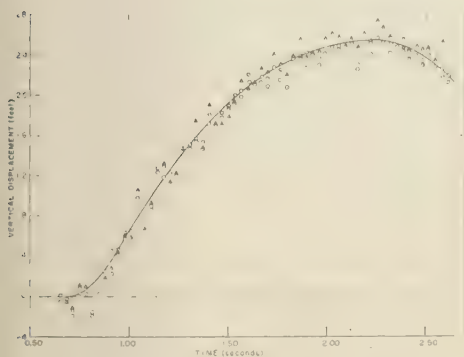


Fig. 21. Surface zero motion, Blanca event, Project 26.5.

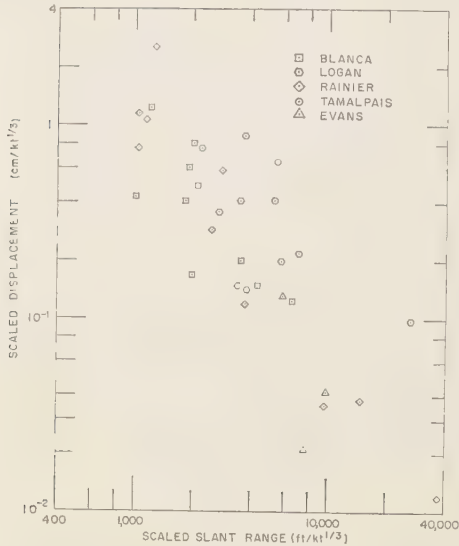


Fig. 22. Scaled surface vertical displacement versus scaled slant range, Rainier, Logan, and Blanca events, Project 26.4.

A comparison of these results with those expected for an assumed free field can be made. Scaled peak vertical displacements (Fig. 22) show considerable scatter. Equation 3, written as

$$D = k \frac{W^{(n+1)/3}}{R^n} \tag{18}$$

relates the exponents of yield and range. The coefficients of log R in equations 15 through 17 give the following comparison of $(n + 1)/3$ and the coefficients of log W :

$\frac{n + 1}{3}$	Fitted coefficient of log W
0.75	0.69
0.89	0.94
0.91	0.82

The agreement here is surprisingly better than that in the analysis of acceleration. The reason for this good agreement is that the maximum displacement occurs at a significantly lower frequency than the maximum acceleration. Therefore, the displacement is less seriously affected by interface phenomena.

The exponent of the yield is of considerable importance in the prediction of motion parameters from increased yields. Peak vertical displacement data for a constant slant range of 3500 feet are plotted in Figure 23, together with the line of best fit derived from all observations of peak vertical surface displacement at all ranges. The scatter about the line is large, and it suggests the need for caution in predicting displacement for yields larger than those which produced the present experimental data.

Recent work on amplitudes of seismic body waves from underground nuclear explosions has been presented in papers by *Carder and Cloud* [1959] and by *Romney* [1959].

Stress and strain. BRL obtained the only stress data during the Tamalpais event. Five observations were made in the tunnel in the radial range between 100 and 425 feet (Table A.19). Both record traces (radial and tangential components) at the 100-foot range went off the edge of the record paper. However, a rough estimate of the peak values, made by extrapolating the peak slopes, assuming no increase in rate of

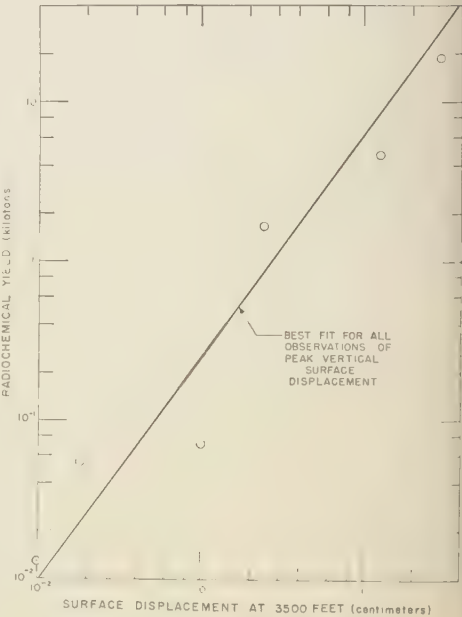


Fig. 23. Surface vertical displacement versus yield, Rainier, Logan, and Blanca events, Project 26.4.

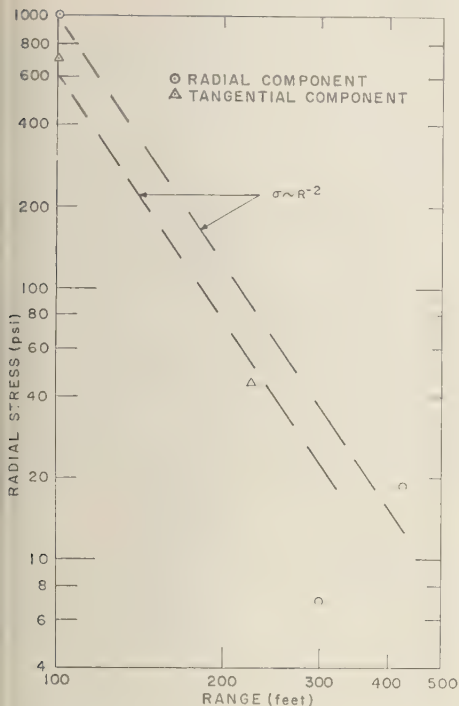


Fig. 24. Radial stress versus range, Tamalpais event, Project 26.8.

ise, and allowing some rounding of the curve at the peak, yielded about 1000 psi radial and 700 psi tangential stresses. Instrument stations at different ranges were also at widely different azimuths from the Tamalpais burst point, with the result that at least one gage, that at 425 feet, was in appreciably harder rock than the others.

These data, plotted on logarithmic scales of stress versus range (Fig. 24), suggest variation of both components with the inverse cube of radial range. The data point for 300 feet appears to be low by an order of magnitude. There is no evident reason for this low value, but the Project 26.8 report [Perkins and Thompson, 1958] suggests that poor coupling between the gage and rock could be responsible.

Ten ERDL strain gages provided legible records of radial strain for Tamalpais (Tables A.1, A.20, and A.21). Five of these were at the same borings as three of the BRL stress gages at 100- and 300-foot ranges. Comparison of the

stress and strain records is desirable, but, unfortunately, construction of a stress-strain curve is not justified by the results because (1) peaks are absent at the 100-foot stress gage, (2) there is an apparent low response for the 300-foot stress gages, (3) there is low response of the 300-foot strain gages, and (4) the strain gages were wholly contained within gypsum cement cylinders and are nearer than one tunnel diameter to the free surface. However, a comparison of the estimated peak stress at the 100-foot range with the observed peak strain gives a ratio of about 1.6×10^6 psi, which appears to be more nearly characteristic of the grout than of the rock.

A plot of observed peak strain versus range may be somewhat more relevant (Fig. 25). There is considerable scatter, some of which may be attributable to differences in gage environment, which includes five geologically different rock units and appreciable changes in degree of water saturation. The plotted data suggest that strain

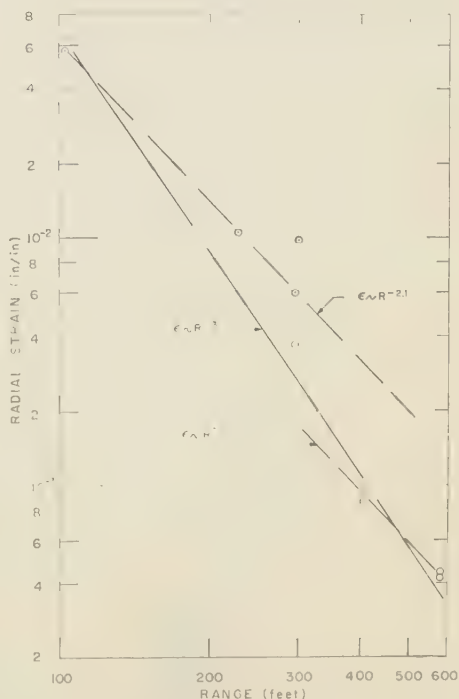


Fig. 25. Radial strain versus range, Tamalpais event, Project 26.3.

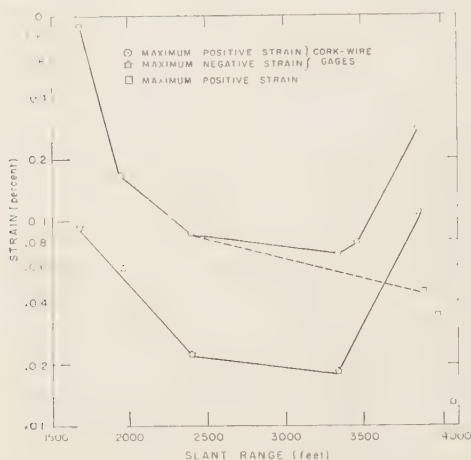


Fig. 26. Surface strain, Blanca event, Project 26.1.

attenuates at a rate between inverse cube and inverse square of range.

No significant data on surface strain were obtained on Evans.

All the cork-wire strain gages produced data from Blanca (Fig. 26 and Table A.22). When the data are plotted versus range, it is evident that the curve decays regularly with range and increases abruptly at the farthest station. This behavior is possibly indicative of refracted or reflected energy coming from subsurface layers of the medium.

Included in Figure 26 are the peak positive strain data obtained from the long-span electronic gages which yielded useful data on Blanca (Table A.23). All these data fall below the cork-wire peak strain; however, it must be noted that the three most remote cork-wire stations were near Rainier surface zero whereas the electronic gages were nearer the Blanca surface zero. Thus, perhaps a more realistic curve for the decay of peak horizontal strain with distance would be that indicated in Figure 26 by the dashed line.

CONCLUSIONS

Information that was anticipated from Program 26 was adversely affected by the very low yield of the Evans event for which primary instrumentation was installed. However, surface motion data from near and remote strong-motion

and teleseismic stations were satisfactory for the various Hardtack-II events. Data from the subsurface instrumentation are fragmentary but do provide some substantiation for Rainier data and a few pieces of information not previously available.

Strong-motion data from surface stations out to 9 miles indicate that vertical, radial, and tangential components of surface acceleration follow an equation of the form

$$A = 3.2 \times 10^6 W^{0.7} R^{-2}$$

where A is peak acceleration in parts of gravity, W is the yield in kilotons, and R is the slant range in feet.

Different components of peak surface displacements follow different scaling relationships of the form

$$D = k W^{(n+1)/3} R^{-n}$$

where D is the peak displacement in centimeters, W is the yield in kilotons, and R is the slant range in feet. Here both the coefficient k and the exponent n differ for different components. The displacement relationships are considered to be more suitable for extrapolation to higher yields than is the acceleration equation because of the lower-frequency content of the displacement. However, for lack of data in other geological structures and media, it will be necessary in prediction to extrapolate from these results, although various known differences between media preclude accurate prediction. For accuracy of prediction, scaling shots must be fired in the new environment.

Subsurface data indicate that peak radial accelerations decrease as the inverse third or fourth power of range, similarly to the pattern shown for horizontal radius data from Rainier. Low precision of the data from Projects 26.1 and 26.2, caused by a yield from Evans of only about 1 per cent of that for which instrumentation was adjusted, make these results significant only in a qualitative sense.

Measured radial stress in the rock near Tamalpais was not definitive because peak signals from gages closest to the explosion were lost. However, rough estimates were feasible; indication of pressure magnitude is probably good to within a factor of 2, and wave shapes are well defined.

Absolute displacements observed by two gages

new design at a single range agree very well with doubly integrated acceleration (displacement) data derived from Rainier at the same scaled range.

Surface motion photography established the pattern of motion at surface zero for Blanca during the initial upheaval and at two points on the mesa top during the initial phase and during later periods of settlement. Maximum upheaval at surface zero was 25.5 feet, and on the mesa surface at a point offset 750 feet laterally from surface zero it was about 2.5 feet. There appears to be no simple scaling relationship between the Blanca, Neptune, and Rainier transient surface displacements.

The tuff has a velocity of 6200 ft/sec, with the underlying dolomite velocity 11,700 ft/sec. A two-layer crustal model for NTS gives layer thicknesses and corresponding velocities of 24 m and 5.69 km/sec for the upper layer, and 6 km and 7.65 km/sec for the second layer. The top of the mantle has a velocity of 8.12 m/sec and dips eastward.

The results of strong-motion observations from

Rainier and the underground nuclear explosions of Phase II of Operation Hardtack are hardly adequate for development of a very complete picture of the reaction of massive tuff to a large source of explosively released energy or for very effective correlation with theoretical studies. However, there is still strong reason to recommend continuing efforts toward meeting the goals of Rainier and Hardtack-II projects. The developing interest in problems of seismic detection and the recognition of underground nuclear explosions as described and analyzed in a report of the Panel of Seismic Improvement [*U. S. Dept. of State*, 1959] has greatly increased the need for understanding the effect of the environment of an underground explosion on the seismically transmitted energy. It is in the medium immediately surrounding an explosion that energy is partitioned between dissipative processes and the elastic region.

The work described in this report was performed under auspices of both the U. S. Atomic Energy Commission and the U. S. Department of Defense.

APPENDIX. TABLES OF RESULTS

TABLE A.1. Maximum Subsurface Strain and Acceleration, Tamalpais (Project 26.3 Data)

Tunnel Station*	Gage	Range, ft	Travel Time, msec	Indicated Peak Strain, %	Peak Acceleration, g
02 2 + 12	Strain gage	100.7	13.5	0.0630	...
02 2 + 12	Strain gage	100.7	13.0	0.0570	...
02 0 + 90	Strain gage	228.2	37.0(poor)	0.0105	...
02 0 + 90	Strain gage	228.2	NR†	NR	...
7 + 06	Strain gage	296.3	NR	0.0060	...
7 + 06	Strain gage	296.3	NR	0.0037	...
10 + 70	Strain gage	300.9	56.5(poor)	0.0097	...
10 + 70	Strain gage	300.9	NR	NR	...
12 + 15	Accelerometer	405.2	NR	...	NR
12 + 15	Strain gage	405.2	84.0(poor)	0.00085	...
12 + 15	Accelerometer	405.2	55.5	...	1.60
12 + 15	Strain gage	405.2	74.0(poor)	0.00095	...
14 + 20	Accelerometer	583.3	NR	...	1.05
14 + 20	Strain gage	583.3	74.5	0.0042	...
14 + 20	Accelerometer	583.3	75.5	...	1.04
14 + 20	Strain gage	583.3	NR	0.0044	...

* See Figure 4 for station locations.

† NR = no record.

TABLE A.2. Vertical Acceleration, Deep Hole, Evans
(Project 26.1 Data)

Depth, ft	Range, ft	Travel Time, sec	Acceleration					Time Max. Peak, sec
			First Peak, g	Time First Peak, sec	Second Peak, g	Time Second Peak, sec	Max. Peak, if other, g	
0	850	0.132	0.51	0.150	-0.45	0.194	0.59	0.240
50	790	0.121	0.64	0.133	-0.53	0.142		
100	740	0.112	0.70	0.124	-0.63	0.135		
150	690	0.105	0.75	0.118	-0.62	0.126		
200	640	0.101	0.80	0.112	-0.94	0.120		
250	590	0.093	0.80	0.104	-0.63	0.116		
350	490	0.077	1.93	0.086	-1.79	0.097		
450	390	0.058	2.94	0.068	-3.11	0.078		
500	340	0.051	3.87	0.061	-3.38	0.070		
550	290	0.044	1.87	0.052	-0.86	0.064		
600	240	0.037	16.10	0.042	-12.51	0.055		
650	190	0.028	11.20	0.033	-5.10	0.046		

TABLE A.3. Vertical Acceleration, Deep and Shallow Borings, Evans
(Project 26.2 Data)

Depth, ft	Radial Range, ft	Travel Time, sec	Maximum Acceleration	
			Up, g	Down, g
Deep Boring				
1	849	0.132	1.07	0.60
65	785	0.118	0.73	0.73
215	635	0.100	0.92	0.92
315	535	0.088	2.4	5.2
364	486	0.052	1.6	1.6
365	485	0.077	3.3	4.8
415	435	0.054	4.8	4.8
465	385	0.048		9.5*
...	No record
515	335	0.041		30.*
563	287	0.044		97.*
565	285	0.044		98.*
615	235	No data
.				
Shallow Boring				
1	849	0.132	0.90	0.67
39	811	0.120	0.67	0.50
89	761	0.102	0.69	0.59
139	711	0.114	0.72	0.63
189	661	0.102	0.69	0.67
239	611	0.094	0.92	0.92
289	561	0.085	1.72	2.25
339	511	0.079	1.86	2.0

* Peak-to-peak data.

TABLE A.4. Vertical Acceleration, Evans Deep Hole, Blanca
(Project 26.1 Data)

Slant Range, ft	Angle to Vertical, deg.	Travel Time, sec	Acceleration					Time Max. Peak, sec
			First Peak, g	Time First Peak, sec	Second Peak, g	Time Second Peak, sec	Max. Peak, if other, g	
3599	68.3	0.458	0.99	0.562	-0.97	0.628		
3577*	69.2	0.439	0.34	0.482	0.72	0.547	-0.86	0.600
3560	70.0	0.429	0.35	0.468	0.79	0.535	-0.41	0.551
3543	70.7	0.432	0.28	0.462	0.80	0.530	-0.73	0.560
3527	71.5	0.426	0.76	0.526	-0.78	0.556		
3513	72.3	0.413	0.31	0.450	0.88	0.524	-0.66	0.550
3482†	73.8	0.416	-0.65	0.468	0.96	0.509	-1.60	0.539
3456	75.4	0.393	0.62	0.413	0.97	0.495	-1.54	0.527
3443	76.2	0.393	-0.41	0.451	1.09	0.489	-1.23	0.525
3432	77.0	...	0.38	0.481				
3421	77.9	0.405	-1.98	0.428	2.09	0.475	-4.71	0.501
3411	78.7	0.390	-1.36	0.420	1.21	0.465	-3.24	0.494

* High-frequency disturbance near 0.584 sec.

† High-frequency disturbance near 0.580 sec.

TABLE A.5. Vertical Acceleration, Deep and Shallow Borings, Blanca
(Project 26.2 Data)

Depth, ft	Slant Range, ft	Travel Time, sec	Maximum Acceleration	
			Up, g	Down, g
Deep Boring				
1	3598	0.456	1.86	1.32
65	3482	0.430	0.89	0.86
215	3431	0.410	1.69	0.95
315	3399	...	3.2*	
364	3385	0.382	2.0*	
365	3385	...	2.1	2.1
415	3371	...	3.4*	
465	3358	No data		
...	...	No record		
515	3345	No data		
563	3333	No data		
565	3334	No data		
615	3322	No data		
Shallow Boring				
1	3598	0.454	1.82	1.18
39	3492	0.438	0.95	1.22
89	3474	0.422	0.92	0.63
139	3456	0.418	0.98	0.71
189	3439	0.412	0.80	0.61
239	3423	0.412	1.06	0.88
289	3407	0.406	0.95	0.98
339	3392	0.400	1.29	1.44

* Peak-to-peak data.

TABLE A.6. Vertical and Radial Surface Acceleration, Tamalpais
(Project 26.2 Data)

Direction of Measurement	Range		Travel Time, sec	Acceleration		
	Ground, ft	Slant, ft		Initial Positive,* g	Maximum Positive, g	Maximum Negative, g
Vertical	1355	1597	0.274	0.069	0.069	0.112
Vertical	1722	1910	0.364	0.044	0.108	0.159
Radial			0.344	0.036	0.151	0.104
Vertical	3530	3613	0.578	0.030	0.052	0.052
Radial			0.586	0.014	0.073	0.069
Vertical	4019	4091	0.604	0.010	0.101	0.081
Radial				Gage damaged before test		
Vertical	4859	4925	0.656	0.004	0.049	0.062
Radial			0.656	0.003	0.039	0.023

* Positive signal represents upward motion for vertical gages, outward motion for radial gages.

TABLE A.7. Maximum Surface Acceleration and Displacement, Tamalpais and Mars
(Project 26.4 Data)

Station and Distance	Component	Maximum Acceleration, g	Approximate Period, sec	Maximum Displacement, cm	Approximate Period, sec
Tamalpais					
1200.09	Vertical
45,771 ft	Radial	0.00031	1.1
(slant)	Transverse	0.00039	0.5
7.202	V
43,812 ft	R	0.0016	1.1
	T	0.0011	0.8
1200.05	V	0.098	0.1	0.27	0.7
2222 ft	R	0.064	0.1	0.19	0.6
	T	0.052	0.1	0.28	0.6
1200.04	V	0.18	0.2	0.17	0.3
2180 ft	R	0.18	0.1	0.44	0.4
	T	0.33	0.1	0.45	0.3
Mars					
1200.04	V	0.038	0.1	0.033	0.3
1944 ft	R	0.049	0.2	0.052	0.4
(slant)	T	0.049	0.2	0.047	0.3

TABLE A.8. Vertical and Radial Surface Acceleration, Evans
(Project 26.1 Data)

Direction of Measurement	Range		Travel Time, sec	Acceleration					
	Ground, ft	Slant, ft		First Peak, g	Time First Peak, sec	Second Peak, g	Time Second Peak, sec	Max. Peak, if other, g	Time Max. Peak, sec
Vertical	200	867	0.142	0.40	0.158	-0.19	0.200		
Radial	200	867	0.142	0.38	0.161	-0.35	0.190		
Vertical	400	932	0.170	-0.12	0.178	0.12	0.178	-0.23	0.202
Radial	400	932	0.167	0.20	0.182	-0.24	0.214	0.24	0.263
Vertical	600	1014	...	-0.09	0.320	0.09	0.365		
Radial	600	1014	0.200	0.06	0.220	-0.23	0.240	0.23	0.426
Vertical	800	1136	0.225	0.09	0.262	-0.05	0.312	0.23	0.337
Radial	800	1136	0.237	-0.16	0.302	0.26	0.352	-0.29	0.446

(Project 26.2 Data)

Direction of Measurement	Range		Travel Time, sec	Acceleration*		
	Ground, ft	Slant, ft		Initial Positive, † g	Maximum Positive, g	Maximum Negative, g
Vertical	0	849	0.134	0.651	0.651	0.397
Vertical	563	996	0.192	0.028	1.428	0.943
Radial			0.180	0.37	1.016	1.193
Vertical	2292	2416	0.446	0.007	0.065	0.072
Radial			0.436	0.011	0.024	0.033
Vertical	2778	2880	0.516	0.002	0.011	0.007
Radial			0.497	0.001	0.006	0.008
Vertical	3613	3701	0.586	0.002	0.019	0.020
Radial			0.608	0.003	0.009	0.009

* Signal lost on all channels except O-AV at 0.846 second through accidental erasure.

† Positive signal represents upward motion for vertical gages, outward motion for radial gages.

TABLE A.9. Maximum Surface Acceleration and Displacement, Evans
(Project 26.4 Data)

Station and Distance	Component	Maximum Acceleration, g	Approximate Period, sec	Maximum Displacement, cm	Approximate Period, sec
1200.09	Vertical
47,019 ft	Radial	0.00008	...
(slant)	Transverse	0.0001	...
7.202	<i>V</i>
44,995 ft	<i>R</i>	0.00008	...
	<i>T</i>	0.00008	...
1200.01	<i>V</i>	0.0007
18,075 ft	<i>R</i>	0.0005
	<i>T</i>	0.0004
1200.02	<i>V</i>
12,026 ft	<i>R</i>	0.0005
1200.08	<i>V</i>	0.001
10,141 ft	<i>R</i>	0.0008
1200.07	<i>V</i>	0.002
6320 ft	<i>R</i>	0.003
	<i>T</i>	0.003
1200.03	<i>V</i>	0.005
4854 ft	<i>R</i>	0.009
	<i>T</i>	0.008
1200.06	<i>V</i>	0.009
4166 ft	<i>R</i>	0.009
	<i>T</i>	0.009
1200.14	<i>V</i>	0.042	0.1	0.016	...
3698 ft	<i>R</i>	0.031	0.1	0.010	...
	<i>T</i>	0.040	0.1	0.022	...
1200.04	<i>V</i>	0.033	0.2	0.008	...
3266 ft	<i>R</i>	0.065	0.2	0.03	...
	<i>T</i>	0.065	0.2	0.04	...
1200.10	<i>V</i>	0.049	0.1
2877 ft	<i>R</i>	0.058	0.1
	<i>T</i>	0.063	0.1
1200.05	<i>V</i>	0.034	0.1	0.05	...
2235 ft	<i>R</i>	0.031	0.1	0.05	...
	<i>T</i>	0.052	0.1	0.07	...

TABLE A.10. Maximum Surface Acceleration and Displacement, Logan
(Project 26.4 Data)

Station and Distance	Component	Maximum Acceleration, g	Approximate Period, sec	Maximum Displacement, cm	Approximate Period, sec
1200.09	Vertical
47,057 ft	Radial	0.046	1.3
(slant)	Transverse	0.044	1.3
7,202	V	0.16	1.2
43,234 ft	R	0.076	1.3
	T
1200.01	V	0.026	0.4
17,060 ft	R	0.038	0.2	0.16	0.8
	T	0.032	0.5	0.25	0.7
1200.02	V	0.055	0.3	0.36	0.6
11,417 ft	R	0.063	0.2	0.33	0.7
	T	0.049	0.2	0.24	0.5
1200.08	V	0.10	0.2	0.33	0.5
9289 ft	R	0.08	0.2	0.44	0.7
	T	0.06	0.2	0.35	0.5
1200.14	V	0.18	0.2	0.22	0.4
6241 ft	R	0.14	0.2	1.73	1.7
	T	0.13	0.2	1.33	1.2
1200.05	V	0.13	0.3	1.45	0.8
6056 ft	R	0.14	0.3	1.66	1.7
	T	0.19	0.2	1.47	1.2
1200.10	V	0.34	0.1	0.67	0.6
5701 ft	R	0.22	0.3	1.81	1.7
	T	0.38	0.1	1.62	1.1
1200.03	V	Instrument failure		0.25	?
5474 ft	R			0.87	0.5
	T			0.36	0.6
1200.07	V	0.20	0.1	0.58	0.7
4446 ft	R	0.26	0.1	0.64	0.7
	T	0.12	0.1	0.28	?
1200.04	V	0.80	0.1	1.25	?
3527 ft	R	1.68	0.1	6.12	0.6
	T	1.03	0.2	2.78	0.6
1200.06	V	0.83	0.3	Instrument failure	
2621 ft	R	1.12	0.04		
	T	0.55	0.1		

TABLE A.11. Vertical and Radial Surface Acceleration, Blanca
(Project 26.1 Data)

Direction of Measurement	Range		Travel Time, sec	Acceleration					
	Ground, ft	Slant, ft		First Peak, g	Time First Peak, sec	Second Peak, g	Time Second Peak, sec	Max. Peak, if other, g	Time Max. Peak, sec
Vertical	3494	3736	0.480*	0.77	0.571	-0.78	0.626		
Radial	3494	3736	0.460	0.34	0.504	-0.14	0.532	0.75	0.565
Vertical	3659	3888	0.555*	0.68	0.585	-0.60	0.643	1.22	0.671
Radial	3659	3888	0.498	0.28	0.528	0.89	0.592	-0.68	0.648
Vertical	3756	3974	0.521	0.52	0.571	-0.33	0.643	2.13	0.683
Radial	3756	3974	0.540	-0.68	0.667	0.71	0.690		
Vertical	3865	4075	0.528	0.58	0.564	-0.40	0.594	2.13	0.672
Radial	3865	4075	0.557	0.40	0.581	-1.13	0.664	1.22	0.679

(Project 26.2 Data)

Direction of Measurement	Range		Travel Time, sec	Acceleration		
	Ground, ft	Slant, ft		Initial Positive, † g	Maximum Positive, g	Maximum Negative, g
Vertical	3343	3598	0.450	0.585	1.078	0.900
Radial			0.448	0.160	0.944	0.548
Vertical	3774	3992	0.502	0.472	1.228	1.065
Radial			0.498	0.293	1.103	1.043
Vertical	4601	4766	0.552	0.268	0.627	0.431
Radial			0.562	0.114	0.522	0.678
Vertical	4921	5075	0.578	0.208	0.561	0.416
Radial			0.593	0.079	0.321	0.409
Vertical	5508	5655	0.608	0.190	0.286	0.302
Radial			0.602	0.071	0.258	0.261
Vertical	12002	12094	1.174	0.074	0.167	0.135

* Travel time indefinite.

† Positive signal represents upward motion for vertical gages, outward motion for radial gages.

TABLE A.12. Maximum Surface Acceleration and Displacement, Blanca
(Project 26.4 Data)

Station, Distance, and Foundation	Component	Maximum Acceleration, g	Approximate Period, sec	Maximum Displacement, cm	Approximate Period, sec
1200.09	Vertical
17,181 ft (slant)	Radial	0.128	1.4
Granitic rock	Transverse	0.088	1.4
7.202	V
13,635 ft	R	0.431	1.4
Deep alluvium	T	0.137	1.4
1200.01	V	0.074	0.2	0.332	0.6
17,311 ft	R	0.054	0.2	0.618	1.3
Quartzite	T	0.073	0.2	0.358	0.6
1200.02	V	0.14	0.1	0.400	0.6
11,570 ft	R	0.19	0.1	0.645	0.5
Limestone	T	0.17	0.1	0.314	0.6
1200.08	V	0.19	0.1	0.53	0.7
1463 ft	R	0.14	0.1	1.21	0.8
Limestone	T	0.17	0.1	0.66	0.7
1200.14	V	0.44	0.2	1.29	?
5644 ft	R	0.26	0.2	5.60	1.9
Welded tuff	T	0.36	0.1	2.11	2.2
1200.05	V	0.40	0.1	2.16	1.4
5469 ft	R	0.33	0.2	4.75	0.9
Welded tuff	T	0.52	0.2	5.18	1.6
1200.03	V	0.69	0.2	0.46	0.2
5310 ft	R	0.69	0.2	1.90	0.5
Bedded tuff	T	0.48	0.1	0.50	0.2
1200.10	V	0.54	?	1.63	0.8
5081 ft	R	0.38	0.3	5.12	1.9
Welded tuff	T	0.50	0.1	3.06	1.3
1200.07	V	0.27	0.1	1.10	0.8
1710 ft	R	0.27	0.1	0.70	0.6
Limestone	T	0.28	0.1	0.32	?
1200.04	V	1.67	0.1	3.30	0.5
3300 ft	R	1.04	0.07	3.10	0.6
Bedded tuff	T	1.37	0.07	2.2	0.5
1200.06	V	2.10	0.04	1.15	?
2679 ft	R	1.58	0.07	2.00	?
Limestone	T	1.50	0.04	3.80	0.4

TABLE A.13. Vertical Velocity, Deep Hole, Evans
(Project 26.1 Data)

Depth, ft	Distance from Detonation, ft	Velocity				Integration	
		First Peak, ft/sec	Time First Peak, sec	Second Peak, ft/sec	Time Second Peak, sec	Max. Vel., ft/sec	Time of Max., sec
0	850	NR			
50	790	0.28	0.136			0.23	0.138
100	740	0.19	0.130			0.22	0.130
150	690	0.23	0.116			0.23	0.120
200*	640	0.19	0.115			0.22	0.116
250	590	0.21	0.108			0.23	0.109
350	490	0.48	0.091	-0.32	0.121	0.54	0.090
500	340	1.12	0.063	-0.16	0.090	0.94	0.063
600	240	1.53	0.048	-0.45	0.092	3.36	0.047

* Nonlinear baseline.

TABLE A.14. Vertical Velocity, Evans Deep Hole, Blanca
(Project 26.1 Data)

Slant Range, ft	Angle to Vertical, deg	First Peak, ft/sec	Time First Peak, sec	Second Peak, ft/sec	Time Second Peak, sec	Integration	
						Max. Vel., ft/sec	Time of Max., sec
3599	68.3	1.90	0.571	-1.10	0.790	1.0	0.578
3577	69.2	1.66	0.554			0.99	0.562
3560	70.0	NR	NR		
3543	70.7	0.98	0.542	-0.44	0.700	0.95	0.545
3527*	71.5	0.79	0.540			0.86	0.540
3513	72.3	1.51	0.535	-0.50	0.715	0.81	0.537
3482†	73.8	(0.95)	0.520		
3443	76.2	1.08	0.500	-0.61	0.565	1.10	0.500
3421	77.9	0.74	0.485	-0.73	0.575	OAV-10	small

* Nonlinear baseline.

† Wavy baseline; peak estimated.

TABLE A.15. Reed Gage Data, Blanca
(Project 26.1 Data)

Range (ft) Radial: Vert.: Location:	(See Fig. 2) 9				(See Fig. 2) 4				(See Fig. 2) 15				(See Fig. 2) 5				(See Fig. 2) 23				(See Fig. 2) 18			
	Nat. Freq., cps	Max. Deflec., in.	Nat. Freq., cps	Max. Deflec., in.	Nat. Freq., cps	Max. Deflec., in.	Nat. Freq., cps	Max. Deflec., in.	Nat. Freq., cps	Max. Deflec., in.	Nat. Freq., cps	Max. Deflec., in.	Nat. Freq., cps	Max. Deflec., in.	Nat. Freq., cps	Max. Deflec., in.	Nat. Freq., cps	Max. Deflec., in.	Nat. Freq., cps	Max. Deflec., in.				
825 1443 Mesa (SRI Sta 8)	2.9	6.375	3.0	4.984	3.3	3.689	3.0	1.518	2.8	1.627	3.0	2.288	3.0	0.744	3.0	0.316	23	0.0275	1290	0.0051				
	10.0	1.085	9.7	0.907	9.9	0.677	10.0	0.314	10.0	0.257	9.7	0.361	10.6	0.316	10.6	0.0275	1320	0.0275	Evans 800					
	23	0.218	23	0.174	23	0.157	22	0.0552	23	0.0251	23	0.0726	23	0.0275	23	0.0275	Evans 400							
	49	0.0472	48	0.0407	51	0.0349	49	0.0070	50	0.0098	51	0.0066	49	0.0051	51	0.0051								
	90	0.0096	91	0.0104	91	0.008	90	0.0020	90	0.0012	86		91		91									
	136	0.0039	138	0.0042	138	0.0046	136		138		138		138		138									
	182	0.0022	180	0.0022	181	0.0066	178		180	0.0011	180		181		181									
	220	0.0011	219		221	0.0060	218		221		222		222		222									
	256		263		262	0.0035	258		262	0.0010	260		264		264									
	288		288		288		287		288		284		283		283									

TABLE A.16. Peak Subsurface Displacement, Tamalpais
(Project 26.8 Data)

Station Location*	Distance from Detonation, ft	Peak Displacement		Component Measured
		First Pulse, in.	Duration of Positive Pulse, msec	
7 + 06 U12b	300	0.6	90	Radial
10 + 70 U12B	300	0.7	180	Radial

* See Figure 4 for station locations.

TABLE A.17. Surface Displacement at Distant Stations, Tamalpais
(Project 26.8 Data)

Event*	Horizontal Component			Vertical Component		
	Travel Time, sec	Amplitude, mils	Frequency, cps	Travel Time, sec	Amplitude, mils	Frequency, cps
Station 1200.02 (Distance, 10,715 feet)						
A Re- fracted <i>P</i>	0.71	0.5	4	0.77	0.5	4
B Direct <i>P</i> (?)	1.11	1.2	2	1.24	1.2	2
C	1.86	0.8	2.5	1.96	0.9	2.5
D	2.05	1.9	2.5	2.42	0.5	2.5
E	2.80	...	2.5			
Station 1200.01 (Distance, 16,855 feet)						
A Re- fracted <i>P</i>	1.27	0.2	4	1.25	0.5	4
B Direct <i>P</i> (?)	1.83	1.2	2	2.00	0.9	2
C	2.21	1.1	2.5	2.42	0.7	2.5
D	2.8	1.1
E	3.54	0.7	2	3.47	0.7	2
F	4.26	0.8

* *P* represents the longitudinal wave in events A and B. Longitudinal wave velocity; near surface, 8500 ft/sec; and subsurface, 10,900 ft/sec.

TABLE A.18. Summary of Teleseismic Results, Blanca and Logan

Station	Kilometers	Blanca—P			First Motion	Logan—P			First Motion
		h	m	s		h	m	s	
Beatty	58.6	15-00	10.4		C*	06-00	10.5		C
Desert Rock	63.9	00-10	7		C	00-(07)			
Alamo	95.4	00-16	5		C	00-16	4		C
Lockes	130.5	00-23	6		C	00-23	7		C
Tonopah	132.8	00-23	1		C	NR			
Las Vegas	147.7	00-27			R†	00-25	6		C
Tinenaga	180.7	00-30			C	00-30			C
Boulder City	181.2	00-29			C	00-30			C
Hoover Dam	185.4	NR†				NR			
Haiwee	195.2	00-32			C	00-32			C
China Lake	197.5	00-31			C	00-31			C
Eureka	258.1	00-40			C	00-40			C-D
Isabella	267.0	00-40			C	00-40			C
Woody	289.0	00-44			C	00-44			C
Fresno	323.5	00-48			C	00-48			C
Ft. Tejon	352.8	00-52			R	00-52			C
Dalton	365.8	00-53			C	00-53			C
Mt. Wilson	370.2	NR				00-53			
Riverside	370.8	00-54			C	00-53			C
King Taneh	379.8	NTC§			C	NTC			C
Pasadena	382.2	00-55			C	00-55			C
Hayfield	389.1	00-55			C	00-56			C
Reno	408.8	00-59			C	00-59			R
Palos Verdes	423.3					01-02			
Palomar	430.5	01-01			C	01-01			C
Santa Barbara	439.5	NTC			C	01-(04)			—
Mt. Hamilton	482.8	01-08			C	01-08			C
Monterey	500.5	01-15							
Barrett	502.8	01-10			C	01-10			—?
Palo Alto	530.4	01-14			R	NR			
San Nicholas	530.9	01-13			C	01-13			R
Berkeley	540.6	01-16			C	01-16			C
Salt Lake City	548.1	01-19			C	01-19			D
San Francisco	556.7	01-22			?	NR			
Mineral	582.9	01-10			R	01-21			—
Ukiah	649.0	01-47			R	NR			
Logan	659.8	01-27			R				
Shasta	662.1	01-30			C	NR			
Tucson	735.8	01-39			R	01-39			D
Rifle	820.8	01-48			—	01-49			—
Boulder	1001.3	02-14			C	02-14			C
Corvallis	1014.5	NR				NR			
Laramie	1024.1	02-16			C	02-16			C
Butte	1026.5	02-20			C	02-20			D?
Boseman	1035.7	NR				02-22			C
Hungry Horse	1253.2	02-45			—	02-45			C
Seattle	1264.5	NR				NR			
Rapid City	1338.0	02-55			R	02-53			R
Lubbock	1351.6	03-00			—	03-01			—
Victoria	1389.2	02-13			C	NR			
Banff	1552.7	03-24							
Blue Hill	1560.7	03-24				NR			
Dallas	1832.7	NR							
Lawrence	1845.0	03-53			—	NR			
Fayetteville	1967.6	04-09			C	04-09			C

TABLE A.18. Continued

Station	Kilometers	Blanca—P	First Motion	Logan—P	First Motion
Little Rock	2161.5	NR		NR	
Star Lake, Canada	2182.4	NR		04-35	—
Fort Madison	2185.0	04-33	—		
East Merrick, Canada	1916.0	NR		NR	
Florissant	2268.7	04-41	h¶	04-42	h
St. Louis	2281.6	04-41	h	04-42	C
Linko, Canada	2494.9	NR		05-01	?
Geraldton, Canada	2717.6	NR		NR	
Flynn Lake, Canada	2808.5	NR		NR	
Alpena		05-32			
Opasatika	2997.6	05-44	—	NR	
Buffalo	3282.4	06-38	—		
Chapel Hill	3307.8	06-09	—	NR	
Ottawa, Canada	3472.9	06-23	C	06-24	C
Shawnigan Falls, Canada	3703.1	06-40	C	NR	
College, Alaska	3716.6	06-42	C	06-42	C
Seven Falls	3851.1	NTC	R	06-56	R

* C Compressional wave

† R Rarefactional wave

‡ NR No Record

§ NTC No time correction

|| — Direction of first motion not determined

¶ h Horizontal component

TABLE A.19. Peak Subsurface Stress, Tamalpais
(Project 26.8 Data)

Location*	Distance from Detonation, ft	Peak Stress Value, psi	Travel Time, msec	Component Measured	Remarks
2 + 12 U12b.02	100	~1000	13.0	Radial	Estimate; trace went off scale. Crystal pressure gage that was installed to measure peak did not record due to power failure.
2 + 12 U12b.02	100	~700	13.0	Transverse	
0 + 75 U12b.02	225	45	33.8	Transverse	
7 + 06 U12b	300	7	44.0	Radial	
0 + 50 U12b.01	425	18.8	66.0	Radial	This gage was in a harder rock than the other gages.

* See Figure 4 for station locations.

TABLE A.20. Residual Subsurface Strain, Tamalpais
(Project 26.3 Data)

Range,* ft	Static E $\times 10^{-6}$ psi	Peak Transient Strain, † $\mu\text{in./in.}$	Residual Strain †		
			2½ hrs, $\mu\text{in./in.}$	24 hrs, $\mu\text{in./in.}$	240 hrs, $\mu\text{in./in.}$
100.7	0.66	630C	NR	NR	NR
100.7	0.66	570C	NR	NR	NR
228.2	2.44	105C	25T	45T	NR
228.2	2.44	NR	NR	NR	NR
296.3	1.65	60C	50T	65T	NR
296.3	1.65	37C	28T	70T	NR
300.9	0.96	97C	12T	5T	5T
300.9	0.96	NR	30T	60T	25T
405.2	NR	8.5C	18T	30T	62T
405.2	1.85	9.5C	30T	25T	10C
583.3	0.93	42C	5C	2C	NR
583.3	NR	44C	30C	18C	NR

* Station locations same as in Table A-1.

† C = compression, T = tension, NR = no record.

TABLE A.21. Reduced Subsurface Strain, Tamalpais
(Strain in arbitrary units of compression)*
(Project 26.3 Data)

Range, † ft	Peak Transient Strain	Residual Strain	
		2½ hrs	24 hrs
228.2	366	49	0
296.3	206	25	0
296.3	176	69	0
300.9	105	0	7
405.2	73	0	9
583.3	37	3	0

* State of maximum tension assumed to be state of no strain.

† Station locations same as in Table A.1.

TABLE A.22. Surface Strain, Blanca
(Project 26.1 Data)

Component Measured	Ground Range, ft	Slant Range, ft	Strain			
			First Peak, ppk	Time First Peak, sec	Second Peak, ppk	Time Second Peak, sec
Transverse	3344	3599	-0.31	0.709		
Radial	3344	3599	(Deflections unreadable)			
Radial	3494	3736	-0.11	0.863		
Radial	3659	3888	-0.17	0.596	0.45	0.822
Radial	3756	3974	0.12	0.662	0.34	0.803
Radial	3865	4075	-0.03	0.671	0.13	1.004

See Figure 2 for location of first 4 stations.

TABLE A.23. Cork-Wire Surface Strain, Blanca (Project 26.1 Data)

Ground Range,* ft	Slant Range, ft	Effective Gage Length, ft	Max. Positive Deflection, ft	Max.† Positive Strain, ppk	Max. Negative Deflection, ft	Max. Negative Strain, ppk	Residual Strain, ppk
912	1699	50.55	0.450	8.90	0.047	0.93	+2.26
1525	2055	49.75	0.083	1.67	0.029	0.58	+0.58
2000	2403	45.50	0.039	0.86	0.010	0.22	+0.69
3051	3341	56.60	0.039	0.69	0.010	0.18	+0.28
3184	3459	37.80	0.029	0.77	0	0	0
3600	3853	44.90	0.125	2.78	0.049	1.09	0
3658	3888	47.37†	0.076	1.61	0.052	1.10	0

* See Figure 2 for station locations.

† Positive strain is increase of wire span length; negative strain is decrease of wire length.

‡ Wire disturbed inadvertently before readings taken; data uncertain.

REFERENCES

- Anthony, M. V., Ground motion measurements, *ERDL, Project 26.3, Operation Hardtack-II, ITR-1704*, February 1959.
- Barton, M. V., Ground shock environment—measurements and application, *Space Technol. Labs., GM-TR-293-A*, December 11, 1957, Confidential.
- Carder, D. S., and L. F. Bailey, Seismic wave travel times from nuclear explosions, *Bull. Seism. Soc. Am.* 48, 377-398, 1958.
- Carder, D. S., W. K. Cloud, L. M. Murphy, and J. H. Hershberger, Surface motions from an underground explosion, *USC&GS, Project 26.4d, Operation Plumbbob, WT-1530*, November 1958.
- Carder, D. S., W. K. Cloud, T. H. Pearce, and L. M. Murphy, Surface motions from a series of underground nuclear tests, *USC&GS, Project 26.4, Operation Hardtack-II, ITR-1705*, 1959.
- Carder, D. S., and W. K. Cloud, Surface motion from large underground explosions, *J. Geophys. Research*, 64, 1471-1487, 1959.
- Chaszeyka, M. A., and F. B. Porzel, Study of blast effects in soil, *Armour Research Foundation Rept. ARF-D119*, August 1, 1958.
- Edgerton, Germeshausen & Grier, Inc., Photographic analysis of earth motion, *Rainier, Project 26.4f, Operation Plumbbob, WT-1532*, 1958.
- Halsey, J. F., and M. V. Barton, Spectra of ground shocks produced by nuclear detonations, *AFBMD, Project 1.9, Operation Plumbbob, WT-1487*, 1959, Confidential.
- Johnson, G. W., G. T. Pelsor, R. G. Preston, and C. E. Violet, The underground nuclear detonation of September 19, 1957, *Rainier, Operation Plumbbob, Lawrence Radiation Lab. Rept. UCRL-5124*, February 1958.
- Morris, R. H., and R. C. Schneiderhan, Earth motion studies, *EG & G, Project 26.5, Operation Hardtack-II, WT-1706*, to be published.
- Perkins, B., Jr., and A. A. Thompson, Preliminary report on medium studies, *BRL, Project 26.8, Operation Hardtack-II, ITR-1709*, December 1958.
- Perret, W. R., Subsurface motions from a confined underground detonation, 1, *SC, Project 26.4b, Operation Plumbbob, ITR-1529*, October 1957.
- Perret, W. R., and R. G. Preston, Preliminary summary report of strong-motion measurements from a confined underground nuclear detonation, *Operation Plumbbob, ITR-1499*, June 15, 1958.
- Perret, W. R., Surface and subsurface strong motion measurements, *SC, Projects 26.2 and 26.10, Operation Hardtack-II, ITR-1703*, 1959.
- Pieper, F. A., A. C. Tiemann, and R. H. Sievers, Jr., Subsurface accelerations and strains from an underground detonation, 2, *ERDL, Project 26.4e, Operation Plumbbob, WT-1531*, October 1958.
- Press, F., Further studies of the phase velocity method of exploration, Annual Meeting, Soc. Exploration Geophysicists, November 9-12, 1959, Los Angeles, California.
- Romney, C. F., Amplitudes of seismic body waves from underground nuclear explosions, *J. Geophys. Research*, 64, 1489-1498, 1959.
- Swift, L. M., and D. C. Sachs, Surface motion from an underground detonation, *SRI, Project 26.4a, Operation Plumbbob, WT-1528*, 1959.
- Swift, L. M., D. C. Sachs, and W. M. Wells, Earth motion measurements, 1, Seismic studies and cavity studies, *Project 26.1, SRI, Operation Hardtack-II, ITR-1702*, January 1959.
- U. S. Dept. of State, The need for fundamental research in seismology, Report of the Panel on Seismic Improvement, July 1959.

(Manuscript received August 27, 1960.)

A Method of Concealing Underground Nuclear Explosions¹

A. L. LATTER, R. E. LELEVIER,
E. A. MARTINELLI, AND W. G. McMILLAN

The RAND Corporation, Santa Monica, California

Abstract. It is shown theoretically that the seismic signal from an underground nuclear explosion can be greatly reduced by carrying out the explosion in a large cavity. An estimate of the effectiveness of the method indicates that a yield of more than 300 kilotons (HE-equivalent) could be made to look seismically like a yield of 1 kiloton. Experiments with both chemical and nuclear explosions are needed to test the theory.

Introduction. The possibility of concealing nuclear explosions is of vital importance in connection with the Geneva Conference on test suspension. In this report we shall show theoretically that the seismic signal from an underground explosion can be greatly reduced by exploding the bomb in a large cavity.

Last summer (1958) this idea was considered, but was rejected for reasons that we now know to be fallacious. The argument went as follows. If a pressure p is suddenly applied in a cavity of radius a in an infinite elastic medium, the displacements at large distances are proportional [Bullen, 1953] to pa^2 . Because the energy W of the explosion is essentially proportional to pa^3 , the displacement for a given energy is inversely proportional to a , and hence it appears that the coupling can be reduced by increasing the radius of the cavity. In this reasoning, however, an important physical effect is ignored. Because of preferential absorption of high frequencies in the earth, only the low-frequency components of the wave are contained in the distant seismic signal. When this effect is taken into account, the displacement at great distances turns out to be proportional, as will be shown, not to pa^2 but rather to pa^3 ; therefore the distant signal is independent of the radius of the cavity. On this basis it was concluded that a cavity would not be effective in decoupling the signal.

Actually, the above argument is completely correct only for holes that are sufficiently big to keep the pressure below the elastic limit of the surrounding medium. In other words, once the

hole exceeds some critical size it does not pay to make it any bigger. The new discovery is that it is advantageous to have a hole that is big enough to eliminate any nonelastic behavior of the rock. Nonelastic behavior causes increased coupling because the medium can flow as a liquid and thus undergo large displacements.

Analysis of the method. Consider a nuclear explosion of yield W in a spherical cavity of radius a , sufficiently large so that the pressure developed on the wall does not exceed the elastic limit of the medium. Assume that the energy W is suddenly distributed uniformly over the volume of the cavity and produces a step-function pressure on the wall, given by

$$p = (\gamma - 1)W/(4\pi a^3/3) \quad (1)$$

where γ is a constant which is characteristic of the gas in the hole. It is possible to achieve such a rapid and uniform distribution of the energy by increasing the radius of the fireball during the radiation phase of its growth, as will be discussed.

The Fourier transform of the elastic displacement produced by the step pressure p , at a distance r in the wave zone, is [Latter, Martinelli, and Teller, 1959]

$$\hat{\xi}(\omega) = \frac{pa}{8\pi\mu r} \frac{c}{\omega_0^2 + i\omega_0\omega} - \frac{c}{\lambda + 2\mu} \frac{1}{\omega} \quad (2)$$

where λ and μ are the Lamé constants, c is the speed of sound, ω is the angular frequency, and

$$\omega_0 = c/a \quad (3)$$

We are interested in those values of ω for which elastic displacements are propagated to large distances with negligible attenuation in the earth. For the seismic network considered

¹ This work was performed under USAF contract AF 49(638)700 and was originally reported in essentially its present form as RAND Corporation Report R-348, dated March 30, 1959 (declassified October 20, 1959).

by the Geneva Conference, the important range in ω is from 0 to about 6 sec^{-1} , corresponding to frequencies below 1 cps. For such low frequencies the first term in the denominator of (2) dominates in the cases of interest, and (2) becomes

$$\hat{\xi}(\omega) = \frac{pa^3}{8\pi\mu rc} = \frac{3(\gamma - 1)W}{32\pi^2\mu rc} \quad (4)$$

Thus we find, as was pointed out by Latter, Martinelli, and Teller, that the amplitude of the distant seismic signal is proportional to pa^3 ; that is, it is proportional to W and independent of a . This is the basis of our earlier remark that the size of the hole does not affect the distant signal.

*Comparison with Rainier.*² It has been possible to give a simple analysis for the hole because the medium is assumed to be elastic. In the case of Rainier, however, we must deal with a shock wave in a medium whose equation of state is not known, and with a transition (from the shock wave to an elastic wave) which is not well understood. For these reasons we shall not base our comparison on any theory of Rainier, but rather on direct experimental observations.

Measurements were made by Perret [1957] of the accelerations produced by the Rainier shot at distances of a few hundred feet from the explosion. The measurements made in the vertical direction at 371 ft and 451 ft are particularly useful because the medium was homogeneous and apparently elastic in this region, and the records were relatively free of extraneous reflections. The accelerometer records at these points have the form of a damped oscillatory wave; this form is characteristic of an elastic medium. It is easily shown [Latter, Martinelli, and Teller, 1959] that the Fourier transform of the displacement at a distance r is, in general,

$$\hat{\xi}(\omega) = \frac{\hat{p}a}{8\pi\mu} \left(\frac{1}{r^2} + \frac{i\omega}{rc} \right) \frac{c^2}{\omega_0^2 + i\omega_0\omega - \frac{\lambda + 2\mu}{4\mu}\omega^2} \quad (5)$$

where a is the (unknown) radius at which the medium begins to behave elastically, \hat{p} is the

(unknown) Fourier transform of the pressure that acts at a , and where $\omega_0 = c/a$ as before.

The Fourier transform of the acceleration is, of course, $-\omega^2\hat{\xi}(\omega)$. We have tried to fit the experimental data by choosing various values for a and different forms for \hat{p} . We find that the best value of a is about 300 ft, with ω_0 about 25, essentially independent of the form of \hat{p} . More generally, for an explosion of any yield W_{kt} (in kilotons) is the Rainier environment, the characteristic angular frequency ω_0 must scale as $W_{kt}^{-1/3}$ and hence

$$\omega_0 = 25(1.7/W_{kt})^{1/3} \text{ sec}^{-1} \quad (6)$$

since the yield of Rainier was 1.7 kt.

From (5) and the experimental acceleration data we can now determine the Fourier transform of the displacement in the wave zone and then compare this transform directly with the same quantity for the hole given in (4). Denoting by r_0 the radius at which the accelerations were measured (371 ft and 451 ft), and by r any radius in the wave zone, we find for $r \gg c/\omega \gg r_0$,

$$\hat{\xi}(\omega) = (r_0^2 i\omega/rc) \hat{\xi}_0(\omega) \quad (7)$$

where $\hat{\xi}_0$ is evaluated at r_0 . The quantity $\hat{\xi}_0$ is easily evaluated from the following expression:

$$\hat{\xi}_0(\omega) = \frac{1}{2\pi i\omega} \int_0^\infty \dot{\xi}_0(\tau) e^{-i\omega\tau} d\tau \quad (8)$$

where $\dot{\xi}_0(\tau)$ is the radial velocity at r_0 as a function of time. For the values of ω which are of interest, namely those below about 6 sec^{-1} , we see from (6) that ω is less than ω_0 provided $W < 100 \text{ kt}$. In this case the exponential in (8) is approximately unity for the important part of the integration ($0 < \tau < 1/\omega_0$), and (8) reduces to

$$\hat{\xi}_0(\omega) = d_0/2\pi i\omega \quad (9)$$

where d_0 is the permanent displacement at r_0 .

From (7) and (9),

$$\hat{\xi}(\omega) = r_0^2 d_0/2\pi rc \quad (10)$$

This quantity is to be compared with the corresponding quantity for the hole given in (4). In what follows we affix the subscript h to all quantities referring to the hole. Taking the ratio of (10) to (4), we obtain

$$\frac{\hat{\xi}(\omega)}{\hat{\xi}_h(\omega)} = \frac{16\pi}{3(\gamma - 1)} \frac{c_h}{c} \frac{\mu_h r_0^2}{W} d_0 \quad (11)$$

² Rainier is the name given to the 1.7-kiloton nuclear explosion conducted at a depth of about 900 ft at the AEC Nevada site in September 1957 [Johnson, Higgins, and Violet, 1959].

For Rainier the quantity $r_0^2 d_0 = 2 \times 10^9 \text{ cm}^3$ or $1.4 \times 10^9 \text{ cm}^3$, depending on the measurement station. Choosing the smaller value, setting $V = 1.7 \text{ kt} = 7 \times 10^{10} \text{ ergs}$, and letting $\gamma = 1.2$, which is appropriate for air under the conditions of interest, we find for the decoupling factor

$$\hat{f}(\omega)/\hat{f}_h(\omega) = 2.4\mu_h c_h/c \quad (12)$$

where μ_h is in kilobars (kb). If the hole were in the Rainier medium, $c_h = c$ and $\mu_h \sim 20 \text{ kb}$, and the decoupling factor would be ~ 50 . Obviously it is desirable to make the hole in a stronger medium, e.g., salt, in which $c_h \sim 2.5c$ and $\mu_h \sim 100 \text{ kb}$. The decoupling factor in this case is ~ 600 . This number should be reduced somewhat because the soft Rainier medium couples to harder rock below the explosion point, thus decreasing the transmitted signal. This effect is difficult to estimate but is probably less than a factor of 2, and therefore we expect a decoupling factor of at least 300.

Another comparison with Rainier can be made on the basis of the U. S. Coast and Geodetic Survey seismic measurements at a distance of about 1 km. These measurements showed that the energy in the near seismic field, outside a radius of a few hundred feet, was approximately 5 per cent of the total yield [Carder, Cloud, Murphy, and Hershberger, 1958].

The total seismic energy radiated by the hole is

$$E_h = \pi p^2 a^3 / 2\mu \quad (13)$$

where, as before, p is the step pressure in the hole of radius a , and is related to the total yield W through (1). To ensure that the frequency analysis of the seismic wave produced by the hole is comparable to that of the Rainier shot, we must choose a to be about 300 ft. Again setting $\mu = 20 \text{ kb}$, we find that $E_h = 2 \times 10^{-6} W$. Hence the seismic energy from Rainier was about $5 \times 10^{-2} / 2 \times 10^{-6} = 2500$ times as great as that expected from the hole. Because the displacement is proportional to the square root of the energy E_h , it follows that the decoupling factor is $(2500)^{1/2} = 50$. This figure is in excellent agreement with our previous estimate for a hole in the Rainier medium.

Size and shape of the hole. We have shown theoretically that the seismic signal produced by an explosion in a hole in a strong medium will be hundreds of times smaller than that from an explosion of the same yield under Rainier

conditions (in Nevada tuff, without a hole). To what extent such a large decoupling factor can be realized in practice depends mainly on our being able to obtain a big hole in the right kind of medium.

The volume of the hole required is proportional to the yield of the explosion and is inversely proportional to the pressure to which the surrounding medium can be subjected without behaving nonelastically. Both plasticity and cracking must be avoided. The latter may impose a severe limit because most rocks possess little strength in tension. Precisely what the limiting pressure is must be determined from experiment, but in the meantime it seems safe to say that the elastic requirement will be fulfilled if the explosion pressure does not greatly exceed the overburden pressure. The reason for this is that the overburden produces a compressive stress that can be relieved by the explosion without putting the medium into tension.

Considering the depth at which cavities can be easily 'washed out' in salt domes (salt seems to be a particularly suitable medium), it seems feasible to contain an average explosion pressure of about 150 atmospheres. With this value of p it is easily calculated from (1) that the volume of the hole must be $3 \times 10^6 \text{ ft}^3$ (a radius of 90 ft) for a yield of 1.7 kt, and for $\gamma = 1.2$ (this is an appropriate value for air under the assumed conditions). In general, the volume of the hole must be approximately

$$V = 3 \times 10^6 W_{kt} / p_{kb} \text{ ft}^3 \quad (14)$$

where W_{kt} is the yield in kilotons, and p_{kb} is the maximum permissible pressure in kilobars.

It may be necessary, for practical reasons, to use a nonspherical hole. If so, the ratio of the major to the minor radius must not be so large that the explosion energy is effectively trapped in less than the total volume of the cavity. This problem has not been studied in detail, but it seems clear that a ratio of 3 or 4 is quite safe.

Assuming that pressure spikes on the wall of a nonspherical cavity can be avoided, we still must determine the nature of the seismic radiation which is produced, how much, and at what frequencies. These problems, too, remain to be studied. A crude analysis suggests that, for a class of prolate spheroids of fixed volume, the total seismic energy will not vary significantly. Furthermore, the frequency spectrum

may be shifted somewhat toward higher values corresponding to the minor dimension of the spheroid. If the spectrum is shifted upward, and if the total seismic energy is the same, then making the hole nonspherical will further reduce the distant seismic signal.

Nature of the pressure pulse. In air of density ρ , the shock wave from an explosion of W kilotons forms at a radius given by

$$R = 11.5 W_{kt}^{0.5} (\rho_0/\rho)^{0.5} \text{ ft} \quad (15)$$

where ρ_0 is the density of normal sea-level air (F. R. Gilmore, and A. L. Latter, unpublished work, 1956). If the radius of the hole is larger than R , a shock wave will form in the air and the pressure experienced by the wall will, for a short time, rise considerably above the average pressure in the hole. If such a pressure spike does not cause the surrounding medium to behave nonelastically, the distant seismic signal will not be increased because the spike lasts for a time that is very short compared with the periods of the waves that can be propagated to large distances. As an example, consider an explosion of 1.7 kt in a spherical hole with a radius of 130 ft. If the hole contains air at normal density, the wall will experience a pressure spike of about 1 kb acting for a few milliseconds. Thereafter the pressure on the wall will be sensibly the same as the average pressure in the hole, namely, about 50 atmospheres.

We do not know whether a kilobar acting for a few milliseconds will cause any important nonelasticity. Such a pressure may well be below the plastic limit and of too short duration to produce large tensile hoop stresses. However, if it should be necessary, it appears that it would be easy to reduce the pressure spike or to eliminate it entirely by partially evacuating the cavity or by partially replacing the air with hydrogen gas. Either of these measures will extend the radiation phase of the growth of the fireball, allowing less energy to go into shock motion. For example, if in the case we have just considered the air density in the cavity is reduced to 0.01 normal, the radiation phase will extend to the full 130-ft radius. In this way the pressure on the wall can be made to approximate a step pressure of 50 atmospheres, with no spikes.

In addition to the possible pressure spike from the shock wave, the hot gas in the cavity will interact with the wall and cause some vaporiza-

tion of the surface. This effect will produce a recoil shock pressure that must be added to the pressure of the gas. The magnitude of the shock depends on the rate of vaporization and hence critically on the temperature of the hot gas. For an explosion of 1.7 kt in a 130-ft hole containing air of normal density, the average temperature is equivalent to only ~ 1 ev, and the pressure due to vaporization is utterly negligible. If, however, the hole is evacuated to 0.01 normal density to eliminate the shock, the temperature will be equivalent to ~ 12 ev, and it is not quite certain that the vaporization pressure will still be negligible, although rough calculations suggest that this is likely. If the vaporization pressure should prove to be appreciable, it can be eliminated simply by introducing additional material into the hole to soak up energy and to lower the temperature. This additional material should be in the form of foils that are thin, to absorb energy rapidly, and that are oriented along radial lines so as not to impede the growth of the isothermal sphere.

A possible further advantage of the use of foils is that some of the energy they absorb goes into nonpressure forms such as latent heats of melting and vaporization. Although it does not seem likely that the pressure could be greatly reduced in this way in a time that is short compared with the period of the important seismic waves, it might be reduced by as much as one-half to two-thirds. This point needs further investigation.

Acknowledgment. We wish to thank Professors Edward Teller and David T. Griggs for their interest and criticism during the course of this work.

REFERENCES

- Bullen, K. E., *An Introduction to the Theory of Seismology*, Cambridge University Press, 1953.
- Carder, D. S., W. K. Cloud, L. M. Murphy, and J. H. Hershberger, Surface motions from an underground explosion, *U. S. Coast and Geodetic Survey Rept. WT 1530*, November 14, 1953.
- Johnson, G. W., G. H. Higgins, and C. E. Violet, *J. Geophys. Research*, **64**, 1457-1470, 1959.
- Latter, A. L., E. A. Martinelli, and E. Teller, A seismic scaling law for underground explosions, *Phys. Fluids*, **2**, 280-282, 1959.
- Perret, W. R., Subsurface motion from a confined underground detonation, *1, Sandia Corp. Rept. ITR-1529*, October, 1957.

Particle Motions near Explosions in Halite

BYRON F. MURPHEY

Sandia Laboratory, Albuquerque, New Mexico

Abstract. Peak particle velocities and displacements were measured for tamped (coupled) and cavity (decoupled) explosions in halite. Recordings are illustrated of particle velocity versus time in the salt medium and of pressure versus time on the cavity wall. Peak particle velocities from tamped shots decrease as $d^{-1.65}$ over distances equivalent to 40 to 800 feet for 1000 pounds of high explosive.

Decoupling factors that were directly observed apply only to close-in stations. One method of extrapolating close-in data yields distant decoupling factors ranging from 40 to 100 for these particular experiments. Actual measurements (verbal communication from Herbst, 1960) of distant decoupling factors give larger numbers by a factor of 2. Extrapolation to nuclear explosions is not attempted here.

Introduction. Project Cowboy was an experiment designed to determine to what extent underground explosions could be effectively concealed simply by firing the explosion in a large cavity. Comparative measurements of earth motion were obtained from tamped charges of high explosives and high-explosive (HE) charges of similar yield fired in large cavities in halite. The tamped explosions are referred to as coupled shots and the explosions in cavities as decoupled shots. The function of the cavity is to decouple the explosion from the surrounding medium and thus conceal the explosion by reducing the amount of energy transmitted to the medium at low frequencies.

Instrumentation was included to measure ground motion, both in the salt near the explosions and on the earth's surface out to ranges of several miles.

Measurements close to the explosions were required for two main reasons: to indicate the actual pressure-time histories on the walls of the cavities and to show comparative motions of the salt from coupled and decoupled explosions of identical yield.

Measurement of the cavity pressure-time history and particle displacement in the salt medium provided data for comparison with and verification of theoretical calculations. Actually, precise measurement of *permanent* displacement is difficult to achieve. Values of peak transient velocities and *peak* displacements are readily obtainable.

For tamped explosions, the most useful quantity to measure is permanent displacement,

although, again, values of transient peak velocities and displacements are also useful.

Background. The idea that underground explosions can be concealed has been published in a RAND Corporation report and is republished in this Journal [Latter, LeLevier, Martinelli, and McMillan, 1961]. Since the ideas involved a combination of elasticity theory in the behavior of cavities in hard rock and experimental observation of particle motion near a 1.7-kt nuclear explosion (Rainier), it seemed highly desirable to obtain more experimental confirmation of the theory. Lawrence Radiation Laboratory was requested to conduct the experiment, designated Project Cowboy. Sandia Laboratory was requested by LRL to provide strong-motion instrumentation within the surrounding rock at various distances from the explosions.

At the time the experiment was planned (early summer, 1959) we decided to use available commercial instruments because of the anticipated short time scale. Since displacement gages were not available, we suggested that the primary instrumentation be velocity gages. Use of accelerometers was also planned in the event velocity gages were not adequate; velocity gages were, however, satisfactory.

The experiment was conducted at depths near 800 feet in the Carey Company salt mine near Winnfield, Louisiana. All instrumentation provided by Sandia was located in the mine. Since both coupled and decoupled shots were fired in the salt medium, factors describing concealment refer to comparable shots in salt.

Theory. The ratio of the distant signals in the

limit of low frequencies between a coupled and a decoupled explosion is given by equation 11 of *Latter, LeLevier, Martinelli, and McMillan* [1961]:

$$\text{decoupling factor} = \frac{16}{3(\gamma - 1)} \frac{c_h}{c} \mu_h \frac{r_0^2 d_0}{W} \quad (1)$$

where

γ = ratio of specific heats applicable to explosion in cavity.

c_h = velocity of sound in medium around cavity.

c = velocity of sound in medium around tamped shot.

μ_h = shear modulus in medium around cavity.

r_0 = distance from tamped explosion at which permanent displacement d_0 is measured in elastic zone.

W = explosion energy release.

This expression involves the assumption that energy W is distributed uniformly over the cavity volume, giving a step-function pressure p on the wall [*Latter, LeLevier, Martinelli, and McMillan*, 1961, eq. 1]:

$$p = \frac{(\gamma - 1)W}{(4/3)\pi a^3} \quad (2)$$

where a is the radius of the cavity. Of course the actual pressure observed on the wall was not simply that given by (2) because expected short-duration pressure pulses did occur.

This fact emphasizes the necessity for using the observed (or, more accurately, calculated) pressure-time history at the cavity wall to determine close-in particle motion. Actually, in the direct application of (1) values of p are not needed; only W is used. A difficulty in the use of (1) is the inability to determine the permanent displacement d_0 accurately. Observed transient displacements can be used to verify the assumption of elastic behavior of the cavity walls.

In the Cowboy experiments spherical charges of Pelletol (TNT at 1 g/cm³) were placed at the center of the cavity, which was then evacuated to about 1/20 of an atmosphere. Nothing is stated in (1) about the maximum value of W which can be released in the cavity. One purpose of these experiments was to determine how great W could be, and the close-in measurements indicated whether displacements were proportional to W for large W .

Some insight into the experiment can be obtained from an approximate elementary theory of the behavior of peak velocities and displacements. We assume that the effective pressure on the cavity wall is p_0 , and that p_0 is small enough in magnitude for the pressure at radius r from the center of a cavity of radius a to vary as

$$p = p_0(a/r) \quad (3)$$

The $1/r$ dependence at large r is a valid approximation [*Sharpe*, 1942]. We assume also that

$$p = \rho c u \quad (4)$$

where

u = peak particle velocity.

c = velocity of sound.

ρ = density.

Equation 4 is a close approximation at large r . We may then write

$$u = (p_0/\rho c)(a/r) \quad (5)$$

If it is assumed that u varies sinusoidally with time, it is permissible to obtain peak displacement from $d = u/\omega$. If, in addition, it is true that $\omega = c/a$ because of the elastic behavior of the cavity walls, then

$$d \propto (p_0/\rho c^2)(a^2/r) \quad r > a \quad (6)$$

(Equations 5 and 6 will not hold at distances so close to the cavity that inductive mass motion occurs involving dependence on $1/r$ and $1/r^2$.)

For the tamped explosion some effective pressure p_0 exists at some effective radius a_i , such that peak velocities and displacements are given by

$$u_i = (p_{0i}/\rho_i c_i)(a_i/r) \quad (7)$$

and

$$d_i \propto (p_{0i}/\rho_i c_i^2)(a_i^2/r) \quad (8)$$

To obtain close-in decoupling factors for peak values, we need only look at the observed ratios u_i/u and d_i/d . When $\rho = \rho_i$ and $c = c_i$, as in the Cowboy experiments, we find

$$\frac{u_i}{u} = \frac{p_{0i} a_i}{p_0 a} \quad r \gg a, a_i \quad (9)$$

$$\frac{d_i}{d} = \frac{p_{0i} a_i^2}{p_0 a^2} \quad r \gg a, a_i \quad (10)$$

The distant decoupling factor is further increased in proportion to ω_0/ω_{0t} , where $\omega_{0t} = c/a_t$ and $\omega_0 = c/a$ [Latter, LeLevier, Martinelli, and McMillan, 1961]. Such an increase in decoupling would be observed at large distances or close in with low-pass measuring instruments for which $\omega_0 \ll \omega_{0t}$. The low-frequency limit of the Fourier transform of displacement related to ω_{0t} is higher than the corresponding limit for ω_0 as the ratio ω_0/ω_{0t} . As a result the amplitudes and waveforms of initial driving pressures at the elastic radii are similar,

$$\frac{d_t(\omega < \omega_0)}{d(\omega < \omega_0)} = \frac{p_{0t}a_t^3}{pa^3} \\ = \text{distant decoupling factor}, \quad (11)$$

see also Latter, Martinelli, and Teller [1959].

The ratios

$$p_{0t}/p_0 \quad \text{and} \quad a_t/a$$

are calculable from ratios of observed peak velocities and displacements. Therefore, the distant decoupling factor is calculable from (11). However, (10) will apply in case the measuring station has instruments that respond near ω_0 and the station is not far enough away for waves of this frequency to be attenuated by solid friction.

If the transient peak pressure on the cavity wall has large amplitude compared with the pressure calculated from (2) and if its duration is shorter than a time comparable to $1/\omega_0$, then the propagated pressure pulse may not be characterized by ω_0 , and (6) may not be strictly applicable. Nevertheless, equations 9 through 11 seem to be useful for an understanding of strong-motion data obtained, but the equations do not reveal why a may be, and usually is, significantly smaller than a_t .

The exact manner in which pressure falls off with distance in salt was not known at the start of Project Cowboy. We did know that in air or soil, in the range of measurement planned for salt, dependence would be r^{-3} , and that in water [Cole, 1948], dependence had been observed to be $r^{-1.12}$. Presumably, the exponent for salt would be between these, since a dependence near $r^{-2.3}$ had been calculated for nuclear shots in tuff (unpublished notes by John Nuckolls, 1959). In calculating velocities to be anticipated, a further difficulty arose, since, at close distances, mass

motion of material near the explosion introduced an r^{-2} term.

In practice, for the tamped explosion, our method of predicting velocity was to make a guess and hope that we would be correct within a factor of 5. After one shot had been fired and measurements obtained at two distances, empirical formulas were then established for prediction for later explosions. For high explosives, the similarity principle can be invoked for explosions of different size, namely, equal velocities are anticipated at corresponding distances scaled in proportion to $W^{1/3}$. Incidentally, this cannot be done for nuclear explosions generally, since the starting pressure at the edge of the nuclear explosive on the cavity wall depends on the yield of the explosion. For similar high-explosive charges (closely tamped Pelletol was always used in the coupled Cowboy shots), the starting pressure at the edge of the tamped explosion is independent of the yield.

Results of the tamped explosions soon indicated that we could write the empirical expression for peak velocities as $u \propto r^{-1.65}$ over the range of $r/W^{1/3} = 4$ to 80, where r is in feet and W is yield in pounds. It is quite probable that this relation is nearly correct for high explosives in any hard rock.

We now consider the term $r_0^2 d_0$ which occurs in (1). This term represents the permanent mass motion which would occur after an explosion in a perfectly elastic incompressible medium. That is, the increase in volume of the cavity is observable at any distance r_0 as a permanent displacement d_0 such that the permanent volume change in the cavity is equal to $4\pi r_0^2 d_0$. Latter, LeLevier, Martinelli, and McMillan [1961] were naturally hopeful that we might obtain a good measurement of d_0 . The intent was to integrate the velocity-time records. It turned out that this could not be done accurately because the peak displacements were quite large compared with the permanent displacements, even for the tamped explosions. This problem is mentioned here to point out the fact that the assumption that a coupled explosion injects a step function of pressure at some elastic radius is valid only for frequency components much lower than the dominant information frequency as observed close to the explosion. This is a basic assumption of the decoupling theory.

The above discussion should serve to show that

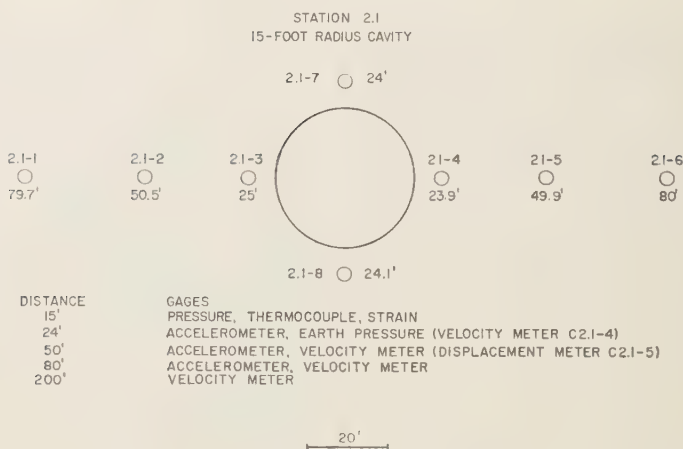


Fig. 1. Schematic gage layout near 15-foot cavity.

primary close-in measurements should be (a) pressure versus time at the cavity wall and (b) velocities and displacements in the medium near coupled and decoupled explosions. Of course, distant seismic signals provide direct measurement of decoupling factors, modified by the response and location of the seismometers.

Description of experiment. The Cowboy experimental area is located in an unused portion

of the Carey Salt Company mine near Winnfield, Louisiana. Tamped explosions were placed in drill holes at depths of 45 and 110 feet below the tunnel floor. Cavities 6 and 15 feet in radius were constructed at the ends of new tunnels driven about 75 feet from existing tunnel walls. Cavity explosives consisted of spherical charges placed at the centers of the cavities.

A schematic drawing of instrument locations

TABLE 1. Summary of Shot Data, Project Cowboy

Shot No.	Date	Time* (CST) h m s	Yield,† lbs	Station	Type
1	Dec. 17	00 15	20	1.2	Coupled, 45-ft hole
2	Dec. 17	00 45	20	1.1	Decoupled, 12-ft-dia. sphere
3	Dec. 19	00 00	100	1.1	Decoupled, 12-ft-dia. sphere
4	Dec. 19	00 15	100	1.3	Coupled, 45-ft hole
5	Jan. 23	00 00 00.113	198.35	2.1	Decoupled, 30-ft-dia. sphere
6	Jan. 30	00 01 00.112	200.0	2.1	Decoupled, 30-ft-dia. sphere
7	Jan. 30	01 01 00.112	199.65	2.2	Coupled, 110-ft hole
8	Feb. 6	00 01 00.115	477.4	2.1	Decoupled, 30-ft-dia. sphere
9	Feb. 6	01 01 00.113	499.7	2.3	Coupled, 110-ft hole
10	Feb. 13	19 01 00.113	954.0	2.1	Decoupled, 30-ft-dia. sphere
11	Feb. 13	20 01 00.114	1003.0	2.4	Coupled, 110-ft hole
12	Feb. 20	00 01 00.112	929.0	1.1	Decoupled, 12-ft-dia. sphere
13	Feb. 20	01 00 59.614	987.6	2.5	Coupled, 110-ft hole
14	Feb. 27	00 01 00.127	1902.4	1.1	Decoupled, 12-ft-dia. sphere
15	Feb. 28	04 01 00.131	936.2	2.6	Coupled, 110-ft hole
16	Mar. 3	23 01 00.128	199.5	1.4	Coupled, 45-ft hole
17	Mar. 4	00 01 00.130	199.8	1.3-1	Coupled, 45-ft hole

* All times for shots 5 through 17 are derived from comparisons with WWV. Accuracies are ± 0.001 sec, except for shot 15, which is ± 0.003 sec.

† All yields include 'Nitramon' booster and detonator weights of either 2 or 3 pounds.

near the 15-foot-radius cavity is shown in Figure 1. Gages were placed to measure radial particle motion. Similar gage positions were used for the tamped explosions. Although a variety of gages was used, it is sufficient in this paper to consider measurements made by velocity and pressure gages only.

In the cavity of 15-foot radius, four pressure gages were used to indicate pressure as a function of time. Two of these gages were located in a plate near the entrance to the cavity. The other two were placed 45° and 90° away on the horizontal great circle. A pressure gage with a long fill time was used to read pressure in the cavity at long times compared with the duration of the transient pressure pulse.

A summary of the shots fired during Project Cowboy is given in Table 1. The explosive used in all cases was Pelletol, which was contained in

plastic spherical shells for all decoupled shots.

Results. Values of observed peak velocities and peak displacements for all explosions are listed in Tables 2, 3, and 4. Except for displacements from the gages listed as -DR, all peak displacements were obtained by integrating velocity-time recordings. The -DR gages are experimental displacement gages which were installed late in the program.

Peak velocities and displacements observed for the three 200-pound tamped explosions are plotted in Figure 2 to illustrate the degree to which the data are consistent. An example of a velocity-time recording and the corresponding integration is shown in Figure 3.

All peak-velocity data for tamped explosions (20 pounds through 1000 pounds) have been plotted in Figure 4 as a function of distance divided by the cube root of the charge weight.

TABLE 2. Peak Velocities and Displacements, Tamped Explosions

Gage	Distance, ft	Shot No.	W, lbs	Peak Vel., in/sec	$W^{1/3}$	Peak Displ., mils	Mils/ $W^{1/3}$	$D/W^{1/3}$
1.2-3-V	19.4	1	20	12	2.71	...		7.15
1.2-4-V	36			9.4			low	13.3
1.3-7-V	19.3	4	100	90	4.64	...		4.16
1.3-8-V	35.9			28.4		...		7.73
2.2-3-V	49	7	200	40	5.84	24	4.11	8.4
2.2-2-V	50.3			42		26	4.46	8.6
2.2-1-V	79.4			15.5		10.4	1.79	13.6
2.2-4-V	80.6			10		8	1.37	13.8
2.1-17-VB	452.5			1.0		1.0	0.172	77.5
1.2-4-V	157	16	200	3.9	5.84	3.0	0.515	26.9
1.2-3-V	173			3.0		2.3	low 0.395	29.7
1.3-7-V	223			3.4		2.5	0.429	38.2
1.3-8-V	207			3.7		2.5	0.429	35.5
2.1-17-VB	431			1.1		0.8	0.137	73.8
2.1-17-VC	431			1.0		0.8	0.137	73.8
1.3-7-V	99	17	200	11.2	5.84	8.2	1.4	17
1.3-8-V	116			9.1		8.1	1.39	19.9
1.2-3-V	150			4.4		3.4	0.583	25.7
1.2-4-V	167			4.1		3.2	0.55	28.6
2.1-17-VC	274			1.8		1.5	0.257	47
2.3-2-V	50.5	9	500	48	7.92	48	6.07	6.38
2.3-1-V	79.6			20		22.5	2.85	10
2.3-4-V	79.7			23		20	2.53	10
2.1-17-VB	368.8			2.0		2.9	0.37	46.6
2.4-1-V	77.5	11	1000	46	10	42	4.2	7.75
2.4-15-V	208.2			6.5		9.3	0.93	20.8
2.4-15-DR				...		11.6	1.16	20.8
2.1-17-VB	477.7			2.1		3.2	0.32	47.8
2.5-4-V	80.9	13	1000	40		39	3.9	8.1
2.4-15-V	351.7			4.3		5.6	0.56	35.2
2.4-15-DR				...		6.1	0.61	35.2
2.1-17-VB	585.5			1.3		1.7	0.17	58.6

TABLE 3. Peak Velocities and Displacements, 15-Foot Cavity

Gage	Distance, ft	Shot No.	W, lbs	Peak Vel., in/sec	Peak Displ., mils
2.1-2-V	50.5	5	200	1.4	0.53
2.1-1-V	79.7			0.45	0.25
2.1-4-V	23.9	6	200	2.2	1.44
2.1-2-V	50.5			1.0	0.5
2.1-1-V	79.7			0.4	0.25
2.1-6-V	80			0.4	0.26
2.1-11-V	200.1			0.17	0.09
2.1-4-V	23.9	8	500	7.8	2.5
2.1-2-V	50.5			3.8	1.2
2.1-5-V	49.9			3.4	1.2
2.1-5-DR	49.9			...	1.2
2.1-1-V	79.7			2.0	0.55
2.1-6-V	80			1.6	0.5
2.1-11-V	200.1			0.6	0.2
2.1-17-VA	366.6			0.28	0.1
2.1-4-V	23.9	10	1000	13	5
2.1-5-V	49.9			5.1	1.8
2.5-5-DR				...	2.2
2.1-2-V	50.5			6	2.1
2.1-1-V	79.7			2.6	0.9
2.1-6-V	80			2.4	0.6
2.1-11-V	200.1			0.83	0.28
2.1-17-VA	366.6			0.4	0.14

This plot shows that, over the range of scaled distances from 4 to 80, peak velocities fall off with distance as $r^{-1.65}$.

Similarly, Figure 5 is a plot of observed peak displacements for all tamped explosions. However, peak displacement divided by $W^{1/3}$ must be used in the scaled plot. $d/W^{1/3}$ is found to depend on distance as $r^{-1.65}$.

Apparent differences in the frequencies of signals from tamped and cavity explosions may be inferred qualitatively from inspection of the corresponding velocity-time recordings. Copies of actual velocity measurements made by an oscillograph recording on film are reproduced in Figures 6 and 7.

Notable for the coupled shots is the fact that rise time for the change in particle velocity is slow enough for the gage to follow the motion with some accuracy. Such is not the case for the decoupled shots. The high frequency to be seen on the recordings of velocities from decoupled explosions is caused by ringing of the canister containing the gages. The degree of ringing varies from gage to gage because of variation in precautions taken to avoid the ringing. This ringing

TABLE 4. Peak Velocities and Displacements, 6-Foot Cavity

Gage	Distance, ft	Shot No.	W, lbs	Peak Vel., in/sec	Peak Displ., mils
1.1-2-V	20.7	3	20	0.7	...
1.1-1-V	35.1			0.5	...
1.1-6-V	36.2			0.45	...
1.1-5-V	19.6	4	100	3.4	...
1.1-2-V	20.7			2.1	...
1.1-1-V	35.1			1.3	...
1.1-6-V	36.2			1.9	...
1.1-5-V	19.6	12	929	32	21.3
1.1-2-V	20.7			24.5	16
1.1-1-V	35.1			12.5	6.7
1.1-6-V	36.2			10.5	7.8
1.1-9-V2	100.7			4	2.4
2.1-17-VB	461.2			0.3	0.3
1.1-5-V	19.6	14	1903.4	71	52
1.1-2-V	20.7			54	43
1.1-1-V	35.1			26.5	18.5
1.1-6-V	36.2			27	19
1.1-9-V2	100.7			6.7	5.5
2.1-17-VB	461.2			0.6	0.6

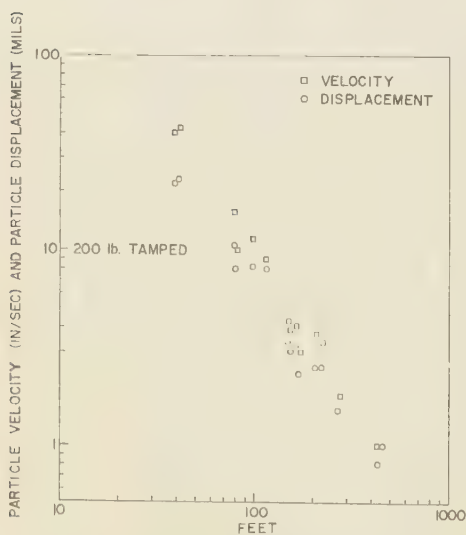


Fig. 2. Peak velocity and displacement versus distance for 200-pound tamped explosions.

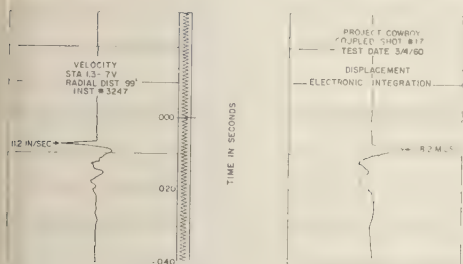


Fig. 3. Velocity-time recording and corresponding integration.

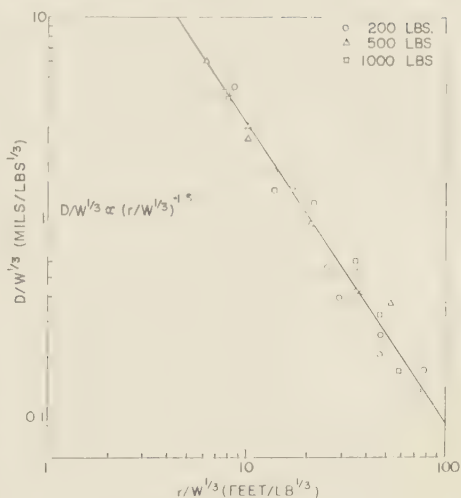


Fig. 5. Scaled peak displacements versus scaled distance for all tamped explosions.

can be filtered out in playing back data from magnetic-tape recordings; indeed this is done automatically during integration to give displacement. It is questionable whether actual peak particle velocity is always recorded accurately for decoupled explosions. The inaccuracy involved can be guessed at by extrapolating back to arrival time of the shock front, if it is assumed that a step shock front existed.

Since the pressure on the cavity wall from an explosion is not truly a step function, actual pressure-time histories in the cavity were desired over both short and long time intervals. Pressure gages were placed near the door and at horizontal angles of 45° and 90° from the door. A slow-response pressure gage was also placed near the

door to measure cavity pressure at long times after the explosion.

The best illustration of pressure versus time in the cavity is provided by results from shot 10. Data recorded from one of the gages is illustrated in Figure 8 for 1000 pounds of Pelletol in the cavity of 15-foot radius. The first pressure pulse had an amplitude near 900 psi, the second about 300 psi, and the third about 100 psi. The gas pressure continued to oscillate for some time. Figure 9 illustrates the cavity pressure at long times for the same explosion. This gage was purposely arranged to have a long fill time so that it would not record peak transient pressures. The cavity pressure at 100 milliseconds is 90 psi, or about one-tenth of the initial peak pressure.

Comparative peak pressures and pressures at 100 msec after zero time for explosions in the 15-foot cavity are listed in Table 5.

TABLE 5. Pressures in 15-Foot Cavity

W, lbs	Shot No.	Peak Pressure, psi	Pressure at 100 msec, psi	$p = \frac{(\gamma - 1)W}{4/3\pi 15^3}$, psi
198	5	~300	22	28
477	8	500	44	67
954	10	900	92	135

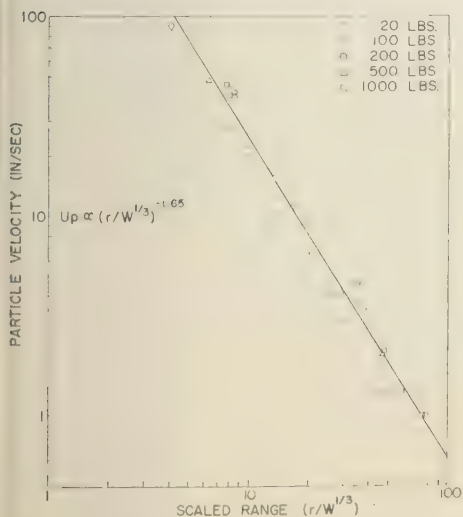


Fig. 4. Peak velocity versus distance/ $W^{1/3}$ for all tamped explosions.

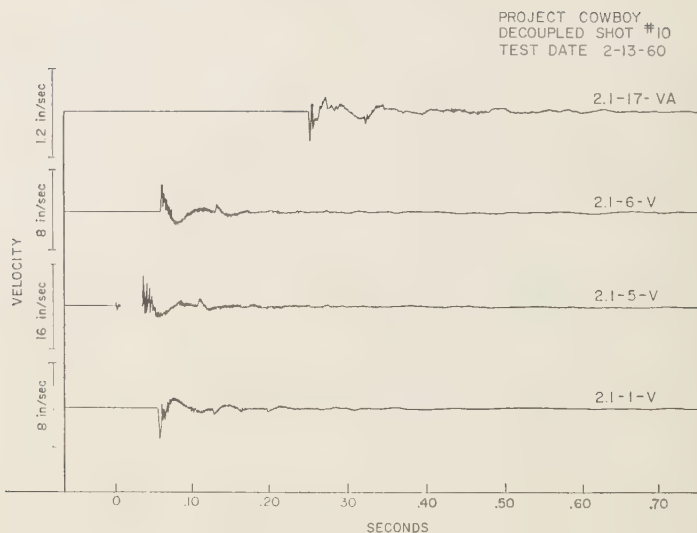


Fig. 6. Particle velocity versus time (1000 pounds, decoupled, 15-foot cavity, shot 10, Feb. 13, 1960).

In the table, $\gamma = 1.2$ has been used because the cavity was evacuated and the energy release of Pelletol was assumed to be 1000 cal/g. If the pressure at 100 msec is extrapolated back to zero time and if peak pressure is ignored, values closer to calculated pressures are obtained.

Analysis of results. Given observed data for tamped chemical explosions in halite and theoretical behavior of a cavity, a decoupling factor can be calculated. This calculation will be compared with data obtained from the cavity explosions.

From the peak velocity and displacement for tamped explosions, plotted in Figures 4 and 5, an effective elastic radius as a function of distance can be computed from the expression

$$a_i \cong c d/u$$

(For a precise expression the exact form of the stress curve would have to be taken into account; the above expression gives a low estimate of a_i .) The velocity of sound c is observed from transit time between gage positions to be about 14,500 ft/sec. The equation then gives, for a charge of 1000 pounds, an effective elastic radius of 22.8 ft as observed from 1000 ft away, or a radius of 16 ft as observed from 50 ft.

This variation in radius reflects a variation in d/u with distance. Presumably the ratio will not

continue to change much more at greater distance, although complete change-over to $1/r$ behavior is not yet evident at 1000 feet. At scaled distances $r/W^{1/3} = 100$, the value of a_i will be $2.3W^{1/3}$ for explosions of Pelletol in halite. If the approximation that $c/a_i = 2\pi f$ is valid, the observed positive phase duration T of the velocity pulse should be approximately equal to $1/2f$ or $\pi a_i/c$. Since $\pi a_i/c = 5$ msec and $T = 3$ to 4 msec, it is unlikely that a_i is much larger than 23 feet for explosions of 1000 pounds of Pelletol in halite. However, assumptions of elastic behavior beyond the 'elastic radius' a_i are not entirely correct because a_i depends on the distance of observation.

The effective value of p_0 at a can be calculated from

$$u = (p_0/\rho c)(a_i/r)$$

If we take

$$\begin{aligned} r &= 1000 \text{ feet} \\ u &= 0.59 \text{ in/sec} = 1.5 \text{ cm/sec} \\ a_i &= 23 \text{ feet} \\ \rho &= 2.13 \text{ g/cm}^3 \\ c &= 14,500 \text{ ft/sec} = 4.4 \times 10^6 \text{ cm/sec, then} \\ p_0 &= 61 \text{ bars} = 900 \text{ psi} \cong 1000 \text{ psi.} \end{aligned}$$

Provided that the cavity can withstand 1000 psi and that an explosion yield is chosen to give

PROJECT COWBOY
COUPLED SHOT #11
TEST DATE 2-13-60

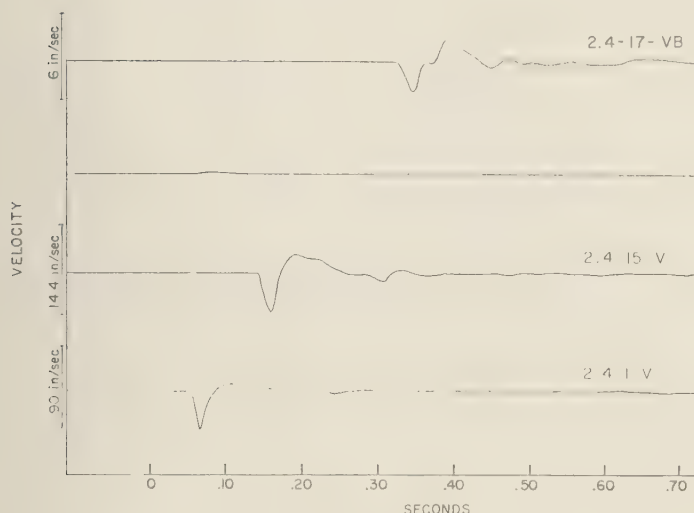


Fig. 7. Particle velocity versus time (1000 pounds, coupled, shot 11, Feb. 13, 1960).

1000 psi in the cavity, the theoretical distant decoupling factor is simply a_i^3/a^3 , where a_i is the tamped elastic radius and a is the cavity radius. From (2), the value of W required to give 1000 psi in a 15-foot cavity is 6900 pounds. The corresponding a_i is 44 feet. This 'theoretical' distant decoupling factor a_i^3/a^3 is 25 for halite. Comparison with close-in observation follows.

Observed decoupling factors for peak velocities and displacements permit calculation of distance decoupling factors for each halite experiment. From (9), (10), and (11), the distant decoupling factor is given by $d_i^2 u_c / d_o^2 u_i$.

Results in Table 6 yield numbers as much as 4 to 5 times larger than the number calculated above.

The third column gives distant decoupling factors which would be observed by distant velocity or displacement meters that were responsive at low frequencies. *The numbers apply only to the specific experiment to which they refer, i.e., tamped and cavity HE explosions in halite.* Smaller numbers could easily be observed in the Cowboy experiments by nearby surface instruments of proper frequency response.

The numbers listed in column 3, Table 6, are not precise, since the condition that the comparison be made in the region where velocities

fall off inversely as distance is not fulfilled. Table 7 shows how the numbers vary with distance of comparison.

The reason the decoupling factor is higher for the higher-yield explosions in the 15-foot cavity is simply that the recorded pulse from the cavity is relatively sharper for the higher-yield ex-

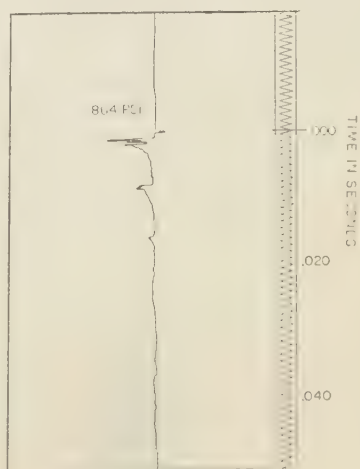


Fig. 8. Pressure versus time (1000 pounds, decoupled, 15-foot cavity, Feb. 13, 1960).

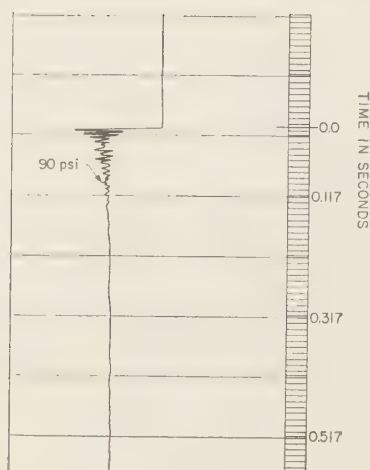


Fig. 9. Cavity pressure at long times (1000 pounds, decoupled, 15-foot cavity, Feb. 13, 1960).

plosions. The duration of the velocity pulse from the tamped explosion increases with yield as $W^{1/3}$. Velocity pulses for the cavity retained a higher-frequency content than would be characteristic for the oscillating cavity and are really more characteristic of the driving pressure pulses.

The reason that the observed distant decoupling factors are nearer 100 than 25 appears to be that more of the energy is concentrated in high frequencies than is allowed for in the calculation. The after pressure at 100 msec is also smaller than was calculated from (2). Experimentally, the after pressure at 100 msec from 1000 pounds in the 15-foot cavity was 92 psi. According to this observation, 11,000 pounds of Pelletol would be required to give 1000 psi at

TABLE 6. Decoupling Factors for HE in Halite (from peak values)

u_i/u_o	d_i/d_o	$(d_i/d_o)^2$ u_i/u_o	W , lbs	r , ft	Shot No. (cavity)	Cavity Radius, ft
20	30.5	47	200	200	6	15
7.3	23	72	500	370	8	15
7.5	30	120	1000	365	10	15
35	20	35	2	6
25	100	35	3	6
6.7	10	15	1000	460	12	6
5	8.6	15	2000	460	14	6

TABLE 7. Decoupling versus Distance of Close-in Observation

u_i/u_o	d_i/d_o	$(d_i/d_o)^2$ u_i/u_o	r , ft	Shot No.
15	39.2	100	50	8
13.9	43.8	138	80	8
9.3	29	91	200	8
7.3	23	72	370	8

100 msec after the explosion. On this basis, a_i for 11,000 pounds is 51 feet and a_i^3/a^3 would be 40. Since the effective value of a_i calculated from distant observations would be larger than that used here, distant decoupling factors between 40 and 100 can be estimated from the close-in observed peak velocities and displacements for these particular Cowboy experiments in the 15-foot cavity.

The same calculation made for the 15-foot cavity can be made for the 6-foot cavity and should give the same result. The filling weight to give 1000 psi is 710 pounds, for which $a_i = 20.6$ feet and $a_i^3/a^3 = 40$.

Extrapolation of peak velocities and displacements from Tables 2 and 4 to the 6-foot cavity wall gives peak velocity = 130 in/sec and peak displacement = 0.1 in. The corresponding peak radial-compressive strain and peak tangential-tensile strain are, therefore, for 929 pounds of Pelletol:

$$E_r = u/c = 750 \mu\text{in/in} \quad \text{compression}$$

$$E_t = d/r = 1400 \mu\text{in/in} \quad \text{tension}$$

Similarly, for 1900 pounds in the 6-foot-radius cavity:

$$E_r = 1800 \mu\text{in/in} \quad \text{compression}$$

$$E_t = 4200 \mu\text{in/in} \quad \text{tension}$$

Unconfined halite specimens in laboratory tests exhibit a Young's modulus near 800,000 psi and tensile failure at less than 100 psi. Tensile strength of the cavity wall is almost entirely due to overburden compressive stress that must be overcome before the wall goes into tension. Since large tensile strains occurred, the wall developed tensile cracks. Compressive strains were too small to result in failure in compression, a value of several thousand $\mu\text{in/in}$ would be required.

At the time of maximum tangential-tensile strain, the radial strain is zero. Shortly afterwards small tensile radial strain develops, so that some spalling would occur if a large enough shot were fired in the cavity. As yield increases from small values, radial cracking extends farther and farther from the wall, causing the cavity to be inelastic. Apparently serious cracking does not occur until the confining overburden pressure is considerably exceeded.

Propagation velocities in the halite were observed from transit time between velocity gages to be 14,500 to 15,000 ft/sec. In this report we have used $c = 14,500$ ft/sec for halite and $\rho = 2.13$ g/cm³. With these numbers, $\lambda + 2\mu = 415$ kilobars. If $\lambda = \mu$, then $\sigma = 0.25$ and $\mu = 137$ kilobars, or if $\lambda = 2\mu$, then $\sigma = 0.3$ and $\mu = 103$ kilobars.

Shear-wave velocity was not determined from our records, since gages were always radial except for the distant accelerometers where reflections obscure the data.

Conclusions. Radial motion close to tamped explosions in halite was adequately determined over scaled distances from 6 to 80 ft/lb^{1/3}. Permanent displacements at the closest ranges were considerably less than would be expected for incompressible motion. Evidently, measurements as close as a scaled distance of 2 ft/lb^{1/3} are needed to obtain an accurate measure of permanent displacement from tamped explosions. It is suggested that, for 1000-pound explosions, measurements be obtained at distances of 20, 30, and 50 feet, but it should be noted that accelerometers or long-base displacement gages would have to be used. Larger explosions would make measurements easier to obtain. Radial stress measurements should also be made in the halite at the same distances, as a check on the degree of elasticity.

Adequate measure of motion near the cavities is difficult to obtain because the centrally located charge gives a fast-rising, short-duration pulse that is difficult to measure unless the HE charges are large. Measurements for charges of 500 pounds and larger appear to be good enough. Low-frequency motions near the cavities were too small to measure. Use of gas in the cavities would presumably make the fast pressure pulse less significant and make measurement easier.

Enough transient measurements were obtained to make possible a calculation of the motion near

the 15-foot cavity. For such calculations we need use only the observed pressure-time history on the wall as an input to equation described by *Sharpe* [1942] or *Blake* [1952]. Computed transient velocities may then be compared with observations of velocity versus time. Such calculations will be published separately. Clearly, motion of the medium near the cavity depends on details of the pressure-time history in the cavity. Empirically, motion at large distances from the cavity falls off faster than r^{-1} . If this is due to attenuation of high frequencies caused by frictional effects, it will not occur to the same extent for larger cavities and larger explosions. Scaling of these data to very large chemical explosions is not necessarily accurate.

Data obtained from Cowboy definitely prove that decoupling in halite of from 40 to 100 can be obtained for high explosives. Actual measurements (verbal communication from Herbst, 1960) of distant decoupling factors give larger numbers by a factor of 2. Experimental proof of the degree of decoupling that could be obtained from nuclear explosions can be obtained only from nuclear explosions, for two reasons: (1) A tamped nuclear explosion causes a very high initial pressure in the medium. In fact, the starting pressure increases with nuclear yield, so that nuclear explosions of different yield do not even exhibit similar behavior. Thus, the similarity principle invoked for various-yield chemical explosions cannot be used in the same way for nuclear explosions. (2) A nuclear explosion in a cavity will behave in a manner different from a chemical explosion simply because of the very different pressure-time history of the nuclear explosion. However, a nuclear shot in a cavity has been calculated [*Latter, LeLievier, Martinelli and McMillan*, 1961] to give the same signal at large distances as a chemical explosion of the same yield.

Acknowledgments. Sandia Laboratory measurements during Project Cowboy, Winnfield, Louisiana, were carried out under the general supervision of A. Dean Thornbrough. Ed. S. Ames and Hervey L. Hawk were responsible for the successful operation of the instrumentation system. Frank Adelman of Lawrence Radiation Laboratory provided scientific liaison between Sandia and theoreticians at LRL and RAND Corporation. All field support was obtained through the LRL engineering staff.

This research was a part of Operation Cowboy, carried out under the auspices of the Atomic Energy Commission.

REFERENCES

- Blake, F. G., Jr., Spherical wave propagation in solid media, *J. Acoust. Soc. Am.* 24, 211-215, 1952.
- Cole, R. H., *Underwater Explosions*, Princeton Univ. Press, 1948.
- Latter, A. L., R. E. LeLevier, E. A. Martinelli, and W. G. McMillan. A method of concealing underground nuclear explosions, *J. Geophys. Research*, 66, 943-946, 1961.
- Latter, A. L., E. A. Martinelli, and E. Teller, A seismic scaling law for underground explosions, *Phys. Fluids*, 2, 280-282, 1959.
- Sharpe, J. A., The propagation of elastic waves by explosive pressures, *Geophysics*, 7, 144-154, 311-321, 1942.
- (Manuscript received September 22, 1960; revised December 1, 1960.)

Use of Large Cavities to Reduce Seismic Waves from Underground Explosions

ROLAND F. HERBST, GLENN C. WERTH, AND DONALD L. SPRINGER

*Lawrence Radiation Laboratory, University of California
Livermore, California*

Abstract. An analysis is given of an experiment designed to test the theory of seismic decoupling of underground explosions proposed by *Latter, LeLevier, Martinelli, and McMillan* [1961]. The amplitude of the seismic signal from a 1.7-kiloton nuclear explosion in a hole in salt was calculated and compared with the measured value from the 1.7-kt Rainier shot in tuff at the same distance. A decoupling factor of about 300 resulted. The experiment, called Cowboy,¹ was designed to test the decoupling principle by carrying out a series of eight high-explosive shots in two spheres made in a salt dome, and nine tamped shots for comparison. The seismic data reported here were obtained primarily at ranges of 14,000 and 22,000 feet and at frequencies of 10 to 30 cps. A salt-to-salt decoupling factor of 100 was obtained which is consistent with the predicted tuff-to-salt factor of 300. When the sphere was overdriven so that the walls did not move elastically (which violates a condition of the theory for full decoupling), decoupling factors of 10 and 30 were measured. The seismic data are interpreted to give the dependence of decoupling on the various parameters of the experiment. The decoupling deduced from measurements made 80 feet from the shot points is found to be consistent with that deduced from the measurements at 14,000 and 22,000 feet.

INTRODUCTION

This report is an interpretation of the surface seismic data obtained in Project Cowboy. This project, sponsored by the Atomic Energy Commission, was designed as an experimental test with high explosives in salt of the decoupling theory published by *Latter, LeLevier, Martinelli, and McMillan* [1961].

The idea, in brief, is that the coupled or tamped explosion causes the surrounding medium to flow plastically, crack, and behave nonlinearly until the wave has propagated far enough out for the stress to be reduced to a 'critical stress' (dependent only on medium characteristics and depth) at which time elastic propagation begins. If, however, the explosive is placed in a hole just large enough for the critical stress to occur on the walls, the radius and volume of the hole are much smaller than the radius and volume at which the tamped shot reaches the critical stress. For the low frequencies of interest, the amplitude of the seismic waves radiated away is directly proportional to the product of stress and volume at the critical radius. The spherical cavity,

having a much smaller volume at critical stress than the tamped case, radiates a much smaller seismic wave.

At large distances, *Latter, LeLevier, Martinelli, and McMillan* [1961] predict that the wave amplitude from a tamped nuclear shot in tuff is 300 times the wave amplitude from a nuclear shot in a cavity in salt. In the Cowboy experiment we are comparing amplitudes from tamped high-explosive shots in salt to those from high-explosive shots in a cavity in salt. Experimental measurements from tamped explosions are required in the prediction of the amplitude or decoupling ratio. Since no such measurements were available prior to Cowboy, it was not possible to predict the Cowboy results.

Seismic records which illustrate the decoupling effect are presented in Figure 1. The six traces show signal amplitude (particle velocity) versus time for six different seismometers located 200 feet apart, starting at 44,600 feet. In the upper panel a 1000-pound tamped shot is clearly seen. In the lower panel a 1000-pound shot in the 30-foot-diameter sphere gives no visible signal despite the fact that amplifier gains have been increased by a factor of 8.

To obtain a quantitative measure of the decoupling it is necessary to use seismograms taken near enough so that the decoupled shot

¹ Project Cowboy was sponsored by the Atomic Energy Commission and carried out under the technical direction of the Lawrence Radiation Laboratory, University of California.

gives a measurable signal. In Figure 2 records taken at 14,400 feet are reproduced. The signal from the decoupled shot has been amplified by a factor of 64 relative to that from the tamped shot. Since the amplitude of the tamped signal (at the dominant frequency of 30 cps) is roughly 50 per cent larger than the sphere signal, a decoupling ratio of about 100 results.

In this report we examine the dependence of decoupling on the various parameters of the experiment. We have answered the following questions. Can the different seismic waves be identified as to path traveled in the particular geologic environment of the experiment? (Yes.) Does the decoupling depend on wave type? (Yes.) Which wave is least affected by local geology and shot location so that it can be extrapolated out of the particular geologic environment? (The so-called 'direct' wave.) What is a reasonable range of decoupling for this wave? (90 to 125, although extraneous values ranging from 60 to 200 can be found for specific shots and geophones.) What causes this variation? (Geology, shot location differences, and non-reproducibility of shots.) Does decoupling change if the pressure due to the explosive is changed? (No, not as long as the walls remain elastic.)

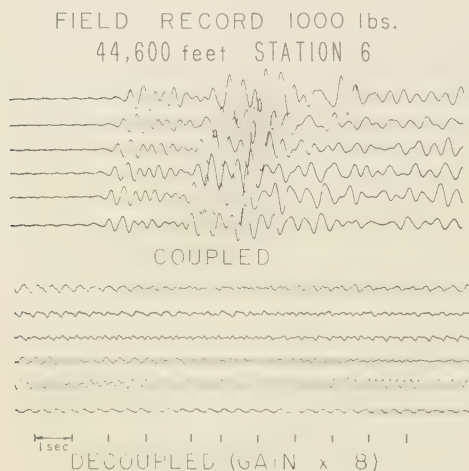


Fig. 1. Seismograms recorded at station 6. The seismometers are 200 feet apart and are in-line with the shot point, the first one at 44,600 feet. The coupled record is from shot 11, 1003 pounds of Pelletol. The decoupled record is from shot 10, consisting of 954 pounds of Pelletol in a 30-foot-diameter sphere in salt.

FIELD RECORD 1000 lbs.
14,400 feet STATION 4

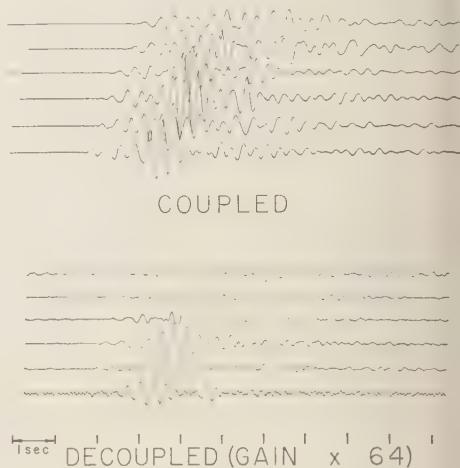


Fig. 2. Same shots as Figure 1, but recorded at station 4 located 14,400 feet from ground zero.

What happens at lower frequencies? (The data show that the decoupling remains essentially constant.) Are these results consistent with the measurements made close in? (Yes.) What happens if a small sphere is used and the elastic limit is exceeded? (The decoupling reduces to 25 and is even smaller at lower frequencies.)

THE PLAN OF THE EXPERIMENT

Salt was chosen as the test medium because the theory predicts a large decoupling factor for a cavity in salt, and salt cavities are easier to excavate than cavities in other strong media. Arrangements were made with the Carey Salt Company to use its salt mine at Winnfield, Louisiana. The shots were located in the unused northeast workings of the mine which are sketched in Figure 3. These workings are 800 feet below the surface.

The spheres were dug with diameters of 30 and 12 feet. The $2\frac{1}{2}$ -ft-diameter doors to the spheres were made of steel and were sealed with rubber gaskets. The plan was to detonate high explosive located in the center of one of the spheres, record the seismic waves, wait 15 minutes, detonate the same weight of explosive in a tamped hole, and record again. These paired

shots are connected by lines as shown in Figure 3.

Typically, the tamped holes were made in the following manner. An 8-inch shaft was drilled 110 feet down from the mine floor. The bottom 3 feet was reamed to a 2-foot diameter and filled with the appropriate amount of Pelletol explosive. The hole was then grouted to the surface. Instruments designed to measure particle velocity and acceleration were placed within the mine at distances ranging from 40 to 800 feet from the shots. The pressures inside the spheres were also recorded. This work was done by Sandia Corporation [Murphey, 1961], the Bureau of Mines, and representatives of the United Kingdom.

Surface seismic stations were set up at various intervals ranging out to 30 miles. Records from stations directly over the dome are not useful because of the large shot separation within the dome. Useful records for the decoupled shots were obtained at stations 4 and 5 at ranges of 14,400 feet and 22,100 feet from ground zero. The instruments were supplied by the National Geophysical Company and were of two types. The 'low frequency' instruments had a passband

from 2 to 20 cps. The 'high frequency' instruments had a passband from 20 to 100 cps. Benioff 1- to 3-cps seismographs were also used at these two stations but the only decoupled shot that gave a signal large enough above the noise to be useful was a 2000-pound overdriven sphere shot. The surface seismic instrumentation was supervised by the U. S. Coast and Geodetic Survey [Carder and Mickey, 1960; see also Adams and Allen, 1960].

THE THEORETICAL SEISMOGRAMS

A difficult part of the interpretation was to estimate what effect the particular Winnfield, Louisiana, salt dome and surrounding geology had on the measurements. If geology is not considered, the data seem to have large variation. With even a crude geologic model and rough calculation, however, much of this variation can be understood with fair assurance of reproducibility of results if the experiment is repeated elsewhere.

A discussion of the procedure for making a theoretical seismogram has been placed in the Appendix. For our purposes here, we shall mention only the method and the results so that we can proceed with the interpretation of the seismic data.

The first step in making a theoretical seismogram is to construct a geologic model. Data from oil wells in the vicinity are insufficient to delineate the edge of the salt dome, so we assume a 'possible' salt dome configuration. Hence, the theoretical seismograms show typical behavior rather than actual behavior. Nonetheless, we believe them to be useful in the interpretation.

The calculation is simplified by first computing the response of the model to a δ -function or impulse source. The results are shown in Figure 4. The series of impulses received are identified by the name of the deepest geologic formation that they have passed through.

We convolve this impulse response with assumed equivalent source functions for the tamped and sphere shots to produce theoretical response records for the equivalent sources. In view of the crude geologic model, we do not deem it worth while to derive equivalent source functions from the information that was available concerning the actual source waveform, the attenuation, and the instrument response. The waveforms assumed for the tamped and sphere shots are given

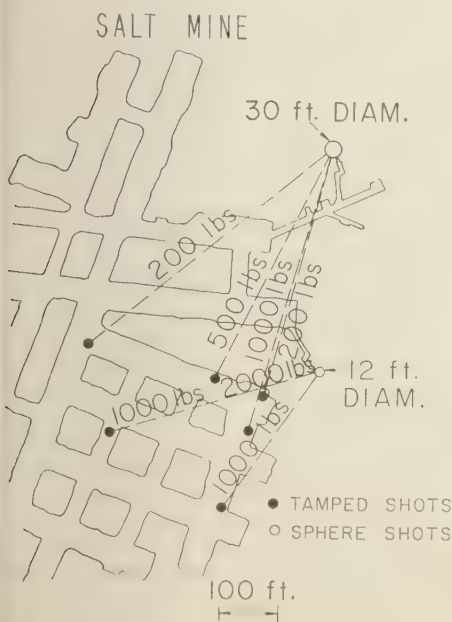


Fig. 3. Subsurface plan of the northeast workings of the Carey Salt Mine at Winnfield, Louisiana. The coupled and decoupled comparison shots are connected by dashed lines.

THEORETICAL SEISMOGRAMS

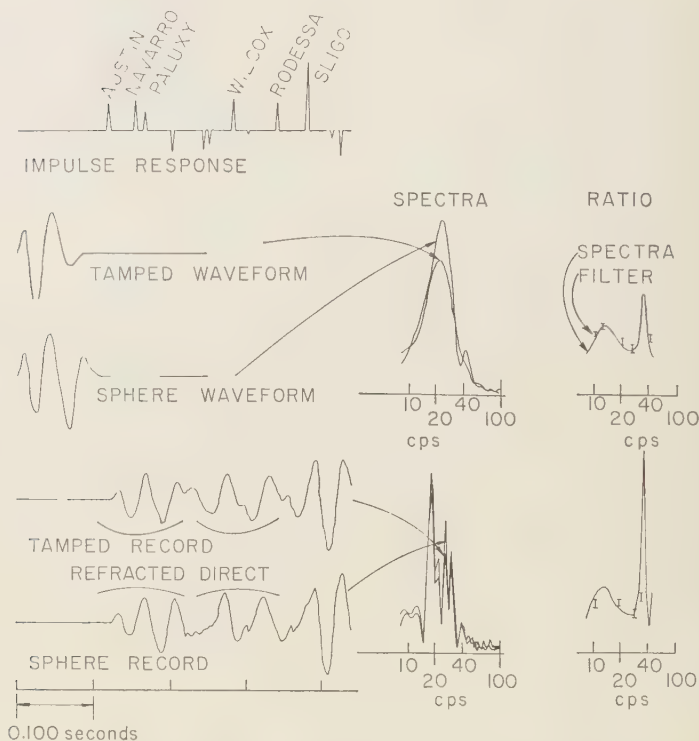


Fig. 4. Theoretical seismograms used to illustrate interpretation problems. Within the passband the ratio of the spectra of the records is equal to the ratio of the spectra of the assumed source waveforms.

in Figure 4. The ratios of their spectra are merely illustrative and are not to be construed as a prediction of the frequency dependence of decoupling. The two lower left panels of Figure 4 show the theoretical records obtained by convolving the impulse response with the two assumed waveforms. In the next several sections, these theoretical seismograms will be used in the interpretation of the experimental records.

PROBLEMS IN THE INTERPRETATION

Identification of the major arrivals. Figure 5 shows a plot of the experimental records in the digital form. In a program of this nature it was thought useful to cover the frequency range of interest with different instruments. It is unfortunate that the frequency band of major interest, 10 to 40 cps, straddled the crossover frequency of 20 cps between the two sets of

instruments referred to as 'high frequency' and 'low frequency.'

Three bursts of energy can be identified on all six of the displayed records. A time correlation of these bursts with the impulse response identifies the first as that due to refractions by the Austin Chalk, Navarro, and Paluxy formations (the geologic model is shown in the Appendix). The second burst is primarily due to refraction by the Wilcox formation and will be called the 'direct' arrival since the energy travels out essentially horizontally, directly to the receiver, merely refracting up through the weathering layer. The third burst is believed due to refractions from the Rodessa and Sligo formations. Purely reflected waves, which have not been calculated, probably also come in at this time. No easily identifiable surface waves appear on the records.

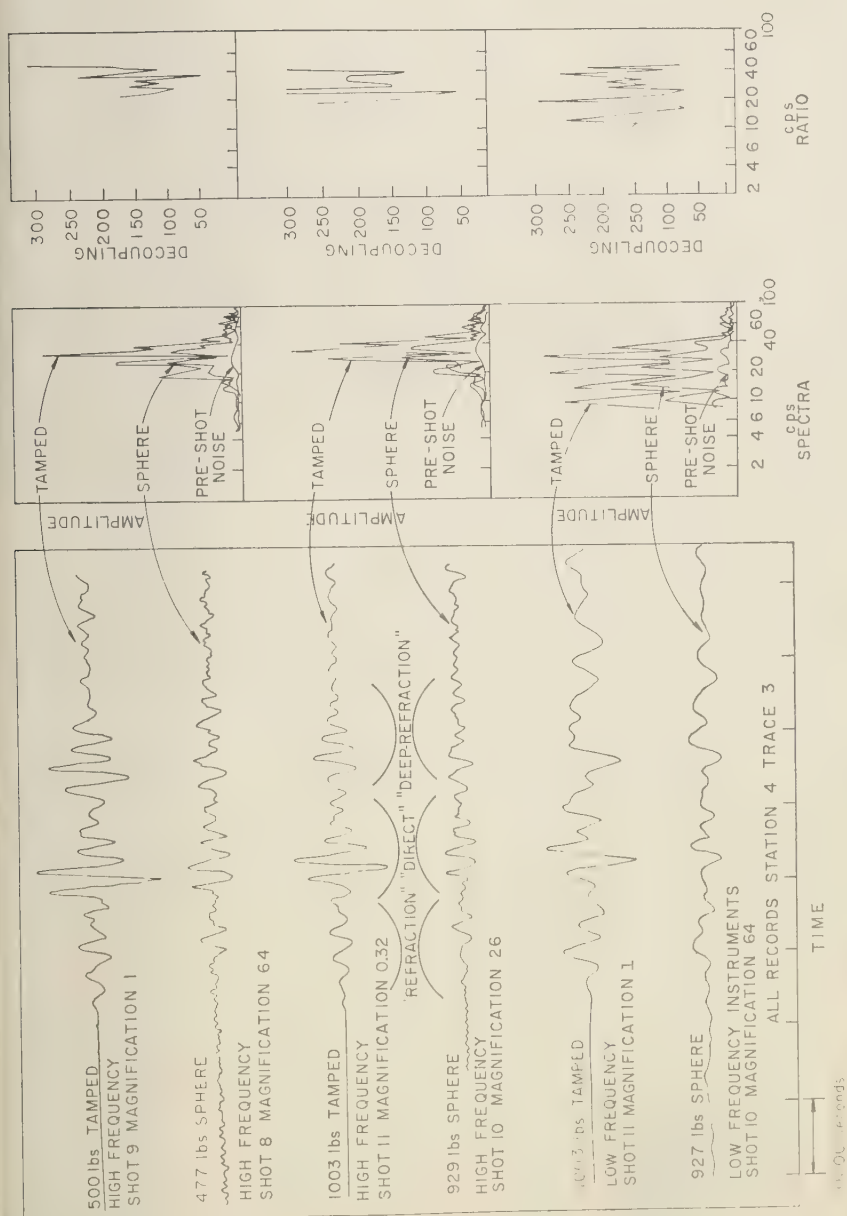


Fig. 5. Experimental records at station 4. The magnification of the high frequency instruments is relative to the 500-pound tamped shot. Likewise the magnification of the low-frequency instruments is relative to the 1003-pound tamped shot. The tamped spectra have been plotted at reduced scale so that geologic effects can be more clearly seen. The ratio of tamped to sphere spectra is called decoupling.

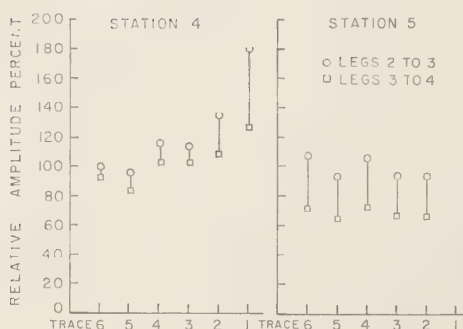


Fig. 6. Theoretical trace-to-trace variation in decoupling for the refraction arrivals. The traces are 200 feet apart. The circles are measurements from the second to third leg (trough to peak) and the squares from third to fourth. The variation is relative because actual source functions have not been used. The trends indicate the trace-to-trace variation that can be caused by geologic factors.

Although the energy bursts seen on the experimental records can be observed on the theoretical records, the detailed comparison is poor. This is to be expected since we are dealing with a boundary value problem in wave propagation in which the field (seismic record) is known at a few points, the actual boundaries are unknown (the model is only a first approximation), and the source function is to be determined. Such a problem, in principle, is theoretically indeterminable.

But the experiment must be interpreted with the effects of geology considered if we wish the results to have meaning for other locations. Despite a lack of detailed agreement between the experimental and theoretical records, we can still use the theoretical records profitably in the interpretation because they represent the types of complications introduced into the interpretation by the geology. The geologic model and the theoretical records do identify the wave types, do explain the structure of the spectra, do predict trace-to-trace variation of decoupling, and do aid in understanding the scaling problem.

The effect of geology on the Fourier spectra. The Fourier spectra of the field records are shown in Figure 5. In a later section we examine in some detail the spectra of the outgoing wave in the salt from both the sphere and tamped shots. No sharp, dominant peaks or troughs occur below 30 cps in either wave, and we must therefore

conclude that all the structure in the spectra analysis is caused by the geology.

Such structure is indeed evident when the theoretical records are examined by Fourier analysis (Fig. 4). The Cowboy experiment was designed to give information about the source from the distant seismic signals. Yet we find that virtually all the complexities in the spectra and the manifold arrivals in the time domain are due to the geology. This complication in the interpretation is no surprise to seismologists.

In principle, taking a ratio of tamped to sphere shot spectra cancels out the geologic effects and leaves only the source effects, provided, of course, that the two impulse responses are identical. In Figure 4, the ratio of the assumed tamped to sphere source functions is shown, as well as the ratio of the theoretical records. In the passband the two ratios are equal. Out of the passband the ratios of nearly zero quantities give wild answers. Higher precision in the digital analysis undoubtedly would bring these ratios into agreement.

The ratios of the experimental records are given in Figure 5. Even in the passband wild numbers occur. The preshot noise spectrum has been calculated, and in these cases it is too small to cause the wild answers. The explanation appears to be that the impulse response for the tamped shot is not identical to that of the sphere shot. Tamped and sphere shots were located some 500 feet apart in the mine (over a quarter of a wavelength at 10 cps; see Fig. 3). It is reasonable

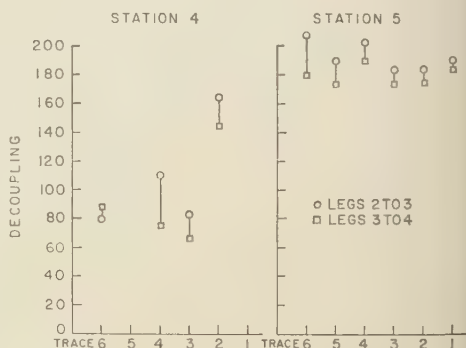


Fig. 7. Experimental trace-to-trace variation in decoupling for refraction arrivals. The decoupling is calculated from shot 11 (1003 pounds tamped) and shot 10 (954 pounds in the 30-foot-diameter sphere).

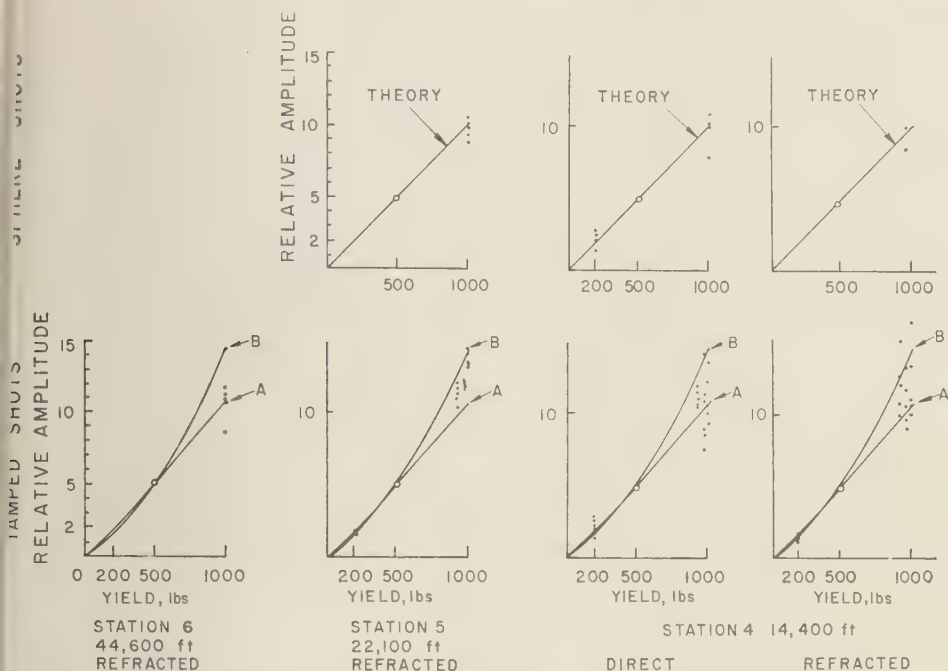


Fig. 8. Summary of seismic amplitude scaling relative to charge size. The data have been normalized to the 500-pound shots at an amplitude of 5. Amplitudes from tamped shots 11, 13, and 15 have been plotted at 1003, 987, and 936 pounds, respectively. The theory cited for sphere shots is for elastic propagation away from a spherical hole. Curves A and B are scaling deduced from the measurement of shot 11 at a range of 80 feet.

to believe that this shift in location can change the impulse response of one shot relative to the other so that the impulse responses do not cancel out in taking a ratio. The theoretical seismograms show that the impulse response controls the structure of the spectra. A small shift of a peak or trough will yield a wild ratio.

An alternative to Fourier spectrum analysis to obtain decoupling is narrow-band filtering. Figure 4 shows that the ratio of the two theoretical records, narrow-band filtered, is the same as that of the two filtered source functions. Filtering, being a smoothing process, does not yield wild decoupling ratios. Furthermore, filtering has an additional advantage over spectrum analysis because, if the waveforms of the filtered sphere and tamped records do not agree reasonably well, noise can be suspected and the point downgraded accordingly in the interpretation.

The high-frequency records themselves are approximately equivalent to narrow-band filter-

ing at 30 cps (see Fig. 5). The high frequency cutoff is controlled by attenuation in the medium, the low by instrumental limitations. Direct analysis of the high-frequency records (Fig. 1) is satisfactory and quite convenient.

The results at 30 cps have particular significance, since 30 cps from 1000 pounds of high explosive scales to about 1 cps for 15-kiloton nuclear shots. (Time scales as the cube root of the yield, as we shall see in a later section.) The first motion of seismic waves at about 1000 km from a 15-kt underground nuclear detonation is at a frequency of about 1 cps and was recognized by the Conference of Experts in Geneva as the principal means of both locating and identifying underground nuclear tests.

Trace-to-trace variation of decoupling. We next examine the variation of decoupling with trace or geophone location. The impulse response for each trace has been calculated for both station 4 and station 5. After convolving these responses

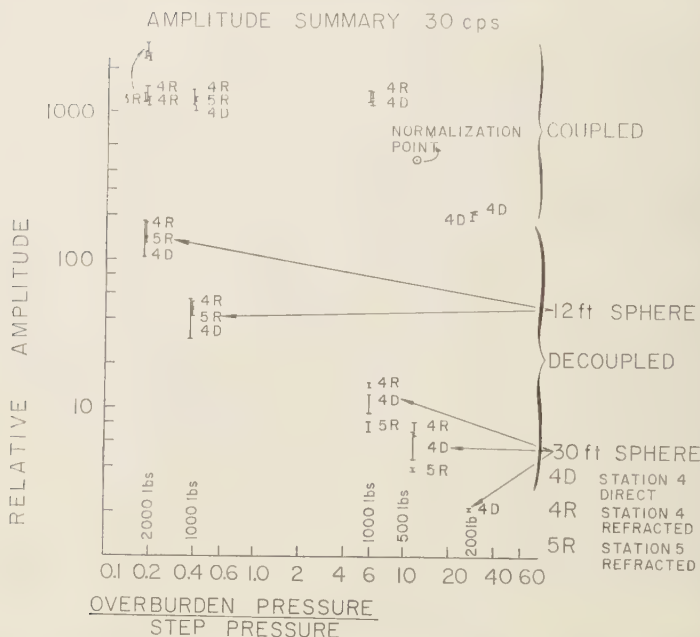


Fig. 9. Amplitude summary at the dominant frequency. The amplitudes of paired coupled and decoupled shots are plotted against the ratio of overburden pressure to step pressure for the sphere shots. The step pressure is the pressure existing in the sphere after the transient spike has passed. The nominal weights of explosives are shown. The arrow indicates that the value for the 1000-pound shot should be doubled before a decoupling factor for the 2000-pound sphere is computed.

with the assumed source functions, we calculated the amplitude ratio of the refraction arrivals. Of course, only the relative value or variation was deduced.

The results are plotted in Figure 6. A large trace-to-trace variation is seen for station 4 and essentially no variation at station 5, although the absolute answer depends on which particular legs, or peak and trough, are picked for the calculation. The effect of the guided waves is more important for station 5, since it is farther away. For that reason, the impulse response at station 5 is less complete.

The experimental trace-to-trace variation is shown in Figure 7. A large variation occurs for station 4 and very little for station 5, just as was predicted theoretically.

Station-to-station variation of decoupling. The experimental data in Figure 7 point out still another problem. Station 5 decoupling values for the 1000-pound shot are significantly higher than the station 4 values. The problem is demon-

strated by plotting the amplitude against charge size for the various arrivals at the various stations (Fig. 8). The data have been normalized to the 500-pound shot to eliminate trace-to-trace variation.

The decoupled shots follow a first-power scaling law rather well. In a later section we shall show that a first-power law is correct.

The scaling of the tamped shots is not as simple. We should expect shots 11, 13, and 15 (1003, 987, and 936 pounds, respectively) to scale the same way at each station, yet they do not. Shot 11 at station 5 is particularly inconsistent. The energy arriving at the various stations leaves the shot at different solid angles. It may be that the different shots produce different amounts of low-frequency energy in the various solid angles pertinent to the measurements at the distant stations. This point will be explored further in a subsection on tamped shots.

Differences in shot location may also be partially responsible for the station-to-station

discrepancies. In the Appendix it is shown that the refracted rays approach grazing angles on the dome walls. Transmission coefficients change rapidly with angle under such conditions. Shots 11, 13, and 15 are over a quarter of a wavelength apart in the dome (see Fig. 3) and, for certain dome configurations, we believe there is enough change of the angles to get a significant amplitude change with change in source location. We have already seen that location differences of 500 feet between tamped and sphere shots are important enough to produce wild decoupling ratios. Curves A and B for the tamped shots show scaling deduced from close-in measurements. Discussion of these curves is reserved until later (see section entitled 'Comparison with close-in data.')

The direct wave to station 4 should be the least affected by location differences of the shot points since the energy propagates out of the dome at normal incidence. We conclude that the station-to-station and trace-to-trace variations in decoupling are a manifestation of the particular wave path and shot location in the Winnfield geology. Decoupling ratios of paired shots are valid but apply only to the particular circumstances of the Cowboy experiment.

It is highly desirable to obtain a decoupling value independent of the Winnfield geology. Since we cannot theoretically reproduce the experimental seismograms, we attempt to average out the geologic effect before taking decoupling ratios.

DECOUPLING FOR THE DOMINANT FREQUENCY

In the scaling study in the last section the importance of studying the amplitudes of the tamped and sphere shots separately before taking ratios has been pointed out. The high-frequency data are summarized in Figure 9. Traces 3, 4, and 5 are used for station 4, and traces 1 and 6 for station 5. These are the most noise-free traces on all the records. The amplitudes have been normalized by trace number to the 500-pound tamped shot. Large spreads occur in the sphere shots; however, if a sphere shot had been chosen for normalization, large spreads would also have occurred in the tamped shots.

The decoupling is summarized in Figure 10. The circles are the ratios of the mean values of the direct wave at station 4. These are considered best values because they are least affected by

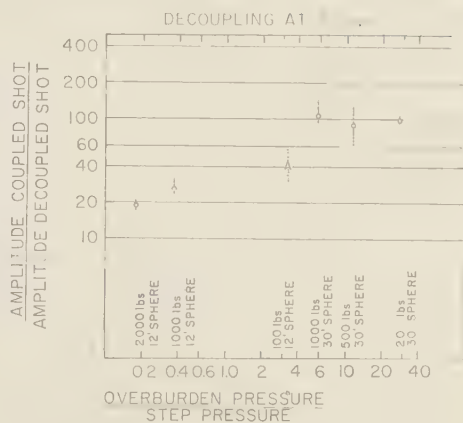


Fig. 10. Decoupling summary at the dominant frequency. The ratios of the mean values of the direct arrivals at station 4 are given as circles indicating best values. The A indicates that the shot was recorded only at a temporary station, 5000 feet away. The pressure ratio must be greater than 5 for the latter decoupling theory to apply.

changes in shot location and have the highest amplitudes. We arbitrarily define the range by taking the ratio of the two maxima to the two minima for a pair of shots given in Figure 9. The results should be less dependent on the local geologic influence that affects the paired-shot method of computing decoupling. An exception to this method has been made for the 100-pound shot in the 12-foot sphere. A temporary station was set up at a distance of 5000 feet for this shot, and a direct ratio was taken.

The amplitudes and decoupling factors have been plotted against the ratio of overburden to step pressure. The overburden pressure is due to the weight of the rock above, which places the sphere in a state of initial preshot compression. The step pressure (\bar{p}) is the pressure that the hot gases exert against the walls of the sphere after the initial spike has passed. This pressure ratio is equivalent to a volume-to-yield ratio.

If there were no spike, the walls of the sphere would remain elastic for a pressure ratio greater than 1 (i.e., for $\bar{p} < \rho gh$) where ρ is the density, g is the acceleration due to gravity, and h is the depth. In the past a pressure ratio of 2 (i.e., $\bar{p} < \rho gh/2$) has been considered as safe for nuclear explosions even with the spike. However,

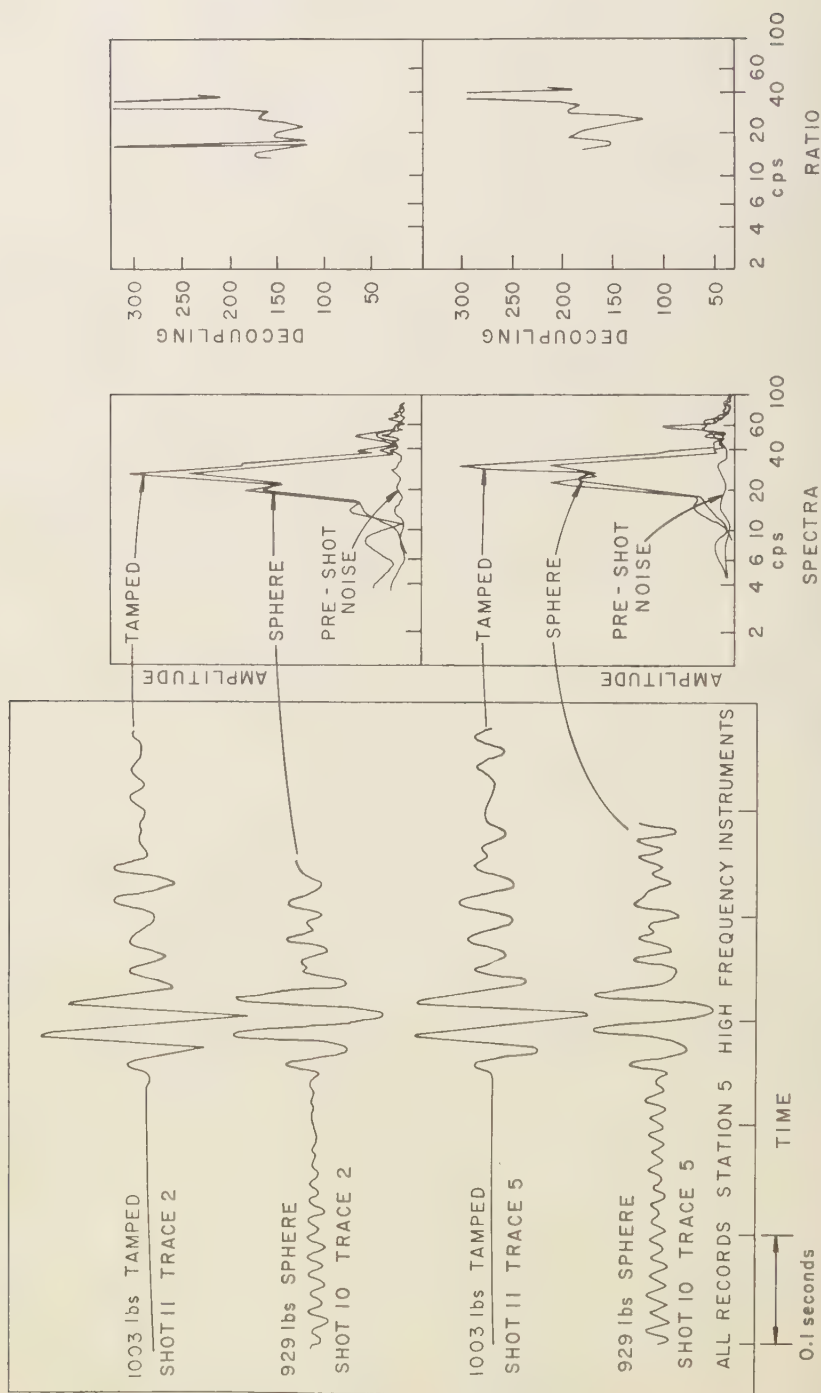


Fig. 11. Records for station 5 located 22,000 feet from ground zero.

the spike for high explosives has greater momentum than for nuclear explosives, and A. Latter (private communication) has noted that a ratio of 5 (i.e., $\bar{p} < \rho gh/5$) may be necessary to insure completely elastic behavior for Cowboy.

The experimental data show that there is no significant change in decoupling if the pressure ratio (or volume-to-yield ratio) exceeds the critical ratio for keeping the walls elastic. This result is in accord with the decoupling theory.

The decoupling for overdriven or nonelastic sphere shots cannot be calculated by using linear theory. Experimental values are shown in Figure 10. Since it was not practical to shoot a 2000-pound tamped shot in the mine, the nominal decoupling for the 2000-pound sphere shot was obtained by doubling the amplitude of a 1000-pound tamped shot. Until the phenomenon of the overdriven sphere is understood, the validity

of any extrapolation to other situations is uncertain.

FREQUENCY DEPENDENCE OF DECOUPLING

The decoupling values given in the last section are for the dominant frequency on the high-frequency records, namely 30 cps. It is interesting to determine what happens to these values at lower frequencies.

A low signal level prevents the use of the low-frequency records at station 5. Attempts to obtain low-frequency information from the high-frequency records at station 5 lead to problems as illustrated in Figure 11. The spectra are cut off abruptly on the low side, partly because of the instrumental cutoff but also partly by a geologically caused minimum in the spectra.

Data from the low frequency instruments at station 4 are the best hope of obtaining decoupling

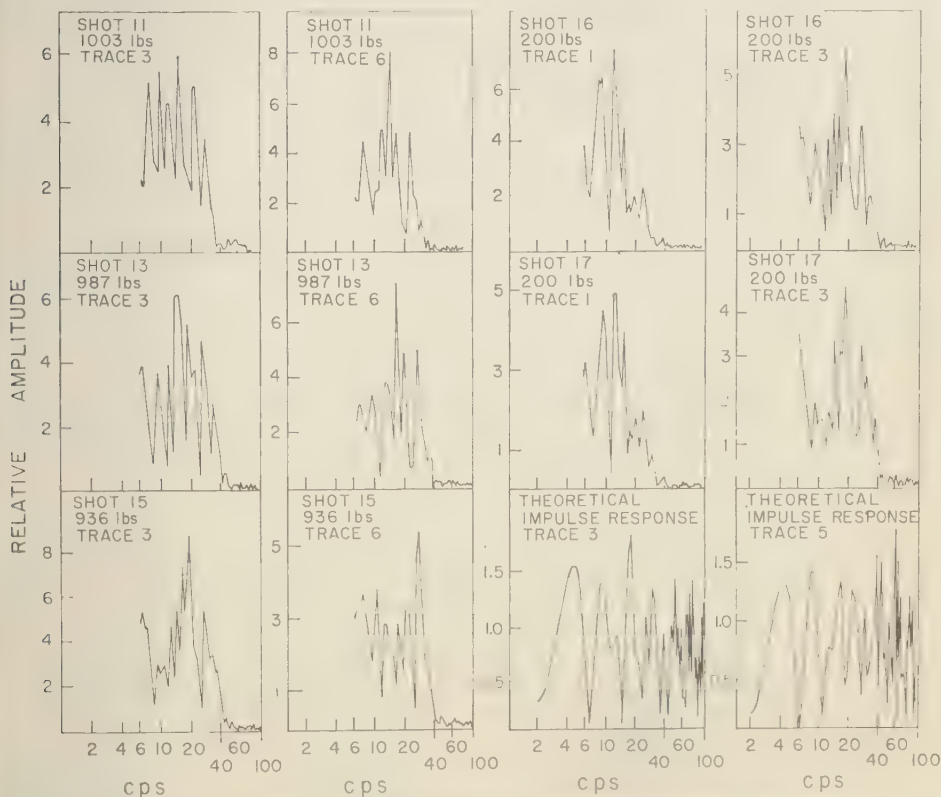


Fig. 12. Comparison of Fourier spectra for station 4, low-frequency instruments, and a comparison of two theoretically computed impulse responses.

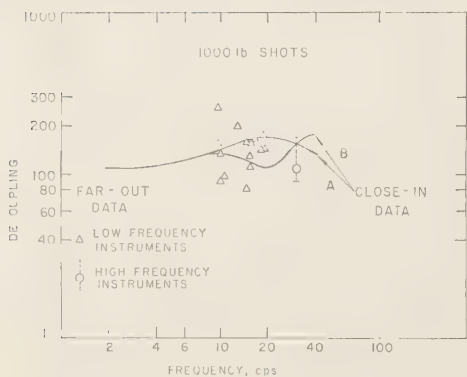


Fig. 13. Frequency dependence of decoupling showing the comparison of close-in and far-out data (shots 11, 1003 pounds, and 10, 954 pounds). The data from the high-frequency instruments have been replotted from Figure 10. The data from the low-frequency instruments are from station 4.

at low frequencies. Low-frequency spectra of various shots at station 4 are presented in Figure 12. A problem of reproducibility is immediately apparent. Shots 11, 13, and 15 did not have identical charge configuration but shots 16 and 17 did, and yet variations occur. As an explanation we offer the observation that shots 16 and 17 were located 330 feet apart, which is almost $\frac{1}{4}$ of a wavelength at 10 cps. This same effect could have been operative for the 1000-pound shots. Shots 13 and 15 are separated from shot 11 by 140 and 250 feet, respectively. As was mentioned earlier, it is probably the proximity of the dome edge which makes the effect so large. The disturbing aspect is that even for the same trace number the trends are not reproducible.

The lack of reproducibility from trace to trace can be demonstrated by spectral analysis of the impulse responses for two traces located 400 feet apart. As is shown in Figure 12, maxima and minima are materially shifted.

This lack of reproducibility in the data is discouraging, but it is still worth while to see if a trend can be established for the decoupling variation with frequency. As before, we shall use narrow-band filtering and pair each of the 1000-pound tamped shots with the 1000-pound decoupled shot to produce a decoupling ratio. The result is shown in Figure 13. Only two traces of the decoupled shot are sufficiently free of

noise to be valid. The data are widely scattered and give no indication that the decoupling decreases at lower frequencies. The A and B curves are deduced from close-in measurements and will be discussed in a subsection on tamped shots.

The frequency dependence of decoupling for the overdriven sphere is shown in Figure 14. Both the 1000- and 2000-pound shots show that decoupling decreases at lower frequencies. The 2000-pound shot gave usable signals at lower frequencies because the decoupling was less. Experimentally, we see the decoupling leveling off at low frequencies to a value of about half that obtained at 30 cps.

Both the 1000- and 2000-pound shots caused the sphere to be vented through the sphere plug. The gas from the 1000-pound shot leaked through a break in the plug gasket but instruments near the plug showed that this happened sometime after 1 second from shot time and hence would not affect the signals. The 2000-pound shot

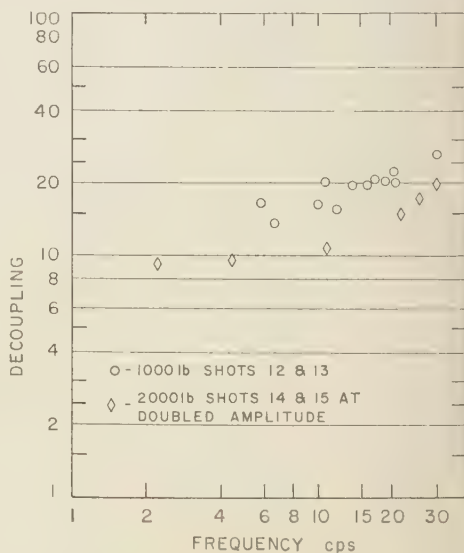


Fig. 14. Decoupling for overdriven spheres. The values at 30 cps are from Figure 9. Other values of shots 12 and 13 are from narrow-band filtering of data taken from the low-frequency instruments at station 4. Values below 5 cps for shots 14 and 15 come from the Benioff seismographs at stations 4 and 5. The remaining values are from the low-frequency instruments at stations 4, 5, and 6.

destroyed the plug sometime after 0.1 second from shot time. If the sphere vented rapidly at about 0.1 second, the signal would be altered. Although this possibility cannot be ruled out, we can find no evidence of it in the records.

The fact that sizable decouplings were obtained when the sphere was overdriven is significant. If this result can be extrapolated to nuclear yields, it means that a sizable decoupling can be obtained with a volume much smaller than previously considered.

COMPARISON WITH CLOSE-IN DATA

Decoupling theory. The decoupling theory may be illustrated in the following way. Near an explosion, but beyond some elastic radius r_e , we assume that the motion can be represented approximately by the elasticity equations for a spherically symmetric infinite material. Then a 'reduced' displacement potential $A(\tau)$ can be defined by

$$u(r, t) = \frac{\partial}{\partial r} \frac{A(\tau)}{r} \quad (1)$$

where $\tau = t - r/c$, and $u(r, t)$ is the displacement. It can be shown that $A(\tau)/r$ represents elastic outgoing waves. The Fourier transform is

$$\hat{u}(r, \omega) = -(1/r^2 + i\omega/rc) \hat{A}(\omega) \quad (2)$$

$\hat{A}(\omega)$ is a convenient quantity since it is independent of r .

The distant signal will be given by

$$S(\tau) = \mathbf{O} A(\tau) \quad (3)$$

where \mathbf{O} is some operator representing the earth. After transforming,

$$\hat{S}(\omega) = \hat{\mathbf{O}}(\omega) \hat{A}(\omega) \quad (4)$$

The operator \mathbf{O} corresponds to the impulse response, attenuation, and instrument effects discussed in earlier sections.

Now if there are two explosions, 1 and 2, for which the conditions inside r_e differ but outside r_e are the same, then

$$\frac{\hat{S}_1(\omega)}{\hat{S}_2(\omega)} = \frac{\hat{\mathbf{O}}(\omega) \hat{A}_1(\omega)}{\hat{\mathbf{O}}(\omega) \hat{A}_2(\omega)} = \frac{\hat{A}_1(\omega)}{\hat{A}_2(\omega)} \quad (5)$$

Thus we see that the operator representing the earth cancels out as was demonstrated in Figure 4. Or for a tamped and a sphere shot, the decoupling factor is

$$D(\omega) = \left| \frac{\hat{S}_s(\omega)}{\hat{S}_t(\omega)} \right| = \left| \frac{\hat{A}_t(\omega)}{\hat{A}_s(\omega)} \right| \quad (6)$$

Since $i\omega \hat{A}(\omega)$ is a better-behaved function than $\hat{A}(\omega)$, we shall use

$$D(\omega) = \left| \frac{i\omega \hat{A}_t(\omega)}{i\omega \hat{A}_s(\omega)} \right| \quad (7)$$

In the decoupling theory \hat{A}_t is estimated from experiment and \hat{A}_s from elastic theory.

Since earth motions were measured near the Cowboy explosions by Sandia Corporation, one should be able to compare the distant decoupling factors with the close-in measurements. However, since the distant decoupling factors have a considerable experimental spread and since the close-in data are incomplete, one can only show consistency.

Sphere shots. The response of the 30-foot sphere should be completely elastic. The solution of the problem of the signal from an elastic spherical cavity driven by a pressure is given by several writers [Blake, 1952; Sharpe, 1942; Jeffreys, 1931]. For the 'reduced' potential, it is

$$i\omega \hat{A}(\omega) = i\omega \hat{p}(\omega) (a^3 K / \rho c^2) \cdot [1 + (1 - 2K)x^2 + K^2 x^4]^{-1/2} \quad (8)$$

where

$$K = \frac{1}{2} (1 - \sigma) (1 - 2\sigma)^{-1},$$

$$x = \frac{a}{c},$$

a = radius of sphere.

c = compressional velocity.

σ = Poisson's ratio.

ρ = density.

ω = circular frequency.

\hat{p} = Fourier transform of the driving pressure.

For the low frequencies of interest,

$$1 + (1 - 2K)x^2 + K^2 x^4 \approx 1$$

and therefore $i\omega \hat{p}(\omega)$ contains all the frequency dependence.

The pressure in the cavity may be written as

$$p(t) = p_s(t) + \bar{p}, \quad t > 0 \quad (9)$$

where $p_s(t)$ is a transient pressure spike and \bar{p} is the step pressure, given by

$$\bar{p} = (\gamma - 1) W / 4,$$

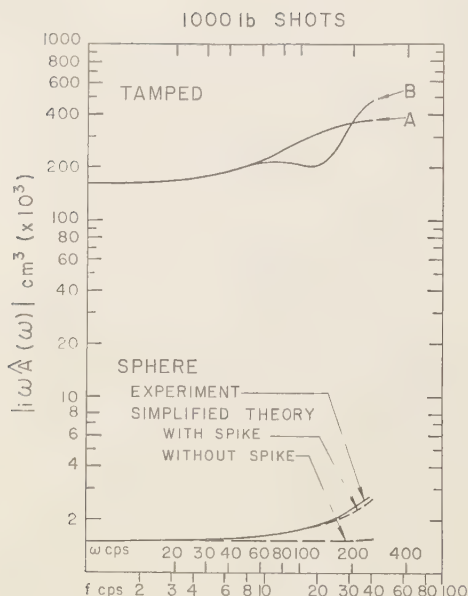


Fig. 15. $|i\omega\bar{A}|$ for the tamped and sphere explosions. The A and B curves are calculations from extrapolations of measurements at 80 feet (see Fig. 17). The measurement for the 30-foot-diameter sphere is calculated from the pressure record at the sphere wall for shot 10. The theory is given by equations 8 and 15.

where

V_s = the volume of the sphere.

W = the yield of the explosion.

γ = the ratio of the specific heats of the gases in the cavity.

For both air and low-density high-explosive combustion products, γ is about 1.2.

The Fourier transform of \bar{p} is $\bar{p}/i\omega$. For nuclear explosions the signal due to $p_s(t)$ is small at frequencies of interest, but for solid chemical explosions it is not. This is due to the large mass of explosive hitting the wall.

An approximate evaluation of $p_s(\omega)$ for low frequencies can be given by

$$\begin{aligned} \hat{p}_s(\omega) &= \int p_s(t) e^{-i\omega t} dt \\ &\approx \int p_s(t) dt, \quad \omega \text{ small} \end{aligned} \quad (10)$$

or

$$\hat{p}_s(\omega) \approx I \quad (11)$$

where I is the impulse on the wall.

Now if we equate I to the momentum per unit area of the high explosive,

$$I = \frac{\sqrt{2mW}}{4\pi a^2} = \frac{\sqrt{2W}}{4\pi a^2 \epsilon^{1/2}} \quad (12)$$

where ϵ is the specific energy of detonation, then

$$\hat{p}(\omega) = \frac{(\gamma - 1)W}{i\omega V_s} + \frac{\sqrt{2W}}{4\pi a^2 \epsilon^{1/2}} \quad (13)$$

and

$$\begin{aligned} i\omega \hat{p}(\omega) &= \frac{(\gamma - 1)W}{V_s} \\ &\cdot \left[1 + i\omega \frac{\sqrt{2a}}{3(\gamma - 1)\epsilon^{1/2}} \right] \end{aligned} \quad (14)$$

For the 954-pound explosion (nominal 1000 pounds) in the 30-foot sphere (shot 10),

$$i\omega \hat{p}(\omega) = 8.4[1 + i\omega(0.0053)] \text{ bars} \quad (15)$$

where $\gamma = 1.2$ and $\epsilon = 926 \text{ cal/g}$ for low-density TNT [Jones and Miller, 1948].

Equation 15 has been substituted into equation 8 and the results for the 1000-pound shot are shown as *Theory* in Figure 15. The pressure was measured [Murphey, 1961] in the sphere, and its time history is given in Figure 16. The step component averages to about 8 bars and the initial spike rises to 73 bars. Later spikes are reverberations in the sphere of the combustion products. The structure of the spike is thought to be an interaction between the combustion products and the small amount of residual air in the sphere. (The sphere was partially evacuated to eliminate burn-back and to reduce the size of the spike). The Fourier transform, $|i\omega\bar{A}|$, calculated from this pressure profile is shown as *Experiment* in Figure 15. The agreement between the measurement and the theory deduced from the momentum of the high explosive hitting the wall is good. The measured spikes have larger momentum than that in our simple calculation because of the reverberations of combustion products.

The experimental pressure record has been used to calculate the displacement at 80 feet. John Nuckolls, of our laboratory, has devised a machine code that numerically integrates the elasticity equations. The resulting theoretical displacement is shown in Figure 16 along with the measured displacement. Again the agreement is good.

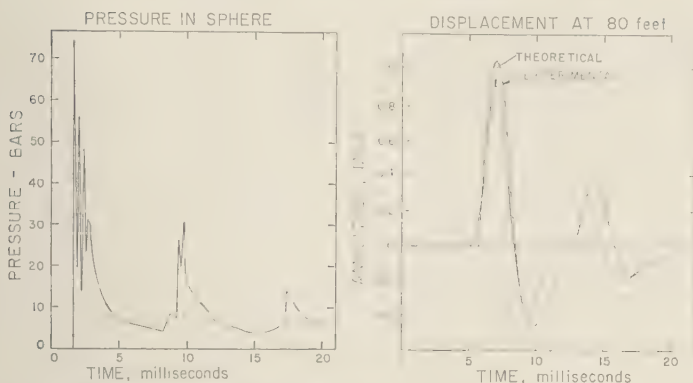


Fig. 16. The left panel shows the pressure recorded on the wall of the 30-foot-diameter sphere due to shot 10 (954 pounds). The theoretical curve in the right panel results from elastic calculations in which the pressure function is used as input. The experimental curve at the right results from the integration of a velocity instrument record located 80 feet from the center of the sphere.

Tamped shots. Figure 17 shows the displacement at 80 feet from two 1000-pound tamped shots. These displacements were obtained by integrating the velocity as measured by Murphey. The two measurements agree rather well at early times but not at late times. The same effect takes place with measurements on opposite sides of the 500-pound shot. Evidently there is asymmetry at later times on the records.

Postshot excavation of the area around one of the 1000-pound tamped shots showed an asymmetric crack pattern. Wright and Press (private communications) have both pointed out that shear-to-compressional wave ratios are larger for tamped than for sphere shots. Asymmetric motion about a tamped shot would tend to generate shear components. This asymmetry may be responsible for the fact that two 1000-pound tamped shots measured by the Benioff seismographs near 2 cps at both stations 4 and 5 differed in amplitude by a factor of approximately 2.

We have sketched two possible late-time extrapolations (A and B) for the tamped shots in Figure 17. These are meant to represent two possible average motions at 80 feet. The final value is the permanent displacement as computed from the measured increases in the volume of the hole.

The increase in volume for 100-, 500-, and 1000-pound tamped shots turned out to be about 0.065 ft³ per pound of explosive. This results in an average displacement of about 10 mils for the

1000-pound shot at 80 feet. The assumption is made that no void spaces in the medium are closed by the tamped explosion. We believe that this is a reasonable assumption since the volume which experiences pressures greater than the yield strength of salt should not contain enough void space to take up much of the 65 ft³.

Figure 15 shows $[\omega\hat{A}]$ for these curves, and the resultant decoupling is given in Figure 13. The two different extrapolations on the tamped data are so labeled. The results are completely consistent with the far-out data, giving values between 100 and 180. The asymmetry problem of the close-in tamped measurements causes the same degree of uncertainty in decoupling that we had already found in the far-out data.

Scaling laws. Equation 14 shows that for

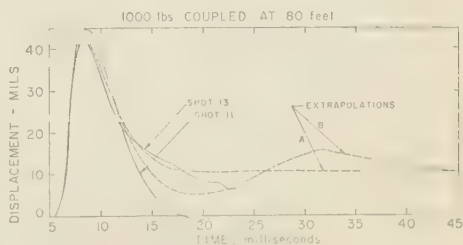


Fig. 17. Displacement at 80 feet due to shot 11 (1003 pounds) and shot 13 (987 pounds). Curves A and B are two different extrapolations of the experimental data to the final value at 45 milliseconds; the calculations were based upon consideration of the sizes of the holes.

sphere shots $\tilde{p}(\omega)$ is proportional to W . Hence, for the decoupled shots, $|\omega \hat{A}(\omega)|$, and therefore the distant signal at any given frequency, obeys a first-power law. The first-power law is compared with surface data in Figure 8, and adequate agreement is found.

For tamped shots more involved reasoning is necessary. For point sources of energy in infinite homogeneous media, one expects lengths and times to scale as $W^{1/3}$ if there are no characteristic distances or times. To state the law more exactly, if there are two explosions W_i and W_j with displacements $u_i(r, t)$ and $u_j(r, t)$, respectively, the scaling law is

$$u_i[(W_i/W_j)^{1/3}r, (W_i/W_j)^{1/3}t] \\ = (W_j/W_i)^{1/3}u_j[r, t] \quad (16)$$

Although no real explosions completely satisfy the stated conditions, there is much experimental evidence to indicate that the $W^{1/3}$ law is approximately satisfied close to the shot point. For the Cowboy experiment all the Sandia data for tamped shots approximately satisfy equation 16. If we set $\omega \hat{A}(\omega) = B_i(\omega)$ for a shot of yield W_i , then these laws imply that

$$B_i[(W_i/W_j)^{1/3}\omega] = (W_j/W_i)B_j[\omega] \quad (17)$$

Then for the distant signal (from eq. 5),

$$\frac{S_1(\omega)}{S_2(\omega)} = \frac{B_1[\omega]}{B_2[\omega]} = \frac{W_1}{W_2} \frac{B_2[(W_1/W_2)^{1/3}\omega]}{B_2[\omega]} \quad (18)$$

We now have the distant scaling law in terms of B for one reference yield.²

We have used equation 18 to derive the 30-cps

² It is interesting to examine these equations for the following simple assumptions concerning the time dependence of the source. If $A(t)$ can be considered a step function for the frequencies of interest, i.e., $B(\omega)$ is a constant, then $S \sim W$ will result—a first-power law. If $A(t)$ approximates a δ function, i.e., $B(\omega) \sim \omega$, then $S \sim W^{4/3}$.

These scaling laws have been examined for nuclear explosions by *Latter, Martinelli, and Teller* [1959], who used assumptions which are equivalent to ours. *O'Brien* [1960] has considered a first-power scaling law for chemical explosions. However, his assumptions do not seem to be consistent with the $W^{1/3}$ law close in. He assumes an effective elastic radius that is proportional to $W^{1/3}$; but, at that radius, he assumes a sharp pressure spike whose impulse is a constant for all yields. The $W^{1/3}$ scaling, which is experimentally observed in Cowboy, requires this impulse to scale as $W^{1/3}$.

scaling law for Cowboy from curves *A* and *B*. The comparison is made in Figure 8. The close-in and far-out data are again consistent.

Overdriven spheres. As indicated in Figure 9, the 200-, 500-, and 1000-pound explosions in the 30-foot sphere should have produced no inelastic response. However, the 1000- and 2000-pound explosions in the 12-foot sphere should have produced inelastic response.

The 100-pound shot in the 12-foot sphere is a borderline case. Cracking should have occurred only during the transient phase. Unfortunately the shot was detected only at a temporary station about 1 mile away and the decoupling factors there have a large spread. We do not know what the correct average is.

The 1000- and 2000-pound shots in the 12-foot sphere gave much useful surface data because they provided comparatively large signals. Although the sphere was intact after these detonations, many cracks were visible in the wall. The only crack which approximated a great circle was on the equator, but, since the velocity gages were on the equatorial plane, we believe they cannot be used for analyzing the motion around the sphere. Hence, we cannot compare surface data and close-in data for the overdriven sphere shots.

Significance of the results for nuclear shots. In the decoupling theory worked out by *Latter, LeVier, Martinelli, and McMillan*, the decoupling factor was the ratio of the signal amplitude from the Rainier nuclear explosion in tuff to the theoretical amplitude from a decoupled nuclear explosion of the same yield in a hole in salt. The predicted value was 300. In the Cowboy experiments small chemical explosives were used for the tamped shots as well as for the sphere shots in salt. Differences between chemical and nuclear explosions and the difference between tuff and salt for tamped explosions have not been theoretically calculated. Nor should one expect to be able to scale exactly tamped chemical explosions to nuclear explosions larger by factors of 10,000. For these reasons the Cowboy experiments were not expected to confirm or deny the key Rainier measurement.

However, one could hope for confirmation of the basic theoretical assumptions of the decoupling theory, namely, the conditions for the elastic behavior of the hole and for linear propagation to distant stations. Figures 16 and 13

verify these assumptions within the accuracy of the experiment.

Despite problems in scaling and differences in chemical and nuclear yield it is interesting to compare Cowboy tamped explosions with the current interpretation of Rainier.

For Rainier, $|\omega A|$ is approximately independent of frequency below 2 cps and is approximately 3 times as large as the value obtained by scaling the low-frequency limit of a 1000-pound tamped high explosive in salt to the Rainier yield.

In scaling high explosive decoupled shots to nuclear yields it must be remembered that the effects of the large spike caused by the high mass-to-yield ratio of chemical explosives would be absent. The $|\omega A|$ for a decoupled nuclear explosion in a cavity in salt would be approximately independent of frequency up to 2 cps at the very least and would have a value equal to that obtained by scaling the low-frequency limit of 1000-pound tamped high explosive in salt.

Hence $|\omega A|$ for both a tamped nuclear explosion in tuff and a decoupled nuclear explosion in salt is approximately independent of frequency up to 2 cps, and the ratio is equal to about 3 times the value (~ 300) obtained in the Cowboy experiment. We therefore expect both first motions (1 cps) and crustal surface waves (18-sec periods) to decouple.

It is more difficult to deal with the overdriven sphere problem because theory is not available to guide the discussion. We believe that the measured decoupling at the low frequencies of Figure 14 should be multiplied by 3 to allow for differences of tamped shots as explained above. At 30 cps an allowance should be made for the spike, and it is our opinion that decoupling should be multiplied by something less than 3.

CONCLUSION

The Cowboy experiment verifies the prediction made by Latter, LeLevier, Martinelli, and McMillan that seismic signals from explosions in cavities that yield elastically will be very small compared with the seismic signal from fully tamped shots. The surface measurements and the close-in measurements are consistent with one another and with the decoupling theory. The experiment shows further that, at least in these circumstances, an explosion in a sphere which is smaller than necessary to insure elasticity will still decouple.

APPENDIX. THE CALCULATION OF THE THEORETICAL SEISMOGRAMS

Formation of the geologic model. The first step is to form a geologic model—that is, a cross section of the earth showing the various rock strata extending from the Winnfield dome in a southwesterly direction along the line of seismic stations. Electric logs (*E logs*) taken from oil wells along this line are presented in Figure A-1. The identification of geologic horizons and the correlations have been made with the help of a stratigraphic section (located 8 miles to the north) published by the Shreveport Geological Society. The velocity information for the lower part comes from an interval velocity log (sonic) located 45 miles to the north. The velocities in the shallow beds are estimated. The velocities

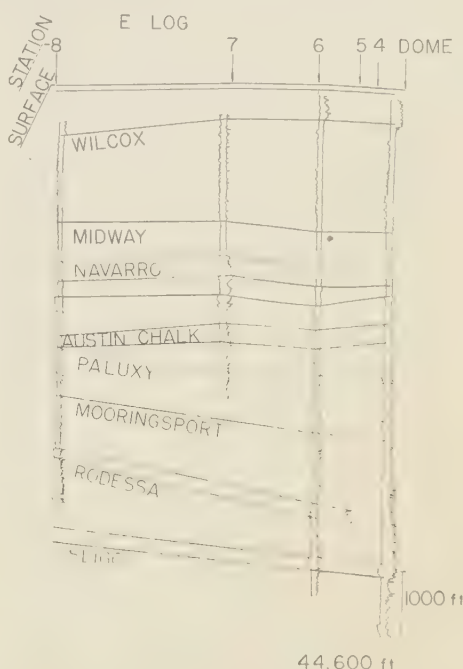


Fig. A-1. Electric Log Section along the line of seismic stations. Wells used, left to right, are Southern Prod. Co., #1 L.L.L.L. Co.; Fort Bend Oil Co., #1 Dunkleman; Hunt, #F-135 Goodpine; and Sinclair, #1 Louisiana Nebo. Correlations and formation identification have been drawn with reference to 'Structural and Stratigraphic Cross Sections' of the Publication Committee of the Shreveport Geological Society.

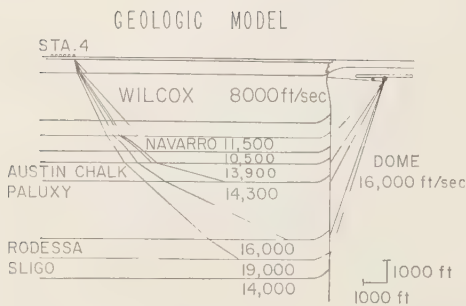


Fig. A-2. Geologic model for theoretical studies for station 4. The layering is from Figure A-1. Only paths of refracted compressional waves have been drawn. Waves that were converted to shear were also calculated. The rays emanate from the location of the 30-foot-diameter sphere. The dot to the left of the sphere represents the location of the tamped shots.

have been checked against velocity-depth functions for the area supplied by the National Geophysical Company, Inc.

Ideally, we should have a section made from interval velocity logs, but they do not exist. Since velocity is primarily dependent on porosity and since the resistivity measured by electric logs is also primarily dependent on porosity, the use of E logs in the model is not unreasonable. The division into strata is made primarily on the basis of common velocity rather than geologic formation.

Although tamped signals were received as far out as station 8, the decoupled signals (down in amplitude by a factor of 100) were not. Hence, we need a model giving the detail from the dome out to station 4 at 14,400 feet. The layering in Figure A-2 is taken from the E -log section (simplified for ease of calculation) and the distance to the edge of the salt dome from drilling records made by the Carey Salt Company. Undoubtedly, the actual geologic section is far more complicated. Faults and structural complexities surely exist in the vicinity of the dome. More log information is required for an accurate determination of the dip. This model is considered to be a first approximation to the actual geology.³

³ The Shreveport Geological Society has recently published a guide book which gives about a 20° slope (from the vertical) for the opposite side of the Winnfield dome.

Method of calculation. The model is far too complicated to allow us to entertain the idea of making an exact elastic-wave-equation calculation for the motion at station 4 due to an outgoing spherically symmetric wave originating in the dome. We use, therefore, the plane wave or ray-amplitude approximation. The first step in the calculation is to find the Green's function or response of the system to an impulse or δ -function source. This impulse response is then convolved with the source function, the attenuation function, and the function representing the effects of the instruments, or with a function representing the combined effects of all three.

The technique is approximate, because only an approximate impulse response is found by tracing rays. The rays start with unit amplitude. Changes in amplitudes caused by the geologic boundaries are computed by using the plane wave elastic transmission and reflection coefficients. The use of these coefficients is equivalent to the assumption that the wave fronts are locally plane when crossing boundaries. If a sufficiently large number of the higher-amplitude rays are calculated, an adequate approximation of the impulse response is obtained.

Spencer [1960] has shown how exact solutions can be expressed as sums of the plane wave solution and a correction term. The correction term for a given solution is small and can be ignored if the frequencies of interest are sufficiently high. Knopoff [1958] has obtained exact solutions and reduced them to an approximate solution which is the plane wave solution. The approximation is valid, provided the pulse duration is short compared with the total travel time involved. Low-frequency interface waves are ignored in any plane wave approximation.

Many oil companies have used this approximation in calculating theoretical seismograms for reflection prospecting (normal incidence only). One of us (Werth) has found good agreement between the actual field record and theory, when enough is known about the geology to insure that the interfaces are plane and parallel. Several examples are given by Wuenchel [1960].

Angle dependence must be included in our calculation. Furthermore, refractions, or head waves, require special treatment because a plane wave theory will not yield a head wave. Knopoff, Gilbert, and Pilant [1960], following Cagniard, have developed a first-motion approximation for

head waves (in two dimensions), which is equivalent to the plane wave approximation used for incidence at less than the critical angle. *Malinovskaya* [1957] outlined the Russian method of calculating an impulse response in their equivalent approximation. She presented moduli and phase angles for the various types of head waves.

Knopoff used the approximation to calculate a single-layer two-dimensional laboratory model record. He obtained a partial confirmation of the method as applied to non-normal incidence problems, but more rays should be calculated for a more complete experimental check. We know of no field application of the technique for non-normal incidence. However, ray-time (no amplitude) procedures have had outstanding success in outlining salt domes [*Musgrave, Wooley, and Gray*, 1960].

Theoretical seismograms. Physical insight is used in coding the problem for the required machine calculations. Basically, it is a refraction prospecting problem with the source complicated by the dome. A spherically symmetric longitudinal (P wave) source is assumed. The first arriving waves travel down the dome, spill over into the various layers, propagate in these layers, refract up, split into P and S (shear) components at each interface, and arrive at the surface, where they are recorded and reflected back into the section. These waves are followed by waves reflected from the surface above the dome and from the sides of the dome. Next come waves which have traveled more or less horizontally out from the dome in the lower-speed layers near the surface. Finally, waves from deep refractions and reflections arrive.

Since the geologic data poorly define the dome edge, it is pointless to labor the precise mechanisms by which the energy gets out of the dome and into the layers. Some of it is undoubtedly transmitted into low-velocity strata and then critically refracted. Other energy is transmitted directly from the dome into the refracting beds. We considered not only the ray paths in the dome shown on the model but also rays reflected from the back side of the dome and from the surface.

A complete solution should contain the wave guide effect of multiple reflections in the layers as the energy is propagated horizontally. The farther the energy is propagated, the more important is this effect. We did not attempt the

calculation, since the layers forming the guides do not have high velocity contrasts and since the distances propagated in them are short (at least for station 4). Furthermore, we would have difficulty in determining how the guides are excited, since we do not know the detail of the edge of the dome.

We do calculate all the rays that leave each of the beds as a critical refraction for either P or S . *Malinovskaya's* curves are used to give their relative amplitude. At every interface above the refractor, the waves split into new P and S waves. The transmission coefficients are used to calculate the amplitudes of all P - S splits all the way to the surface. All possible refractions for the actual source and for the surface-reflected and back-dome-reflected image sources have been calculated for a total of 2937 rays with their identifications, amplitudes, angles, and times. The vertical component of motion is computed and then plotted against time in the top panel of Figure 4.

Only twelve rays have sufficient amplitude to be plotted. Six have traveled as compressional waves all the way from the source. The other six are their surface reflections above the source. Although we do not question the importance of shear waves in a refraction problem [*Vasil'ev*, 1957], they have too low an amplitude to be of importance in this problem.

We have reflected these twelve P waves from the surface and again at each of the interfaces physically possible in the model. None of the resultant waves has sufficient amplitude to be plotted. Since the back-dome reflection has too low an amplitude, further internal dome reflections are unimportant. No attempt has been made to calculate the purely reflected arrivals.

The impulse response that results from this calculation is shown in Figure 4 and discussed in the section on theoretical seismograms.

Acknowledgments. Discussions with John Nuckolls were particularly helpful in developing a better understanding of tamped and decoupled sources. William Adams assisted in providing information about the field program. The several digital machine codes used were written by George Powles, David Brooks, Alex Cecil, and Frances Petersen.

This work was done under the auspices of the U. S. Atomic Energy Commission.

REFERENCES

Adams, W. M., and D. C. Allen, Seismic decoupling

- for explosions in spherical cavities, *UCRL-6086, Project Cowboy*, 1960.
- Blake, F. C., Jr., Spherical wave propagation in solid media, *J. Acoust. Soc. Am.*, **24**, 211-215, 1952.
- Carder, D. S., and W. V. Mickey, Seismic ground effects from coupled and decoupled shots in salt, *U. S. Coast and Geodetic Survey* (to be published).
- Jeffreys, H., On the cause of oscillatory movement in seismograms, *Monthly Notices Roy. Astron. Soc., Geophys. Suppl.* **2**, 407-416, 1931.
- Jones, H., and A. R. Miller, The detonation of solid explosives: the equilibrium conditions in the detonation wave-front and the adiabatic expansion of the products of detonation, *Proc. Roy. Soc. London, A*, **194**, 480-507, 1948.
- Knopoff, L., Surface motions of a thick plate, *J. Appl. Phys.*, **29**, 661-670, 1958.
- Knopoff, L., F. Gilbert, and W. L. Pilant, Wave propagation in a medium with a single layer, *J. Geophys. Research*, **65**, 265-278, 1960.
- Latter, A. L., R. E. LeVier, E. A. Martinelli, and W. G. McMillan, A method of concealing underground nuclear explosions, *J. Geophys. Research*, **66**, 943-945, 1961.
- Latter, A. L., E. A. Martinelli, and E. Teller, Seismic scaling law for underground explosions, *Phys. Fluids*, **2**, 280-282, 1959.
- Malinovskaya, I. N., On the methodology of calculating the dynamic characteristics of seismic waves, *Izvest. Akad. Nauk SSSR, Ser. Geofiz.*, **4**, 426-439, 1957.
- Murphey, B. F., Particle motions near explosions in halite, *J. Geophys. Research*, **66**, 947-958, 1961.
- Musgrave, A. W., W. C. Wooley, and G. Gray, Outlining of salt masses by refraction methods, *Geophysics*, **25**, 141-167, 1960.
- O'Brien, P. N. S., Seismic energy from explosions, *Geophys. J., Roy. Astron. Soc.*, **3**, 29-44, 1960.
- Sharpe, J. A., The production of elastic waves by explosion pressures, 1, Theory and empirical field observations, *Geophysics*, **7**, 144-145, 1942.
- Spencer, T. W., The method of generalized reflection and transmission coefficients, *Geophysics*, **25**, 625-641, 1960.
- Vasil'ev, Yu J., Study of alternating refracted waves in seismic prospecting, *Izvest. Akad. Nauk. SSSR, Ser. Geofiz.*, **3**, 301-318, 1957.
- Wuenchel, P. C., Seismogram synthesis including multiples and transmission coefficients, *Geophysics*, **25**, 106-129, 1960.

(Manuscript received November 9, 1960;
revised December 12, 1960.)

Geomagnetic and Solar Data

J. VIRGINIA LINCOLN

CRPL, National Bureau of Standards
Boulder, Colorado

INTERNATIONAL DATA ON MAGNETIC DISTURBANCES

This report continues the series which has appeared regularly in this JOURNAL since Vol. 54, No. 3, 295 (1949). Please refer to that first report for an explanation of the data given, and to Vol. 59, No. 3, 423 (1954) for the definition of *Ap*.

Note: Additional and final Geomagnetic and Solar Data appears in due course in the following international publications: "Quarterly Bulletin on Solar Activity," International Astronomical Union, c/o Eidgen. Steinwarte, Zurich, Switzerland; "IAGA Bulletins, Geomagnetic Indices *K* and *C*" by J. Bartels, A. Romaña and J. Veldkamp, International Union of Geodesy and Geophysics, Association of Geomagnetism and Aeronomy, c/o V. Laursen, Meteorologisk Institut, Charlottenlund, Denmark.

SUDDEN COMMENCEMENTS AND SOLAR-FLARE EFFECTS, SECOND QUARTER 1960

Preliminary Report of Sudden Commencements

S.c.'s given by ten or more stations are in italics. Times are mean values obtained from normal magnetograms.

Sudden commencements followed by a magnetic storm or a period of storminess (s.s.c.)

1960 April 01d 03h 07m: Db Ci (si: Es).—02d 23h 13m: fifty-four (ssc: 53; si: 1).—05d 13h 00m: forty-nine (ssc: 37; si: 11; sfe: H1).—07d 15h 11m: forty-four (ssc: 30; si: 13; bs: 1).—10d 01h 26m: forty-four (ssc: 40; si: 2; sfe: PM, Gn).—27d 20h 20m: fifty-five (ssc: 54; si: 1).—30d 01h 32m: fifty-one (ssc: 42; si: 9).—30d 12h 13m: forty-two (ssc: 36; si: 6).

1960 May 06d 11h 21m: Nu Ta Bn (si: Qu).—06d 16h 50m: fifteen (ssc: 14; si: 1).—06d 17h 18m: Cm Db IK Ci Mc Lr Lu Tn (si: Wn V1 Ma Pr Fr Ka Qu).—08d 04h 21m: fifty-three (ssc: 52; si: 1).—11d 04h 35m: forty-seven (ssc: 42; si: 5).—16d 11h 20m: Mb Ka Ky Lr (sfe:

Fr).—16d 13h 51m: forty-seven (ssc: 43; si: 4).—23d 11h 36m: Ma Ka Qu Ta (si: So Sw IK).—28d 20h 29m: fifty-six.—31d 07h 50m: Qu MB.—31d 12h 13m: Lg Ta (si: Be).

1960 June 04d 02h 48m: forty-six (ssc: 44; si: 2).—21d 00h 13m: H1 Wn V1 Ma IK Ks Qu (si: Be; b: Sw Tn; bp: Lg T1; bps: Eb Od; pt: Cm Aq).—26d 20h 15m: Tr So (pt: Cm).—27d 01h 45m: fifty-five (ssc: 54; si: 1).—29d 19h 39m: fifty-six (ssc: 52; si: 4).—30d 17h 20m: twenty-eight (ssc: 22; si: 6).—

Sudden impulses found in the magnetograms (s.i.)

1960 April 03d 08h 55m: eighteen (si: 14; ssc: 4).—03d 18h 32m: Cm Fr Ks Ta MB.—04d 04h 03m: eighteen (si: 15; ssc: 3).—04d 13h 38m: Cm Fu Ci Va.—05d 08h 42m: fourteen (si: 13; ssc: 1).—06d 16h 28m: fifty-two (si: 27; ssc: 25).—07d 14h 20m: Cm Ks Bi (ssc: IK).—09d 23h 45m: H1 (sfe: Si).—10d 22h 34m: Es MB Gu (pt: Wn Ma).—13d 13h 14m: Be MB (sfe: Fr).—15d 14h 41m: Sw Lg T1 Ks MB Mc (sfe: Fr).—17d 16h 09m: Cm Fr.—23d 10h 33m: Lu Hr.—25d 07h 43m: H1 Wn Pr Lg IK.—30d 16h 11m: Mb (ssc: Wi).—

1960 May 02d 09h 13m: Mc Lu Hr.—06d 19h 06m: Qu (ssc: Am; sfe: Hu).—06d 21h 42m: Le Es Wn V1 Pr (bp: Hr; pt: Cm).—07d 01h 23m: Gu (ssc: Lu).—07d 09h 27m: twenty (si: 16; ssc: 3; sfe: Db).—07d 11h 08m: Es Mb Ka Ky Lu (ssc: 2).—07d 12h 05m: Mb Ka Ky.—08d 23h 29m: Es Lr Bi.—09d 05h 06m: Ka Bi (sfe: Gn).—09d 10h 34m: Wn V1 Pr (sfe: Le).—11d 19h 30m: Es V1 Ma Lu Hr (sfe: Db Fr Hu).—15d 10h 09m: twenty-six (si: 17; ssc: 3; bs: 2; sfe: Ma? Aq? Mc Lr).—16d 14h 50m: Es Mb Ka Ky Lu (ssc: V1 Ta).—16d 20h 36m: seventeen (si: 15; ssc: 2).—17d 06h 25m: Es Wn V1 Ha Pr Fu Mb Ka Ky (ssc: Qu; sfe: Db).—22d 14h 38m: forty-eight (si: 29; ssc: 18; sfe: Fr).—29d 01h 06m: Mb Ka Ky MB PM.—29d 06h 31m: Mb Ka Ky.—29d 13h 34m: Es Mb Ka Ky MB.—29d 23h 43m: H1 Cm Lg Qu Lu Hr.

1960 June 02d 13h 59m: H1 St Be.—04d 09h

PRINCIPAL MAGNETIC STORMS

(Advance knowledge of the character of the records at some observatories as regards disturbances)

Observatory (Observer- in-Charge)	Green- wich date	Storm-time		Sudden commencement			C- figure, degree of ac- tivity ⁴	Maximal activity on K-scale 0 to 9			Ranges			
		GMT of begin.	GMT of ending ¹	Type ²	Amplitudes ³			Gr. day	Gr. 3-hr. period	K- index	D	H	Z	
					D	H								Z
(1)	(2)	(3)	(4)	(5)	(6)	(7)	(8)	(9)	(10)	(11)	(12)	(13)	(14)	(15)
Elisabethville/ Karavia (Ngandu, Ntambwe)	1960	<i>h m</i>	<i>d h</i>		<i>'</i>	<i>γ</i>	<i>γ</i>					<i>'</i>	<i>γ</i>	<i>γ</i>
					January no principal storms									
					February no principal storms									
	Mar. 31	10 35	1 22	s.c.*	-2	+49	x	ms	1	3,6		23	622	62
	Apr. 30	12 12	1 10	s.c.*	-6	+99	-16	s	30	5,6,7		25	761	85
	May 8	04 21	8 24	s.c.*	+2	+49	-4	m	8	2,6		14	351	36
					June no principal storms									
				July no principal storms										
	Aug. 16	14 09	17 23	s.c.	-11	+35	-2	m	17	1,8		17	210	25
				September no principal storms (no measurements 6,7,8 September).										

¹Approximate time of ending of storm construed as the time of cessation of reasonably marked disturbance movements in the traces; more specifically, when the K-index measure diminished to 2 or less for a reasonable period.²s.c. = sudden commencement; s.c.* = small initial impulse followed by main impulse (the amplitude in this case is that of the main impulse only, neglecting the initial brief pulse); ... = gradual commencement.³Signs of amplitudes of D and Z taken algebraically; D reckoned positive if towards the east and Z reckoned positive if vertically downward.⁴Storm described by three degrees of activity: m for moderate (when K-index as great as 5); ms for moderately severe (when K = 6 or 7); s for severe (when K = 8 or 9).

42m: Es Lu.—04d 20h 39m: V1 Od (bs: Mc).—
04d 21h 17m: fifteen (si: 12; ssc: 1; bs: 1; pt: 1).—
09d 12h 25m: Mo IK.—10d 11h 27m: Le H1 V1
Cm Ma (ssc: Db; sfc: Od Su Ks).—18d 22h 15m:
Mo Su SF.—21d 03h 09m: Mb Ka Ky MB.—
27d 21h 16m: Mo Wn V1 Cm Pr Fu Mb MB Mc
(ssc: Db).—28d 00h 30m: H1 Ta MB Mc.—28d
05h 24m: Mb Ka Ky SF Ta Lr (ssc: Ks Mc Lu;
sfc: Db).—28d 07h 21m: Mb Ka Ky.—29d 06h
50m: Nu Wn V1 Ma Pr Fu (ssc: Es Kv; b: Ir;
bs: Mo; bp: Ka Ky Lu; bps: Gu.)

Preliminary report on solar-flare effects (s.f.e.)

Effects confirmed by ionospheric or solar observations are in italics.

1960 April 02d 08h 36m–08h 55m: Es Lr Hr
(si: Bi; bp: Ky To).—02d 18h 19m–18h 28m: Db
Hu (si: Es MB).—04d 08h 51m–09h 00m: Es.—
05d 16h 01m: Le Es.—06d 11h 32m–12h 00m:
Le Es Wn Wi V1 Ha IK? Ks Mc? Lr Hr (si: Lg
MB Bi Lu).—09d 10h 50m–11h 22m: Le Es Mc
Lr (si: Lu).—12d 09h 15m–09h 38m: Le.—16d
11h 34m–11h 45m: Cm.—16d 13h 59m: Hu.—
17d 13h 28m: Fr.—18d 09h 25m: Mc (b: Bn).—
19d 16h 30m: Fr.—20d 12h 24m: IK.—22d 10h
20m: IK Fr Ks Mc? (si: Lu Hr; bs: Bn; pt:
SM).—22d 15h 11m: Fr.—22d 16h 42m: Fr.—
23d 19h 22m: Hu.—24d 02h 41m: Gu.—27d 15h
47m: Fr.—29d 16h 26m: Hu.

1960 May 01d 15h 58m: Hu.—old 18h 30m:

Fr.—04d 10h 13m–11h 00m: Le Hr (b: Qu Ta;
bp: Ks).—04d 14h 54m: Fr.—06d 15h 13m:
Le.—06d 23h 24m–23h 50m: Gu.—08d 10h 11m:
Le.—10d 12h 24m: Fr.—11d 19h 30m: Db Fr Hu
(si: Es V1 Ma Hr).—13d 05h 18m–05h 25m: Le
Es Mb Ka Ky PM (bp: Lu).—14d 23h 12m:
Si.—15d 11h 52m: Wi.—16d 15h 01m: Hu.—
16d 19h 02m: Hu.—18d 15h 33m: Fr.—25d 15h
43m: Hu (bp: MB).—26d 08h 40m–09h 00m:
Es.—26d 09h 14m: Mc? Lr.

1960 June 01d 08h 30m: Hr?—01d 16h 50m:
He.—02d 09h 00m: IK Lr.—02d 09h 36m: Mc
Lr.—03d 17h 30m: od.—06d 16h 12m: Hu.—
08d 13h 56m: Hu.—10d 06h 34m: Lr.—10d 16h
21m: Hu.—13d 17h 10m: Hu.—14d 13h 30m:
Hu.—15d 02h 52m: Mb? Ka? (si: Gu).—17d 01h
38m: od.—19d 13h 32m–13h 41m: Le Es Wn?
Wi Hu.—20d 01h 28m: Mb? Ka? Ky? PM Gn
(si: Tu Gu; ssc: Sr).—21d 10h 20m: Od (si:
Ka).—21d 11h 07m: V1.—21d 14h 35m: Ir.—
25d 04h 17m–04h 23m: Gu.—25d 10h 24m: Lr
(ssc: MB).—26d 04h 30m: Mb? Ka? Ky?—26d
13h 58m–14h 02m: Es. Hu.—27d 11h 48m: Es
Hu.—27d 18h 40m: Hu (si: V1).—28d 18h 38m:
Hu (ssc: Wk).

COMMITTEE ON RAPID VARIATIONS AND
EARTH CURRENTSA. ROMAÑA, *Chairman*, Observatorio del Ebro,
Tortosa, Spain

SELECTED GEOMAGNETIC AND SOLAR DATA

 K_p , C_i , C_p , A_p , K_{F_r} , R_z and Selected Days

November 1960

Day ¹	Three-hour Range Indices K_p^2									Prel. ³ C_i	C_p^4	A_p^5	3-hr. Range Indices K_{Fr}^6		Prov. ⁷ R_z	
	1	2	3	4	5	6	7	8	Sum				Values	Sum		
1	3-	3o	3o	2+	2+	2+	2-	3+	21-	0.6	0.7	12	2431	1103	15	76
2	3o	3-	4-	3o	3+	1+	3o	4-	24-	0.8	0.9	16	3333	3133	22	80
3	4+	3-	3-	3+	3o	2o	3-	5-	25+	1.0	1.0	18	5223	2224	22	69
4 D	6-	6-	6-	5-	5+	5+	4-	5-	41-	1.5	1.6	52	6544	4424	33	58
5 q	4-	4o	2+	2o	3-	1o	0+	0+	16+	0.5	0.6	11	3422	2000	13	73
6 q	0o	1o	2+	2+	2-	0+	2+	2o	12o	0.2	0.3	6	0132	2021	11	90
7 Q	3o	3-	3-	2-	1-	0+	0o	0o	11o	0.2	0.3	6	3232	1000	11	116
8 Q	0o	0o	2o	2-	1-	1-	0+	1+	7-	0.1	0.1	3	0011	2111	07	125
9 Q	2-	2o	2o	2+	2-	0+	0o	1o	11o	0.1	0.2	5	1332	2000	11	125
10 q	0o	0o	2+	2+	3o	2+	1o	1-	12-	0.3	0.3	6	0021	3311	11	125
11	2+	3+	4-	5-	3+	2o	3o	3-	25o	1.0	1.0	18	3334	3232	23	134
12	2o	1o	2o	2-	5o	6o	8-	8o	33+	1.7	1.7	67	1121	5667	29	132
13 D	9-	9-	9o	9o	9-	8+	8o	6+	67-	2.0	2.3	280	8899	9875	63	128
14 D	7+	5-	5o	4o	3-	4+	5+	4o	37+	1.6	1.6	49	6553	2444	33	132
15 D	5+	4o	4+	3o	6o	6o	6o	8-	42+	1.7	1.7	69	5332	6547	35	133
16 D	8+	8+	6o	5+	6-	5-	3+	3+	45o	1.6	1.9	94	7654	4433	36	121
17	4-	3o	3+	3o	3-	4-	4o	3-	26o	1.0	1.0	18	4334	2234	25	103
18 Q	3+	2o	1o	1+	1-	1-	0+	0o	9+	0.2	0.2	5	3111	0100	07	82
19 Q	0o	2o	1+	3-	3o	1-	0+	1+	11+	0.4	0.3	6	0213	3112	13	74
20 q	2o	2+	2+	3-	3o	3-	1o	2-	18-	0.6	0.5	9	2223	3222	18	82
21	1o	4+	6-	5-	5o	5o	6o	5-	36+	1.5	1.5	45	2345	4444	30	65
22	6-	5+	5-	4-	3+	3-	2o	4-	31o	1.3	1.3	30	5543	3223	27	57
23	3-	3-	4-	2+	2o	1o	2-	2o	18o	0.5	0.6	10	3433	2112	19	57
24	4-	2+	3+	1o	2o	2o	3o	5o	22+	0.9	0.9	16	3232	2235	22	41
25	4o	5-	5+	5+	5-	4+	4+	4+	37o	1.4	1.4	39	3554	4344	32	42
26	3-	4+	4-	3+	4-	1+	3o	3-	25-	0.9	0.9	17	2443	3132	22	60
27	3-	3o	3+	3o	3+	4o	5-	4-	28-	1.2	1.1	21	2333	3342	23	58
28	5o	5-	4-	3+	4-	2o	1+	1o	25-	1.0	1.1	21	5333	3221	22	56
29 q	3+	2+	2-	3-	2-	1+	2-	3-	17+	0.4	0.5	9	3322	1113	16	53
30	2o	3o	2-	1o	2-	2-	4o	6-	21-	1.0	0.9	17	1311	2145	18	63
Means:										0.91	0.95	32			87.0	
No. of days:										30	30	30			30	

Notes:

¹ Five quiet days (Q), ten quiet days (Q or q), five disturbed days (D) selected by Committee on Characterization of Magnetic Disturbances, J. Veldkamp, Kon. Nederlandsch Meteorologisch Instituut, DeBilt, Holland.

² Geomagnetic planetary three-hour-range indices K_p prepared by Committee on Characterization of Magnetic Disturbances, J. Bartels, Chairman, University, Göttingen, Germany.

³ Preliminary magnetic character-figures, C_i , prepared by J. Veldkamp.

⁴ Magnetic character-figures, C_p , prepared by J. Bartels.

⁵ Average amplitudes A_p (unit 2γ), prepared by J. Bartels.

⁶ Fredericksburg three-hour-range indices K ($K_9 = 500\gamma$); scale-values of variometers in γ: mm: $D = 2.7$; $H = 2.5$, $Z = 3.1$ prepared by Robert E. Gebhardt, Observer-in-Charge, Fredericksburg Magnetic Observatory, Corbin, Virginia.

⁷ Provisional sunspot-numbers (dependent on observations at Zurich Observatory and its stations at Locarno and Arosa) prepared by M. Waldmeier, Swiss Federal Observatory, Zurich, Switzerland.

Letters to the Editor

Effect of the Magnetic Field in Ionospheric Backscatter

E. E. SALPETER

*Laboratory of Nuclear Studies and Center for Radiophysics and Space Research
Cornell University, Ithaca, New York*

Theoretical results have been derived recently [Dougherty and Farley, 1960; Fejer, 1960; Salpeter, 1960] for the frequency spectrum of the return signal in radar backscatter from free electrons in the high ionosphere and exosphere, assuming perfect thermodynamic equilibrium. In these calculations the earth's magnetic field B was neglected and some effects due to this field are discussed in the present note.

Let n be the number particle density of electrons, m the electron mass, M the mass of the (singly charged) positive ions in the plasma, T the temperature, and λ the radar wavelength. We define some characteristic frequencies by

$$\left. \begin{aligned} \omega_e &= (4\pi/\lambda)(2kT/m)^{1/2}, \\ \omega_p &= (4\pi ne^2/m)^{1/2}, \quad \omega_c = eB/mc \\ \omega_i &= (4\pi/\lambda)(2kT/M)^{1/2}, \\ \omega_{pi} &= (4\pi ne^2/M)^{1/2}, \quad \omega_{ci} = eB/Mc \end{aligned} \right\} \quad (1)$$

where ω_e and ω_i are characteristic Doppler broadening frequencies for electrons and ions, ω_p is the electron plasma frequency, and ω_c , ω_{ci} are the gyromagnetic frequencies for electrons and ions, respectively. We define some dimensionless parameters

$$\left. \begin{aligned} \alpha &= \lambda(ne^2/4\pi kT)^{1/2} = \omega_p/\sqrt{2}\omega_e \\ \epsilon &= \omega_c/\omega_e, \quad \epsilon_i = \omega_{ci}/\omega_i = (m/M)^{1/2}\epsilon \end{aligned} \right\} \quad (2)$$

We shall assume that complete thermodynamic equilibrium holds, that collisions can be neglected, that the radar frequency is large compared with ω_e , ω_c and ω_p , and that $m \ll M$. For radar frequencies between 40 and 500 Mc/s we have $\alpha > 1$ at all heights up to 2000 km or more. If $\epsilon = 0$ (or if the direction of the magnetic field is parallel to the radar beam) the frequency spectrum consists of two parts: (1) The 'ion component' has width $\sim \omega_i$ and dominates if

$\alpha \gg 1$. (2) If $\alpha \ll 1$ the 'electron component' has width $\sim \omega_e \gg \omega_i$ and dominates. If $\alpha \gg 1$ the weak 'electron component' consists of two sharp weak lines displaced from the central frequency by frequencies approximately $\pm \omega_p$ with integrated intensity $1/\alpha^2$ times the total intensity.

For the limit of $\alpha \rightarrow 0$, i.e. neglecting electrostatic forces altogether, Laaspere [1960] has derived in detail the frequency spectrum for general values of ϵ and for any angle $(\phi - \frac{1}{2}\pi)$ between the magnetic field and the radar beam. If $\phi = 0$ he obtains a series of sharp lines spaced exactly ω_e apart; if $\phi \neq 0$ the lines have a width of the order of $\omega_e \sin \phi$. If $\epsilon \ll 1$ (and $\phi = 0$), Laaspere finds the envelope of the line spectrum to be identical with the spectral distribution for $\epsilon = 0$; if $\epsilon \gg 1$ the main intensity is in the central line with much weaker lines displaced $\pm \omega_c$, etc.

The present writer has derived a formal expression for the frequency spectrum for general values of α , ϵ , and ϕ . Numerical evaluation of this expression is required in general, but certain limiting cases are simple. If $\alpha \gg 1$ (or $\epsilon \ll 1$) the results are of course similar to Laaspere's (or to those without a magnetic field). Results are described below only for cases where

$$\alpha \gg 1 \quad \epsilon \gg 1 \quad \epsilon_i \lesssim 1 \quad (3)$$

which holds in most ionospheric experiments proposed for the near future.

1. Consider first $\phi = 0$ (radar beam *exactly* perpendicular to the magnetic field).

a. The 'electron component' consists of two weak symmetrically placed spectral lines, as for $\alpha \gg 1 \gg \epsilon$, but at frequencies displaced by approximately $\pm(\omega_p^2 + \omega_c^2)^{1/2}$ with integrated intensity $(\alpha^2 + 2\epsilon^2)^{-1}$ times the total intensity. This component corresponds to the well-known longitudinal electron plasma oscillations in the presence of a static magnetic field.

b. For $\alpha \gg 1$ the 'ion component' of the frequency spectrum dominates and it has been conjectured [Bowles, 1959] that an appreciable fraction of the intensity resides in lines displaced by multiples of the ion gyrofrequency ω_{ci} as long as $\epsilon_i \lesssim 1$ although $\epsilon \gg 1$. In fact, the bulk of the intensity resides in a single, central, undisplaced line for the following reason: since $\epsilon \gg 1$, the electron's motion is mainly confined¹ to distances of the order of the electron's gyro-radius R_e which is small compared with $\lambda/4\pi$, where λ is the radar wavelength. On the other hand, we have charge neutrality to a good approximation, since $\alpha \gg 1$, and the ions are also confined to within small distances of the order of R_e even though the ion's own gyroradius may be larger than $\lambda/4\pi$. Besides the strong central line there appear other spectral lines which, although weak, may be of interest.

If ϵ^2 and α^2 are both large compared with $|\log \epsilon_i|$ (as well as with unity) we have two symmetric lines displaced by frequencies $\pm\omega_r$, where

$$\begin{aligned} \omega_r^2 &= \omega_i^2 \frac{\alpha^2 \epsilon^2}{(\alpha^2 + 2\epsilon^2)} = \frac{M}{m} \omega_{ci}^2 \frac{\alpha^2}{(\alpha^2 + 2\epsilon^2)} \\ &= \frac{m}{M} \frac{\omega_e^2 \times \omega_p^2}{(\omega_e^2 + \omega_p^2)} \quad (4) \end{aligned}$$

The intensity of this pair of lines is $\alpha^2(\alpha^2 + 2\epsilon^2)^{-1} \times (2\epsilon^2)^{-1}$ times the intensity of the main central line. If (in addition to the inequalities above) $\epsilon \ll \alpha$, then ω_r reduces to $\omega_{ci} (M/m)^{1/2}$ the geometric mean of the electron and ion gyro-frequencies, and the intensity to $(2\epsilon^2)^{-1}$ times that of the central line.

The ratio α/ϵ is independent of the radar wavelength used and is probably slightly larger than unity at heights above about 300 km. The value of ϵ decreases with increasing height and increases with increasing radar wavelength. At a height of a few hundred kilometers, for instance, one might have $n \sim 2 \times 10^6$, $T \sim 2,000^\circ\text{K}$, $B \sim 0.5$ Gauss, and, for a radar frequency of 450 Mc/s, $\alpha \sim 8$ and $\epsilon \sim 2$. Writing $\nu = \omega/2\pi$ for each circular frequency ω , and assuming positive ions of atomic weight 16, we then have

$\nu_p \sim 4$ Mc/s, $\nu_e \sim 1.5$ Mc/s, $\nu_r \sim 8$ kc/s, $\nu_i \sim 4$ kc/s, and $\nu_{ci} \sim 0.05$ kc/s. If $\alpha > \epsilon > 1$ but ϵ is still sufficiently small for the weak lines at $\pm\nu_r$ to be detectable then one can, *in principle*, measure M , B , and T as well as n , provided thermodynamic equilibrium really holds. With the radar beam perpendicular to the magnetic field a measurement of the frequency ν_r essentially gives $B/(M)^{1/2}$ and the intensity of the line at $\pm\nu_r$ relative to that of the central lines gives ϵ and hence $B/(T)^{1/2}$. With the radar beam parallel to the magnetic field, the spectrum is as for $\epsilon = 0$, and the width of the spectrum gives ν_i and hence T/M . Finally, the absolute total intensity (or, better still, the value of the plasma frequency ν_p if the very weak lines at $\pm\nu_p$ could be detected) gives n .

2. *In practice*,² however, it will be very difficult to make use of the results of case 1b, since the frequency spectrum is strongly altered if $\sin \phi > (m/M)^{1/2} \ll 1$. This is due to the fact that the electrons can drift unhindered along the magnetic field lines with the electron thermal velocity which exceeds that of the ions by a factor of $(M/m)^{1/2}$. In the last expression for ω_r in equation 4 the factor m/M is replaced by $[(m/M) + \sin^2 \phi]$, so that this line furnishes little information on the ion mass if $\sin^2 \phi \gg m/M$. On the other hand, Bowles' conjecture becomes essentially correct if the double inequality $(m/M)^{1/2} \ll \sin \phi \ll \epsilon_i$ holds. The strong sharp central line of case 1b is replaced by a pattern of width $\sim \omega_i$ which carries most of the intensity and consists of a series of slightly broadened but well separated lines. The spacing of these lines can be calculated numerically (for each value of ϵ_i) and is close to ω_{ci} . The envelope to this line spectrum is found to be close to the spectral distribution in the absence of a magnetic field as long as $\epsilon_i \lesssim 0.2$ and can be calculated for larger values of ϵ_i . Bowles' [1959] suggested method for measuring the ion mass M should then be feasible in principle if $\epsilon \gg 1$, which is true for low enough radar frequencies.

² Even if ϕ is exactly zero the effects described under 1b may be difficult to obtain in practice, since they are sensitive to even quite slight disturbances due to (1) deviations from complete thermodynamic equilibrium, (2) occasional collisions suffered by electrons, (3) fluctuating electric fields if nD^3 is not sufficiently large. Practical results at $\phi = 0$ will probably be closer to our case 2 than to case 1b.

¹ At least this is the effect in our case where we are considering electron density fluctuations which extend over very many wavelengths λ in directions perpendicular to the radar beam and where $nD^3 \gg 1$ (D being the Debye length).

3. In experiments carried out at Lincoln Laboratories and those proposed for Puerto Rico we have $\epsilon_i \ll \sin \phi$. In this event the main 'ion component' is essentially the same as that in the absence of a magnetic field, even though $\epsilon > 1$.

Acknowledgments. This study was supported in part by a joint contract with the U. S. Atomic Energy Commission and the Office of Naval Research. Part of the work was carried out at the School of Physics, University of Sydney.

REFERENCES

Bowles, K. L., Incoherent scattering by free elec-

- trons, *Nat. Bur. Stand. Rept. 6070*, September 18, 1959.
 Dougherty, J. P., and D. T. Farley, Incoherent scattering of radio waves by a plasma, 1960 (in press).
 Fejer, J. A., Scattering of radio waves by free electrons, *Canad. J. Physics*, 1960 (in press).
 Laaspere, T., The effect of a magnetic field on the spectrum of incoherent scattering, Ph.D. thesis, Cornell University, September 1960.
 Salpeter, E. E., Scattering of radio waves by electrons above the ionosphere, *J. Geophys. Research*, 65, 1851-1852, 1960.
 Salpeter, E. E., Electron density fluctuations in a plasma, *Phys. Rev.*, 120, 1528-1535, 1960.

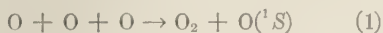
(Received January 3, 1961.)

The 5577 Å Airglow Emission Mechanism

C. A. BARTH AND A. F. HILDEBRANDT

*Physical Sciences Division, Jet Propulsion Laboratory
California Institute of Technology, Pasadena 3, California*

The atomic oxygen 5577 Å line is the most prominent emission in the visible part of the airglow spectrum. Of the many excitation theories that have been proposed to explain the appearance of this spectral line, the chemical excitation mechanism proposed by Chapman [1931] appeared to be the most plausible. In this mechanism, an oxygen atom is excited to the 1S state (the upper state of the 5577 Å transition) by the three-body recombination of two other oxygen atoms.

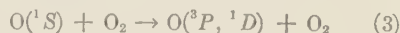


Rocket measurements of the vertical distribution of the 5577 Å airglow emission have repeatedly shown that the maximum in airglow intensity is near 100 km [Tousey, 1958], which is the region where the maximum atomic oxygen density should occur [Nicolet, 1959]. Since the intensity of the emission from the three-body recombination, reaction 1, would be proportional to the cube of the oxygen atom density, the rocket measurements of the airglow height have been used as evidence supporting the Chapman theory.

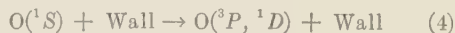
This letter is a report of the measurement of the rate coefficient for the 5577 Å emission resulting from the three-body recombination of atomic oxygen by means of the combined techniques of electron paramagnetic resonance spectrometry and optical spectroscopy. In a low-pressure flow system a mixture of 10 per cent oxygen atoms and 90 per cent oxygen molecules was produced at 1 mm Hg pressure. The density of atoms, measured with the electron paramagnetic resonance spectrometer, was found to be 3.0×10^{16} atoms/cm³. The recombining atoms were contained in a tube 35 mm in inner diameter and 486 mm long. The reacting atoms were observed by a grating spectrograph with an $f/2$ camera. The spectrograph was calibrated by means of a standard lamp and was found to have

a sensitivity sufficient to enable it to detect spectral line emissions with an intensity of 1 kilorayleigh (10^3 photons/cm² sec) or greater in the green part of the spectrum. The experiment carried out under these conditions showed that the intensity of the 5577 Å radiation was less than the minimum detectable.

In the laboratory experiment, the excited oxygen atoms that are formed in reaction 1 may also be lost by collisional deactivation with oxygen molecules



and with the wall



as well as by radiation, reaction 2. The equilibrium density of $O(^1S)$ atoms may be obtained by equating the rate equations for reactions 1 to 4:

$$k(O)^3 = A(O, ^1S) + d(O_2)(O, ^1S) + W(O, ^1S) \quad (5)$$

where k is the three-body recombination rate coefficient for reactions resulting in excited 1S atoms, (O) and (O_2) are the atom and molecular densities, A is the radiative transition probability, and d and W are the molecular and wall deactivation coefficients. The intensity of 5577 Å radiation expressed in rayleighs is equal to the product of the number of $O(^1S)$ atoms, the transition probability, and the length of the emission region

$$I = k(O)^3 L \frac{1}{1 + \frac{d(O_2)}{A} + \frac{W}{A}} \quad (6)$$

where L is the length of the experimental tube.

The wall and molecular deactivation coefficients were obtained from two additional experiments that measured their ratio to the radiative transition probability. Oxygen atoms in the excited 1S state were produced in a mixture of

nitrogen and oxygen atoms by using the technique of Schade and Kaplan (to be published). In this case, equation 6 may be rewritten as

$$I = \frac{KL}{1 + \frac{d}{A}(\text{O}_2) + \frac{W}{A}} \quad (7)$$

where K is the production rate of O (^1S) atoms. The wall deactivation coefficient was obtained by measuring the intensity of the 5577 Å radiation from two observation tubes of different diameters. The two tubes contained the same density of reacting atoms and the same production rate of O(^1S) atoms. Since the wall deactivation coefficient, W , is inversely proportional to the diameter of the tube, the ratio of W/A was obtained from the ratio of the 5577 Å intensities and equation 7. The value of W/A was found to be 1.3 for the observation tube of 35 mm i.d. The molecular deactivation coefficient was measured in the second additional experiment. Molecular oxygen was added to the 35 mm i.d. observation tube while the production rate of ^1S oxygen atoms was held constant. The intensity of the 5577 Å line was measured for varying amounts of molecular oxygen. When the experimental values were substituted into equation 7, the value of $3.5 \times 10^{-16} \text{ cm}^3$ was obtained for the ratio of d/A .

The results of the three laboratory experiments were substituted into equation 6: the upper limit of 5577 Å intensity, the oxygen atom density, the oxygen molecule density and the length of the observation tube from the experiment on the

mixture of oxygen atoms and molecules, and the deactivation coefficient values from the experiments on the mixtures of oxygen and nitrogen atoms. An upper limit of $8 \times 10^{-38} \text{ cm}^6 \text{ sec}^{-1}$ was found for k , the three-body recombination rate coefficient for reactions resulting in excited ^1S atoms.

When values for the upper atmosphere atomic and molecular oxygen densities [Nicolet, 1959] are substituted into equation 6 together with the laboratory value for k , the maximum intensity of airglow radiation calculated for the three-body atomic oxygen mechanism is 0.2 rayleigh (2×10^6 photons/cm 2 sec). This result is to be compared with a typical airglow intensity of 250 rayleighs. Therefore, these laboratory measurements do not support the Chapman mechanism as the source of the 5577 Å airglow emission.

Acknowledgments. This research was sponsored by the National Aeronautics and Space Administration. These results were presented at the XII General Assembly of the International Union of Geodesy and Geophysics, Helsinki, July 1960. The experimental data were obtained by M. Patapoff. We thank W. J. Schade for many discussions throughout the course of this work.

REFERENCES

- Chapman, S., Some phenomena of the upper atmosphere, *Proc. Roy. Soc. London, A*, 132, 353-374, 1931.
 Nicolet, M., La thermosphère, *Ann. géophys.*, 15, 1-22, 1959.
 Tousey, R., Rocket measurements of the night airglow, *Ann. Géophys.*, 14, 186-195, 1958.

(Received November 25, 1960.)

Thermal Radiation Spectrum of the Arctic Sky

W. B. MURCRAJ

*University of Washington
and**Geophysical Institute, University of Alaska
College, Alaska*

The spectrum of atmospheric thermal emission to about 15 microns wavelength has been observed by several investigators [Buller, 1952; Sloan, Shaw, and Williams, 1955]. All these observations were made at low latitudes on comparatively warm atmospheres, and with much liquid water close by. Industrial activity and decaying vegetation were present also in the near vicinity.

The spectrum shown in Figure 1 was obtained under quite different conditions. It was taken at Point Barrow at about 01:00 AM local time on February 12, 1960. The instrument was pointed out over the Arctic Ocean at an elevation angle of about 25° so that the optical path included about 2.5 air masses. At this time the temperature had been below 0° F for over 2 months. The sunlight had returned some time before, but the days were still only about 4 hours long. The land for hundreds of miles southward had been solidly frozen for months, so that CO_2 production from decaying vegetation in the vicinity would be small. There were, however, large areas of open water in the Bering Sea not so very far away, and there were some open leads in the Arctic Ocean near by. Ground-level air temperature at the time of the observation was about -30° F.

The spectrum shown was obtained with a Perkin-Elmer single beam monochromator with thermocouple detector and NaCl prism. Because of the difficulty of obtaining a good ground in the frozen tundra, the records were somewhat noisy, so the automatic wavelength sweep of the instrument was not used. Instead, manual control was used, and the instrument was set at a particular wavelength until a reading was obtained, the procedure being repeated until the wavelength range 4–14 microns was covered. (There was no measurable radiation shorter than 4 microns.)

The recorder deflection at a given wavelength is proportional to the difference in radiation from the sky and from a reference source at room tem-

perature, the proportionality constant being different at each wavelength because of such things as effective slit width, etc. (Actual slit width was maintained at 1.25 mm throughout.) Calibration was accomplished by readings on a block of snow with a hollow carved in it, after it had stood at room temperature until it had become wet. This was considered a blackbody at 0°C , and the proportionality constant obtained for each wavelength. The difference between sky radiation and room radiation could then be calculated, and the room temperature radiation being known, the sky radiation could be obtained.

Because of the roughness of the calibration it is perhaps best not to take the intensity scale of Figure 1 too seriously. It does not seem likely to be far wrong, however, at least in the main features. Bearing in mind, then, that the uncertainties are considerable, the spectrum shows some interesting features. The most noticeable,

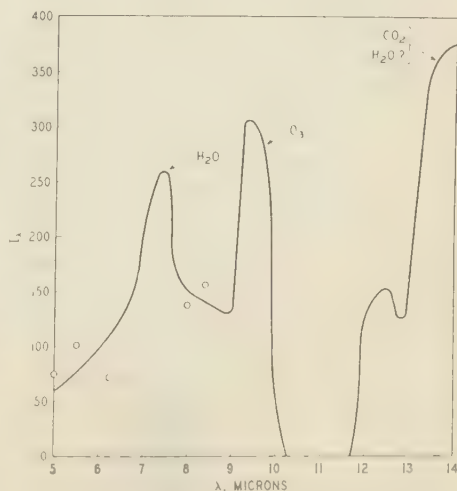


Fig. 1. Thermal emission spectrum of atmosphere at -30°F . I_λ in 10^{-5} cal cm^{-2} min^{-1} for unit angle, and $\Delta\lambda = 1\mu$.

of course, is the importance of the ozone band between 9 and 10 microns and the emission beyond 13 microns (probably mostly CO_2) as compared with the water vapor emission between 4 and 8 microns. Under temperate conditions the 6-micron band is by far the most prominent. It should be noted, however, that even under the arctic conditions the atmosphere is radiating essentially as a blackbody at air temperature in the 4–8 micron region. The figure shows quite a bit of radiation in the 8-micron 'window', which should not be there if the atmosphere is really transparent in this region. It is not known whether this emission is real or represents measurement errors, but its presence is consistent with other observations [Sloan, Shaw, and Williams, 1955]. If it is real, this region is not a very good 'window' even under such extreme atmospheric conditions. The 10–12 micron region, on the other hand, shows little or nothing.

The ozone emission at 9.6μ is interesting in that it represents a contribution from higher in the atmosphere. If the assumption is made that 2.5 air masses are enough to make the emissivity of the ozone region unity, one may follow Adel [1949] and derive an 'effective radiation temperature of the ozone region.' If this is done, the result is a radiation temperature for the ozonosphere of about -40 to -45°F , which is not far from that obtained in New Mexico by Adel.

The small feature between 12 and 13 microns has no legitimate place on the record as the data are not that good. It is included mostly because it has been seen on other records, and others have reported something in this region [Butler, 1952].

The emission in the region beyond 13 microns probably comes mainly from CO_2 . It should be noticed that this radiation is well below that of a blackbody at -30°F , indicating that at least the lower atmosphere is not opaque at these wavelengths.

The main features of the spectrum are explainable by the changes in the Planck radiation curve as the temperature decreases, and by the small amount of water vapor in the atmosphere after such long periods of low temperature.

It is evident that there will be some emission from the air at room temperature in the portion of the radiation path that lies inside the room, and that there will be some absorption of chopped radiation inside the spectrometer. No correction was made for this. The path length in air at room

temperature was about 1 meter to the chopper, and the path of the chopped radiation to the detector was somewhat longer than this. The equipment was in an isolated building a mile or so from the main camp, housing no activities that would increase the water content of the atmosphere except for the respiration of the observer himself. From humidity observations made at a meteorological site some distance away, it seems probable that the total precipitable water content of the 1 meter of path that was at room temperature was less than 1 micron. The carbon dioxide content is not known, but it is hoped that the short path length kept the error due to CO_2 radiation small.

In the calibration runs, the water vapor content of the air was higher, and the calibration curve was smoothed in essentially the manner described by Sloan [1956] to take absorption of the chopped radiation into account. The source was very close to the chopper in this instance to minimize room temperature emission.

Other spectra taken using the mechanical wavelength sweep showed essentially the same features, but, because of the instrumental damping necessary to obtain a good record, were not considered suitable for quantitative treatment.

It is hoped that observations will be obtained by more refined techniques in the near future.

Acknowledgment. The logistic support of the Arctic Research Laboratory of the University of Alaska made these observations possible. The research reported here was supported by the Office of Naval Research.

REFERENCES

- Adel, A., Effective radiation temperatures of the ozonosphere over New Mexico, *Geophysical Research Paper No. 2*, Base Directorate for Geophysical Research, Air Force Cambridge Research Laboratories, Cambridge, Massachusetts, 1949.
- Butler, C. P., On the exchange of radiant energy between the earth and sky, *NRL Report 3984*, June 11, 1952.
- Sloan, R., J. Shaw, and D. Williams, Infrared emission spectrum of the atmosphere, *JOSA*, **45**, *n6*, 455–460, June 1955.
- Sloan, R., The infrared emission spectrum of the atmosphere, *Scientific Report No. 3*, Contract AF 19(604)-1003, Air Force Cambridge Research Center GRD, Hanscom Field, Bedford, Massachusetts, March 1956.

(Received November 14, 1960; revised December 15, 1960.)

Reply to Some Comments by Malville concerning the Midnight Auroral Maximum

E. H. VESTINE AND J. W. KERN

*Department of Planetary Sciences, The RAND Corporation
Santa Monica, California*

In a recent letter, Malville has discussed the movement of geomagnetically trapped radiation toward lower latitudes on the night side of the earth in relation to the observed preferential 'dumping' of auroral particles near magnetic midnight [Malville, 1960]. This possibility has been suggested by several writers as a consequence of distortion of the geomagnetic field by solar streams [Vestine, 1960; Chamberlain, Kern, and Vestine, 1960]. The writers tentatively visualized both day side 'compression' and night side 'stretching' of geomagnetic field lines, and they noted that the mirror point for geomagnetically trapped radiation would be at a lower height above the ground near magnetic midnight. This effect was predicted by integrating the function $(1 - F/F_m)^{1/2}$, where F is the geomagnetic field intensity, along geomagnetic field lines between northern and southern mirror points F_m , and treating the result in all longitudes as invariant [Vestine and Sibley, 1960]. Because of the stretched length of the field line near midnight, the particle was supposed to intersect the surface $F_m = \text{constant}$ deeper in the atmosphere at this time, and hence would be more likely to produce the aurora. As the particles drift in longitude and drift to lower latitudes, their mirror points are lowered in altitude, dumping them preferentially on the night side. It has since come to our notice that a somewhat similar lowering of mirror-point height is predicted for the night side on the basis of the transverse integral invariant, which depends on the difference between distorted field intensities on the day side as compared with the night side of the earth [Rees and Reid, 1959]. The two statements are, in fact, complementary. Chamberlain, Kern, and Vestine considered physical effects on the auroral particles based on the longitudinal integral invariant, especially at times of geomagnetic bays or auroras, and not specifically for the initial phase of magnetic storms. Such

magnetic bays are often closely associated with auroral displays [Heppner, 1954]. Shortening of field lines on the day side was not emphasized, the principal effect being ascribed to lengthening of field lines on the night side near magnetic midnight.

According to Malville, a drop of 150 km in mirror-point height is of negligible importance in promoting auroral phenomena. Though this may well be true for the case he cites, where the drop is from 1000 to 850 km, a similar drop below 200 km is not negligible in an exponential atmosphere. In fact, a drop in mirror-point height of only 10 km may be of considerable interest, especially if atmospheric heating and expansion occurs because of impinging particles [Krassovski, 1958; Jastrow, 1960].

The 71° to 63° equatorward shift in latitude and the 150-km drop in mirror-point height estimated by Malville (for a fourfold increase in field-line length from day side to night side beyond 4 earth radii) are typical of previous estimates made by one of us. The particle-trapping ability of lengthened nighttime field lines would be restricted to much lower energy particles, and would be indeed questionable if the lines were 'blown away' [Piddington, 1960] as mentioned by Malville. If trapping of auroral and electrojet particles occurs on the day side, however, the particle will drift equatorward, away from extended lines, as the geomagnetic field undergoes diurnal rotation or the particle experiences longitudinal drift.

A shift of only a few degrees in latitude with a drop of a few tens of kilometers may be highly significant if other mechanisms exist that can augment the effect. An instance of this kind may arise in connection with the polar electrojets. These seem likely to be driven by nearly meridional electric fields, acting in the electrically conducting E region [Chamberlain, Kern, and Vestine, 1960]. This suggests radiation draining

continuously from the geomagnetic field with a latitudinal separation of particles of opposite sign. For the eastward-directed electrojet, an excess of positive charge may impinge on the equatorward side of the jet, with some excess of negative charge to the north. This charge distribution would be reversed for the early morning westward-directed electrojet at times of magnetic bays [Silsbee and Vestine, 1942]. If the excess of impinging charge locally is positive, the resulting electric field, directed outward from the space charge region, will drive Hall currents which will lower the mirror points inside the region. The Hall conductivity increases rapidly with decreasing height in the F region. Thus, for a given charge excess, any mirror-point lowering, by a mechanism based on conservation of the longitudinal integral invariant, may lead to a further substantial drop toward the ground due to Hall currents [Kern and Vestine, 1960]. This effect also exists in the event of an excess of electrons, which may exist on the equatorward side of the westward-directed electrojet. The mirror points of incident particles depend on pitch angle and, because of atmospheric absorption, on particle energy. Hence, if the energy distribution in incident electrons is different from that of protons, the incident-particle distribution as a function of height may differ in the two cases. Thus the hydrogen emission often noted in homogeneous arcs during a positive bay is compatible with an excess of incident protons. The higher base of illumination of a ray arc developing from a homogeneous arc can be ascribed to a change to an excess of incident electrons. Such shifts in the charge composition of incident particles have been invoked by some authors to explain the eastward- and westward-directed electrojets (Watanabe, personal communication). However, such a transition may result from changes in the incident-particle energy spectrum with time, owing to mirror-point lowering by Hall currents [Kern and Vestine 1960] or to acceleration of auroral primaries by electric fields associated with charge separation. We believe a mechanism for charge separation may be supplied by geomagnetic field gradients perpendicular to meridional planes. Such gradients, associated with solar stream distortion of the geomagnetic field, would be closely related to the changes in

longitudinal integral invariant discussed above.

A reversal of meridional electric field near magnetic midnight would produce electron drift within auroral arcs and rays opposite in direction to the electrojet currents, and would therefore agree with observations by Heppner [1958], Nichols [1959], and Kim and Currie [1958]. The charge-separation mechanism mentioned above would produce auroral arcs aligned more or less parallel to current flow in the polar ionospheric interzonal current sheet. Adjacent pairs of arcs produced by electrons are often seen linked in horseshoe form opened away from the midnight meridian [Nichols, 1959]. This effect would be expected if the charge excess is different in sign before and after midnight. The writers therefore believe that the explanation suggested for the average preponderance of aurora near magnetic midnight based on predictions using adiabatic invariants merits further careful consideration. This question will be considered in a later communication by one of us. The effects of Hall currents in auroral sheets are discussed in a forthcoming paper presenting a new theory of auroral morphology by Kern and Vestine [1961].

REFERENCES

- Chamberlain, J. W., J. Kern, and E. H. Vestine, Some consequences of local acceleration of auroral primaries, *J. Geophys. Research*, **65**, 2535-2537, 1960.
- Heppner, J. P., Time sequences and spatial relations in auroral activity during magnetic bays at College, Alaska, *J. Geophys. Research*, **59**, 329-338, 1954.
- Jastrow, R., Geophysical effects of the trapped particle layer, *Space Research, Proceedings of the First International Space Science Symposium, Nice, January 11-16, 1960*, edited by Hilde Kallmann Bijl, North Holland Publishing Company, Amsterdam, pp. 1009-1016, 1960.
- Kern, J., and E. H. Vestine, Theory of auroral morphology, *J. Geophys. Research*, **66**, 713-723, 1961.
- Kim, J. S., and B. W. Currie, Horizontal movements of aurora, *Can. J. Phys.*, **36**, 160-170, 1958.
- Krassovsky, V. I., Report on results of Sputnik III, *Fifth CSAGI Assembly*, Moscow, July 1958.
- Malville, J. M., The effect of the initial phase of a magnetic storm upon the outer Van Allen belt, *J. Geophys. Research*, **65**, 3008-3010, 1960.
- Nichols, B., Auroral ionization and magnetic disturbances, *Proc. IRE*, **47** (2), 245-254, 1959.
- Piddington, J. H., Geomagnetic storm theory, *J. Geophys. Research*, **65**, 93-106, 1960.

Rees, M. H., and G. C. Reid, The aurora, the radiation belt and the solar wind: a unifying hypothesis, *Nature*, 184, 539-540, 1959.

Silsbee, H. C., and E. H. Vestine, Geomagnetic bays, their frequency and current-systems, *Terrest. Magnetism and Atmospheric Elec.* 47, 195-208, 1942.

Vestine, E. H., Polar auroral, geomagnetic, and

ionospheric disturbances, *J. Geophys. Research*, 65, 360-361, 1960.

Vestine, E. H., and W. L. Sibley, The geomagnetic field in space, ring currents, and auroral iso-chasms, *J. Geophys. Research*, 65, 1967-1979, 1960.

(Received December 5, 1960.)

A Note on Phase Velocity of VLF Radio Waves

JAMES R. WAIT AND KENNETH P. SPIES

National Bureau of Standards
Boulder, Colorado

The phase of the carrier signal from a distant VLF transmitter is very sensitive to changes of the lower edge of the ionosphere. This subject has been discussed in a number of recent papers [Pierce, 1957; Crombie, Allan, and Newman, 1958; Casselman, Heritage, and Tibbals, 1959] for frequencies of the order of 16 kc/s. The diurnal variation of the phase could be interpreted as a change of the effective reflecting height of the ionosphere. Using a simplified wave-guide approach, this diurnal height change

was deduced to be of the order of 16 km [Wait, 1959]. This result was based on a model that replaced the earth and ionosphere by perfectly reflecting surfaces. The phase shift at the lower boundary (i.e., the earth) was assumed to be zero and that at the upper boundary was 180° . For low-order waveguide modes this is an adequate first approximation [Wait, 1958]. Unfortunately, however, the equations employed in interpreting these experimental results are not sufficiently accurate for *absolute* determinations of phase velocity. Although this does not modify the deduced diurnal change of height, it is desirable to seek a more accurate relation between v , the phase velocity, and h , the ionospheric reflecting height.

An earlier paper by Wait and Spies [1960] presented the more accurate formulas. On the basis of equation 2 of that paper (with $q = 0$, $q_1 = \infty$) values of phase velocity were computed for the dominant mode (i.e., $n = 1$). To this end the quantity $v/c - 1$ is shown plotted in Figure 1 where c is the velocity of light in vacuo. The abscissa is frequency f in kilocycles and the curves are parametric in h , the height of the reflecting layer.

It is interesting to observe, from the computed curves, that the phase velocity may actually be equal to c in some instances. The physical explanation for such behavior is that the influence of earth curvature tends to decrease the phase velocity whereas the waveguide characteristic of the mode tends to increase the phase velocity. As can be seen, these two effects may balance one another for certain combinations of h and f .

The influence of the finite conductivity of the earth and the ionosphere and of the earth's magnetic field is to shift these curves by a small amount (equivalent to change of several kilometers in h).

More extensive computations of this kind for higher modes and for a range of ionospheric conditions will be reported at a later date.

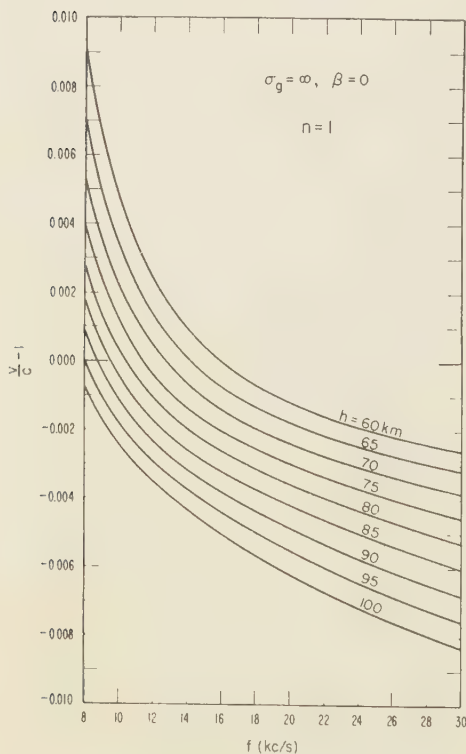


Fig. 1. Phase velocity deviation as a function of frequency for various ionospheric heights.

REFERENCES

- Casselman, C. J., D. P. Heritage, and M. L. Tibbals, VLF propagation measurements for the Radux-Omega navigation system, *Proc. IRE*, 47, 829-839, 1959.
- Crombie, D. D., A. H. Allan, and M. Newman, Phase variations of 16 kc/s transmissions from Rugby as received in New Zealand, *Proc. Inst. Elect. Engrs.*, B21, 301-304, 1958.
- Pierce, J. A., Intercontinental frequency comparison by very-low-frequency radio transmission, *Proc. IRE*, 45, 794-803, 1957.
- Wait, J. R., The propagation of VLF pulses to great distances, *J. Research NBS*, 61, 187-203, 1958.
- Wait, J. R., Diurnal change of ionospheric heights deduced from phase velocity measurements at VLF, *Proc. IRE*, 47, 998, 1959.
- Wait, J. R., and Kenneth Spies, Influence of earth curvature and the terrestrial magnetic field on VLF propagation, *J. Geophys. Research*, 65, 2325-2331, 1960.

(Received December 12, 1960.)

Discussion of Paper by J. N. Nanda, 'The Origin of Microseisms'

M. S. LONGUET-HIGGINS

*National Institute of Oceanography
Wormley, Godalming, Surrey, England*

May I call attention to some misstatements that have appeared in a recent paper in the June number of this Journal [Nanda, 1960]. Present comments are confined solely to cases where Dr. Nanda refers to a previous paper [Longuet-Higgins, 1950].

1. In the Introduction Dr. Nanda states: 'The Longuet-Higgins theory does not show a direct influence of depth of the sea at the origin.' In fact, it is shown in §5.1 and 5.2 of my paper that the response depends quite markedly on the local depth; the response curves for the different modes of oscillation are given in Figure 2 of that paper.

2. A little later Dr. Nanda states: 'The Longuet-Higgins theory would require the existence of standing waves.' Such is not the case, for the requisite pressure fluctuations are produced by opposite wave trains whose amplitudes need not be equal; the pressure fluctuations are simply proportional to the product of the amplitudes of opposite components in the spectrum.

3. On p. 1819 he states: 'Usually standing waves can arise only from sources which have

definite phase relationships.' However, the main purpose of §3 and 5 of my paper is to allow for the random phase relationships between different components in the two-dimensional spectrum; and it is shown that the requisite pressure fluctuations do occur even in an incoherent sea.

4. On the last page Dr. Nanda states: 'A similar calculation on the Longuet-Higgins theory, when wave heights are assumed to be 3 meters, is 16 mm.' I do not know how this figure is arrived at, unless Dr. Nanda has assumed that the second-order pressure fluctuations are in-phase over the whole generating area, an assumption which is quite unsupportable, and which is certainly not made in my paper.

REFERENCES

- Nanda, J. N., The origin of microseisms, *J. Geophys. Research*, **65**, 1815-1820, 1960.
Longuet-Higgins, M. S., A theory of the origin of microseisms, *Phil. Trans. Roy. Soc. London A*, **243**, 1-35, 1950.

(Received November 18, 1960.)

Corrigendum

The author, Dr. J. H. Rosenbaum, has called attention to several errors in his paper, 'The Long-Time Response of a Layered Elastic Medium to Explosive Sound,' in the May 1960 issue of this Journal. His corrections follow.

Page 1579, first column, following equation 3:

$$R^2 = r^2 + (d - z)^2.$$

Page 1586, second column, line 33:

$$|e^{\sigma(K)}|.$$

Page 1587, first column, equation 38, second line:

$$e^{-i\gamma/2}.$$

Page 1590, second column, following equation 45:

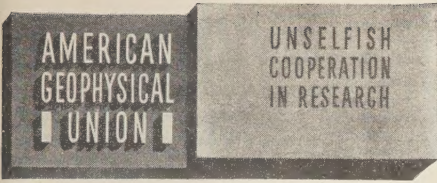
define $\psi^c = \text{phase}(Q_n^c) + \pi$ (omit the rest of the definition); also define $-\pi < \text{phase}(-i\tilde{\omega}_n'') < \pi$.

Page 1592, second column, last paragraph, and page 1593, first column, top of page:

points where $\alpha_{2n} = 0$ are *not* branch points of the period equation $\tilde{\omega}_n$ as a function of K ; however, points where $\tilde{\omega}_n = 0$, and $d\tilde{\omega}_n/dK$ becomes infinite, are also branch points.

Page 1593, column 2, line 7:

real values of K .



AMERICAN GEOPHYSICAL UNION

1515 Massachusetts Avenue, N.W., Washington 5, D. C.
Established by the National Research Council in 1919 for the development of the science of geophysics through scientific publication and the advancement of professional ideals.

QUALIFICATIONS FOR MEMBERSHIP

The Membership of the AGU shall consist of Members, Associate Members, Student Members, Corporation Members, and Supporting Members.

Those eligible as candidates for election to the grade of MEMBER shall be:

MEMBER (a) Persons who have made an active contribution to geophysical research through observation, publication, teaching, or administration. Definite evidence should be presented to the Membership Committee. "Publication" may include books, articles, unpublished manuscripts, inventions, or development of geophysical instruments.

(b) Persons who have made active practical application of geophysical research. It should be shown that the nominee's work has not been purely routine, but that it has tended to create new knowledge of, or to broaden or strengthen the application of, geophysical research. In general, the minimum qualifications for membership will be not less than three years of professional experience in some phase of geophysics.

(Continued on next page)

Cut along this line

APPLICATION FOR MEMBERSHIP

Please refer to qualifications on reverse side and designate below type of membership desired:

Member (\$10) ☐ Associate (\$10) ☐ Student (\$4.50) ☐
(1961)

Application forms for Corporation and Supporting Membership are available upon request.

1. _____
Surname First Name Middle Name

2. _____
Preferred mailing address for publications

Permanent address

3. _____ 4. _____
Place Month Day Year of Birth Country of citizenship/naturalization

5. _____
Nature of work and title and/or military rank; name and address of organization with which you are associated.

6. Check section or sections with which affiliation is desired.

- | | |
|--|---|
| <input type="checkbox"/> Geodesy | <input type="checkbox"/> Oceanography |
| <input type="checkbox"/> Seismology | <input type="checkbox"/> Volcanology, Geochemistry, and Petrology |
| <input type="checkbox"/> Meteorology | <input type="checkbox"/> Hydrology |
| <input type="checkbox"/> Geomagnetism and Aeronomy | <input type="checkbox"/> Tectonophysics |

7. **EXPERIENCE (List below, use added sheets as necessary)**

Dates: From To Name and address of organization Title, duties, nature of work

8. **EDUCATION (List Below, use added sheets as necessary)**

Dates: From To School Address Major Subject Degree, if any; year

(over)

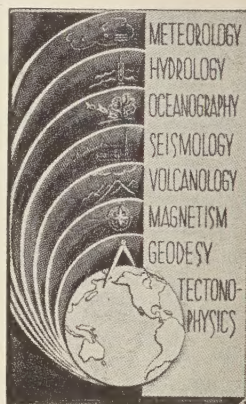
(Continued from previous page)

Those eligible as candidates for election to the grade of ASSOCIATE MEMBER shall be:

ASSOCIATE MEMBER Persons who have an active interest in physical processes of the Earth or technical assistance in the application of geophysics. In general, the minimum qualification for associate membership will be acceptable training or experience in some field of geophysics or allied science.

CORPORATION AND SUPPORTING MEMBER Corporations and other interested organizations shall be eligible as candidates for election to CORPORATION or SUPPORTING MEMBERSHIP. They shall have the privilege of designating a representative who has the rights and privileges of Members (use special form).

STUDENT MEMBER Those eligible as candidates for election to the grade of STUDENT MEMBER shall be persons who are graduate or undergraduate students in residence at least half-time and who are specializing in the geophysical sciences. Teaching or research assistants enrolled in more than half of a full-time academic program may also be eligible for Student Membership. Student Members shall have all the privileges of Members except that they shall not vote or hold office.



Cut along this line

*9. References: Please list below names and addresses of two or three references; include members of the AGU or others who know you well.

*10. Titles of technical contributions or publications, particularly those in the geophysical sciences, and where published.

*11. Brief statement of any special interests or qualifications in the geophysical sciences.

Date _____
Written Signature _____

12. (STUDENT MEMBERS ONLY) The person whose signature appears above is known to me and is a student majoring in _____ (subject) at _____

(Name of college or university) expected to graduate in _____ (year) with the degree of _____

☐ He is a full-time student, or ☐ a teaching or research assistant enrolled in more than half of a full-time academic program.

(Signature of faculty sponsor) ☐ Check here if faculty sponsor is a member of AGU and willing to act as a regular sponsor for associate membership as well.

(Typed or printed name of sponsor) (Title) _____

* Applicants for student membership may omit Questions 9, 10, and 11, but must fill in Question 12. Please return form with check or money order payable to American Geophysical Union, 1515 Massachusetts Ave., N.W., Washington 5, D. C.

Contents

(Continued from back cover)

PAGE

The Principal Factors Influencing the Seasonal Oscillation of Sea Level <i>Eugenie Lisitzin and June G. Pattullo</i>	845
Estimates of Vertical Motions and Meridional Heat Exchange in Gulf Stream Eddies, and a Comparison with Atmospheric Disturbances. <i>Chester W. Newton</i>	853
Glaciological Regime at Little America Station, Antarctica <i>A. P. Crary</i>	871
Directional Properties and Phase Relations of the Magnetotelluric Fields at Austin, Texas. <i>H. W. Smith, L. D. Provazek, and F. X. Bostick, Jr.</i>	879
The Record in the Meteorites. 6. On the Chronology of the Early Solar System <i>Gordon G. Goles and Edward Anders</i>	889
Determination of Sedimentary Thickness in the Mexican Geosyncline by Rayleigh Wave Dispersion. <i>D. H. Shurbet</i>	899
Summary Report of Strong-Motion Measurements, Underground Nuclear Detonations <i>W. M. Adams, R. G. Preston, P. L. Flanders, D. C. Sachs, and W. R. Perret</i>	903
A Method of Concealing Underground Nuclear Explosions <i>A. L. Latter, R. E. LeLevier, E. A. Martinelli, and W. G. McMillan</i>	943
Particle Motions near Explosions in Halite. <i>Byron F. Murphey</i>	947
Use of Large Cavities to Reduce Seismic Waves from Underground Explosions <i>Roland F. Herbst, Glenn C. Werth, and Donald L. Springer</i>	959
Geomagnetic and Solar Data. <i>J. Virginia Lincoln</i>	979
Letters to the Editor:	
Effect of the Magnetic Field in Ionospheric Backscatter. <i>E. E. Salpeter</i>	982
The 5577 Å Airglow Emission Mechanism . . . <i>C. A. Barth and A. F. Hildebrandt</i>	985
Thermal Radiation Spectrum of the Arctic Sky. <i>W. B. Murcray</i>	987
Reply to Some Comments by Malville concerning the Midnight Auroral Maximum. <i>E. H. Vestine and J. W. Kern</i>	989
A Note on Phase Velocity of VLF Radio Waves <i>James R. Wait and Kenneth P. Spies</i>	992
Discussion of paper by J. N. Nanda, "The Origin of Microseisms" <i>M. S. Longuet-Higgins</i>	994
Corrigendum. <i>J. H. Rosenbaum</i>	994

Contents

	PAGE
Cosmic-Ray Neutron Demography <i>W. N. Hess, E. H. Canfield, and R. E. Lingenfelter</i>	665
Scintillation-Counter Observations of Auroral X Rays during the Geomagnetic Storm of May 12, 1959..... <i>P. D. Bhavsar</i>	679
Effect of Hydromagnetic Waves in a Dipole Field on the Longitudinal Invariant <i>E. N. Parker</i>	693
Equation of a Charged Particle Shell in a Perturbed Dipole Field <i>Ralph H. Pennington</i>	709
Theory of Auroral Morphology..... <i>J. W. Kern and E. H. Vestine</i>	713
The Relationship between Unique Geomagnetic and Auroral Events..... <i>Y. Sobouti</i>	725
Influence of Sunspots on Geomagnetic Disturbance... <i>Fred Ward and Ralph Shapiro</i>	739
Low-Latitude and High-Latitude Geomagnetic Agitation..... <i>E. R. Hope</i>	747
Some Properties of Radio Waves Reflected from the Moon and Their Relation to the Lunar Surface..... <i>Tor Hagfors</i>	777
Daytime and Nighttime Atmospheric Properties Derived from Rocket and Satellite Observations..... <i>H. K. Kallmann-Bijl</i>	787
A Subtropical Convergence Line of the South Pacific: A Case Study Using Meteorological Satellite Data..... <i>Lester F. Hubert</i>	797
Evidence of a Downward-Propagating, Annual Wind Reversal in the Equatorial Stratosphere <i>Richard J. Reed, William J. Campbell, Lowell A. Rasmussen, and Dale G. Rogers</i>	813
Analysis of a Falling-Sphere Experiment for Measurement of Upper-Atmosphere Density and Wind Velocity..... <i>J. Otterman, I. J. Sattinger, and D. F. Smith</i>	819
Technique for Introducing Low-Density Space Charge into the Atmosphere <i>B. Vonnegut, K. Maynard, W. G. Sykes, and C. B. Moore</i>	823
Calculations of Cloud Electrification Based on a General Charge-Separation Mechanism..... <i>J. D. Sartor</i>	831
Effects of Wind-Induced Advection on Sea Surface Temperature..... <i>L. E. Eber</i>	839

(Continued inside back cover)